

Strong-Field Physics in QED and QCD: From Fundamentals to Applications

Koichi Hattori,^{1,2*} Kazunori Itakura,^{3,4†} and Sho Ozaki^{5‡}

¹Zhejiang Institute of Modern Physics, Department of Physics,
Zhejiang University, Hangzhou, Zhejiang 310027, China

²Research Center for Nuclear Physics, Osaka University,
10-1 Mihogaoka, Ibaraki, Osaka 567-0047, Japan

³Nagasaki Institute of Applied Science, Nagasaki 851-0193, Japan

⁴KEK Theory Center, Institute of Particle and Nuclear Studies,
High Energy Accelerator Research Organization,
1-1, Oho, Ibaraki, 305-0801, Japan

⁵ Graduate School of Science and Technology, Hirosaki University,
3 Bunkyo, Hirosaki, Aomori, 036-8561, Japan

July 18, 2023

Abstract

We provide a pedagogical review article on fundamentals and applications of the quantum dynamics in strong electromagnetic fields in QED and QCD. The fundamentals include the basic picture of the Landau quantization and the resummation techniques applied to the class of higher-order diagrams that are enhanced by large magnitudes of the external fields. We then discuss observable effects of the vacuum fluctuations in the presence of the strong fields, which consist of the interdisciplinary research field of nonlinear QED. We also discuss extensions of the Heisenberg-Euler effective theory to finite temperature/density and to non-Abelian theories with some applications. Next, we proceed to the paradigm of the dimensional reduction emerging in the low-energy dynamics in the strong magnetic fields. The mechanisms of superconductivity, the magnetic catalysis of the chiral symmetry breaking, and the Kondo effect are addressed from a unified point of view in terms of the renormalization-group method. We provide an up-to-date summary of the lattice QCD simulations in magnetic fields for the chiral symmetry breaking and the related topics as of the end of 2022. Finally, we discuss novel transport phenomena induced by chiral anomaly and the axial-charge dynamics. Those discussions are supported by a number of appendices.

*koichi.hattori@outlook.com

†kazunori.itakura@kek.jp

‡sho.ozaki@hirosaki-u.ac.jp

Contents

1	Introduction	4
2	Landau quantization in a constant magnetic field	8
2.1	Gauge-invariant consequences	10
2.1.1	Landau quantization	10
2.1.2	Kinetic momentum	11
2.1.3	Pseudomomentum, guiding center, and the magnetic translation	12
2.1.4	Angular momenta	15
2.1.5	Zeeman effect and resultant energy spectrum	18
2.2	Wave functions for the Landau levels	19
2.2.1	Landau gauge	19
2.2.2	Symmetric gauge	21
2.3	Relativistic fermions in a magnetic field	23
2.3.1	Dirac equation in magnetic fields	23
2.3.2	Mode expansion with the Ritus basis	25
2.3.3	Massless fermions, spectral flow, and chiral anomaly	27
3	Resummation by the proper-time method	30
3.1	Generalities of the proper-time method	30
3.2	Spin- $\frac{1}{2}$ particles	32
3.2.1	The Fock-Schwinger gauge and the Schwinger phase	32
3.2.2	Proper-time representation	35
3.2.3	Spectrum and spin polarizations	36
3.3	Charged scalar particles	38
3.4	Simplest extension to QCD: Covariantly constant fields	39
3.4.1	Resummed quark propagator	41
3.4.2	Resummed ghost propagator	42
3.4.3	Resummed gluon propagator	42
4	Heisenberg-Euler effective action	44
4.1	Resummed effective action	45
4.1.1	Constant electromagnetic fields	46
4.1.2	Beyond the Heisenberg-Euler effective action	48
4.2	Schwinger mechanism in constant fields	50
4.2.1	Pair production from purely electric fields	50
4.2.2	Schwinger mechanism as quantum tunneling	53
4.2.3	Effects of magnetic fields on the pair production	56
4.2.4	Landau-level decomposition	57
4.3	Schwinger mechanism beyond constant fields	59
4.3.1	Pair production from time-dependent electric fields	59
4.3.2	Pair production from spatially inhomogeneous electric fields	62
5	Vacuum fluctuations and nonlinear effects	64
5.1	Vacuum polarization tensor in strong fields	65
5.2	Photon's vacuum birefringence and decay into an e^+e^- pair	67
5.2.1	Low-energy photons (I): Weak fields	70
5.2.2	Low-energy photons (II): Wrenchless fields	71
5.2.3	High-energy photons: Beyond Heisenberg-Euler effective theory	74

5.3	Photon splitting	81
6	Heisenberg-Euler effective action revisited: Extensions to finite temperature/density and QCD	83
6.1	Extension to finite temperature/density	84
6.2	Spontaneous chiral symmetry breaking: A preview of the magnetic catalysis	88
6.2.1	Gap equation at zero temperature	89
6.2.2	Chiral phase transition temperature	90
6.3	Extension to non-Abelian theories	91
6.3.1	Ghost- and gluon-loop contributions	94
6.3.2	Quark-loop contribution	98
6.4	Schwinger mechanism in chromo-fields	99
6.4.1	Gluon production in chromo-electromagnetic fields	99
6.4.2	Quark pair production in QCD+QED fields	102
6.5	Effective potential in QCD+QED fields: Magnetic-gluon condensation	103
6.5.1	Singularities in proper-time integrals	103
6.5.2	Computation of effective Lagrangians	105
6.5.3	Vacuum paramagnetism and the asymptotic freedom	107
6.5.4	Dislocated minimum of the effective potential	110
6.6	Polyakov-loop potential in QCD+QED fields at finite temperature	113
6.6.1	GPY-Weiss potential at finite temperature	114
6.6.2	GPY-Weiss potential in a magnetic field	116
7	Low-energy dynamics in strong magnetic fields	117
7.1	Analogy with the dense system, effective dimensional reduction, and infrared scaling dimensions	118
7.2	Magnetic catalysis of the chiral symmetry breaking	122
7.2.1	Renormalization-group analysis	124
7.2.2	Magnetic catalysis in weak-coupling gauge theories	126
7.3	The QCD Kondo effect	133
7.3.1	The QCD Kondo effect in dense quark matter	134
7.3.2	The magnetically induced QCD Kondo effect	137
7.4	Magnetic catalysis in QCD	139
7.4.1	Results from lattice QCD simulations	140
7.4.2	Quark excitations in strong magnetic fields	157
7.4.3	Debye screening effect and the deconfinement phase transition	163
7.4.4	Mesonic excitations toward the phase transitions	165
8	Quantum anomaly in transport phenomena	166
8.1	Chiral magnetic/separation effect	166
8.2	Manifestation of the chiral anomaly	169
8.3	Axial-charge dynamics: Helicity conversion and the chiral plasma instability	172
9	Summary	178
A	Wave functions in magnetic fields	179
A.1	Landau gauge	179
A.2	Symmetric gauge	180

B	Solutions for the resummed propagators	181
B.1	Schwinger phases on polygons	181
B.2	Fermion propagator	183
B.3	Equivalence with the Ritus basis method	185
B.4	Gluon propagator	187
C	Perturbative propagators in weak external fields	188
C.1	Scalar QED	188
C.2	Spinor QED	189
D	QCD Lagrangian in external chromo-electromagnetic fields	190
D.1	Decomposition into external and fluctuation fields	190
D.2	Covariantly constant external fields	191
D.2.1	Fundamental representation	191
D.2.2	Adjoint representation	192
E	QCD effective action in a chromo-magnetic field	194
E.1	Vacuum energy in the Landau levels	194
E.2	Yang-Mills part	194
E.3	Quark part	196
E.4	Scalar QED	196
F	Gluon/photon self-energy in magnetic fields	197
F.1	General form of gluon/photon propagator	197
F.2	Anomalous dynamics in the lowest Landau level	199
F.2.1	Vacuum contribution: Massless and massive cases	199
F.2.2	Chiral anomaly: Massless and massive cases	202
F.2.3	Chiral anomaly from dispersion integral	204
F.3	Fermion-mass dependences of the anomaly diagrams	206
F.3.1	Massive triangle diagrams and the limit of constant magnetic fields	207
F.3.2	The lowest Landau level in effective (1+1) dimensions	211
F.4	Thermal contributions at finite temperature and density	212
F.4.1	Thermally induced imaginary parts	213
F.4.2	Photon masses from the polarization effects	215
F.4.3	Axial Ward identity at finite temperature and density	218
F.5	Gluon/photon self-energy in a weak magnetic field	220
G	Chiral magnetic/separation effect with massive fermions	224

1 Introduction

Since the seminal paper by Heisenberg and Euler [1], the strong-field physics, quantum dynamics in external strong electromagnetic fields, has been studied in various research fields which include high-energy physics, condensed matter physics, high-intensity laser physics, and astrophysics. It is still growing as one of the most exciting interdisciplinary research fields in modern physics.

Recent progress in laboratory experiments and astronomical observations has been driving intensive and extensive theoretical studies on the strong-field physics. To name a few, as proposed in classic papers [2–5], highly accelerated nuclei can be used as a source of strong electromagnetic fields. Ultrarelativistic heavy-ion collisions with Relativistic Heavy Ion Collider (RHIC) and the Large Hadron Collider (LHC)

create the ever strongest electromagnetic fields [6–10] (see also Refs. [11, 12] for reviews on the estimates of the strengths). We have basically two types of opportunities. When the accelerated nuclei smash each other, the quark-gluon plasma is created under the strong electromagnetic fields, enabling us to study the interplay between QCD and QED [11–16]. In ultraperipheral collision events where the nuclei pass by each other, electromagnetic processes in vacuum play dominant roles without the matter effects (see recent experimental progress at the LHC [17–20] and RHIC [21]). Also, observations of compact stars, especially magnetars, have been providing us with an opportunity to investigate effects of strong magnetic fields [22, 23] that are stable in time and have an extension over a macroscopic spatial scale. The existence of a strong magnetic field in the early universe has been also suggested by observations and there are hot discussions about its generation mechanism [24–29]. The world record of the laser intensity has been increased, aiming at probing the nonperturbative modifications of the vacuum properties such as the Schwinger pair creation and the vacuum birefringence [30–34].

This review paper is composed of two parts to provide a consistent picture of the strong-field physics in fundamentals and applications. There are great review papers and textbooks that are useful even beyond the scope of each research field such as a basic textbook [35], those in astrophysics [36, 37], and in condensed matter physics [38, 39]. We will try to provide a complementary review that starts with fundamentals but includes more recent developments. Below, we give some more detailed survey of this paper and then remarks on general properties of constant electromagnetic fields and conventions.

Fundamentals

In the first part from Sec. 2 to Sec. 3, we will provide fundamental materials that we think important to understand the basic picture of the dynamics in external fields and to be prepared for applications discussed in the later sections.

In Sec. 2, we first address the most fundamental fact that the spectrum of a charged particle is quantized in magnetic fields as known as the Landau quantization. To provide the simplest demonstration, we start with nonrelativistic quantum mechanics. We put an emphasis on the gauge-invariant formulation and the physical meaning of the quantum numbers specifying the energy eigenstates which include not only the principal quantum numbers but also the other auxiliary quantum numbers. We then discuss a relativistic extension for a Dirac fermion.

Bearing this in mind, we proceed to the resummation technique by means of the proper-time method in Sec. 3. After suggestive papers by Nambu [40], Feynman [41], and Schwinger’s seminal paper [42], this method is widely used in the strong-field physics and allows us to work on the resummation of the higher-order diagrams that are enhanced by large magnitudes of external fields. Namely, they are equally important as the leading-order diagram in the naive perturbation theory.

We first explain the resummation in QED where the charged fermions are interacting with external Abelian electromagnetic fields. Treatment of photons does not require the same resummation, since they do not have self-interactions with the external fields. We apply the same technique to scalar QED. Then, we explain an extension of the resummation technique to QCD. In contrast to QED, the external chromo-electromagnetic fields interact with all the constituents, i.e., quarks, gluons, and ghosts. In general, this resummation is a quite tough task because of the non-Abelian nature of QCD. We therefore confine ourselves to the simplest extension, that is, the so-called covariantly constant fields. In this specific configuration of an external chromo-electromagnetic field, we only need to investigate the diagonal sector of the $SU(N_c)$ color symmetry.

Applications to classic but unsolved problems

We review classic problems which have been addressed since the very early times of Heisenberg and Euler [1]. We will, however, encounter unestablished aspects of the nonlinear QED.

As mentioned above, photons do not directly interact with the external fields. Nevertheless, we first observe that photons can interact with the external fields through the virtual fermion pairs in vacuum, and, importantly, those quantum processes are not suppressed in sufficiently strong external fields as compared to the process in the absence of the external fields. This fact poses a fundamental question about the vacuum properties in the strong fields. This is the subject discussed in Sections 4 and 5.

We are able to construct the effective theory by integrating out the fermion loop. This is called the Heisenberg-Euler effective theory and is understood as the low-energy effective theory of photons in the zero frequency and momentum limits. We derive the effective Lagrangian as an application of the resummation technique established in the preceding sections, and discuss the consequences of the nonlinear interactions with the external fields, such as the Schwinger mechanism.

We next discuss one of the drastic changes of the photon properties in external fields. We will see that photons acquire nontrivial refractive indices in external fields, so that the photon propagation in external fields is far nontrivial and reflects the modifications of the vacuum as if propagating in dielectric substances. When the photon energy is small, one may use the low-energy effective theory in computing refractive indices, which offers another application of the Heisenberg-Euler Lagrangian. However, when the photon carries a hard momentum, we need to explicitly include the photon momentum and encounter computation of the two-point function, that is, the vacuum polarization tensor. We review a recent progress on the general analysis of the photon's refractive index. Also, we briefly discuss the photon splitting in magnetic fields arising from the three-point functions.

Those phenomena are expected to be observed with the developments of laser fields, astrophysical observations, and relativistic heavy-ion collisions.

Developments of further interdisciplinary fields

From Sec. 6, we move on to the topics that are newly proposed and have been intensively studied in the last two decades.

In Sec. 6, we begin with discussing extensions of the Heisenberg-Euler effective theory to non-Abelian theories as well as to finite temperature/density. By using the results from the covariantly constant fields, we are able to obtain the low-energy effective theory of QCD in the coexisting Abelian and non-Abelian fields. In the last decade, there appeared a number of suggestive results from lattice QCD simulations and ultrarelativistic heavy-ion collisions that have been providing driving force for the study of QCD in the presence of the external fields.

In Sec. 7, we focus on the low-energy dynamics in strong magnetic fields. The central topics of this section is the quantum many-body effect induced by the dimensional reduction in the LLL and its analogy to the low-energy dynamics in the vicinity of the large Fermi surface where a similar dimensional reduction occurs. We discuss the chiral symmetry breaking in strong magnetic fields induced by the pairing between fermions and antifermions in parallel to the Cooper pairing in superconductor. Also, we discuss another pairing phenomenon occurring between light fermions and a heavy and dilute impurity embedded in a bulk of conducting light fermions. Such a situation is known occurs in alloys and was recently suggested to occur in quark matter with heavy-quark impurities, serving as platforms of the Kondo effect.

We provide a unified point of view of all these systems in terms of the renormalization-group (RG) method. It is noteworthy that the Kondo effect was one of main motivations for Wilson to develop his concept of the renormalization group and effective field theories [43]. The first basic observation in this section is the fact that the four-Fermi interaction becomes a marginal operator irrespective of the magnitude of the coupling constant thanks to the dimensional reduction. With this suggestive result, we construct the RG equations for weak-coupling theories at zero temperature. This allows us to understand the very basic concept of the dimensional reduction and how it manifests itself in all of the aforementioned phenomena. We then proceed to the low-energy QCD in strong magnetic fields with

a body of summary for recent lattice QCD simulations and discuss interpretations of the interesting results that are induced by the interplay between nonperturbative QCD and strong magnetic fields.

In Sec. 8, we discuss the novel transport phenomena induced by quantum anomaly that opened a new interdisciplinary avenue toward applications to ultrarelativistic heavy-ion collisions, the Weyl/Dirac semimetals in condensed matter physics, and astrophysics/cosmology. We discuss a diagrammatic derivation of the anomalous currents and an exponential amplification of a helical magnetic field as a consequence of chiral anomaly.

Concluding remarks and appendices

Finally, we devote Sec. 9 to our summary and brief remarks on recent developments which are not covered in earlier sections. In appendices, we provide details of the basic formulation which we think are useful as the machinery for the future studies.

Preparations: Generalities of constant electromagnetic fields and conventions

In this review paper, we mostly focus on the dynamics in external constant electromagnetic fields. The field strength tensor and its dual are, respectively, given by

$$F^{\mu\nu} = \partial^\mu A^\nu - \partial^\nu A^\mu, \quad (1a)$$

$$\tilde{F}^{\mu\nu} = \frac{1}{2}\epsilon^{\mu\nu\alpha\beta}F_{\alpha\beta}. \quad (1b)$$

We use the mostly minus convention for the Minkowski metric $g^{\mu\nu} = \text{diag}(1, -1, -1, -1)$ and the completely antisymmetric tensor with $\epsilon^{0123} = +1$. An electric and magnetic field can be expressed as $E^i = -\nabla^i A^0 - \dot{A}^i = F^{i0}$ and $B^i = \sum_{j,k} \epsilon^{ijk} \nabla^j A^k = -\sum_{j,k} \epsilon^{ijk} F^{jk}/2$ with $\nabla^i = -\partial^i$ and the antisymmetric tensor $\epsilon^{123} = +1$, respectively. Their components are explicitly given as

$$F^{\mu\nu} = \begin{pmatrix} 0 & -E_x & -E_y & -E_z \\ E_x & 0 & -B_z & B_y \\ E_y & B_z & 0 & -B_x \\ E_z & -B_y & B_x & 0 \end{pmatrix}, \quad F_{\mu\nu} = \begin{pmatrix} 0 & E_x & E_y & E_z \\ -E_x & 0 & -B_z & B_y \\ -E_y & B_z & 0 & -B_x \\ -E_z & -B_y & B_x & 0 \end{pmatrix}, \quad (2a)$$

$$\tilde{F}^{\mu\nu} = \begin{pmatrix} 0 & -B_x & -B_y & -B_z \\ B_x & 0 & E_z & -E_y \\ B_y & -E_z & 0 & E_x \\ B_z & E_y & -E_x & 0 \end{pmatrix}, \quad \tilde{F}_{\mu\nu} = \begin{pmatrix} 0 & B_x & B_y & B_z \\ -B_x & 0 & E_z & -E_y \\ -B_y & -E_z & 0 & E_x \\ -B_z & E_y & -E_x & 0 \end{pmatrix}, \quad (2b)$$

Since the field strength tensors have antisymmetric Lorentz indices, one can only construct two Lorentz invariants of mass-dimension four:

$$\mathcal{F} \equiv \frac{1}{4}F_{\mu\nu}F^{\mu\nu} = \frac{1}{2}(\mathbf{B}^2 - \mathbf{E}^2), \quad (3a)$$

$$\mathcal{G} \equiv \frac{1}{4}F_{\mu\nu}\tilde{F}^{\mu\nu} = -\mathbf{B} \cdot \mathbf{E}, \quad (3b)$$

where the three-dimensional vectors \mathbf{E} and \mathbf{B} are electric and magnetic fields in an arbitrary Lorentz frame. Regarding $F_\mu{}^\nu$ as a matrix, one finds that the equation $F_\mu{}^\nu\phi^\nu = \lambda\phi^\mu$ has four independent eigenvalues,¹ of which the pairwise forms $\pm a$ and $\pm ib$ are written in terms of the invariants (3a) and (3b) as

$$a = \sqrt{\sqrt{\mathcal{F}^2 + \mathcal{G}^2} - \mathcal{F}}, \quad (4a)$$

¹This is because the matrix $F_\mu{}^\nu$ is not antisymmetric in the sense that $F_\mu{}^\nu \neq -F_\nu{}^\mu$.

$$b = \sqrt{\sqrt{\mathcal{F}^2 + \mathcal{G}^2} + \mathcal{F}}. \quad (4b)$$

The field configurations are characterized by these Lorentz invariants.

As long as the electromagnetic field has a finite invariant \mathcal{G} , there exists a Lorentz frame such that the invariant is given by $\mathcal{G} = \mp |\mathbf{B}_0| |\mathbf{E}_0|$. This means that the electric and magnetic fields are parallel or antiparallel to each other depending on the sign of \mathcal{G} which is, of course, invariant under the proper Lorentz transform. Therefore, the appropriate choice of the Lorentz frame, in general, simplifies analyses of the strong-field physics. In such a frame, one finds $a = |\mathbf{E}_0|$ and $b = |\mathbf{B}_0|$.²

If the invariant is vanishing $\mathcal{G} = 0$, i.e., the electric and magnetic fields are orthogonal to each other in a Lorentz frame, they are also orthogonal in any other frame. In this case, we have $a = 0$ and $b = \sqrt{|\mathbf{B}|^2 - |\mathbf{E}|^2}$ when the other invariant is positive $\mathcal{F} > 0$, or $a = \sqrt{|\mathbf{E}|^2 - |\mathbf{B}|^2}$ and $b = 0$ when negative $\mathcal{F} < 0$. Therefore, there exists a Lorentz frame in which either an electric or magnetic field vanishes. We shall denote the electric and magnetic fields in such a frame as $|\mathbf{E}_0|$ and $|\mathbf{B}_0|$, respectively. In the former case ($|\mathbf{B}| > |\mathbf{E}|$), one can take a vanishing electric field ($|\mathbf{E}_0| = 0$) in the above expression, leaving only a magnetic field with a magnitude $|\mathbf{B}_0| = b$. Similarly, in the latter case ($|\mathbf{E}| > |\mathbf{B}|$), one finds that $|\mathbf{B}_0| = 0$ and $|\mathbf{E}_0| = a$.

A pair of vanishing invariants $\mathcal{F} = \mathcal{G} = 0$ corresponds to not only the absence of the field but also the so-called ‘‘crossed field’’ such that $|\mathbf{E}| = |\mathbf{B}|$ and $\mathbf{E} \cdot \mathbf{B} = 0$. This feature is invariant under the Lorentz transform.

In the second rank of mass-dimension four, one can again construct two tensors by the use of the field strength tensors. In the parallel configuration with E and B being the magnitudes of the fields, their explicit forms read

$$F^{\mu\lambda} F^\nu{}_\lambda = -E^2 g_{\parallel}^{\mu\nu} + B^2 g_{\perp}^{\mu\nu}, \quad (5a)$$

$$F^{\mu\lambda} \tilde{F}^\nu{}_\lambda = -EB g^{\mu\nu}. \quad (5b)$$

Therefore, we are naturally led to introduce two additional metrics for the longitudinal and transverse subspaces with respect to the fields. They are, respectively, defined as

$$g_{\parallel}^{\mu\nu} = \text{diag}(1, 0, 0, -1) \quad \text{and} \quad g_{\perp}^{\mu\nu} = \text{diag}(0, -1, -1, 0). \quad (6)$$

Without loss of generality, we have taken the directions of the fields in the positive z direction when $E, B > 0$.³ Accordingly, the momenta in these subspaces are introduced as $p_{\parallel}^\mu = g_{\parallel}^{\mu\nu} p_\nu$ and $p_{\perp}^\mu = g_{\perp}^{\mu\nu} p_\nu$. Also, for the gamma matrices obeying the Clifford algebra $\{\gamma^\mu, \gamma^\nu\} = 2g^{\mu\nu}$, we introduce $\gamma_{\parallel}^\mu = g_{\parallel}^{\mu\nu} \gamma_\nu$ and $\gamma_{\perp}^\mu = g_{\perp}^{\mu\nu} \gamma_\nu$. We will often use these notations throughout this review paper together with $\gamma^5 = i\gamma^0\gamma^1\gamma^2\gamma^3$.

2 Landau quantization in a constant magnetic field

In this section, we provide a pedagogical discussion about the energy spectrum of charged particles in magnetic fields. We first analyze a nonrelativistic Hamiltonian to demonstrate the essence of the Landau quantization [44, 45] (see also Sec. 2.5 in Ref. [46] for an anecdotal review) and then proceed to QED in Sec. 2.3.

The quantum mechanical Hamiltonian is given as

$$\hat{\mathcal{H}} = \hat{\mathcal{H}}_{\perp} + \frac{\hat{p}_z^2}{2m} - \hat{\mu}_B B. \quad (7)$$

²Occasionally, the definitions of a and b are interchanged in the literature. However, the definitions in Eqs. (4a) and (4b) may be more convenient in the sense that the b reduces to the B field by the Lorentz transform.

³It is also useful to note frame-independent identities $F^{\mu\lambda} F^\nu{}_\lambda - \tilde{F}^{\mu\lambda} \tilde{F}^\nu{}_\lambda = 2\mathcal{F} g^{\mu\nu}$ and $F^{\mu\lambda} \tilde{F}^\nu{}_\lambda = \mathcal{G} g^{\mu\nu}$.

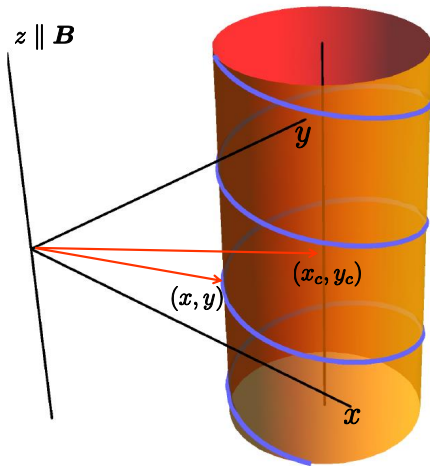


Figure 1: Cyclotron motion in a magnetic field ($\mathbf{B} \parallel \hat{z}$) with a finite longitudinal momentum p_z . The transverse coordinates of the classical trajectory (blue curve) and of the center of the cyclotron orbit is given by (x, y) and (x_c, y_c) , respectively.

Without loss of generality, we apply a constant magnetic field $\mathbf{B} = (0, 0, B)$ in the z direction, so that the longitudinal momentum \hat{p}_z is a constant of motion and can be replaced by a c-number. The last term is responsible for the Zeeman effect for the nonrelativistic magnetic moment $\hat{\mu}_B \equiv q_f g \frac{\hbar}{2m} \hat{s}_z$, which is given by the g -factor, an electrical charge q_f , and the spin operator \hat{s}_z along the magnetic field. The transverse part of the Hamiltonian is given as

$$\hat{\mathcal{H}}_{\perp} = \frac{1}{2m} \{ \hat{\mathbf{p}}_{\perp} - q_f \mathbf{A}_{\perp}(\hat{\mathbf{x}}_{\perp}) \}^2 = \frac{1}{2m} (\hat{\pi}_x^2 + \hat{\pi}_y^2), \quad (8)$$

where the gauge field $\mathbf{A}_{\perp}(\hat{\mathbf{x}}_{\perp})$ generates the constant external magnetic field. The subscript \perp denotes the components transverse to the external magnetic field, that is, the x and y components.

The commutation relation is imposed on the *canonical momentum* $\hat{\mathbf{p}}$ as

$$[\hat{x}^i, \hat{p}^j] = i\hbar \delta^{ij}. \quad (9)$$

It is very important to note that, in the presence of the gauge field, the canonical momentum $\hat{\mathbf{p}}$ is different from the *kinetic momentum* defined by

$$\hat{\boldsymbol{\pi}} \equiv \hat{\mathbf{p}} - q_f \mathbf{A}(\hat{\mathbf{x}}). \quad (10)$$

This momentum corresponds to the covariant derivative. Its kinetic nature, relation to the mass and velocity, is suggested by the Heisenberg equation for the coordinate, i.e., $\dot{\hat{\mathbf{x}}} = (i\hbar)^{-1} [\hat{\mathbf{x}}, \hat{\mathcal{H}}] = \hat{\boldsymbol{\pi}}/m$. Also, the Heisenberg equation for the kinetic momentum reads $\dot{\hat{\boldsymbol{\pi}}} = (i\hbar)^{-1} [\hat{\boldsymbol{\pi}}, \hat{\mathcal{H}}] = q_f \hat{\boldsymbol{\pi}} \times \mathbf{B}/m$, indicating that the kinetic momentum evolves in time independently of the gauge choice for \mathbf{A}_{\perp} and that the transverse components $\hat{\boldsymbol{\pi}}_{\perp}$ are not conserved quantities in a magnetic field. The transverse components of the canonical momentum $\hat{\mathbf{p}}_{\perp}$ are, in general, not conserved quantities either, i.e., $[\hat{\mathbf{p}}_{\perp}, \hat{\mathcal{H}}] \neq 0$, because of the coordinate dependence of the gauge field $\mathbf{A}_{\perp}(\mathbf{x})$ under the canonical commutation relation (9): Whether or not the canonical momentum is conserved depends on the gauge choice.

The presence of a conserved and gauge-invariant momentum is suggested by the above Heisenberg equations of motion that describe the effects of the Lorentz force. Integrating the both sides of the equation for $\dot{\hat{\boldsymbol{\pi}}}$, we define the *pseudomomentum* as

$$\hat{\mathbf{k}} \equiv \hat{\boldsymbol{\pi}} - q_f \hat{\mathbf{x}} \times \mathbf{B}. \quad (11)$$

	Kinetic momentum	Canonical momentum	Pseudo-momentum	Kinetic AM	Canonical AM	Pseudo-AM
	$\hat{\boldsymbol{\pi}}$	$\hat{\boldsymbol{p}}$	$\hat{\boldsymbol{k}}$	$(\hat{\boldsymbol{x}} - \hat{\boldsymbol{x}}_c) \times \hat{\boldsymbol{\pi}}$	$\hat{\boldsymbol{x}} \times \hat{\boldsymbol{p}}$	$\hat{\boldsymbol{x}}_c \times \hat{\boldsymbol{k}}$
Gauge invariance	✓	✗	✓	✓	✗	✓
Conservation	✗	Up to gauges	✓	✓	Up to gauges	✓

Figure 2: Properties of the three linear momenta and the associated angular momenta (AM).

The pseudomomentum commutes with the Hamiltonian, i.e., $[\hat{\boldsymbol{k}}, \hat{\mathcal{H}}] = 0$, independently of the gauge choice. Figure 1 shows a classical trajectory of the cyclotron motion in a constant magnetic field. The classical solution for the center coordinate of a cyclotron orbit is found to be

$$(\hat{x}_c, \hat{y}_c) = \left(\hat{x} + \frac{\hat{\pi}_y}{q_f B}, \hat{y} - \frac{\hat{\pi}_x}{q_f B} \right). \quad (12)$$

We lifted $\hat{\boldsymbol{x}}_\perp$ and $\hat{\boldsymbol{\pi}}_\perp$ to quantum operators on the right-hand side, which defines the center coordinate (\hat{x}_c, \hat{y}_c) as a quantum operator. This coordinate, which is sometimes called the *guiding center*, is also a constant of motion both in classical and quantum theories, i.e., $[\hat{x}_c, \hat{\mathcal{H}}] = 0 = [\hat{y}_c, \hat{\mathcal{H}}]$. In fact, those two conserved quantities are not independent of one another and are related as

$$(\hat{k}_x, \hat{k}_y) = q_f B (-\hat{y}_c, \hat{x}_c). \quad (13)$$

Figure 2 summarizes the properties of the three distinct momenta as well as the associated angular momenta that we will discuss in detail. Based on the above observations, we will carefully examine quantum picture of the cyclotron motion.

2.1 Gauge-invariant consequences

We first discuss the gauge-invariant consequences that can be extracted from the Hamiltonian (8) and gauge-invariant algebra. We will not choose a particular gauge for $\mathbf{A}_\perp(\hat{\boldsymbol{x}}_\perp)$ until Sec. 2.2 where we look for explicit forms of the wave functions. As mentioned above, neither kinetic nor canonical momentum is a conserved quantity in general. The canonical momentum, even if it is conserved, does not provide a gauge-invariant formulation of the Landau quantization. We formulate the Landau quantization in a gauge-invariant way by the use of eigenstates of the center coordinates (\hat{x}_c, \hat{y}_c) , and thus of the pseudomomentum (\hat{k}_x, \hat{k}_y) , that are the simultaneous eigenstates of the Hamiltonian $\hat{\mathcal{H}}_\perp$. We will, however, find that \hat{x}_c and \hat{y}_c do not commute with each other in quantum theory, i.e., $[\hat{x}_c, \hat{y}_c] \neq 0$. Until Sec. 2.1.5, we focus on the transverse part of the Hamiltonian \mathcal{H}_\perp .

2.1.1 Landau quantization

According to the canonical commutation relation (9), one can immediately show that the kinetic momentum satisfies a commutation relation

$$[\hat{\pi}_x, \hat{\pi}_y] = i\hbar q_f \left(\frac{\partial A_y}{\partial x} - \frac{\partial A_x}{\partial y} \right) = i\hbar q_f B. \quad (14)$$

This is a gauge-invariant relation and can be regarded as a canonical commutation relation after an appropriate normalization is applied. Motivated by this observation, one can define a set of “creation

and annihilation operators”

$$\hat{a} = \frac{\ell_f}{\hbar\sqrt{2}}(\hat{\pi}_x + is_f\hat{\pi}_y) \quad \hat{a}^\dagger = \frac{\ell_f}{\hbar\sqrt{2}}(\hat{\pi}_x - is_f\hat{\pi}_y), \quad (15)$$

which satisfies the commutation relation $[\hat{a}, \hat{a}^\dagger] = 1$. Here, we defined a sign function $s_f = \text{sgn}(q_f B)$ and $\ell_f = \sqrt{\hbar/|q_f B|}$ called the magnetic length. One can diagonalize the Hamiltonian (8) in the same manner as that for the harmonic oscillator. That is, we get

$$\hat{\mathcal{H}}_\perp = \hbar\omega_f \left(\hat{a}^\dagger \hat{a} + \frac{1}{2} \right). \quad (16)$$

The cyclotron frequency $\omega_f = |q_f B|/m$ naturally appears in the spectrum since a cyclotron motion is a sort of harmonic motion. We have found that the energy spectrum is quantized in constant magnetic fields, and is specified by the eigenvalue n of the “number operator $\hat{a}^\dagger \hat{a}$ ” as

$$\epsilon_n = \hbar\omega_f \left(n + \frac{1}{2} \right). \quad (17)$$

This is called the Landau levels. As usual, the corresponding eigenvectors are constructed as

$$\hat{a}|0\rangle = 0, \quad |n\rangle = \frac{(\hat{a}^\dagger)^n}{\sqrt{n!}}|0\rangle, \quad (18)$$

which are orthonormal among themselves, i.e.,

$$\langle n|n'\rangle = \delta_{nn'}. \quad (19)$$

Below, we investigate the properties and the expectation values of the linear and angular momentum operators with the eigenvectors (18).

2.1.2 Kinetic momentum

The kinetic momentum does not commute with the Hamiltonian, i.e., $[\hat{\pi}_{x,y}, \hat{\mathcal{H}}_\perp] \neq 0$, and does not serve as a good quantum number. This is expected from classical intuition for a cyclotron motion where the direction of the kinetic momentum is changing in time.

The expectation value of the kinetic momentum reads

$$\langle n|\hat{\pi}_{x,y}|n\rangle \propto \langle n|(\hat{a} \pm \hat{a}^\dagger)|n\rangle = 0, \quad (20)$$

where the upper and lower signs are for the x and y components, respectively. The expectation value of the velocity $\hat{\mathbf{v}} = \hat{\boldsymbol{\pi}}/m$ is also vanishing. This is again expected from the classical motion on a cyclotron orbit due to the alternating direction of motion.⁴ The mean square is also easily obtained as

$$\langle n|\hat{\pi}_{x,y}^2|n\rangle = \frac{\hbar^2}{\ell_f^2} \left(n + \frac{1}{2} \right) = \hbar|q_f B| \left(n + \frac{1}{2} \right), \quad (21)$$

where both the components take the same value. Then, we find an uncertainty relation $\langle (\Delta\hat{\pi}_x)^2 \rangle \langle (\Delta\hat{\pi}_y)^2 \rangle \geq |[\hat{\pi}_x, \hat{\pi}_y]|^2/4 = \hbar^2|q_f B|^2$ with $\Delta\hat{\mathcal{O}} := \hat{\mathcal{O}} - \langle \hat{\mathcal{O}} \rangle$ (cf., e.g., Ref. [48]). Therefore, the ground state, called the lowest Landau level (LLL), satisfies the minimal uncertainty as anticipated from the analogy with the harmonic oscillator.

⁴The velocity will have a finite expectation value when there is an electric field applied perpendicularly to the magnetic field because of the drift motion. This leads to the (classical) Hall effect, but not quantum Hall effect without effects of disorder (see, e.g., Ref. [38, 47]).

2.1.3 Pseudomomentum, guiding center, and the magnetic translation

We have obtained the energy spectrum (17) from the manifestly gauge-invariant algebra. One would, however, wonder if there is a mismatch in the number of degrees of freedom. Whereas we had two components of the transverse momenta in the transverse Hamiltonian (8), the energy spectrum is only specified by one quantum number n in Eq. (17). To resolve this mismatch, we examine the eigenstates of the pseudomomentum [36, 37, 49, 50].

As mentioned in Eq. (13), the pseudomomentum is related to the center coordinate of the cyclotron orbit called the guiding center. It should be noticed that there is no preferred position for a center of cyclotron orbit in a constant magnetic field, so that the energy spectrum is expected to be independent of the center coordinate. Namely, there must be energy degeneracy.

One can easily show commutation relations for the center coordinate $[\hat{x}_c^i, \hat{\pi}^j] = 0$ for any combination of the components and other two sets of important commutation relations

$$[\hat{x}_c, \hat{\mathcal{H}}] = 0 = [\hat{y}_c, \hat{\mathcal{H}}], \quad (22)$$

and

$$[\hat{x}_c, \hat{y}_c] = -is_f \ell_f^2. \quad (23)$$

According to Eq. (13), these relations also imply the corresponding relations for the pseudomomentum, $[\hat{k}^i, \hat{\pi}^j] = 0$ and so on. The first relation (22) indicates that the center coordinate is a constant of motion in quantum theory. However, this quantum number does not appear in the energy spectrum (17), explicitly indicating that the Landau levels are degenerated with respect to the center coordinate (or the pseudomomentum). One can therefore use the center coordinate to label the degenerate energy eigenstates. However, the second relation (23) indicates quantum nature that one cannot simultaneously determine both components of the center coordinate, meaning that only one of the components, or any one of functions of \hat{x}_c, \hat{y}_c , serves as a simultaneous eigenstate of the Hamiltonian. One can choose, for example, one of the followings

$$\hat{x}_c, \quad \hat{y}_c, \quad \hat{r}_c^2 \equiv \hat{x}_c^2 + \hat{y}_c^2, \quad (24)$$

and so on. The existence of this one simultaneous quantum number resolves the aforementioned mismatch in the number of degrees of freedom. In Sec. 2.2, we discuss two of an infinite number of possible choices.

The commutation relation (23) leads to an uncertainty relation $\langle(\Delta\hat{x}_c)^2\rangle\langle(\Delta\hat{y}_c)^2\rangle \geq |\langle[\hat{x}_c, \hat{y}_c]\rangle|^2/4 = \ell_f^4/4$. The existence of the uncertainty in the center coordinate can be understood by convincing oneself that an energy eigenstate is not corresponding to one (classical) cyclotron orbit but to superposition of cyclotron orbits of the same radius. To see this, recall the existence of the uncertainty in the kinetic momentum (14). In the energy eigenstate $|n\rangle$, the magnitude of the kinetic momentum is determined via the Hamiltonian (8). However, the direction of the kinetic momentum is uncertain in quantum theory. As a consequence, there are infinitely many cyclotron orbits that pass through a given coordinate position with the same magnitude of the kinetic momentum. See Fig. 3 drawn in the coordinate space where the arrows and circles in the same colors show the uncertainty in the directions of the kinetic momentum and the corresponding cyclotron orbits tangential to the kinetic momentum, respectively. The uncertainty in the center coordinate originates from the superposition of the cyclotron orbits, and thus the magnitude of the uncertainty is of the order of the cyclotron radius. We find that the LLL satisfies the lower bound in the uncertainty relation. The lower bound decreases as we increase the magnetic field strength since the cyclotron radius itself shrinks with an increasing magnetic field strength.

As we increase the magnetic-field strength, more and more orbits are packed in the transverse plane. The density of degenerate states for a given n can be obtained from the phase space volume of the

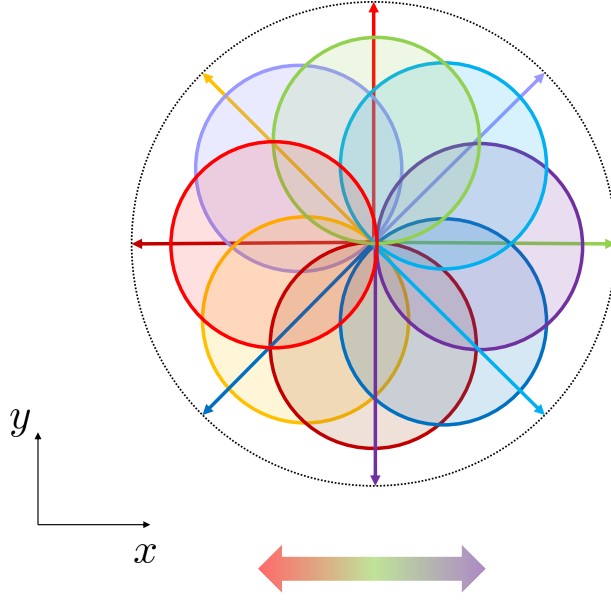


Figure 3: Superposition of cyclotron orbits that all pass through a given coordinate position. The arrows show the uncertainty in the direction of the kinetic momentum at a given energy eigenvalue (shown by dotted circle) and the circles in the same colors show the corresponding cyclotron orbits tangential to the arrows. The two-headed arrow in the bottom shows the magnitude of the standard deviation of the order of the cyclotron radius in the x direction; The same holds in the y direction.

canonical pair in Eq. (23). When the system size is given by $0 \leq x_c, y_c \leq L_{x,y}$, one finds the density of states often called the Landau degeneracy factor

$$\frac{1}{L_x L_y} \left(\frac{L_x L_y |q_f B|}{2\pi\hbar} \right) = \frac{|q_f B|}{2\pi\hbar}, \quad (25)$$

where the factor of $|q_f B|$ comes from the normalization of the canonical pair in Eq. (23). The density of states is common to all the Landau levels.⁵ Note also that there could be further spin degeneracies depending on particle species as discussed in Sec. 2.1.5.

We remark on an interesting property of \hat{r}_c^2 defined in Eq. (24) that is the distance between a cyclotron orbit and the coordinate origin. The eigenvalue of \hat{r}_c^2 is quantized independently of the gauge choice, and the degenerate states are labeled by integers (when we decide to choose this label among other choices). Led by the canonical commutation relation (23) between \hat{x}_c and \hat{y}_c , we can construct a set of “creation and annihilation operators”

$$\hat{b} = \frac{1}{\sqrt{2\ell_f}} (\hat{x}_c - i s_f \hat{y}_c), \quad \hat{b}^\dagger = \frac{1}{\sqrt{2\ell_f}} (\hat{x}_c + i s_f \hat{y}_c), \quad (26)$$

which satisfy the commutation relation $[\hat{b}, \hat{b}^\dagger] = 1$. They commute with \hat{a} and \hat{a}^\dagger . The radial coordinate is expressed by the “number operator” as

$$\hat{r}_c^2 = 2\ell_f^2 \left(\hat{b}^\dagger \hat{b} + \frac{1}{2} \right). \quad (27)$$

⁵This may not be a rigorous statement for finite-volume systems. Charged particles feel boundary effects when their orbits touch the boundary, and, actually, the cyclotron radius depends on the Landau levels [cf. Eq. (35)]. Nevertheless, one may neglect the contribution of such states near the boundary as compared to a large number of states in the bulk as long as $L_x L_y / \ell_f^2 \gg 1$ and we focus on bulk properties. One should note that boundary contributions can be crucial when bulk contributions are suppressed for some reason like in quantum Hall effect.

Therefore, the degenerate states are labeled by an integer m that is the eigenvalue of $\hat{b}^\dagger \hat{b}$.⁶ The above algebraic properties are gauge-invariant ones. We will use those properties in Sec. 2.2.2.

In classical mechanics, the system in a constant magnetic field has a translational invariance in the transverse plane that manifests itself in a shift of cyclotron orbit. In quantum theory, neither the kinetic nor canonical momentum is a gauge-invariant generator of such a translation operator. Nevertheless, we expect the existence of a translational invariance since it is the very origin of the Landau degeneracy discussed above. The reason for the apparent breaking is that the usual translation operator, generating a linear coordinate shift $\hat{\mathbf{x}}_\perp \rightarrow \hat{\mathbf{x}}'_\perp = \hat{\mathbf{x}}_\perp + \Delta \mathbf{x}_\perp$, transforms the vector potential as $\mathbf{A}_\perp(\hat{\mathbf{x}}_\perp) \rightarrow \mathbf{A}_\perp(\hat{\mathbf{x}}'_\perp)$, which breaks the translational invariance of the Hamiltonian. This translation, however, does not contradict with the translation invariance of the system since the magnitude of the magnetic field is invariant, i.e., $\nabla \times \mathbf{A}_\perp(\hat{\mathbf{x}}_\perp) = \mathbf{B} = \nabla \times \mathbf{A}_\perp(\hat{\mathbf{x}}'_\perp)$. That is, the translational invariance is hidden behind the gauge dependence induced by the translation of the vector potential. Below, we find that the pseudomomentum serves as the generator of the translation operator connecting two degenerate states at different center coordinates with an appropriate phase rotation. Likewise, the rotational symmetry with respect to the direction of the magnetic field should imply the existence of an associated conserved angular momentum as we will indeed find below.

We introduce the ‘‘magnetic translation operator’’ generated by the pseudomomentum as [51, 52]⁷

$$T(\mathbf{x}) = \exp\left(-\frac{i}{\hbar} \mathbf{x} \cdot \hat{\mathbf{k}}\right). \quad (28)$$

One can show that the pseudomomentum is canonical conjugate to the cyclotron center, i.e.,

$$[\hat{x}_c^i, \hat{k}^j] = i\hbar \delta^{ij}, \quad (29)$$

as well as to $\hat{\mathbf{x}}$. Therefore, this translation connects the degenerate energy eigenstates labeled by different eigenvalues of $\hat{\mathbf{x}}_c$.⁸ Namely, when a state $|n, \mathbf{x}_c\rangle$ is an energy eigenstate of the Landau level n , so is a new state $|n, \mathbf{x}_c + \mathbf{x}\rangle \equiv T(\mathbf{x})|n, \mathbf{x}_c\rangle$. Note, however, that the two components of $\hat{\mathbf{k}}$ do not commute with each other⁹

$$[\hat{k}_x, \hat{k}_y] = -i\hbar q_f B. \quad (30)$$

Accordingly, the translation operators do not commute either, and interchanging the order of the magnetic translation operators gives rise to a phase factor as

$$T(\mathbf{x}_2)T(\mathbf{x}_1) = T(\mathbf{x}_1)T(\mathbf{x}_2) e^{\frac{1}{\hbar^2}[\mathbf{x}_1 \cdot \hat{\mathbf{k}}, \mathbf{x}_2 \cdot \hat{\mathbf{k}}]} = T(\mathbf{x}_1)T(\mathbf{x}_2) e^{-i\frac{q_f}{\hbar} \Phi_B}. \quad (31)$$

The phase is proportional to $\Phi_B = (\mathbf{x}_1 \times \mathbf{x}_2) \cdot \mathbf{B}$, which is the magnetic flux penetrating the area spanned by \mathbf{x}_1 and \mathbf{x}_2 , and vanishes only when the magnetic flux is an integer multiple of the magnetic flux quantum, i.e., $\Phi_B = (h/q_f)n_B$ with n_B being an integer. This phase is essentially the Aharonov-Bohm phase (though the magnetic field is directly interacting with a charged particle in the present case).

⁶We follow this frequently used notation for m , which should not be confused with a mass parameter.

⁷See also Ref. [53] for an application to quantum Hall effect.

⁸For notational brevity, we use the vector form of $\hat{\mathbf{x}}_c$. However, remember that the two transverse components do not commute with each other and cannot be simultaneous eigenstates of the Hamiltonian at the same time as shown in Eq. (23). Also, we do not include the coordinate z into the label as it is not a good quantum number.

⁹The pseudomomentum can be generalized to a center-of-mass momentum of multi-body systems in constant magnetic fields, and is conserved if the system is charge neutral in total [54, 55]. This generalized pseudomomentum commutes with the Hamiltonian as long as the interaction Hamiltonian has a translational invariance, so that it serve as a good quantum number of bound states in a magnetic field. This conserved momentum was, for example, used in the study of quarkonium spectrum in a magnetic field [56–59] (see Ref. [12, 60] for reviews). However, if a bound state carries a total nonzero charge, the transverse components do not commute with each other. Therefore, one of the components cannot persist as a good quantum number, and, instead, an integer specifies a bound-state spectrum [61].

2.1.4 Angular momenta

We focus on the rotational motion of a cyclotron orbit and associated angular momenta. At abstract level, an angular momentum is introduced as the generator of the spatial rotations. We examine whether or not there is any representation of such generators in the Hilbert space of energy eigenstates in the current situation. For this purpose, it is useful to examine concrete forms of angular momenta that can be introduced as the exterior product of a coordinate and momentum in analogy with classical mechanics. In general, properties of as such introduced angular momenta depend on the reference point in the coordinate system. Besides, one can here define distinct angular momenta by the use of the three linear momenta introduced above which are the kinetic momentum, canonical momentum, and pseudomomentum. Among those various options, there are, however, few conserved angular momenta since a magnetic field breaks the rotational symmetries except for the one with respect to the direction of the magnetic field and the vector potential can completely break the rotational symmetries depending on a gauge choice. Not all the components of an angular momentum are conserved in any definition introduced below. Recall also that the classical picture of cyclotron motion is a rotational motion around the center of a cyclotron orbit (\hat{x}_c, \hat{y}_c) distributed in the transverse plane that is different from the coordinate origin. Such a classical intuition is useful below.

Motivated by the classical picture, we first define the *kinetic angular momentum* around the center coordinate of a cyclotron orbit as

$$\hat{\mathbf{M}} \equiv \hat{\boldsymbol{\xi}} \times \hat{\boldsymbol{\pi}}, \quad (32)$$

with the kinetic momentum $\hat{\boldsymbol{\pi}}$. We take $\hat{\boldsymbol{\xi}} = (\hat{x} - \hat{x}_c, \hat{y} - \hat{y}_c, \hat{z})$ that is canonical conjugate to the kinetic momentum, i.e., $[\hat{\xi}^i, \hat{\pi}^j] = i\hbar\delta^{ij}$. By the use of Eq. (12), one can immediately rewrite the Hamiltonian as

$$\hat{\mathcal{H}}_{\perp} = -\frac{1}{2}\omega_f s_f \hat{M}_z. \quad (33)$$

Clearly, the z component along the magnetic field is a conserved quantity, i.e., $[\hat{M}_z, \hat{\mathcal{H}}] = 0$, which is anticipated from the rotational symmetry around the center of cyclotron orbit. Kinetic nature is made clear if one writes it by the use of Eq. (12) as

$$\hat{M}_z = -s_f I_z \omega_f, \quad \hat{\mathcal{H}}_{\perp} = \frac{1}{2} I_z \omega_f^2, \quad (34)$$

where one can define the ‘‘moment of inertia’’ of a point-like particle as $I_z \equiv m\hat{R}^2$ with the distance from the center coordinate $\hat{R}^2 \equiv (\hat{x} - \hat{x}_c)^2 + (\hat{y} - \hat{y}_c)^2$. The average radius of the cyclotron orbit depends on the Landau level as

$$\langle n | \hat{R}^2 | n \rangle = \ell_f^2 (2n + 1). \quad (35)$$

The average radius is proportional to the magnetic length ℓ_f and shrinks as we increase the magnetic-field strength. The average radius increases with an increasing n for the higher Landau levels (hLLs). The cyclotron motion gives rise to a nonzero expectation value of the kinetic angular momentum

$$\langle n | \hat{M}_z | n \rangle = -s_f \hbar (2n + 1). \quad (36)$$

The magnitude depends on the Landau level, but is independent of the magnetic-field strength. The sign of the expectation value depends on the direction of the cyclotron motion via the sign function s_f . Moreover, due to the overall minus sign in Eq. (36), the magnetic moment of the orbital current is opposite to the applied magnetic field, implying occurrence of the *Landau diamagnetism* [44]. None of

the other components of $\hat{\mathbf{M}}$ nor the kinetic angular momenta around the coordinate origin, $\hat{\mathbf{x}} \times \hat{\boldsymbol{\pi}}$ and $\hat{\mathbf{x}}_c \times \hat{\boldsymbol{\pi}}$, are conserved in a magnetic field due to the absence of associated rotational symmetries.

Recalling that $\hat{\boldsymbol{\xi}}$ and $\hat{\boldsymbol{\pi}}$ are canonical conjugate to each other, one can show the following commutation relations

$$[\hat{M}_y, \hat{M}_z] = 2i\hbar\hat{M}_x, \quad [\hat{M}_z, \hat{M}_x] = 2i\hbar\hat{M}_y. \quad (37)$$

These relations indicate that the kinetic angular momentum satisfies a part of the algebra for the rotation generators when it is normalized as $\hat{\mathbf{M}}/2$. The factor of 2 stems from the fact that $\hat{\pi}_x$ and $\hat{\pi}_y$ do not commute with each other. For the same reason, we find that the algebra is not closed, i.e., $[\hat{M}_x, \hat{M}_y] \neq 2i\hbar\hat{M}_z$. One of the components $\hat{M}_z/2$ generates a rotation of the coordinate $\hat{\boldsymbol{\xi}}$ with respect to the direction of the magnetic field. That is, we can define a rotation operator

$$\hat{D}_z(\theta) = e^{-\frac{i}{\hbar}\theta\hat{M}_z}, \quad (38)$$

by an angle θ around the center coordinate of a cyclotron orbit. Then, the coordinate operator $\hat{\boldsymbol{\xi}}$ is rotated in the transverse plane as

$$\hat{D}_z^{-1}(\theta)\hat{\xi}_x\hat{D}_z(\theta) = \hat{\xi}_x \cos \theta - \hat{\xi}_y \sin \theta. \quad (39)$$

Applying a rotation by an angle $\theta = 2\pi$ to the energy eigenstate, we find a phase factor

$$\hat{D}_z(2\pi)|n\rangle = e^{i\frac{q_f}{\hbar}\hat{\Phi}_B}|n\rangle = e^{is_f(2n+1)\pi}|n\rangle = -|n\rangle, \quad (40)$$

where $\hat{\Phi}_B = B\pi\hat{R}^2$ is the magnetic flux penetrating through a cyclotron orbit $\hat{\Phi}_B|n\rangle = s_f\frac{\hbar}{q_f}(2n+1)\pi|n\rangle$. We obtained a negative sign generated by a 2π rotation similar to that appearing in the spin precession (see, e.g., Sec. 3.2 in a textbook [48]).

One can also define the *canonical angular momentum*

$$\hat{\mathbf{L}} \equiv \hat{\mathbf{x}} \times \hat{\mathbf{p}}. \quad (41)$$

This angular momentum satisfies the algebra $[\hat{L}_i, \hat{L}_j] = i\hbar \sum_k \epsilon_{ijk} \hat{L}_k$ required for the rotation generators and serves as the representation in the three-dimensional coordinate space. This property is solely guaranteed by the canonical commutation relation (9) and is intact in the presence a magnetic field. However, the canonical angular momentum does not serve as a representation in the Hilbert space of the energy eigenstates since it is, in general, not a conserved quantity unless the gauge configuration $\mathbf{A}_\perp(\hat{\mathbf{x}})$ holds a rotational symmetry. Whether or not it is conserved depends on the gauge choice (see Eq. (64) and below for the ‘‘symmetric gauge’’ where it becomes a conserved quantity).

Finally, we define another angular momentum by the pseudomomentum as

$$\hat{\mathbf{K}} \equiv \hat{\mathbf{x}}_c \times \hat{\mathbf{k}}, \quad (42)$$

where we introduced a three dimensional vector $\hat{\mathbf{x}}_c \equiv (\hat{x}_c, \hat{y}_c, \hat{z})$. This is just for the notational convenience¹⁰ and the z components of $\hat{\mathbf{x}}_c$ and $\hat{\boldsymbol{\xi}}$ are the same. Then, $\hat{\mathbf{x}}_c$ and $\hat{\mathbf{k}}$ are canonical conjugate to each other as shown in Eq. (29) and imposed in Eq. (9). Here, we call $\hat{\mathbf{K}}$ the *pseudo angular momentum*. This is a gauge-invariant quantity. Notice that its component along the magnetic field is proportional to the radius defined in Eq. (24) as

$$\hat{K}_z = q_f B \hat{r}_c^2, \quad (43)$$

¹⁰While the transverse components (\hat{x}_c, \hat{y}_c) are originally introduced as conserved quantities, \hat{z} and thus $\hat{\mathbf{x}}_c$ as a three-vector are of course not conserved quantities.

and is a conserved quantity, i.e., $[\hat{K}_z, \hat{\mathcal{H}}] \propto [\hat{r}_c^2, \hat{\mathcal{H}}] = 0$ as discussed there. As clear in Eq. (43), \hat{K}_z does not have kinetic nature since it is independent of particle mass and velocity and only depends on the magnetic-field strength and the center coordinate. Neither the other possible quantities, $\hat{\mathbf{x}} \times \hat{\mathbf{k}}$ nor $(\hat{\mathbf{x}} - \hat{\mathbf{x}}_c) \times \hat{\mathbf{k}}$, is a conserved angular momentum because we have $\hat{\mathbf{x}} \times \hat{\mathbf{k}} = \hat{\mathbf{x}} \times \hat{\boldsymbol{\pi}}$ which is not conserved as mentioned above.

One can immediately show that \hat{K}_z satisfies the following commutation relations

$$[\hat{K}_y, \hat{K}_z] = 2i\hbar\hat{K}_x, \quad [\hat{K}_z, \hat{K}_x] = 2i\hbar\hat{K}_y. \quad (44)$$

Similar to Eq. (37) for the kinetic angular momentum, these commutation relations stem from the canonical commutation relation between $\hat{\mathbf{x}}_c$ and $\hat{\mathbf{k}}$. Due to the non-commutative property (30) between \hat{k}_x and \hat{k}_y , there is an additional factor of 2 on the right-hand side as compared to the algebra for the rotation generators and the other combination does not satisfy the algebra required for the rotation generators, i.e., $[\hat{K}_x, \hat{K}_y] \neq i\hat{K}_z$. The normalized operator $\hat{K}_z/2$ serves as the generator of spatial rotation with respect to the direction of the magnetic field

$$\hat{R}_z(\theta) = e^{-\frac{i}{\hbar}\theta\hat{K}_z}, \quad (45)$$

by an angle θ around the coordinate origin. According to the canonical commutation between $\hat{\mathbf{x}}_c$ and $\hat{\mathbf{k}}$, this operator rotates $\hat{\mathbf{x}}_c$ in the transverse plane as

$$\hat{R}_z^{-1}(\theta)\hat{x}_c\hat{R}_z(\theta) = \hat{x}_c \cos \theta - \hat{y}_c \sin \theta. \quad (46)$$

Since the center of rotation is the coordinate origin, this operator also rotates $\hat{\mathbf{x}}$ as expected from the canonical commutation relation $[\hat{x}^i, \hat{k}^j] = i\hbar\delta^{ij}$. When we label the degenerate states with \hat{r}_c^2 in Eq. (24) and apply a rotation by an angle $\theta = 2\pi$, we again find a phase factor (see Eq. (31) for the phase factor from the magnetic translation along a closed path)

$$\hat{R}_z(2\pi)|n, r_c^2\rangle = e^{-i\frac{qf}{\hbar}\Phi_B}|n, r_c^2\rangle = e^{-is_f(2m+1)\pi}|n, r_c^2\rangle = -|n, r_c^2\rangle, \quad (47)$$

where the magnetic flux penetrating through the area πr_c^2 is quantized as $\Phi_B = (\pi r_c^2)B = \hbar s_f/q_f(2m+1)\pi$ according to Eq. (27). Also, in analogy with the familiar theory of angular momentum, we define the ladder operators

$$\hat{K}_{\pm} = \frac{1}{2}(\hat{K}_x \pm is_f\hat{K}_y), \quad (48)$$

which satisfy the commutation relations $[\hat{K}_z/2, \hat{K}_{\pm}] = \pm s_f\hbar\hat{K}_{\pm}$. According to the relation (43), these are equivalent to $[\hat{r}_c^2, \hat{K}_{\pm}] = \pm 2\ell_f^2\hat{K}_{\pm}$. Therefore, these ladder operators shift the eigenvalue of \hat{r}_c^2 as

$$\hat{r}_c^2\hat{K}_{\pm}|n, r_c^2\rangle = (r_c^2 \pm 2\ell_f^2)\hat{K}_{\pm}|n, r_c^2\rangle. \quad (49)$$

This relation indicates that the ladder operators \hat{K}_{\pm} connect the degenerate states in a given Landau level n and that the eigenvalue of \hat{r}_c^2 is quantized as we have already seen in Eq. (27). Accordingly, the 2π rotation gives rise to a non-vanishing phase in Eq. (47) that flips the sign of the state vector. Here, we stress that the algebraic structures for $\hat{\mathbf{K}}$ have been constructed in a gauge-invariant way. In Sec. 2.2.2, we will use the quantized eigenvalue of \hat{r}_c^2 to label the degenerate states.

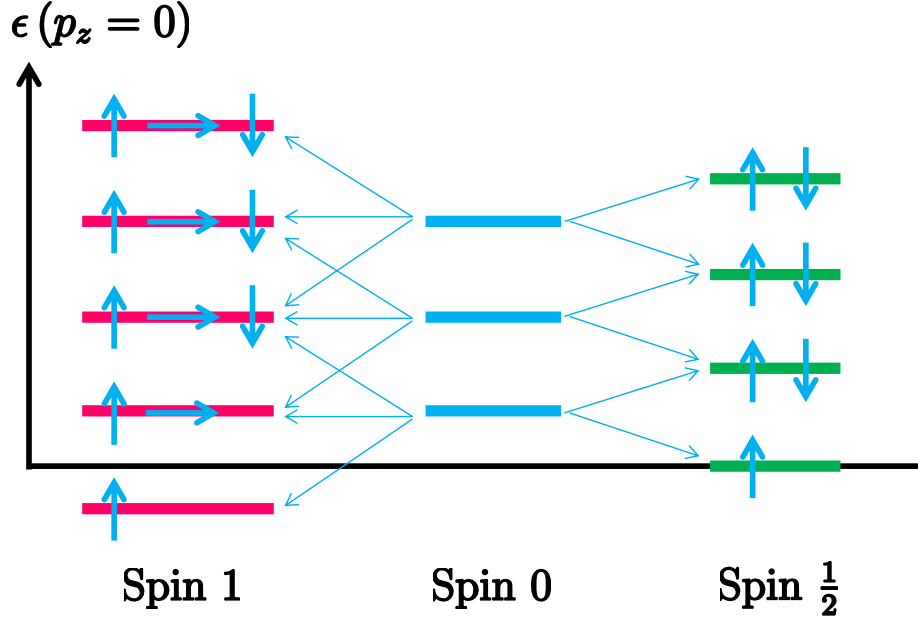


Figure 4: Landau-level discretization and Zeeman splitting with the vanishing longitudinal momentum $p_z = 0$. The ground states of spin- $\frac{1}{2}$ and spin-1 particles have unique spin directions, of which the spectra could become zero modes and tachyonic, respectively.

2.1.5 Zeeman effect and resultant energy spectrum

We now include the Zeeman effect given by the last term in Eq. (7), which resolves the spin degeneracy in each Landau level. Including the Zeeman splitting and longitudinal momentum in Eq. (7), we obtain the energy spectrum for a spin- $\frac{1}{2}$ particle

$$\epsilon_{\text{spin}-\frac{1}{2}} = \frac{p_z^2}{2m_f} + \hbar\omega_f n, \quad (50)$$

with an integer $n \geq 0$. Figure 4 shows the resultant energy levels in Eq. (50). The LLL has a unique spin direction, while there is still a spin degeneracy in each hLL due to the coincidence between the Landau-level spacing and the magnitude of the Zeeman effect for $g = 2$. The Zeeman energy cancels the “zero-point energy” in the Landau quantization when $g = 2$.

As for a spin-1 particle, we have

$$\epsilon_{\text{spin}-1} = \frac{p_z^2}{2m} + \hbar\omega_f \left(n - \frac{1}{2} \right), \quad (51)$$

with an integer $n \geq 0$. Similar to the spin-1/2 particles, higher states are degenerated with respect to the spin directions, while the ground state is a unique spin eigenstate. The lowest energy takes a negative value, $\epsilon_{\text{spin}-1} = -\hbar\omega_f/2$.¹¹

Summarizing this subsection, we have introduced the quantum-mechanical concept of the cyclotron center and the magnetic translation in the gauge-invariant way. One can draw two gauge-invariant

¹¹As we will see in Sec. 3.4.3 with the field-theoretical framework, the relativistic form of the energy spectrum is given by $\epsilon_{\text{spin}-1} = \sqrt{p_z^2 + m^2 + \hbar|q_f B|(2n - 1)}$. When $m^2 \gg p_z^2, |q_f B|$, the mass expansion leads to the real-valued spectrum (51). On the other hand, when $\hbar|q_f B| > (p_z^2 + m^2)$, the low-energy spectrum becomes an imaginary number, $\epsilon_{\text{spin}-1} = i\sqrt{\hbar|q_f B| - (p_z^2 + m^2)}$. A well-known example of such unstable modes is the Nielsen-Olesen instability [62] which occurs due to the self-interactions between the (massless) gauge bosons and external magnetic fields in non-Abelian theories, e.g., electroweak theory and QCD (cf. Sec. 6).

conclusions. (i) The energy level is quantized into the Landau levels. Each Landau level is infinite-fold degenerated with respect to the center coordinate of the cyclotron motion with the density (25). (ii) The degenerate states can be labeled by any function of the conserved \hat{x}_c according Eq. (22). Those degenerate states are connected by the magnetic translation introduced in Eq. (28). However, the commutation relation (23) indicates that only one of such functions can be a simultaneous energy eigenstate. The simplest choice would be the eigenstate of either \hat{x}_c or \hat{y}_c . Alternatively, one can take the eigenstate of the radius \hat{r}_c^2 defined in Eq. (24). We will examine those two cases separately in the next subsection.

2.2 Wave functions for the Landau levels

Here, we look for explicit forms of the wave functions, that is, the coordinate representation of the eigenvectors (18). As discussed in Sec. 2.1.3, the degenerate states are labeled by any function of \hat{x}_c and \hat{y}_c . However, \hat{x}_c and \hat{y}_c do not commute with each other [cf. Eq. (23)]. Specifying a function of the center coordinates is intimately, though *not* necessarily, related to the gauge choice. We will examine two choices of such functions, and choose a convenient gauge in each case to get an explicit form of the wave function.

2.2.1 Landau gauge

We first choose \hat{x}_c as the label of the degenerate energy eigenstates that satisfy

$$\hat{x}_c|n, x_c\rangle = x_c|n, x_c\rangle, \quad (52)$$

where x_c is an eigenvalue. Note that making this choice itself is independent of the gauge choice and that the y_c cannot be determined due to the quantum uncertainty (23). One can write \hat{x}_c as $\hat{x}_c = \hat{x} + \frac{1}{q_f B} \{\hat{p}_y - q_f A_y(\hat{\mathbf{x}})\}$. This form suggests that a suitable gauge choice will be the ‘‘Landau gauge’’:

$$A_y = B\hat{x}, \quad A_t = A_x = A_z = 0, \quad (53)$$

where the above relation reduces to

$$\hat{x}_c = \frac{\hat{p}_y}{q_f B}. \quad (54)$$

The canonical momentum \hat{p}_y is a constant of motion, while \hat{p}_x is not conserved. Therefore, the operator \hat{p}_y can be replaced by its eigenvalue as

$$\hat{p}_y|n, x_c\rangle = q_f B x_c|n, x_c\rangle. \quad (55)$$

This equality only holds in the Landau gauge. In this gauge, the energy eigenstate is labeled by the principle quantum number n and the conserved canonical momentum p_y that is equivalent to x_c chosen in Eq. (52). On the other hand, the gauge configuration apparently breaks the rotational symmetry around the direction of the magnetic field. The rotational symmetry should be restored in gauge-invariant quantities in the end of the day after correct computations.

Now that we have completely specified the labels of the energy eigenstates, we can obtain the wave function $\phi_n(x, y) \equiv \langle x|n, x_c\rangle$. First, according to Eq. (55), we can factorize the plane-wave component as

$$\phi_{n,p_y}(x, y) = e^{i\frac{p_y y}{\hbar}} \tilde{\phi}_n(x), \quad (56)$$

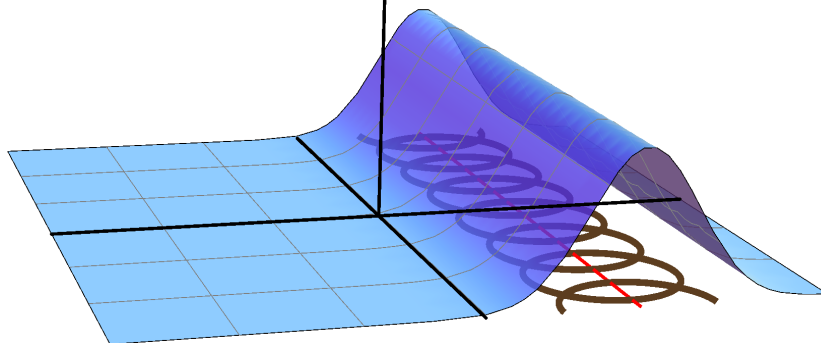


Figure 5: The LLL wave function in the Landau gauge composed of the superposition of cyclotron motions (circles) of which the center coordinates are aligned on a red line at $x_c = p_y/(q_f B)$. A similar picture holds in the higher Landau levels ($n \geq 1$).

where $p_y = q_f B x_c$. In the previous subsection, we have already constructed the complete set of the eigenstates in Eq. (18), so that the remaining part $\tilde{\phi}(x)$ can be obtained by using the explicit representations of the creation and annihilation operators in the Landau gauge. Following the detailed account in Appendix A.1, we obtain the wave function for the general Landau level n :

$$\phi_{n,p_y}(\xi, y) = e^{i\frac{p_y y}{\hbar}} i^n \mathcal{H}_n(\xi), \quad (57)$$

where we have defined $\xi = (x - x_c)/\ell_f$ and the normalized Hermite function

$$\mathcal{H}_n(\xi) = \sqrt{\frac{1}{2^n n! \pi^{1/2} \ell_f}} e^{-\frac{\xi^2}{2}} H_n(\xi), \quad (58)$$

with the Hermite polynomial $H_n(x)$ is defined as

$$H_n(\xi) = (-1)^n e^{\xi^2} \frac{\partial^n}{\partial \xi^n} e^{-\xi^2}. \quad (59)$$

This means that the wave function in the Landau gauge is given by that of the displaced harmonic oscillator with the center located at x_c (see Fig. 5). Some useful properties of the Hermite function are summarized as

$$\int dx \mathcal{H}_m(\xi) \mathcal{H}_n(\xi) = \delta_{m,n}, \quad (60a)$$

$$\sum_n \mathcal{H}_n(\xi) \mathcal{H}_n(\xi') = \ell_f^{-1} \delta(\xi - \xi'), \quad (60b)$$

$$\int dx x \mathcal{H}_m(\xi) \mathcal{H}_n(\xi) = \ell_f \left[\sqrt{\frac{n}{2}} \delta_{m,n-1} + \sqrt{\frac{n+1}{2}} \delta_{m,n+1} \right], \quad (60c)$$

$$\partial_x \mathcal{H}_n(\xi) = \ell_f^{-1} \left[\sqrt{\frac{n}{2}} \mathcal{H}_{n-1}(\xi) - \sqrt{\frac{n+1}{2}} \mathcal{H}_{n+1}(\xi) \right]. \quad (60d)$$

Note a difference between x and ξ which have different mass dimensions.

As already discussed in the gauge-invariant manner, the density of degenerate states can be counted in a finite box with the side L_x in the x direction. Since $0 \leq x_c \leq L_x$, we have $0 \leq p_y \leq q_f B L_x$ when

$s_f > 0$, and $-|q_f B|L_x \leq p_y \leq 0$ when $s_f < 0$. Therefore, we get the density of states

$$\frac{1}{L_x} \int_0^{|q_f B|L_x} \frac{dp_y}{2\pi\hbar} = \frac{|q_f B|}{2\pi\hbar}. \quad (61)$$

This expression agrees with that in Eq. (25). Here, there is no p_x integral since p_x is not a quantum number specifying our phase space.

2.2.2 Symmetric gauge

We shall examine another way of labeling the degenerate states by the eigenvalue of \hat{r}_c^2 which is the distance between the cyclotron center and the coordinate origin as defined in Eq. (24). In Eq. (27), we have found that the eigenvalue of \hat{r}_c^2 is quantized with the creation and annihilation operators, \hat{b} and \hat{b}^\dagger , in Eq. (26). Therefore, one can construct the complete set of the energy eigenstates by starting out with the “ground state” annihilated by both of the annihilation operators

$$\hat{a}|0, 0\rangle = 0 = \hat{b}|0, 0\rangle. \quad (62)$$

The other states can be obtained by operating the creation operators as

$$\phi_{nm} \equiv \langle \mathbf{x} | n, m \rangle = \langle \mathbf{x} | \frac{(\hat{a}^\dagger)^n (\hat{b}^\dagger)^m}{\sqrt{n!} \sqrt{m!}} | 0, 0 \rangle. \quad (63)$$

Note that operating \hat{b}, \hat{b}^\dagger does not change the Landau level n as \hat{a}, \hat{a}^\dagger and \hat{b}, \hat{b}^\dagger commute with each other. Also, operating \hat{a}, \hat{a}^\dagger does not change the degeneracy label m . As in Eq. (52), making this choice itself is independent of the gauge choice since the commutation relations (22) with the Hamiltonian are gauge-invariant properties. The algebraic properties for \hat{b}, \hat{b}^\dagger as well as for \hat{a}, \hat{a}^\dagger are gauge-invariant as well. Remember also that, in the gauge-invariant language of the pseudo angular momentum \hat{K} , the quantization of \hat{r}_c^2 , which is found to be proportional to \hat{K}_z , is led by the ladder operators (48) that connects the degenerate states. One needs to specify the gauge only when getting an explicit form of the wave function ϕ_{nm} from the coordinate representations of the creation and annihilation operators. The coordinate representations of the creation and annihilation operators depend on the gauge choice.

It is also straightforward to show that the canonical angular momentum operator (41), $\hat{L}_z = \hat{x}\hat{p}_y - \hat{y}\hat{p}_x$, can be written by $\hat{\mathbf{x}}_c$ and $\hat{\boldsymbol{\pi}}$ in a general gauge as

$$\hat{L}_z = \frac{s_f}{\omega_f} \left(\frac{1}{2} m_0 (\hat{r}_c \omega_f)^2 - \hat{\mathcal{H}}_\perp \right) + q_f \left[\{ \hat{x} A_y(\hat{\mathbf{x}}) - \hat{y} A_x(\hat{\mathbf{x}}) \} - \frac{1}{2} B \hat{r}^2 \right], \quad (64)$$

where $\hat{r}^2 \equiv \hat{x}^2 + \hat{y}^2$ and a mass parameter is denoted as m_0 in this subsection (to avoid a possible confusion with the quantum number m). The first two terms between the parentheses are diagonalized by the creation and annihilation operators as discussed above. However, those terms between the square brackets do not commute with the Hamiltonian in a general gauge. Nevertheless, it is clear from the symmetry argument that, if one takes a rotationally symmetric gauge, the canonical angular momentum is also a simultaneous eigenstate of the Hamiltonian. Therefore, one can make a suitable choice with the so-called “symmetric gauge”

$$A_x = -\frac{1}{2} B \hat{y}, \quad A_y = \frac{1}{2} B \hat{x}, \quad A_t = A_z = 0. \quad (65)$$

In this gauge, the last term in Eq. (64) cancels away, and the canonical angular momentum is diagonalized as

$$\hat{L}_z = s_f \hbar (\hat{b}^\dagger \hat{b} - \hat{a}^\dagger \hat{a}). \quad (66)$$

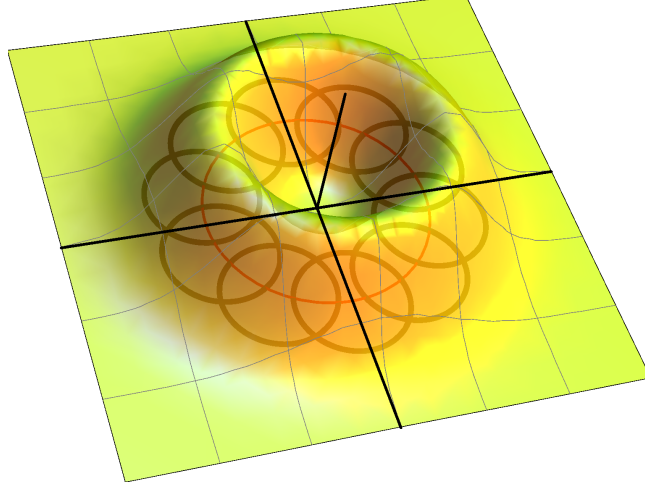


Figure 6: The LLL wave function in the symmetric gauge composed of superposition of cyclotron motions (circles), of which the center coordinates are aligned on a red circle. The radius of each cyclotron motion and the location of the center coordinate are given by $R^2 = (2n + 1)\ell_f^2$ and $r_c^2 = (2m + 1)\ell_f^2$, respectively.

The canonical angular momentum is a gauge-dependent quantity, and is not an observable quantity as clear from its definition by the canonical momentum. We find an eigenvalue of the angular momentum as

$$\hat{L}_z |n, m\rangle = s_f \hbar (m - n) |n, m\rangle. \quad (67)$$

For each Landau level, the angular momentum $\ell \equiv m - n$ takes an integer from $-n$ to the positive infinity ($\ell \geq -n$), according to the lower bounds, $m, n \geq 0$. Since the integer m specifies the center of the cyclotron motion, a larger angular momentum at a fixed n corresponds to an outer orbit that is more distant from the origin of the coordinate system (cf. Fig. 6).

Following detailed descriptions in Appendix A.2, the coordinate representation of the wave function is obtained as

$$\begin{aligned} \phi_{nm}(r, \theta) &= C_S (-i)^n e^{is_f \ell \theta} \sqrt{\frac{n!}{m!}} e^{-\frac{r^2}{4\ell_f^2}} \left(\frac{r^2}{2\ell_f^2}\right)^{\frac{\ell}{2}} L_n^\ell \left(\frac{r^2}{2\ell_f^2}\right) \\ &= C_S i^n (-1)^{\min(n, m)} e^{is_f \ell \theta} \sqrt{\frac{n!}{m!}} e^{-\frac{r^2}{4\ell_f^2}} \left(\frac{r^2}{2\ell_f^2}\right)^{\frac{|\ell|}{2}} L_{\min(n, m)}^{|\ell|} \left(\frac{r^2}{2\ell_f^2}\right), \end{aligned} \quad (68)$$

with the associated Laguerre polynomial $L_k^\alpha(z)$ defined as

$$L_k^\alpha(\rho) = \frac{\rho^{-\alpha} e^\rho}{k!} \frac{\partial^k}{\partial \rho^k} (\rho^{k+\alpha} e^{-\rho}). \quad (69)$$

The radial coordinate and the normalization constant are denoted as $r = \sqrt{x^2 + y^2}$ and $C_S = (2\pi\ell_f^2)^{-\frac{1}{2}}$, respectively. In the second line of Eq. (68), we used the formula (501) to have a positive index in the

upstairs of the Laguerre polynomial and promise to take the smaller integer in $\min(n, m)$. Especially, the LLL wave function is found to be

$$\phi_{0m}(r, \theta) = C_S e^{is_f m \theta} \sqrt{\frac{1}{m!}} e^{-\frac{r^2}{4\ell_f^2}} \left(\frac{r^2}{2\ell_f^2}\right)^{\frac{m}{2}}. \quad (70)$$

Notice that the last factor can be any positive power of r . Therefore, any linear combination of those wave functions, that is a product of any polynomial of r and the Gaussian, serves as the wave function of the LLL.

When the transverse area of the system is given by S_\perp , the quantum number m is bounded according to an inequality $S_\perp \geq \pi r_c^2$. From this inequality, we immediately find the density of degenerate states

$$\frac{m_{\max}}{S_\perp} \sim \frac{|q_f B|}{2\pi\hbar}. \quad (71)$$

Here, we assumed $m_{\max} \gg 1$ or, in other words, $S_\perp \gg \pi(2\ell_f^2)$ where the latter is the area enclosed by each cyclotron orbit. Although the spatial profiles of the wave functions and the labels of the degenerate states strongly depend on the gauge choice, the density of states is a gauge-invariant quantity [cf. Eqs. (25) and (61)].

2.3 Relativistic fermions in a magnetic field

In the previous subsection, we have examined the Landau quantization in terms of nonrelativistic quantum mechanics. In this section, we proceed to a field theoretical framework for relativistic fermions in magnetic fields. Specifically, we will introduce the Ritus-basis method [63, 64] to find the eigenspinor of the Dirac operator in magnetic fields. Hereafter, we work in natural units.

2.3.1 Dirac equation in magnetic fields

Interactions between relativistic fermion and an external electromagnetic field are described by the spinor QED Lagrangian:

$$\mathcal{L} = \bar{\psi} (i\not{D} - m) \psi. \quad (72)$$

Here, we use the following convention of the covariant derivative

$$D^\mu = \partial^\mu + iq_f A^\mu(x). \quad (73)$$

The Abelian gauge field $A^\mu(x)$ is for an external field, and we do not include a dynamical photon (see, e.g., Ref. [65]). The Euler-Lagrange equation results in the Dirac equation in the external field:

$$(i\not{D} - m) \psi = 0. \quad (74)$$

By using an identity, $\gamma^\mu \gamma^\nu = \frac{1}{2}[\gamma^\mu, \gamma^\nu] + \frac{1}{2}\{\gamma^\mu, \gamma^\nu\}$, we get

$$\left(D^2 + m^2 + \frac{q_f}{2} F^{\mu\nu} \sigma_{\mu\nu}\right) \psi = 0, \quad (75)$$

with $\sigma_{\mu\nu} = \frac{i}{2}[\gamma_\mu, \gamma_\nu]$.

In the presence of a magnetic field in the z -direction, we have a non-vanishing commutation relation for the transverse components of the covariant derivative

$$[iD^1, iD^2] = -iq_f F^{12} = iq_f B. \quad (76)$$

One can use the covariant derivative as a pair of the ‘‘canonical variables’’ as in Eq. (14) for non-relativistic quantum mechanics. Therefore, one can apply the techniques discussed in the previous subsection. Identifying the variables in the present and previous discussions as $iD^i \leftrightarrow \hat{\pi}^i$, one can define the ‘‘creation and annihilation operators’’ for the Landau levels [cf. Eq. (15)]:

$$\hat{a} = \frac{1}{\sqrt{2|q_f B|}}(iD^1 - s_f D^2), \quad \hat{a}^\dagger = \frac{1}{\sqrt{2|q_f B|}}(iD^1 + s_f D^2). \quad (77)$$

Then, we find a simple relation

$$D^2 + m^2 = \partial_t^2 - \partial_z^2 + (2\hat{a}^\dagger \hat{a} + 1) |q_f B| + m^2. \quad (78)$$

Here and below, the creation and annihilation operators, \hat{a}^\dagger and \hat{a} , should be understood as their coordinate representations and act on the wave function $\phi_n(x)$ in the coordinate representation. The above Klein-Gordon operator represents the relativistic Landau quantization for charged scalar particles.

One may easily guess that the remaining term $\frac{q_f}{2} F^{\mu\nu} \sigma_{\mu\nu}$ in Eq. (75) is responsible for the Zeeman effect. To explicitly see this, we shall introduce spin projection operators¹²

$$\mathcal{P}_\pm = \frac{1}{2} (1 \pm i s_f \gamma^1 \gamma^2). \quad (79)$$

In the standard (Dirac or Weyl) representation, they are expressed as

$$\mathcal{P}_\pm = \frac{1}{2} \begin{pmatrix} 1 \pm s_f \sigma_z & \\ & 1 \pm s_f \sigma_z \end{pmatrix}, \quad (80)$$

with the Pauli matrix $\sigma_z = \text{diag}(1, -1)$. Then, we indeed find a spin decomposition

$$\frac{q_f}{2} F^{\mu\nu} \sigma_{\mu\nu} = |q_f B| (-\mathcal{P}_+ + \mathcal{P}_-). \quad (81)$$

Therefore, the (squared) energy of the spin state $\psi_+ \equiv \mathcal{P}_+ \psi$ decreases by $|q_f B|$, while that of the opposite spin state $\psi_- \equiv \mathcal{P}_- \psi$ increases by the same amount. This is nothing but the Zeeman effect for a spin-1/2 particle. The energetically favored spin direction depends on the direction of the magnetic field and the electric charge, which is thus encoded in the sign function $s_f = \text{sgn}(q_f B)$ in \mathcal{P}_\pm . Including the Zeeman splitting term, we have

$$[\partial_t^2 - \partial_z^2 + (2\hat{a}^\dagger \hat{a} + 1 \mp 1) |q_f B| + m^2] \psi_\pm = 0. \quad (82)$$

Note that the g -factor in the Dirac equation is $g = 2$, up to higher-order corrections by interactions. The zero-point energy in the LLL is canceled by the Zeeman shift as in Fig. 4 for nonrelativistic fermions.

In the previous subsections, we have already obtained the transverse wave functions in magnetic fields such that $\phi_{n,\chi}(x_\perp) = \langle x_\perp | n, \chi \rangle$ with $\hat{a}^\dagger \hat{a} |n, \chi\rangle = n |n, \chi\rangle$.¹³ Recall that this ‘‘number operator’’ has been defined in a gauge-invariant manner and its eigenvalue n corresponds to the Landau levels. The longitudinal part is the same as the (1+1)-dimensional free theory. Therefore, one can write the eigenfunction in a factorized form $\psi \propto e^{-ip_\parallel x} \phi_{n,\chi}(x_\perp)$ to find the relativistic dispersion relation

$$\epsilon_n = \pm \sqrt{p_z^2 + 2n|q_f B| + m^2}. \quad (83)$$

¹²These operators have useful properties: $\mathcal{P}_\pm^\dagger = \mathcal{P}_\pm$, $\mathcal{P}_+ + \mathcal{P}_- = 1$, $\mathcal{P}_\pm \mathcal{P}_\pm = \mathcal{P}_\pm$, and $\mathcal{P}_\pm \mathcal{P}_\mp = 0$. Therefore, one also finds that $\mathcal{P}_\pm \gamma^\mu \mathcal{P}_\pm = \gamma_\parallel^\mu \mathcal{P}_\pm$ and $\mathcal{P}_\pm \gamma^\mu \mathcal{P}_\mp = \gamma_\perp^\mu \mathcal{P}_\mp$, which will be useful for diagrammatic calculations.

¹³Recall that the wave functions were denoted as ϕ_{n,p_y} and ϕ_{nm} in the Landau and symmetric gauges, respectively. Here, $\phi_{n,\chi}$ is a generalized notation for an arbitrary gauge. The quantum numbers specifying a state $|n, \chi\rangle$ are denoted as subscripts of the wave function $\phi_{n,\chi}$ regardless of whether they are discrete or continuous ones, while the coordinate basis is denoted as the argument.

The upper and lower signs are for the positive and negative energy solutions, respectively, and the non-negative integer n is the resultant quantum number after the sum of the Landau level and the Zeeman shift. Similar to the nonrelativistic fermions discussed in Sec. 2.1.5, the LLL has a unique spin direction, while the higher levels ($n \geq 1$) are two-fold degenerated with respect to the spin directions (cf. Fig. 4). One can reproduce the nonrelativistic expression as an expansion in the limit, $m^2 \gg p_z^2, |q_f B|$. While the Landau-level spacing is given by the cyclotron frequency ω_c in the nonrelativistic case, the relativistic energy levels are not equally spaced. The level spacing is now of the order of $\sqrt{q_f B}$.

2.3.2 Mode expansion with the Ritus basis

Next, we examine the Dirac spinor structure of ψ . As clear from the above discussion, the spin projection operators provides an appropriate basis for the solution of the Dirac equation as

$$\mathcal{R}_{n,\chi}(x_\perp) = \phi_{n,\chi}(x_\perp)\mathcal{P}_+ + \phi_{n-1,\chi}(x_\perp)\mathcal{P}_-, \quad (84)$$

where $\phi_{-1} \equiv 0$ is understood. This expression reflects the two-fold spin degeneracy in the hLLs, while the uniqueness in the LLL is guaranteed by the prescription $\phi_{-1} = 0$. This is called the *Ritus basis*, which was proposed for computation of the fermion self-energy in external fields [63, 64]. By the use of the Ritus basis, one may put an Ansatz

$$\psi(x) = e^{-ip_\parallel x} \mathcal{R}_{n,\chi}(x_\perp) u, \quad (85)$$

where u is a four-component spinor to be determined by the Dirac equation. In both the Landau and symmetric gauges, we have $A_0 = A_3 = 0$, so that $i\mathcal{D} = i\mathcal{D}_\parallel - iD^1\gamma^1 - iD^2\gamma^2$. Then, by the use of the \hat{a} , \hat{a}^\dagger and \mathcal{P}_\pm , the Dirac operator is cast into a more convenient form

$$i\mathcal{D} = i\mathcal{D}_\parallel - \sqrt{2|q_f B|} \gamma^1 (\hat{a}\mathcal{P}_+ + \hat{a}^\dagger\mathcal{P}_-). \quad (86)$$

Acting the Dirac operator on the above Ansatz, we find that

$$i\mathcal{D}\psi(x) = e^{-ip_\parallel x} \mathcal{R}_{n,\chi}(x_\perp) \left(\not{p}_\parallel - \sqrt{2n|q_f B|} \gamma^1 \right) u. \quad (87)$$

The ansatz (85) provides us with a solution for the Dirac equation (74) if the spinor u satisfies the “free” Dirac equation

$$(\not{p}_n - m)u(p_n) = 0, \quad (88)$$

with the four momentum $p_n^\mu \equiv (\epsilon_n, \sqrt{2n|q_f B|}, 0, p^3)$. This is one of the most fundamental equations in quantum field theory, and the solutions are available in numerous textbooks, e.g., Ref. [66]. This equation has two solutions corresponding to the two “spin states” labeled as $u^\kappa(p_n)$.¹⁴ Similarly, we can put an ansatz for the negative-energy solution:

$$\psi(x) = e^{ip_\parallel x} \mathcal{R}_{n,\chi}(x_\perp) v, \quad (89)$$

where the sign of the longitudinal momentum p_\parallel^μ is flipped. Inserting it into the Dirac equation (74), we have

$$i\mathcal{D}\psi(x) = -e^{ip_\parallel x} \mathcal{R}_{n,\chi}(x_\perp) \left(\not{p}_\parallel + \sqrt{2n|q_f B|} \gamma^1 \right) v. \quad (90)$$

¹⁴The general solution for the Dirac equation (88) can be written as $u^\kappa(p_n) = (\sqrt{p_n \cdot \sigma} \xi^\kappa, \sqrt{p_n \cdot \bar{\sigma}} \xi^\kappa)$ with $\sigma^\mu = (1, \boldsymbol{\sigma})$, $\bar{\sigma}^\mu = (1, -\boldsymbol{\sigma})$, and a still arbitrary spinor ξ^κ , according to $(p_n \cdot \sigma)(p_n \cdot \bar{\sigma}) = p_n^2 = m^2$ [66]. Precisely speaking, the “spin label κ ” in the notations of Ref. [66] refers to an arbitrary spinor basis ξ^κ . While ξ^κ can be chosen as an eigenstate of arbitrary operator, e.g., a spin operator σ_z , the solutions $\sqrt{p_n \cdot \sigma} \xi^\kappa$ and $\sqrt{p_n \cdot \bar{\sigma}} \xi^\kappa$ do not remain eigenstates of the same operator if it does not commute with $\boldsymbol{\sigma}$. In the present case, the spinors are eventually projected with \mathcal{P}_\pm in the Ritus basis $\mathcal{R}_{n,\chi}(x;p)$ whatever the basis is chosen.

Therefore, the ansatz (89) provides us with the solution for the Dirac equation (74) if the spinor v satisfies the “free” Dirac equation

$$(\bar{\not{p}}_n + m)v(\bar{p}_n) = 0. \quad (91)$$

We defined $\bar{p}_n^\mu \equiv (\epsilon_n, -\sqrt{2n|q_f B|}, 0, p^3)$ that needs to be distinguished from p_n^μ in Eq. (88): Since the sign of p_{\parallel}^μ has been flipped in the above, \bar{p}_n^1 has a relative minus sign against those longitudinal components. Those spinors satisfy the useful relations [66]

$$\sum_{\kappa=\pm} u^\kappa(p_n)\bar{u}^\kappa(p_n) = (\not{p}_n + m), \quad \sum_{\kappa=\pm} v^\kappa(\bar{p}_n)\bar{v}^\kappa(\bar{p}_n) = (\bar{\not{p}}_n - m). \quad (92)$$

Using the obtained eigenspinors, we can organize a mode expansion. For the notational brevity, we hereafter take a specific gauge, i.e., the Landau gauge (53), where p_y plays the role of χ . In the Landau gauge, the mode expansion with the Ritus basis reads¹⁵

$$\psi(x) = \sum_{\kappa=\pm} \sum_{n=0}^{\infty} \int \frac{dp_z}{2\pi} \int \frac{dp_y}{2\pi} \frac{1}{\sqrt{2\epsilon_n}} \mathcal{R}_{n,p_y}(x_\perp) \left[a_{p_n,p_y}^\kappa e^{-ip_{\parallel}x} u^\kappa(p_n) + b_{\bar{p}_n,p_y}^{\kappa\dagger} e^{ip_{\parallel}x} v^\kappa(\bar{p}_n) \right], \quad (93a)$$

$$\bar{\psi}(x) = \sum_{\kappa=\pm} \sum_{n=0}^{\infty} \int \frac{dp_z}{2\pi} \int \frac{dp_y}{2\pi} \frac{1}{\sqrt{2\epsilon_n}} \left[b_{\bar{p}_n,p_y}^\kappa e^{-ip_{\parallel}x} \bar{v}^\kappa(\bar{p}_n) + a_{p_n,p_y}^{\kappa\dagger} e^{ip_{\parallel}x} \bar{u}^\kappa(p_n) \right] \mathcal{R}_{n,p_y}^\dagger(x_\perp), \quad (93b)$$

where κ is for the “spin sum” and $p^0 = \epsilon_n$. Note also that $\mathcal{P}_\pm^\dagger = \mathcal{P}_\pm$. Each mode is specified by n and p_z in p_n or \bar{p}_n as well as the gauge-dependent quantum number p_y , which are indicated explicitly on the creation and annihilation operators. The operators a_{p_n,p_y}^κ and $b_{\bar{p}_n,p_y}^\kappa$ annihilate the vacuum, i.e., $a_{p_n,p_y}^\kappa |0\rangle = 0 = b_{\bar{p}_n,p_y}^\kappa |0\rangle$ for any p_n , \bar{p}_n , and p_y . The creation and annihilation operators satisfy the anticommutation relations $\{a_{p_n,p_y}^\kappa, a_{p'_{n'},p'_y}^{\kappa'\dagger}\} = \{b_{\bar{p}_n,p_y}^\kappa, b_{\bar{p}'_{n'},p'_y}^{\kappa'\dagger}\} = (2\pi)^2 \delta(p_y - p'_y) \delta(p_z - p'_z) \delta_{nn'} \delta_{\kappa\kappa'}$, while those for all the other combinations vanish. The anticommutation relations imposed on the creation and annihilation operators are consistent with the equal-time anticommutation relation for the fermion field, $\{\psi(x), \psi^\dagger(x')\}|_{x^0=x'^0} = \delta^{(3)}(\mathbf{x} - \mathbf{x}')$.

One can show orthogonal relations

$$\sum_{n=0}^{\infty} \int \frac{dp_y}{2\pi} \mathcal{R}_{n,p_y}(x_\perp) \mathcal{R}_{n,p_y}^\dagger(x'_\perp) = \delta^{(2)}(x_\perp - x'_\perp), \quad (94a)$$

$$\int d^2x_\perp \mathcal{R}_{n,p_y}(x_\perp) \mathcal{R}_{n',p'_y}^\dagger(x_\perp) = 2\pi \delta(p_y - p'_y) \delta_{nn'} I_n, \quad (94b)$$

where a “unit matrix” is introduced as

$$I_n = \begin{cases} \mathcal{P}_+ & (n = 0) \\ \mathbb{1}_{\text{spinor}} & (n \geq 1) \end{cases}. \quad (95)$$

Note that the explicit forms of those orthogonal relations depend on the choice of the label for the Landau degeneracy as discussed in Sec. 2.1. However, as long as the Landau degeneracy is specified by a Hermite operator composed of \hat{x}_c and \hat{y}_c , one can organize an orthonormal set of eigenstates in a corresponding choice of gauge, which serves as good a choice as the Landau gauge with Eq. (55). Mode expansions in other choices of the label and gauge can be organized in a similar way.

In Sec. 8.1, we will apply the Ritus-basis method to computation of currents (one-point functions). The reader is also referred to the literature, e.g., Ref. [61, 65, 67–78], for more examples. In Appendix B.3, we discuss a fermion propagator in the Ritus-basis method.

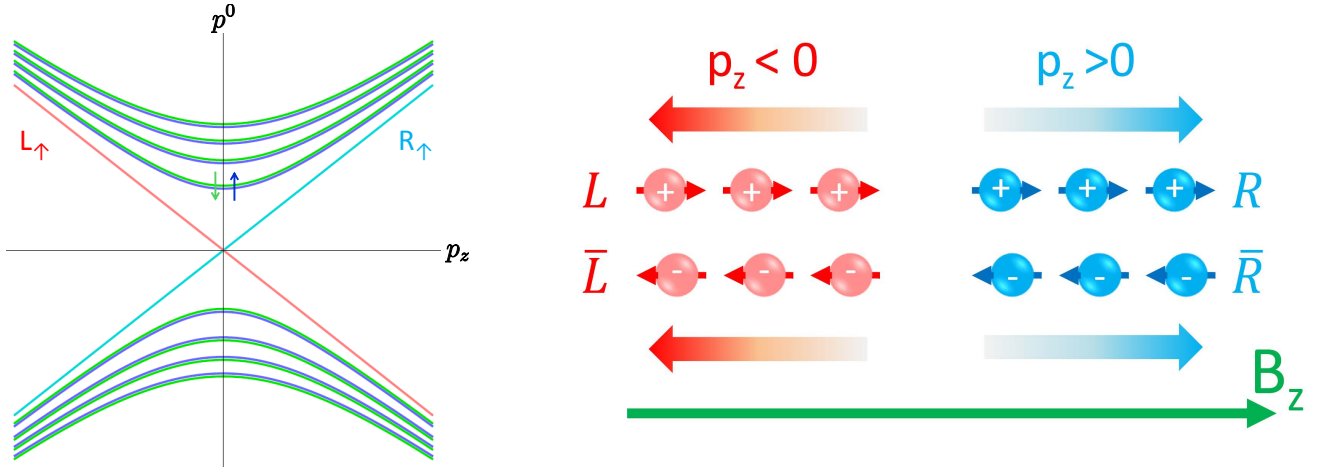


Figure 7: Dispersion relations of the massless fermions in a constant magnetic field when $s_f > 0$ (left). Arrows denote the spin directions. The right figure shows the momentum directions (long arrows), the spin directions (short arrows) and the electric charges (\pm). Bars on \bar{R}/\bar{L} denote the antiparticle states contained in the R/L spinors. The particles and antiparticles contained in the spinor of a given chirality, say the blues, obey the one-way motion in the *same* direction (cf. the color correspondence between the left and right figures).

2.3.3 Massless fermions, spectral flow, and chiral anomaly

In this transient subsection, we discuss some special properties of massless fermions in the LLL. In the massless limit ($m = 0$), the solutions for the free Dirac equations (88) and (91) are given by the chirality eigenstates, i.e., $\gamma^5 u = \pm u$, and so is the solution for ψ because the \mathcal{P}_\pm commutes with $\gamma^5 = i\gamma^0\gamma^1\gamma^2\gamma^3 = \text{diag}(-\mathbb{1}, \mathbb{1})$. As shown in Fig. 7, the hLLs still have the quadratic dispersion relations and are degenerated with respect to the spin directions or now the chirality.

On the other hand, the massless LLL exhibits some special properties originating from the fact that the positive- and negative-energy states are directly connected with each other on each linear dispersion relations (see blue and red diagonal lines in Fig. 7). Such a diagonal dispersion relation often induces interesting phenomena as well as confusions, so that we will carefully identify the quantum numbers of the physical excitations and discuss the spectral flow, an adiabatic acceleration along the dispersion lines in response to an external electric field, which serves as an intuitive interpretation of the chiral anomaly [79, 80] (see also Ref. [81] for a review article).

To get the correct dispersion relation, it is important to note that Eq. (82) from the squared Dirac operator does not determine the relative sign between p^0 and p_z in the dispersion relation, which could be $p^0 = \pm|p_z|$, $p^0 = \pm p_z$, or anything else. Thus, one should refer the original Dirac equation that can be arranged as

$$(p^0 - s_f p_z \gamma^5) \psi_{\text{LLL}} = 0, \quad (96)$$

where we used the facts that the LLL spinor satisfies $\hat{a}\psi_{\text{LLL}} = 0$ and $(i\gamma^1\gamma^2)\psi_{\text{LLL}} = s_f\psi_{\text{LLL}}$. We denote the right/left chirality eigenstate as $\gamma^5\psi_{\text{LLL}}^{R/L} = \pm\psi_{\text{LLL}}^{R/L}$. The dispersion relation for each chirality is found to be

$$p^0 = \pm s_f p_z, \quad (97)$$

without the symbol of the absolute value. Here, the upper and lower signs are for the right- and left-handed chirality eigenstates, respectively, and should not be mixed up with the signs for positive- and

¹⁵The creation and annihilation operators for particle states should not be confused with \hat{a} and \hat{a}^\dagger defined in Eq. (77).

	Spin (s)	Chirality (γ^5)	Axial charge (n_A)	Momentum (p)	Helicity (h)
Particles	$+s_f \frac{1}{2}$	\pm	\pm	$\pm s_f$	$\pm \frac{1}{2}$
Antiparticles (positive energy)	$-s_f \frac{1}{2}$	\pm	\mp	$\pm s_f$	$\mp \frac{1}{2}$

Figure 8: Quantum numbers characterizing the massless fermions in the LLL. All upper (lower) signs are for the right (left) chirality. The momentum and helicity are automatically assigned once the spin direction and the chirality are specified.

negative-energy solutions. The sign of p^0 depends on that of p_z , so that each chirality eigenstate contains both positive- and negative-energy states connected by the diagonal dispersion relation in Fig. 7. The correct dispersion relation (97) is different from the naive massless limit of Eq. (83) that erroneously results in an absolute value of p_z and thus separate Dirac cones in the positive- and negative-energy regions.

Below, by antiparticles, we mean the physical excitations carrying positive energies. In each of $\psi_{\text{LLL}}^{R/L}$, the momentum direction of *antiparticles*, as holes of the negative-energy particle states, is the same as that of particles (cf. the right panel of Fig. 7). This is because, in the linear dispersion relation (97), the positive- and negative-energy states have the opposite momenta (cf. each diagonal line in the left panel of Fig. 7). On the other hand, in each of $\psi_{\text{LLL}}^{R/L}$, the particles and *antiparticles* carry the opposite helicity h and the opposite axial charge n_A ,¹⁶ meaning that those quantities for the antiparticles have the opposite signs to the chirality, i.e., the eigenvalue of γ^5 . To explicitly check the correspondence between the chirality and the helicity, one can arrange the Dirac equation (96) as

$$\hat{h} \psi_{\text{LLL}} = \frac{1}{2} \text{sgn}(p^0) \gamma^5 \psi_{\text{LLL}}, \quad (98)$$

where we used $(\gamma^5)^2 = 1$ and defined the helicity operator $\hat{h} = (i\gamma^1\gamma^2/2)(p_z/|p^0|)$ with the spin operator $(i\gamma^1\gamma^2/2)$ and momentum direction along the magnetic field. According to Eq. (98), the relative sign between the chirality and the helicity depends on the sign of energy p^0 . Therefore, ψ_{LLL}^R (ψ_{LLL}^L) contains the right-handed helicity particles and left-handed helicity antiparticles (the left-handed helicity particles and right-handed helicity antiparticles).

In Fig. 8, we summarize the correspondences among the quantum numbers. All upper and lower signs are for ψ_{LLL}^R and ψ_{LLL}^L , respectively. The momentum direction and the chirality (or the helicity) are locked with each other in the LLL (cf. the right panel of Fig. 7): One needs two quantum numbers out of chirality, spin, and, momentum to specify the massless excitations and the spin direction is frozen in the unique direction along a magnetic field, leaving only one independent quantum number. The spin direction depends on the sign function s_f , and so does the momentum direction according to the locking. The massless LLL fermions are equivalent to the chiral fermions in purely (1+1) dimensions that do not have spin degrees of freedom.¹⁷

¹⁶The axial charge density, or the chiral charge density, is defined as the temporal component of the axial current $n_A = j_A^{\mu=0} = \bar{\psi}\gamma^0\gamma^5\psi = \psi_R^\dagger\psi_R - \psi_L^\dagger\psi_L$. The particles in ψ_{LLL}^R (ψ_{LLL}^L) carry the axial charge $n_A = +1$ ($n_A = -1$), while the antiparticles in ψ_{LLL}^R (ψ_{LLL}^L) carry the opposite axial charge $n_A = -1$ ($n_A = +1$).

¹⁷We should keep it in mind that the wave function of the LLL fermions have a transverse part and that charge-neutral particles such as photons and gluons are not confined in the (1+1) dimensions, that makes big differences in, e.g., the spontaneous symmetry breaking and bound-state problems (or the confinement).

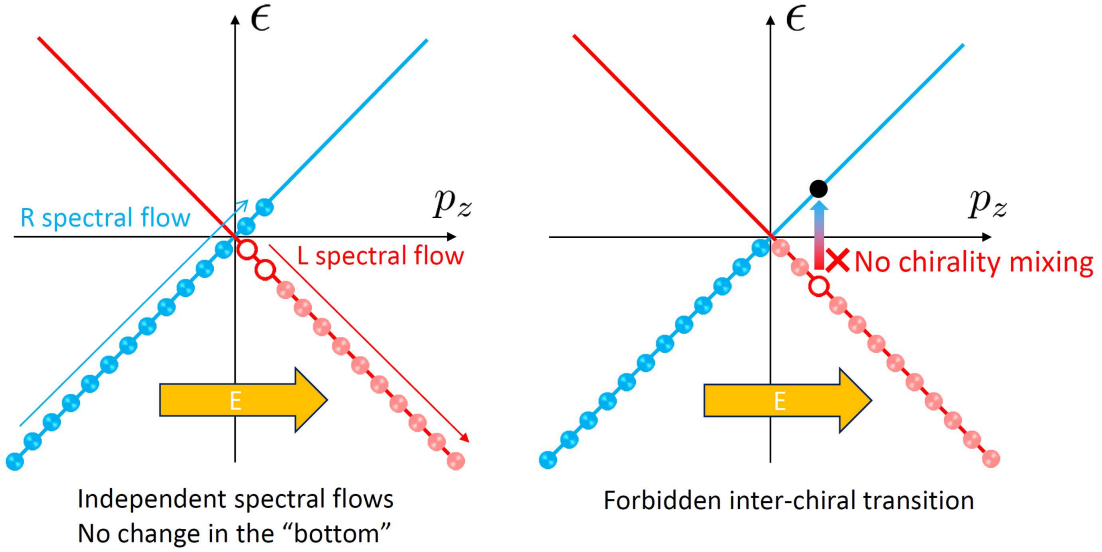


Figure 9: Spectral flow (left) and a forbidden inter-chiral-state transition (right) in an electric and magnetic field applied in a parallel direction. We take a case $q_f > 0$, $B > 0$, and $q_f E > 0$ to draw a figure.

Now, we consider applying an external electric field along the magnetic field adiabatically, which will in general accelerate particles along dispersion curves. Such an adiabatic shift along dispersion curves is often referred to as the spectral flow. Here, an infinitesimal electric field can create particles and antiparticles out of the Dirac sea, i.e., vacuum, since the positive- and negative-energy states are smoothly connected with each other on the diagonal dispersion lines. However, the creation of particles or antiparticles would possibly violate the charge conservation. This anomalous charge violation is offset only if particles and antiparticles are created with the same amount. Nevertheless, the total energy of the system seems to increase even if the total charge is somehow conserved. To understand how this issue is cured and if there is any consequence of the deposited energy, we should recall the quantum numbers of the massless LLL fermions discussed above and identify the quantum numbers created by an electric field.

Since particles and antiparticles are accelerated in opposite directions in an electric field, we immediately notice that they are belonging to the *different* chirality eigenstates (cf. Fig. 7). Therefore, each chirality eigenstate gains the same amount of charge with a relative minus sign, i.e., $n_R = -n_L$ (cf. Fig. 8). This means that the net charge remains zero $n_R + n_L = 0$ thanks to the cancellation. However, the particles and antiparticles in the final state carry the same amount of chiral charges created out of vacuum, providing a nonzero axial charge $n_A = n_R - n_L \neq 0$. This clearly indicates violation of the chirality conservation, and of the chiral symmetry. Namely, the spectrum flow across the surface of the Dirac sea, shown in the left panel of Fig. 9, serves as an intuitive interpretation of the chiral anomaly [82, 83] in massless fermion systems as discussed in Refs. [79, 80] (see also Ref. [81] for a review article).

Notice that the creation of particles and antiparticles occurs independently of each other along each diagonal line (cf. left panel in Fig. 9). During the spectral flow, the occupied states shift altogether since the electric field accelerates all of them. In this way, the occupied states in the infrared (IR) region near the surface is entangled with those in the ultraviolet (UV) region in the bottom of the Dirac sea. The UV behavior of a theory is still crucial though the axial charge creation reveals itself as a consequence in the IR region [80]. Counting of the created quantum numbers depends on whether the Dirac sea is bottomless or not and whether there is, for example, a periodicity in the finite cases like lattice systems. That is, regularization of the UV region matters.

Chiral anomaly is not explained just by processes in the infrared region such as an inter-chirality

transition from an occupied negative-energy state to a positive-energy state in the other chirality state (cf. right panel in Fig. 9). This transition is prohibited due to the absence of chirality mixing in massless QED Lagrangian. In fact, adiabatic creation of the axial charge is not induced by a vertical transition from the lower to upper half of the $p_z - \epsilon$ plane but by a horizontal transition between the left- and right-half planes due to acceleration of particles across a vanishing momentum $p_z = 0$. At this instant, the helicity is flipped. In the massless LLL systems, those transitions occur simultaneously in the diagonal way. For massive cases, the spectral flow goes along the parabolic dispersion curves. In vacuum, the spectral flow under the Dirac sea does not create an axial charge [80]. However, an axial charge can be created when there are pre-occupied positive-energy states in medium at finite temperature and/or density where the helicity of massive particles can be flipped due to acceleration by an electric field [84]. Things are more intricate when one considers diabatic processes such as the Schwinger pair production induced by nonperturbatively strong electric fields (see, e.g., Refs. [80, 85] and Sec. 4.2) and/or transitions induced by finite-frequency electric fields (see Ref. [84] and Appendix F). We will discuss how the created axial charge manifests itself in physical quantities in Sec. 8.

3 Resummation by the proper-time method

In this section, we review the proper-time method in external electromagnetic fields. After describing generalities of the method, we will apply it to the construction of the propagators of spin- $\frac{1}{2}$ and spinless particles in external Abelian fields. In particular, we will elaborate the Schwinger phase which is responsible for the gauge dependence of the propagators and the Landau levels encoded in the propagator. We will, then, discuss an extension to the case of external chromo-electromagnetic fields that is straightforwardly performed when we focus on the so-called covariantly constant field configurations. We discuss the gluon propagator in the external chromo-electromagnetic field in detail. In Appendix B.3, we discuss an equivalence between the proper-time method and the Ritus-basis method introduced in the previous section.

3.1 Generalities of the proper-time method

Nambu [40] and Feynman [41] discussed quantum field theories on the basis of the idea of Fock [86] where a proper-time variable is introduced to parametrize the worldline in the four dimensional spacetime. Schwinger applied the proper-time method to reformulation of the Heisenberg-Euler effective action and further investigated fundamental properties of vacuum in strong electromagnetic fields [42]. He established a systematic way of studying the strong-field physics with the proper-time method which makes it simpler to perform the resummation of propagators or effective actions in terms of external fields. Here, we first explain the essence of the proper-time method by taking scalar field theory as a simple example [87, 88].

Consider the Feynman propagator in the coordinate space:

$$G(x, y) = \int \frac{d^4 p}{(2\pi)^4} e^{ip(x-y)} \frac{i}{p^2 - m^2 + i\epsilon}. \quad (99)$$

We rewrite this by using a mathematical identity

$$\frac{i}{X + i\epsilon} = \int_0^\infty ds e^{is(X+i\epsilon)}, \quad (100)$$

where X is a real quantity. An infinitesimal small number $\epsilon > 0$, which serves as a damping factor $e^{-\epsilon s}$, ensures the convergence of integral at infinity. Integrating both sides of Eq. (100) with respect to X

from B to A , we find another formula

$$\ln \frac{A + i\epsilon}{B + i\epsilon} = - \int_0^\infty \frac{ds}{s} (e^{is(A+i\epsilon)} - e^{is(B+i\epsilon)}) . \quad (101)$$

We will later find that this identity is useful for evaluating the effective action. The integration variable s introduced in these formulas is called the proper time for the reason explained later. By using the first formula (100), the propagator (99) is rewritten as

$$G(x, y) = \int \frac{d^4 p}{(2\pi)^4} e^{ip(x-y)} \int_0^\infty ds e^{is(p^2 - m^2 + i\epsilon)} . \quad (102)$$

Introduction of the proper time makes the inverse operator $i(p^2 - m^2 + i\epsilon)^{-1}$ (where the external fields will appear) more tractable with an exponential form $e^{is(p^2 - m^2 + i\epsilon)}$.

Instead of performing the Gaussian integral over the momentum p in Eq. (102), we examine another way. Let us introduce the Hilbert spaces spanned by $|x\rangle$ and $|p\rangle$ where x and p are *four-dimensional* vectors x^μ and p^μ , respectively. Namely, we define $|x\rangle$ and $|p\rangle$ as eigenstates of the ‘‘operators’’ \hat{x} and \hat{p} :

$$\hat{x}^\mu |x\rangle = x^\mu |x\rangle , \quad \hat{p}^\mu |p\rangle = p^\mu |p\rangle . \quad (103)$$

These states are normalized as

$$\langle p' | p \rangle = \delta^4(p' - p) , \quad \int \frac{d^4 p}{(2\pi)^4} |p\rangle \langle p| = 1 , \quad (104)$$

and so on, and the inner product between $|x\rangle$ and $|p\rangle$ is defined as

$$\langle p | x \rangle = e^{ip^\mu x_\mu} . \quad (105)$$

By using these properties, one can rewrite Eq. (102) in a compact and suggestive form:

$$G(x, y) = \int_0^\infty ds e^{-s\epsilon} e^{-ism^2} \langle y | e^{-i\hat{H}_0 s} | x \rangle , \quad (106)$$

where we have defined an operator $\hat{H}_0 = -\hat{p}^2$ and used $e^{isp^2} \langle p | x \rangle = \langle p | e^{-is\hat{H}_0} | x \rangle$. As is evident from this expression, we notice that the matrix element $\langle y | e^{-i\hat{H}_0 s} | x \rangle$ can be regarded as a kind of transition amplitude with \hat{H}_0 being the ‘‘Hamiltonian’’ and s being the ‘‘time’’. In this picture, the four-vectors x^μ and y^μ are parametrized by s . Recall that, in the special relativity, the proper time s of a particle is defined by the worldline element $ds^2 = g_{\mu\nu} dx^\mu dx^\nu$ along the trajectory of a particle, and is conjugate to an operator $\hat{H} = g_{\mu\nu} \partial^\mu \partial^\nu$. Therefore, we can indeed regard s , introduced above, as the proper time and $\hat{H}_0 = -\hat{p}^2$ as the Hamiltonian generating the ‘‘proper-time’’ evolution of a state $|x(s)\rangle = e^{-i\hat{H}_0 s} |x(0)\rangle$ (it is customary to define the Hamiltonian without the mass contribution).

Then we are left with the problem to compute the transition matrix element $\langle y | e^{-i\hat{H}_0 s} | x \rangle$ [42]. Similar to the ordinary quantum mechanics, this transition amplitude satisfies a counterpart of the Schrödinger equation for the proper-time evolution. Alternatively, we can work in the Heisenberg picture with the Heisenberg equations of motion for the operators \hat{x}^μ and \hat{p}^μ .¹⁸ In any case, the result turns out to be $\langle y | e^{-i\hat{H}_0 s} | x \rangle = -i/(16\pi^2 s^2) \exp\{-i(x - y)^2/(4s)\}$ and reproduces the result directly obtained from the Gaussian integral in Eq. (102) (See, e.g., Ref. [42, 89] for more detailed discussions).

¹⁸With the proper-time evolution operator, the Heisenberg equation of motion is given by $d\hat{x}^\mu/ds = i[\hat{H}, \hat{x}^\mu]$, etc. We impose the canonical commutator at the equal ‘‘proper time’’ $[\hat{x}^\mu(s), \hat{p}^\nu(s)] = -ig^{\mu\nu}$.

In interacting field theories, we are able to apply the proper-time method for the computation of propagators. Then, in place of the transition amplitude defined by \hat{H}_0 in Eq. (106), we will encounter a transition amplitude $\langle y|e^{-i\hat{H}s}|x\rangle$ with a Hamiltonian \hat{H} which includes the interaction effects. Nevertheless, we can compute the transition amplitude in a similar way as discussed above by solving the Schrödinger equation or the Heisenberg equation of motion. An application to the spinor QED was suggested by Nambu [40]. Soon later, Feynman also discussed a similar idea for Klein-Gordon particles [41]. An advantage of the proper-time method is that the amplitude can be cast into a path-integral form in analogy with quantum mechanics [41, 90–95]. Then, one can apply conventional techniques that have been accumulated for evaluation of the path integral such as the Monte Carlo sampling and the saddle-point method with the so-called “worldline instanton” solutions (see Ref. [88, 96] for reviews and more references therein for applications).

3.2 Spin- $\frac{1}{2}$ particles

In this subsection, we elaborate the proper-time method for spin- $\frac{1}{2}$ particles in constant external electromagnetic fields. We derive the proper-time representation of the fermion propagator $S(x, y|A)$, where the argument A indicates the presence of an external electromagnetic field. In the presence of the external field $A^\mu(x)$, we encounter an issue when transforming the propagator into the Fourier space: Namely, the gauge field and, thus the propagator $S(x, y|A)$, do not have a manifest translational invariance, which spoils the Fourier transform by a single momentum. Nevertheless, we have already learned in Sec. 2.1 that the translational invariance is merely hidden behind the gauge dependence since constant electric and magnetic fields do not break the translational invariance. Putting it the other way round, one can take an advantage of the gauge choice to bypass the above issue as follows.

Notice that, as long as the gauge field is a linear function of the coordinate [cf. Eqs. (53) and (65)], the choice of the origin of the coordinate is arbitrary; A gauge field $A^\mu(x - x_0)$ shifted by x_0 produces the same external field as $A^\mu(x)$ does. Setting the origin to be $x_0 = y$, the Green’s function will satisfy the equation of motion in a translation-invariant form

$$(i\mathcal{D}_x - m) S(x - y|A) = i\delta^4(x - y), \quad (107)$$

where the covariant derivative (73) includes the gauge field $A^\mu(x - y)$. This gauge choice enables us to perform the Fourier transform of the Green’s function by a single momentum. Then, we need to restore a general gauge by examining the gauge-transformation property of the obtained propagator to guarantee that there is no conflict of gauge choices among all the fermion lines in Feynman diagrams.

Below, we will introduce a useful gauge called the Fock-Schwinger gauge [42, 86] and will carefully examine the gauge covariance of the propagator that is expressed in the form of the so-called Schwinger phase. There are several ways to solve Eq. (107). Here, we employ the strategy given in Refs. [97–99] and extend the discussions to more general cases. As an alternative way, one may evaluate the inverse Dirac operator by using the complete set of the wave functions discussed in the previous section. In Appendix B.3, we explicitly show the equivalence between the proper-time method and the Ritus basis method. The reader is also referred to, e.g., appendices in Refs. [100, 101] for this alternative derivation of the Schwinger phase and the resummed propagator. It is also interesting to look up the original derivation by Schwinger on the basis of the “equations of motion” for the proper-time evolution [42] (see also Refs. [89, 102] for reviews).

3.2.1 The Fock-Schwinger gauge and the Schwinger phase

We introduce the Fock-Schwinger (FS) gauge for a constant field strength tensor $F^{\mu\nu}$ [42, 86]:

$$A_{\text{FS}}^\mu(x) = -\frac{1}{2}F^{\mu\nu}(x_\nu - x_{0\nu}), \quad (108)$$

where x_0^μ is a free parameter. By choosing $x_0^\mu = y^\mu$, we can get the translation-invariant form (107). This gauge is sometimes called the fixed-point gauge because x_0^μ specifies a particular point in spacetime [103, 104]. This is an extension of the symmetric gauge (65) that we have used for a constant magnetic field in Sec. 2.2.2. The FS gauge allows us to include an electric field as well as a magnetic field in terms of the gauge-invariant field strength tensor $F^{\mu\nu}$. While we here focus on constant fields, this gauge can be extended to inhomogeneous cases [103, 104]. The general gauge condition is given by

$$(x^\mu - x_0^\mu)A_\mu^{\text{FS}}(x) = 0. \quad (109)$$

If the field strength tensor has a weak spacetime dependence, one can solve Eq. (109) on an order-by-order basis in a derivative expansion. Such a gauge configuration has been used for calculations of the Wilson coefficients in the operator product expansion [103, 104] and for constructions of the Heisenberg-Euler Lagrangian. We will discuss the latter in Sec. 4.1.2.

To get the fermion propagator in a general gauge, we carefully examine how the fermion propagator is transformed in a gauge transformation. Under the $U(1)$ gauge transformation by a local angle $\alpha(x)$, we have

$$\psi(x) \rightarrow \psi' = e^{i\alpha(x)}\psi(x), \quad (110)$$

$$A^\mu(x) \rightarrow A'^\mu(x) = A^\mu(x) - \frac{1}{q_f}\partial^\mu\alpha(x). \quad (111)$$

According to the definition (107), the Green's function $S(x, y|A')$ with the transformed field $A'_\mu(x)$ should satisfy $(i\mathcal{D}'_x - m)S(x, y|A') = i\delta^4(x - y)$ with $D'_\mu = \partial_\mu + iq_f A'_\mu$. By using the covariance of the Dirac operator, this equation can be rewritten as

$$\begin{aligned} i\delta^4(x - y) &= e^{i\alpha(x)}(i\mathcal{D}_x - m)e^{-i\alpha(x)}S(x, y|A') \\ &= (i\mathcal{D}_x - m)e^{-i\{\alpha(x) - \alpha(y)\}}S(x, y|A'), \end{aligned} \quad (112)$$

where we have replaced $\alpha(x)$ by $\alpha(y)$ because the overall exponential factor is relevant only when $x = y$ as implied by the delta function. Comparing Eq. (112) with Eq. (107), the propagator transforms under the gauge transformation from the FS gauge (108) to an arbitrary gauge $A(x)$ as

$$S(x, y|A) = e^{i\Phi_A(x, y)}S(x - y|A_{\text{FS}}). \quad (113)$$

The transformation property is solely encoded in the Schwinger phase $\Phi_A(x, y)$ given by

$$\Phi_A(x, y) \equiv -\{\alpha(x) - \alpha(y)\} = -q_f \int_y^x \left(A_\mu(\xi) + \frac{1}{2}F_{\mu\nu}(\xi^\nu - y^\nu) \right) d\xi^\mu. \quad (114)$$

It is important to remember that the origin of the coordinate was taken at $x_0 = y$ in the FS gauge (108) for *each* propagator. This choice is reflected in the integrand of the Schwinger phase and apparently breaks the translational invariance. The rest of the propagator $S(x - y|A_{\text{FS}})$ is expressed with the field strength tensor $F^{\mu\nu}$, and has a manifest gauge invariance. Thus, we conclude that the gauge dependence and the translation-breaking part are both factorized as the Schwinger phase. In short, insertion of a gauge link between the fermion fields at x and y is necessary for the gauge covariance of the two-point function. The Schwinger phase guarantees that there is no conflict of gauge choices among fermion lines. The total Schwinger phase in Feynman diagrams should be automatically organized into a gauge- and translation-invariant form when one computes a gauge-invariant quantity.

In prior to getting the explicit form of $S(x - y|A_{\text{FS}})$ in the next subsection, we summarize some basic properties of the Schwinger phase. We find in Eq. (114) that the integrand of the Schwinger phase

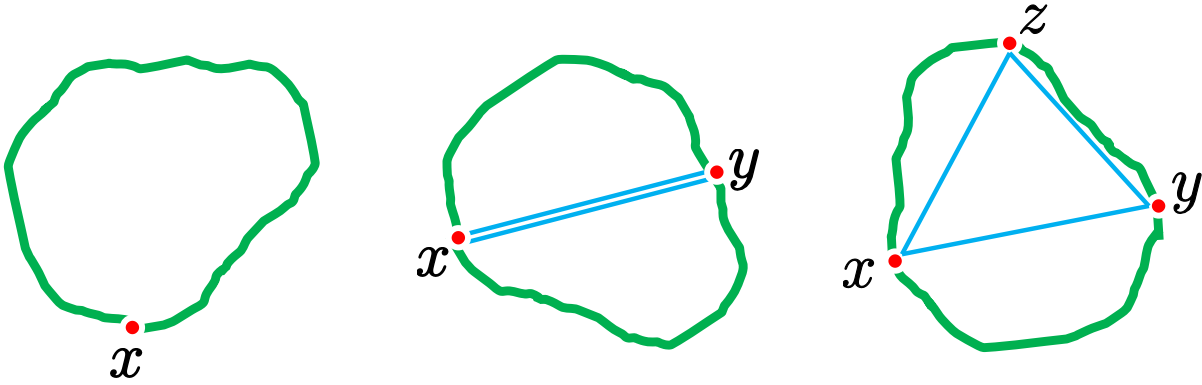


Figure 10: Schwinger phases on closed paths.

$[\equiv f_\mu(\xi; y)]$ is curl-free, i.e., $\partial_\xi^\mu f^\nu(\xi; y) - \partial_\xi^\nu f^\mu(\xi; y) = 0$. Therefore, first of all, the result of the integral is independent of the path, and the integral along a closed path vanishes¹⁹

$$\Phi_A(x, x) = -q_f \oint f_\mu(\xi; x) d\xi^\mu = 0. \quad (115)$$

It is important to note that this means neither $\Phi_A(x, y) = \Phi_A(x', y')$ for $x \neq x'$ and $y \neq y'$ nor the absence of the Schwinger phase on an arbitrary closed loop when there are more than two vertices. This is because the integrand $f_\mu(\xi; y)$ does not have a translational invariance since we have chosen the different values of the parameter x_0^μ for different fermion lines in a Feynman diagram.

In Fig. 10, we show closed loops with different numbers of vertices, $n_v = 1, 2$, and 3 . When $n_v = 1$ which includes the case of the Heisenberg-Euler effective action discussed in the subsequent section, one finds the vanishing phase as in Eq. (115). However, when $n_v \geq 2$, the Schwinger phase on a closed loop is nonvanishing due to the breaking of translational invariance.²⁰ Nevertheless, one can show that the Schwinger phase for a closed fermion loop is a gauge-invariant quantity and can be cast into a translation-invariant form (506) as shown in Appendix B.1, though the Schwinger phase on each side of polygons is not a gauge- or translation-invariant quantity.

When considering derivative couplings, one needs to take the derivative of the Schwinger phase at the interaction vertices. This is required not only in a theory/model with derivative couplings but also in the correlators of the energy-momentum tensor which may contain derivatives. One can show that (see Appendix B.1)

$$D_x^\mu e^{i\Phi_A(x, y)} = e^{i\Phi_A(x, y)} \left\{ \partial_x^\mu - \frac{i}{2} q_f F^{\mu\nu} (x_\nu - y_\nu) \right\} = e^{i\Phi_A(x, y)} \left\{ \partial_x^\mu + i q_f A_{\text{FS}}^\mu (x_0 \rightarrow y) \right\}. \quad (116)$$

After the derivative went through the Schwinger phase, the terms between the braces are given in a manifestly gauge- and translation-invariant form and are the covariant derivative expressed in the Fock-Schwinger gauge (108) with $x_0^\mu = y^\mu$. This result is expected from the covariance of the derivative operator. When the Dirac operator $(i\mathcal{D}_x - m)$ is operated on the both sides of Eq. (113), the derivative relation (116) also implies that

$$(i\mathcal{D}_x - m)S(x, y|A) = e^{i\Phi_A(x, y)} i\delta^{(4)}(x - y), \quad (117)$$

¹⁹This statement is true only when the closed path can be continuously squeezed to a point. For example, in the imaginary-time formalism of thermal field theory, the integral around the compact temporal direction results in a finite winding number (see Sec. 6).

²⁰As shown in Appendix B.1, we find that $n_v = 2$ is an exceptional case where the Schwinger phase identically vanishes.

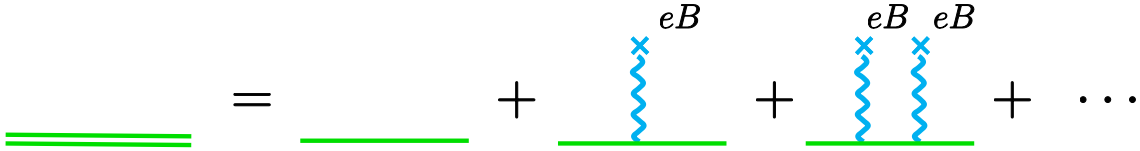


Figure 11: Resummed propagator in a strong external field (double line). The higher-order terms with respect to the coupling constant are not suppressed when the smallness of the coupling constant is compensated by the large field strength of the external field appearing in the combination $q_f F^{\mu\nu}$.

where we used Eq. (107). Recalling that $\Phi_A(x, x) = 0$, we notice that the right-hand side reads $i\delta^{(4)}(x - y)$ when $x = y$ and, otherwise, vanishes. Therefore, we confirm that the resummed propagator $S(x, y|A)$ in a general gauge is the Green's function of the Dirac operator, although it does not have a translation invariance like in familiar cases.

3.2.2 Proper-time representation

By using the trick discussed below Eq. (107), one can Fourier transform the both sides of Eq. (107) as

$$(\not{p} - q_f \not{A} - m) S(p|A) = i, \quad (118)$$

with the single momentum p . The coordinate dependence in the gauge field is understood to be replaced by the derivative operator with respect to the momentum. The above equation in the momentum space can be solved in a formal way

$$S(p|A) = \frac{i}{\not{p} - q_f \not{A} - m} = i(\not{p} - q_f \not{A} + m) \Delta(p|A), \quad (119)$$

where

$$\Delta(p|A) = \frac{1}{i} \int_0^\infty ds e^{is\{(\not{p} - q_f \not{A})^2 - m^2 + i\epsilon\}}. \quad (120)$$

As mentioned in Sec. 3.1, the integral variable s is called the proper time, and this integral is convergent at the infinity owing to an infinitesimal imaginary part, $i\epsilon$. As clear from the appearance of the Dirac operator in Eq. (119), the $\Delta(p|A)$ transforms in precisely the same way as the $S(p|A)$ does in Eq. (113) by the Schwinger phase. When the external field is weak, one may perform a perturbative expansion of the full propagator (119) with respect to the coupling constant e (in q_f). However, when $eA \gtrsim m$, the higher-order terms, which is of the order of $(eA)^n$ ($n \geq 1$), are all as important as the leading term without the external field ($n = 0$), and a naive perturbative expansion breaks down (cf. Fig. 11). In such a case, the proper-time method is useful for organizing the full propagator into the compact form (120).

Following Eq. (118), we obtain the equation for the $\Delta(p|A)$:

$$\left[(\not{p} - q_f \not{A})^2 - m^2 \right] \Delta(p|A) = 1. \quad (121)$$

By using the FS gauge and an identity, $\gamma^\mu \gamma^\nu = \frac{1}{2}[\gamma^\mu, \gamma^\nu] + \frac{1}{2}\{\gamma^\mu, \gamma^\nu\}$, we have

$$\left[p^2 + \frac{q_f^2}{4} F^{\mu\alpha} F_\alpha^\nu \frac{\partial}{\partial p^\mu} \frac{\partial}{\partial p^\nu} - \kappa^2 \right] \Delta(p|A_{\text{FS}}) = 1, \quad (122)$$

where $\kappa^2 := (m^2 - i\epsilon) + \frac{q_f}{2} F^{\mu\nu} \sigma_{\mu\nu}$. We have dropped a term proportional to $F_{\mu\nu} p^\mu \partial_p^\nu$, which is the generator of the Lorentz transform by an ‘‘angle matrix $F^{\mu\nu}$ ’’. Since the operator in Eq. (122) has a manifest Lorentz invariance, the solution for $\Delta(p|A_{\text{FS}})$ is expected to be a Lorentz-scalar function, and thus the increment in an infinitesimal transform $\sim p^\mu \partial_p^\nu \Delta(p|A_{\text{FS}})$ should vanish.

To obtain the resummed propagator, one needs to solve Eq. (122). This can be carried out by using an ansatz, which is explained in detail in Appendix B.2. After some computations, one finds the following solution:

$$\Delta(p|A_{\text{FS}}) = -i \int_0^\infty ds \exp \left[-i\kappa^2 s + ip_\mu X^{\mu\nu}(s) p_\nu + Y(s) \right], \quad (123a)$$

$$X^{\mu\nu}(s) = \left[(q_f F)^{-1} \tanh(q_f F s) \right]^{\mu\nu}, \quad (123b)$$

$$Y(s) = -\frac{1}{2} \text{Tr} \left[\ln \{ \cosh(q_f F s) \} \right], \quad (123c)$$

where F^{-1} is the inverse matrix of the field strength tensor, and the Lorentz indices are suppressed for notational simplicity. Inserting $\Delta(p|A_{\text{FS}})$ back to Eq. (119) with the gauge field in the FS gauge (108), we find the proper-time representation of the resummed propagator

$$S(p|A_{\text{FS}}) = \int_0^\infty ds \left[\not{p} + q_f \gamma^\mu F_{\mu\nu} X^{\nu\lambda}(s) p_\lambda + m \right] e^{-i\kappa^2 s + ip^\mu X_{\mu\nu}(s) p^\nu + Y(s)}. \quad (124)$$

It is straightforward to confirm that the free propagator is reproduced in the vanishing field limit and to obtain the order-by-order expansion with respect to the external field in the weak field limit (see Appendix C). As discussed in Sec. 3.2.1, one should remember that the above result is obtained in the FS gauge, and transforms with the Schwinger phase under a gauge transformation as in Eq. (113).

3.2.3 Spectrum and spin polarizations

In this subsection, we shall more closely look into the proper-time representation (124) and clarify the physical meaning of the spinor structures and the energy spectrum encoded therein. To this end, we first specify an explicit form of the field strength tensor. As discussed below Eq. (4b), one can choose the Lorentz frame in which the external electric and magnetic fields are parallel/antiparallel to each other. Therefore, without loss of generality, we work with this field configuration where the external electric and magnetic fields are both oriented in the z direction. This configuration also covers the cases where either of the electric or magnetic field vanishes as one can easily take such a limit.

In this Lorentz frame, the square of the field strength tensor has the diagonal form (5a), so that the following calculations are greatly simplified. Especially, since the $X^{\mu\nu}$ and Y in Eqs. (123b) and (123c) are even functions of $F^{\mu\nu}$, they also have diagonal forms:

$$X^{\mu\nu}(s) = \frac{1}{q_f E} \tanh(q_f E s) g_{\parallel}^{\mu\nu} + \frac{1}{q_f B} \tanh(q_f B s) g_{\perp}^{\mu\nu}, \quad (125)$$

$$Y(s) = -\ln \left\{ \cosh(q_f E s) \cos(q_f B s) \right\}. \quad (126)$$

The remaining ingredient is the spin coupling $F^{\mu\nu} \sigma_{\mu\nu} = 2i(E\gamma^0\gamma^3 - B\gamma^1\gamma^2)$ in Eq. (123a). One can decompose the exponential factor there as

$$e^{-i\kappa^2 s} = e^{-im^2 s} \left(\cosh(q_f E s) + \gamma^0 \gamma^3 \sinh(q_f E s) \right) \left(\cos(q_f B s) - \gamma^1 \gamma^2 \sin(q_f B s) \right), \quad (127)$$

where we have utilized the fact that $\gamma^0 \gamma^3$ and $\gamma^1 \gamma^2$ commute with each other. The signs of E and B only matter in this exponential factor related to spin configurations: The other parts of the propagator are

even functions of E and B as seen above. The decomposition in Eqs. (125)–(127) casts the resummed propagator (124) into the following form

$$\begin{aligned}
S(p|B, E) &= \int_0^\infty ds \left[\frac{1 - \gamma^1 \gamma^2 \tan(q_f B s)}{\cosh^2(q_f E s)} \not{p}_\parallel + \frac{1 + \gamma^0 \gamma^3 \tanh(q_f E s)}{\cos^2(q_f B s)} \not{p}_\perp \right. \\
&\quad \left. + m(1 - \gamma^1 \gamma^2 \tan(q_f B s))(1 + \gamma^0 \gamma^3 \tanh(q_f E s)) \right] \\
&\quad \times \exp \left(-im^2 s + i \frac{p_\perp^2}{q_f B} \tan(q_f B s) + i \frac{p_\parallel^2}{q_f E} \tanh(q_f E s) \right). \tag{128}
\end{aligned}$$

It should be noticed that there is a duality under the following simultaneous interchanges:

$$(B, p_\perp^\mu, \gamma^1 \gamma^2) \longleftrightarrow (iE, p_\parallel^\mu, i\gamma^0 \gamma^3), \tag{129}$$

whereas the ordinary electromagnetic duality under the interchange $B \longleftrightarrow E$ is broken due to the coupling to the matter fields.

To investigate the basic properties of the resummed propagator (128), we focus on a purely magnetic-field case without an electric field ($B \neq 0, E = 0$). The expression for a purely electric-field case ($E \neq 0, B = 0$) can be obtained by using the extended duality (129). Taking the limit of the vanishing electric field in Eq. (128), one finds that

$$\begin{aligned}
S(p|B, E = 0) &= \int_0^\infty ds \left[(\not{p}_\parallel + m)(1 - s_f \gamma^1 \gamma^2 \tan(|q_f B|s)) + \not{p}_\perp \cos^{-2}(|q_f B|s) \right] \\
&\quad \times \exp \left(-im^2 s + ip_\parallel^2 s + i \frac{p_\perp^2}{|q_f B|} \tan(|q_f B|s) \right). \tag{130}
\end{aligned}$$

As discussed in Sec. 2.2.2, the wave functions of charged particles in magnetic fields are given by the associated Laguerre polynomial $L_k^\alpha(x)$ in the symmetric gauge that is nothing but the FS gauge when $E = 0$. Therefore, it is natural to expect that the resummed propagator can be decomposed in terms of $L_k^\alpha(x)$. To use the generating function of the associated Laguerre polynomial

$$(1 - z)^{-(1+\alpha)} \exp\left(\frac{xz}{z-1}\right) = \sum_{n=0}^{\infty} L_n^\alpha(x) z^n, \tag{131}$$

we put

$$z = -e^{-2i|q_f B|s}. \tag{132}$$

Then, the tangent in the exponential is rewritten in a desired form

$$\exp\left(i \frac{p_\perp^2}{|q_f B|} \tan(|q_f B|s)\right) = \exp\left(-\frac{u_\perp}{2}\right) \exp\left(\frac{u_\perp z}{z-1}\right), \tag{133}$$

where $u_\perp = -2p_\perp^2/|q_f B|$. The second factor is identified with the exponential factor in the generating function (131), and thus can be decomposed into the polynomial of z by the use of Eq. (131). The other trigonometric functions in Eq. (130) are also rewritten in terms of z .

After all, the fermion propagator is written by the polynomial of z , leading to a simple expression in terms of the exponential factor of s :

$$S(p|B) = 2 e^{-\frac{u_\perp}{2}} \sum_{n=0}^{\infty} (-1)^n \hat{B}_n(u_\perp) \int_0^\infty ds e^{i(p_\parallel^2 - m^2 + i\epsilon - 2n|q_f B|)s}, \tag{134}$$

where

$$\hat{B}_n(x) = (\not{p}_\parallel + m)\{\mathcal{P}_+L_n(x) - \mathcal{P}_-L_{n-1}(x)\} - 2\not{p}_\perp L_{n-1}^1(x). \quad (135)$$

Here, $L_n(x) = L_n^0(x)$ and $L_{-1}(x) = 0 = L_{-1}^1(x)$ are understood. Now, the proper-time integral can be easily performed, and the resummed propagator is represented in the form of summation over the Landau levels [105, 106]

$$S(p|B) = 2i e^{\frac{p_\perp^2}{|q_f B|}} \sum_{n=0}^{\infty} \frac{(-1)^n \hat{B}_n(u_\perp)}{p_\parallel^2 - m^2 - 2n|q_f B|}, \quad (136)$$

where $p_\perp^2 = -|\mathbf{p}_\perp|^2$. The origin of the spin projection operators $\mathcal{P}_\pm = (1 \pm i s_f \gamma^1 \gamma^2)/2$ is traced back to the spin coupling $F^{\mu\nu} \sigma_{\mu\nu}$ in Eq. (127) as encountered earlier in Eq. (79). Note that the sign of $q_f B$ only appears in the spin projection operator. As discussed below Eq. (526), the first two terms in $\hat{B}_n(u_\perp)$ correspond to the degenerate spin eigenstates, while the last term originates from the overlap between the wave functions of those states. The last point is more clearly seen in the Ritus basis method discussed in Appendix B.3.

There are an infinite number of poles located at $p_\parallel^2 - m^2 - 2n|q_f B| = 0$. The dispersion relation $p^0 = \pm \sqrt{(p^3)^2 + m^2 + 2n|q_f B|}$ represents nothing but the resultant energy levels from the Landau quantization and the Zeeman effect (cf. Fig. 4). The propagator in the LLL is given by a particularly simple form

$$S_{\text{LLL}}(p|B) = 2i e^{\frac{p_\perp^2}{|q_f B|}} \frac{\not{p}_\parallel + m}{p_\parallel^2 - m^2} \mathcal{P}_+, \quad (137)$$

with $L_0(x) = 1$. The LLL propagator only has one term because of the absence of the spin degeneracy. Notice that this expression is the same as the free fermion propagator in (1+1) dimensions up to two residual factors due to the presence of (frozen) spin \mathcal{P}_+ and the wave function in the transverse plane given by the Gaussian factor. This propagator is useful to compute physical quantities in the strong field limit.

3.3 Charged scalar particles

The proper-time representation of the propagator for charged scalar particles can be obtained in a similar manner as we have done for the fermion propagator in the preceding subsections. The Lagrangian of scalar QED is given by

$$\mathcal{L} = (D^\mu \phi)^* (D_\mu \phi) - m^2 \phi^* \phi, \quad (138)$$

where the covariant derivative (73) contains an external field. The propagator of the scalar particles obeys the equation of motion

$$(D^2 + m^2)G(x, y|A) = i\delta^4(x - y). \quad (139)$$

Similar to the procedure in the preceding sections, this equation can be solved formally as

$$G(p|A) = i \times \frac{1}{i} \int_0^\infty ds e^{is\{(p-eA)^2 - m^2 + i\epsilon\}} \equiv \Delta_{\text{scalar}}(p|A). \quad (140)$$

Here, we notice a correspondence between $\Delta(p|A)$ in Eq. (120) for spin- $\frac{1}{2}$ particles and $\Delta_{\text{scalar}}(p|A)$ in Eq. (140) for scalar particles. They only differ by the spinor structure $F^{\mu\nu} \sigma_{\mu\nu}$ which arises from the

square of the Dirac operator $\not{D}\not{D}$ and thus is absent for spinless particles. We find a useful relation in a formal limit at $\sigma_{\mu\nu} \rightarrow 0$ as

$$\Delta_{\text{scalar}}(p|A) = \Delta(p|A)|_{\sigma^{\mu\nu}=0}, \quad (141)$$

where one should get rid of an implicit unit matrix in the spinor space on the right-hand side. The absence of the spinor structure should result in the absence of the Zeeman effect in the energy spectrum of spinless particles as explicitly seen below. Also, we can apply the discussion around Eq. (113) to the Klein-Gordon equation (139) using the covariance of the Klein-Gordon operator to find the gauge-transformation property

$$G(x, y|A) = e^{i\Phi_A(x, y)} G(x - y|A_{\text{FS}}), \quad (142)$$

where $\Phi_A(x, y)$ is the Schwinger phase (114).

Borrowing the result for spin-1/2 fermions shown in Eqs. (123a)–(123c), one can immediately obtain the propagator of charged scalar particles

$$G(p|A) = \int_0^\infty ds e^{-i(m^2 - i\epsilon)s + ip_\mu X^{\mu\nu}(s)p_\nu + Y(s)}. \quad (143)$$

In the vanishing and weak field limits, the free propagator $G(p|B = E = 0) = i/(p^2 - m^2)$ and the perturbative expansion are reproduced from Eq. (143) (see Appendix C). When $E = 0$, the resummed propagator is simplified and decomposed into the Landau levels as

$$G(p|B, E = 0) = \int_0^\infty ds \frac{1}{\cos(q_f B s)} \exp \left\{ -i(m^2 - i\epsilon)s + ip_\parallel^2 s + i \frac{p_\perp^2}{q_f B} \tan(q_f B s) \right\} \quad (144a)$$

$$= 2i e^{-\frac{|p_\perp|^2}{|q_f B|}} \sum_{n=0}^\infty (-1)^n L_n \left(\frac{|p_\perp|^2}{2|q_f B|} \right) \frac{1}{p_\parallel^2 - m^2 - (2n + 1)|q_f B|}. \quad (144b)$$

As mentioned in the previous section, the proper-time integral is convergent thanks to the infinitesimal imaginary part $i\epsilon$. In the second line, the decomposed propagator has an infinite number of poles precisely at the Landau levels $\omega^2 = m^2 + p_z^2 + (2n + 1)|q_f B|$ without the Zeeman effect. Again, the expression in a constant electric field E is obtained by using the extended duality (129).

3.4 Simplest extension to QCD: Covariantly constant fields

In this subsection, we further extend the resummation techniques discussed in the previous subsections for QED. Here, we will obtain the resummed propagators for quarks, gluons, and ghosts in the presence of an external chromo-electromagnetic field in QCD. In general, QCD contains much richer and more complex dynamics than QED, so that we confine ourselves to the so-called *covariantly constant fields*. As shown below, the covariantly constant chromo-electromagnetic field is decomposed into three Abelian fields, and thus one can apply the resummation techniques to QCD without a technical leap. We will use those propagators to derive the non-Abelian Heisenberg-Euler effective action in Sec. 6.3.1.

We first briefly recapitulate the QCD Lagrangian in an external chromo-electromagnetic field, following the “background field method.” We shall start with the full QCD action of the $SU(N_c)$ gauge group:

$$S_{\text{QCD}} = \int d^4x \left[\bar{\psi} (i\not{D}_A - m) \psi - \frac{1}{4} \mathcal{F}_{A\mu\nu}^a \mathcal{F}_A^{a\mu\nu} \right], \quad (145)$$

where we use the following conventions of the covariant derivative

$$D_A^\mu = \partial^\mu - ig\mathcal{A}^{a\mu}t^a. \quad (146)$$

The associated field strength tensor is given by $\mathcal{F}_A^{a\mu\nu} = \partial^\mu \mathcal{A}^{a\nu} - \partial^\nu \mathcal{A}^{a\mu} + gf^{abc}\mathcal{A}^{b\mu}\mathcal{A}^{c\nu}$. The generator of the non-Abelian gauge symmetry obeys the algebra $[t^a, t^b] = if^{abc}t^c$ and the normalization $\text{Tr}[t^a t^b] = C\delta^{ab}$ with $C = 1/2$ and $C = N_c = 3$ for the fundamental and adjoint representations, respectively. While we consider one-flavor case for notational simplicity, extension to multi-flavor cases is straightforward.

We divide the non-Abelian gauge field into a dynamical and external fields as

$$\mathcal{A}^{a\mu} = a^{a\mu} + \mathcal{A}_{\text{ext}}^{a\mu}. \quad (147)$$

Accordingly, the coupling between the quark and gluon fields in the covariant derivative is also divided as

$$\bar{\psi}(i\mathcal{D}_A)\psi = \bar{\psi}(i\mathcal{D})\psi - ig\bar{\psi}\phi^a(t^a)\psi. \quad (148)$$

Hereafter in this section, we frequently use the covariant derivative defined with the external chromo-field (without any suffix)

$$D^\mu \equiv \partial^\mu - ig\mathcal{A}_{\text{ext}}^{a\mu}t^a. \quad (149)$$

Based on the decomposition (147), one can also decompose the Yang-Mills part. As summarized in Appendix D.1, this procedure provides the kinetic and interaction terms of the fluctuation field a^a in the presence of the external field. Then, the kinetic terms, from which we get the propagators in the external field, are obtained as

$$\begin{aligned} \mathcal{L}_{\text{kin}} = & \bar{\psi}(i\mathcal{D} - m)\psi - \bar{c}^a(D^2)^{ac}c^c \\ & - \frac{1}{2}a_\mu^a \left(-(D^2)^{ac}g^{\mu\nu} + (1 - \frac{1}{\xi_g})D^{ab\mu}D^{bc\nu} + ig(\mathcal{F}_{\alpha\beta}^b\mathcal{J}^{\alpha\beta})^{\mu\nu}f^{abc} \right) a_\nu^c, \end{aligned} \quad (150)$$

where the ghost field and the gauge parameter (for the dynamical gauge field) are denoted as c^a and ξ_g , respectively. We also introduced the field strength tensor of the external field

$$\mathcal{F}^{a\mu\nu} \equiv \partial^\mu \mathcal{A}_{\text{ext}}^{a\nu} - \partial^\nu \mathcal{A}_{\text{ext}}^{a\mu} - ig(t^b)^{ac}\mathcal{A}_{\text{ext}}^{b\mu}\mathcal{A}_{\text{ext}}^{c\nu}, \quad (151)$$

and the generator of the Lorentz transformation $\mathcal{J}_{\alpha\beta}^{\mu\nu} = i(\delta_\alpha^\mu\delta_\beta^\nu - \delta_\beta^\mu\delta_\alpha^\nu)$. Using those quantities, we can write the spin interaction term as $(\mathcal{F}_{\alpha\beta}^b\mathcal{J}^{\alpha\beta})^{\mu\nu} = \mathcal{F}^{b\alpha\beta}\mathcal{J}_{\alpha\beta}^{\mu\nu} = 2i\mathcal{F}^{b\mu\nu}$. The interaction vertices in the external field are summarized in Appendix D.1.

While we have not assumed any specific configuration of the external field in the above arrangement, we now focus on the covariantly constant external field which is introduced as an extension of constant Abelian fields that satisfy $\partial_\lambda F_{\mu\nu} = 0$. For this extension, we require that a covariant derivative of the field strength tensor vanishes as follows [107–115]

$$D_\lambda^{ab}\mathcal{F}_{\mu\nu}^b = 0. \quad (152)$$

To find a solution for this condition, we evaluate a quantity $[D_\lambda, D_\sigma]^{ab}\mathcal{F}_{\mu\nu}^b$ in two ways. First, the above condition immediately leads to $[D_\lambda, D_\sigma]^{ab}\mathcal{F}_{\mu\nu}^b = 0$. On the other hand, the commutator can be written by the field strength tensor and the structure constant. Therefore, the covariantly constant field satisfies a condition

$$f^{abc}\mathcal{F}_{\mu\nu}^b\mathcal{F}_{\lambda\sigma}^c = 0. \quad (153)$$

Since the four Lorentz indices are arbitrary, this condition is satisfied only when the contractions of the color indices vanish. Therefore, we find the solution in a factorized form

$$\mathcal{F}_{\mu\nu}^a = \mathcal{F}_{\mu\nu}n^a, \quad (154)$$

where n^a is a vector in the color space and is normalized as $n^a n^a = 1$. On the right-hand side of Eq. (154), the vector n^a represents the color direction, while an Abelian-like field $\mathcal{F}^{\mu\nu}$ does not carry the color index and only quantifies the magnitude of the external field.

Accordingly, the external gauge field in the covariant derivative (149) is also factorized into the color direction and the magnitude. As explained in Appendix D.2, the color structures in the covariant derivatives are diagonalized as

$$D^{ij\mu} = \delta^{ij} (\partial^\mu - iw_i \mathcal{A}_{\text{ext}}^\mu), \quad (155a)$$

$$D^{ab\mu} = \delta^{ab} (\partial^\mu - iv^a \mathcal{A}_{\text{ext}}^\mu), \quad (155b)$$

where the first and second lines are for the fundamental and adjoint representations, respectively. Note that the Einstein summation convention is not applied to the color indices represented with the Roman alphabets. For $N_c = 3$, the effective color charges w_k have the three components

$$w^k = \frac{g}{\sqrt{3}} \sin\left(\frac{2}{3}k\pi - \theta\right), \quad k = 1, 2, 3. \quad (156)$$

As shown in Eq. (564), the color direction θ is specified by the second Casimir invariant. The effective color charges v^a for the adjoint representation are given by

$$\begin{aligned} v^a &= \frac{g}{2} \sin\left(\frac{2}{3}a\pi - \theta_{\text{ad}}\right), & a = 1, 2, 3, \\ v^a &= -\frac{g}{2} \sin\left(\frac{2}{3}a\pi - \theta_{\text{ad}}\right), & a = 5, 6, 7, \\ v^a &= 0, & a = 4, 8. \end{aligned} \quad (157)$$

Again, the color direction θ_{ad} is given by a gauge-invariant form (569). Similarly, we also get the diagonal form of the spin-interaction term

$$ig(\mathcal{F}_{\alpha\beta}^b \mathcal{J}^{\alpha\beta})^{\mu\nu} f^{abc} = v^a \delta^{ac} (\mathcal{F}_{\alpha\beta} \mathcal{J}^{\alpha\beta})^{\mu\nu}. \quad (158)$$

With the help of these simplifications, we will obtain the resummed propagators in the covariantly constant fields below, which goes along the procedure in the previous sections for the Abelian field.

3.4.1 Resummed quark propagator

In the covariantly constant field, the kinetic term of the quark field is given as

$$\bar{\psi}^i (i\not{D}^{ij} - m)\psi^j = \bar{\psi}^i i\delta^{ij} (\not{\partial} - iw^i \mathcal{A}_{\text{ext}} - m)\psi^j. \quad (159)$$

This means that the interaction with the external field does not cause a rotation of the color carried by the fermion, and thus that the color index only provides additive degrees just like the flavor index (within QCD). We can still use the Fock-Schwinger gauge for the Abelian-like field $\mathcal{F}^{\mu\nu}$ in Eq. (154). Therefore, the resummed propagator is obtained simply by using Eq. (124) with the replacement of the coupling constant (156) as

$$q_f \rightarrow -w^i. \quad (160)$$

Explicitly, the Fourier transformation of the quark propagator $\mathcal{S}^{ij}(x, y|\mathcal{A}_{\text{FS}}) = \langle 0|T\psi^i(x)\bar{\psi}^j(y)|0\rangle$ reads

$$\mathcal{S}^{ij}(p|\mathcal{A}_{\text{FS}}) = \delta^{ij} S^i(p|\mathcal{A}_{\text{FS}}), \quad (161)$$

where $S^i(p|\mathcal{A}_{\text{FS}})$ denotes the fermion propagator (124) with the effective charge, $-w^i$. The Einstein notation is not applied to the index i . We should introduce the Schwinger phase as in the Abelian case [cf., Eq. (113)], which now has the color index in the diagonal form. Therefore, we have

$$\mathcal{S}^{ij}(x, y|\mathcal{A}_{\text{ext}}) = \delta^{ij} e^{i\Phi_A^i} \mathcal{S}^i(x - y|\mathcal{A}_{\text{FS}}), \quad (162)$$

where $\mathcal{S}^i(x - y|\mathcal{A}_{\text{FS}})$ is the coordinate representation of $\mathcal{S}^i(p|\mathcal{A}_{\text{FS}})$ and Φ_A^i is the Schwinger phase (114).

3.4.2 Resummed ghost propagator

The covariant derivative in the adjoint representation, is diagonal in the color structure as well. Therefore, each diagonal component of the ghost propagator is also obtained from the propagator (143) for charged scalar particles in the Abelian field. This amounts to the replacement of the coupling constant (157) as

$$q_f \rightarrow -v^a. \quad (163)$$

Explicitly, we have

$$\mathcal{G}_{\text{ghost}}^{ab}(p|\mathcal{A}_{\text{FS}}) = \delta^{ab} G^a(p|\mathcal{A}_{\text{FS}}), \quad (164)$$

where $G^a(p|\mathcal{A}_{\text{FS}})$ denotes the scalar propagator (143) with the effective charge $-v^a$. According to the discussion around Eq. (142), the Schwinger phase should be introduced. This is simply done with the replacement of the charge as in the fermion propagator mentioned just above (but for the adjoint representation).

One should remember that the ghost and the Klein-Gordon fields have different statistics: The ghost fields anticommute with each other. Therefore, one should put a minus sign to each ghost loop as in the familiar Feynman rules without external fields.

3.4.3 Resummed gluon propagator

Finally, we examine the gluon propagator in the Feynman gauge (for the dynamical fields). Setting $\xi_g = 1$ in the Lagrangian (150), the kinetic term reads

$$\mathcal{L}_{\text{Feynman}} = -\frac{1}{2} a_\mu^a \delta^{ac} \{ -(D^2) g^{\mu\nu} + v^a (\mathcal{F}_{\alpha\beta} \mathcal{J}^{\alpha\beta})^{\mu\nu} \} a_\nu^c. \quad (165)$$

Interactions with the covariantly constant external field do not induce color rotations. Therefore, the color structure of the resummed gluon propagator is factorized as

$$\mathcal{D}_{\mu\nu}^{ac}(p|\mathcal{A}_{\text{ext}}) = \delta^{ac} \mathcal{D}_{\mu\nu}^{(a)}(p|\mathcal{A}_{\text{ext}}). \quad (166)$$

By using the trick discussed below Eq. (107), the equation of motion for the gluon propagator in the momentum space is obtained as

$$\left[-(p - v^a \mathcal{A}_{\text{ext}}(p))^2 g^{\mu\nu} - v^a (\mathcal{F}_{\alpha\beta} \mathcal{J}^{\alpha\beta})^{\mu\nu} \right] \mathcal{D}_{\nu\sigma}^{(a)}(p|\mathcal{A}_{\text{ext}}) = i \delta_\sigma^\mu, \quad (167)$$

where summation of the color index is not assumed. Because of the covariance in the this expression, the gluon propagator again transforms with the same Schwinger phase as the quark and ghost propagators do.

The propagator is formally given by the inverse of the operator in Eq. (167), i.e.,

$$\mathcal{D}_{\mu\nu}^{(a)}(p|\mathcal{A}_{\text{ext}}) = -i \left[(p - v^a \mathcal{A}_{\text{ext}}(p))^2 \mathbb{1} - v^a (\mathcal{F}_{\alpha\beta} \mathcal{J}^{\alpha\beta}) \right]_{\mu\nu}^{-1} = i \Delta_{\mu\nu}^{(a)}(p|\mathcal{A}_{\text{ext}}). \quad (168)$$

Similar to the case of the fermion propagator, we have exponentiated the inverse operator by the use of the proper-time integral

$$\Delta_{\mu\nu}^{(a)}(p|\mathcal{A}_{\text{ext}}) = \frac{1}{i} \int_0^\infty ds e^{-is(p - v^a \mathcal{A}_{\text{ext}}(p))^2} \left[e^{-isv^a \mathcal{F}_{\alpha\beta} \mathcal{J}^{\alpha\beta}} \right]_{\mu\nu}. \quad (169)$$

At this point, one can easily confirm that the above propagator reduces to the free propagator $\mathcal{D}_{\text{free}}^{(a)\mu\nu}(p) = -\frac{i}{p^2}g^{\mu\nu}$ in the vanishing field limit. Now, we adopt the FS gauge for the Abelian part of the covariantly constant field $\mathcal{A}_{\text{ext}}^\mu$. Then, the resummed gluon propagator obeys an equation

$$-\left[\left(p^2 + \frac{(v^a)^2}{4} \mathcal{F}^{\alpha\beta} \mathcal{F}_\beta^\gamma \frac{\partial}{\partial p^\alpha} \frac{\partial}{\partial p^\gamma} \right) g^{\mu\nu} + v^a (\mathcal{F}_{\alpha\beta} \mathcal{J}^{\alpha\beta})^{\mu\nu} \right] \Delta_{\nu\sigma}^{(a)}(p|\mathcal{A}_{\text{FS}}) = \delta_\sigma^\mu. \quad (170)$$

As explained in Appendix B.4, this equation can be solved by using an ansatz in the same manner as that we have done for the fermion propagator in Sec. 3.2.2. In fact, after the replacement of the effective color charge $q_f \rightarrow -v^a$, the gluon propagator can be written in terms of $X_{\mu\nu}(s)$ and $Y(s)$ already given in Eqs. (123b) and (123c), respectively. Namely, the resummed gluon propagator in the Feynman gauge is obtained as

$$\mathcal{D}_{\mu\nu}^{(a)}(p|\mathcal{A}_{\text{FS}}) = i\Delta_{\mu\nu}^{(a)}(p|\mathcal{A}_{\text{FS}}) = \int_0^\infty ds e^{-ip_\alpha X^{\alpha\beta}(s)p_\beta + Y(s)} \exp[-isv^a (\mathcal{F}_{\alpha\beta} \mathcal{J}^{\alpha\beta})]_{\mu\nu}. \quad (171)$$

Compared with the fermion propagator in Eq. (123a), the exponential factor, $\exp(-isq_f F_{\alpha\beta} \sigma^{\alpha\beta}/2)$, is replaced by $\exp(-isv^a (\mathcal{F}_{\alpha\beta} \mathcal{J}^{\alpha\beta}))_{\mu\nu}$. This replacement originates from the difference between the spin degrees of freedom of fermions and the gluons, which should manifest themselves in the Zeeman effects. We will explicitly see this point below after the decomposition of the gluon propagator into the Landau levels.

We shall closely look into the gluon spectrum and the spin structure encoded in the propagator (171) as we did in Sec. 3.2.3 for fermions. We again work in the Lorentz frame where the electric and magnetic fields are parallel/antiparallel to each other. Then, the expressions of $X^{\mu\nu}(s)$ and $Y(s)$ are simplified to those in Eqs. (125) and (126) with the replacement of the charge $q_f \rightarrow -v^a$. To decompose the exponential factor in Eq. (171), we introduce two antisymmetric tensors

$$\epsilon_{\parallel}^{\mu\nu} = \begin{pmatrix} & & -1 & \\ & 0 & & \\ & 0 & & \\ 1 & & & \end{pmatrix}, \quad \epsilon_{\perp}^{\mu\nu} = \begin{pmatrix} & & & 0 \\ & & 1 & \\ & -1 & & \\ 0 & & & \end{pmatrix}, \quad (172)$$

and separate the electric and magnetic components of the field strength tensor as $\mathcal{F}^{\mu\nu} = \mathcal{E}\epsilon_{\parallel}^{\mu\nu} - \mathcal{B}\epsilon_{\perp}^{\mu\nu}$. Since those antisymmetric tensors are orthogonal to each other and have properties $\epsilon_{\parallel\sigma}^\mu \epsilon_{\parallel}^{\sigma\nu} = g_{\parallel}^{\mu\nu}$ and $\epsilon_{\perp\sigma}^\mu \epsilon_{\perp}^{\sigma\nu} = -g_{\perp}^{\mu\nu}$, one can arrange the even- and odd-power terms in the form

$$\exp[-isv^a (\mathcal{F}_{\alpha\beta} \mathcal{J}^{\alpha\beta})]_{\mu\nu} = \cosh(2v^a \mathcal{E}s) g_{\parallel}^{\mu\nu} + \sinh(2v^a \mathcal{E}s) \epsilon_{\parallel}^{\mu\nu} + \cos(2v^a \mathcal{B}s) g_{\perp}^{\mu\nu} - \sin(2v^a \mathcal{B}s) \epsilon_{\perp}^{\mu\nu}. \quad (173)$$

The gluon propagator is then given by

$$\mathcal{D}_{\mu\nu}^{(a)}(p) = \int_0^\infty ds \frac{\exp[-isv^a (\mathcal{F}_{\alpha\beta} \mathcal{J}^{\alpha\beta})]_{\mu\nu}}{\cos(v^a \mathcal{B}s) \cosh(v^a \mathcal{E}s)} \exp\left(-i \frac{p_{\perp}^2}{v^a \mathcal{B}} \tan(v^a \mathcal{B}s) - i \frac{p_{\parallel}^2}{v^a \mathcal{E}} \tanh(v^a \mathcal{E}s) \right), \quad (174)$$

where the exponential factor is understood to be decomposed as already shown in Eq. (173). Similar to the case of the fermion propagator, there is an extended duality between the electric and magnetic fields [cf. Eq. (129)]. Namely, the gluon propagator (174) is invariant under the simultaneous interchanges

$$(\mathcal{B}, p_{\perp}^\mu, g_{\perp}^{\mu\nu}, \epsilon_{\perp}^{\mu\nu}) \longleftrightarrow (i\mathcal{E}, p_{\parallel}^\mu, g_{\parallel}^{\mu\nu}, i\epsilon_{\parallel}^{\mu\nu}). \quad (175)$$

Below, we shall elaborate the gluon propagator with a magnetic component without an electric component. The propagator with an electric component can be deduced from the expression with

a magnetic component owing to the extended duality (175). To use the generating function of the Laguerre polynomial (131), we introduce a variable²¹

$$z = -e^{2i|v^a \mathcal{B}|s}. \quad (176)$$

Then, the tangent appearing in Eq. (174) is rewritten as

$$\exp\left(-i\frac{p_\perp^2}{v^a \mathcal{B}} \tan(v^a \mathcal{B}s)\right) = \exp\left(-\frac{u_\perp}{2}\right) \exp\left(\frac{u_\perp z}{z-1}\right), \quad (177)$$

where $u_\perp = -2p_\perp^2/|v^a \mathcal{B}|$ as in the case of the fermion propagator. Then, the last exponential factor in Eq. (177) can be decomposed into polynomials of z by the use of the generating function (131). In addition, all of the trigonometric functions appearing in the gluon propagator (174) can be rewritten by z . Therefore, after some arrangements, the gluon propagator in the covariantly constant magnetic field is found to be

$$\begin{aligned} \mathcal{D}^{(a)\mu\nu}(p) &= 2e^{-\frac{u_\perp}{2}} \sum_{n=0}^{\infty} (-1)^n \hat{\mathcal{B}}_n^{\mu\nu} \int_0^\infty ds e^{-is(p_\parallel^2 - (2n-1)|v^a \mathcal{B}|) - \epsilon s} \\ &= 2ie^{-\frac{u_\perp}{2}} \sum_{n=0}^{\infty} \frac{(-1)^n \hat{\mathcal{B}}_n^{\mu\nu}}{p_\parallel^2 - (2n-1)|v^a \mathcal{B}|}, \end{aligned} \quad (178)$$

$$\hat{\mathcal{B}}_n^{\mu\nu} = L_n(u_\perp) \mathcal{Q}_+^{\mu\nu} - L_{n-1}(u_\perp) g_\parallel^{\mu\nu} + L_{n-2}(u_\perp) \mathcal{Q}_-^{\mu\nu}. \quad (179)$$

We promise again that the Laguerre polynomials with negative indices vanish, i.e., $L_{-1} = 0 = L_{-2}$, and introduce new operators $\mathcal{Q}_\pm^{\mu\nu} = (g_\perp^{\mu\nu} \pm is^a \epsilon_\pm^{\mu\nu})/2$ with $s^a = \text{sgn}(-v^a \mathcal{B})$.²²

The pole positions in Eq. (178) specify the gluon dispersion relations as $(p^0)^2 = (p^3)^2 + (2n-1)|v^a \mathcal{B}|$. This is nothing but the spectrum of spin-1 particles in a magnetic field that results from the Landau quantization and the Zeeman effect (cf. Fig. 4). Especially, the ground state ($n=0$) takes a negative value, $(p^0)^2 = p_z^2 - |v^a \mathcal{B}|$, when $p_z^2 < |v^a \mathcal{B}|$. In this case, the energy $p^0 = \sqrt{p_z^2 - |v^a \mathcal{B}|}$ is a pure imaginary number, indicating the presence of a tachyonic mode called the Nielsen-Olesen instability [62, 116, 117].

The operators $\mathcal{Q}_\pm^{\mu\nu}$ work as the helicity-projection operators for the transverse polarization modes. Those operators have the eigenvectors $\varepsilon_\pm^\mu = (0, 1, \pm is^a, 0)/\sqrt{2}$ that have unit eigenvalues $\mathcal{Q}_\pm^{\mu\nu} \varepsilon_{\pm\nu} = \varepsilon_\pm^\mu$ and are orthogonal to the other eigenvectors $\mathcal{Q}_\pm^{\mu\nu} \varepsilon_{\mp\nu} = 0$. The eigenvectors are nothing but the circular polarization vectors with the spin directions oriented along the magnetic field. This helicity projection is also evident in the energy levels: The terms proportional to $\mathcal{Q}_\pm^{\mu\nu}$ correspond to the lower and higher energy levels in the Zeeman splitting for a given n (as schematically shown in Fig. 4 *albeit* for the nonrelativistic case). The second term in Eq. (179) corresponds to the longitudinal mode. The spin direction is perpendicular to the magnetic field, so that the energy level is not shifted by the Zeeman effect. When computing gauge-invariant quantities, this term is expected to be canceled out with the ghost contribution given in Sec. 3.4.2. We will explicitly confirm this cancellation in the derivation of the non-Abelian Heisenberg-Euler effective action in Sec. 6.3.1.

4 Heisenberg-Euler effective action

The previous sections were devoted to a review of the fundamental techniques of quantum field theories under strong electromagnetic fields. From this section, we are going to discuss applications of the

²¹In Eq. (132) for the fermion propagator, we chose $z = -e^{-2i|q_f \mathcal{B}|s}$ with an opposite sign in the exponential. This is because the bilinear $p_\alpha X^{\alpha\beta} p_\beta$ had an opposite sign stemming from the overall sign conventions in the free propagators.

²²The sign of the spin interaction depends on that of the (color) charge specified by the convention of the covariant derivative (146). In our conventions following those in a standard textbook [66], a particle carries a color charge, $-g$, while a fermion carries an electric charge, $+q_f$, as specified in the covariant derivative (73).

machinery to various physical phenomena. As the first and important application, we discuss the Heisenberg-Euler effective action for low-energy electromagnetic fields by including quantum corrections from the one-loop vacuum fluctuations. We then discuss the Schwinger mechanism signaled by an imaginary part of the effective action, which indicates the electron-positron pair production from vacuum driven by electric fields. We have already seen that the effect of external fields on propagation of charged particles is in general nonlinear in nature and becomes non-negligible even if the coupling to the external field is small when the magnitude of the external field is strong.

It was Heisenberg and Euler who for the first time constructed the effective action for the electromagnetic fields [1]. They obtained the effective action through the evaluation of the vacuum energy shift induced by electromagnetic fields before the systematic machinery of diagrammatic calculations or renormalization is established. Later, Schwinger applied the proper-time formalism, discussed in Sec. 3, to the field-theoretical derivation of the Heisenberg-Euler effective action [42]. Since then, quantum field theories in external fields have been developed in various directions.

This includes, for example, analyses for the fields with spacetime inhomogeneity, computation of the effective action beyond the one-loop level, and application to the other gauge theories such as QCD. Note also that the physical processes induced by an electric field are not static phenomena but are inevitably dynamical ones because of the energy injection to the system by the electric field. There have been a number of studies addressing the real-time dynamics of the pair production including the back-reactions [85, 118–124] (see also Refs. [34, 125–127] for reviews on the Heisenberg-Euler effective action, the Schwinger mechanism, and beyond).

Below, we first present a derivation of the Heisenberg-Euler effective action by utilizing the resummed propagators already obtained in the previous section (see also Ref. [89] for a review of the original derivation by Schwinger [42]). An analog of the Heisenberg-Euler effective action in QCD (and in the presence of both QCD and QED fields) will be discussed in Sec. 6. For now, we only briefly mention that the quark-loop contribution in the chromo-electric field was applied to the description of the quark and antiquark pair production in the color flux tubes [128, 129] and the particle production mechanism in the relativistic heavy-ion collisions [110, 130, 131]. See a review article [127] for more developments in the particle production in the early-time dynamics of the relativistic heavy-ion collisions that leads to the creation of the quark-gluon plasma and a recent review article [34] for particle production in various systems.

4.1 Resummed effective action

The effective action for the gauge fields $S_{\text{eff}} = \int d^4x \mathcal{L}_{\text{eff}}[A_\mu]$ is formally obtained through the path integration of the QED action with respect to the fermion field:

$$S_{\text{eff}}[A_\mu] = -i \ln \det(i\mathcal{D} - m) = -\frac{i}{2} \ln \det(\mathcal{D}^2 + m^2), \quad (180)$$

with $D_\mu = \partial_\mu + iq_f A_\mu$ for the external field A^μ . The electrical charge is negative for electrons ($q_f = -|e|$). Without the dynamical photon field, this corresponds to a series of the one-loop contributions (see Fig. 12).²³ Thus, together with the original Maxwell part $\mathcal{L}^{(0)} = -\frac{1}{4}F_{\mu\nu}F^{\mu\nu}$, we write the total effective Lagrangian as $\mathcal{L}_{\text{eff}} = \mathcal{L}^{(0)} + \mathcal{L}^{(1)}$. In the last equality of Eq. (180), we have used a relation $\det(i\mathcal{D} - m) = (-1)^d \det(i\mathcal{D} + m)$ obtained from the operation of the charge conjugation $C\mathcal{D}C^{-1} = -\mathcal{D}^T$ and $\det(-1) = (-1)^4 = 1$ in the four dimensions.

As discussed in Sec. 3.1, we can rewrite Eq. (180) by using the formula (101) with the proper time

²³As mentioned in the beginning of Sec. 5.3, Furry's theorem states that the odd-order diagrams vanish identically in charge-conjugation even environments and that only even-order diagrams contribute to the series [132].

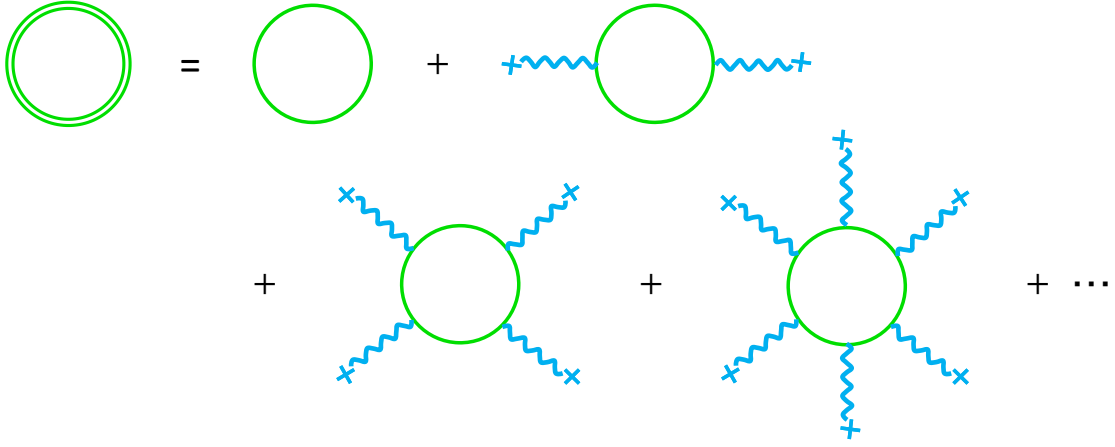


Figure 12: One-loop diagrams contributing to the Heisenberg-Euler effective action. The first diagram without external legs is subtracted in Eq. (181).

s:

$$\mathcal{L}^{(1')} = \frac{i}{2} \int_0^\infty \frac{ds}{s} e^{-\epsilon s} e^{-ism^2} \text{tr} \left[\langle x | e^{-i\hat{H}s} | x \rangle - \langle x | e^{-i\hat{H}_0 s} | x \rangle \right], \quad (181)$$

where we have recovered an infinitesimal parameter $\epsilon > 0$. We factorized the trace over the coordinate space in the form of the corresponding integral measure and will take the remaining trace over the Dirac spinor space denoted as “tr”. The “Hamiltonian” is defined as (see also Sec. 3.1)

$$\hat{H} = D^2 + \frac{q_f}{2} F^{\mu\nu} \sigma_{\mu\nu}, \quad (182)$$

where we defined the Hamiltonian without including the mass term. The mass dependence only appears in the overall exponential factor. We subtracted the contribution in the absence of external fields, which corresponds to the second term in Eq. (181) with the free Hamiltonian $\hat{H}_0 = \partial^2$.

So far, there is no restriction to the configuration of the external electromagnetic fields, and thus the action (181) is valid for electromagnetic fields with arbitrary spacetime dependence. Here, we first focus on a constant electromagnetic fields without a spacetime dependence, which yields the original Heisenberg-Euler effective action. The non-constant cases will be discussed in Sec. 4.1.2.

4.1.1 Constant electromagnetic fields

Consider the transition matrix element in the proper-time formalism:

$$K(x, x'; s | A_{\text{FS}}) \equiv \langle x | e^{-i\hat{H}s} | x' \rangle, \quad (183)$$

whose special case with $x = x'$ appears in Eq. (181). As we discussed in Sec. 3.1, we can compute this quantity by solving the Schrödinger-like equation with the proper time s being the evolution parameter, or in the path-integral formalism. This is the strategy taken by Schwinger (see Sec. III of Ref. [42] and a review part in Ref. [89]). However, we can in fact utilize the fermion propagator under external fields which was already computed in Sections 3.2.2 and 3.2.3. While this derivation of the Heisenberg-Euler effective action is somewhat different from those known in the literature, we can take the shortest path by the efficient use of our previous results.

One finds that a proper-time integral of $K(x, x'; s | A_{\text{FS}})$ corresponds to the coordinate representation of $\Delta(p|A)$ defined in Sec. 3.2.2 as

$$\Delta(x, x' | A_{\text{FS}}) = \frac{1}{i} \int_0^\infty ds e^{-im^2 s} K(x, x'; s | A_{\text{FS}}). \quad (184)$$

For constant electromagnetic fields in the Fock-Schwinger gauge, $\Delta(x, x'|A_{\text{FS}})$ becomes a function of the coordinate difference, and can be Fourier-transformed as

$$\Delta(x - x'|A_{\text{FS}}) = \int \frac{d^4 p}{(2\pi)^4} e^{ip(x-x')} \Delta(p|A_{\text{FS}}). \quad (185)$$

Consider the parallel field configuration as defined in Sec. 3.2.3. Since we already know the explicit form of the propagator for this configuration, let us utilize it for computation of the effective action. Recall that $\Delta(p|A_{\text{FS}})$ is defined by Eqs. (123b)–(123c). Using the explicit forms for the parallel field configurations in Eqs. (125) and (126), we find that

$$\begin{aligned} \Delta(p|A_{\text{FS}}) &= \frac{1}{i} \int_0^\infty ds e^{-im^2 s} (1 - \gamma^1 \gamma^2 \tan(q_f B s)) (1 + \gamma^0 \gamma^3 \tanh(q_f E s)) \\ &\quad \times \exp\left(i \frac{p_\perp^2}{q_f B} \tan(q_f B s) + i \frac{p_\parallel^2}{q_f E} \tanh(q_f E s)\right). \end{aligned} \quad (186)$$

Now, comparing Eqs. (184) and (185), it is straightforward to read off the expression for $\text{tr} \langle x | e^{-i\hat{H}s} | x \rangle$:

$$\begin{aligned} \text{tr} \langle x | e^{-i\hat{H}s} | x \rangle &= \text{tr} K(x, x; s | A_{\text{FS}}) \\ &= -\frac{i}{4\pi^2} \frac{q_f B}{\tan(q_f B s)} \cdot \frac{q_f E}{\tanh(q_f E s)}. \end{aligned} \quad (187)$$

The imaginary unit i in the last line comes from the Gaussian integration over $p_\parallel^\mu = (p^0, 0, 0, p^3)$. Remember that the gauge dependence of $\Delta(p|A)$ has been factorized in the form of the Schwinger phase as mentioned below Eq. (120). Therefore, the transition amplitude $\langle x' | e^{-i\hat{H}s} | x \rangle$ has the manifest gauge invariance in the coincidence limit $x' \rightarrow x$, and so does the Heisenberg-Euler effective Lagrangian represented by the closed loop diagrams in Fig. 12 (see also discussions in Sec. 3.2.1).

Plugging the matrix element (187) into Eq. (181), we arrive at the Heisenberg-Euler effective action $\mathcal{L}_{\text{HE}} = \mathcal{L}^{(0)} + \mathcal{L}^{(1)}$ for the parallel field configurations:

$$\mathcal{L}_{\text{HE}} = \frac{1}{2}(E^2 - B^2) + \frac{1}{8\pi^2} \int_0^\infty \frac{ds}{s} e^{-i(m^2 - i\epsilon)s} \left[\frac{(q_f E)(q_f B)}{\tanh(q_f E s) \tan(q_f B s)} - \frac{1}{s^2} \right], \quad (188)$$

where the second term in the bracket corresponds to the term in Eq. (181), which was added to subtract the one-loop contribution without the external fields. The first term in the bracket is nonlinear with respect to the electromagnetic fields E and B , which are multiplied by the electric charge q_f as they originate from the interactions with the fermion loop in Fig. 12. The effective action is invariant under the interchange $B \leftrightarrow iE$.

Recall that the quantities a and b , which are the eigenvalues of a field strength tensor $F_\mu{}^\nu$, correspond to E and B in the parallel configurations. Therefore, by replacing E and B in the previous results by a and b , we can easily obtain the Heisenberg-Euler effective action for arbitrary constant configurations as a function of those two Lorentz invariants [see Eqs. (4a) and (4b)]:

$$\mathcal{L}_{\text{HE}} = -\mathcal{F} + \frac{1}{8\pi^2} \int_0^\infty \frac{ds}{s} e^{-i(m^2 - i\epsilon)s} \left[\frac{(q_f a)(q_f b)}{\tanh(q_f a s) \tan(q_f b s)} - \frac{1}{s^2} \right]. \quad (189)$$

We can find several different representations of the Heisenberg-Euler effective action. Among them, the following expression is useful in the sense that the action looks obviously real (we will discuss the appearance of an imaginary part for $E \neq 0$ in the next subsection):

$$\mathcal{L}_{\text{HE}} = -\mathcal{F} - \frac{1}{8\pi^2} \int_0^\infty \frac{ds}{s} e^{-m^2 s} \left[q_f^2 \mathcal{G} \frac{\Re \left[\cosh \left\{ q_f s \sqrt{2(\mathcal{F} + i\mathcal{G})} \right\} \right]}{\Im \left[\cosh \left\{ q_f s \sqrt{2(\mathcal{F} + i\mathcal{G})} \right\} \right]} - \frac{1}{s^2} - \frac{2}{3} q_f^2 \mathcal{F} \right]. \quad (190)$$

Here we have replaced the proper time s by the “imaginary” proper time $s \rightarrow -is$ on the basis of the Wick rotation.

The last term in Eq. (190) has been added in order to renormalize the effective action: The last two terms cancel the divergent terms $1/s^2 + (2/3)q_f^2\mathcal{F}$ that appear in the expansion of the first term with respect to q_f (or weak fields) [cf. Fig. 12]. The term $1/s^2$ is the divergent vacuum energy density in the absence of external fields, which comes from a fermion loop without external fields attached. The term $(2/3)q_f^2\mathcal{F}$ has a quadratic dependence on the external fields that comes from the diagram with two insertions of the external field in Fig. 12. This diagram contains a logarithmic divergence and requires the charge renormalization. The higher-order diagrams do not yield UV divergences.²⁴ To regularize the ultraviolet divergences, one can simply insert a cutoff as the lower boundary of the integral region.²⁵ This simple regularization, called the proper-time regularization, is a gauge-invariant one, which serves as one of the merits of the proper-time method. We will discuss renormalization in more detail in Sec. 6.5.3.

All the calculations discussed so far can be equally applied to scalar QED defined by Eq. (138). By using the resummed propagator (143) for scalar fields, one can easily obtain the effective action for scalar QED [42]. The result is obtained as (see also Ref. [89] for a comparison between scalar and spinor QED)

$$\mathcal{L}_{\text{scalar QED}} = -\frac{1}{16\pi^2} \int_0^\infty \frac{ds}{s} e^{-is(m^2 - i\epsilon)} \left[\frac{(q_f a)(q_f b)}{\sinh(q_f a s) \sin(q_f b s)} - \frac{1}{s^2} \right]. \quad (191)$$

4.1.2 Beyond the Heisenberg-Euler effective action

The Heisenberg-Euler effective action is obtained for constant electromagnetic fields. However, as mentioned before, the very first expression (181) in the proper-time formalism is valid for any non-constant field. In many actual situations where strong fields appear, we encounter time-dependent and/or spatially inhomogeneous electromagnetic fields. Except for a few special cases some of which we will discuss later, it is difficult to exactly compute the effective actions in non-constant electromagnetic fields. We thus discuss some approximations.

A useful method is the derivative expansion with respect to the electromagnetic fields. Since we treat the spacetime variation of the electromagnetic fields (instead of the gauge potentials), it is again convenient to work in the Fock-Schwinger gauge introduced in Sec. 3.2.1. According to the gauge condition (109), one finds an identity

$$x'_\alpha F^{\alpha\mu}(x) = (1 + x'_\alpha \partial^\alpha) A_{\text{FS}}^\mu(x), \quad (192)$$

where $F^{\alpha\mu}(x) = \partial^\alpha A_{\text{FS}}^\mu(x) - \partial^\mu A_{\text{FS}}^\alpha(x)$ and $x'^\mu := x^\mu - x_0^\mu$. Performing a scale transformation $x'^\mu \rightarrow \sigma x'^\mu$, we have

$$\sigma x'_\alpha F^{\alpha\mu}(\sigma x' + x_0) = \frac{d}{d\sigma} [\sigma A_{\text{FS}}^\mu(\sigma x' + x_0)]. \quad (193)$$

If the field strength tensor takes a constant value $F^{\alpha\mu}(\sigma x' + x_0) = F^{\alpha\mu}$, one can easily integrate the both sides as

$$A_{\text{FS}}^\mu(x) = \int_0^1 d\sigma \sigma (x_\alpha - x_{0\alpha}) F^{\alpha\mu} = -\frac{1}{2} F^{\mu\alpha} (x_\alpha - x_{0\alpha}). \quad (194)$$

This reproduces the constant case (108). When the spacetime dependence is weak, one can organize a derivative expansion for the field strength tensor. Then, we are able to solve Eq. (193) on an order-by-order basis of the derivative expansion to express the gauge potential in terms of the electromagnetic

²⁴The actual degrees of divergences are lower than the superficial ones due to the gauge symmetry (see e.g., Ref. [66]).

²⁵Note that the proper time s has a mass dimension “-2”, and the small s regime corresponds to the ultraviolet regime.



Figure 13: Two-loop diagram contributing to the Heisenberg-Euler effective action.

fields as

$$\begin{aligned}
 A_\nu^{\text{FS}}(x) &= \frac{1}{2}(x^\mu - x_0^\mu)F_{\mu\nu}(x_0) + \frac{1}{3}(x^\mu - x_0^\mu)(x^\sigma - x_0^\sigma)\partial_\sigma F_{\mu\nu}(x_0) + \dots \\
 &= \sum_{n=0}^{\infty} \frac{(x^\mu - x_0^\mu)(x^{\sigma_1} - x_0^{\sigma_1}) \dots (x^{\sigma_n} - x_0^{\sigma_n})}{n!(n+2)} \partial_{\sigma_1} \partial_{\sigma_2} \dots \partial_{\sigma_n} F_{\mu\nu}(x_0). \quad (195)
 \end{aligned}$$

The leading term corresponds to the constant case (194). Since the spacetime derivative ∂_μ has a mass dimension, it must be accompanied by a characteristic scale in the system, the electron mass m_e . The derivative expansion is a good approximation when the ratio ∂_μ/m_e is small enough. In other words, the Heisenberg-Euler effective action is valid when the electromagnetic fields are almost constant over the Compton wavelength $\lambda = 1/m_e$, which means $\partial_\mu/m_e \ll 1$. The effective action in the derivative expansion will read

$$\mathcal{L}_{\text{eff}} = \mathcal{L}_{\text{HE}}(F_{\mu\nu}) + \partial_\sigma F_{\alpha\beta} \partial_\rho F_{\gamma\delta} \mathcal{L}_1^{\sigma\alpha\beta\gamma\delta\rho}(F_{\mu\nu}) + \dots \quad (196)$$

Calculation of the first correction to the Heisenberg-Euler action was explicitly done in Refs. [133–135]. In Ref. [136], the result of the derivative expansion is compared with that from a solvable model.

Another direction to go beyond the Heisenberg-Euler effective action is evaluation of the higher-loop contributions. In deriving the Heisenberg-Euler effective action, we treated the electromagnetic field as an external background field and did not treat it as a dynamical field. Let us allow a photon field to fluctuate around the external classical field: $A^\mu = A_{\text{ext}}^\mu + a^\mu$. Then the path-integration over a photon fluctuation field a_μ in addition to the electron field ψ , $\bar{\psi}$ formally defines the effective action including higher-loop effects. The two-loop diagram is just an electron's one-loop diagram with a virtual photon propagator connecting two points on the loop (see Fig. 13). Compared to the one-loop diagram, this contribution is down by a factor of e^2 due to the coupling between a photon and an electron loop (at two vertices).²⁶ It is in general difficult to exactly evaluate the higher-loop contributions, but a conjecture about the imaginary part of the effective action (corresponding to the pair production rate as discussed in the next subsection) has been suggested based on the results of strong-coupling and weak-field case [90]. A concise review about higher-loop effects including relevant references is available in Ref. [137] (see also Refs. [138, 139]).

²⁶In QED with a small coupling constant, the higher-loop contributions are of course small compared to the one-loop contribution. However, when the coupling is relatively large as in QCD near the QCD scale, the higher-loop effects will become important.

Since the physical degrees of freedom of the effective action are the low-energy electromagnetic fields, the effective action cannot be directly applied to the situations involving energetic particles. For example, if we wish to understand how energetic electrons or photons propagate in strong electromagnetic fields, we need to evaluate the self-energy diagrams that have two external lines with a large energy/momentum flow together with infinitely many insertions of external fields. Such an investigation also goes beyond the Heisenberg-Euler effective action. We will discuss this direction in Sec. 5.

4.2 Schwinger mechanism in constant fields

4.2.1 Pair production from purely electric fields

As we will see shortly, the Heisenberg-Euler effective action acquires an imaginary part in a non-vanishing electric field ($E \neq 0$). According to the Cutkosky's cutting rule, the presence of an imaginary part implies creation of on-shell particles out of, otherwise, virtual states forming bubble diagrams in vacuum. While the real part of the Heisenberg-Euler effective action describes electromagnetism, the production of electron-positron pairs in the electric fields is signaled by the emergence of an imaginary part [1, 140]. This is often called the Schwinger mechanism [42].

In the presence of an external background field A_{ext} , the vacuum state in the infinite past $|\Omega_{\text{in}}\rangle$ is in general not equal to the one in the infinite future $|\Omega_{\text{out}}\rangle$. In the present case, an electric field will inject energy to the system in the form of the acceleration of the particles and antiparticles, which causes the mixing between the positive- and negative-energy states. Therefore, the definition of vacuum does not uniquely persist throughout the time evolution, and the vacuum persistence probability (VPP) $|\langle\Omega_{\text{out}}|\Omega_{\text{in}}\rangle_{A_{\text{ext}}}|^2$ is not equal to unity. In fact, the transition amplitude defines the effective action

$$\langle\Omega_{\text{out}}|\Omega_{\text{in}}\rangle_{A_{\text{ext}}} = e^{iW[A_{\text{ext}}]} = \exp\left\{i \int d^4x \mathcal{L}_{\text{eff}}[A_{\text{ext}}]\right\}. \quad (197)$$

Accordingly, the origin of the transition from the initial to final vacua is identified with the particle-antiparticle pair production process from the vacuum, and is signaled by the emergence of the imaginary part in the effective action. Then, we define the complement of the VPP as

$$\Gamma \equiv 1 - |\langle\Omega_{\text{out}}|\Omega_{\text{in}}\rangle_{A_{\text{ext}}}|^2 = 1 - e^{-2\Im m W[A_{\text{ext}}]}.$$

When the imaginary part of the effective action is small, we have

$$\Gamma \simeq 2 \Im m W[A_{\text{ext}}] = 2 \int d^4x \Im m \mathcal{L}_{\text{eff}}[A_{\text{ext}}]. \quad (198)$$

Note that the VPP is by definition different from the pair production rate (PPR) that should be defined with the expectation value of the number operator for the produced pairs. Indeed, the direct computation of the PPR has shown that those quantities have similar but different forms [141, 142]. We will come back to this issue in Sec. 4.2.2.

Here, we compute the imaginary part of the Heisenberg-Euler effective action (188) in a constant electromagnetic field at the one-loop level. In Eq. (188), the integrand for the proper-time integral has the form $ds s^{-1} f(s)$ with $f(s)$ being a real-valued and even function of s . Thus, its imaginary part may be written as

$$\begin{aligned} \Im m \mathcal{L}_{\text{HE}} &= \frac{1}{2i} \cdot \frac{1}{8\pi^2} \left[\int_0^\infty \frac{ds}{s} e^{-i(m^2 - i\epsilon)s} f(s) - \int_0^\infty \frac{ds}{s} e^{i(m^2 + i\epsilon)s} f(s) \right] \\ &= \frac{1}{2i} \cdot \frac{1}{8\pi^2} \int_{-\infty}^\infty \frac{ds}{s} e^{-i(m^2 - i\text{sgn}(s)\epsilon)s} f(s). \end{aligned} \quad (199)$$

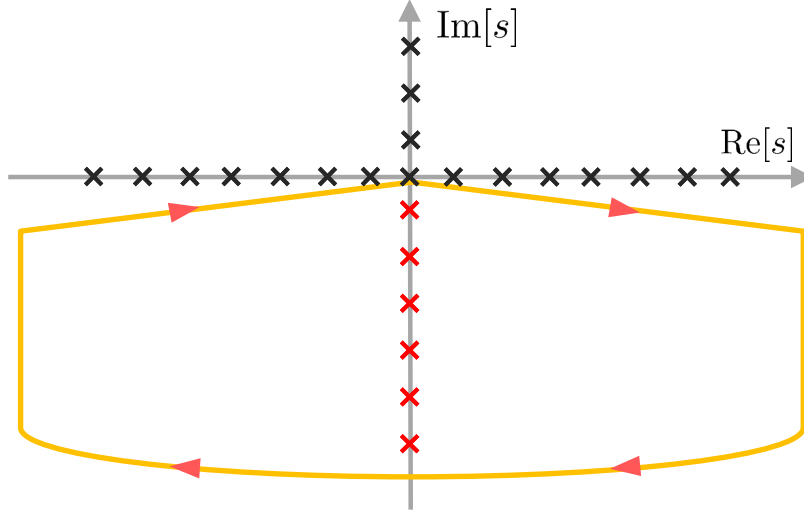


Figure 14: Contour on the complex s -plane with the poles on the real and imaginary axes induced by a magnetic and electric field, respectively. The path along the real axis is inclined with the ϵ parameter.

We can easily perform this integral with the help of the residue theorem. A positive-definite mass term ($m^2 > 0$) suggests closing the contour in the lower-half plane (see Fig. 14). When analytically continued to the complex s -plane, the function $f(s)$ has poles on the real and imaginary axes. The pole on the origin is common to the free-theory contribution, and is nothing to do with the Schwinger mechanism. Since the poles on the real axis are avoided due to the inclined contour specified by the ϵ parameter, we should only pick up the poles on the imaginary axis at $s = -in\pi/(q_f E)$ ($n = 1, 2, \dots$).²⁷ Note that the poles on the real and imaginary axes are induced by a magnetic and electric field, respectively. This means that only an electric field is responsible for the emergence of the imaginary part. Therefore, we first consider the case only with an electric field. Effects of a magnetic field on the pair production will be examined in Sec. 4.2.3 for QED and in Sec. 6 for QCD.

The effective action in the presence of an electric field is easily obtained from the previous result (188) by taking the limit $B \rightarrow 0$:

$$\begin{aligned} \mathcal{L}_{\text{HE}}(E \neq 0, B = 0) &= \frac{1}{2}E^2 + \frac{1}{8\pi^2} \int_0^\infty \frac{ds}{s^3} e^{-im^2 s} f_e(s), \\ f_e(s) &\equiv s^2 \lim_{B \rightarrow 0} f(s) = q_f E s \coth(q_f E s) - 1. \end{aligned} \quad (200)$$

At this point, we took the limit $\epsilon \rightarrow 0$ (though this is not mandatory), since the integrand damps fast enough $f_e(s)/s^3 \rightarrow q_f E/s^2$ as $s \rightarrow \infty$. Then, we obtain the integral value as the summation of the residues

$$\begin{aligned} \Im m \mathcal{L}_{\text{HE}}(E \neq 0, B = 0) &= \frac{1}{2i} \cdot \frac{1}{8\pi^2} \cdot (-2\pi i) \sum_{n=1}^{\infty} \text{Res} \left[\frac{e^{-im^2 s}}{s^3} f_e(s) \right]_{s=-i \frac{n\pi}{q_f E}} \\ &= \frac{|q_f E|^2}{8\pi^3} \sum_{n=1}^{\infty} \frac{1}{n^2} e^{-\frac{E_c}{E} n\pi}, \end{aligned} \quad (201)$$

where the summation over n can be represented by the dilogarithm function $\text{Li}_2(z) = \sum_{n=1}^{\infty} z^n/n^2$ as

²⁷The poles in the lower half plane should be denoted by $s = -in\pi/|q_f E|$ ($n = 1, 2, \dots$) when $q_f E < 0$. We will, however, suppress the symbol of absolute value for notational simplicity.

$\Im m\mathcal{L}_{\text{HE}}(E) = q_f^2 E^2 / (8\pi^3) \text{Li}_2(e^{-\frac{E_c}{E}\pi})$. Here, we defined the critical electric field [1]

$$E_c \equiv \frac{m^2}{|q_f|}. \quad (202)$$

The first term of this series ($n = 1$) in Eq. (201) was obtained by Sauter in the form of the transmission rate between the negative- and positive-energy states [140]. Then, Heisenberg and Euler recognized the correspondence between the Sauter's result and the imaginary part of their effective Lagrangian at $n = 1$ as well as the presence of the other sequential poles (though an explicit result was not shown) [1]. Sometime later, the complete form of the series was systematically derived by Schwinger [42].

The imaginary part of the effective Lagrangian is a monotonically increasing function of E and finally increases quadratically without the exponential suppression when the electric field exceeds the critical value E_c . Then, the VPP decreases significantly. The exponential factor crucially controls the visibility of the Schwinger mechanism in real systems. Nevertheless, even an infinitesimally weak electric field induces a finite imaginary part, though it is exponentially suppressed, which implies that the Schwinger mechanism is a quantum phenomenon. The Schwinger mechanism is also an inherently non-perturbative phenomenon because the exponential factor $\exp(-\frac{E_c}{E}n\pi) = \exp(-n\pi\frac{m^2}{q_f E})$ behaves non-analytically when the coupling constant q_f is formally sent to zero, which cannot be obtained from a finite order of the perturbative theory with respect to q_f . In other words, the pair production can be captured only when the infinitely many insertions of external fields are summed.

One may wonder whether the imaginary part of the effective Lagrangian provides the pair production rate (PPR) per unit spacetime volume. Since the PPR is essentially an expectation value of the number operator, there is no *a priori* reason that it coincides with the imaginary part representing the overlap of the vacua. It should be emphasized that an explicit comparison between those quantities has shown that they are indeed given by different expressions [141, 142]. The PPR is actually given by the first term ($n = 1$) of the Schwinger's formula (201). Therefore, the two quantities approximately agree with each other only when the exponential factors are small. Those facts also suggest that one cannot interpret the n -th term in the summation as a probability for production of n pairs: If it were so, the expectation value computed with this would-be probability should agree with the PPR. The difference between the VPP and PPR has been discussed repeatedly in pedagogical ways [122, 143–146], although there are yet confusions in some literature. We will come back to this issue in terms of the quantum-tunneling picture in the next subsection.

While the pair production has been discussed in the seminal papers [1, 42] on the basis of the effective-action formalism as above, it actually may not be a suitable framework for explicitly describing the real-time dynamics of the pair production process since the fermionic degrees of freedom are already integrated out. To define the particle number and discuss the dynamical issues including the (kinetic) momentum distribution of the produced particles, one needs to begin with defining the particle and antiparticle states by the Bogoliubov transformation at each step of the time evolution [109, 141–143, 147], since an amount of energy injected by the electric field inevitably causes the mixing between the positive- and negative-energy states. In other words, one needs to define the vacuum that varies dynamically. For those dynamical issues, the reader is referred to, e.g., Refs. [34, 122, 127, 148] and references therein.

One can similarly compute the imaginary part for scalar QED [42]. The imaginary part of the effective action (191) reads

$$\Im m\mathcal{L}_{\text{scalar QED}} = \frac{|q_f E|^2}{16\pi^3} \sum_{n=1}^{\infty} \frac{(-1)^{n-1}}{n^2} e^{-\frac{E_c}{E}n\pi}. \quad (203)$$

Here, q_f and m in the critical field $E_c = m^2/|q_f|$ are the charge and mass of the complex scalar field. The result looks similar to Eq. (201) for spinor QED except for an overall numerical factor and the

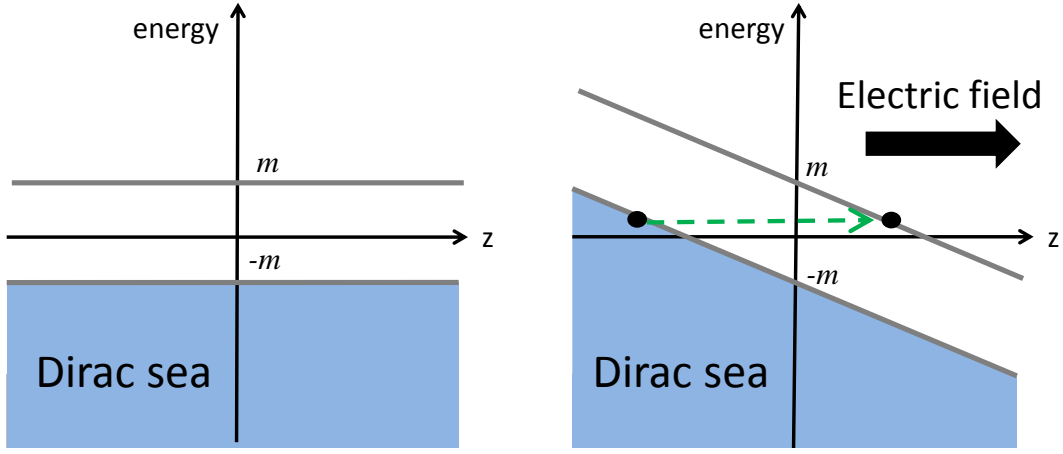


Figure 15: The static Dirac sea at $E = 0$ (left) and the Schwinger mechanism as tunneling through the mass gap at $E \neq 0$ (right).

alternating sign of each term in the summation over n . The statistics in the Gaussian path integral, which is now for the two degrees of freedom in a complex scalar field without the Grassmann nature, is reflected in the numerical factor, while the absence of the spin-interaction term in the Hamiltonian (182) is reflected in both the numerical factor and the alternating sign (see Ref. [89] for the comparisons). As we mention in Sec. 4.2.3, a difference between scalar and spinor QED is more prominent when there is a coexisting magnetic field [89]. This is because the ground-state energy is lowered in spinor QED owing to the Zeeman shift that reduces the exponential suppression.

4.2.2 Schwinger mechanism as quantum tunneling

The result in Eq. (201) can be interpreted in an intuitive way as quantum tunneling. First of all, the critical electric field E_c in Eq. (202) is consistent with the minimum work necessary for exciting a virtual pair of a fermion and an antifermion to become a real excitation: Namely, the E_c satisfies a relation $2|q_f|E_c d \sim 2m$ where $d \sim 1/m$ is the Compton length of a fermion and $2m$ on the right-hand-side is the threshold energy.²⁸ Next, the result is understood as the tunneling probability for a fermion in the Dirac sea going out across the mass gap [128]. When an electric field is generated by a potential $A^0 = -Ez$, the dispersion relation of a charged fermion is tilted in the coordinate space as $(\epsilon + q_f E z)^2 - |\mathbf{p}|^2 = m^2$. For the notational simplicity, we take $q_f E > 0$. For fixed values of ϵ , $|\mathbf{p}_\perp| \neq 0$ and $p_z = 0$, one can define the tilted band gap $z_- < z < z_+$ with $z_\pm = (-\epsilon \pm m_T)/q_f E$ and the transverse mass $m_T = \sqrt{m^2 + |\mathbf{p}_\perp|^2}$ (see Fig. 15). This band is the mass gap region and plays a role of a potential barrier for the pair production. The Dirac sea is occupied in the vacuum and the quantum tunneling will take place from the top of the occupied state at $z = z_-$ to the vacant state at $z = z_+$. Therefore, the tunneling probability in the WKB approximation, for a fermion carrying a transverse momentum \mathbf{p}_\perp , is given by

$$P(\mathbf{p}_\perp) = \exp\left(-2 \int_{z_-}^{z_+} dz \sqrt{m_T^2 - (\epsilon + q_f E z)^2}\right) = \exp\left(-\frac{\pi m_T^2}{q_f E}\right). \quad (204)$$

The tunneling probability defines the pair production rate (PPR) κ and vacuum persistence proba-

²⁸This is consistent with the validity condition for the Heisenberg-Euler effective action that the electromagnetic field should be almost constant over the scale of the Compton wavelength.

bility (VPP) in the summation and product forms, respectively, as

$$\kappa = \frac{1}{TL^3} \sum_{\text{spin}} \sum_{t,z} \sum_{\mathbf{p}_\perp} P(\mathbf{p}_\perp), \quad (205a)$$

$$|\langle \Omega_{\text{out}} | \Omega_{\text{in}} \rangle_{A_{\text{ext}}} |^2 = \prod_{\text{spin}} \prod_{t,z} \prod_{\mathbf{p}_\perp} [1 - P(\mathbf{p}_\perp)] = \exp \left[\sum_{\text{spin}} \sum_{t,z} \sum_{\mathbf{p}_\perp} \ln [1 - P(\mathbf{p}_\perp)] \right], \quad (205b)$$

where TL^3 is the spacetime volume. The summation over transverse coordinates x, y is replaced by the summation over $\mathbf{p}_\perp = (p_x, p_y)$. Then, we take summation over small cells $(\Delta p_x, \Delta p_y, \Delta z, \Delta t)$ and replace each sum as²⁹

$$\sum_{\mathbf{p}_\perp} = L^2 \int \frac{d^2 \mathbf{p}_\perp}{(2\pi)^2}, \quad \sum_t = \frac{m_T}{\pi} \int dt, \quad \sum_z = \frac{q_f E}{2m_T} \int dz. \quad (206)$$

On the basis of these replacements, we immediately get the PPR

$$\kappa = \frac{|q_f E|^2}{4\pi^3} \exp \left(-\frac{\pi m^2}{q_f E} \right). \quad (207)$$

As for the VPP, we define γ such that $|\langle \Omega_{\text{out}} | \Omega_{\text{in}} \rangle_{A_{\text{ext}}} |^2 = \exp(-TL^3\gamma)$. Then, we have

$$\gamma = \frac{|q_f E|^2}{4\pi^3} \sum_{n=1}^{\infty} \frac{1}{n^2} \exp \left(-\frac{\pi m^2}{q_f E} n \right), \quad (208)$$

where the summation appears from an expansion $\ln(1-x) = -\sum_{n=1}^{\infty} \frac{1}{n} x^n$. The tunneling picture reproduces the VPP obtained from the Heisenberg-Euler effective action, i.e., $\gamma = 2\Im m \mathcal{L}_{\text{HE}}(E \neq 0, B = 0)$ [cf. Eqs. (197) and (201)] [128, 144, 149–151]. As mentioned earlier, the PPR κ coincides with the first term of the series ($n = 1$) in the VPP γ , which confirms the previous observations [122, 141, 142, 144–146]. This point is already clear in Eq. (205b) where the expansion of the logarithm results in the summation over n :

$$\gamma = \sum_{n=1}^{\infty} \frac{1}{n} \left[\frac{1}{TL^d} \sum_{\text{spin}} \sum_{t,z} \sum_{\mathbf{p}_\perp} P(\mathbf{p}_\perp)^n \right]. \quad (209)$$

This expression is valid for a general $(d+1)$ -dimensional case with the $(d-1)$ -dimensional transverse-momentum integral $\sum_{\mathbf{p}_\perp}$. Thus, κ is given by the first term in γ in any dimensions. For example, the corresponding expressions in the $(1+1)$ -dimension are obtained as

$$\kappa = \frac{q_f E}{2\pi} e^{-\frac{\pi m^2}{q_f E}}, \quad (210a)$$

$$\gamma = \frac{q_f E}{2\pi} \sum_{n=1}^{\infty} \frac{1}{n} e^{-\frac{\pi m^2}{q_f E} n}, \quad (210b)$$

where there is no spin degrees of freedom or transverse-momentum integral in the pure $(1+1)$ dimensions. Without the transverse-momentum integral, the order of the inverse n factor is lower than that in the four dimensional case (208). This makes a prominent difference in the strong-field limit or the small-mass

²⁹One can evaluate the summation as follows [128, 149]: A pair creation occurs in a volume $\Delta t \Delta z$. According to the uncertainty principle, we have $\Delta t = 2\pi/\omega = \pi/m_T$, where the frequency ω counts how often the tunneling occurs and the threshold energy is given as $2m_T$. The longitudinal extension Δz is given by the penetration length through the barrier $\Delta z = z_+ - z_- = 2m_T/q_f E$.

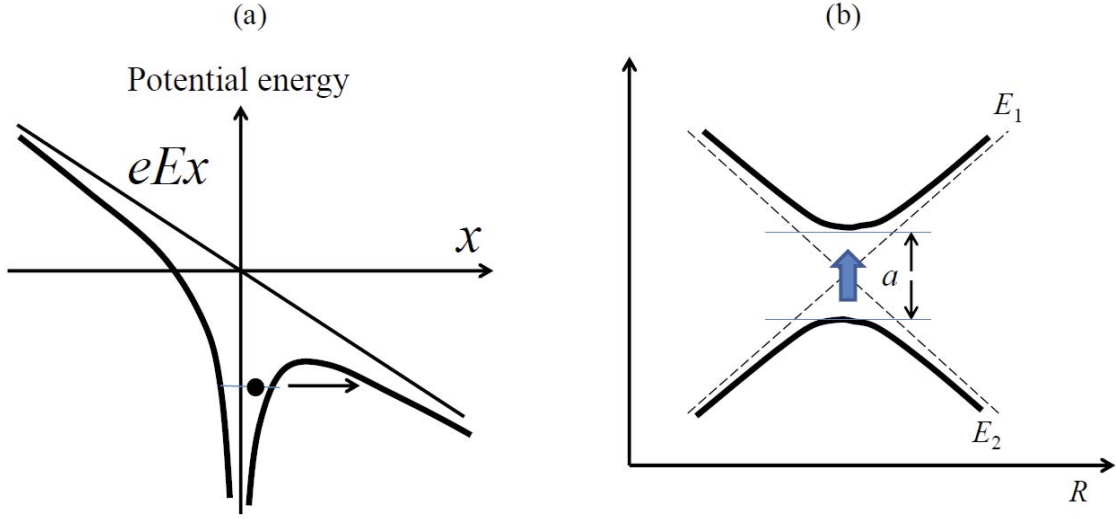


Figure 16: (a) Ionization of a hydrogen atom by a static electric field. A bound electron can escape from the atom due to quantum tunneling. (b) Diabatic transition between two states at the avoided crossing point with an energy gap a . Figure shows two energy levels that typically appear in a system of two molecules at a distance R .

limit where the exponential factor reduces to unity as $m^2/(q_f E) \rightarrow 0$. In such a limit, the summation over n diverges in the (1+1) dimensions [146, 152, 153], while it remains finite in the (3+1) dimensions where $\sum_{n=1}^{\infty} 1/n^2 = \zeta(2) = \pi^2/6$. Note that $P(\mathbf{p}_{\perp})$ itself depends on the spatial dimensions via the transverse momentum in m_T . Creating pairs with nonzero transverse momentum causes an additional energy cost for filling up the transverse phase space. Accordingly, a suppression of $P(\mathbf{p}_{\perp})^n$ by a Gaussian factor $\exp[-n\pi|\mathbf{p}_{\perp}|^2/(q_f E)]$ results in a faster convergence of the series in a higher-dimensional system. Once again, one should note that the n -th term cannot be interpreted as the probability of n -pair production [154]. In the context of the worldline instanton, the summation over n is reproduced from a periodic motion along a classical path parametrized by the proper time [155, 156] (see also Ref. [90]).

The tunneling interpretation of the Schwinger mechanism reminds us of the essential similarity with the other related phenomena. For example, as shown in Fig. 16, the PPR is very similar to the ionization rate of a hydrogen atom by a static electric field E [157, 158] (see also Refs. [125, 159, 160] for more details)

$$P_{\text{ionization}} = \exp\left(-\frac{2m^2 e^5}{3E}\right), \quad (211)$$

and the Landau-Zener formula for non-adiabatic transition [161, 162] (see also section 90 in Ref. [45])

$$P_{\text{LZ}} = \exp\left(-\frac{2\pi a^2}{\left|\frac{d}{dt}(E_1 - E_2)\right|}\right), \quad (212)$$

where a is the closest energy gap between two levels (corresponding to the mass gap in the Schwinger mechanism), and $\frac{d}{dt}(E_1 - E_2)$ is a velocity of the energy-level difference under the change of time dependent parameters (corresponding to the applied electric field). The interested reader is referred to Ref. [163] for further discussions about similarities to condensed matter systems.

4.2.3 Effects of magnetic fields on the pair production

When both electric and magnetic fields are applied in vacuum, we need to generalize the formula (201) to include effects of a magnetic field. This extension can be simply carried out by the use of the Lorentz invariants a and b . Therefore, we start with the expression in Eq. (189).

The integrand has poles both on the real and imaginary axes in the s plane. Nevertheless, the actual integral contour is displaced downward from the real axis because of the infinitesimal imaginary part $i\epsilon$, as discussed below Eq. (199). Therefore, we can again close the integral contour in the lower half plane as shown in Fig. 14, and only need to pick up the residues on the imaginary axis. Then, we obtain the the imaginary part of the effective Lagrangian and the PPR κ :

$$2\Im \mathcal{L}_{\text{HE}}(a, b) = \frac{q_f^2}{4\pi^2} \sum_{n=1}^{\infty} \left[\frac{ab}{n} \coth\left(\frac{b}{a}n\pi\right) \right] e^{-\frac{E_c}{a}n\pi}, \quad (213a)$$

$$\kappa(a, b) = \frac{q_f^2}{4\pi^2} \left[ab \coth\left(\frac{b}{a}\pi\right) \right] e^{-\frac{E_c}{a}\pi}. \quad (213b)$$

As discussed above, the PPR κ coincides with the first term of the series ($n = 1$) in $2\Im \mathcal{L}_{\text{HE}}(a, b)$. Of course, this result reproduces the previous result (201) for purely electric fields in the limit $a \rightarrow E$, $b \rightarrow 0$, and the imaginary part vanishes when $a \rightarrow 0$.

Now, we fix the magnitude of the electric field $|\mathbf{E}|$, and investigate how a magnetic field modifies the PPR as compared to the one in a purely electric field. To see a dependence on the relative direction between the electric and magnetic fields, we first consider two particular configurations in which those fields are applied in parallel/antiparallel and orthogonal to each other.

When a magnetic field is applied in *parallel/antiparallel* to the electric field, we have $a = |\mathbf{E}|$ and $b = |\mathbf{B}|$. Compared with the purely electric field configuration, we get a finite b without changing the value of a . Thus, there is no modification in the exponent. The prefactor, shown between the square brackets, should be compared with $E^2/\pi n^2$ in the purely electric case. It has a positive first derivative with respect to b for any positive value $a, b > 0$. One can also show that the prefactor is always larger than $E^2/\pi n^2$. This means that the PPR (213) is enhanced as we increase the magnetic-field strength (with a fixed electric field). Therefore, the *parallel/antiparallel* magnetic field ‘‘catalyzes’’ the pair production. We will discuss a more intuitive picture below on the basis of the Landau-level decomposition.

When a magnetic field is applied in *orthogonal* to the electric field, i.e., when $\mathcal{G} = 0$ (with $\mathcal{F} \neq 0$), any field configuration reduces to either a purely electric or magnetic field by a Lorentz transform. Since the production rate is a Lorentz scalar, we may evaluate the PPR in such a particular frame and then go back to the original frame in which we have the orthogonal field configuration. When $\mathcal{F} < 0$, i.e., $|\mathbf{B}| < |\mathbf{E}|$, we have $a = \sqrt{|\mathbf{E}^2 - \mathbf{B}^2|}$ and $b = 0$. Therefore, we observe a pair production induced by a purely electric field with a strength a . Because of a smaller value $a < |\mathbf{E}|$, the PPR is suppressed by the magnetic field. As we increase the magnetic field (with the electric field fixed), we have a smaller a and observe a stronger suppression. As we further increase the magnetic field, we reach the ‘‘crossed-field’’ configuration specified by $\mathcal{F} = \mathcal{G} = 0$, where the electric and magnetic fields have the same strengths. In this case, we have $a = b = 0$, and thus observe no pair production eventually. With a stronger magnetic field, we have $\mathcal{F} > 0$, i.e., $a = 0$, so that we again find a vanishing PPR, $\kappa = 0$. Therefore, the *orthogonal* magnetic field suppresses the PPR and eventually prohibits the pair production when $|\mathbf{E}| \leq |\mathbf{B}|$.

In the presence of an orthogonal magnetic field, a fermion and antifermion drift in the same direction perpendicular to both the electric and magnetic fields. This cyclic motion prevents the pair from receding from each other along the electric field, which may cause a suppression of the PPR. In the beginning of Sec. 4.2.2, we discussed a semi-classical picture in which the critical electric field strength

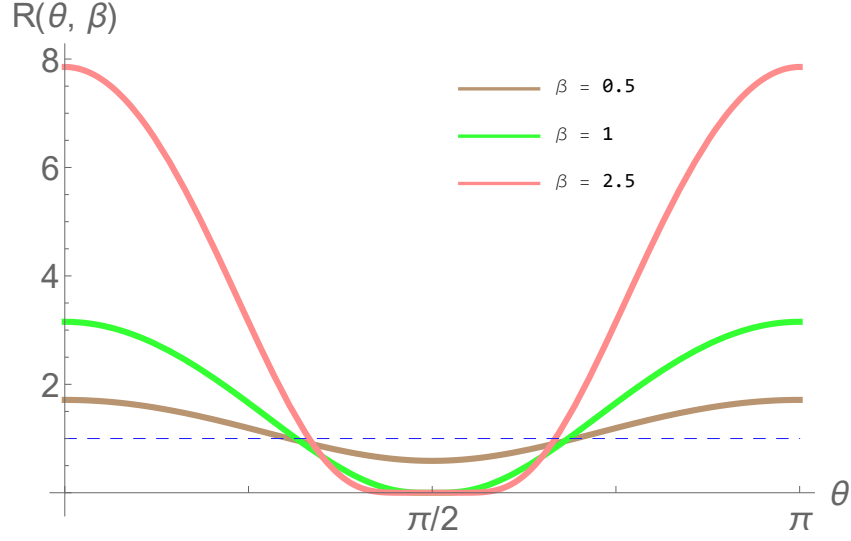


Figure 17: Effects of a magnetic field on the pair production rate as a function of the relative strength $\beta \equiv |B/E|$ and the relative angle θ .

is interpreted as a minimum strength that can separate a pair over the Compton length. Therefore, it is reasonable to compare the Compton length ($= 1/\sqrt{|q_f E_c|}$) and the cyclotron radius ($= 1/\sqrt{|q_f B|}$). In the presence of a magnetic field stronger than the electric field, i.e., $|B| > |E_c|$, the cyclotron radius is smaller than the Compton length. Therefore, there is little chance for a pair to separate over the Compton length. However, in the opposite case, i.e., $|B| < |E_c|$, the cyclotron radius is larger than the Compton length. Therefore, a pair can be separated from each other along the electric field in a cycle of the cyclotron motion, which may lead to a finite, *albeit* suppressed, production rate.

For a general configuration with an arbitrary angle, we shall see a numerical plot. We focus on the PPR at the critical field strength $|E| = E_c$ which may be of our interest. Nevertheless, qualitative features shown below do not depend on the magnitude of the electric field. We investigate the ratio

$$R(\theta, \beta) \equiv \frac{\kappa(a, b)}{\kappa(E, 0)} = \frac{ab \coth\left(\frac{b}{a}\pi\right) e^{-\frac{|E|}{a}\pi}}{(2\pi)^{-1} E^2 e^{-\pi}}, \quad (214)$$

where we set $|E| = E_c$. This ratio can be regarded as a function of a normalized magnetic-field strength $\beta \equiv |B/E|$ and of the relative angle θ between the directions of the electric and magnetic fields. In Fig. 17, all the aforementioned behaviors at $\theta = 0, \pi$ and $\theta = \pi/2$ are confirmed, and are interpolated for a general value of θ .

4.2.4 Landau-level decomposition

In the presence of a parallel/antiparallel magnetic field, we could pursue the origin of the enhanced PPR by performing the Landau-level decomposition as we have done in Sec. 3.2.3. To see this, we apply the formula (131) to the transition amplitude (187) before performing the transverse-momentum integral [89]. Then, we get

$$\text{tr} \langle x | e^{-i\hat{H}s} | x \rangle = 2 \sum_{n=0}^{\infty} g_n(q_f B) (-z)^n \left[\frac{i}{(2\pi)^2} \frac{\pi q_f E}{i \tanh(q_f E s)} \right], \quad (215)$$

where we defined $z = -\exp(-2iq_f B s)$. The longitudinal-momentum integral has been performed, and the transverse-momentum integral is left in the form

$$g_n(q_f B) = 2 \int \frac{d^2 p_{\perp}}{(2\pi)^2} e^{\frac{p_{\perp}^2}{q_f B}} (-1)^n L_n^{-1} \left(-\frac{2p_{\perp}^2}{|q_f B|} \right). \quad (216)$$

Note that the transition amplitude (215) has been completely factorized into the longitudinal (1+1)-dimensional part and the residual transverse part. The integral in the transverse part can be performed as³⁰

$$g_n(q_f B) = \frac{|q_f B|}{4\pi} (-1)^n \int_0^\infty d\zeta e^{-\zeta/2} L_n^{-1}(\zeta) = \kappa_n \frac{|q_f B|}{2\pi}. \quad (217)$$

Interestingly, the dependence on the integer index appears only in the prefactor $\kappa_n = 2 - \delta_{n0}$. This result for the integral is actually anticipated, since this is nothing but the Landau degeneracy factor for each Landau level with κ_n being the spin degeneracy factor for the two-fold degenerated hLLs.

Inserting those expressions into Eq. (181), we obtain the Heisenberg-Euler Lagrangian in the Landau-level representation:

$$\mathcal{L}_{\text{HE}} = \frac{1}{2}(E^2 - B^2) + \sum_{n=0}^{\infty} \left[\kappa_n \frac{|q_f B|}{2\pi} \right] \frac{i}{4\pi} \int_0^\infty \frac{ds}{s} e^{-i(m_n^2 - i\epsilon)s} \frac{q_f E}{\tanh(q_f E s)}. \quad (218)$$

We did not include the counter term since there is no divergence in the imaginary part. We have defined the effective mass $m_n^2 = m^2 + 2n|q_f B|$ where the integer n specifies the Landau level as foreseen from our prior experience that the Landau levels are eigenstates of the Dirac operator. The covariant form is obtained by simple replacements, $|\mathbf{E}|, |\mathbf{B}| \rightarrow a, b$ (see Ref. [89]). In fact, one can directly obtain the same result from the Heisenberg-Euler action for the parallel field configuration (188) by the use of an identity [89, 139]:

$$\cot x = i \left[1 + \frac{2e^{-2ix}}{1 - e^{-2ix}} \right] = i \sum_{n=0}^{\infty} \kappa_n e^{-2inx}. \quad (219)$$

We can also apply this formula to $\cot(q_f b s)$ in the HE effective action (189) for arbitrary configuration to get an infinite-series expansion. As long as $b \neq 0$, there exists such a Lorentz frame where it reduces to the magnetic-field strength $b = |\mathbf{B}|$. Accordingly, we can identify the Landau levels in that frame. One may not consider the vanishing limit $b \rightarrow 0$ naively, since this limit and the summation over n do not commute with each other. The physical origin of this non-commutativity comes from the fact that the infinite tower of the discrete Landau levels collapses into the ground state if a finite value of b is not maintained in the summation form. Therefore, the summation must be performed before the limit $b \rightarrow 0$.

As before, one can obtain the imaginary part of the effective Lagrangian by picking up the residues of the poles on the imaginary axis:

$$\begin{aligned} 2\Im m \mathcal{L}_{\text{HE}} &= \frac{2}{2i} \cdot \frac{i}{4\pi} \sum_{n=0}^{\infty} \left[\kappa_n \frac{|q_f B|}{2\pi} \right] \Im m \int_0^\infty \frac{ds}{s} e^{-i(m_n^2 - i\epsilon)s} \frac{q_f E}{\tanh(q_f E s)} \\ &= \sum_{n=0}^{\infty} \left[\kappa_n \frac{|q_f B|}{2\pi} \right] \left[\frac{|q_f E|}{2\pi} \sum_{\sigma=1}^{\infty} \frac{1}{\sigma} e^{-\frac{E_c^n}{|\mathbf{E}|} \sigma \pi} \right]. \end{aligned} \quad (220)$$

Alternatively, one can again apply the expansion (219) to the previous results (213). Here, we have defined $E_c^n = m_n^2/|q_f|$ for each Landau level. Therefore, there is an infinite number of the ‘‘Landau-Schwinger limits’’ specifying the critical field strengths for the pair production. It is quite natural that the exponential suppression is stronger for the higher Landau level that has a larger energy gap

³⁰Putting $I_n := \int_0^\infty d\zeta e^{-\zeta/2} L_n^{-1}(\zeta)$, one can find a simple recursive relation $I_{n+1} = -I_n$ for $n \geq 1$. Use the derivative formula $dL_n^\alpha(\zeta)/d\zeta = -L_{n-1}^{\alpha+1}(\zeta)$ and the recursive relation $L_{n+1}^{\alpha-1}(\zeta) = L_{n+1}^\alpha(\zeta) - L_n^\alpha(\zeta)$ to show this relation, and then $L_0^{-1}(\zeta) = 1$ and $L_1^{-1}(\zeta) = -\zeta$ to get $I_0 = 2$ and $I_1 = -4$, respectively [164].

measured from the Dirac sea. Once we overcome the exponential suppression with a sufficiently strong electric field, the PPR is enhanced by the Landau degeneracy factor [89, 152, 153]. This is because an energy provided by the external electric field can be consumed only to fill up the one-dimensional phase space along the magnetic field, and the degenerated transverse phase space can be filled without an additional energy cost. Although we have an infinite tower of the Landau levels, the hLL contributions are exponentially suppressed in the strong magnetic field limit. In contrast, the LLL contribution is still enhanced by the Landau degeneracy factor as long as $E \gtrsim E_c^{n=0}$. The simple point is that the lowest critical field strength, $E_c^{n=0} = m^2/|q_f|$, is independent of the magnetic field, while the higher levels are gapped out in a strong magnetic field. This one-dimensional structure of the phase space is the origin of the catalysis phenomenon, leading to the enhancement of the PPR found in Fig. 17.³¹ Consistent with those observations, the expression between the second brackets in the Landau-Schwinger formula (220) is nothing but the (1+1)-dimensional Schwinger formula. The pair production in the parallel electric and magnetic fields was recently studied with the kinetic equation from the Wigner-function formalism as well [165].

Now, it is a straightforward exercise to get the imaginary part for scalar QED [89]:

$$2\Im m\mathcal{L}_{\text{scalar QED}} = \left[\frac{|q_f B|}{2\pi} \right] \sum_{n=0}^{\infty} \left[\frac{|q_f E|}{2\pi} \sum_{\sigma=1}^{\infty} \frac{(-1)^{\sigma-1}}{\sigma} e^{-\frac{E_c^n}{|E|}\sigma\pi} \right]. \quad (221)$$

In addition to the alternating sign mentioned previously, there appear two-fold differences between spinor and scalar QED because of the absence of spin degrees of freedom. First, there is not a factor of κ_n without a spin degeneracy in each Landau level. Second, the critical field strength is now given by $E_c^n = \{m^2 + (2n+1)|q_f B|\}/|q_f|$ due to the absence of the Zeeman shift. The “zero-point energy”, that increases with $|q_f B|$, yields a huge difference in the exponential suppression factor. Thus, the Schwinger mechanism is suppressed in scalar QED as we increase the strength of the parallel magnetic field.

4.3 Schwinger mechanism beyond constant fields

4.3.1 Pair production from time-dependent electric fields

We have discussed the Schwinger mechanism in a constant electric field as a nonperturbative phenomenon. Recall that the pair production is described by the imaginary part of the Heisenberg-Euler effective action, and thus is diagrammatically represented as a one-loop diagram with a cut. Since there is no energy-momentum flow at each interaction vertex from a constant electric field, massive particles have a chance of becoming on-shell excitations only when their dispersion relations are modified by the infinitely many insertions. This is the rough understanding for the reason why the Schwinger mechanism is a nonperturbative process. When the electric field is time-dependent, however, the situation is qualitatively different. A generic time-dependent electric field $E(t)$ can be Fourier-transformed into a power spectrum $\tilde{E}(\omega)$. Thus, if the power spectrum has a large support above the threshold energy $\omega \gtrsim 2m$, particle production becomes possible with only a few insertions of electric fields. In other words, the pair production in a generic time-dependent electric field contains both nonperturbative and perturbative contributions.

If the characteristic energy ω_0 in the spectrum $\tilde{E}(\omega)$ is much *smaller* than m (meaning that we can ignore the time-dependence) and the strength of electric field E_0 at that energy is *larger* than the critical electric field E_c , the pair production predominantly occurs with the nonperturbative mechanism. On the other hand, if the characteristic energy ω_0 is much *larger* than m and the electric field E_0 at that

³¹In Sec. 7, we will discuss consequences of the effective dimensional reduction in more detail. One can get a covariant form by replacing E, B by a, b in Eq. (220), respectively. The quickest way to get the LLL contribution is to simply take the strong magnetic field limit $|B/E| \rightarrow \infty$ in Eq. (213).

energy is *smaller* than E_c , the pair production is mainly realized with the perturbative mechanism, i.e., a few insertions of electric fields. These two limiting cases are distinguished by the ‘‘Keldysh parameter’’ $\gamma_K^{(\text{time})}$ defined by

$$\gamma_K^{(\text{time})} \equiv \frac{\omega_0}{m} \cdot \frac{E_c}{E_0} = \frac{m\omega_0}{eE_0}, \quad (222)$$

where $\gamma_K^{(\text{time})} \ll 1$ and $\gamma_K^{(\text{time})} \gg 1$ correspond to nonperturbative and perturbative regimes, respectively. This dimensionless parameter, sometimes also called the adiabaticity parameter, was first introduced by Keldysh in the analysis of ionization of an atom by laser [166]. As mentioned before, ionization can take place in a static electric field due to quantum tunneling. Ionization is also possible by absorption of multiple photons which assists a bound electron to be liberated. These two cases correspond to nonperturbative and perturbative mechanisms, respectively. Such an interplay between the perturbative and nonperturbative mechanisms in the scalar and spinor QED was demonstrated by Brezin and Itzykson [154]. They computed particle creations from an oscillating electric field $E_z(t) = E_0 e^{i\omega_0 t}$ and obtained an approximate formula connecting the perturbative and nonperturbative regimes. Interestingly, they found that the exponential suppression in the production ratio (the leading $n = 1$ contribution in Eq. (201)) is now modified as

$$\exp \left[-\frac{\pi m^2}{eE_0} g(\gamma_K^{(\text{time})}) \right], \quad (223)$$

where $g(\gamma_K^{(\text{time})})$ is a smooth decreasing function with a boundary condition $g(0) = 1$. This reproduces the Schwinger’s formula and the perturbative result for $\gamma_K^{(\text{time})} \ll 1$ and $\gamma_K^{(\text{time})} \gg 1$, respectively. In fact, at large $\gamma_K^{(\text{time})}$, the $g(\gamma_K^{(\text{time})})$ behaves as $g(\gamma_K^{(\text{time})}) \sim (4\pi/\gamma_K^{(\text{time})}) \ln(2\gamma_K^{(\text{time})})$, so that the nonperturbative dependence $\propto 1/eE_0$ in the exponent is canceled and a perturbative power dependence is reproduced.

More recently, the authors of Ref. [167] have carefully investigated this interplay by using a pulsed electric field called the Sauter-type field. The electric field is oriented to the z -direction [$\mathbf{E} = (0, 0, E(t))$] and its time-dependence has a pulsed shape:

$$E(t) = \frac{E_0}{\cosh^2(t/\tau)}, \quad (224)$$

where E_0 is the peak value of the field and τ is the duration of the pulse. The Sauter-type field is one of the few examples with non-constant electromagnetic fields which allow us to solve the equation of motion to exactly compute the pair production rate.³² The Fourier transformation of the electric field (the power spectrum) is given by

$$\tilde{E}(\omega) = \frac{i\pi E_0 \tau^2 \omega}{\sinh \frac{\pi \tau \omega}{2}}, \quad (225)$$

which is plotted in Fig. 18 for a normalized frequency (putting $\pi\tau/2 = 1$). The characteristic spectrum $|\omega| \lesssim \frac{2}{\pi\tau}$ is determined by the time duration of the pulse τ . Therefore, a shorter pulse involves a wider spectrum that could contain the frequency above the threshold value $2m$ and could induce the pair production perturbatively. On the other hand, an electric field with a large τ has a sharp spectrum near $\omega \sim 0$ and will induce the nonperturbative pair production (the Schwinger mechanism). This expectation is explicitly verified by analytic results for the number density of produced pairs:

$$\frac{(2\pi)^3}{V} \frac{d^3 N}{dp^3} \rightarrow \begin{cases} \left(1 - \frac{p_z^2}{p_0^2}\right) \left| \frac{eE_0}{p_0^2} \right|^2 \frac{(\pi p_0 \tau)^4}{\pi^2 |\sinh(\pi p_0 \tau)|} & (\gamma_K^{(\text{time})} \gg 1) \\ \exp\left(-\frac{\pi m^2}{|eE_0|}\right) & (\gamma_K^{(\text{time})} \ll 1), \end{cases} \quad (226)$$

³²In fact, this is an alternative (and more direct) method for the calculation of the pair production rate. It is not easy to compute the effective action itself for electric fields with generic time dependences.

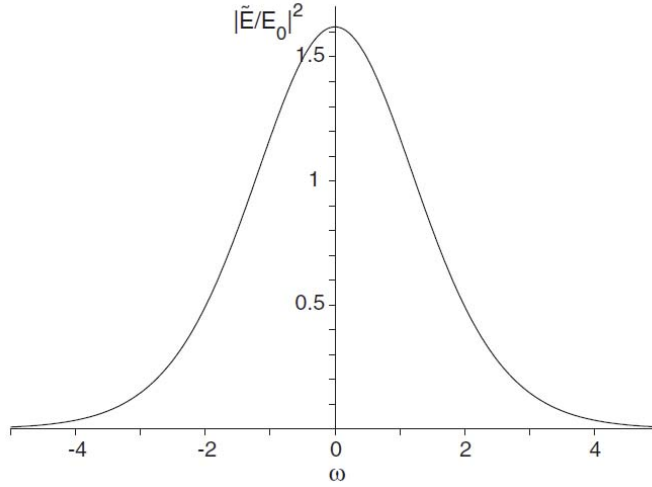


Figure 18: Spectrum $|\tilde{E}(\omega)/E_0|^2$ of the Sauter-type electric field for $\tau = 2/\pi$.

where the Keldysh parameter is now given by $\gamma_K^{(\text{time})} = \frac{m}{|\epsilon E_0| \tau}$. The result with $\gamma_K^{(\text{time})} \gg 1$ corresponds to the perturbative pair production from one photon, and is a good approximation when the pulse duration is small enough $\tau \ll 1/m$.

In recent years, another interesting development has been seen. Based on the observation discussed above, we can also think of superposition of two pulsed electric fields. In particular, it is interesting to consider the mixed situation where one pulsed field induces nonperturbative pair production while the other perturbative one:

$$E(t) = \frac{E_1}{\cosh^2(t/\tau_1)} + \frac{E_2}{\cosh^2(t/\tau_2)}. \quad (227)$$

Here, $E_1 \gg E_2$ and $\tau_1 \gg \tau_2$ and thus the first (second) term is for the strong and long (weak and short) pulse. In this case, even if E_1 has a subcritical strength $E_1 \ll E_c$, we can gain a large number of particle production due to the assist of the weaker short pulse. This kind of pair production is called the “dynamically assisted Schwinger mechanism” and was first discussed in Ref. [168]. Physically, the tunneling barrier is reduced thanks to the absorption of perturbative photons, and the pair production rate is significantly enhanced [169]. It was explicitly demonstrated that in the perturbative treatment of the short pulse around the long pulse, the pair production rate is indeed enhanced [170]. This opened up an interesting question what is the optimized pulse shape that maximizes the pair-creation rate. For example, it was recently found that the pair-creation rate strongly depends on the shape of the short (perturbative) pulse [171], effects of envelope profiles of laser fields were investigated in Ref. [172], and lastly, optimization of the pulse shape was discussed for rotating fields in Ref. [173].

In fact, there is a condensed matter analog of the dynamically assisted Schwinger mechanism. In semiconductor physics, photo absorption plays a fundamental role since it directly reflects the band structure of a bulk material. It has been known both theoretically and experimentally that the photo absorption rate is significantly modified if a strong slow electric field is applied to the semiconductor in such a way that the rate becomes finite even below the band gap energy and oscillates above the gap energy. This phenomenon, called the Franz-Keldysh effect [174, 175] (see also a review article [176]), has a similar situation as the dynamically assisted Schwinger mechanism since the absorptive photons correspond to perturbative electric fields which coexist with a slow strong electric field. Very recently, the Franz-Keldysh effect was formulated in QED and it was found that the similar interplay between the perturbative and nonperturbative pair production indeed occurs [177].

4.3.2 Pair production from spatially inhomogeneous electric fields

As we discussed above, the crucial point of time-dependent fields is that those fields are able to directly inject a significant amount of energy to the pairs of virtual excitations so that they can become real excitations over a smaller energy barrier. Those “hard” processes can occur within a short spacetime scale. Contrary, time-independent electric fields provide energies to the pairs only by consuming the electric energies for the acceleration of the pairs. This process, as a sequence of the “soft” interactions, requires a quantum coherence over a certain spatial length as well as the time duration before the virtual pairs acquire energy enough to become real particles. Therefore, the spatial profile of the electric fields is crucial for the realization of the pair production. This observation is consistent with the demand for the resummation of external-field insertions, which leads us to the Heisenberg-Euler effective action.

To understand the effects of spatial inhomogeneity, let us reexamine the condition for pair production to occur. For simplicity, we assume that the electric field is oriented to the z direction and has only z -dependence, $\mathbf{E} = (0, 0, E(z))$. The condition for the pair production to occur is that the work done by the electric field for the virtual pair is larger than the mass gap:

$$2 \int_0^\ell |q_f| E(z) dz \geq 2m. \quad (228)$$

For a given $E(z)$, we can determine the minimum length ℓ_{\min} by the length ℓ that satisfies the equality. The ℓ_{\min} will be short when $E(z)$ is large over a wide range of space, while it may be long for a weak electric field. However, the length ℓ cannot be too long because the pair is a (virtual) quantum fluctuation before the condition is satisfied. Typically, the formation length ℓ will be shorter than or of the order of the Compton wavelength $\lambda = 1/m$. In other words, in the tunneling picture, the Compton wavelength roughly corresponds to a typical penetration length in a mass gap region. Therefore, the pair production will be realized when the condition (228) is satisfied for the length scale $\ell \lesssim \lambda = 1/m$. When the electric field is spatially constant and present in the whole region of z , $E(z) = E_0 (> 0)$, the threshold condition reads $E_0 \ell = m/|q_f|$. For the length scale $\ell \lesssim \lambda = 1/m$, one finds that there is a minimum strength for the electric field: $E_0 \gtrsim E_c = (m/|q_f|)(1/\lambda) = m^2/|q_f|$. This is the critical field strength which we previously obtained. Notice that the minimum length ℓ_{\min} necessary for the pair production is given by $\ell_{\min} = (m/|q_f|)(1/E_0)$ and thus becomes shorter than the Compton wavelength for a super-critical field strength $E_0 \gtrsim E_c$.

Now let us turn to inhomogeneous electric fields. The simplest example is the case where the electric field is applied only in a finite extent as in a capacitor: $E(z) = E_0 > 0$ only for $-L < z < L$. Consider a strong (super-critical) electric field $E_0 \gtrsim E_c$. If the electric field is applied in a whole space, then the length ℓ for the pair production to occur is $\ell_{\min} = m/(|q_f|E_0) \lesssim \lambda = 1/m$. Therefore, if the extent L is larger than ℓ_{\min} , there will be a spatial region where the condition (228) will be satisfied and thus the pair production occurs. On the other hand, when L is shorter than ℓ_{\min} , it is not possible to satisfy the condition (228) and thus the pair production does not occur. This means that there is a critical extent L_{crit} for the onset of pair production and it is simply given by

$$L_{\text{crit}} = \frac{m}{|q_f|E_0}. \quad (229)$$

In fact, by exactly solving the Dirac equation with a finite-extent electric field, one can confirm the presence of the critical extent as explicitly demonstrated in Ref. [178] (see also Ref. [179] for the calculation in the worldline formalism and Ref. [180] for a recent analysis). When $E_0 = E_c$, the critical extent coincides with the Compton wavelength $L_{\text{crit}} = 1/m = \lambda$.

Next, consider the electric field with a generic but mild z -dependence [181]. Assuming that the electric field takes its maximum value at $z = 0$ and slowly decays to zero at large $|z|$, we may use the

following expansion of the electric field (for $z > 0$)

$$E(z) = E_0 + z \left. \frac{dE(z)}{dz} \right|_{z \sim 0} + \dots \quad (230)$$

The coefficient of the first derivative term is roughly evaluated as

$$\left. \frac{dE(z)}{dz} \right|_{z \sim 0} \sim -\frac{E_0}{\sigma},$$

with σ being a typical width of the profile. By using this expression, the work done by the electric field $\mathcal{W}(\ell) \equiv 2|q_f| \int_0^\ell E(z) dz$ is also expanded as $\mathcal{W}(\ell) = \mathcal{W}_0(\ell) + \mathcal{W}_1(\ell) + \dots$. Now if we take a ratio between the zeroth term $\mathcal{W}_0(\ell)$ and the first-derivative term $\mathcal{W}_1(\ell)$, we find that the result is expressed by the ratio between two characteristic length scales:

$$\left| \frac{\mathcal{W}_1(\ell)}{\mathcal{W}_0(\ell)} \right| = \frac{\frac{E_0}{\sigma} \frac{\ell^2}{2}}{E_0 \ell} = \frac{\ell}{2\sigma}. \quad (231)$$

When the ratio is small enough, the pair production occurs predominantly by the zeroth term, and we are able to ignore the effects of inhomogeneity. In this case, we can approximate ℓ as $\ell \sim \ell_{\min}$ which is determined for the electric field with an infinite extent. On the other hand, if the ratio is large enough, the derivative expansion breaks down and the effects of inhomogeneity is significant. Therefore, it is natural to define an inhomogeneity parameter in analogy with the Keldysh parameter for adiabaticity [155]:

$$\gamma_K^{(\text{space})} \equiv \frac{\ell_{\min}}{\sigma}. \quad (232)$$

Plugging the explicit form $\ell_{\min} = m/(|q_f|E_0)$ and introducing an inverse width $k = 1/\sigma$, one finds

$$\gamma_K^{(\text{space})} = \frac{mk}{|q_f|E_0}, \quad (233)$$

which has the same representation as the Keldysh adiabaticity parameter (222) under the replacement of the typical frequency ω_0 by the typical momentum scale k . If we take E_0 strong enough, the inhomogeneity parameter can become small even though the electric field has a narrow width. In such a case, we can forget about the effects of inhomogeneity and can use the ordinary formula of the Schwinger mechanism.

In the above case with mild z -dependences, the inhomogeneity parameter $\gamma_K^{(\text{space})}$ in Eq. (233) makes sense only for $\gamma_K^{(\text{space})} \ll 1$. However, it can be applied to more generic z -dependent electric fields. Similar to the case with time-dependent electric fields, the Sauter profile

$$E(z) = \frac{E_0}{\cosh^2 kz}$$

can be exactly treated [142], and the inhomogeneity parameter indeed plays the role of distinguishing the homogeneous case from the strongly inhomogeneous case [155, 182]. Since the Sauter profile has a width $1/k$, we define the condition for the pair production to occur as

$$|q_f| \int_{-\infty}^{\infty} E(z) dz \geq 2m. \quad (234)$$

The left-hand side yields $2|q_f|E_0/k$, and we find that the condition is rewritten as $\gamma_K^{(\text{space})} \leq 1$ with $\gamma_K^{(\text{space})}$ defined by Eq. (233). Therefore, the Sauter profile with $\gamma_K^{(\text{space})} > 1$ does not allow pair production,

and $\gamma_K^{(\text{space})} = 1$ corresponds to the critical value. Incidentally, the critical extent (229) for the capacitor also gives $\gamma_K^{(\text{space})} = 1$ under the identification $k = 1/L_{\text{crit}}$.

So far we discussed three examples of inhomogeneous electric fields: the capacitor-like profile, the mild decaying profile, and the Sauter profile. All these cases allow for the pair production depending on parameters characterizing the profiles (the magnitude at the peak E_0 and the inverse width k). In particular, the onset of pair production is equally specified by the inhomogeneity parameter $\gamma_K^{(\text{space})} = 1$. This brings us into awareness that there are in fact infinitely many profiles that can satisfy the condition (234). This is, of course, simply because the condition is written in terms of the integration over the space, and only the integral value matters. Then, one may ask if the spatial profiles obey any classification. Recently, the authors of Refs. [183, 184] found a similarity between the pair production and phase transitions in critical phenomena. Recall that the onset of pair production is expressed as a nonzero value of the imaginary part of the effective action $\Im m \mathcal{L}_{\text{eff}}$. The authors of Refs. [183, 184] regarded the imaginary part of the effective action as an order parameter for the pair production, and claimed that the notion of universality appears at the “critical point” $\gamma_K^{(\text{space})} = 1$. We shall write the electric fields as $E(z) = E_0 f'(u)$, where the normalized potential function f is an antisymmetric and monotonic function of $u = kz$. Then, this field indeed yields the imaginary part of the effective action around the critical point

$$\Im m \mathcal{L}_{\text{eff}} \sim \left[1 - (\gamma_K^{(\text{space})})^2 \right]^\beta, \quad (235)$$

with β being a critical exponent. The generic profiles $E(z)$ are subdivided into several “universality classes” depending on numerical values of β . Interestingly, the exponent β only depends on the large-scale behavior of the profile, and is insensitive to microscopic details. We also point out that the Landau-Zener transition, mentioned above as an analog of the Schwinger mechanism, was analyzed in terms of the Kibble-Zurek mechanism [185, 186] that has been originally developed to connect defect production during the phase transition to the universal critical exponents [187–189] (see Ref. [190] for a review). It is quite interesting to pursue the connection between the production rate and the “universality class” for the inhomogeneous electric field by the Kibble-Zurek mechanism.

5 Vacuum fluctuations and nonlinear effects

Many studies in physics have addressed how the systems respond to externally applied fields in various ways. When an external field is weak, one may focus on the linear responses to the external field. In the strong-field physics, we however explore the nonlinear regime beyond the linear order. For example, “nonlinear optics” is the research field where one studies nonlinear responses of media [191, 192]. An electric polarization \mathbf{P} of a medium in the *linear* optics is assumed to be proportional to the applied electric field $\mathbf{P} = \epsilon_0 \chi \mathbf{E}$ where ϵ_0 is the vacuum permittivity and χ is the electric susceptibility. However, it is called the *nonlinear* optics when the same quantity is subject to significant nonlinear corrections like $\mathbf{P} = \epsilon_0 [\chi^{(1)} \mathbf{E} + \chi^{(2)} \mathbf{E}^2 + \chi^{(3)} \mathbf{E}^3 + \dots]$. Such nonlinear dependences can be assembled in the form of the nonlinear response function, e.g., the nonlinear electric susceptibility $\chi = \chi(\mathbf{E})$ in this example.

In quantum field theories, vacuum accommodates perpetual fluctuations of the matter fields, and is mixed with the states having a nonzero number of particle-antiparticle pairs. Moreover, due to the presence of interactions between (charged) particles and gauge fields, the external fields are coupled with such fluctuations and induce nontrivial responses of the *vacuum* as if the vacuum plays a role of a medium. This observation was one of the motivations that drove Heisenberg and Euler to compute the effective action of the electromagnetic fields [1], and was clearly recognized by Weisskopf [193, 194]. With the vacuum behaving like a medium, we can expect various phenomena to occur in parallel to the

nonlinear optics. Such examples include “birefringences” (cf. a photo in Fig. 19),³³ “wave mixing” and “high harmonic generation.”

In this section, we study how the properties of photons are modified by strong electromagnetic fields. As we discussed in Sec. 4, electromagnetism of slowly varying fields is described by the Heisenberg-Euler (HE) effective action (190) [1], which contains nonlinear terms in addition to the Maxwell term. In fact, similar to the nonlinear optics, one can compute an electric polarization \mathbf{P} and a magnetization \mathbf{M} of the vacuum from the HE action \mathcal{L}_{HE} as $\mathbf{P} = \mathbf{D} - \mathbf{E}$ and $\mathbf{M} = \mathbf{H} - \mathbf{B}$ with $\mathbf{D} \equiv \partial\mathcal{L}_{\text{HE}}/\partial\mathbf{E}$ and $\mathbf{H} \equiv -\partial\mathcal{L}_{\text{HE}}/\partial\mathbf{B}$ (see, for example, §129 in Ref. [196]). In other words, one can define the electric and magnetic permeability tensors $(\bar{\epsilon}^{ij}, \bar{\mu}^{ij})$ of the vacuum as $D^i = \bar{\epsilon}^{ij}E^j$ and $B^i = \bar{\mu}^{ij}H^j$. Since they are just unity ($\bar{\epsilon}^{ij} = \epsilon_0\delta^{ij} = \delta^{ij}$, $\bar{\mu}^{ij} = \mu_0\delta^{ij} = \delta^{ij}$) in the ordinary vacuum without a strong electromagnetic field, deviations from unity signals the polarization and magnetization of the vacuum.

Recall that the combination of the electric and magnetic permeability provides the speed of light c_0 which is, of course, unity $c_0^{-1} = \sqrt{\epsilon_0\mu_0} = 1$ in the natural unit according to the Lorentz and gauge symmetries in the ordinary vacuum.³⁴ However, when an external field is applied, the symmetries of the “vacuum” will be changed. The external field breaks the Lorentz and full spatial rotational symmetries, so that the speed of light, as consequences of the response from the vacuum, will acquire a nontrivial modification and moreover becomes not only anisotropic but also polarization-mode dependent. This is the *vacuum birefringence*. In the soft-photon regime, we can compute its velocity from the HE action through \mathbf{P} and \mathbf{M} , which will be obtained in the tensor forms consistent with the residual spatial symmetries. In this way, properties of propagating photons are intimately related to the properties of the vacuum under strong fields. It is also important to notice that a photon having no electric charge gets modified by the electromagnetic fields only through quantum fluctuations creating a virtual electron-positron pair. Without a strong field, such effects are higher order in the perturbation theory. However, as we have already seen, the coupling between the fluctuating matter field and the strong external field can be enhanced by a large field strength.

Nonlinear physics in vacuum under strong electromagnetic fields has a long history. After the pioneering work by Heisenberg and Euler [1], Schwinger re-derived the effective action from a modern view of quantum field theory by using the proper-time method [42] as we have seen in the previous section. Then people started discussing the vacuum birefringence and the photon splitting for low-energy photons as a result of the effective theory including nonlinear corrections to the Maxwell part [199–205]. Analysis beyond the first nonlinear correction to the Maxwell theory was also performed in order to treat higher energy photons and/or stronger electromagnetic fields [199, 205–213]. There are many studies which discussed the photon polarization tensor in limited kinematical regimes with appropriate approximations (see Fig. 20 for summary of the representative regimes in external magnetic fields). The reader is also referred to Ref. [102] for more references until 2000. Most recently, an analytic evaluation of the double parameter integral for the polarization tensor was performed in Refs. [214, 215]. Below, we discuss how to describe the vacuum birefringence and the photon splitting with relevant references.

5.1 Vacuum polarization tensor in strong fields

There are mainly two different ways to compute the vacuum polarization tensor of a photon in external fields. The first one is to extract the vacuum polarization tensor from the effective action for the electromagnetic fields, and the second one is to directly compute it from the polarization diagram. In

³³Birefringence of a medium induced by an electric (magnetic) field is called the optical Kerr effect (the Cotton-Mouton effect). When both \mathbf{E} and \mathbf{B} are present, birefringences induced by the parallel configuration $\mathbf{E} \parallel \mathbf{B}$ and perpendicular configuration $\mathbf{E} \perp \mathbf{B}$ are, respectively, called Jones and magneto-electric birefringences. All of these are already observed in experiments [195].

³⁴As is well-known, photons become massive in a gauge invariant way in the (1+1)-dimensional QED called the Schwinger model [197, 198]. A similar situation occurs in a strong magnetic field (see also Appendix F.2.1).

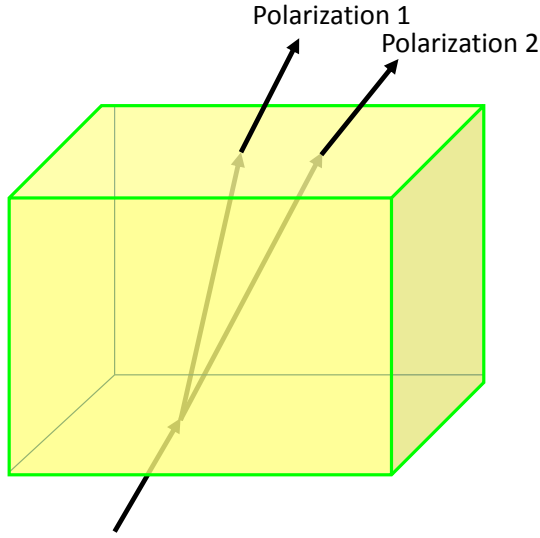


Figure 19: Ray splitting on the faces of a calcite caused by the birefringence.

both cases, the proper-time method turns out to be very useful. In the present review, we explain the latter approach in detail, while the former is only briefly outlined below.

One can use the effective Lagrangian (181) to derive the polarization tensor for a dynamical photon field. Since we have not specified the gauge field $A_\mu(x)$ at the level of Eq. (181), we can regard it as consisting of an external field and a dynamical field: $A^\mu = A_{\text{ext}}^\mu + a^\mu$. Using this decomposition and expanding Eq. (181) with respect to the dynamical gauge field, we obtain $\mathcal{L}^{(1')}[A^\mu] = \mathcal{L}^{(1')}[A_{\text{ext}}^\mu] + \delta\mathcal{L}^{(1')}[A_{\text{ext}}^\mu, a^\mu]$ where the second term is quadratic in a_μ :

$$\delta\mathcal{L}^{(1')}[A_{\text{ext}}^\mu, a^\mu] = -\frac{1}{2} \int d^4x' a_\mu(x) \Pi^{\mu\nu}(x, x'|F_{\text{ext}}) a_\nu(x'). \quad (236)$$

Here, the polarization tensor of a propagating photon is obtained from the second-order variation of the action

$$\Pi^{\mu\nu}(x, x'|F_{\text{ext}}) = -\frac{\delta^2}{\delta a_\mu(x) \delta a_\nu(x')} \int d^4x \delta\mathcal{L}^{(1')}[A_{\text{ext}}^\mu, a^\mu]. \quad (237)$$

It has a nonlinear dependence on the field strength of the external field $F_{\text{ext}}^{\mu\nu} = \partial^\mu A_{\text{ext}}^\nu - \partial^\nu A_{\text{ext}}^\mu$. This approach was adopted, for example, by Tsai and Erber [207, 208]. When the spacetime dependence of an electromagnetic field is smaller than the electron's Compton wavelength $|\nabla F|/F \ll m$, the effective action can be explicitly evaluated and yields the HE effective action. In this “soft photon limit,” one may use the previous result on the HE effective action.

One can also explicitly compute the same quantity from the polarization diagrams. At the one-loop level, the diagram is drawn in Fig. 21. Accordingly to the standard Feynman rules, its momentum representation reads

$$i \Pi^{\mu\nu}(q|F_{\text{ext}}) = (-1)(-ie)^2 \int \frac{d^4p}{(2\pi)^4} \text{tr} \left[\gamma^\mu S(p|F_{\text{ext}}) \gamma^\nu S(p+q|F_{\text{ext}}) \right], \quad (238)$$

where “tr” is taken for the spinor indices and $S(p|F_{\text{ext}})$ is (the gauge-invariant part of) the electron propagator in a strong field as defined in Eq. (121). As we discussed in Sec. 3.2.1, the Schwinger phase identically vanishes for the two-point diagram in Fig. 21 and we are left with the gauge-invariant part, implying the gauge invariance of the polarization tensor.³⁵ In contrast to the effective-action approach,

³⁵Here, we mean the gauge invariance of $\Pi^{\mu\nu}$ with respect to the external gauge field A_{ext}^μ . We discuss the gauge for the dynamical gauge field a^μ just below.

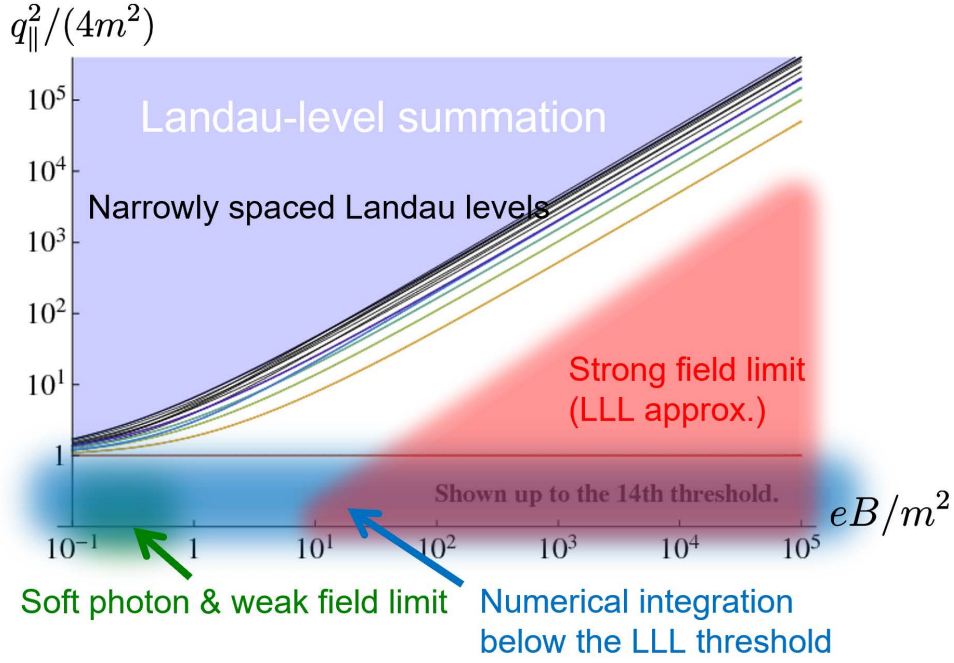


Figure 20: Summary of scales involved in the analyzes of the vacuum fluctuations in magnetic fields. The photon momentum q_{\parallel}^2 and the magnetic field strength eB are normalized by the mass scale of the fluctuation.

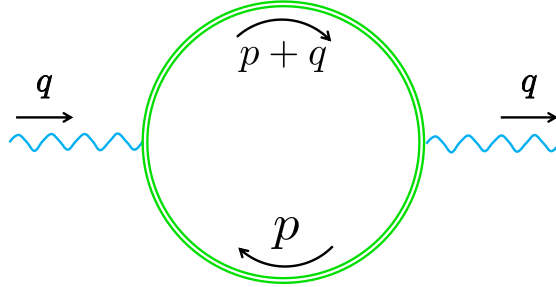


Figure 21: One-loop diagram of the vacuum polarization tensor in a strong magnetic field. Double lines denote the dressed electrons interacting with the external field treated by the proper-time method.

there is no *a priori* restriction on the momentum scale q of the incoming photon. Since the resummed propagator is expressed by the use of the proper-time method, the explicit form (238) contains two proper times corresponding to the two electron propagators. This approach was taken, for example, in Refs. [214, 215] (see also the literature therein). In the next subsection, we will give its explicit form and discuss how to analytically perform the proper-time integrals.

5.2 Photon's vacuum birefringence and decay into an e^+e^- pair

Consider the case where the external field only consists of a magnetic field. As we discussed in previous sections, the direction of the magnetic field can be taken along the z axis without loss of generality. In the ordinary vacuum, the Lorentz structure of the polarization tensor is proportional to the transverse projection $P_0^{\mu\nu}(q) = q^2 g^{\mu\nu} - q^\mu q^\nu$ so that the Ward identity is satisfied, $q_\mu \Pi_0^{\mu\nu}(q) = 0$. On the other hand, in the presence of a magnetic field, we need to distinguish the longitudinal and transverse directions with respect to the magnetic field, which can be performed with the help of the additional metrics $g_{\parallel}^{\mu\nu}$ and $g_{\perp}^{\mu\nu}$ defined in Eq. (6). Thus, in addition to $P_0^{\mu\nu}$, we can construct two additional tensor structures

$P_1^{\mu\nu} = q_{\parallel}^2 g_{\parallel}^{\mu\nu} - q_{\parallel}^{\mu} q_{\parallel}^{\nu}$ and $P_2^{\mu\nu} = q_{\perp}^2 g_{\perp}^{\mu\nu} - q_{\perp}^{\mu} q_{\perp}^{\nu}$. By using them, the general form of the vacuum polarization tensor is given as³⁶

$$\Pi^{\mu\nu}(q|B) = -(\chi_0 P_0^{\mu\nu} + \chi_1 P_1^{\mu\nu} + \chi_2 P_2^{\mu\nu}). \quad (239)$$

While we have suppressed arguments of the Lorentz-scalar functions χ_i ($i = 0, 1, 2$), they are in general functions of q_{\parallel}^2 and q_{\perp}^2 according to the boost invariance and rotational symmetry with respect to the direction of the magnetic field. By construction, the Ward identity is satisfied $q_{\mu} \Pi^{\mu\nu} = 0$ thanks to the transversality $q_{\mu} P_i^{\mu\nu} = 0$ for $i = 0, 1, 2$.

In the presence of an external magnetic field, we need to analyze the equation of motion for the dynamical photon field including the effect of the vacuum polarization. Namely, with the quantum correction to the Lagrangian (236), the Maxwell equation is modified as

$$\left[q^2 g^{\mu\nu} - \left(1 - \frac{1}{\xi_g}\right) q^{\mu} q^{\nu} - \Pi^{\mu\nu}(q_{\parallel}, q_{\perp}|B) \right] a_{\nu}(q) = 0, \quad (240)$$

where ξ_g is a parameter in the gauge-fixing term, $\mathcal{L}_{\text{GF}} = -\frac{1}{2\xi_g}(\partial^{\mu} a_{\mu})^2$. Substituting the general form of the vacuum polarization tensor (239), one finds

$$\left[(1 + \chi_0) P_0^{\mu\nu} + \chi_1 P_1^{\mu\nu} + \chi_2 P_2^{\mu\nu} + \frac{1}{\xi_g} q^{\mu} q^{\nu} \right] a_{\nu}(q) = 0. \quad (241)$$

We shall examine modifications in a refractive index of photon

$$n^2 = \frac{|\mathbf{q}|^2}{\omega^2}, \quad (242)$$

where ω and \mathbf{q} are the frequency and spatial momentum of the propagating photon, respectively. We relate the dielectric constant ϵ to the refractive index as $\epsilon = n^2$ assuming that the modification of the magnetic permeability is small. By selecting an appropriate basis for the photon polarization modes, we find two independent dispersion relations³⁷ in terms of the distinct dielectric constants:

$$\epsilon_{\perp} = \frac{1 + \chi_0}{1 + \chi_0 + \chi_2 \sin^2 \theta}, \quad (243a)$$

$$\epsilon_{\parallel} = \frac{1 + \chi_0 + \chi_1}{1 + \chi_0 + \chi_1 \cos^2 \theta}, \quad (243b)$$

where θ is the angle between the magnetic field \mathbf{B} and the photon momentum \mathbf{q} . With a nonzero χ_i , the ϵ_{\perp} and ϵ_{\parallel} are in general not equal to unity and are also different from each other. Thus, there are two propagating modes whose velocities are not equal to the speed of light in the ordinary vacuum. This phenomenon is called the *vacuum birefringence* after a similar phenomenon in the birefringent substances such as calcite crystal. The birefringence in a material causes, for example, splitting of the polarization modes of the transmitting ray and then induces a double image as shown in Fig. 19. Intuitively, the vacuum birefringence originates from the anisotropic response of charged particles to the photon field in the presence of an external magnetic field. As we already saw in Sec. 2, motions of charged particles in the directions parallel and transverse to the magnetic field are completely different.

³⁶When there are both electric and magnetic fields, there is one additional tensor structure (see, e.g., Ref. [102]).

³⁷The dynamical photon field a^{μ} can be decomposed into two modes having different polarizations. They are specified by vectors $\varepsilon_{(1)}^{\mu} \propto (0, q^2, -q^1, 0)$ and $\varepsilon_{(2)}^{\mu} \propto (q^3, 0, 0, q^0)$ so that $a^{\mu} = N(\varepsilon_{(1)}^{\mu} e^{-i(\omega_{(1)} t - \mathbf{q} \cdot \mathbf{x})} + \varepsilon_{(2)}^{\mu} e^{-i(\omega_{(2)} t - \mathbf{q} \cdot \mathbf{x})})$ with N being a normalization constant. The polarization modes $\varepsilon_{(1)}^{\mu}$ and $\varepsilon_{(2)}^{\mu}$ correspond to ϵ_{\perp} and ϵ_{\parallel} , respectively. One can also read off the dispersion relation and corresponding polarization from the resummed photon propagator (see Appendix C and D of Ref. [214] and Ref. [216]).

Especially, the (1+1)-dimensional motion of the LLL fermions behaves like a polarizer which modifies the propagation of the parallel mode ($\epsilon_{\parallel} \neq 1$) but transmits the perpendicular mode ($\epsilon_{\perp} = 1$) [see Eq. (273a) and below for the analysis in the LLL approximation]. It should be emphasized that, while the modified Maxwell equation (240) is linear in the dynamical field a_{μ} , the vacuum birefringence is a result of the nonlinear effects with respect to the external fields. The polarization tensor carries the information about the interaction between the virtual fluctuations and the external fields. Here are a few comments in order:

- Both of the two dielectric constants ϵ_{\perp} and ϵ_{\parallel} are independent of the gauge fixing parameter ξ_g , meaning that they are gauge invariant quantities (the same result is indeed available in the radiation gauge). The dependence on ξ_g only appears in the unphysical mode.
- In the ordinary vacuum, both ϵ_{\perp} and ϵ_{\parallel} are unity in accordance with the Lorentz symmetry. As mentioned before, quantum fluctuations in the ordinary vacuum without an external field induces nonzero χ_0 while the other two are vanishing ($\chi_0 \neq 0, \chi_1 = \chi_2 = 0$). In this ordinary case, we confirm that $\epsilon_{\perp} = \epsilon_{\parallel} = 1$ as it should be.
- Due to the breaking of the Lorentz and rotational symmetries by an external magnetic field, the dielectric constants explicitly depend on the zenith angle with respect to the magnetic field direction, while they do not depend on the azimuthal angle according to the residual rotational symmetry. On the other hand, the system maintains a boost invariance in the direction of the constant external magnetic field, and thus photon propagations in the directions at $\theta = 0, \pi$ are special. Substituting these angles into Eqs. (243a) and (243b), we find that both of the dielectric constants reduce to unity $\epsilon_{\perp}(\theta = 0, \pi) = \epsilon_{\parallel}(\theta = 0, \pi) = 1$, as a consequence of the boost invariance.

Let us assume that the scalar functions χ_i have imaginary parts in general. Then, the dielectric constants also have imaginary parts: $\epsilon = \epsilon_{\text{real}} + i \epsilon_{\text{imag}}$. Since the dielectric constants and refractive indices are related with each other via $n^2 = \epsilon$, we can similarly define real and imaginary parts of the refractive indices: $n = n_{\text{real}} + i n_{\text{imag}}$. Then, one can easily find relations

$$n_{\text{real}} = \frac{1}{\sqrt{2}} \sqrt{|\epsilon| + \epsilon_{\text{real}}}, \quad n_{\text{imag}} = \frac{1}{\sqrt{2}} \sqrt{|\epsilon| - \epsilon_{\text{real}}}, \quad (244)$$

where $|\epsilon| = (\epsilon_{\text{real}}^2 + \epsilon_{\text{imag}}^2)^{1/2}$. As is well explained in standard textbooks of optics [217], refractive indices have clear physical meaning: The real and imaginary parts of the refraction index provide a *phase velocity* $v_{\text{phase}} = 1/n_{\text{real}}$ and an *extinction coefficient* $\kappa = n_{\text{imag}}$ of a propagating photon, respectively. In the photon field $\Psi(t, \mathbf{x})$, they appear in a phase factor and damping factor, respectively,

$$\Psi(t, \mathbf{x}) \propto \exp\{-i\omega(t - v_{\text{phase}}^{-1} \hat{\mathbf{q}} \cdot \mathbf{x})\} \exp\{-\omega \kappa \hat{\mathbf{q}} \cdot \mathbf{x}\}, \quad (245)$$

where $\hat{\mathbf{q}}$ is a unit vector along the photon momentum. Thus, it is natural to define a *decay length* at which the intensity of the photon field falls off

$$\lambda \equiv \frac{1}{2\omega\kappa} = \frac{1}{2\omega n_{\text{imag}}}. \quad (246)$$

As we will explain later, the coefficient functions χ_i indeed acquire imaginary parts, and there emerges complex refractive indices, which originates from the fact that even a real photon can decay into an electron-positron pair in a strong magnetic field.³⁸

³⁸We know that the cyclotron radiation occurs in a magnetic field and is a representative example of the 1-to-2 processes. Those 1-to-2 (2-to-1) processes are, however, prohibited in the absence of a magnetic field for the kinematical reason.

5.2.1 Low-energy photons (I): Weak fields

Let us first consider the case where the energy of propagating photon is small enough. More precisely, the photon energy is assumed to be much smaller than the electron mass $\omega \ll m \simeq 0.5 \text{ MeV}$ so that the HE effective Lagrangian is valid. This condition is satisfied by visible lights (with a few eV) and X-rays (with 1-100 keV), and thus typically matters when we consider photon propagation in a high-intensity laser or in the magnetospheres of neutron stars or magnetars. The refractive indices are always real quantities for such a low-energy photon (well below the threshold of the pair production). Here we compute the refractive indices from the HE effective Lagrangian.

When the external fields are not stronger than the critical value $|F^{\mu\nu}| \ll m^2/|e|$, we are able to expand the HE effective Lagrangian with respect to the external fields. The expansion with respect to the gauge-invariant quantities \mathcal{F} and \mathcal{G} , defined in Eqs. (3), reads

$$\mathcal{L}_{\text{HE}} = \mathcal{L}_{\text{HE}}^{(0)} + \mathcal{L}_{\text{HE}}^{(1)} + \dots \quad (247)$$

with the Maxwell term $\mathcal{L}_{\text{HE}}^{(0)} = -\mathcal{F}$. The nonlinear part in the HE effective Lagrangian (190) is evaluated as (we take $q_f = e < 0$ for electrons)

$$(es)^2 \mathcal{G} \frac{\Re \left[\cosh \left\{ es \sqrt{2(\mathcal{F} + i\mathcal{G})} \right\} \right]}{\Im m \left[\cosh \left\{ es \sqrt{2(\mathcal{F} + i\mathcal{G})} \right\} \right]} = \frac{1 + (es)^2 \mathcal{F} + \frac{1}{6}(es)^4 (\mathcal{F}^2 - \mathcal{G}^2) + \dots}{1 + \frac{1}{3}(es)^2 \mathcal{F} + \frac{1}{90}(es)^4 (3\mathcal{F}^2 - \mathcal{G}^2) + \dots} \quad (248)$$

Note that the discrete symmetries of electromagnetic fields are the following: $(C, P, T) = (-, -, +)$ for the electric field \mathbf{E} and $(C, P, T) = (-, +, -)$ for the magnetic field \mathbf{B} . Consequently, \mathcal{F} is $(C, P, T) = (+, +, +)$ and \mathcal{G} is $(C, P, T) = (+, -, -)$. Therefore, the effective Lagrangian can have \mathcal{F} with odd powers, but \mathcal{G} must always appear with even powers unless the theory has any parameter that breaks those symmetries. Therefore, we find the leading nonlinear corrections [42]

$$\begin{aligned} \mathcal{L}_{\text{HE}}^{(1)} &= -\frac{1}{8\pi^2} \int_0^\infty \frac{ds}{s^3} e^{-m^2 s} \left[-\frac{(es)^4}{45} (4\mathcal{F}^2 + 7\mathcal{G}^2) \right] \\ &= \frac{2\alpha^2}{45m^4} (4\mathcal{F}^2 + 7\mathcal{G}^2). \end{aligned} \quad (249)$$

This is called the Euler-Kockel Lagrangian [218] as they first derived it before the paper by Heisenberg and Euler [1].

As we mentioned in the begining of this section, we are able to compute the electric and magnetic permeability tensor $\bar{\epsilon}^{ij}$ and $\bar{\mu}^{ij}$ through $D^i = \partial \mathcal{L}_{\text{HE}} / \partial E^i = \bar{\epsilon}^{ij} E^j$ and $H^i = -\partial \mathcal{L}_{\text{HE}} / \partial B^i = (\bar{\mu}^{-1})^{ij} B^j$. By using the Euler-Kockel Lagrangian (249), the leading nonlinear corrections to those quantities are obtained as

$$\bar{\epsilon}^{ij} = \delta^{ij} + \frac{4\alpha^2}{45m^4} [2(\mathbf{E}^2 - \mathbf{B}^2)\delta^{ij} + 7B^i B^j], \quad (250a)$$

$$\bar{\mu}^{ij} = \delta^{ij} + \frac{4\alpha^2}{45m^4} [-2(\mathbf{E}^2 - \mathbf{B}^2)\delta^{ij} + 7E^i E^j]. \quad (250b)$$

This result implies that the polarization $\mathbf{P} = \mathbf{D} - \mathbf{E}$ and the magnetization $\mathbf{M} = \mathbf{H} - \mathbf{B}$ of the vacuum acquire the nonlinear corrections

$$P^i = \frac{4\alpha^2}{45m^4} [2(\mathbf{E}^2 - \mathbf{B}^2)\delta^{ij} + 7B^i B^j] E^j, \quad (251a)$$

$$M^i = \frac{4\alpha^2}{45m^4} [2(\mathbf{E}^2 - \mathbf{B}^2)\delta^{ij} - 7E^i E^j] B^j. \quad (251b)$$

This result is similar to that in (nonlinear) optics. However, unlike optics, the above vacuum result does not have a linear term in the electromagnetic fields and starts from the third order. Note also that there is mixing between \mathbf{E} and \mathbf{B} .

Consider the case where a low-energy photon propagates in vacuum in the presence of only a magnetic field $\mathbf{B} = \mathbf{B}_{\text{ext}} = (0, 0, B)$. To compute the refractive indices, we can again use the Euler-Kockel Lagrangian in which we substitute $\mathbf{B} = \mathbf{B}_{\text{ext}} + \mathbf{b}$ and $\mathbf{E} = \mathbf{e}$ with \mathbf{b} and \mathbf{e} being the propagating modes. From the modified Maxwell equations, we can find two independent polarization modes: the “ \perp -mode” is that the propagating electric field \mathbf{e} is perpendicular to the plane spanned by the photon momentum \mathbf{k} and the magnetic field \mathbf{B}_{ext} (\mathbf{b} is in the plane), and the “ \parallel -mode” is that the propagating magnetic field \mathbf{b} is perpendicular to the same plane (\mathbf{e} is in the plane).³⁹ The refractive indices of these two modes are found to be

$$n_{\perp} = 1 + \frac{8\alpha^2}{45m^4} B^2 \sin^2 \theta, \quad (252a)$$

$$n_{\parallel} = 1 + \frac{14\alpha^2}{45m^4} B^2 \sin^2 \theta, \quad (252b)$$

where θ is the angle between the direction of propagation and the magnetic field. Those results are valid only when $B \ll B_c = m^2/e$. Therefore, it is useful to rewrite them with respect to the ratio B/B_c in the form $n_{\perp, \parallel} = 1 + \Delta n_{\perp, \parallel}$. The corrections are given by $\Delta n_{\perp} = (7/4)\Delta n_{\parallel} = (2\alpha/45\pi)(B/B_c)^2 \sin^2 \theta$, so that the deviations of the refractive indices from unity are quite small $\Delta n_{\perp, \parallel} \ll 1$. This regime corresponds to the “soft-photon and weak-field limit” in Fig. 20.

One of the possible experimental setup to measure the vacuum birefringence is to use the ultra-high-intensity laser⁴⁰ such as to be built in Extreme-Light Infrastructure (ELI) in Europe [223–225]. A probe laser will get affected during its propagation in a high-intensity laser, yielding a small amount of change in the polarization direction. This change could be detected as an interference pattern between the original and modified probe laser fields. Some of the recent attempts are discussed in Ref. [195]. Intensity of the laser field in ELI will reach the current highest value $I = E^2 = B^2 \sim 10^{25} \text{ W/cm}^2$, which is however far below the intensity of the critical field $I_c = E_c^2 = B_c^2 = 4.4 \times 10^{29} \text{ W/cm}^2$. Thus, even with such a high-intensity laser, the ratio B/B_c is small $\sim 10^{-2}$, and we should treat it as a weak field. If one uses Eqs. (252a) and (252b), one finds that deviation of the refractive indices from unity will be quite tiny $\Delta n \sim 10^{-9}$. Extremely high precision measurement will be necessary to detect this small deviation. Nevertheless, considering that the vacuum birefringence as a dispersive effect occurs in external fields whose strengths are well below the critical value, we expect that, in laboratory experiments, it is much easier to detect the vacuum birefringence than the Schwinger mechanism which at least requires strong electric fields of the order of the critical field $E_c = m^2/e$.

5.2.2 Low-energy photons (II): Wrenchless fields

Low-energy photon propagation in a strong field should be investigated with the full nonlinear expression of the HE effective Lagrangian. While it is still tough to analytically treat the HE Lagrangian for arbitrary values of \mathcal{F} and \mathcal{G} , one could find other expansion parameters instead. One such example is the “wrenchless” fields specified as $\mathcal{F} \neq 0$, $\mathcal{G} = 0$ and its first correction with respect to a nonzero \mathcal{G}

³⁹Note that these definitions are interchanged in some literature, e.g., Ref. [219].

⁴⁰Another setup is to measure the rotation angle of the polarization direction of laser photons that travel in a static homogeneous magnetic field. The merit of this setup is that the deflecting angle should be proportional to the propagation length so that a large effect is expected if one could prepare a homogeneous magnetic field of a large size. Typical experiment is the PVLAS collaboration, which also searches for axions in the same facility. Although it was once reported that they observed a small rotation of the photon polarization, it turned out later that it was due to an instrumental artifact and was not of physical origin [220, 221]. See also Ref. [222] for current status of the experiment.

as was shown by Heyl and Hernquist [212, 213]. The wrenchless fields cover the weak- to strong-field regimes within the constraint that \mathcal{G} is a small quantity.

The HE Lagrangian for the wrenchless fields and its corrections are simply given in the series expansion with respect to \mathcal{G}^2 :

$$\mathcal{L}_{\text{HE}} = \mathcal{L}_{\text{HE}}(\mathcal{F} \neq 0, \mathcal{G} = 0) + \left. \frac{\partial \mathcal{L}_{\text{HE}}}{\partial \mathcal{G}^2} \right|_{\mathcal{G}^2=0} \mathcal{G}^2 + \dots, \quad (253)$$

where each term is given as a function of a dimensionless variable $\rho \equiv \sqrt{B_c^2/(2\mathcal{F})}$ with $B_c = m^2/|e|$. It is quite straightforward to perform the expansion and obtain explicit forms of the first two terms⁴¹

$$\mathcal{L}_{\text{HE}}(\mathcal{F}, \mathcal{G} = 0) = -\mathcal{F} \left[1 - 2 \frac{e^2}{8\pi^2} X_0(\rho) \right], \quad (254a)$$

$$\left. \frac{\partial \mathcal{L}_{\text{HE}}}{\partial \mathcal{G}^2} \right|_{\mathcal{G}^2=0} = \frac{e^2}{8\pi^2} \frac{1}{4\mathcal{F}} X_1(\rho), \quad (254b)$$

with

$$X_0(\rho) = \int_0^\infty \frac{ds}{s} e^{-i(1-i\epsilon)\rho s} \left[\frac{1}{s} \cot s - \frac{1}{s^2} + \frac{1}{3} \right], \quad (255a)$$

$$X_1(\rho) = \int_0^\infty \frac{ds}{s^2} e^{-i(1-i\epsilon)\rho s} \frac{1}{3} [(3 + 2s^2) \cot s - 3s \csc^2 s]. \quad (255b)$$

Both of those integrals are convergent. Notice that $X_1(\rho)$ can be expressed with $X_0(\rho)$ by integrating by parts as

$$X_1(\rho) = -2X_0(\rho) + \rho X_0^{(1)}(\rho) + \frac{2}{3} X_0^{(2)}(\rho) - \frac{2}{9\rho^2}, \quad (256)$$

where $X_0^{(n)}(\rho) \equiv d^n X_0(\rho)/d\rho^n$.

Now we evaluate the coefficient function $X_0(x)$ that appears in the purely electric or magnetic case ($\mathcal{G} = 0$), and has been well investigated in the classic literature after the seminal papers [1, 218]. One can also find the literature in the modern languages [98, 226, 227] as well as Refs. [212, 213] (see also review articles [99, 125, 228]). Assuming a real-valued ρ for a positive value of $\mathcal{F} > 0$, i.e., the purely magnetic-field case, one can rotate the integral contour as

$$X_0(\rho) = \lim_{\delta \rightarrow 0} \mu^{2\delta} \int_0^\infty \frac{ds}{s^{2-\delta}} e^{-\rho s} \left[-\coth s + \frac{1}{s} + \frac{s}{3} \right]. \quad (257)$$

While this integral is finite in total (as the counter terms have been already included), each term in the integrand diverges at the lower boundary $s = 0$. It is, thus, helpful to regularize each term in the intermediate steps of the computation. One such way is to introduce a cut-off to the proper-time integral as mentioned earlier. In the above expression, we employed an alternative way via the dimensional regularization [98, 226, 227] and introduced a displacement δ that is assumed to be $\delta > 2$ and is sent to zero in the end of computation. Accordingly, we have introduced an overall factor composed of a dimension-one parameter μ since the proper-time s is a dimensional variable.⁴² These schemes provide

⁴¹Note correspondences between the notations here and in Refs. [212, 213]: $\mathcal{F} = I/4$, $\mathcal{G} = K/4$, and $\rho = \xi^{-1}$. Also, the effective Lagrangian therein is smaller by an overall factor of $1/(8\pi^2)$ according to the difference in electromagnetic units.

⁴²Nevertheless, this (renormalization) scale does not appear in the final result of $X_0(\rho)$ which has been already made a finite quantity by the subtraction of the second and third terms in its integrand. For the same reason, we did not explicitly include the factor of $(-1)^d$ mentioned below Eq. (180) which depends on the dimension d . We will restore these factors in Sec. 6.5 to discuss renormalization in QCD.

gauge-invariant regularizations and finally a finite result. One can immediately identify the second and third terms with the integral representation of the gamma function $\Gamma(z)$ and the the first term with the Hurwitz zeta function $\zeta(z, a) = \sum_{n=0}^{\infty} (n+a)^{-z}$ after some arrangements. The integral representation of $\zeta(z, a)$ is given as [229]

$$\zeta(z, a) = \frac{1}{\Gamma(z)} \int_0^{\infty} \frac{ds}{s^{1-z}} \frac{e^{-as}}{1 - e^{-s}}, \quad \Re e [z] > 1, \quad \Re e [a] > 0. \quad (258)$$

Therefore, one can find a useful formula

$$\int_0^{\infty} \frac{ds}{s^{1-z}} e^{-as} \coth s = \frac{\Gamma(z)}{2^{z-1}} \left[\zeta\left(z, \frac{a}{2}\right) - 2^{z-1} a^{-z} \right], \quad (259)$$

and arrive at a well-known result (see Ref. [227] for alternative expressions)

$$\begin{aligned} X_0(\rho) &= \lim_{\delta \rightarrow 0} \mu^{2\delta} \left[-\Gamma(-1 + \delta) \left\{ 2^{2-\delta} \zeta\left(-1 + \delta, \frac{\rho}{2}\right) - \rho^{1-\delta} \right\} + \rho^{2-\delta} \Gamma(-2 + \delta) + \frac{1}{3} \rho^{-\delta} \Gamma(\delta) \right] \\ &= \left(\frac{\rho}{2}\right)^2 - \frac{1}{3} + 4\zeta\left(-1, \frac{\rho}{2}\right) \ln \frac{\rho}{2} + 4\zeta'\left(-1, \frac{\rho}{2}\right), \end{aligned} \quad (260)$$

where we have the first derivative of the Hurwitz zeta function $\zeta'(z, a) \equiv \partial\zeta(z, a)/\partial z$ and a polynomial form $\zeta(-1, a) = -(2a^2 - 2a + 1/3)/4$. Since we do not have constraints on the magnitude of \mathcal{F} , we may consider both the weak- and strong-field limits such that $\rho \gg 1$ and $\rho \ll 1$, respectively. In the weak-field limit ($\rho \gg 1$), the above results correctly reproduce the Euler-Kockel Lagrangian (249) and systematically yields higher-order corrections in $1/\rho$. In the strong-field limit ($\rho \ll 1$), the leading behavior of $X_0(\rho)$ reads $X_0(\rho) \sim \frac{1}{3} \ln(2/\rho)$ with constants under the logarithm. On the other hand, we get $X_1(\rho) \sim 2/(3\rho)$, and the coefficient of the \mathcal{G}^2 term reads $\partial\mathcal{L}_{\text{HE}}/\partial\mathcal{G}^2|_{\mathcal{G}^2=0} \propto (e^4/m^4)\rho^2 X_1(\rho) \sim (e^4/m^4)\rho$ which becomes less and less important as we increase \mathcal{F} with fixed values of \mathcal{G} , e , and m . Therefore, one finds the leading behavior of the HE effective Lagrangian $\mathcal{L}_{\text{HE}} \sim -\mathcal{F} \left(1 - \frac{e^2}{12\pi^2} \ln \frac{2\sqrt{2}e^2\mathcal{F}}{m^2}\right)$. While we assumed a positive value of $\mathcal{F} > 0$ in the above, we can obtain expressions for the other case with a negative value of $\mathcal{F} < 0$, i.e., the purely electric case, with the help of analytic continuation applied to the above results. In this case, an imaginary part of the effective Lagrangian should appear from analytic continuation in accordance with the Schwinger mechanism discussed in the previous section [98, 125, 212, 213, 227].

By using the above result up to the first order with respect to \mathcal{G}^2 , one obtains the electric and magnetic permeability tensors as ($B_c = E_c = m^2/|e|$)

$$\bar{\epsilon}^{ij} = \delta^{ij} + \frac{\alpha}{2\pi} \left[\left\{ -2X_0(\rho) + \rho X_0^{(1)}(\rho) \right\} \delta^{ij} - \rho^2 X_1(\rho) \frac{B^i B^j}{B_c^2} \right], \quad (261a)$$

$$(\bar{\mu}^{-1})^{ij} = \delta^{ij} + \frac{\alpha}{2\pi} \left[\left\{ -2X_0(\rho) + \rho X_0^{(1)}(\rho) \right\} \delta^{ij} + \rho^2 X_1(\rho) \frac{E^i E^j}{E_c^2} \right]. \quad (261b)$$

To extract the photon polarization tensor, we need the second derivative of the HE Lagrangian with respect to E^i or B^i . We can obtain a modified Maxwell equation for the propagating fields, and again find two independent modes. When there is only a magnetic field, we find the following refractive indices ($\mathcal{F} = \mathbf{B}^2/2$ and thus $\rho = B_c/|\mathbf{B}|$):

$$n_{\perp} = 1 - \frac{\alpha}{4\pi} X_1(\rho) \sin^2 \theta, \quad (262a)$$

$$n_{\parallel} = 1 + \frac{\alpha}{4\pi} \left\{ \rho^2 X_0^{(2)}(\rho) - \rho X_0^{(1)}(\rho) \right\} \sin^2 \theta. \quad (262b)$$

The deviations from unity could be much larger than those in Eqs. (252a) and (252b) for the weak magnetic fields.

It has been discussed in the literature [230–232] that the vacuum birefringence in strong magnetic fields could give rise to a visible effect on the low-energy photon radiation emitted from neutron stars or magnetars, where the strength of magnetic fields would be close to or beyond the critical value $B_c = m^2/e$ (see a review [22] for more references). In particular, it is expected that the polarization properties of radiation emitted by isolated neutron stars will be strongly influenced by strong magnetic fields of stars. To minimize possible background effects originating from the QED plasma, “isolated” neutron stars have been thought to be the best candidates for the observation of the vacuum birefringence. Recently, it was reported that radiation from the famous isolated neutron star, RX J1856.5-3754, having a dipolar surface magnetic field $B \sim 10^{13}$ - 10^{14} Gauss is substantially polarized, which cannot be explained by known effects and thus would suggest other new effects such as the vacuum birefringence. Indeed, the measured values of polarization are consistent with the picture that they are from the vacuum birefringence[233]. The polarization measurement of neutron stars and magnetars is very important and one of the main targets in future experiments such as PRAXyS (the Polarimeter for Relativistic Astrophysical X-ray Sources) [234]. More precise measurement in a wide range of radiation energies will be necessary for definitive identification of the effects with that of the vacuum birefringence, which will also improve our understanding of the magnetic structure of the neutron stars or magnetars. There is also an attempt to detect the vacuum birefringence by relativistic heavy-ion collisions in recent years [21, 235]. The maximum magnitudes of the electromagnetic fields can be as large as the QCD scale ~ 200 MeV that is much larger than the critical field strength defined by electron mass. The above expansion may be relevant for the field configurations created there.

5.2.3 High-energy photons: Beyond Heisenberg-Euler effective theory

The HE Lagrangian is no longer a useful effective theory when the photon field varies in spacetime at scales shorter than the electron’s Compton wavelength. Propagation of such a high-energy photon in a slowly varying magnetic field is a typical situation which requires to go beyond the HE Lagrangian. Such situation will be relevant when we consider high-energy photons emitted in heavy-ion collisions or γ ray propagation in astrophysical jets, both of which are accompanied by strong magnetic fields. In order to study such problems, we need to go back to the original representation (181) of the effective action for arbitrary gauge fields or directly evaluate the polarization tensor (238) as shown in the diagram, Fig. 21. While the formal expression of the polarization tensor (at the one-loop level) had been known for a long time [206, 209, 211, 236], analytic insights in a whole kinematical region have not been available until recently due to technical difficulties in the expression in terms of the double-parameter integral [237]. Here, based on Refs. [214, 215], we outline the way to reach an analytic representation of the polarization tensor under magnetic fields with arbitrary strength.

Double-integral representation of the polarization tensor

Again, let us focus on the case with only a homogeneous magnetic field $\mathbf{B} = (0, 0, B)$ directed to the z direction. The polarization tensor (238) has integrals with respect to the internal momentum p , and two proper times which we denote as τ_1 and τ_2 originating from the two resummed propagators. The integration over p is just a Gaussian integral and is straightforwardly carried out. We are left with the remaining proper-time integrals which can be rewritten by using two dimensionless variables $\tau = eB(\tau_1 + \tau_2)/2$ and $\beta = eB(\tau_1 - \tau_2)/\tau$. Notice that the scalar functions χ_i ($i = 0, 1, 2$) defined in Eq. (239) are dimensionless, and thus we further introduce three dimensionless variables, $B_r = B/B_c = eB/m^2$, $r_{\parallel}^2 = q_{\parallel}^2/(4m^2)$ and $r_{\perp}^2 = q_{\perp}^2/(4m^2) = -|\mathbf{q}_{\perp}|^2/(4m^2)$, which are taken as the axes of Fig. 20. Then, the

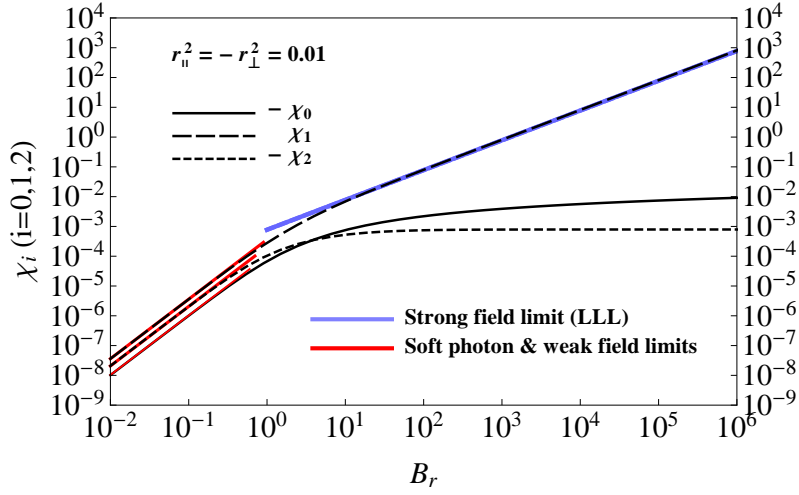


Figure 22: Numerical results of χ_i in the soft-photon regime, compared with the analytic expressions both in the weak and strong field limits, taken from [215].

scalar functions χ_i are expressed as

$$\chi_i(r_{\parallel}^2, r_{\perp}^2; B_r) = \frac{\alpha}{4\pi} \int_{-1}^1 d\beta \int_0^{\infty} d\tau \frac{\Gamma_i(\tau, \beta)}{\sin \tau} e^{-iu \cos(\beta\tau)} e^{i\eta \cot \tau} e^{-i\phi_{\parallel} \tau}. \quad (263)$$

Here, we have introduced two shorthand notations, $\eta \equiv -2r_{\perp}^2/B_r$ and $u \equiv \eta/\sin \tau$, which are useful to proceed to the analytic calculation below. Lastly, ϕ_{\parallel} and Γ_i are known functions given by the following forms [205–211, 238, 239] (see also Refs. [99, 102] for details):

$$\phi_{\parallel}(r_{\parallel}^2, B_r) = \frac{1}{B_r} \{1 - (1 - \beta^2) r_{\parallel}^2\}, \quad (264)$$

and

$$\begin{aligned} \Gamma_0(\tau, \beta) &= \cos(\beta\tau) - \beta \sin(\beta\tau) \cot \tau, \\ \Gamma_1(\tau, \beta) &= (1 - \beta^2) \cos \tau - \Gamma_0(\tau, \beta), \\ \Gamma_2(\tau, \beta) &= 2 \frac{\cos(\beta\tau) - \cos \tau}{\sin^2 \tau} - \Gamma_0(\tau, \beta). \end{aligned} \quad (265)$$

In Eq. (263), the coupling constants in the overall factor $\alpha = e^2/4\pi$ come from the two vertices at which the propagating photon is coupled to the electron one-loop. The others are from the interactions between the electron-positron fluctuations and the external magnetic field, as is evident from the fact that they always appear with the magnetic field in the form of eB .

This representation contains involved integration with respect to β and τ . In fact, this complexity has prevented previous studies from complete analytical understanding of the vacuum birefringence [205, 207, 208, 210], and even from performing numerical computation except in a limited kinematical region where there is no imaginary part (cf. Fig. 20) [240]. All the studies started from this representation and had to resort to some kind of approximations depending on interested kinematics and conditions.

Soft-photon and weak-field limit

It would be instructive to first look at one of these approximations in the soft-photon and weak-field limit, which turns out to reproduce the results in Eqs. (252a) and (252b) obtained earlier from the HE

Lagrangian. Consider the simultaneous limits for the soft photon $\omega^2 \ll 4m^2$ and weak field $B_r \ll 1$. In Eq. (264), the integrands of the τ -integral is damped within a scale $\sim B_r$ when $r_{\parallel}^2 \ll 1$. Therefore, when $B_r \ll 1$, we can expand the integrands with respect to the small value of τ . In this limit, the exponential factor is approximated as

$$\exp(-i\phi_{\parallel}\tau) \sim \left[1 + (1 - \beta^2)r^2 \frac{\tau}{B_r} \right] e^{-\frac{\tau}{B_r}}, \quad (266)$$

where $r^2 = q^2/(4m^2)$. The Γ_i are also expanded as

$$\frac{1}{\sinh \tau} (\Gamma_0 - \Gamma_0^{\text{free}}) = -\frac{1}{6}(1 - \beta^2)^2 \tau, \quad (267a)$$

$$\frac{1}{\sinh \tau} \Gamma_1 = \frac{1}{6}(1 - \beta^2)(3 - \beta^2) \tau, \quad (267b)$$

$$\frac{1}{\sinh \tau} \Gamma_2 = -\frac{1}{12}(1 - \beta^2)(3 + \beta^2) \tau. \quad (267c)$$

A function Γ_0^{free} is the contribution in the absence of the magnetic field that is equal to the vanishing B limit of Γ_0 , and removes the logarithmic singularity $\sim 1/s$ coming from the ultraviolet divergence.⁴³ After performing the elementary integrals, we obtain

$$\chi_0 = -\frac{2\alpha}{315\pi} B_r^2 (7 + 12r^2), \quad (268a)$$

$$\chi_1 = \frac{\alpha}{315\pi} B_r^2 (49 + 80r^2), \quad (268b)$$

$$\chi_2 = -\frac{4\alpha}{315\pi} B_r^2 (7 + 11r^2). \quad (268c)$$

In Fig. 22, the above analytic results are shown with the numerical results in the soft-photon limit. They agree with each other in the soft-photon and weak-field limit, which is indicated as an overlap region in Fig. 20. The analytic expression for the strong field limit, the LLL approximation, will be discussed below. Plugging the weak-field results into the refractive indices given in Eq. (242)–(243b), we find that the results from the HE Lagrangian (252a) and (252b) are reproduced in the vanishing momentum limit $r^2 \rightarrow 0$. The above results provide the leading corrections with respect to the photon momentum r^2 .

These approximates are, however, valid only in the limited kinematical regions and the other regions were not fully investigated. After almost 40 years since the expression (263) was obtained, an analytic result for the double integral was obtained in Ref. [214], and the result was soon confirmed numerically⁴⁴ [241]. The final analytic representation for the scalar functions χ_i obtained in Ref. [214] is given by an infinite series of functions composed of the associated Laguerre polynomials $L_{\ell}^n(x)$. The appearance of the associated Laguerre polynomials is quite natural because they appear in the wave functions of charged fermions in a magnetic field as we saw in Sec. 2.2.2.⁴⁵

Full analytic result and the Landau levels

Below, we give the outline to reach the analytic expression and explain the physical meaning of the result. The main difficulties in performing the double integral in the scalar functions χ_i (263) come

⁴³In case of the two-point function, the vacuum contribution, without any insertion of the external field, has the logarithmic divergence, while all the other diagrams with insertions of the external magnetic field are convergent.

⁴⁴The authors of Ref. [241] also gave a renormalization prescription when Γ_0 is given by the discrete sum of contributions from the Landau levels, while the subtraction term Γ_0^{free} , which is not affected by the magnetic field, is a continuous function.

⁴⁵Nevertheless, the vacuum polarization diagram is invariant with respect to the gauge of the external magnetic field as mentioned earlier.

from the fact that trigonometric functions appear in the exponentials in the integrands. Actually, those double-exponential forms generate arbitrarily higher harmonic modes due to nonlinear nature. Those difficulties are overcome as follows: First of all, the factor $e^{-iu \cos(\beta\tau)}$ can be “expanded” by using the partial wave decomposition which is an established technique in quantum mechanics. This exponential factor is expressed as an infinite series including the modified Bessel functions $I_n(-iu)$. Next, we can further rewrite the product of the modified Bessel function $I_n(-iu)$ with the other exponential factor $e^{in \cot \tau}$ by using another infinite series including the associated Laguerre polynomials $L_\ell^n(x)$. After those decompositions, all the exponential factors have simple shoulders linear in τ , and we are able to exactly perform the double integrals with respect to τ and then β to obtain the final result. The details are written in Ref. [214].

After all, we have two integer indices n and ℓ to be summed from zero to infinity. Although both of them were originally introduced in the above decompositions for the technical purposes, they actually correspond to the Landau-level indices of the fermion-antifermion pair. This interpretation is justified by the following observation. Each term in the infinite summation contains the function:

$$I_{\ell\Delta}^n(r_{\parallel}^2) \equiv \int_{-1}^1 \frac{d\beta}{r_{\parallel}^2 \beta^2 - nB_r \beta + (1 - r_{\parallel}^2) + (2\ell + n)B_r}. \quad (269)$$

Its kinematical property is specified by a discriminant for the second-order function of β in the denominator: $\mathcal{D} \equiv (-nB_r)^2 - 4r_{\parallel}^2 \{(1 - r_{\parallel}^2) + (2\ell + n)B_r\}$. Depending on the sign of \mathcal{D} , the integral $I_{\ell\Delta}^n(r_{\parallel}^2)$ takes either real or complex value. Therefore, the solutions to an equation, $\mathcal{D}(r_{\parallel}) = 0$, specify the threshold for the emergence of imaginary part:

$$r_{\parallel}^2 = \frac{1}{4} \left[\sqrt{1 + 2\ell B_r} \pm \sqrt{1 + 2(\ell + n)B_r} \right]^2 \equiv s_{\pm}^{\ell n}. \quad (270)$$

One can prove that an imaginary part appears only when $s_{+}^{\ell n} < r_{\parallel}^2$. In terms of dimensionful quantities, the threshold condition $r_{\parallel}^2 = s_{+}^{\ell n}$ is rewritten as

$$q_{\parallel}^2 = \left[\sqrt{m^2 + 2\ell eB} + \sqrt{m^2 + 2(\ell + n)eB} \right]^2. \quad (271)$$

Recall that the fermion dispersion relation in a magnetic field is given as $\varepsilon_n(p_z) = \sqrt{m^2 + p_z^2 + 2neB}$ with $n \geq 0$. The right-hand side of Eq. (271) exactly agrees with the invariant mass of a fermion-antifermion pair with a vanishing longitudinal momentum, and the integers ℓ and $\ell + n$ specify the Landau levels. Therefore, the infinite summations over n and ℓ correspond to summing all the Landau levels associated with the fermion-antifermion pair constituting the one-loop. The lowest threshold is given by the lowest Landau levels $n = \ell = 0$, which agrees with the strong-field limit obtained in other methods [210, 214, 215, 242].

The appearance of an imaginary part indicates that a *real photon* decays into an electron-positron pair in the magnetic field above the threshold energy. Clearly, this contrasts to the case without a magnetic field where the on-shell conditions for the fermion-antifermion pair require a nonzero invariant mass of photon, $q^2 \geq (2m)^2$. The kinematics in a magnetic field can be understood as follows. If we regard the Landau level and the transverse photon momentum as an “effective mass” of the fermion and the photon, respectively, their dispersion relations may be interpreted as (1+1)-dimensional ones. Then, the kinematics in a magnetic field can be identified with that for the decay of a “massive” gauge boson to a fermion-antifermion pair in the (1+1) dimensions: There is no kinematical prohibition of decay of a massive boson. Consistent to this observation, the threshold condition (271) constrains only the longitudinal part of the photon momentum q_{\parallel}^2 .⁴⁶ Setting $q_z = 0$ in Eq. (271),⁴⁷ we find the

⁴⁶Remember also that the transverse components of the kinetic momentum are not good quantum numbers and that those of the canonical momentum are not conserved either in a general gauge (cf. Sec. 2.3).

⁴⁷One can always move to such a Lorentz frame where the longitudinal photon momentum vanishes $q_z = 0$, thanks to the boost invariance along the magnetic field.

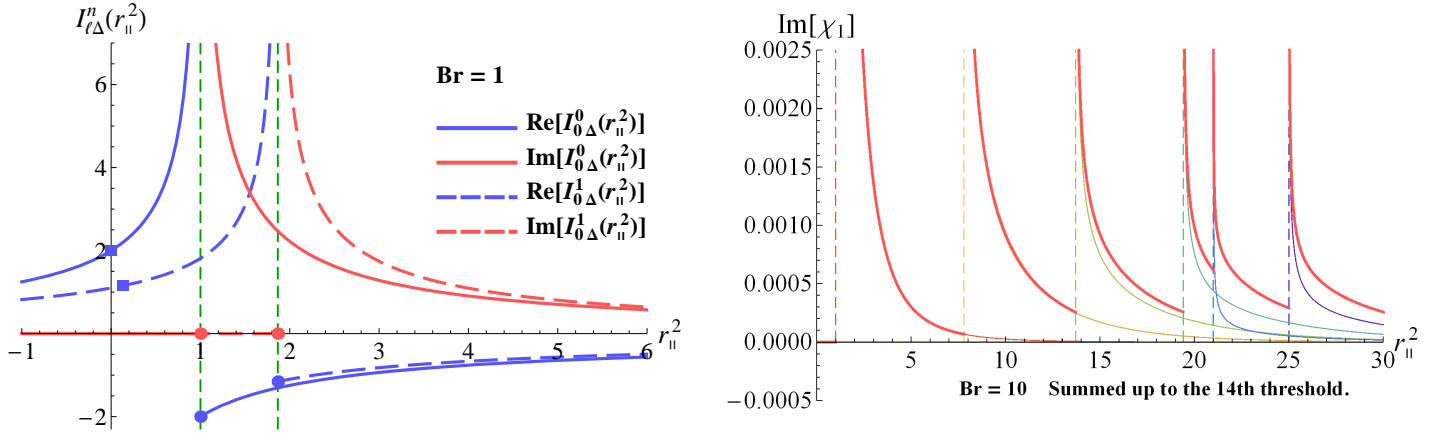


Figure 23: Real and imaginary parts of the function $I_{\ell\Delta}^n(r_{\parallel}^2)$ for the lowest and first Landau levels ($n = \ell = 0$ and $n = 1, \ell = 0$) [left]. The imaginary part of χ_1 with many thresholds which show contributions of each Landau level (thin lines) and the sum (solid line) [right]. Both figures are taken from Ref. [214].

threshold photon energy $\omega_{\text{th}}(n, \ell) = \sqrt{m^2 + 2\ell eB} + \sqrt{m^2 + 2(\ell + n)eB}$. In the LLL, the threshold does not depend on B , and is simply given by $\omega_{\text{th}}(0, 0) = 2m$. Therefore, even in a magnetic field, a real photon does not decay if its energy is less than $2m$.

The function $I_{\ell\Delta}^n(r_{\parallel}^2)$ has a characteristic behavior around the threshold $r_{\parallel}^2 = s_+^{\ell n}$, which is common to any pair of the Landau levels $(\ell, \ell + n)$. In Fig. 23, we show threshold structures of the real and imaginary parts of $I_{\ell\Delta}^n(r_{\parallel}^2)$ for the lowest and first Landau levels ($n = \ell = 0$ and $n = 1, \ell = 0$). The real part of $I_{\ell\Delta}^n(r_{\parallel}^2)$ increases as r_{\parallel}^2 approaches the threshold from below, and diverges at the threshold. On the other hand, the imaginary part is zero below the threshold, but has an inverse-square-root dependence $\sim 1/(r_{\parallel}^2 - s_+^{\ell n})^{1/2}$ above the threshold. This is the typical threshold behavior in the (1+1) dimensions, determine by the phase-space volume. As a result of such a divergent behavior of $I_{\ell\Delta}^n(r_{\parallel}^2)$ at each threshold, the scalar coefficients $\chi_i(r_{\parallel}^2)$ have divergences at infinitely many points, exhibiting a comb-shaped dependence on r_{\parallel}^2 (see Fig. 23). It is important to notice that these divergences are harmless for the physical quantities, i.e., the dielectric constants $\epsilon_{\perp, \parallel}$ and the refractive indices $n_{\perp, \parallel}$. This is easily understood from the explicit representation of the dielectric constants, Eqs. (243a) and (243b). First, all the coefficients χ_i ($i = 0, 1, 2$) contain the function $I_{\ell\Delta}^n(r_{\parallel}^2)$, and thus they have divergences of the same order at the same r_{\parallel}^2 . Second, these coefficients appear both in the denominators and numerators of Eqs. (243a) and (243b). Therefore, the singularities are canceled to give finite values of the dielectric constants and the refractive indices.

Refractive indices in a strong magnetic field

Having obtained the explicit forms of the scalar functions χ_i , we are able to compute the dielectric constants $\epsilon_{\perp, \parallel}$ or equivalently the refractive indices $n_{\perp, \parallel}$. The formulas are already given in Eqs. (243a) and (243b). However, it should be noticed that these equations must be solved self-consistently with respect to ϵ_{\perp} and ϵ_{\parallel} since χ_i are functions of r_{\perp}^2 and r_{\parallel}^2 [215]. In fact, we have not yet specified any dispersion relation for the external photon momentum when we computed the scalar coefficient functions χ_i . For an on-shell photon, the dispersion relations should be determined by Eqs. (243a) and (243b), which do contain the dielectric constants on the right-hand sides through the photon momenta, r_{\parallel}^2 and r_{\perp}^2 . According to the definition of the dielectric constant (242), those photon momenta are rewritten in terms of ϵ, ω and θ as (by using $q_z^2 = |\mathbf{q}|^2 \cos^2 \theta = \epsilon \omega^2 \cos^2 \theta$, $\mathbf{q}_{\perp}^2 = |\mathbf{q}|^2 - q_z^2 = |\mathbf{q}|^2(1 - \cos^2 \theta) =$

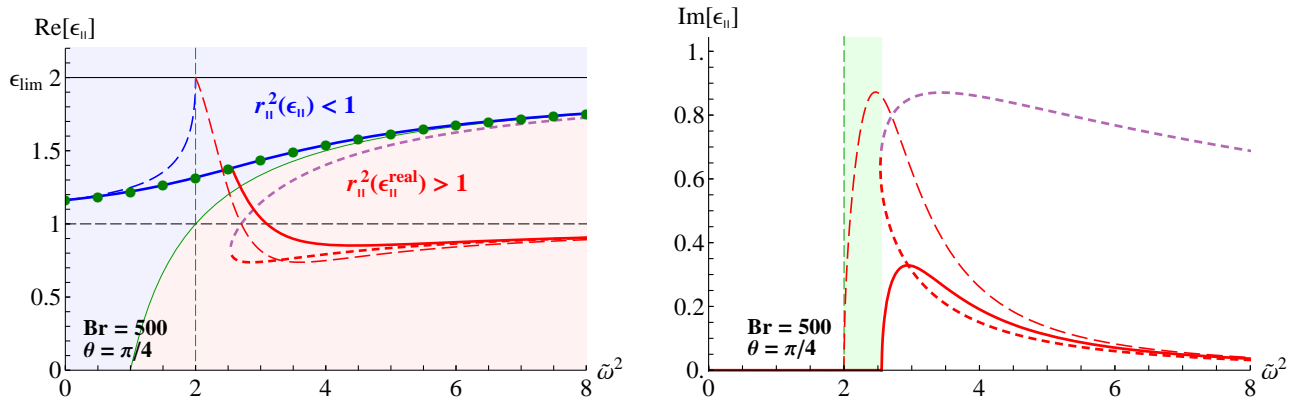


Figure 24: Energy dependence of the dielectric constant $\epsilon_{||}$ in the LLL approximation. The angle θ between the photon momentum and the magnetic field is taken as $\theta = \pi/4$ and $B_r = B/B_c = 500$. Taken from Ref. [215].

$\epsilon \omega^2 \sin^2 \theta$),

$$r_{||}^2 = \tilde{\omega}^2(1 - \epsilon \cos^2 \theta), \quad (272a)$$

$$r_{\perp}^2 = -\epsilon \tilde{\omega}^2 \sin^2 \theta, \quad (272b)$$

where we introduced a scaled photon energy, $\tilde{\omega}^2 = \omega^2/(4m^2)$. This fact indicates that we have to solve these relations in a self-consistent way with respect to the dielectric constant appearing on the both sides. Physically, self-consistent treatment corresponds to including the backreaction of the vacuum against the incident photon field.

Such procedure will demand careful treatments of χ_i with the infinitely many divergences. However, analysis is greatly simplified if we take the limit of a strong magnetic field and focus on the region of photon energies around the first threshold. In this limit, we are allowed to approximate χ_i by the lowest Landau levels (LLL) $n = \ell = 0$. This is because the higher Landau levels are all gapped by the energy scale $\sim \sqrt{eB}$ and go far away from the LLL as the magnetic field increases. With such a simplification, we are able to explicitly study how the self-consistent treatment affects the solution [215]. Since χ_i behaves in the same manner in the vicinity of all the thresholds, which goes like the inverse square root as mentioned above, the behaviors of the refractive indices near the threshold regions should share qualitatively the same character as that in the LLL.

The scalar coefficient functions in the LLL approximation are given as (see Appendix F for more details)

$$\chi_0^{\text{LLL}} = \chi_2^{\text{LLL}} = 0, \quad (273a)$$

$$\chi_1^{\text{LLL}}(r_{||}^2, r_{\perp}^2; B_r) = \frac{\alpha B_r}{4\pi} e^{-\eta} \times \frac{1}{r_{||}^2} [I_{0\Delta}^0(r_{||}^2) - 2]. \quad (273b)$$

In Fig. 22, we confirm the agreement between this analytic expression and the numerical result, and clearly see the dominance of χ_1 . The linear growth of χ_1 with respect to eB is attributed to the Landau degeneracy factor. Then, the dielectric constants are obtained as

$$\epsilon_{\perp}^{\text{LLL}} = 1, \quad (274a)$$

$$\epsilon_{||}^{\text{LLL}}(\tilde{\omega}, \theta; B_r) = \frac{1 + \chi_1^{\text{LLL}}(r_{||}^2, r_{\perp}^2; B_r)}{1 + \chi_1^{\text{LLL}}(r_{||}^2, r_{\perp}^2; B_r) \times \cos^2 \theta}. \quad (274b)$$

Here, we explicitly write the arguments of $\epsilon_{||}^{\text{LLL}}$ and χ_1^{LLL} . The photon momenta $r_{||}^2$ and r_{\perp}^2 on the right-hand side should be expressed as Eqs. (272a) and (272b), respectively, with $\epsilon = \epsilon_{||}$.

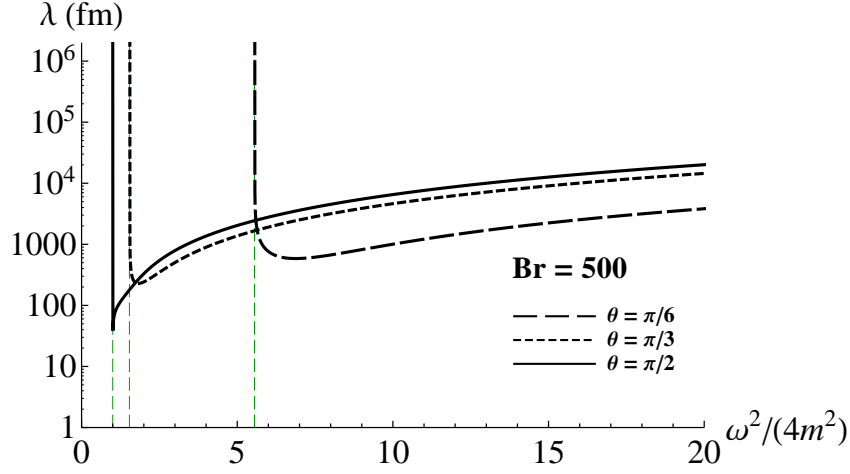


Figure 25: The decay length of real photons against the photon energy, taken from Ref. [215]. θ is an angle between the photon momentum and the magnetic field.

Even with the above simplified case, we need to solve Eq. (274b) numerically. The result for $B_r = 500$ and $\theta = \pi/4$ is shown in Fig. 24. Solid lines correspond to the self-consistent solutions, and the other lines are all incomplete solutions where some kind of approximations are adopted. First of all, look at the green solid line on the left panel. This corresponds to the threshold line $r_{\parallel}^2 = 1$ which is rewritten as $\epsilon = (1 - 1/\tilde{\omega}^2)/\cos^2\theta$. In the high energy limit $\tilde{\omega} \rightarrow \infty$, we find $\epsilon \rightarrow 1/\cos^2\theta \equiv \epsilon_{\text{lim}}$. This is the largest value for ϵ , and can be also obtained from Eq. (274b) in the limit $\chi_1^{\text{LLL}} \rightarrow \infty$. The blue shaded region on the left-hand side of the green solid line corresponds to the region below the threshold $r_{\parallel}^2 < 1$. Second, notice that the blue thick solid line (the real part of ϵ_{\parallel}) largely deviates from unity and increases with increasing photon energies. At some energy, another red solid line appears, which is accompanied by a nonzero imaginary part (the right panel). Therefore, these red lines correspond to unstable decaying states. Lastly, comparing with the other lines, one finds that the effect of the self-consistent treatment is rather large, in particular around the threshold. We can also study the magnetic field dependence and angle dependence which are all available in Ref. [215].

We can perform the same calculation for the refractive index $n_{\parallel}^{\text{LLL}}$. The result is qualitatively the same as for $\epsilon_{\parallel}^{\text{LLL}}$. In particular, $n_{\parallel}^{\text{LLL}}$ is clearly larger than unity (for the same B_r and θ), and its largest value is given by $n_{\parallel}^{\text{LLL}} = \sqrt{\epsilon_{\text{lim}}} \equiv n_{\text{lim}}$. For example, at the angle $\theta = \pi/4$, the refractive index n_{\parallel} keeps increasing with increasing magnetic fields, and approaches the limiting value $n_{\text{lim}} = \sqrt{2}$. This is comparable to the values which we encounter in ordinary life. To name a few, atmosphere of the earth (1 atm, 0 °C) and water (20 °C) have refractive indices, $n_{\text{air}} = 1.000293$ and $n_{\text{water}} = 1.333$, respectively, and “calcite” known as a representative birefringent material shown in Fig. 19 has refractive indices $n_o = 1.6584$ and $n_e = 1.4864$ for ordinary and extraordinary modes, respectively. At a magnetic field strength $B_r \sim (m_{\pi}/m_e)^2 \sim 10^{4-5}$ which could be realized in the ultrarelativistic heavy-ion collisions⁴⁸ (see Ref. [12] and references therein), the refractive index is close to the limiting value $n_{\text{lim}} = \sqrt{2}$, and thus can be larger than that of gas, and even comparable to those of liquid and solid.

In Fig. 25, we show the decay length (246) obtained from the imaginary part of the polarization tensor in the LLL approximation. The magnitude of the magnetic field is taken to be supercritical $B_r = 500$, which may be relevant for physics in the magnetosphere near magnetars (see, e.g., Refs. [22, 23] for reviews). The locations of the thresholds depend on the angle θ between the photon momentum and the magnetic field. We find that the photons having energy larger than the threshold value decay into e^+e^- within a microscopic scale $\sim 0.1\text{-}10$ pm near the thresholds. This implies an importance of

⁴⁸ m_{π} and m_e are masses of a pion $m_{\pi} \sim 140$ MeV and an electron $m_e \sim 0.5$ MeV, respectively.

the real-photon decay in the magnetic fields of magnetars which extend over the macroscopic scales. Corresponding to the large value of the imaginary part near the threshold (see Fig. 23), the decay length is small near the threshold and increases with an increasing photon energy. Then, approaching the threshold for the next Landau level, we will again find a minimum of the decay length. As mentioned before, the behaviors of the imaginary parts near the thresholds are essentially common to all Landau levels, so that the decay length scales as $\sim 1/\omega$ in Eq. (246). When the photon energy is of the order of GeV, the decay length falls in 0.1-10 fm. Therefore, the real-photon decay could be an interesting effect in the relativistic heavy-ion collisions [65, 215, 243, 244]. On the other hand, photons below the threshold energy can survive without decaying into e^+e^- pairs. Photon spectrum after traversing the magnetic regions will be modified so that higher energy modes are cut off.

A couple of the next directions will be the inclusion of electric fields and/or inhomogeneities (depending on the systems). Recently, the refractive indices were investigated in a monochromatic plane-wave configuration of external electromagnetic field [245]. The inhomogeneity was included on the basis of the derivative expansion.

5.3 Photon splitting

Another interesting phenomenon induced by strong fields is the *photon splitting* $\gamma \rightarrow \gamma + \gamma$ for on-shell photons. As well-known as Furry's theorem [132], diagrams having an odd number of external photon lines do not contribute in charge-conjugation even systems, because contracting the fermion fields in all possible ways results in the pairwise diagrams with the opposite charge flows that turn out to exactly cancel each other in the total amplitude.⁴⁹ Therefore, in vacuum without external fields, it does not make any sense to discuss a diagram having three external photon legs. However, in the presence of an external field, it becomes possible to have a nonzero amplitude which persists with the help of an additional odd number of legs for external fields. This means that a real photon can split into two photons in the presence of an external field.

Let us see this in a higher order QED diagram. The lowest order diagram for the effective interactions among photons is given by the box diagram shown in Fig. 26 (a). Its cross section is proportional to α^4 , and experimental detection of such processes is challenging.⁵⁰ But if we replace one photon leg by a strong external field such as a Coulomb field of an atomic nucleus having a charge number Z [Fig. 26 (b)], the cross section is enhanced by a factor of Z^2 . This corresponds to the lowest order photon splitting diagram in the perturbation theory.⁵¹ In fact, such an enhancement and Z^2 -scaling of the cross section were already observed long time ago in the scattering of synchrotron lights off atomic targets with various charge numbers [249]. More recently, direct observation of the same process by back-scattered laser lights was also reported [250]. When the external field is much stronger than the atomic Coulomb field and approaches the critical field, we need to sum up all the diagrams having

⁴⁹This can be easily verified by using the charge-conjugation property $C\gamma^\mu C^{-1} = -(\gamma^\mu)^T$ with C and T being the charge conjugation operator and the transpose of the spinor indices, respectively. Since the trace (for the spinor index) is invariant under the transpose, one can invert the ordering of the vertices by the use of the above property, and finds that the pairwise diagrams have the same amplitudes but with a relative sign $(-1)^{n_v}$ for the number of vertices n_v (see also Ref. [246] for a pedagogical explanation). When the charge-conjugation symmetry is broken by, e.g., a finite chemical potential, the exact cancellation may not occur.

⁵⁰When all the photon legs are on-shell, this process is called the light-by-light scattering. There are intensive experimental studies of this process at the Large Hadron Collider (LHC) in recent years [17–20] (see Ref. [247] for a pre-experiment estimate of signal efficiency). This measurement is made possible by an enhancement of the cross section by a large photon flux induced by highly accelerated nuclei and a suppression of medium-induced backgrounds in the ultraperipheral collision events where the nuclei pass by each other and the medium, or the quark-gluon plasma, is not created.

⁵¹Similarly, if we replace two photon legs by the atomic Coulomb fields, the cross section gets a huge enhancement factor Z^4 for a large Z . This process is called the Delbrück scattering, and is already observed in experiments. See Ref. [248] for the current status of experiments and theoretical description including higher order corrections.

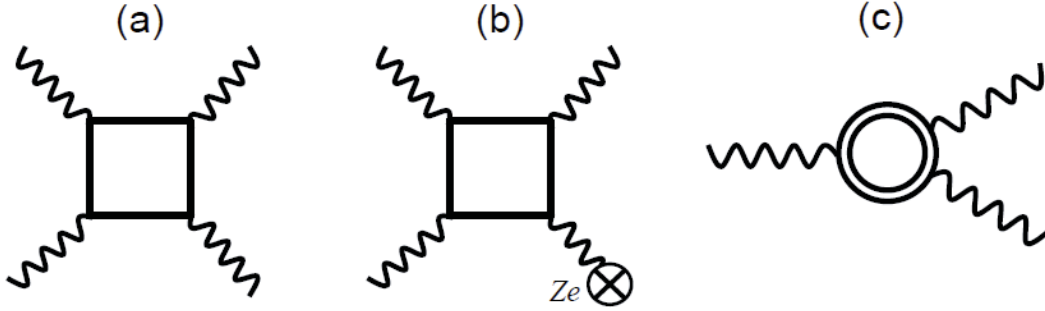


Figure 26: (a) Photon-photon scattering at lowest order in QED, (b) photon splitting in atomic Coulomb field, (c) photon splitting in strong external fields.

multiple interactions with the external field, and the photon splitting shown in Fig. 26 (c) is expected to occur. There, the double line corresponds to a dressed electron in strong external field that was introduced in previous sections.

Similar to the vacuum birefringence in strong fields, if photon's energy is small enough $\omega \ll m$, we can study the photon splitting by using the HE effective theory. This was done by Adler, et al. [205, 219], who discussed a weak-field approximation. They found that the lowest contribution comes from the hexagonal diagram with six photon fields attached,⁵² among which three are propagating photons and the rest are external fields. The absorption coefficient κ for the photon splitting in the magnetic field is computed as $\kappa \sim \int dk_1 dk_2 |\mathcal{M}(\gamma(k) \rightarrow \gamma(k_1) + \gamma(k_2))|^2 \delta^4(k - k_1 - k_2)$ with \mathcal{M} being the photon splitting amplitude, and is estimated as

$$\kappa = c \frac{\alpha^3}{60\pi^2} \left(\frac{\omega}{m}\right)^5 \left(\frac{B \sin \theta}{B_c}\right)^6 m, \quad (275)$$

where c is a numerical constant which depends on the polarization, ω is the energy of an incoming photon $k^\mu = (\omega, \mathbf{k})$, and θ is the angle between the incoming photon momentum \mathbf{k} and the external magnetic field. The hexagonal diagram having six vertices should amount to $(e^6)^2 = e^{12}$ in total. In the above result, a half of them appears in $\alpha^3 = (e^2/4\pi)^3$ and the other half in $(B/B_c)^6 = (eB/m^2)^6$. Being suppressed by small numbers $\alpha \ll 1$, $\omega/m \ll 1$, and $B/B_c \ll 1$, this cross section is quite small.

However, for the photon energy below the threshold of the decay into an e^+e^- pair, the photon splitting is the only process at work. Besides, when the magnetic field is strong enough, we can again use the analytic representation of the HE effective theory for the wrenchless fields [212, 213]. The result shows that the coefficient κ increases with an increasing B , and saturates at a high value for extremely strong magnetic fields beyond the critical field. Thus, we may expect to have observable effects, for example, around neutron stars or magnetars: There, a lot of photons will traverse a strong magnetic fields over a large spatial scale, which will compensate the smallness of the absorption coefficient to make the effects sizable. Summary of applications to neutron stars and magnetars is available in Refs. [23, 251].

When the photon energy is close to or larger than the electron mass, one needs to compute the triangle diagrams with the resummed fermion propagators (see, e.g., Refs. [252–262]). In this case, one would need to examine the competition between the photon splitting and the decay into an e^+e^- pair possibly in the magnetosphere of magnetars [252, 254, 259].

⁵²To draw this conclusion, one assumes the light-like dispersion relation of photons: Otherwise, the square diagrams have finite contributions. This implies an interplay between the vacuum birefringence and the photon splitting changes the splitting rate. In nonlinear optics, it is well-known that the “phase matching” is important to observe the nonlinear processes such as high-harmonic generation and can be achieved by use of birefringent materials.

6 Heisenberg-Euler effective action revisited: Extensions to finite temperature/density and QCD

There is a long history in the investigations of low-energy effective actions in pure Yang-Mills theories and QCD. One of the motivations for studying this problem is to determine the ground state of QCD. While this may require nonperturbative analyses of strongly coupled quantum dynamics, perturbative analyses have also been playing some roles in understanding and modeling the QCD ground state. Of course, a simple fixed-order perturbative calculation may not suffice because a class of diagrams would be enhanced by nonperturbative physics underlying in the QCD vacuum. Assuming that the physical degrees of freedom relevant for the low-energy dynamics are the non-Abelian electromagnetic fields which we call the *chromo*-electromagnetic fields, one may perform resummed perturbative calculations of the effective actions in a similar way that we analysed the HE effective action in Sec. 4. In this sense, the early investigations of the low-energy effective actions can be understood as the *non-Abelian extensions of the HE effective action*.

The first attempt in this direction was performed for the pure Yang-Mills theory with $SU(N)$ symmetry [263], and the result was expressed with the proper-time integral. Explicit evaluation of the proper-time integration was later done in the pure $SU(2)$ Yang-Mills theory [107, 264, 265]. In particular, the authors computed the effective potential in homogeneous chromo-magnetic fields and found that the effective potential has a local minimum at a nonzero chromo-magnetic field, suggesting the realization of paramagnetism in the ground state of the Yang-Mills theories known as the Savvidy vacuum [107, 264] (see Ref. [266] for a recent retrospective review).

It was important to notice that this local minimum is induced by the logarithmic term arising from the gluon-loop contribution to the effective action (see Ref. [267] for an early observation), and that the prefactor of the logarithm has the opposite sign as compared to those both in spinor and scalar QED (remember the logarithmic behavior mentioned below Eq. (260) for spinor QED). The authors explicitly showed that this logarithm leads to the renormalization-group equation with the negative beta function [107, 264, 265], which had been known to give rise to the asymptotic freedom [268, 269]. Under the constraint of the Lorentz symmetry $\epsilon\mu = 1$, the charge antiscreening effect ($\epsilon < 1$) and the paramagnetism ($\mu > 1$) imply each other, and one may attribute the asymptotic freedom to a consequence of the vacuum paramagnetism [270–274].⁵³

After those effective-potential studies, Nielsen and Olesen found the presence of a tachyonic unstable mode in fluctuations around the non-Abelian magnetic fields [62] (see also Refs. [108, 275, 276]). Namely, the spin-1 Zeeman effect in a chromo-magnetic field causes a negative value of the energy square in the lowest Landau levels. We have already seen a similar behavior in Fig. 4 with a (hypothetical) electrically charged spin-1 boson in an Abelian magnetic field (see Ref. [277] for an early observation). As we will explicitly see in this section, the unstable mode provides about a half of the total logarithmic contributions to the effective action among the infinite tower of the Landau levels, and also gives rise to an imaginary part of the effective action (even in the absence of an electric field). It is worth mentioning that similar implications were obtained in an earlier study [267] where the authors considered the vacuum fluctuation of a spin-1 vector boson in an Abelian electromagnetic field. The authors observed a charge antiscreening effect in their concluding remarks, which implies the essential role of the spin interaction, although the presence of such a vector boson was not located in the Abelian theory.

Since a nonzero chromo-magnetic field having specific color and spatial directions breaks the gauge and Lorentz symmetries, it cannot be regarded as the true vacuum by itself. However, Ambjorn and Olesen later proposed that the ground state of pure Yang-Mills theories would be realized by the so-called “Spaghetti vacuum” which consists of nonzero non-Abelian magnetic fields having a nontrivial spatial structure (Kagome-like configuration in the transverse plane) so that the gauge and Lorentz

⁵³We discuss recent lattice QCD studies on magnetization in Sec. 7.4.1.

symmetries are recovered on average at large scales [117, 278]. On the other hand, to determine the ground state in QCD, we need to include the contribution of quarks. Actually, as was done in Ref. [279], this procedure is just a straightforward extension of the HE effective action. Calculation of the effective action of the Yang-Mills theory or QCD at finite temperature also followed in Refs. [280–283] (see also Refs. [284–289] for the QED effective action at finite temperature). These studies based on the perturbative effective actions provided significant insights into the understanding of the QCD ground state, which then followed by various nonperturbative analyses [290–297].

Recently, we have seen a revival of interest in strong non-Abelian electromagnetic fields motivated by a modern picture of relativistic heavy-ion collisions. When the collision energy is high enough, colliding nuclei can be described as “color glass condensates” (weakly interacting high-density gluonic states) [298, 299] which, after the collision, produce color electromagnetic fields whose strength is very large compared with the quark mass: $g\mathcal{F} \gg m_q^2$. This strong color electromagnetic field is a transitional state in between the color glass condensate and a quark-gluon plasma, and is called the “glasma” [300–302]. While the glasma is generated by color sources made of valence-like partons of each colliding nucleus (partons carrying larger fractions of momentum), we are able to treat it as a source-free field in the forward light cones (i.e., in the region between two receding nuclei). Therefore, to describe the particle production from the glasma we are able to use the non-Abelian analog of the HE effective action. Moreover, it has been also recognized that the heavy-ion collisions of two electrically charged nuclei produce extremely strong electromagnetic fields [6–9, 303]. Thus, there comes a theoretical interest in the interplay between the electromagnetic fields and the color electromagnetic fields. For example, analytic representation of the HE effective action in the presence of both fields was recently obtained at zero temperature [115, 304] and at finite temperature [305]. At finite temperature, the effective action also contains the Polyakov loop as well as the color electromagnetic fields. Since the Polyakov loop is an order parameter for the deconfinement phase transition, the generalized HE effective action allows us to study the effects of electromagnetic fields on the deconfinement phase transition [305].

This section is devoted to the outline of such recent extensions of the HE effective action. After we explain the derivation of general form of the effective action at zero and finite temperatures, we discuss physical applications of the results to the Schwinger mechanism and the analyses of the QCD effective potential for color electromagnetic fields at zero temperature and the Polyakov-loop effective action at finite temperature.

6.1 Extension to finite temperature/density

We extend the HE effective action discussed in Sec. 4.1 to finite temperature/density by the use of the imaginary-time formalism. This extension was carried out for the effective action in a magnetic field in an early work [284] and that for electric and magnetic fields in Ref. [288]. It was further elaborated by Gies in Ref. [289], and the technical details were reviewed in Ref. [102].

First of all, the Lorentz symmetry is broken in the presence of medium, and our reference frame may be specified by the medium flow vector u^μ . This means that configurations of constant electromagnetic fields are not completely classified by the Lorentz invariants a and b like in vacuum. Therefore, one cannot simply deduce the general form of the effective action by starting out from the parallel/antiparallel configuration, which is now not uniquely connected to the class of field configurations specified by a , b by a Lorentz transformation. We will need to introduce the covariant form of the electric field $E^\mu \equiv F^{\mu\nu}u_\nu$ to express the effective action in a general Lorentz frame. Moreover, since the temporal component of the gauge field is distinguished from the spatial components, the extended duality (129) under the interchange between the electric and magnetic components, ia and b does not hold in the presence of medium.

Next, one should be careful of the gauge transformation in a compact spacetime. In the imaginary-time formalism for thermal field theory, the temporal coordinate is compactified with the periodic and

antiperiodic boundary conditions $\psi(\tau = 0, \mathbf{x}) = \pm\psi(\tau = \beta, \mathbf{x})$ for bosons in scalar QED and fermions in spinor QED; We introduce the imaginary time $t \rightarrow \tau = -it$, and the period is set by an inverse temperature, $\beta = 1/T$. Those boundary conditions are, however, not invariant under general gauge transformations. Thus, one should keep track of the pair of the covariant derivative and the boundary conditions when a gauge transformation is performed.

We recapitulate a general discussion with a covariant derivative under an external field A_{ext}^μ :

$$iD_\tau = \partial_\tau - q_f A_{\text{ext}}^0 \quad \text{with} \quad \psi(\tau = 0, \mathbf{x}) = \pm\psi(\tau = \beta, \mathbf{x}). \quad (276)$$

Here, we focus on the temporal component since the spatial directions are the same as in vacuum. We examine whether A_{ext}^0 can be gauged away as

$$\psi(\tau, \mathbf{x}) \rightarrow \psi'(\tau, \mathbf{x}) = e^{q_f \int_0^\tau d\tau' A_{\text{ext}}^0(\tau')} \psi(\tau, \mathbf{x}). \quad (277)$$

As we should expect, we cannot simply remove A_{ext}^0 from the theory and find a modification of the boundary condition as

$$iD_\tau \rightarrow \partial_\tau \quad \text{with} \quad \psi(\tau = 0, \mathbf{x}) = \pm e^{q_f \int_0^\beta d\tau' A_{\text{ext}}^0(\tau')} \psi(\beta, \mathbf{x}). \quad (278)$$

The modification of the boundary condition gives rise to a shift of the Matsubara frequency

$$p^0 = i\omega_k^{B/F} + q_f T \int_0^\beta d\tau' A_{\text{ext}}^0(\tau'), \quad (279)$$

where $\omega_k^{B/F} = 2k\pi T, (2k+1)\pi T$ are the Matsubara frequency for a boson and fermion field, respectively. This is just similar to the shift by a chemical potential: $p^0 \rightarrow i\omega_k + \mu$ (see, e.g., Ref. [306, 307]).⁵⁴ The integral over the temporal period is invariant under a periodic gauge transformation where the gauge parameter is taken to be the same at $\tau = 0$ and $\tau = \beta$. Namely, if we perform another gauge transformation, the integral in Eq. (279) gives a vanishing surface term that is a vanishing difference between the gauge parameter at $\tau = 0$ and β .

Below, we discuss the case where A_{ext}^0 can contain not only a constant external field but also other external fields. To include the constant fields with the FS gauge as in vacuum, we perform a gauge transformation

$$\psi(\tau, \mathbf{x}) \rightarrow \psi'(\tau, \mathbf{x}) = e^{q_f \int_0^\tau d\tau' \{A_{\text{ext}}^0(\tau') - A_{\text{FS}}^0(\tau')\}} \psi(\tau, \mathbf{x}). \quad (280)$$

Accordingly, the pair of the covariant derivative and the boundary condition is transformed to

$$iD_\tau = \partial_\tau - q_f A_{\text{FS}}^0 \quad \text{with} \quad \psi(\tau = 0, \mathbf{x}) = \pm e^{q_f \int_0^\beta d\tau' \{A_{\text{ext}}^0(\tau') - A_{\text{FS}}^0(\tau')\}} \psi(\beta, \mathbf{x}). \quad (281)$$

The modification of the boundary condition (281) gives rise to the shift of the Matsubara frequency

$$p^0 = i\omega_k^{B/F} + q_f T \int_0^\beta d\tau' \{A_{\text{ext}}^0(\tau') - A_{\text{FS}}^0(\tau')\}. \quad (282)$$

Since only the FS gauge component is left in the covariant derivative (281) after the gauge transformation, the temporal component does not contribute to the Schwinger phase (114). Instead, one should

⁵⁴The shift in Eq. (279) is also analogous to the periodic energy shift due to the Aharonov-Bohm phase on a circle; The energy degeneracy between the clockwise and counterclockwise propagation is lifted due to the AB phase (see, e.g., Ref. [308]). One could interpret the above gauge-invariant integral (or a chemical potential) in a similar way (though the Matsubara frequency is not an energy spectrum in the imaginary world). The shift in Eq. (279) is periodic for an Euclidean gauge field when the integral value coincides with an integer multiple of $2\pi/q_f$, i.e., $\int_0^\beta d\tau' A_{\text{ext}}^0(\tau', \mathbf{x}) = i(2\pi/q_f)\lambda$ with an integer λ ; Such a shift can be absorbed into the Matsubara frequency.

include the shift in Eq. (282). The constant-field component in A_{ext}^0 is subtracted by A_{FS}^0 ; Namely, if A_{ext}^0 is just gauge-equivalent to A_{FS}^0 , the integral gives a vanishing surface term under a periodic gauge transformation. For notational simplicity, we denote the shift as $p^0 = i\omega_k^{B/F} + q_f\varphi$ with

$$\varphi := T \int_0^\beta d\tau' \{A_{\text{ext}}^0(\tau') - A_{\text{FS}}^0(\tau')\}. \quad (283)$$

A non-Abelian analog of the shift is the Polyakov loop discussed in Sec. 6.6.

Bearing these points in mind, we compute the thermal contribution to the effective action in Eqs. (188) and (189) by adopting the imaginary-time formalism with the replacement rules $\int dp^0 \rightarrow iT \sum_{k=-\infty}^\infty$ and of Eq. (282). First, we focus on the effective action in the presence of the parallel electric and magnetic fields in the medium rest frame. The matrix element (187) in the imaginary-time formalism is now given as

$$\text{tr} \langle x | e^{-i\hat{H}s} | x \rangle = 4iT \sum_{k=-\infty}^\infty \int \frac{d^3p}{(2\pi)^3} \exp \left(i \frac{p_{\parallel}^2}{q_f E} \tanh(q_f E s) + i \frac{p_{\perp}^2}{q_f B} \tan(q_f B s) \right) \Bigg|_{p^0=i(2k+1)\pi T+q_f\varphi}, \quad (284)$$

where $\hat{H} = D^2 + \frac{q_f}{2} F^{\mu\nu} \sigma_{\mu\nu}$ as defined in Eq. (182). The Schwinger phase $\Phi_A(x, x')$ after the gauge transformation (280) vanishes in the coincidence limit, $x \rightarrow x'$. Performing the three-dimensional momentum integral and reorganizing the Matsubara sum by using the Poisson summation formula,⁵⁵ we obtain the effective Lagrangian

$$\begin{aligned} \mathcal{L}^{(1)} &= \sum_{f=1}^{N_f} \frac{1}{8\pi^2} \int_0^\infty \frac{ds}{s} e^{-i(m_f^2 - i\epsilon)s} \frac{(q_f E)(q_f B)}{\tanh(q_f E s) \tan(q_f B s)} \\ &\quad \times \left[1 + 2 \sum_{\bar{k}=1}^\infty (-1)^{\bar{k}} e^{iq_f E \coth(q_f E s) \frac{\bar{k}^2}{4T^2}} \cosh(q_f \varphi \beta) \right]. \end{aligned} \quad (285)$$

The first term in the square brackets, which is the term with $\bar{k} = 0$ in the Poisson summation, agrees with the zero-temperature contribution in Eq. (188). Therefore, we find that the first and second terms in the square brackets account for the zero- and finite-temperature contributions, respectively.⁵⁶ The alternating sign, $(-1)^{\bar{k}}$, originates from the antiperiodic boundary condition [cf. Eq. (315) below for the periodic boundary condition, where the alternating sign is absent]. The HE effective Lagrangian (285) at finite temperature reproduces that in a magnetic field [284] and in electric and magnetic fields [288].

At this stage, we should note that the system is assumed to be in a thermal equilibrium by construction of the imaginary-time formalism. For a system to reach such an equilibrium state, an external electric field, which is pumping an energy to the system, should be screened by the thermal particles

⁵⁵The Poisson summation formula for a generic function reads

$$\sum_{k=-\infty}^\infty f(x+k) = \sum_{\bar{k}=-\infty}^\infty e^{2\pi i \bar{k} x} \int_{-\infty}^\infty dx' f(x') e^{-2\pi i \bar{k} x'}.$$

If one takes a Gaussian $f(x) = e^{-\sigma x^2}$, one finds a formula useful in the present calculation [102, 284, 289, 309]:

$$\sum_{k=-\infty}^\infty e^{-\sigma(k-z)^2} = \sum_{\bar{k}=-\infty}^\infty \sqrt{\frac{\pi}{\sigma}} e^{-\frac{\pi^2}{\sigma} \bar{k}^2 - 2\pi i z \bar{k}}.$$

⁵⁶The index \bar{k} should not be confused with the one in the Matsubara summation. The Poisson summation formula is applied in order to separate the vacuum part from the temperature-dependent part.

and damped out [310–312]. Therefore, it is not legitimate to address effects of an external electric field within the imaginary-time formalism in the rigorous sense, so that one should carefully check the validity of the framework for a phenomenological application to each physical situation. For example, there is a controversy on the medium modification of the Schwinger mechanism [285, 288, 289, 313–319].⁵⁷ Nevertheless, a finite-volume system in an electric field may reach a steady state, and one could measure relevant physical quantities (see Ref. [320] for a recent study on an electric susceptibility).

The generalization to the expression in an arbitrary Lorentz frame was addressed in Ref. [289] with a detailed account (see also Ref. [102]). Therefore, we only quote the result:

$$\mathcal{L}^{(1)} = \sum_{f=1}^{N_f} \frac{1}{8\pi^2} \int_0^\infty \frac{ds}{s} e^{-i(m_f^2 - i\epsilon)s} \frac{(q_f a)(q_f b)}{\tanh(q_f a s) \tan(q_f b s)} \times \left[1 + 2 \sum_{\bar{k}=1}^{\infty} (-1)^{\bar{k}} e^{i \frac{q_f h(s)}{4T^2} \bar{k}^2} \cosh(q_f \varphi \beta \bar{k}) \right], \quad (286)$$

where the explicit temporal component A^0 in φ should be also replaced by the projection $A_u \equiv A_{\text{ext}}^\mu u_\mu$ along the medium flow vector u^μ . As in Eq. (285), the first term in the square brackets corresponds to the vacuum contribution, so that the parallel electromagnetic fields, E , B , are simply replaced by the invariants, a , b , outside the brackets. However, as mentioned above, this simple Lorentz transform does not work for the thermal contribution (the second term in the brackets), and the explicit dependence on the flow vector u^μ appears. In addition to A_u just mentioned above, $h(s)$ in the exponent also depends on u^μ :

$$h(s) \equiv a \frac{b^2 + e_u^2}{a^2 + b^2} \coth(q_f a s) + b \frac{a^2 - e_u^2}{a^2 + b^2} \cot(q_f b s), \quad (287)$$

where the power of the electric field $e_u^2 = -E^\mu E_\mu$ is defined with the covariant form of the electric field, $E^\mu \equiv F^{\mu\nu} u_\nu$. In the medium rest frame, we have $u^\mu = (1, 0, 0, 0)$ and $E^\mu = (0, \mathbf{E})$, so that $e_u^2 = |\mathbf{E}|^2$, which reproduces Eq. (285) obtained in an earlier work [288].

It would be also instructive to reproduce the familiar result in the absence of the external fields. We focus on the thermal part. Taking the vanishing field-strength limit and maintaining only φ , we have

$$\mathcal{L}_T^{(1)} = \sum_{f=1}^{N_f} \frac{1}{4\pi^2} \sum_{\bar{k}=1}^{\infty} (-1)^{\bar{k}} \cosh(q_f \varphi \beta \bar{k}) \int_0^\infty \frac{ds}{s^3} e^{-i(m_f^2 - i\epsilon)s} e^{\frac{i}{4T^2 s} \bar{k}^2}. \quad (288)$$

After the rotation of the integral contour to the negative imaginary axis, the proper-time integral can be identified with the modified Bessel function of the second kind $K_n(z)$ with the help of the integral representations [321, 322]⁵⁸

$$K_n(z) = \frac{1}{2} \int_0^\infty \frac{dt}{t^{1-n}} e^{-\frac{z}{2}(t + \frac{1}{t})} \quad (289a)$$

⁵⁷Seemingly, there is no medium modification from the one-loop effective action [288, 289, 313], while medium modifications were put forwarded in some literature (see discussions and references in another review article [283]). On the other hand, the interaction between a thermal photon and a fermion pair appears in the two-loop level, and absorption of the thermal photon by the fermion pair may “assist” the virtual fermion-antifermion pair to penetrate the potential barrier for the pair creation. This point was discussed with an explicit calculation in the low-temperature limit, $T \ll m$ [102, 314], where the population of thermal photons is sizeable, but that of the thermal fermions is suppressed by the Boltzmann factor. (Thus, possible effects of the thermal fermions, e.g., Pauli blocking, were not included.) Further investigations may be needed not only for technical details but also for finding a reasonable setup of the problem depending on phenomenological situations.

⁵⁸The integral in Eq. (288) can be identified with the first representation (289a) according to a property $K_n(z) = K_{-n}(z)$ which follows from the change of the integral variable $t \rightarrow 1/t$. The second representation is obtained by integrating Eq. (7) in Ref. [322] by parts.

$$= \frac{\sqrt{\pi}}{\Gamma(n - \frac{1}{2})} \left(\frac{z}{2}\right)^{n-1} \int_1^\infty dy y (y^2 - 1)^{n-\frac{3}{2}} e^{-yz}, \quad (289b)$$

for $\text{Re}[z] > 0$ and $n > 1/2$. It is found that

$$\mathcal{L}_T^{(1)} = -2 \frac{(m_f T)^2}{\pi^2} \sum_{f=1}^{N_f} \sum_{\bar{k}=1}^{\infty} \frac{(-1)^{\bar{k}}}{\bar{k}^2} \cosh(q_f \varphi \beta \bar{k}) K_2\left(\frac{m_f}{T} \bar{k}\right). \quad (290)$$

By changing the integral variable as $p = m_f (y^2 - 1)^{1/2}$ in the second integral representation (289b), one can retrieve the familiar momentum-integral form as

$$K_2\left(\frac{m_f}{T} \bar{k}\right) = 2\pi^2 \left(\frac{\bar{k}}{m_f^2 T}\right) \int_0^\infty \frac{d^3 p}{(2\pi)^3} e^{-\beta \sqrt{p^2 + m_f^2} \bar{k}}, \quad (291)$$

where $\beta = 1/T$ and $\Gamma(\frac{3}{2}) = \sqrt{\pi}/2$. Plugging this expression back to the effective Lagrangian and identifying the Poisson summation with the Taylor series $\ln(1+x) = -\sum_{\bar{k}=1}^{\infty} \frac{(-x)^{\bar{k}}}{\bar{k}}$, we find the familiar form (see, e.g., a standard textbook [306])

$$\mathcal{L}_T^{(1)} = 2T \sum_{f=1}^{N_f} \int \frac{d^3 p}{(2\pi)^3} \left[\ln\left(1 + e^{-\beta(\epsilon_{\mathbf{p}} - q_f \varphi)}\right) + \ln\left(1 + e^{-\beta(\epsilon_{\mathbf{p}} + q_f \varphi)}\right) \right], \quad (292)$$

where the one-particle energy is given by $\epsilon_{\mathbf{p}} = \sqrt{\mathbf{p}^2 + m_f^2}$. Notice that φ appears in the positions of the chemical potential as anticipated. In the vanishing φ and massless limits, the Stefan-Boltzmann law is reproduced

$$\lim_{q_f \varphi, m_f \rightarrow 0} \mathcal{L}_T^{(1)} = (2 \cdot 2 \cdot N_f) \times \frac{7}{8} \cdot \frac{\pi^2}{90} T^4, \quad (293)$$

where the degeneracy factor comes from two spin states, and particle and antiparticle contributions.

6.2 Spontaneous chiral symmetry breaking: A preview of the magnetic catalysis

In this section, we examine the effective potential $[V^{(1)} \equiv -S_{\text{eff}}^{(1)} / \int d^4 x]$ in strong QED magnetic fields at zero and finite temperature. Focusing on a single-flavor case, we drop the flavor sum for simplicity. Then, taking the vanishing E limit in Eq. (286), we have the effective potential in magnetic fields

$$V^{(1)} = \frac{|q_f B|}{8\pi^2} \int_{1/\Lambda^2}^\infty \frac{ds}{s^2} e^{-m^2 s} \coth(q_f B s) \left[1 + 2 \sum_{\bar{k}=1}^{\infty} (-1)^{\bar{k}} e^{-\frac{1}{4T^2 s} \bar{k}^2} \right], \quad (294)$$

where we work in the fluid rest frame. While we take $\varphi = 0$ and do not introduce a chemical potential, density effects can be studied with the same framework as an extension. Note also that we rotated the integral contour to the negative imaginary axis and inserted a UV cutoff to regularize the divergence in the vacuum part.

6.2.1 Gap equation at zero temperature

Specifically, we discuss the strong-field limit such that $|eB| \gg m^2$, where the LLL contribution plays the dominant role. Remembering the Landau-level decomposition of the HE effective action discussed in Sec. 4.2.4, we find the vacuum part of the effective potential:

$$V_{\text{vac}}^{(1)} \sim \rho_B \left[\frac{1}{4\pi} \int_{1/\Lambda^2}^{\infty} \frac{ds}{s^2} e^{-m^2 s} \right] = \rho_B \frac{m^2}{4\pi} \left[\frac{\Lambda^2}{m^2} - \ln \frac{\Lambda^2}{m^2} + \gamma_E - 1 \right], \quad (295)$$

where $\rho_B = |q_f B|/(2\pi)$ is the density of states introduced in Sec 2 and γ_E is the Euler-Mascheroni constant $\gamma_E = 0.577 \dots$. The proper-time integral has been reduced to the (1+1)-dimensional form when the cutoff is taken to be smaller than the field strength, $\Lambda^2 \lesssim |eB|$, meaning that our cutoff is less than the energy gap of the higher LL.

We demonstrate an interesting property of the fermion effective potential (295) by the use of the Nambu–Jona-Lasinio model (see, e.g., Ref. [323]). Since details of the model are not important for the present discussion,⁵⁹ let us assume the simplest Lagrangian:

$$\mathcal{L}_{\text{NJL}} = i\bar{\psi}\not{\partial}\psi + \frac{\lambda_{\text{NJL}}}{2}(\bar{\psi}\psi)(\bar{\psi}\psi) \sim \bar{\psi}(\not{\partial} - m_{\text{dyn}})\psi - \frac{m_{\text{dyn}}^2}{2\lambda_{\text{NJL}}}. \quad (296)$$

In the rightmost expression, we applied the mean-field approximation for the fermion bilinear field $\bar{\psi}\psi$ which may fluctuate around the expectation value $\langle\bar{\psi}\psi\rangle$. The associated dynamical mass is defined as $m_{\text{dyn}} = -\lambda_{\text{NJL}}\langle\bar{\psi}\psi\rangle$ and the higher order fluctuations are dropped. Hereafter, the mass parameter contained in the potential (295) is also regarded as the dynamical mass m_{dyn} . Combining the mean-field term and the one-loop contribution, we get the effective potential

$$V_{\text{vac}}^{(1)} = \frac{m_{\text{dyn}}^2}{2\lambda_{\text{NJL}}} + \rho_B \frac{m_{\text{dyn}}^2}{4\pi} \left[\frac{\Lambda^2}{m_{\text{dyn}}^2} - \ln \frac{\Lambda^2}{m_{\text{dyn}}^2} + \gamma_E - 1 \right]. \quad (297)$$

Equivalent results were shown in Refs. [106, 324] and Ref. [325], which however have slightly different forms from the above result. The differences may be attributed to the contributions of the higher Landau levels [106, 324] and slightly different cutoff schemes introduced in the momentum integral [325] and in the proper-time integral in Eq. (295), respectively.

We now find an interesting consequence of the dimensional reduction in the effective potential (297). The dynamical mass is determined by the gap equation from the stationary condition $\partial V_{\text{q}}^{\text{vac}}/\partial m_{\text{dyn}} = 0$, i.e.,

$$\frac{\pi}{\rho_B \lambda_{\text{NJL}}} + \frac{\gamma_E}{2} - \ln \frac{\Lambda}{m_{\text{dyn}}} = 0. \quad (298)$$

This gap equation has a nontrivial solution ($m_{\text{dyn}} \neq 0$) regardless of the coupling strength, which we can immediately obtain as

$$m_{\text{dyn}}(T=0) = \Lambda' \exp\left(-\frac{\pi}{\rho_B \lambda_{\text{NJL}}}\right). \quad (299)$$

We absorbed a purely numerical order-one factor into the definition of the cutoff scale, $\Lambda' = \Lambda e^{-\gamma_E/2}$, which does not have any dependence on the parameters in the model. Notice that the above solution has non-analytic dependences on the coupling constants λ_{NJL} and q_f , indicating that the dynamical mass gap emerges as a result of the nonperturbative effect which is captured by the resummation of the

⁵⁹We will discuss the roles of the gauge bosons in the next section.

infinite number of diagrams. The overall coefficient is determined by the cutoff scale. This scale should be small enough $\Lambda^2 \lesssim |q_f B|$, as noted above. We should also ensure that we work within the cutoff scale of the NJL model, $\Lambda^2 \lesssim \Lambda_{\text{NJL}}^2$. Therefore, the smaller value, $\Lambda' \sim \min[\sqrt{q_f B}, \Lambda_{\text{NJL}}]$, determines the size of dynamically generated mass gap (299).

Since the gap equation (298) always has the nontrivial solution, the chiral symmetry breaking takes place in strong magnetic fields without resorting to a large value of the coupling strength. Remember that the NJL model in the absence of magnetic fields exhibits the chiral symmetry breaking only when the coupling strength is larger than a critical value (see, e.g., Ref. [323]). These observations suggest that the mechanism of the chiral symmetry breaking in the strong magnetic field should be qualitatively different from that in the absence of the magnetic field.

It is the growth of the logarithm, $\ln m_{\text{dyn}}$, that forces the effective potential to be convex upward at the origin and the trivial solution ($m_{\text{dyn}} = 0$) to be unstable. The emergence of the logarithm is tracked back to the dimensionality of the integral in Eq. (295), of which the log term goes like $\int (ds/s^2) \cdot (-m_{\text{dyn}}^2 s) \sim m_{\text{dyn}}^2 \ln m_{\text{dyn}}$ in the dimensionally reduced case, while $\int (ds/s^2) \cdot (-m_{\text{dyn}}^2 s)^2/s \sim m_{\text{dyn}}^4 \ln m_{\text{dyn}}$ in the usual four dimensional case at $q_f B = 0$. In the latter case with the quartic prefactor, this term could be subdominant against the quadratic term m^2/λ_{NJL} near the origin $m_{\text{dyn}} = 0$, so that the fate of the vacuum depends on the competition between those terms, yielding the critical coupling strength. In contrast, the effective dimensional reduction gives rise to the logarithm appearing with the quadratic prefactor, which overwhelms the other terms for any value of λ_{NJL} [324, 325].

Therefore, the essential mechanism of the chiral symmetry breaking is identified with the dimensional reduction to the (1+1)-dimensions in the strong magnetic field. Shown above is a quick view of the so-called ‘‘magnetic catalysis’’ of the chiral symmetry breaking [106, 324, 326], of which the various aspects have been investigated in the last two decades. We will discuss this phenomenon more intensively in Sec. 7.

6.2.2 Chiral phase transition temperature

Let us include the finite-temperature contribution to determine the chiral phase transition temperature. As in the vacuum part, we take the strong-field limit

$$V_q^T \sim \rho_B \frac{1}{4\pi} \int_0^\infty \frac{ds}{s^2} e^{-m_{\text{dyn}}^2 s} \sum_{\bar{k}=1}^\infty 2(-1)^{\bar{k}} e^{-\frac{1}{4T^2 s} \bar{k}^2} = \rho_B \frac{m_{\text{dyn}}^2}{4\pi} \sum_{\bar{k}=1}^\infty (-1)^{\bar{k}} \frac{8T}{m_{\text{dyn}} \bar{k}} K_1\left(\frac{m_{\text{dyn}}}{T} \bar{k}\right). \quad (300)$$

It is easy to check again the equivalence between the representations in terms of the proper-time integral and of the momentum integral. Applying the formula (289b) to Eq. (300), we find the (1+1)-dimensional form of the potential as

$$V_T^{(1)} = -\rho_B \times 2T \int_{-\infty}^\infty \frac{dp_z}{2\pi} \ln(1 + e^{-\epsilon_{p_z}/T}), \quad (301)$$

with $\epsilon_{p_z} = \sqrt{p_z^2 + m_{\text{dyn}}^2}$. The UV contribution is suppressed by the exponential factor and is cutoff by the temperature scale as expected.

Since we are interested in the behavior of the effective potential near the phase transition temperature, we may take the small mass limit, $m_{\text{dyn}}(T) \ll T$ assuming the second-order phase transition. Expanding the Bessel function in Eq. (300) and performing the summation with respect to \bar{k} ,⁶⁰ we

⁶⁰The summation can be performed with the help of the Riemann Zeta function as [327]

$$\sum_{\bar{k}=1}^\infty \frac{(-1)^{\bar{k}}}{\bar{k}^s} = (2^{1-s} - 1)\zeta_R(s).$$

obtain the analytic form of the thermal part as

$$V_T^{(1)} \sim -\rho_B \left[\frac{\pi T^2}{6} + \frac{m_{\text{dyn}}^2}{2\pi} \left(\ln \frac{m_{\text{dyn}}}{\pi T} + \gamma_E - \frac{1}{2} \right) \right]. \quad (302)$$

The first term corresponds to the Stefan-Boltzmann limit in the (1+1) dimensions. Including the vacuum part, the total potential is obtained as

$$\begin{aligned} V^{(1)} &\equiv V_{\text{vac}}^{(1)} + V_T^{(1)} \\ &\sim \rho_B \left[\frac{\Lambda^2}{4\pi} - \frac{\pi T^2}{6} + \frac{m_{\text{dyn}}^2}{2\pi} \left(\frac{\pi}{\rho_B \lambda_{\text{NJL}}} + \frac{\gamma_E}{2} - \ln \frac{\Lambda}{\pi T} \right) \right]. \end{aligned} \quad (303)$$

There is no longer the logarithm that played the crucial role in the chiral symmetry breaking at zero temperature. The chiral symmetry can be restored at a certain temperature. The critical temperature is read off from the coefficient of the quadratic term in m_{dyn}^2 that changes its sign across the phase transition. The critical temperature is now found to be

$$T_c = \frac{\Lambda'}{\pi} \exp \left(-\frac{\pi}{\rho_B \lambda_{\text{NJL}}} \right) = \frac{1}{\pi} m_{\text{dyn}}(T=0). \quad (304)$$

Notice that the critical temperature agrees with the dynamical mass at $T=0$ up to the overall factor of π^{-1} . Such relations are established for QED and the NJL model [67, 325, 328–330].

According to Eq. (304), the critical temperature of the chiral symmetry restoration is naturally interpreted as the point at which the thermal energy becomes large enough to overcome the dynamical mass gap and to fill the positive-energy states with thermal excitations. Therefore, we notice a natural behavior that the critical temperature increases as the dynamical mass gap increases at zero temperature. In the history of superconductivity, the BCS theory predicted a similar relation with a universal factor independent of material [331]. In Sec. 7.4, we will see, however, that the lattice QCD simulation do not support this relation to hold in QCD. This is an intriguing implication that the strong-coupling dynamics in the low-energy QCD do not simply follow the results from the NJL model and weak-coupling QED.

6.3 Extension to non-Abelian theories

Here, we invoke on another extension of the HE effective action to non-Abelian theories. QCD is the main target of non-Abelian theories. Before going into details, we briefly comment on the main features of non-Abelian problems that are not seen in the calculation of the HE action in QED. We will perform a one-loop calculation with respect to quantum fluctuations around the background gauge fields assuming that the QCD coupling constant g is small enough. Then we will encounter the following differences.

- In contrast to the electromagnetic fields in QED, the field strengths in non-Abelian gauge theories change covariantly under gauge transformations. Related to this, instead of imposing a gauge-variant condition $\partial_\mu \mathcal{F}_{\nu\rho}^a = 0$, we rather impose the “covariantly constant” condition $D_\lambda^{ab} \mathcal{F}_{\mu\nu}^b = 0$ as introduced in Eq. (152).

Using this formula, one can get another useful formula with the logarithm:

$$\sum_{\bar{k}=1}^{\infty} \frac{(-1)^{\bar{k}}}{\bar{k}^s} \ln \bar{k} = (2^{1-s} - 1) \zeta'_R(s) - (2^{1-s} \ln 2) \zeta_R(s),$$

where the prime denotes the first derivative.

- Under the decomposition of the original gauge field into the background and the (fluctuating) dynamical fields, three-point and four-point interactions, characteristic of the non-Abelian gauge theories, induce a coupling between the background and dynamical fields. Since the decomposition produces quadratic terms in the dynamical gauge fields, we need to treat them as the gluon loop contribution (cf. Fig. 27), in contrast to the QED case where the dynamical photon field only appears at higher loop diagrams.
- Since we have the dynamical non-Abelian gauge fields at the one-loop level, we need to include ghost fields when fixing the gauge of the dynamical gauge field. The ghost field is treated as a pure fluctuation (without background ghost fields), but is coupled to the background chromo-fields.

We shall set up the classical Lagrangian as the starting point. Recall that we have already introduced the QCD action introduced in Eq. (145) and performed the decomposition of the non-Abelian gauge field into the dynamical fluctuation field a_μ^a and classical field $\mathcal{A}_{\text{ext}}^{a\mu}$ as explained in Sec. 3.4 and Appendix D.1. After this procedure, we have obtained the action that describes the dynamics of the quark field ψ , the dynamical gauge field a_μ^a , and the ghost field c^a :

$$S = \int d^4x [\mathcal{L}_{\text{kin}} + \mathcal{L}_{\text{int}}] . \quad (305)$$

The kinetic term \mathcal{L}_{kin} as defined in Eq. (150) is bilinear with respect to the dynamical fields, ψ , a_μ^a , and c^a , while the interaction term \mathcal{L}_{int} given in Eq. (559) in Appendix D.1 contains the coupling terms among more than three fields.

In addition to the external chromo-EM field $\mathcal{A}_{\text{ext}}^{a\mu}$, we here maintain an external Abelian field A_{ext}^μ , which is included in the HE effective action discussed previously, and investigate interplay between QED and QCD fields in the following sections. Such a coexisting field configuration is realized in the ultrarelativistic heavy-ion collisions and lattice QCD simulations. Since the external Abelian field plays a role in the QCD dynamics only through the interaction with quarks, one can immediately include the Abelian field into the action (305) through a modification of the covariant derivative in the fundamental representation

$$\mathbb{D}^\mu \equiv \partial^\mu - ig\mathcal{A}_{\text{ext}}^{a\mu}t^a + iq_f A_{\text{ext}}^\mu = D^\mu + iq_f A_{\text{ext}}^\mu . \quad (306)$$

In the classical action (150), this replaces the covariant derivative D^μ in the quark part, while the covariant derivative acting on the gluon and ghost fields are intact because those fields do not directly interact with the external Abelian field. Here and below, we do not consider electrically charged gauge bosons such as the weak bosons. One can omit the Maxwell part $-\frac{1}{4}F^{\mu\nu}F_{\mu\nu}$ for the constant field and do not consider the dynamical photon field as well. The dynamical photon field needs to be included when we consider the photon dynamics as in Sec. 5, and radiative corrections which, however, will be subdominant to gluon radiative corrections in most of physical situations.

Now, we introduce the covariantly constant chromo-EM field, in which the field strength tensor $\mathcal{F}_{\mu\nu}^a$ associated with $\mathcal{A}_{\text{ext}}^{a\mu}$ is factorized as shown in Eq. (154). Accordingly, one can diagonalize the color structure in the covariant derivative, of which the diagonal component is given by (see Sec. 3.4 & Appendix D.1)

$$\mathbb{D}_{i,f}^\mu = \partial^\mu - iw^i \mathcal{A}_{\text{ext}}^\mu + iq_f A_{\text{ext}}^\mu , \quad (307)$$

where $\mathcal{A}_{\text{ext}}^\mu$ is the Abelian-like strength of the external chromo-EM field [cf., Eq. (155a)], and w^i ($i = 1, 2, 3$) is the effective charge introduced in Eq. (156) that linearly depends on the original strong coupling constant g . Notice that a mixing between the Abelian and non-Abelian fields occurs at this

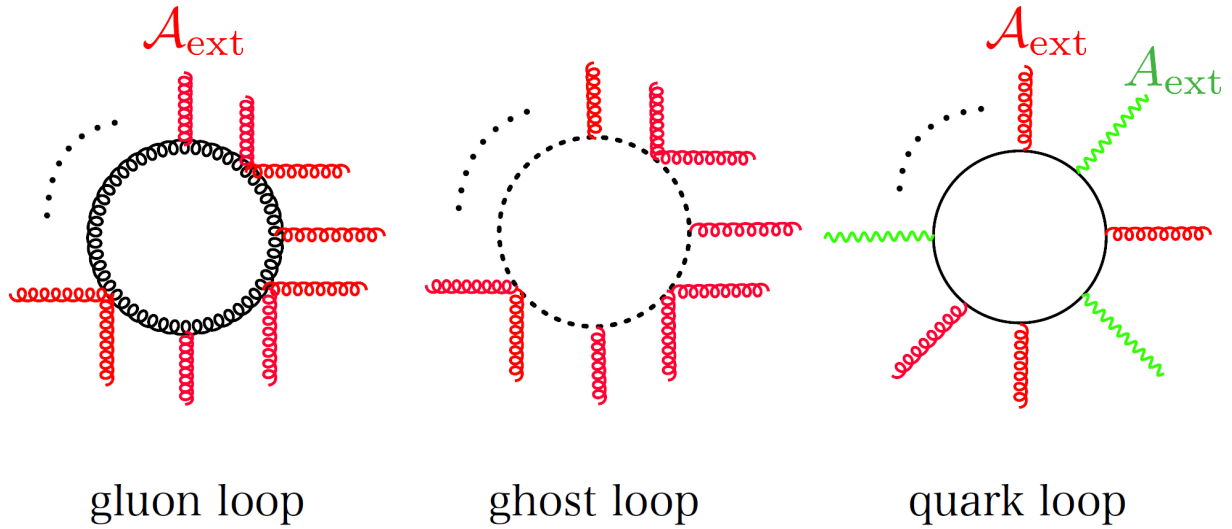


Figure 27: Typical loop diagrams contributing to the resummed effective action.

point. We define the “mixed” field strength tensor⁶¹ $\mathbb{F}_{i,f}^{\mu\nu} \equiv i[\mathbb{D}_{i,f}^\mu, \mathbb{D}_{i,f}^\nu]$ through the covariant derivative $\mathbb{D}_{i,f}^\mu$. It is decomposed as

$$\mathbb{F}_{i,f}^{\mu\nu} = w^i \mathcal{F}^{\mu\nu} - q_f F^{\mu\nu}. \quad (308)$$

$\mathcal{F}^{\mu\nu}$ is for the magnitude of the external chromo-EM field introduced in Eq. (154), which are composed of $\vec{\mathcal{E}}$ and $\vec{\mathcal{B}}$, while $F^{\mu\nu}$ is for the external EM field composed of \vec{E} and \vec{B} as usual. We will use notations $\mathfrak{a}_{i,f}$, $\mathfrak{b}_{i,f}$ for the invariants defined in Eqs. (4a) and (4b) associated with the field strength tensor $\mathbb{F}_{i,f}^{\mu\nu}$ and also \mathfrak{a} , \mathfrak{b} associated with $\mathcal{F}^{\mu\nu}$.⁶² The former and latter appear in the effective actions of the quark part and the Yang-Mills (gluon+ghost) part, respectively.

By integrating out the dynamical fields, we can formally obtain the effective action in the presence of the coexistent external fields $\mathcal{A}_{\text{ext}}^\mu$ and A_{ext}^μ as

$$\exp\left(iS_{\text{eff}}[\mathcal{A}_{\text{ext}}^\mu, A_{\text{ext}}^\mu]\right) \equiv \int \mathcal{D}a^\mu \mathcal{D}c \mathcal{D}\bar{c} \mathcal{D}\psi \mathcal{D}\bar{\psi} \exp\left(iS[\mathcal{A}_{\text{ext}}^\mu, A_{\text{ext}}^\mu, a^\mu, c, \bar{c}, \psi, \bar{\psi}]\right). \quad (309)$$

The effective action S_{eff} has two different types of dependences on the coupling constants g and q_f : One is the type where the coupling constants are accompanied by the field strengths (i.e., $g\mathcal{F}^{\mu\nu}$, $q_f F^{\mu\nu}$), and the other is the type where the coupling constants appear alone without the field strengths. As in the Abelian case discussed in Sec. 4, we consider strong external fields, and sum up the first-type of the dependences to the infinite order. The second-type is treated perturbatively. Then, the leading contribution comes from the bilinear terms in the dynamical (fluctuating) fields which constitute the one-loop diagrams shown in Fig. 27. Performing the path integration over the bilinear terms, we have

$$S_{\text{eff}} = S^{(0)} + S_{\text{quark}}^{(1)} + S_{\text{gluon}}^{(1)} + S_{\text{ghost}}^{(1)}, \quad (310)$$

where $S^{(0)} = \int d^4x \mathcal{L}^{(0)}$ is the pure Yang-Mills action $\mathcal{L}^{(0)} = -\frac{1}{4} \mathcal{F}_{\mu\nu}^a \mathcal{F}^{a\mu\nu}$ and the leading-order (one-loop) contributions are obtained as

$$S_{\text{quark}}^{(1)} = \int d^4x \mathcal{L}_{\text{quark}}^{(1)} = -i \text{Tr} \ln [i\mathbb{D} - m] = -i \text{Tr} \ln [(-1)(\mathbb{D}\mathbb{D} + m^2)]^{\frac{1}{2}}, \quad (311a)$$

⁶¹Compared to the usual definition of the field strength (such as $\mathcal{F}_{\mu\nu}^a t^a = \frac{i}{g}[D^\mu, D^\nu]$), we have defined $\mathbb{F}_{i,f}^{\mu\nu}$ so that it absorbs the two different coupling constants w^i and q_f .

⁶²The definitions of \mathfrak{a} and \mathfrak{b} are interchanged in some literature including Ref. [305].

$$S_{\text{gluon}}^{(1)} = \int d^4x \mathcal{L}_{\text{gluon}}^{(1)} = -i \text{Tr} \ln [-(D^2)^{ab} g^{\mu\nu} + \delta^{ab} v^a (\mathcal{F}_{\alpha\beta} \mathcal{J}^{\alpha\beta})^{\mu\nu}]^{-\frac{1}{2}}, \quad (311b)$$

$$S_{\text{ghost}}^{(1)} = \int d^4x \mathcal{L}_{\text{ghost}}^{(1)} = -i \text{Tr} \ln [(D^2)^{ab}]^{+1}. \quad (311c)$$

We again used the trick on the fermion determinant mentioned below (180) and here maintain the determinant of the sign factor $\det(-1)^{\frac{1}{2}}$ that depends on the number of dimensions. This factor is important when we apply the dimensional regularization in Sec. 6.5. In the gluon contribution, we have taken the Feynman gauge, $\xi_g = 1$, for the dynamical gluon fields. This effective action allows one to explore the dynamics in the strong fields regime $g\mathcal{F}^{\mu\nu}$, $q_f F^{\mu\nu} \gtrsim \Lambda^2$, in which the field strength exceeds the typical energy scale of the system Λ such as the fermion mass, temperature, and density.

The trace ‘‘Tr’’ will be taken for the operator expectation value with the coordinate basis, x , as well as the color, Lorentz, spinor, flavor indices when exist. The color structures in Eqs. (311a)–(311c) are all diagonalized in the covariantly constant field as discussed in Sec. 3.4. The explicit forms of the covariant derivatives and the spin-interaction term in the gluon contribution are shown in Eqs. (155a), (155b), and (158). The summation with respect to the flavor degrees, as well as the color degrees within the covariantly constant field, only appears as the overall sum at the one-loop level. We will introduce these sums just below.

6.3.1 Ghost- and gluon-loop contributions

As far as the one-loop diagrams are concerned, the ghost and gluon contributions do not have any dependence on the quark degrees of freedom, and thus the ordinary (QED) electromagnetic fields are not coupled to those fields. Therefore, computation of the ghost and gluon contributions in QCD is equivalent to that of the pure Yang-Mills (YM) theory. Besides, except for some differences coming from statistics, one can compute the ghost- and gluon-loop contributions in a similar way as in the fermion-loop contribution discussed in Sec. 6.1. We have already obtained all the necessary ingredients in the preceding sections.

Notice again that the logarithms in Eqs. (311b) and (311c) can be both rewritten in the form of the proper-time integral

$$\mathcal{L}_{\text{ghost}}^{(1)} = i \int_0^\infty \frac{ds}{s} e^{-\epsilon s} \text{tr}_c \langle x | e^{-i\hat{H}_{\text{ghost}}s} | x \rangle, \quad (312a)$$

$$\mathcal{L}_{\text{gluon}}^{(1)} = -\frac{i}{2} \int_0^\infty \frac{ds}{s} e^{-\epsilon s} \text{tr}_{c,L} \langle x | e^{-i\hat{H}_{\text{gluon}}s} | x \rangle, \quad (312b)$$

where the ‘‘Hamiltonians’’ in the ghost and gluon contributions are, respectively, given by

$$\hat{H}_{\text{ghost}} = (D^2)^{ab}, \quad (313a)$$

$$\hat{H}_{\text{gluon}} = -(D^2)^{ab} g^{\mu\nu} + \delta^{ab} v^a (\mathcal{F}_{\alpha\beta} \mathcal{J}^{\alpha\beta})^{\mu\nu}. \quad (313b)$$

In Eqs. (312a) and (312b), the different overall factors come from statistics of ghosts and gluons. The traces are taken over the color (c) index in the ghost contribution and the color (c) and Lorentz (L) indices in the gluon contribution. For the notational simplicity in these expressions and below, we do not subtract the contributions independent of background fields that are given by the free Hamiltonians $\hat{H}_0 = \delta^{ab} \partial^2$ or $-\delta^{ab} g^{\mu\nu} \partial^2$. However, one can easily identify these contributions whenever required for subtraction of the divergences in the proper-time integrals.

The computation of the effective action has been reduced to the computation of the transition matrix element $\langle x | e^{-i\hat{H}s} | x \rangle$. Similar to the computation in Sec. 4.1.1, we shall define the transition matrix elements $K(x, x'; s | A_{\text{FS}})$ as in Eq. (183) with the Hamiltonians (313a) and (313b) for the ghost and

gluon contributions, respectively. Then, one can again establish the relation between $K(x, x'; s|A_{\text{FS}})$ and $\Delta(p|A)$ through Eqs. (184) and (185). More specifically, $\Delta(p|A)$ in Eq. (185) is replaced by $\Delta_{\text{scalar}}(p|A)$ in Eq. (140) with a vanishing mass $m = 0$ for the ghost contribution, and by the $\Delta_{\mu\nu}^{(a)}(p|A)$ in Eq. (171) for the gluon contribution. The electric charge q_f in the $\Delta_{\text{scalar}}(p|A)$ is understood to be replaced by the effective charge v^a as explained in Sec. 3.4.2. Note also that the statistics of the ghost field is already taken into account as the difference between the overall factors in Eqs. (312a) and (312b), so that the remaining part of the ghost contribution can be treated as the scalar-particle contribution in Sec. 3.4.2. With these observations, we are ready to write down the transition matrix elements (see also Ref. [89] for a deviation following Schwinger's paper [42])

$$\langle x|e^{-i\hat{H}_{\text{ghost}}s}|x\rangle = \frac{1}{\cosh(v^a \mathbf{a}s) \cos(v^a \mathbf{b}s)} \int \frac{d^4p}{(2\pi)^4} \exp\left(i \frac{p_{\parallel}^2}{v^a \mathbf{a}} \tanh(v^a \mathbf{a}s) + i \frac{p_{\perp}^2}{v^a \mathbf{b}} \tan(v^a \mathbf{b}s)\right), \quad (314a)$$

$$\begin{aligned} \text{tr}_{\text{L}} \langle x|e^{-i\hat{H}_{\text{gluon}}s}|x\rangle &= 2 \frac{\cosh(2v^a \mathbf{a}s) + \cos(2v^a \mathbf{b}s)}{\cosh(v^a \mathbf{a}s) \cos(v^a \mathbf{b}s)} \\ &\times \int \frac{d^4p}{(2\pi)^4} \exp\left(-i \frac{p_{\parallel}^2}{v^a \mathbf{a}} \tanh(v^a \mathbf{a}s) - i \frac{p_{\perp}^2}{v^a \mathbf{b}} \tan(v^a \mathbf{b}s)\right), \end{aligned} \quad (314b)$$

where the invariants \mathbf{a} and \mathbf{b} are defined below Eq. (308). A difference between the integrands in the ghost and gluon contributions appears in the cosine and hyperbolic cosine in the numerator in Eq. (314b) [and also in Eq. (315b) below]. These factors originate from the spin interaction term in Eq. (313b), which was arranged in Eq. (173). However, such a spin interaction is absent for the ghost field. The difference between the signs in the exponents just comes from the relative sign of the ghost and gluon kinetic terms in Eqs. (150) and (313).

At zero temperature, one can immediately perform the Gaussian integrals for the four-dimensional momentum. At finite temperature, one needs to work on the imaginary-time formalism as in the fermion contribution, but with the periodic boundary condition, which leads to the replacements, $\int dp^0 \rightarrow iT \sum_{n=-\infty}^{\infty}$ and $p^0 \rightarrow i2n\pi T + v^a \varphi^a$, where φ^a is defined with $\mathcal{A}_{\text{ext}}^{a0}$ instead of A_{ext}^0 and the corresponding field in the FS gauge in Eq. (283).⁶³ The Matsubara sum is reorganized with the help of the Poisson resummation formula, which we have examined to get the fermion contribution in Eq. (286). Then, we obtain each contribution to the effective action for chromo-EM fields at finite temperature [305]:

$$\mathcal{L}_{\text{ghost}}^{(1)} = \sum_{a=1}^{N_c^2-1} \frac{(v^a \mathbf{a})(v^a \mathbf{b})}{16\pi^2} \int_0^\infty \frac{ds}{s} e^{-\epsilon s} \frac{1}{\sinh(v^a \mathbf{a}s) \sin(v^a \mathbf{b}s)} \left[1 + 2 \sum_{\bar{k}=1}^{\infty} e^{i \frac{v^a \mathfrak{h}(s)}{4T^2} \bar{k}^2} \cosh(\beta v^a \varphi^a \bar{k}) \right], \quad (315a)$$

$$\mathcal{L}_{\text{gluon}}^{(1)} = - \sum_{a=1}^{N_c^2-1} \frac{(v^a \mathbf{a})(v^a \mathbf{b})}{16\pi^2} \int_0^\infty \frac{ds}{s} e^{-\epsilon s} \frac{\cosh(2v^a \mathbf{a}s) + \cos(2v^a \mathbf{b}s)}{\sinh(v^a \mathbf{a}s) \sin(v^a \mathbf{b}s)} \left[1 + 2 \sum_{\bar{k}=1}^{\infty} e^{i \frac{v^a \mathfrak{h}(s)}{4T^2} \bar{k}^2} \cosh(\beta v^a \varphi^a \bar{k}) \right], \quad (315b)$$

where the overall summation is taken over the color index and the field in φ^a is replaced with $\mathcal{A}_u^a \equiv \mathcal{A}_{\text{ext}}^{a\mu} u_\mu$. As we have identified in the fermion-loop contribution (285), the vacuum and finite-temperature contributions are separated into the first and second terms in the square brackets, respectively. The $\mathfrak{h}(s)$ in the exponent is defined as in Eq. (287), but with the replacements of $(q_f a, q_f b, q_f e_u)$ by

⁶³Note that the bosonic boundary condition is taken not only for the gluon field but also for the ghost field, in spite of the fermionic behavior of the ghost field. In the present case, the difference between the periodic and antiperiodic boundary conditions explicitly appears as the alternating signs seen in Eq. (286). Therefore, those fields are expected to take the same boundary conditions so that the ghost contribution cancels the unphysical gluon contributions, as indeed supported by general justifications (see, e.g., Refs. [332, 333] and references therein).

$(v^a \mathbf{a}, v^a \mathbf{b}, v^a \mathbf{e}_u)$, respectively, where the power of the electric field is defined with the field strength tensor of the chromo-field, $\mathbf{e}_u^2 = -\mathcal{F}^{\mu\alpha} \mathcal{F}_{\mu\beta} u_\alpha u^\beta$. Namely, we have

$$v^a \mathfrak{h}(s) = v^a \mathbf{a} \frac{\mathbf{b}^2 + \mathbf{e}_u^2}{\mathbf{a}^2 + \mathbf{b}^2} \coth(v^a \mathbf{a} s) + v^a \mathbf{b} \frac{\mathbf{a}^2 - \mathbf{e}_u^2}{\mathbf{a}^2 + \mathbf{b}^2} \cot(v^a \mathbf{b} s). \quad (316)$$

The sum of the gluon and ghost parts provides the Yang-Mills part of the effective action $\mathcal{L}_{\text{YM}}^{(1)} = \mathcal{L}_{\text{gluon}}^{(1)} + \mathcal{L}_{\text{ghost}}^{(1)}$ in the external chromo-EM fields at finite temperature [305].

Similar to the case of the fermion contribution in Eq. (292), we can reproduce the familiar thermodynamic potential and the Stefan-Boltzmann law for a free gluon gas in the vanishing limit of the external chromo-EM fields. Sending the field strengths to zero and maintaining only φ^a , the temperature-dependent part reads

$$\mathcal{L}_{\text{YM},T}^{(1)}(\mathcal{E}, \mathcal{B} = 0) = - \sum_{a=1}^{N_c^2-1} \frac{1}{8\pi^2} \sum_{\bar{k}=1}^{\infty} \cosh(v^a \varphi^a \beta \bar{k}) \int_0^\infty \frac{ds}{s^3} e^{-\epsilon s} e^{\frac{i}{4T^2 s} \bar{k}^2}. \quad (317)$$

After the rotation of the integral contour to the negative imaginary axis, the proper-time integral and the summation can be performed as

$$\begin{aligned} \mathcal{L}_{\text{YM},T}^{(1)} &= \sum_{a=1}^{N_c^2-1} \frac{1}{8\pi^2} \sum_{\bar{k}=1}^{\infty} \cosh(v^a \varphi^a \beta \bar{k}) \int_0^\infty \frac{ds}{s^3} e^{-\frac{1}{4T^2 s} \bar{k}^2} \\ &= \frac{T^4}{\pi^2} \sum_{a=1}^{N_c^2-1} [\text{Li}_4(e^{v^a \varphi^a \beta}) + \text{Li}_4(e^{-v^a \varphi^a \beta})], \end{aligned} \quad (318)$$

where the summation is identified with a series representation of the polylogarithmic function $\text{Li}_s(z) = \sum_{\bar{k}=1}^{\infty} z^{\bar{k}} / \bar{k}^s$ [334]. The momentum-integral form can be retrieved with the integral representation $\text{Li}_{s+1}(e^\mu) \Gamma(s+1) = - \int_0^\infty dp p^s / (e^{p-\mu} - 1)$ as

$$\mathcal{L}_{\text{YM},T}^{(1)} = -T \sum_{a=1}^{N_c^2-1} \int \frac{d^3 p}{(2\pi)^3} [\ln(1 - e^{-\beta(p-v^a \varphi^a)}) + \ln(1 - e^{-\beta(p+v^a \varphi^a)})]. \quad (319)$$

When $\varphi^a = 0$, we have $\text{Li}_4(1) = \zeta_R(4) = \pi^4/90$ and thus

$$\lim_{\mathcal{A}^0 \rightarrow 0} \mathcal{L}_{\text{YM},T}^{(1)} = (N_c^2 - 1) \cdot 2 \cdot \frac{\pi^2}{90} T^4. \quad (320)$$

The Stefan-Boltzmann limit is reproduced with the number of color degrees of freedom $(N_c^2 - 1)$ and a factor of 2. This factor should come from the two transverse polarization modes after the cancellation of the longitudinal mode by the ghost contribution. Below, we examine how this cancellation occurs in the presence of external chromo-fields in detail.

Cancellation of the longitudinal gluon

When we consider a purely chromo-*electric* background ($\mathcal{E} = |\vec{\mathcal{E}}| \neq 0$, $\mathcal{B} = 0$) in the medium rest frame $u^\mu = (1, 0, 0, 0)$, we have $\mathbf{a} \rightarrow \mathcal{E}$, $\mathbf{b} \rightarrow 0$. Inserting these values into Eqs. (315a) and (315b), one can reproduce Gies' effective action⁶⁴ at finite temperature [283]

$$\mathcal{L}_{\text{YM}}^{(1)}(\mathcal{E} \neq 0, \mathcal{B} = 0) = - \sum_{a=1}^{N_c^2-1} \frac{v^a \mathcal{E}}{16\pi^2} \int_0^\infty \frac{ds}{s^2} e^{-\epsilon s} \frac{\cosh(2v^a \mathcal{E} s)}{\sinh(v^a \mathcal{E} s)} \left[1 + 2 \sum_{\bar{k}=1}^{\infty} e^{i \frac{v^a \mathfrak{h}(s)}{4T^2} \bar{k}^2} \cosh(\beta v^a \varphi^a \bar{k}) \right], \quad (321)$$

⁶⁴More precisely, Gies computed the effective action for the Polyakov loop and the chromo-electric fields, both of which are given by the (imaginary-)time component of the field $\mathcal{A}_{\text{ext}}^0$ (see Sec. 6.6).

where $v^a \mathfrak{h}(s) = v^a \mathcal{E} \coth(v^a \mathcal{E} s)$. Notice that an exact cancellation occurs between the whole ghost contribution and the term proportional to $\cos(2v^a \mathfrak{b} s)$ in the gluon contribution in the limit, $\mathfrak{b} \rightarrow 0$. Such a cancellation is, by construction, expected to occur for the ghost field to eliminate the unphysical gluonic degrees of freedom and is very important when gluons become on-shell particles. The cancellation of the longitudinal mode has been also discussed with the canonical quantization in Refs. [109, 143, 147, 335]. This can occur by the Schwinger mechanism of gluons in chromo-electric fields. While the zero-temperature part in Eq. (321) looks like a real-valued integral, there is a singularity at infinity $s \rightarrow \infty$ as long as there is a finite electric field ($v^a \mathcal{E} > \epsilon$). Therefore, the result of the integral could acquire an imaginary part in the analytic continuation $\epsilon \rightarrow 0$, leading to the gluon Schwinger mechanism in a chromo-electric field.

In case of a purely chromo-magnetic background ($\mathcal{E} = 0$, $\mathcal{B} \neq 0$), we have $\mathfrak{a} \rightarrow 0$, $\mathfrak{b} \rightarrow \mathcal{B}$, and reproduce the results in Refs. [280]. In this case, an exact cancellation occurs between the whole ghost contribution and the term proportional to $\cosh(2v^a \mathfrak{a} s)$ in the gluon contribution.

It is more tempting to explicitly see cancellation of the longitudinal gluon contribution in the Landau-level representation. We speculated this cancellation below Eq. (178) when we identified the Zeeman splitting for gluon spin. Since the following arrangement does not depend on the Poisson summation inside the square brackets in Eq. (315), one can focus on the zero-temperature expression for the notational simplicity. Decomposing the transition matrix elements into the Landau levels in a purely magnetic field ($\mathfrak{a} \rightarrow 0$) [see the computations leading to Eqs. (144b) and (178)], we obtain

$$\langle x | e^{-i\hat{H}_{\text{ghost}} s} | x \rangle = 2 \int \frac{d^4 p}{(2\pi)^4} e^{\frac{p_{\perp}^2}{|v^a \mathcal{B}|}} \sum_{n=0}^{\infty} (-1)^n e^{-\epsilon s} L_n(u_{\perp}) e^{-is(p_{\parallel}^2 - \epsilon_{\perp n}^2)}, \quad (322a)$$

$$\begin{aligned} \text{tr}_{\text{L}} \langle x | e^{-i\hat{H}_{\text{gluon}} s} | x \rangle &= 2 \int \frac{d^4 p}{(2\pi)^4} e^{\frac{p_{\perp}^2}{|v^a \mathcal{B}|}} \sum_{n=0}^{\infty} (-1)^n e^{-\epsilon s} \left[2L_n(u_{\perp}) e^{-is(p_{\parallel}^2 - \epsilon_{\perp n}^2)} \right. \\ &\quad \left. + \{L_n(u_{\perp}) + L_{n-2}(u_{\perp})\} e^{-is(p_{\parallel}^2 - \epsilon_{\perp n-1}^2)} \right], \end{aligned} \quad (322b)$$

where $L_{-2}(u_{\perp}) = L_{-1}(u_{\perp}) = 0$ and we defined $\epsilon_{\perp n}^2 = (2n+1)|v^a \mathcal{B}|$. Performing the momentum integrals in the similar manner as in Eq. (217), we find the Landau-level representation of the effective Lagrangians⁶⁵

$$\mathcal{L}_{\text{ghost}}^{(1)} = \frac{i}{4\pi} \sum_{a=1}^{N_c^2-1} \left| \frac{v^a \mathcal{B}}{2\pi} \right| \int_0^{\infty} \frac{ds}{s^2} e^{-\epsilon s} \sum_{n=0}^{\infty} e^{-is\epsilon_{\perp n}^2}, \quad (324a)$$

$$\mathcal{L}_{\text{gluon}}^{(1)} = -\frac{i}{4\pi} \sum_{a=1}^{N_c^2-1} \left| \frac{v^a \mathcal{B}}{2\pi} \right| \int_0^{\infty} \frac{ds}{s^2} e^{-\epsilon s} \sum_{n=0}^{\infty} \left[e^{-is\epsilon_{\perp n}^2} + \frac{1}{2}(2 - \delta_{n0} - \delta_{n1}) e^{-is\epsilon_{\perp n-1}^2} \right]. \quad (324b)$$

In the gluon contribution, the first and second terms between the square brackets are identified with the contributions of the longitudinal and transverse gluons, respectively. This is understood from the Zeeman splitting of spin-1 particles shown in Fig. 4. The transverse gluon modes in each energy level are counted with the factor of $(2 - \delta_{n0} - \delta_{n1})$; There are two-fold spin degeneracy except for the lowest two levels. Remember also that we explicitly identified the gluon polarization tensors $\mathcal{Q}_{\pm}^{\mu\nu}$ below Eq. (178).

Now, observe an exact cancellation between the longitudinal-gluon and ghost contributions in the all-order Landau levels. After the cancellation, we find the Landau-level representation of the Yang-Mills

⁶⁵Here, the transverse-momentum integral results in an n -independent form

$$2(-1)^n \int \frac{d^2 p_{\perp}}{(2\pi)^2} e^{-\frac{u_{\perp}}{2}} L_n(u_{\perp}) = \left| \frac{v^a \mathcal{B}}{2\pi} \right|. \quad (323)$$

part:

$$\mathcal{L}_{\text{YM}}^{(1)} = -\frac{i}{8\pi} \sum_{a=1}^{N_c^2-1} \left[\frac{v^a \mathcal{B}}{2\pi} \right] \int_0^\infty \frac{ds}{s^2} e^{-\epsilon s} \sum_{n=0}^\infty (2 - \delta_{n0} - \delta_{n1}) e^{-is(2n-1)|v^a \mathcal{B}|}. \quad (325)$$

Incidentally, similar to the discussion below Eq. (218), we can obtain Eq. (325) directly from the effective action $\mathcal{L}_{\text{YM}}^{(1)}$ which has been already obtained in Eqs. (315a) and (315b). To see this, take a purely magnetic configuration ($\mathcal{E} = 0$) and use an identity

$$\frac{\cos 2x}{\sin x} = i \left[e^{ix} + e^{-ix} + 2 \sum_{n=2}^\infty e^{-i(2n-1)x} \right]. \quad (326)$$

The cancellation holds in a coexistent chromo-electric and -magnetic fields. The cancellation of the longitudinal mode in the Schwinger pair production in the coexistent chromo-fields were also explicitly shown on the basis of the HE effective action [89] as well as the canonical quantization [109, 143, 147, 335].

6.3.2 Quark-loop contribution

Next, we compute the quark contribution (311a). Within the covariantly constant chromo-field, this is a straightforward extension of the fermion-loop contributions in the Abelian field already given in Eqs. (285) and (286). The ‘‘Hamiltonian’’ in Eq. (284) is replaced by the one associated with the covariant derivative (307):

$$\hat{H}_{\text{quark}} = \mathbb{D}_{i,f}^2 + \frac{1}{2} \mathbb{F}_{i,f}^{\mu\nu} \sigma_{\mu\nu}. \quad (327)$$

Accordingly, all the associated variables, such as E , B , a , b defined by the covariant derivative and the external gauge field, are replaced as

$$(q_f a, q_f b, q_f \varphi) \rightarrow (\mathbf{a}_{i,f}, \mathbf{b}_{i,f}, \varphi_{i,f}), \quad (328)$$

where $\varphi_{i,f} := T \int_0^\beta d\tau' \{ (q_f A_{\text{ext}}^\mu + w_i \mathcal{A}_{\text{ext}}^\mu) - (q_f A_{\text{FS}}^\mu + w_i \mathcal{A}_{\text{FS}}^\mu) \} u_\mu$ in line with the previous definition (283) and $\mathbf{a}_{i,f}$, $\mathbf{b}_{i,f}$ are introduced below Eq. (308) with $\mathbb{F}_{i,f}^{\mu\nu}$.⁶⁶ Applying those replacements to Eq. (286), we find the quark contribution to the effective action (311a) as [336]

$$\begin{aligned} \mathcal{L}_{\text{quark}}^{(1)} &= \sum_{i=1}^{N_c} \sum_{f=1}^{N_f} \frac{1}{8\pi^2} \int_0^\infty \frac{ds}{s} e^{-i(m_f^2 - i\epsilon)s} \frac{\mathbf{a}_{i,f} \mathbf{b}_{i,f}}{\tanh(\mathbf{a}_{i,f} s) \tan(\mathbf{b}_{i,f} s)} \\ &\quad \times \left[1 + 2 \sum_{\bar{k}=1}^\infty (-1)^{\bar{k}} e^{\frac{i}{4T^2} \mathbf{b}_{i,f}(s) \bar{k}^2} \cosh(\beta \varphi_{i,f} \bar{k}) \right], \end{aligned} \quad (329)$$

with

$$\mathfrak{h}_{i,f}(s) = \mathbf{a}_{i,f} \frac{\mathbf{b}_{i,f}^2 + \mathbf{e}_{i,f}^2}{\mathbf{a}_{i,f}^2 + \mathbf{b}_{i,f}^2} \coth(\mathbf{a}_{i,f} s) + \mathbf{b}_{i,f} \frac{\mathbf{a}_{i,f}^2 - \mathbf{e}_{i,f}^2}{\mathbf{a}_{i,f}^2 + \mathbf{b}_{i,f}^2} \cot(\mathbf{b}_{i,f} s). \quad (330)$$

The power of the electric field $\mathbf{e}_{i,f}^2 = -\mathcal{E}_{i,f}^\mu \mathcal{E}_{i,f\mu}$ is defined with $\mathcal{E}_{i,f}^\mu \equiv \mathbb{F}_{i,f}^{\mu\nu} u_\nu$. In the medium rest frame, we have $u^\mu = (1, 0, 0, 0)$, $\mathcal{E}_{i,f}^\mu = (0, \vec{\mathcal{E}}_{i,f})$, and thus a reduced form $\mathbf{e}_{i,f}^2 = \vec{\mathcal{E}}_{i,f}^2 = (w_i \vec{\mathcal{E}} - q_f \vec{E})^2 = \mathbf{a}_{i,f}^2$.

⁶⁶Note that the charges are included in the definitions of $\varphi_{i,f}$, $\mathbf{a}_{i,f}$, and $\mathbf{b}_{i,f}$ in the same way as the definition of the field strength tensor (308).

One can again perform the Landau-level decomposition of the effective action (329) and also confirm the Stefan-Boltzmann law in the vanishing-field limit. Following the same procedure that led to Eq. (218), one finds the Landau-level representation

$$\mathcal{L}_{\text{quark}}^{(1)\text{vac}} = \sum_{i=1}^{N_c} \sum_{f=1}^{N_f} \sum_{n=0}^{\infty} \left[\kappa_n \frac{|\mathbf{b}_{i,f}|}{2\pi} \right] \frac{i}{4\pi} \int_0^{\infty} \frac{ds}{s} e^{-i(m_n^2 - i\epsilon)s} \frac{\mathbf{a}_{i,f}}{\tanh(\mathbf{a}_{i,f}s)}, \quad (331)$$

where $\kappa_n = 2 - \delta_{n0}$. Here, the effective mass $m_n^2 = m_f^2 + 2n|\mathbf{b}_{i,f}|$ and the Landau degeneracy factor $|\mathbf{b}_{i,f}|/2\pi$ depend on i and f through $\mathbf{b}_{i,f}$. In the absence of external fields and the massless quark limit, the Stefan-Boltzmann law reads

$$\lim_{\mathcal{A}_{i,f}^0, m_f \rightarrow 0} \mathcal{L}_{\text{quark}}^{(1)T} = -(2 \cdot 2 \cdot N_f \cdot N_c) \times \frac{7}{8} \cdot \frac{\pi^2}{90} T^4, \quad (332)$$

where we now have a color factor N_c as compared to Eq. (293).

6.4 Schwinger mechanism in chromo-fields

As mentioned in the beginning of this section, one of the motivations that drove the investigations on the effective action of QCD and QED fields is the interest in the early-time dynamics in high-energy heavy-ion collisions. The effective action can be applied to the problem of particle productions from chromo-EM fields created in the early stages of the heavy-ion collisions. In particular, as we can easily understand from the diagrams relevant for the one-loop effective action (see Fig. 27), the chromo-electric fields allow for *gluon pair* production as well as quark-antiquark pair production, which is a unique feature of the non-Abelian fields. Since these processes are thought to be the essential initial step towards the formation of quark-gluon plasmas, they have been investigated in many papers. By using the effective action in the Yang-Mills theory and QCD, one can immediately find extensions of the Schwinger formula to the problems of gluon/quark production [107–110, 279] (see also Refs. [112, 113, 337] for recent works). Also important is the application to the configurations which could be realized in collisions [128, 129], and the evaluation of dissipative effects of the chromo-EM fields due to particle productions [114, 131, 338]. Refined calculation of the quark and gluon production from chromo-electric fields was performed in Ref. [124], where the effects of expanding geometry was also taken into account. In addition to the Schwinger mechanism in chromo-electric fields, the roles of chromo-magnetic fields were discussed in Refs. [339, 340], where the Nielsen-Olesen (NO) instability is found to take place in a modified way in an expanding geometry.

Below, we briefly discuss the imaginary part of the effective action that provides the vacuum persistent probability (VPP) for the gluon and quark productions in the presence of QED and QCD fields (cf. Sec. 4.2). Furthermore, it is also found that, in the presence of both chromo-electric and chromo-magnetic fields, the gluon production rate is significantly enhanced due to the NO instability [335]. There is, however, a subtlety in this issue. We examine how the quark production rate is affected by the interplay between the chromo-fields and electromagnetic fields [305].

6.4.1 Gluon production in chromo-electromagnetic fields

We here discuss gluon production from chromo-EM fields. Recall that the Yang-Mills part of the effective action is not affected by photon fields at the one-loop level.

Let us first consider the case with purely chromo-electric fields at zero temperature. The Yang-Mills part (321) in chromo-electric fields has a similar proper-time integral as that for the HE effective action in electric fields (200). In a similar way as the contour integral performed there, one can compute

the imaginary part for the Yang-Mills part (321) by picking up the residues on the imaginary axis as [109, 110, 112]

$$\gamma_{\text{gluon}}(\mathcal{E} \neq 0, \mathcal{B} = 0) = 2\Im m \mathcal{L}_{\text{YM}}^{(1)} = \sum_{a=1}^{N_c^2-1} \frac{1}{8\pi^3} (v^a \mathcal{E})^2 \sum_{n=1}^{\infty} \frac{(-1)^{n-1}}{n^2}. \quad (333)$$

The longitudinal gluon component has been canceled by the ghost contribution as discussed below Eq. (321). One finds that this result is consistent with that of the scalar QED (203) except for the following three points: There is the color sum, an overall factor of 2 that counts the number of transverse gluon modes, and no suppression factor such as $e^{-(E_c/E)n\pi} = e^{-m^2 n\pi/(q_f E)}$ for the massless nature of gluons. The alternating series yields a finite positive number $\eta(2) = \frac{\pi^2}{12}$ from $\eta(s) = \sum_{n=1}^{\infty} (-1)^{n-1}/n^s$. Then, the final result is obtained in a quite compact form

$$\gamma_{\text{gluon}}(\mathcal{E} \neq 0, \mathcal{B} = 0) = \frac{N_c}{96\pi} (g\mathcal{E})^2, \quad (334)$$

where the color sum is performed by the use of the identity (572b). The VPP quadratically decreases as a function of \mathcal{E} without an exponential suppression. That is, the threshold energy to create massless gluons is vanishing. See also recent stability analyses against the Schwinger mechanism in non-Abelian electric fields (in the absence of a non-Abelian magnetic field) [341–344].

When the chromo-electric and chromo-magnetic fields coexist, we can still discuss the gluon pair creation with the effective Lagrangian (315). However, there is one subtle point to which we should pay a special attention. As we already saw, the dispersion relation in the lowest energy level has a negative energy squared, known as the NO instability. The gluon pair creation may be significantly modified by the presence of the instability. It is even not clear whether the unstable modes are well-defined on-shell excitation if they are created by chromo-electric fields. Below, we consider a chromo-magnetic field applied in parallel to a chromo-electric field, where the unstable mode can be explicitly identified with the Landau-level decomposition even in the presence of the chromo-electric field.

The effects of the NO instability was investigated in Ref. [335]. The transition amplitude from the in-vacuum to the out-vacuum was computed in a more direct way than the method of effective action. That is, by using explicit solutions for the equations of motion of gluons and ghosts, the transition amplitude was computed as an overlap between the obtained wave functions. Then, the result was obtained as [335]

$$\gamma_{\text{gluon}}(\mathcal{E}, \mathcal{B}) = \frac{N_c}{8\pi^2} g^2 \mathcal{E} \mathcal{B} \sum_{\sigma=\pm} \sum_{n=0}^{\infty} \ln \left[1 + e^{-\pi(2n+1-2\sigma)\frac{\mathcal{E}}{\mathcal{E}}} \right], \quad (335)$$

where σ and n denote the gluon polarization ($\sigma = \pm 1$) and the Landau level, respectively. Notice that the lowest level ($n = 0$ and $\sigma = +1$) has an exponential enhancement factor $e^{+\pi\mathcal{B}/\mathcal{E}}$, while all the other levels have exponential suppression factors. The difference between the enhancement and suppression factors stems from the sign of the squared energy that has a minus sign in the unstable mode. The above result implies that the gluon production is significantly enhanced by the NO instability. It was argued that the unstable modes can become well-defined excitation after the acceleration by the chromo-electric field that pushes the squared energy to a positive value.

Now, we discuss whether the same result is reproduced from the effective Lagrangian (315). We apply the Landau-level decomposition discussed below Eq. (322) to the sum of the ghost and gluon contributions $\mathcal{L}_{\text{YM}}^{(1)} = \mathcal{L}_{\text{ghost}}^{(1)} + \mathcal{L}_{\text{gluon}}^{(1)}$, but now with a chromo-electric field. Sorting the decomposed result into the longitudinal and transverse gluon contributions as $\mathcal{L}_{\text{YM}}^{(1)} = \mathcal{L}_L^{(1)} + \mathcal{L}_T^{(1)}$, we find that

$$\mathcal{L}_L^{(1)} = \sum_{a=1}^{N_c^2-1} \left[\frac{|v^a \mathbf{b}|}{2\pi} \right] \sum_{n=0}^{\infty} \left[-\frac{i}{2\pi} \int_0^{\infty} \frac{ds}{s} e^{-i\epsilon_{1n}^2 s} (v^a \mathbf{a}) \sinh(v^a \mathbf{a} s) \right], \quad (336a)$$

$$\mathcal{L}_T^{(1)} = \sum_{a=1}^{N_c^2-1} \left[\frac{|v^a \mathbf{b}|}{2\pi} \right] \sum_{n=0}^{\infty} \left[-\frac{i}{8\pi} \int_0^{\infty} \frac{ds}{s} \left(e^{-i\epsilon_{\perp n-1}^2 s} + e^{-i\epsilon_{\perp n+1}^2 s} \right) \frac{v^a \mathbf{a}}{\sinh(v^a \mathbf{a} s)} \right]. \quad (336b)$$

We dropped the infinitesimal imaginary parameter because the proper-time integral in each Landau level does not have singularities on the real axis, except for the divergence at the origin which is common to the free theory. Notice that the integrand for the longitudinal mode $\mathcal{L}_L^{(1)}$ is regular everywhere in the complex s plane, indicating that the longitudinal gluon mode is not produced. The NO mode sitting in the ground state of $\mathcal{L}_T^{(1)}$ is a tachyonic mode of which the spectrum is given as $\epsilon_{\perp -1}^2 = -|v^a \mathbf{a}|$. The proper-time integrals for the higher levels are well-defined by themselves and can be performed separately. The imaginary part from each higher-level contribution is just the same as that for the scalar QED (221) with the replacement of the energy spectrum $\epsilon_{\perp n}^2$. Performing the summation in Eq. (221), one can reproduce the result in Eq. (335) from the different method.

Let us focus on the NO mode. The NO mode in Eq. (336b) is extracted as

$$\mathcal{L}_{\text{NO}}^{(1)} = \left[\frac{|v^a \mathbf{b}|}{2\pi} \right] \left[-\frac{i}{8\pi} \int_0^{\infty} \frac{ds}{s} e^{i|v \mathbf{b}|s} \frac{v^a \mathbf{a}}{\sinh(v^a \mathbf{a} s)} \right]. \quad (337)$$

The issue is that the proper-time integral does not converge in the lower-half plane due to the tachyonic dispersion relation. One may not naively close the contour in the lower-half plane as we have done repeatedly (cf. Fig. 14).

One way to make the integral well-behaving is to include a gluon mass m_g so that the tachyonic region is excluded [345, 346]. Namely, it is assumed that $m_g^2 - |v^a \mathbf{b}| > 0$. The massless limit ($m_g \rightarrow 0$) can be taken only after performing the proper-time integral. This looks like a somewhat *ad hoc* way. Yet, adopting this prescription, one can close the contour in the lower-half plane and then take the residues on the *negative* imaginary axis as in the other stable modes. After taking the massless limit, we find an exponential enhancement factor as [89, 346]

$$2\Im m \mathcal{L}_{\text{NO}}^{(1)} = \lim_{m_g \rightarrow 0} \left[\frac{|v^a \mathbf{b}|}{2\pi} \right] \sum_{k=1}^{\infty} (-1)^{k-1} \frac{|v^a \mathbf{a}|}{4\pi k} e^{-\frac{m_g^2 - |v^a \mathbf{b}|}{|v^a \mathbf{a}|} \pi k} = \frac{N_c}{8\pi^2} g^2 |\mathbf{a} \mathbf{b}| \ln \left(1 + e^{|\frac{\mathbf{b}}{\mathbf{a}}| \pi} \right), \quad (338)$$

where the color sum is again performed with the identity (572b). The sum of exponentials results in a finite logarithmic function even in the massless limit ($m_g \rightarrow 0$) thanks to the alternating signs in the residues for bosons. Without the alternating signs, the sum would be divergent, or become a complex-valued logarithm. In the strong electric field limit $|\mathbf{b}/\mathbf{a}| \rightarrow 0$, the exponentially enhanced imaginary part (338) converges to a finite value.

There is another possible way to perform the integral in Eq. (337). There is no mathematical obstacle to close the integral contour in the upper-half plane. In fact, there is a good reason to close the integral contour in the upper-half plane in the absence of chromo-electric fields. In Sec. 6.5, we will see that the QCD beta function is reproduced from the coefficients in the real part of the effective Lagrangian. The correct coefficient is obtained as the sum of coefficients computed with the contours closed in the upper-half plane for the NO mode and in the lower-half plane for the other modes [107, 265]. Collecting the residues on the *positive* imaginary axis, we obtain

$$2\Im m \mathcal{L}_{\text{NO}}^{(1)} = \left[\frac{|v \mathbf{b}|}{2\pi} \right] \sum_{k=1}^{\infty} (-1)^{k-1} \frac{|v^a \mathbf{a}|}{4\pi k} e^{-|\frac{\mathbf{b}}{\mathbf{a}}| \pi k}. \quad (339)$$

This result has an exponential suppression factor and is the same as the scalar QED result (221) up to the replacement of the effective mass by the Landau spacing $|v^a \mathbf{b}|$, as opposed to the previous result (338). One might wonder how the results could be the same as the scalar QED in spite of the big difference between the normal and tachyonic dispersion relations. One can compare the lowest-lying

NO mode and the second lowest normal mode of which the dispersion relations are different only in the signs. In general, the imaginary part of the effective Lagrangian can be written as

$$2i\Im m\mathcal{L}^{(1)} = \left[\frac{|v\mathbf{b}|}{2\pi} \right] \frac{-1}{8\pi} \sum_{n=0}^{\infty} \{ F(\epsilon_{\perp n}^2) - [F(\epsilon_{\perp n}^2)]^* \}. \quad (340)$$

In each energy level, we have

$$F(\epsilon_{\perp n}^2) = i \int_0^{\infty} \frac{ds}{s} e^{-\epsilon s} e^{-i\epsilon_{\perp n}^2 s} \left[\frac{v\mathbf{a}}{\sinh(v\mathbf{a}s)} \right]. \quad (341)$$

It is only a function of the squared form $\epsilon_{\perp n}^2$ and not of a potentially complex-valued quantity $\epsilon_{\perp-1}$. The integral is convergent at the upper boundary ($s \rightarrow \infty$), and one can drop the infinitesimal parameter ϵ . Note that, as long as $\epsilon_{\perp n}^2$ is a real-valued number, we have a simple relation

$$F(\epsilon_{\perp n}^2) - [F(\epsilon_{\perp n}^2)]^* = F(\epsilon_{\perp n}^2) + F(-\epsilon_{\perp n}^2). \quad (342)$$

The right-hand side is symmetric in the sign of $\epsilon_{\perp n}^2$, and the imaginary part (340) may not depend on the sign of $\epsilon_{\perp n}^2$. This especially implies that the imaginary parts from the contributions of the lowest-lying NO mode and the second-lowest normal mode have the same exponential suppression factors. The exponential suppression of the NO mode contradicts the exponential enhancement in Eq. (338) from the gluon-mass prescription, which apparently looks puzzling. As mentioned above, there is, however, a good reason to close the integral contour in the upper-half plane, at least, in the absence of chromo-electric fields. This is a nontrivial suggestion for the choice of contours as elaborated in Sec. 6.5.

The choice of the contour seems to be yet controversial, while there are some other suggestions for the choice of the integral contours and consequent results [275, 276, 347].

6.4.2 Quark pair production in QCD+QED fields

We can study the interplay between the chromo-fields and electromagnetic fields in the quark-antiquark pair creation by the use of the quark-loop contribution (329) computed in the presence of both the QED+QCD fields [305]. The imaginary part reads

$$\gamma_{q\bar{q}} = 2\Im m\mathcal{L}_{\text{quark}}^{(1)} = \sum_{i=1}^{N_c} \sum_{f=1}^{N_f} \frac{\mathbf{a}_{i,f} \mathbf{b}_{i,f}}{4\pi^2} \sum_{n=1}^{\infty} \frac{1}{n} e^{-\frac{m_f^2}{\mathbf{a}_{i,f}} n\pi} \coth \left(\frac{\mathbf{b}_{i,f}}{\mathbf{a}_{i,f}} n\pi \right). \quad (343)$$

When we only have a purely chromo-electric field, the above result reduces to the formula obtained in Refs. [110, 279] (see also Ref. [113]).

The result (343) allows one to study arbitrary combinations of the chromo-fields and electromagnetic fields including the dependences on the relative angles between the fields and the strengths of the fields. Several cases are investigated in Ref. [305]. Of special interest is the ‘‘mixed’’ configuration naturally realized in heavy-ion collisions. For example, in non-central heavy-ion collisions, strong magnetic fields are created in the perpendicular direction to the reaction plane in addition to the ‘‘glasma’’ fields (collinear chromo-EM fields with the same magnitude $|\mathcal{E}| = |\mathcal{B}|$ oriented to the beam direction). In Fig. 28, we show the dependence of the light-quark production rate on the relative angle between the magnetic field and the glasma field. The production ratio is enhanced when the magnetic field exists in parallel/antiparallel to the glasma fields, and is decreased when the magnetic field is perpendicular to the glasma fields. Remember that we observed similar behaviors in Sec. 4.2.3 as the effects of the magnetic field on the pair production rate in the Abelian fields. There, we found that the enhanced production is catalyzed by the Landau degeneracy. One can apply the Landau-level decomposition to the formula (343) as discussed in Sec. 4.2.4.

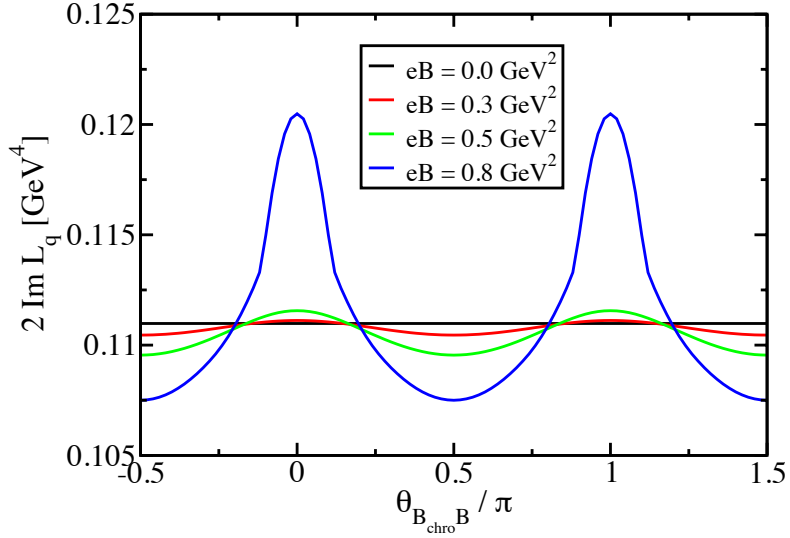


Figure 28: Light-quark production rate $2\Im m\mathcal{L}_{\text{quark}}^{(1)}$ in the collinear glasma fields and a QED magnetic field, plotted as a function of the angle between those fields. We take up quarks mass $m_q = 0.5$ MeV and electric charge $q_u = +2/3|e|$. The strengths of the glasma fields are taken as $g\mathcal{B} = g\mathcal{E} = 1$ GeV².

6.5 Effective potential in QCD+QED fields: Magnetic-gluon condensation

As we have discussed the chiral symmetry breaking in early this section, the effective potential provides us with insight into the vacuum state realized in a system. In this subsection, we discuss the QCD vacuum with the non-Abelian extended effective potential, and find that the QCD vacuum favors spontaneous generation of a nonzero chromo-magnetic field, which is often called the Savvidy vacuum [107, 264, 265]. One finds a logarithm that induces a minimum of the effective potential at a non-zero chromo-magnetic condensation and see that the same logarithm gives rise to a negative beta function leading to the asymptotic freedom in QCD. About a half of the logarithm originates from the lowest Landau level of spin-polarized gluons in a chromo-magnetic field. The contribution of this lowest-lying mode also gives rise to an imaginary part of the effective action called the Nielsen-Olesen instability [62]. We will explicitly observe those points below. Moreover, the asymptotic freedom is discussed as a consequence of magnetism in vacuum rather than the anti-screening of color charges.

We may also discuss effects of an Abelian magnetic field on the Savvidy vacuum. This is related to recent lattice QCD simulations in the presence of strong magnetic fields [348–352], where the authors studied magnetic-field dependences of gluonic observables such as the gluon condensate and the Polyakov loop. It has been found that the gluon condensate acquires an anisotropy induced by the external magnetic field and that the magnitude of the gluon condensate monotonically increases with an increasing magnetic field. The effective potential allows us to capture the qualitative features of those findings.

6.5.1 Singularities in proper-time integrals

We focus on the chromo-magnetic component of the gluon condensate. By taking the limit $\mathbf{a} \rightarrow 0$ in Eqs. (315) and (329), the contributions of the Yang-Mills part $S_{\text{YM}}^{(1)}$ and the quark part $S_{\text{quark}}^{(1)}$ are obtained as

$$S_{\text{YM}}^{(1)} = - \int d^4x \sum_{a=1}^{N_c^2-1} \frac{|v^a \mathcal{B}|}{16\pi^2} \int_0^\infty \frac{ds}{s^2} e^{-\epsilon s} \frac{\cos(2|v^a \mathcal{B}|s)}{\sin(|v^a \mathcal{B}|s)}, \quad (344a)$$

$$S_{\text{quark}}^{(1)} = \int d^4x \sum_{i=1}^{N_c} \sum_{f=1}^{N_f} \frac{\mathbf{b}_{i,f}}{8\pi^2} \int_0^\infty \frac{ds}{s^2} e^{-i(m_f^2 - i\epsilon)s} \cot(\mathbf{b}_{i,f}s). \quad (344b)$$

Quarks are coupled to both the chromo-magnetic field $\vec{\mathcal{B}}$ and the QED magnetic field \vec{B} , so that the invariant $\mathbf{b}_{i,f}$ is expressed with their vector sum

$$\mathbf{b}_{i,f} = \sqrt{|w_i \vec{\mathcal{B}} - q_f \vec{B}|^2} = \sqrt{(w_i \mathcal{B})^2 + (q_f B)^2 - 2w_i q_f \mathcal{B} B \cos \theta_{\mathcal{B}B}}, \quad (345)$$

where $\theta_{\mathcal{B}B}$ stands for the angle between $\vec{\mathcal{B}}$ and \vec{B} in the coordinate space. As we have done in the QED case (see Sec. 5.2.2), we would possibly perform the proper-time integrals in Eq. (344) by rotating the integral contour to the negative imaginary axis via an infinite arc in the lower-half plane. The effective potential is, then, obtained as $V_{\text{eff}} = -S_{\text{eff}}/\int d^4x$ for constant fields. This is still our basic strategy to get an analytic expression of the effective potential. However, one should note that both the integrals contain ultraviolet (UV) divergences, and that the integrand in the YM part contains a component that is not damped out on the arc in the lower-half plane. We shall first briefly look over these issues below.

The proper-time integrals both in Eqs. (344a) and (344b) exhibit UV divergences when the lower boundary of the integral approaches the origin, $s \rightarrow 0$. Expanding the integrands in the small s region, one can identify quartic and logarithmic divergences arising from the integrands of the forms $1/s^3$ and $\mathbf{b}_{i,f}^2/s$, respectively. The quartic divergences are a vacuum energy independent of the magnetic fields, so that we will not discuss them. On the other hand, the logarithmically divergent terms are proportional to $(v^a \mathcal{B})^2 \ln \Lambda$ and $\mathbf{b}_{i,f}^2 \ln \Lambda$ (summation over i and f is understood) with Λ being a UV cutoff of the proper-time integral at $s = 1/\Lambda^2$. This is a gauge-invariant regularization, sometimes called the proper-time regularization. Those logarithmic divergences induce renormalization of the coupling constants e and g . We will reproduce the beta functions in QED and QCD.

The other issue only appears in the YM contribution (344a) in the asymptotic IR region, $|s| \rightarrow \infty$. The asymptotic form of the integrand contains an exponentially growing factor in the lower half of the complex s plane, and one may not naively rotate the integral contour to the negative imaginary axis. The origin of this singular contribution can be identified in the Landau-level decomposition of the effective Lagrangian (325). The singular piece in Eq. (344a) is nothing but the LLL contribution

$$\mathcal{L}_{\text{YM}}^{(1)n=0} = -\frac{i}{8\pi} \sum_{a=1}^{N_c^2-1} \left[\frac{|v^a \mathcal{B}|}{2\pi} \right] \int_0^\infty \frac{ds}{s^2} e^{-\epsilon s + i s |v^a \mathcal{B}|}. \quad (346)$$

The other all Landau levels have phases with the opposite sign that provide damping factors on the negative imaginary axis. In the next subsection, we will fully perform the proper-time integral (344a) with an appropriate choice of the integral contour and of the regularization for the UV divergence ($s \rightarrow 0$). In prior, it is instructive to find an alternative expression of the integral and to see emergence of an imaginary part. To this end, we go back to the Landau-level representation (322), and perform the proper-time integral first, leaving the longitudinal-momentum integral. After introducing a UV regularization (see Appendix E.1), we obtain

$$\mathcal{L}_{\text{YM}}^{(1)} = \sum_{a=1}^{N_c^2-1} \frac{|v^a \mathcal{B}|}{2\pi} \sum_{n=0}^{\infty} \frac{1}{2} (2 - \delta_{n0} - \delta_{n1}) \int \frac{dp_z}{2\pi} \sqrt{p_z^2 + (2n-1)|v^a \mathcal{B}| + i\epsilon}. \quad (347)$$

This expression is nothing but the (divergent) vacuum energy in the Landau levels and is anticipated by construction of the effective action. While the integrands are real-valued for $n \geq 1$, it is evident that the lowest-lying mode ($n = 0$) has an imaginary contribution when $p_z^2 < |v^a \mathcal{B}|$. The imaginary part of

the integral can be straightforwardly computed as⁶⁷

$$\Im m[\mathcal{L}_{\text{YM}}^{(1)n=0}] = \sum_{a=1}^{N_c^2-1} \frac{|v^a \mathcal{B}|}{2\pi} \cdot \frac{1}{2} \int_{-\sqrt{|v^a \mathcal{B}|}}^{\sqrt{|v^a \mathcal{B}|}} \frac{dp_z}{2\pi} \sqrt{|v^a \mathcal{B}| - p_z^2} = \sum_{a=1}^{N_c^2-1} \frac{|v^a \mathcal{B}|}{2\pi} \cdot \frac{1}{8} |v^a \mathcal{B}|. \quad (348)$$

The emergence of this imaginary part in a chromo-magnetic field was originally shown by Nielsen and Olesen [62]. The negative value of the energy square originates from the Zeeman shift for spin-1 particles which is induced by the self-interactions among gauge bosons inherent in non-Abelian gauge theories. The NO instability does not occur in QED.⁶⁸

Bearing those singularities in the UV and IR regions in mind, we now evaluate the proper-time integrals for the Yang-Mills part (344a) and then for the quark part (344b) in order.

6.5.2 Computation of effective Lagrangians

We first need to regularize the UV divergences in the YM part (344a). To focus on the relevant integral, we define a dimensionless integral as

$$\begin{aligned} \mathcal{L}_{\text{YM}}^{(1)} &= - \sum_{a=1}^{N_c^2-1} \frac{|v^a \mathcal{B}|}{16\pi^2} I_{\text{YM}}^{(1)}, \\ I_{\text{YM}}^{(1)} &:= |v^a \mathcal{B}|^{-\delta} \mu^{2\delta} \left(\frac{-i}{4\pi} \right)^{-\delta} \int_0^\infty \frac{ds'}{s'^{2-\delta}} e^{-\epsilon s'} \frac{\cos(2s')}{\sin s'}, \end{aligned} \quad (349)$$

where the integral variable has been scaled as $s \rightarrow s' = |v^a \mathcal{B}|s$. Here, we have already introduced the dimensional regularization, and the integral $I_{\text{YM}}^{(1)}$ is convergent on the both boundaries thanks to the displacement δ as well as ϵ . The overall factor of $\mu^{2\delta}$ is inserted to compensate the mass dimension as before (cf. Sec. 5.2.2). We only applied the displacement to the longitudinal dimension $d_{\parallel} = 2 - 2\delta$, because the transverse momentum does not appear in the dispersion relation and the denominator of the integrand; The transverse-momentum integral just results in the Landau degeneracy factor. The UV divergences will be isolated as singular terms in the limit $\delta \rightarrow 0$. As explained in Appendix E.2, it is important to keep track of the overall factors, especially the imaginary unit $(-i)^\delta$. Such a factor provides a finite contribution of order δ^0 when combined with the divergent integral.

The second crucial step is isolation of the NO mode that diverges on the negative imaginary axis when $s \rightarrow -i\infty$. We decompose the integral as

$$I_{\text{YM}}^{(1)} = I_{\text{NO}}^{(1)} + I_{\text{res}}^{(1)}, \quad (350)$$

where the integrals for the NO mode and the residual all modes are given by [see Eq. (346)]

$$I_{\text{NO}}^{(1)} = \left(\frac{4\pi i \mu^2}{|v^a \mathcal{B}|} \right)^\delta \int_0^\infty \frac{ds}{s^{2-\delta}} e^{-\epsilon s} i e^{is}, \quad (351a)$$

$$I_{\text{res}}^{(1)} = \left(\frac{4\pi i \mu^2}{|v^a \mathcal{B}|} \right)^\delta \int_0^\infty \frac{ds}{s^{2-\delta}} e^{-\epsilon s} \left[\frac{\cos(2s)}{\sin s} - i e^{is} \right]. \quad (351b)$$

⁶⁷Here, the square root is a multi-valued function on the Riemann sheet. However, we get a unique value without the ambiguity in Eq. (576) if we focus on the relevant IR regime from the beginning (see Appendix E.1).

⁶⁸Considering composite particles interacting with an Abelian magnetic field, “ ρ -meson condensation” was put forward according to an analogous spin-1 Zeeman shift of the charged ρ meson spectrum. This observation is based on effective models of QCD [353, 354] and a quenched two-color lattice QCD simulation [355]. It has been pointed out, however, that the ρ -meson condensation conflicts with the Vafa-Witten theorem and that the QCD inequality provides a lower bound of ρ -meson mass by the “connected” neutral pion mass [356]. An indication of the ρ -meson condensation has not been seen in recent quenched lattice QCD simulations [356–359] (see more discussions in Sec. 7.4.1).

Note again that both integrals are well-defined ones without divergences, and also that the integral for the NO mode $I_{\text{NO}}^{(1)}$ is convergent on the positive imaginary axis. Then, one can perform each integral straightforwardly as described in Appendix E.2. It should be emphasized that an imaginary part only appears from the integral $I_{\text{NO}}^{(1)}$ for the NO mode when we carefully include the imaginary unit $(-i)^\delta$ in Eq. (349). Combining the contributions from the NO mode and the residual all modes, we obtain the effective Lagrangian for the Yang-Mills part [107, 115, 264, 275, 276, 360] (see also Ref. [305] for an extension to finite temperature)

$$\mathcal{L}_{\text{YM}}^{(1)} = \frac{1}{96\pi^2} \sum_{a=1}^{N_c^2-1} |v^a \mathcal{B}|^2 \left[11\kappa \left(\frac{\mu^2}{2|v^a \mathcal{B}|} \right) + \ln 2 + 12(1 - \ln G) \right] + iN_c \frac{|g\mathcal{B}|^2}{16\pi}, \quad (352)$$

where G is the Glaisher constant $G = 1.2824\dots$ [327]. The imaginary part agrees with the previous result foreseen in the explicit vacuum-energy computation (348). We defined a UV-divergent quantity

$$\kappa(x) \equiv \left(\frac{1}{\delta} - \gamma_E + \ln(4\pi) \right) + \ln x, \quad (353)$$

with γ_E being the Euler-Mascheroni constant. The first three terms between the brackets are the familiar combination to be subtracted in the $\overline{\text{MS}}$ scheme. Also, we find a logarithmic dependence on the chromo-magnetic field normalized by an arbitrary energy scale μ . Both the integrals $I_{\text{NO}}^{(1)}$ and $I_{\text{res}}^{(1)}$ yield the terms proportional to κ accompanied by numerical factors of 1 and 5/6, respectively. Namely, about a half of the total divergence and logarithm stem from the single lowest-lying mode.

The quark contribution (344b) contains interactions with both the chromo- and Abelian magnetic fields. In the absence of a chromo-magnetic field ($g\mathcal{B} = 0$), it reduces to the HE Lagrangian examined in Sec. 5.2.2 (up to a color factor) [98, 226, 227]. An extension to the effective Lagrangian in a chromo-magnetic field was investigated in Refs. [275, 276]. The complete form in the coexistent QCD+QED fields was obtained in Ref. [115] and was further extended to finite temperature in Ref. [305]. Here, we recapitulate the calculation starting with Eq. (344b) instead of the previous expression (255a) in which the UV divergences had been subtracted. Similar to the YM part, we use the dimensional regularization, and the regularized form of the proper-time integral reads

$$\begin{aligned} \mathcal{L}_{\text{quark}}^{(1)} &= \sum_{i=1}^{N_c} \sum_{f=1}^{N_f} \frac{\mathbf{b}_{i,f}^2}{8\pi^2} I_{\text{quark}}^{(1)}, \\ I_{\text{quark}}^{(1)} &:= \frac{\mu^{2\delta}}{\mathbf{b}_{i,f}^\delta} (-1)^\delta \left(\frac{i}{4\pi} \right)^{-\delta} \int_0^\infty \frac{ds}{s^{2-\delta}} e^{-i(m^2 - i\epsilon)s} \cot(\mathbf{b}_{i,f}s). \end{aligned} \quad (354)$$

To get the correct result with the dimensional regularization, it is again important to keep track of the overall factors (see Appendix E.3). We can perform the remaining integral straightforwardly as done in Sec. 5.2.2). As one can explicitly confirm in Eq. (354) of Appendix E.3, the imaginary units are completely canceled out in the quark part. Then, we arrive at a real-valued result

$$\mathcal{L}_{\text{quark}}^{(1)} = \sum_{i=1}^{N_c} \sum_{f=1}^{N_f} \frac{\mathbf{b}_{i,f}^2}{8\pi^2} \left[-\left(\frac{1}{3} + 2\bar{\mathbf{b}}_{i,f}^{-2} \right) \left\{ \kappa \left(\frac{\mu^2}{m_f^2} \right) + 1 \right\} + 4\zeta(-1, \bar{\mathbf{b}}_{i,f}^{-1}) \ln \bar{\mathbf{b}}_{i,f}^{-1} + 4\zeta'(-1, \bar{\mathbf{b}}_{i,f}^{-1}) \right], \quad (355)$$

where $\bar{\mathbf{b}}_{i,f} \equiv 2\mathbf{b}_{i,f}/m_f^2$, and $\zeta'(z, a) \equiv \partial\zeta(z, a)/\partial z$ and $\zeta(-1, a) = -(2a^2 - 2a + 1/3)/4$ as mentioned below Eq. (260).

Note that the finite piece in Eq. (355) does not vanish in the vanishing field limit $\bar{\mathbf{b}}_{i,f} \rightarrow 0$, whereas the previous result (260) vanishes in the vanishing (Abelian) field limit. This is just because a finite

integral was previously defined with the subtraction of the free Lagrangian. After subtraction of the finite component in the vanishing field limit $\bar{\mathbf{b}}_{i,f} \rightarrow 0$, the finite piece in Eq. (355) agrees with the previous result (260) up to differences in the color and flavor indices and the associate summation [see Eq. (365b) below].

6.5.3 Vacuum paramagnetism and the asymptotic freedom

We have obtained the one-loop quantum corrections to the effective Lagrangian in Eqs. (352) and (355) with the UV divergences isolated in κ . In this subsection, we perform the renormalization of the QED and QCD coupling constants and discuss an interpretation of the asymptotic freedom in terms of the vacuum magnetism.

To perform the renormalization, we shall go back to the original QCD action (145) which we understand is written with the bare fields and coupling constants. As usual, we split the bare fields into the renormalized finite parts and residual divergent parts. Accordingly, the classical Lagrangian is split into the same form of the classical Lagrangian, which is however written with the renormalized fields and coupling constants, and the residual divergent terms, i.e., the counterterms (see, e.g., Ref. [66]). Now, it is understood that the divergent one-loop quantum corrections (352) and (355) have been computed by starting from the renormalized classical Lagrangian. Adding the one-loop quantum corrections to the classical Maxwell and Yang-Mills parts (at vanishing electric components), we find

$$\begin{aligned} \Re[\mathcal{L}_{\text{eff}}^{(1)}(B, \mathcal{B})] &= \mathcal{L}_{\text{classical}} + \Re[\mathcal{L}_{\text{YM}}^{(1)}] + \mathcal{L}_{\text{quark}}^{(1)} \\ &= -\frac{1}{2}(1 + \delta_A)\mathcal{B}^2 - \frac{1}{2}(1 + \delta_A)B^2 \\ &\quad + \frac{11}{96\pi^2} \sum_{a=1}^{N_c^2-1} |v^a \mathcal{B}|^2 \kappa \left(\frac{\mu^2}{2|v^a \mathcal{B}|} \right) - \frac{1}{24\pi^2} \sum_{i=1}^{N_c} \sum_{f=1}^{N_f} \mathbf{b}_{i,f}^2 \kappa \left(\frac{\mu^2}{m_f^2} \right) - (\Re[U_{\text{YM}}^{(1)}] + U_{\text{quark}}^{(1)}). \end{aligned} \quad (356)$$

We do not discuss the imaginary part of $\mathcal{L}_{\text{YM}}^{(1)}$ since it takes a finite value and does not have any UV divergence. All the fields and coupling constants in the above expression are renormalized finite ones and the counterterms are proportional to divergent parameters δ_A, δ_A . The divergent terms proportional to either $|v^a \mathcal{B}|^2$ or $\mathbf{b}_{i,f}^2$ are absorbed by those counterterms equipped in the above expression. Since the one-loop effective action does not contain radiative corrections to the fermion mass and field strength or the vertex form factor, we have suppressed irrelevant counterterms for renormalization of those quantities. We have discarded the term $\propto m_f^4 \kappa(\frac{\mu^2}{m_f^2})$ that originates from the one-loop diagram without any external-field insertion. The residual finite parts are given as

$$U_{\text{YM}}^{(1)}(B, \mathcal{B}) = -\frac{1}{96\pi^2} \sum_{a=1}^{N_c^2-1} |v^a \mathcal{B}|^2 [\ln 2 + 12(1 - \ln G)], \quad (357a)$$

$$U_{\text{quark}}^{(1)}(B, \mathcal{B}) = -\sum_{i=1}^{N_c} \sum_{f=1}^{N_f} \frac{\mathbf{b}_{i,f}^2}{8\pi^2} \left[-\left(\frac{1}{3} + 2\bar{\mathbf{b}}_{i,f}^{-2}\right) + 4\zeta(-1, \bar{\mathbf{b}}_{i,f}^{-1}) \ln \bar{\mathbf{b}}_{i,f}^{-1} + 4\zeta'(-1, \bar{\mathbf{b}}_{i,f}^{-1}) \right]. \quad (357b)$$

Notice that the YM part $U_{\text{YM}}^{(1)}(B, \mathcal{B})$ has only a quadratic dependence on \mathcal{B} in spite of the all-order resummation for the external-field insertion. A simple reason is the massless nature of the YM part which enabled us to factorize all the \mathcal{B} dependences out of the proper-time integral (349). In contrast, the magnetic-field dependences in the quark part $U_{\text{quark}}^{(1)}(B, \mathcal{B})$ cannot be factorized due to the exponential mass dependence in the proper-time integral (354), resulting in an intricate dependence seen in the above.

Explicit forms of the counterterms in the $\overline{\text{MS}}$ scheme should be given as

$$\delta_{\mathcal{A}} = 2 \left[-\frac{11}{96\pi^2} \sum_{a=1}^{N_c^2-1} |v^a|^2 \kappa \left(\frac{\Lambda^2}{2|v^a \mathcal{B}|} \right) + \frac{g^2}{48\pi^2} \sum_{f=1}^{N_f} \kappa \left(\frac{\Lambda^2}{m_f^2} \right) \right], \quad (358a)$$

$$\delta_A = 2 \left[\frac{N_c}{24\pi^2} \sum_{f=1}^{N_f} \bar{q}_f^2 \kappa \left(\frac{\Lambda^2}{m_f^2} \right) \right], \quad (358b)$$

where the summation over the color indices is performed by the use of the identities (566) and (572). The UV divergences have split into the terms proportional to \mathcal{B}^2 and B^2 since the cross terms in $\mathbf{b}_{i,f}^2$ vanish in the color summation. With those counterterms, the effective Lagrangian (356) reads

$$\begin{aligned} \Re e[\mathcal{L}_{\text{eff}}^{(1)}(B'/e, \mathcal{B}'/g)] &= - \left[\frac{1}{g^2} + \frac{1}{24\pi^2} \left(\frac{11}{2} N_c - N_f \right) \ln \left(\frac{\Lambda^2}{\mu^2} \right) \right] \mathcal{B}'^2 \\ &\quad - \left[\frac{1}{e^2} - \frac{1}{12\pi^2} N_c \ln \left(\frac{\Lambda^2}{\mu^2} \right) \sum_{f=1}^{N_f} \bar{q}_f^2 \right] B'^2 - (\Re e[U_{\text{YM}}^{(1)}] + U_{\text{quark}}^{(1)}), \end{aligned} \quad (359)$$

where $\bar{q}_f := q_f/e$. We introduced an arbitrary energy scale Λ . This floating energy scale divides the logarithmic terms into two pieces included in the counterterm and the rest of the effective Lagrangian (359). We rescaled the magnetic-field strengths as $B \rightarrow B' = eB$ and $\mathcal{B} \rightarrow \mathcal{B}' = g\mathcal{B}$. Thanks to this manipulation, one can isolate the coupling constants into the classical part of the effective Lagrangian. The quantum corrections then do not have an explicit dependence on the coupling constants, and can be absorbed into effective coupling constants as

$$\frac{1}{g^2(\Lambda)} := \frac{1}{g^2} + \frac{1}{24\pi^2} \left(\frac{11}{2} N_c - N_f \right) \ln \left(\frac{\Lambda^2}{\mu^2} \right), \quad (360a)$$

$$\frac{1}{e^2(\Lambda)} := \frac{1}{e^2} - \frac{1}{12\pi^2} N_c \ln \left(\frac{\Lambda^2}{\mu^2} \right) \sum_{f=1}^{N_f} \bar{q}_f^2, \quad (360b)$$

where the magnitudes of the quantum corrections depend on the energy scale Λ . The coupling constants g and e on the right-hand sides should be understood as those at the scale $\Lambda = \mu$. Then, the beta functions are found to be⁶⁹

$$\beta_{\text{QCD}}^{(1)} = \Lambda \frac{\partial g(\Lambda)}{\partial \Lambda} = -\frac{g^3}{24\pi^2} \left(\frac{11}{2} N_c - N_f \right), \quad (361a)$$

$$\beta_{\text{QED}}^{(1)} = \Lambda \frac{\partial e(\Lambda)}{\partial \Lambda} = \frac{e^3}{12\pi^2} N_c \sum_{f=1}^{N_f} \bar{q}_f^2. \quad (361b)$$

As clear in the above derivation, the one-loop beta functions are independent of the finite terms in the counterterms (358), i.e., independent of the renormalization scheme. While the QED beta function $\beta_{\text{QED}}^{(1)}$ is positive definite, the QCD beta function $\beta_{\text{QCD}}^{(1)}$ can take a negative value, leading to the asymptotic freedom when $N_f/N_c < 11/2$.

We shall discuss an interpretation of the asymptotic freedom as a consequence of the paramagnetism in the Yang-Mills theory. As mentioned in the beginning of this section, the charge antiscreening effect

⁶⁹We take a positive value for unit electric charge $e > 0$, and the flavor-dependent signs of electric charges are included in a numerical coefficient \bar{q}_f below.

($\epsilon < 1$) and the paramagnetism ($\mu_m > 1$) implies each other under the constraint of the Lorentz symmetry $\epsilon\mu_m = 1$, and one may attribute the asymptotic freedom to a consequence of the vacuum paramagnetism [270–273] (see also Ref. [274] for a concise review on the asymptotic freedom in QCD). They are the susceptibilities at the vanishing field limit, and the Lorentz symmetry can be assumed. For free particles, the magnetic susceptibility has two contributions, which are spin polarization effect known as the Pauli paramagnetism and the orbital magnetic moment induced by the circular current, i.e., the Landau diamagnetism [44]. Therefore, the one-loop beta functions are determined as a consequence of competition between the vacuum energy shifts by these two effects.

Scalar QED.—Without a spin contribution, one can anticipate to have the Landau diamagnetism. There are no photon-polarization contributions to the magnetism in QED without self-interactions among photons. The vacuum diamagnetism ($\mu_m < 1$) implies a charge screening ($\epsilon > 1$) and a positive beta function as it is indeed the case in scalar QED.

Spinor QED.—For particles with nonzero spin, one finds another contribution from the Pauli paramagnetism. As well-known, the magnitude of the Pauli paramagnetism is three times larger than that of the Landau diamagnetism in spinor QED. Then, one may wonder if the total contribution induces a vacuum paramagnetism (as opposed to what we know about QED). However, the fermion contributions to the *vacuum* energy should in general have an overall minus sign originating from the fermionic statistics. The energy gap between the positive- and negative-energy states increases due to the negative energy shift of the filled states in the Dirac sea. With this sign flip, the vacuum diamagnetism still holds in spinor QED [193, 361].

Yang-Mills theory.—Spin-1 gauge bosons have an even larger magnetic moment and are coupled to the chromo-magnetic field due to the non-Abelian nature. The spin-polarization effect dominates over the Landau diamagnetism *without* an overall negative sign for the bosonic statistics. Therefore, the spin-polarization effect gives rise to the vacuum paramagnetism $\mu_m > 1$. The vacuum paramagnetism and the asymptotic freedom is a salient and inherent feature of the Yang-Mills theory arising from the polarization effect of self-interacting spin-1 gauge bosons.

This simple interpretation may suggest that, once an interacting spin-1 boson is allowed to exist in a theory (presumably as an elementary excitation), ubiquitous spin interaction generally leads to the asymptotic freedom. An early implication of the charge antiscreening effect was indeed observed with a (hypothetical) spin-1 vector boson interacting with an Abelian electromagnetic field [267]. Our effective Lagrangian is computed in the covariantly constant chromo-fields which also only have Abelian-like diagonal components in the color space. However, without a non-Abelian gauge symmetry, there is no asymptotic freedom in *renormalizable theories* in the four dimensions [362].

Based on the above discussion, one can divide each beta function into the current-induced and spin-polarization terms:

$$\beta_{\text{QED}}^{(1)} = \frac{e^3}{8\pi^2} (-1) \left(\frac{n_p}{6} - \left(\frac{g}{2} \right)^2 \right) N_c \sum_{f=1}^{N_f} \bar{q}_f^2, \quad (362a)$$

$$\beta_{\text{QCD}}^{(1)} = \frac{g^3}{8\pi^2} \left[(-1) \frac{1}{2} \left(\frac{n_p}{6} - \left(\frac{g}{2} \right)^2 \right) N_f + \frac{N_c}{2} \left(\frac{n_p}{6} - (g \cdot 1)^2 \right) \right], \quad (362b)$$

where n_p is the number of polarization modes for quark and transverse gluons, i.e., $n_p = 2$ and $g = 2$ is the leading-order g -factor. The overall negative sign in the quark contribution originates from the negative-energy states as mentioned above. The quark contribution to the QCD beta function is a half

of that in QED because of the color trace.⁷⁰ Compared to the quark contribution, the YM contribution is multiplied by N_c instead of $1/2$, but a factor of $1/2$ appears for another reason. Namely, the quark contribution includes contributions of particle and antiparticle pairs, and the eight gluons should be also paired into particles and antiparticles, resulting in the factor of $1/2$; Recall that the effective color charges v^a appear in four pairs of positive and negative values (see Eq. (157) and Appendix D.2.2). Most importantly, the spin-1 polarization term gives rise to the negative YM contribution to the QCD beta function, i.e., the vacuum paramagnetism, as discussed above. One can also presume the beta function in scalar QED (without the color group):

$$\beta_{\text{scalar QED}}^{(1)} = \frac{e^3}{8\pi^2} \frac{1}{6} \sum_{f=1}^{N_f} \bar{q}_f^2, \quad (363)$$

with $n_p = 1$ and without the spin-polarization term. Also, the overall sign is plus for bosons. An explicit calculation show that this is indeed the correct beta function in scalar QED (see Appendix E.4).

6.5.4 Dislocated minimum of the effective potential

Having performed the appropriate renormalization in the above, the renormalized pieces provide an effective potential. The real part of the renormalized effective potential reads

$$V_{\text{eff}}(B, \mathcal{B}) \equiv \frac{\mathcal{B}^2}{2} + \frac{B^2}{2} + V_{\text{YM}}^{(1)}(B, \mathcal{B}) + V_{\text{quark}}^{(1)}(B, \mathcal{B}), \quad (364)$$

with the one-loop corrections

$$\begin{aligned} V_{\text{YM}}^{(1)}(B, \mathcal{B}) &= -\frac{11}{96\pi^2} \sum_{a=1}^{N_c^2-1} |v^a \mathcal{B}|^2 \ln \frac{\mu^2}{2|v^a \mathcal{B}|} + U_{\text{YM}}^{(1)}(B, \mathcal{B}) \\ &= N_c \frac{11}{96\pi^2} (g\mathcal{B})^2 \left[\ln \frac{g\mathcal{B}}{\mu^2} + \frac{1}{N_c} \sum_{a=1}^{N_c^2-1} |\lambda_{\text{ad}}^a|^2 \ln |\lambda_{\text{ad}}^a| - \frac{1}{11} (12 + \ln 4 - 12 \ln G) \right], \end{aligned} \quad (365a)$$

$$\begin{aligned} V_{\text{quark}}^{(1)}(B, \mathcal{B}) &= \frac{1}{24\pi^2} \sum_{i=1}^{N_c} \sum_{f=1}^{N_f} \mathfrak{b}_{i,f}^2 \ln \frac{\mu^2}{m_f^2} + \left[U_{\text{quark}}^{(1)}(B, \mathcal{B}) - U_{\text{quark}}^{(1)}(0, 0) \right], \\ &= -\sum_{i=1}^{N_c} \sum_{f=1}^{N_f} \frac{\mathfrak{b}_{i,f}^2}{8\pi^2} \left[\frac{1}{3} \ln \frac{m_f^2}{\mu^2} + \bar{\mathfrak{b}}_{i,f}^{-2} - \frac{1}{3} + 4\zeta(-1, \bar{\mathfrak{b}}_{i,f}^{-1}) \ln \bar{\mathfrak{b}}_{i,f}^{-1} + 4\zeta'(-1, \bar{\mathfrak{b}}_{i,f}^{-1}) \right]. \end{aligned} \quad (365b)$$

The logarithms from κ in Eq. (356) are entirely included in the above effective potential $V_{\text{eff}}(B, \mathcal{B})$. One should thus note that the renormalization scheme here is different from that in Eq. (358) by finite values of the logarithms. We have used the identity (572b) to perform the summation in the YM part after decomposing the logarithm and expressed the result with $\lambda_{\text{ad}}^a (= v^a/g)$ defined there. Note also that the original forms of the one-loop corrections behave in the vanishing-field limit as

$$U_{\text{YM}}^{(1)}(0, 0) = 0, \quad (366a)$$

$$U_{\text{quark}}^{(1)}(0, 0) = -\sum_{i=1}^{N_c} \sum_{f=1}^{N_f} \frac{\mathfrak{b}_{i,f}^2}{8\pi^2} (-3\bar{\mathfrak{b}}_{i,f}^{-2}) = \frac{3N_c}{32\pi^2} \sum_{f=1}^{N_f} m_f^4. \quad (366b)$$

⁷⁰Remember that the logarithmic divergences arise from the diagrams with two external legs, which yield the color trace $\text{Tr}[t^a t^a] = 1/2$, N_c for the fundamental and adjoint representations, respectively.

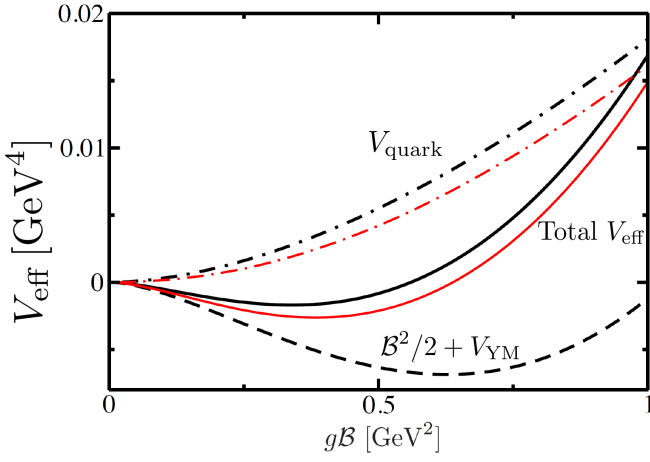


Figure 29: YM and quark parts of the effective potential at $eB = 0$ (0.4) GeV^2 shown with a black (red) line, as well as their sum, in the parallel configuration ($\theta_{BB}=0$) [115].

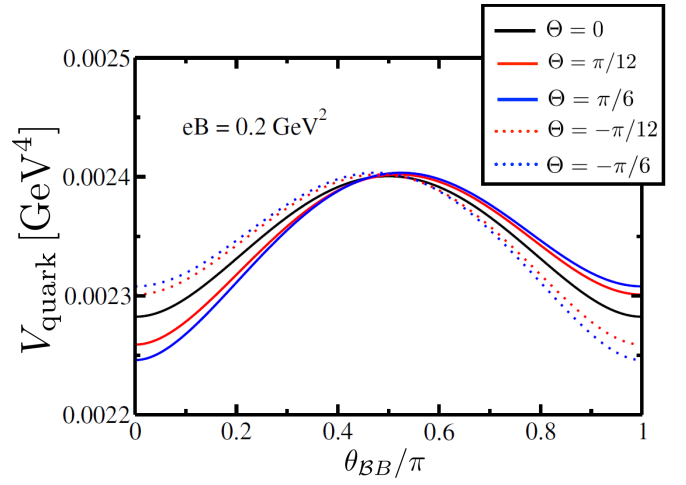


Figure 30: Quark part of the effective potential V_{quark} as a function of θ_{BB} at $g\mathcal{B} = eB = 0.2$ GeV^2 [115]. Note that $\theta = 2\pi/3 - \Theta$ in the current convention.

Therefore, we set the origin of the quark contribution so that it vanishes in this limit, i.e., $V_{\text{quark}}^{(1)}(0,0) = 0$ and $V_{\text{eff}}(0,0) = 0$. It is this subtracted form that agrees with the previous result in the Abelian magnetic field (260). By construction, the effective potential (364) is invariant under the shift of energy scale $\mu \rightarrow \mu + \delta\mu$, if the implicit energy-scale dependences in the running coupling constants are included.

We now discuss the minimum of the effective potential (364). First, we focus on the QCD part with a vanishing QED magnetic field, i.e., $V(\mathcal{B}, B = 0)$. At the classical level, the parabolic effective potential has a minimum at $\mathcal{B} = 0$. Importantly, the one-loop quantum correction contains the logarithmic term $\propto (g\mathcal{B})^2 \ln(g\mathcal{B})$ in the YM part $V_{\text{YM}}^{(1)}$. This logarithm is convex upward at the origin $g\mathcal{B} = 0$, and tends to cause an instability of the effective potential. On the other hand, the same logarithm tends to bound the effective potential at an asymptotically large magnitude of $g\mathcal{B}$. Thus, the quantum correction in the YM part could induce a minimum of the effective potential at a finite strength of $g\mathcal{B}$, implying that the QCD vacuum favors a spontaneous generation of the chromo-magnetic condensation. This point was first realized in Refs. [107, 264, 265] and was tied to the negative beta function of the Yang-Mills theory as we have seen above. Such a vacuum state with the chromo-magnetic condensation is often called the Savvidy vacuum. There are various extensions, e.g., in Refs. [275, 276, 282, 291–297, 360]. Contrary, the quark part does not have such a logarithmic dependence on $g\mathcal{B}$, and tends to make the minimum shallower as confirmed with numerical plots below.

We shall confirm basic behaviors of the effective potential with numerical plots. We need to specify the color configuration to evaluate the remaining color summation in Eq. (365). According to Appendix D.2, we take the eigenvalues $\lambda^i = \{\pm 1/2g, 0\}$ and $\lambda_{\text{ad}}^a = \{\pm 1, \pm 1/2, \pm 1/2, 0, 0\}$ for $N_c = 3$. The YM part (365a), however, depends on the color configuration only in the constant term, which does not change qualitative behavior of the effective potential. We include the three light quarks with the electric charges $q_u = +\frac{2}{3}|e|$ and $q_d = q_s = -\frac{1}{3}|e|$ and the masses $m_u = m_d = 5$ MeV and $m_s = 140$ MeV. Also, we take the strong and the electromagnetic coupling constants in such a way that $g^2/(4\pi) = 1$ and $e^2/(4\pi) = 1/137$ at the renormalization point $\mu = 1$ GeV as a typical hadronic scale.

In Fig. 29, we plot the breakdown of the effective potential as a function of $g\mathcal{B}$ in the absence of an external QED magnetic field with black lines. The quark part is a monotonically increasing function of $g\mathcal{B}$, and tends to make the minimum of the effective potential shallower, competing with the logarithmic behavior in the pure YM part. Nevertheless, the YM part overwhelms the quark part and gives rise to a minimum of the effective potential at a nonzero value of $g\mathcal{B}$.

On top of the Savvidy vacuum, one can investigate effects of an Abelian magnetic field [115]. At

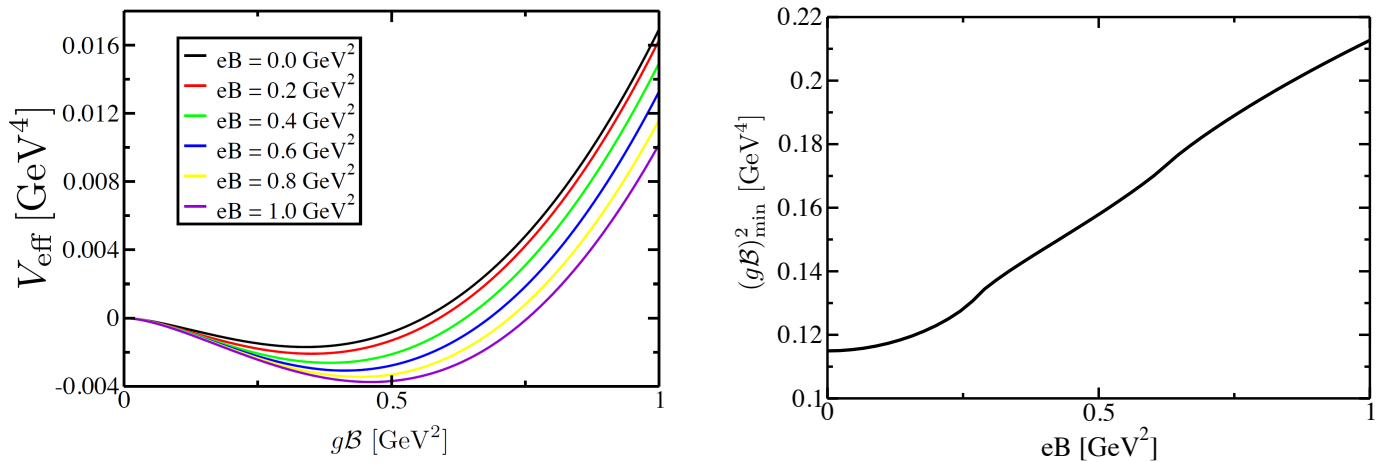


Figure 31: Magnetic-field dependence of the QCD effective potential (left) and of the chromo-magnetic condensate (right) [115].

the one-loop order, effects of the Abelian magnetic field only enters through the quark loop (365b), and can be summarized as a replacement of $g\mathcal{B}$ by an effective strength $\mathbf{b}_{i,f}$ in Eq. (365b). Therefore, the chromo-magnetic condensation would be enhanced (suppressed) when $g\mathcal{B} > \mathbf{b}_{i,f}$ ($g\mathcal{B} < \mathbf{b}_{i,f}$). One should, however, remember that the color index i needs to be summed with a set of w^i defined in Eq. (156). As defined in Eq. (345), the effective strength $\mathbf{b}_{i,f}$ depends on the spatial angle $\theta_{\mathcal{B}\mathcal{B}}$ and the angle θ in the color space through w^i . In Fig. 30, the quark part V_{quark} is plotted as a function of $\theta_{\mathcal{B}\mathcal{B}}$ for $g\mathcal{B} = eB = 0.2 \text{ GeV}^2$ and various values of the color angle θ . The quark part V_{quark} has an invariance under simultaneous discrete transformations $\theta_{\mathcal{B}\mathcal{B}} \rightarrow \pi - \theta_{\mathcal{B}\mathcal{B}}$ and $\theta \rightarrow -\theta$, because the whole set of $\{\mathbf{b}_{1,f}, \mathbf{b}_{2,f}, \mathbf{b}_{3,f}\}$ is invariant under this transformation. The angle dependences in the coordinate and color spaces are entangled with each other. Nevertheless, the parallel spatial configuration ($\theta_{\mathcal{B}\mathcal{B}} = 0$), and the antiparallel one ($\theta_{\mathcal{B}\mathcal{B}} = \pi$) according to the above invariance, is favored for all the values of the color angle θ , suggesting that the QCD vacuum favors the parallel/antiparallel configuration between the chromo- and QED magnetic fields (see Ref. [305] for more discussions). In other words, an anisotropy of the chromo-magnetic field is induced by the QED magnetic field through the interaction with the virtual quark excitations.

Below, we focus on the parallel configuration $\theta_{\mathcal{B}\mathcal{B}}=0$ with the set of λ^i given above. Going back to Fig. 29, we show effects of a finite B with red lines at $eB = 0.4 \text{ GeV}^2$. The quark part V_{quark} is diminished in the presence of the QED magnetic field since it favors a coexistent chromo- and QED magnetic fields as we have seen above. Therefore, adding it to the YM part (which is intact under the application of a finite B), one finds a deeper minimum of the total effective potential induced by the QED magnetic field. Namely, a finite QED magnetic field enhances the magnitude of the chromo-magnetic condensation,

The left panel in Fig. 31 shows the total effective potential $V_{\text{eff}}(\mathcal{B}, B)$ for various strengths of the QED magnetic field in the same configurations of $\theta_{\mathcal{B}\mathcal{B}}$ and w^i as above. The effective potential has a local minimum for all the shown magnetic-field strengths, and the location of the minimum shifts to the right as we increase the strength. This result suggests that the chromo-magnetic condensate $(g\mathcal{B})_{\text{min}}^2$, which is determined from the location of the minimum, monotonically increases with the QED magnetic field. This behavior is explicitly shown in the right panel of Fig. 31. The quark-antiquark polarizations in the vacuum play an important role in this dynamics, since the gluon field is not directly coupled to the external QED field. These behaviors qualitatively agree with the lattice QCD result [350], where the gluonic action density is enhanced in the presence of the magnetic field at zero temperature.

6.6 Polyakov-loop potential in QCD+QED fields at finite temperature

In the previous subsection, we discussed QCD at zero temperature. We here discuss an application of the effective Lagrangians (329), (315a), and (315b) extended to finite temperature. One of important quantities in finite-temperature QCD is the Polyakov loop that serves as an order parameter of the deconfinement phase transition in pure YM theory associated with the breaking of the center symmetry (see a very brief overview below and Ref. [333] for a recent review). A quark field explicitly breaks the center symmetry, and the Polyakov loop should then be understood as an approximate order parameter in the presence of the light-quark fields. The QCD effective action with the background Polyakov loop was first computed at the one-loop level by Gross, Pisarski, and Yaffe (GPY) [363] and also by Weiss [364, 365], and is called the GPY-Weiss potential named after those authors. We will see that the GPY-Weiss potential is reproduced from the extended HE effective action obtained in this section. Moreover, we have further included external QED+QCD fields into the effective Lagrangian, and can use it to discuss how the Polyakov-loop effective potential is modified by those external fields [283, 305]. It is remarkable that the Polyakov loop, as well as the gluon condensate discussed in the previous subsection, has been measured with recent lattice QCD simulations in magnetic fields [348–352] (see Sec. 7.4.1 for more recent developments). These facts motivate us to study the deconfinement phase transition especially in the presence of external electromagnetic fields.

The Polyakov loop is defined by the closed Wilson line in the temporal direction (or imaginary-time direction denoted as the fourth component):

$$\Phi(\vec{x}) = \frac{1}{N_c} \text{Tr} \mathcal{P} \exp \left\{ ig \int_0^\beta d\tau A_4^a(\tau, \vec{x}) t^a \right\}, \quad (367)$$

where $\beta = 1/T$, and \mathcal{P} is the path-ordered product. The thermal average is taken with the QCD action. The confinement phase corresponds to the vanishing value of the Polyakov loop $\langle \Phi \rangle \rightarrow 0$, yielding a diverging free energy F_q of an infinitely heavy quark embedded in the medium, $F_q = -T \ln \langle \Phi \rangle \rightarrow \infty$. On the other hand, a deconfinement phase corresponds to a finite value $\langle \Phi \rangle \neq 0$ which breaks the center symmetry of the color $SU(N)$ group.

We first briefly summarize the basic points, taking the $SU(2)$ case as a simple example. Working in the Polyakov gauge for a time-independent field $A_4^a(\vec{x}) = \phi(\vec{x})\delta^{a3}$, we can perform a functional integral with respect to fluctuations around the field $\phi(\vec{x})$. In this way, one obtains the effective action for $\phi(\vec{x})$. This procedure is nothing but what we have performed in this section: We divided the gluon field A_μ^a into a background field \mathcal{A}_μ^a and a fluctuation field a_μ^a , and then integrated the latter. Therefore, we expect that the aforementioned well-known results are reproduced by the proper-time method.

We divide the background field into the constant part and the coordinate-dependent part as $\mathcal{A}_\mu^a(x) = (\bar{\mathcal{A}}_\mu + \hat{\mathcal{A}}_\mu(x))n^a$. The zeroth component of the first constant term $\bar{\mathcal{A}}_\mu$, after the Wick rotation, gives the Polyakov loop defined in Eq. (367), and the second term generates the external electromagnetic fields, $\mathcal{F}_{\mu\nu}^a$. We work in the Polyakov gauge for $\bar{\mathcal{A}}_4^a$ and the static limit [364]:

$$\bar{\mathcal{A}}_4^a = \bar{\mathcal{A}}_4 \delta^{3a}, \quad \partial_4 \bar{\mathcal{A}}_4 = 0. \quad (368)$$

This gauge condition is compatible with the covariantly constant condition in Eq. (152), so that one can include both of those fields [283]. Note that we employ the Polyakov gauge with the color direction δ^{a3} even for the $SU(N_c)$ case,⁷¹ and the color unit vector n^a should be here understood as $n^a = \delta^{3a}$.

⁷¹In the literature, the temporal component of the gauge field $\bar{\mathcal{A}}_4^a$ in the Polyakov gauge is often expressed by $N_c - 1$ real scalar fields. In our formalism, these color degrees of freedom are encoded in the color eigenvalues w^i ($i = 1, \dots, N_c$) and v^a ($a = 1, \dots, N_c^2 - 1$). Choosing the third direction of the color unit vector, $n^a = \delta^{a3}$, we pick up one particular field $\bar{\mathcal{A}}_4$ (but with the color eigenvalues attached). This convention results in a simple expression for the Polyakov loop shown in Eq. (370) after taking the trace over the eigenvalues v^a .

Introducing a dimensionless field

$$C = \frac{g\bar{\mathcal{A}}_4}{2\pi T}, \quad (369)$$

we can express the Polyakov loop as

$$\begin{aligned} \Phi &= \cos(\pi C) && \text{for SU(2),} \\ \Phi &= \frac{1}{3} \left\{ 1 + 2\cos(\pi C) \right\} && \text{for SU(3).} \end{aligned} \quad (370a)$$

6.6.1 GPY-Weiss potential at finite temperature

Let us proceed to computing the effective potential for the Polyakov loop. First, we only maintain the $\bar{\mathcal{A}}_4^a$ for the Polyakov loop without external electromagnetic fields and confirm that the current formalism correctly reproduces the GPY-Weiss potential [363–365]. In the beginning of the section, we already obtained the general form of the effective action in the presence of the temporal component of the gauge field. Therefore, identifying the $\bar{\mathcal{A}}_4^a$ for the Polyakov loop as $\mathcal{A}_0^a = i\bar{\mathcal{A}}_4^a$ in Eqs. (321) and (329), we obtain the YM and quark contributions to the effective potential as

$$V_{\text{YM}} = -\frac{(4-2)}{16\pi^2} \sum_{a=1}^{N_c^2-1} \sum_{\bar{k}=1}^{\infty} \cos\left(\frac{gv^a \bar{\mathcal{A}}_4 \bar{k}}{T}\right) \frac{16T^4}{\bar{k}^4}, \quad (371a)$$

$$V_{\text{q}} = \frac{N_f}{4\pi^2} \sum_{i=1}^{N_c} \sum_{\bar{k}=1}^{\infty} (-1)^{\bar{k}} \cos\left(\frac{gw^i \bar{\mathcal{A}}_4 \bar{k}}{T}\right) \frac{16T^4}{\bar{k}^4}. \quad (371b)$$

We discarded the vacuum contributions (zero-point energies) which are independent of $\bar{\mathcal{A}}_4$, and took the massless limit for the quark part, assuming that $T \gg m_f$. The last factor in each contribution originates from the proper-time integral which is now finite both in the UV and IR regimes. The cancellation between the unphysical degrees of freedom in the gluon and ghost sectors results in the number of physical degrees of freedom, $4 - 2 = 2$ attached in front of the YM part. The summation over \bar{k} can be analytically performed as⁷²

$$V_{\text{YM}} = -\pi^2 T^4 \sum_{a=1}^{N_c^2-1} \left[\frac{1}{45} - \frac{2}{3} (C^a)^2 (C^a - 1)^2 \right], \quad (372a)$$

$$V_{\text{q}} = 2\pi^2 T^4 N_f \sum_{i=1}^{N_c} \left[\frac{1}{45} - \frac{2}{3} (C^i)^2 (C^i - 1)^2 \right], \quad (372b)$$

⁷²This summation can be regarded as a Fourier series, of which the original function is known as [366]

$$\sum_{\bar{k}=1}^{\infty} \frac{\cos(x\bar{k})}{\bar{k}^4} = -\frac{\pi^4}{3} B_4\left(\frac{x}{2\pi}\right) = -\frac{\pi^4}{3} \left[\left(\frac{x}{2\pi}\right)^2 \left(\frac{x}{2\pi} - 1\right)^2 - \frac{1}{30} \right],$$

where $B_n(z)$ is the Bernoulli polynomial, and its argument is here understood to be z modulo 1 for the first equality to hold for the periodic function. Likewise, one can get the formula for the fermionic part by shifting the argument as

$$\sum_{\bar{k}=1}^{\infty} (-1)^{\bar{k}} \frac{\cos(x\bar{k})}{\bar{k}^4} = -\frac{\pi^4}{3} B_4\left(\frac{x+\pi}{2\pi}\right).$$

A similar formula is easily obtained in the (1+1)-dimensional case, which we will use in the strong magnetic field limit below.

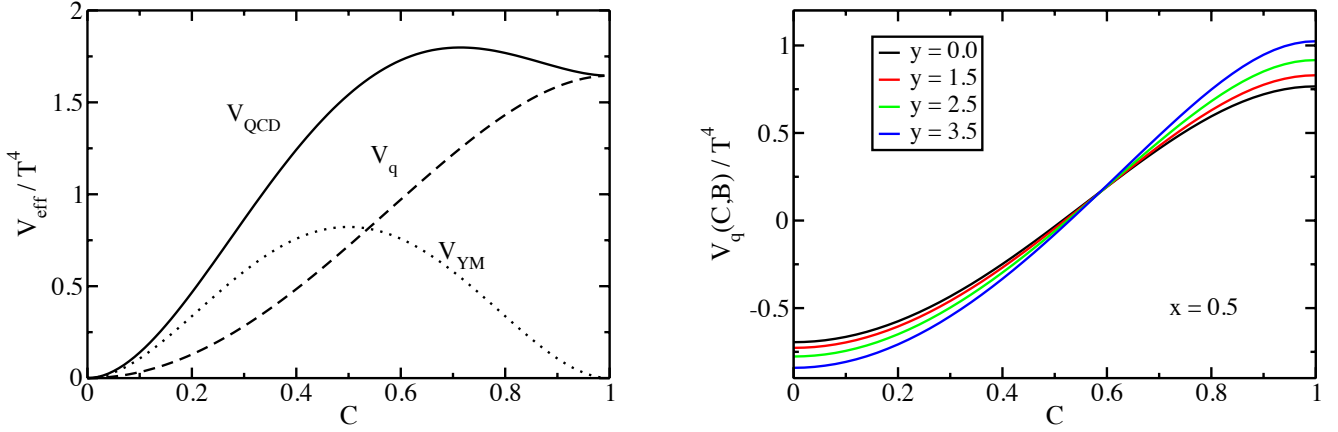


Figure 32: One-loop Polyakov-loop potential as a function of $C = g\bar{\mathcal{A}}_4/(2\pi T)$ without external fields, $E, B, \mathcal{E}, \mathcal{B} = 0$ (left), and the quark part for several values of magnetic fields (right). We defined dimensionless parameters as $x = m^2/T^2$ and $y = eB/T^2$, and subtracted the constant terms which are independent of C .

where $C^a = gv^a\bar{\mathcal{A}}_4/(2\pi T)$ and $C^i = (gw_i\bar{\mathcal{A}}_4/T + \pi)/(2\pi)$ modulo 1. The shift in C^i by a constant term originates from the alternating signs in the Poisson resummation, which, therefore, reflects the fermionic statistics.

To study the essence of the Polyakov loop potential, we shall focus on the case of the color SU(2) group and a single-flavor fermion. Then, using $w^i = \pm 1/2$ and $v^a = 0, \pm 1$,⁷³ one can reproduce the well-known form of the potential [363–365]

$$V_{\text{eff}}[C] = V_{\text{YM}}[C] + V_{\text{q}}[C], \quad (373)$$

where the YM and quark parts are, respectively, given by

$$V_{\text{YM}}[C] = -\frac{3}{45}\pi^2 T^4 + \frac{4}{3}\pi^2 T^4 C^2(1-C)^2, \quad (374a)$$

$$V_{\text{q}}[C] = -\frac{7}{90}\pi^2 T^4 + \frac{1}{6}\pi^2 T^4 C^2(2-C^2). \quad (374b)$$

We normalized the field as $C = g\bar{\mathcal{A}}_4/(2\pi T)$, and these expressions are valid in a cycle of the periodic YM part, $0 \leq C \leq 1$. While the quark part is also periodic as clearly seen in Eq. (372b), its period is now twice as large as that of the YM part because of the difference between the eigenvalues w^i and v^a that reflect the group representations. The first term in each contribution again corresponds to the Stefan-Boltzmann limit, which obviously holds the center symmetry.

In the left panel of Fig. 32, we show the effective potential $V_{\text{eff}}[C]$ and its breakdown. In the YM part, degenerated minima appear at $C = 0$ and $C = 1$, reflecting the center symmetry $C \rightarrow C + 1$ in SU(2). Therefore, selecting one of the two minima spontaneously breaks the center symmetry. This result is thought to be natural, because our one-loop computation is reliable in the high-temperature regime where the system is expected to be in the deconfined phase. The quark part explicitly breaks the center symmetry (due to the doubled period), so that the potential at $C = 0$ and $C = 1$ are no longer degenerated. In the presence of the quark part, the origin $C = 0$ is favored, which corresponds to the deconfined phase.

⁷³These eigenvalues can be found by following the description in Appendix D.2.

This picture of the deconfined phase is intimately related to the color-electric screening of the external field $\bar{\mathcal{A}}_4$ [333, 365]. Since the above potential was obtained from the effective action for the $\bar{\mathcal{A}}_4$, one can immediately read off the thermal mass m_{th} from the quadratic term $(m_{\text{th}}^2/2)\bar{\mathcal{A}}_4$ or the Debye screening mass

$$m_{\text{sc}}^2 = 2m_{\text{th}}^2 = \frac{1}{3} \left(N_c + \frac{N_f}{2} \right) (gT)^2, \quad (375)$$

where $N_c = 2$ in the present case. This expression agrees with the Debye screening mass obtained from the one-loop gluon self-energy in the static limit [307, 363]. The larger the screening mass is, the more the minimum at $C = 0$ is stabilized with a larger potential curvature as expected from the screening of the confining force.

6.6.2 GPY-Weiss potential in a magnetic field

Now we come back to our most general effective Lagrangians (329), (315a), and (315b). By using those formal results, one can study modifications of the Polyakov-loop effective action in an electric field [283, 305] and in a magnetic field [305]. Here, we look into the effects of a magnetic field in some more detail as they are related to lattice QCD simulations [367, 368].

We take the vanishing limit of the electric field and the chromo-EM fields, $E, \mathcal{E}, \mathcal{B} \rightarrow 0$, whereas keep the Polyakov loop $\bar{\mathcal{A}}_4$ and the magnetic field B nonzero in the medium rest frame. The YM part is not coupled to the magnetic field at the one-loop order, which is thus unchanged from Eq. (374a). Therefore, we may write the effective potential as

$$V_{\text{eff}}[C, B] = V_{\text{YM}}[C] + V_{\text{q}}[C, B], \quad (376)$$

where the quark part is given as [305, 367]

$$V_{\text{q}}[C, B] = \sum_{i=1}^{N_c} \sum_{\bar{k}=1}^{\infty} 2(-1)^{\bar{k}} \cos \left(\frac{g w_i \bar{\mathcal{A}}_4 \bar{k}}{T} \right) \frac{\rho_B}{4\pi} \int_0^{\infty} \frac{ds}{s^2} e^{-m_f^2 s - \frac{\bar{k}^2}{4T^2 s}} \coth(|q_f B|s). \quad (377)$$

We again focus on the case of $N_c = 2$ and $N_f = 1$ with $q_f B = eB$ and $m_f = m$. Qualitative features of the following results do not depend on the sign of the quark electrical charge or the direction of the magnetic field, and the fractional factor in the quark electrical charge is neglected for simplicity. In this case, we have

$$V_{\text{q}}[C, B] = \sum_{\bar{k}=1}^{\infty} 2(-1)^{\bar{k}} \cos(C\pi\bar{k}) \frac{\rho_B}{4\pi} \int_0^{\infty} \frac{ds}{s^2} e^{-m^2 s - \frac{\bar{k}^2}{4T^2 s}} \coth(|eB|s). \quad (378)$$

For a general strength of the magnetic field, we need to resort to numerical evaluation. The integral is well convergent. In the right panel in Fig. 32, we show the magnetic-field dependence of the quark part with $x = m^2/T^2 = 0.5$ and various values of $y = |eB|/T^2$. We find an enhancement of the explicit center-symmetry breaking as we increase the magnetic-field strength.

One can confirm this tendency with an analytic form of the potential in the strong magnetic field. As we saw in Sec. 6.2, the effective potential is subject to the effective dimensional reduction in the presence of the strong magnetic field. In the same way, the proper-time integral in Eq. (378) is factorized as a product of the density of states ρ_B and the (1+1)-dimensional form of the potential, when $\coth(|eB|s) \rightarrow 1$ in the strong field limit (see Sections 4.2.4 and 6.3.1 for the Landau-level decompositions). We can perform the proper-time integral and the summation in parallel to the (3+1)-dimensional case demonstrated in Eq. (374b). Then, we find the asymptotic form of the effective potential [305]

$$V_{\text{q}}[C, B] \rightarrow \rho_B \times \pi T^2 \left(-\frac{1}{3} + C^2 \right). \quad (379)$$

This means that the quark contribution, which breaks the center symmetry, is proportional to the magnetic-field strength, confirming the tendency seen in Fig. 32 (right).

As we saw above, the potential curvature is proportional to the electric screening mass or the thermal mass of the $\bar{\mathcal{A}}_4$ field. The screening mass is read off from the asymptotic form of the quark part (379) as

$$m_{\text{sc}}^2 = \rho_B \frac{g^2}{4\pi} + \frac{N_c}{6} (gT)^2. \quad (380)$$

The first term exactly reproduces the screening mass from the LLL quark loop discussed in Sec. 5 and Appendix F.2.1 (with a factor of 1/2 from the color trace). This term grows with ρ_B , while the second term from the YM part is independent of the magnetic field. The minimum at $C = 0$ is more stabilized by the growing quark-loop contribution to the screening mass. This observation is again consistent with the tendency seen in Fig. 32, and implies that the deconfinement phase-transition temperature decreases as we apply a stronger external magnetic field.

Strictly speaking, the above perturbative treatment may not be justified in such a phase-transition region. Nevertheless, from the above analytic results and intuitive discussions, we may learn a qualitative tendency that the center symmetry is more strongly broken when the screening effect is stronger. One should, however, note that the above result is obtained in the vanishing quark mass limit. The screening effect would be suppressed with a finite (constituent) quark mass due to the competition between the temperature scale and the mass gap. A striking question is how strong the screening effect is near the phase transition temperature when the (constituent) quark mass is generated from the inherent strong-coupling nature in QCD and is possibly modified by a strong magnetic field. This poses an interesting question since, in early this section, we have glanced at the fact that the strong magnetic field ‘‘catalyses’’ the chiral symmetry breaking. One might then expect that a strong magnetic field enlarges the mass gap and the phase transition temperature increases due to suppression of the screening effect. However, the recent lattice simulations suggest an opposite behavior, i.e., a decreasing behavior of the transition temperature as we increase the magnetic-field strength [348–352]. A key issue is the non-trivial magnetic-field dependence of the mass gap in the strongly coupled QCD that distinguishes it from weak-coupling QED and possibly naive effective models of QCD. In the next section, we focus on the low-energy dynamics in strong magnetic fields and will come back to the recent results from lattice QCD simulations.

7 Low-energy dynamics in strong magnetic fields

As discussed in Sec. 2, the charged-particle spectrum is subject to the Landau quantization in magnetic fields. Since the Landau-level spacing increases with the magnetic-field strength $\sqrt{q_f B}$, the higher Landau levels are decoupled from the lowest-Landau level (LLL) when one focuses on the low-energy excitations (cf. Fig. 4). For massless fermions, the low-energy spectrum is, therefore, identified with the dispersion relation in the LLL [see Eq. (83)]

$$\epsilon_{\text{LLL}} = \pm p_z, \quad (381)$$

where the magnetic field is again assumed to be applied in the z direction. This dispersion relation is identical to that of a free particle in the (1+1) dimensions, giving rise to an effective dimensional reduction to the longitudinal space along the magnetic field. In this section, we discuss consequences of this dimensional reduction occurring in the low-energy regime. The residual two-dimensional phase space is degenerated since there is no preferred position of a cyclotron motion in the transverse plane. The density of the degenerate states is given by $|q_f B|/(2\pi)$. The (1+1)-dimensional kinetic term for

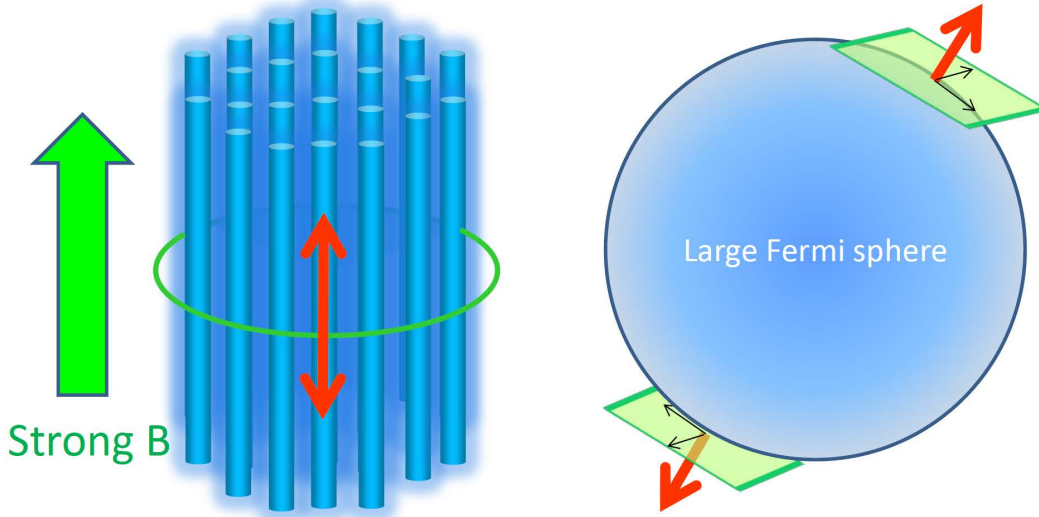


Figure 33: Dimensional reduction in a strong magnetic field and a dense system: Shown are squeezed cyclotron orbits in a strong magnetic field (left) and low-energy excitations near a large Fermi sphere (right). Low-energy excitations only cost energy in the one-dimensional directions along the magnetic field and normal to the Fermi surface (red arrows). There are large degeneracies in the two-dimensional phase spaces transverse to the magnetic field and tangential to the Fermi surface (green planes).

the LLL state reads

$$S_{\text{LLL}}^{\text{kin}} = \int dt \int \frac{dp_z}{2\pi} \bar{\psi}_{\text{LLL}}(p_z) (i\partial_t \gamma^0 - p_z \gamma^3) \psi_{\text{LLL}}(p_z). \quad (382)$$

Here, we have suppressed the degeneracy label for notational simplicity (see Sec. 2 for more details).

7.1 Analogy with the dense system, effective dimensional reduction, and infrared scaling dimensions

To get clear physical insights into consequences of the dimensional reduction, we begin with pointing out an analogy between the systems in the strong magnetic field and at high fermion density. In the presence of a large Fermi sphere, the low-energy excitations near the Fermi surface also exhibits a dimensional reduction (see Fig. 33). This is because, in the small curvature limit, the excitation energy in the vicinity of the Fermi surface is degenerated. Namely, the excitation energy, measured from the Fermi surface, only depends on the one-dimensional momentum normal to the Fermi surface (red arrows). The energy difference among the states on a patch of the tangential plane (green plane) can be infinitesimally small as compared to the Fermi energy as we focus on a lower and lower energy scale.

In condensed matter physics, the dimensional reduction near the Fermi surface has been known to bring about rich physical consequences, i.e., superconductivity [369] and the Kondo effect [370].⁷⁴ They are sometimes called the Fermi surface effects. One may understand these phenomena on the basis of the instabilities induced by the (1+1)-dimensional infrared (IR) dynamics. In high-energy physics under the strong magnetic field, the counterparts will be the chiral symmetry breaking accompanied by the formation of the chiral condensates in QED and QCD as clearly stated by Gusynin et al. [324] and the magnetically induced QCD Kondo effect proposed by Ozaki et al. [336]. According to the analogy, the former implies that the chiral symmetry breaking occurs even in QED in spite of the inherent

⁷⁴The Kondo effect was proposed to explain an anomalous behavior in a temperature dependence of electrical resistance. Existence of a local minimum at a certain temperature had been a long-time mystery since experimentally observed in particular kinds of alloys.

small coupling constant. This is called the “magnetic catalysis” of the chiral symmetry breaking (see Ref. [101] for a large list of references). In Sec. 6.2, we have already previewed the magnetic catalysis in terms of the effective potential in the strong magnetic field. It is worth mentioning here that, while the S -wave Cooper pairs in superconductors are unstable in magnetic fields due to the spin-flip effect, the chiral condensate, where the fermion and antifermion have the magnetic moments with different signs, is a stable configuration against magnetic fields [371–376]. The QCD Kondo effect is a newly proposed phenomenon that leads to a strong correlation between light quarks forming a bulk matter and a heavy quark embedded in it as an impurity [336, 377].

In the modern language, the emergences of the superconductivity and the Kondo effect are informed from the renormalization-group (RG) flow [378–380]. Namely, if an interaction term in a low-energy effective theory is found to be marginal or relevant as the energy scale is reduced to toward the Fermi energy, the effects of the interaction become important and potentially induce an infrared strong-coupling regime. On the other hand, if an interaction term is found to be irrelevant, the system will evolve into a nearly non-interacting Fermi gas. In case of the superconductivity, the four-Fermi operator for conduction electrons turns out to be marginal when a pair of electrons has the opposite momentum, i.e., the BCS configuration [378]. In case of the Kondo effect, the four-Fermi operator for the coupling between a conduction electron and an impurity becomes marginal [43, 381]. One can extract these insights simply by examining the scaling dimensions of the fermion fields. It is thus instructive to first compare the scaling dimensions in the strong magnetic field and in the dense system.

We shall determine the scaling dimension of the LLL fermion field when the excitation energy scale is reduced as $\epsilon_{\text{LLL}} \rightarrow s\epsilon_{\text{LLL}}$ ($t \rightarrow s^{-1}t$) with $s < 1$. Here, we discuss the massless dispersion relation (381) to demonstrate the essential mechanism of the instabilities. Since the LLL fermion has the (1+1)-dimensional dispersion relation (381), the longitudinal momentum p_z is also transformed as $p_z \rightarrow sp_z$. On the other hand, the transverse momentum, which serves as the label of the degenerate states and does not appear in the dispersion relation (381), is not transformed. Therefore, when the kinetic term (382) is invariant under the scale transformation, the LLL fermion field scales as $s^{-1/2}$ in the low-energy dynamics.⁷⁵

As for the dense system, one can explicitly identify the relevant excitations by performing an expansion with respect to a large chemical potential, $1/\mu$. To organize this expansion, we decompose the momentum p^μ into the Fermi momentum $\mu\mathbf{v}_F$ and the small residual momentum $\ell^\mu = (\ell^0, \boldsymbol{\ell})$ as

$$p^0 = \ell^0, \quad p^i = \mu v_F^i + \ell^i, \quad (383)$$

where the energy p^0 is measured from the Fermi surface and the magnitude of the Fermi velocity is unity $|\mathbf{v}_F| = 1$. For a given Fermi velocity, the corresponding plane wave is factorized as

$$\psi(x) = \sum_{\mathbf{v}_F} e^{i\mu\mathbf{v}_F \cdot \mathbf{x}} \psi(x; \mathbf{v}_F). \quad (384)$$

The high-density effective field theory (HDEFT) is an expansion in a phase space around a fixed direction of the Fermi velocity \mathbf{v}_F . The entire phase space is spanned by the patches of those subspaces as represented by the summation over \mathbf{v}_F [382–389]. One can perform a mode expansion with respect to the residual momentum ℓ^μ as

$$\psi(x; \mathbf{v}_F) = \int_{\ell \ll \mu} \frac{d^4\ell}{(2\pi)^4} e^{-i\ell^\mu x_\mu} \psi(\boldsymbol{\ell}; \mathbf{v}_F). \quad (385)$$

⁷⁵We count the scaling dimensions in the mixed representations $\psi_{\text{LLL}}(t, \mathbf{p})$ and so on, since the dimensional reduction occurs in the momentum space.

Projecting out the states above the Dirac sea $\psi_+(x; \mathbf{v}_F) \equiv \frac{1}{2}(1 + \gamma^0 \mathbf{v}_F \cdot \boldsymbol{\gamma})\psi(x; \mathbf{v}_F)$, one gets the leading-order effective Lagrangian

$$\mathcal{S}_{\text{HD}}^{\text{kin}} = \int d^4x \bar{\psi}(x)(i\partial + \mu\gamma^0)\psi(x) = \int dt \sum_{\mathbf{v}_F} \int \frac{d^2\boldsymbol{\ell}_\perp d\ell_\parallel}{(2\pi)^3} \bar{\psi}_+(\boldsymbol{\ell}; \mathbf{v}_F)(i\partial_t - \ell_\parallel)\gamma^0\psi_+(\boldsymbol{\ell}; \mathbf{v}_F) + \mathcal{O}(1/\mu), \quad (386)$$

where we defined $\ell_\parallel \equiv \mathbf{v}_F \cdot \boldsymbol{\ell}$ and $\boldsymbol{\ell}_\perp \equiv \boldsymbol{\ell} - \ell_\parallel \mathbf{v}_F$. The excitations of the fermion field ψ_+ , i.e., particle and hole states, are thus found to satisfy the dispersion relation

$$\ell^0 = \mathbf{v}_F \cdot \boldsymbol{\ell}. \quad (387)$$

Clearly, this is a linear dispersion relation in the (1+1) dimension with the momentum component normal to the Fermi surface as already discussed in an intuitive way (see Fig. 33). The remaining two-dimensional momentum $\boldsymbol{\ell}_\perp$ labels the degenerate states on a patch. Therefore, when the energy scale is reduced to the Fermi energy ($\ell^0 = 0$) as $\ell^0 \rightarrow s\ell^0$ ($t \rightarrow s^{-1}t$) with $s < 1$, only the ℓ_\parallel scales as $\ell_\parallel \rightarrow s\ell_\parallel$, and the tangential momentum $\boldsymbol{\ell}_\perp$ is intact. Following from the invariance of the kinetic term under the scale transformation, one finds that the fermion field $\psi_+(\boldsymbol{\ell}; \mathbf{v}_F)$ scales as $s^{-1/2}$.

In the above, we have found that the fermion fields have the same scaling dimensions in the strong magnetic field and at high density. We now discuss the scaling dimensions of the interaction terms relevant for the superconductivity/magnetic catalysis and then the Kondo effect.

Superconductivity and magnetic catalysis

An effective four-Fermi interaction among conduction electrons or light quarks in dense quark matter can be written as

$$\begin{aligned} \mathcal{S}_{\text{HD}}^{\text{int}} = \int dt \prod_{i=1,2,3,4} \sum_{\mathbf{v}_F^{(i)}} \int \frac{d^2\boldsymbol{\ell}_\perp^{(i)} d\ell_\parallel^{(i)}}{(2\pi)^3} G \left[\bar{\psi}_+(\boldsymbol{\ell}^{(4)}; \mathbf{v}_F^{(4)}) \hat{\gamma}_\parallel^\mu \psi_+(\boldsymbol{\ell}^{(2)}; \mathbf{v}_F^{(2)}) \right] \left[\bar{\psi}_+(\boldsymbol{\ell}^{(3)}; \mathbf{v}_F^{(3)}) \hat{\gamma}_\parallel^\mu \psi_+(\boldsymbol{\ell}^{(1)}; \mathbf{v}_F^{(1)}) \right] \\ \times \delta^{(3)}(\mathbf{p}^{(1)} + \mathbf{p}^{(2)} - \mathbf{p}^{(3)} - \mathbf{p}^{(4)}), \end{aligned} \quad (388)$$

where $\hat{\gamma}_\parallel^\mu = (\gamma^0, (\boldsymbol{\gamma} \cdot \mathbf{v}_F)\mathbf{v}_F)$ and \mathbf{p} is given in Eq. (383). G is an effective coupling constant. Since the Fermi momentum $\sim \mu$ is much larger than the fluctuation near the Fermi surface $\boldsymbol{\ell}$, one may in general neglect the $\boldsymbol{\ell}$ in the momentum conservation. Therefore, the delta function does not scale in this case. By using the scaling dimensions discussed below Eq. (387), the four-Fermi operator turns out to scale as s^+1 , meaning that the interaction is in general irrelevant in the low-energy dynamics.

However, there is an exception. When the scattering fermions have the opposite Fermi momenta, $\mu\mathbf{v}_F^{(1)} + \mu\mathbf{v}_F^{(2)} = 0$, which is called the (S-wave) BCS configuration, the momentum conservation in the order of μ is automatically satisfied. Since the delta function only has the order- ℓ quantities, the delta function scales as s^{-1} when $\ell_\parallel \rightarrow s\ell_\parallel$. Therefore, in the BCS configuration, the four-Fermi operator scales as s^0 and thus is lifted to a marginal operator. This observation suggests that a logarithmic correction emerges in the one-loop scattering diagram shown in Fig. 34, and that the effective coupling constant G grows in attractive channels. The emergence of the Landau pole, where the coupling constant diverges, has been shown for the color superconductivity in the dense quark matter [390–392]. Furthermore, it was shown that the effect of the unscreened magnetic gluon significantly enhances the growth of the coupling constant, so that the Landau pole appears in a larger scale than the would-be scale found in the absence of the long-range interaction [393, 394]. We will also discuss dependences on interaction types with several examples in the following subsections.

Bearing the above discussion in mind, we now proceed to the magnetic catalysis. The effective four-Fermi interaction in the LLL reads

$$\mathcal{S}_{\text{LLL}}^{\text{int}} = \int dt \prod_{i=1,2,3,4} \int dp_z^{(i)} G \left[\bar{\psi}_{\text{LLL}}(p_z^{(4)}) \gamma_\parallel^\mu \psi_{\text{LLL}}(p_z^{(2)}) \right] \left[\bar{\psi}_{\text{LLL}}(p_z^{(3)}) \gamma_{\parallel\mu} \psi_{\text{LLL}}(p_z^{(1)}) \right]$$

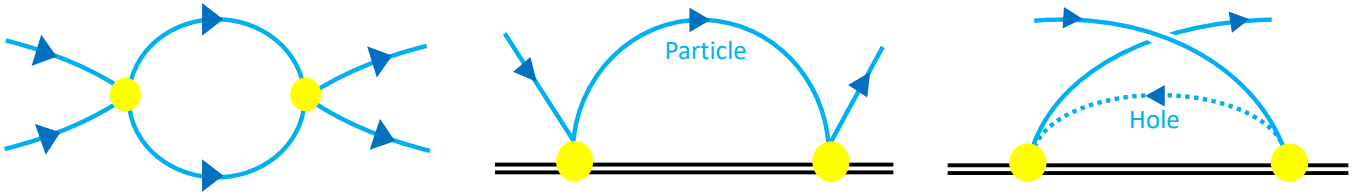


Figure 34: The leading quantum corrections to the four-Fermi interactions in superconductor (left) and in the Kondo effect (right two). In the Kondo diagrams, the double lines denote impurities (heavy quarks for QCD), and the vertices have generators of a non-Abelian symmetry.

$$\times \delta(p_z^{(1)} + p_z^{(2)} - p_z^{(3)} - p_z^{(4)}), \quad (389)$$

where G is an effective coupling constant and $\gamma_{\parallel}^{\mu} = (\gamma^0, 0, 0, \gamma^3)$. Again, the transverse momenta are not written explicitly. Because of the (1+1)-dimensional dispersion relation (381), the delta function scales as s^{-1} . Therefore, when the LLL fermion field scales as $s^{-1/2}$, this interaction term scales as s^0 , meaning that the four-Fermi operator is marginal in the strong magnetic field [395, 396]. Thus, the scattering amplitude is expected to acquire the logarithmic correction, and can be depicted with the same diagram as in the case of superconductivity (cf. Fig. 34). The chiral symmetry will be broken even in weak-coupling theories like QED. This is an analog of the well-known fact that superconductivity is induced by any weak attractive interaction. We readily understand those facts for the dimensional reason. The dimensional reduction occurs in strong magnetic fields enough to compensate the smallness of coupling strengths in underlying theories. Therefore, the magnitudes of the emergent scale can depend on the coupling strengths and are not universal, while the emergence of the Landau pole itself is independent of the coupling strengths.

We are now confident about the occurrence of the logarithmic corrections and are in position to explicitly construct the RG equations. In Sec. 7.2.1, we will see that the effective coupling constant G indeed runs into the Landau pole and induces the magnetic catalysis.

The Kondo effect in dense quark matter and in strong magnetic fields

We proceed to the QCD Kondo effect that occurs in the scattering between the light and heavy quarks [336, 377]. Here, we introduce heavy quarks as impurities. While the bulk properties of a quark matter are predominantly determined by dynamics of light quarks such as up, down, and strange quarks, a small amount of heavy quarks (charm and bottom quarks) can affect the transport properties via impurity scatterings. We shall consider a spatially localized impurity which does not have a spatial velocity. Such a situation is also realized in condensed matter systems as well. In other words, we consider the limit of an infinite heavy-quark mass. In such cases, the spatial translational invariance, and thus the spatial momentum conservation, are absent due to the localized impurities, while the energy remains conserved with the temporal translational invariance.

A systematic expansion with respect to a large heavy-quark mass $1/m_H$ is formulated with the heavy-quark effective field theory (HQEFT) [397]. In the HQEFT, a heavy-quark momentum p^{μ} is divided into hard and residual parts, $p^{\mu} = m_H v^{\mu} + k^{\mu}$ with $v^{\mu} = (1, 0, 0, 0)$ for a static impurity. We factorize the hard-momentum part $e^{-im_H v \cdot x}$ from the heavy-quark field Ψ and define the reduced field $\Psi_+ = \frac{1}{2}(1 + \not{v})e^{im_H v \cdot x}\Psi$ with the positive-energy projection. Then, the kinetic term in the leading order of the HQEFT is given by [397]

$$S_H^{\text{kin}} = \int dt \int \frac{d^3 \mathbf{k}}{(2\pi)^3} \Psi_+^{\dagger}(\mathbf{k}) i \partial_t \Psi_+(\mathbf{k}) + \mathcal{O}(1/m_H), \quad (390)$$

Note that the mass term is absent because we have already removed the hard-scale dynamics in defining the Ψ_+ . When the spatial velocity is vanishing, the spatial derivative does not appear in the kinetic term, and the residual momentum \mathbf{k} does not scale. This kinetic term indicates that the heavy-quark field Ψ_+ does not scale (s^0) when $t \rightarrow s^{-1}t$.

Now that we have determined the scaling dimensions of both the light- and heavy-quark fields, we can investigate their interactions. In the dense light-quark matter, the four-Fermi interaction between the light and heavy quarks is given by

$$S_{\text{HD}}^{\text{int}} = \int dt \sum_{\mathbf{v}_F^{(1)}, \mathbf{v}_F^{(3)}} \int \frac{d^2 \ell_{\perp}^{(1)} d\ell_{\parallel}^{(1)}}{(2\pi)^3} \frac{d^2 \ell_{\perp}^{(3)} d\ell_{\parallel}^{(3)}}{(2\pi)^3} \int \frac{d^3 \mathbf{k}^{(2)}}{(2\pi)^3} \frac{d^3 \mathbf{k}^{(4)}}{(2\pi)^3} \times G \left[\bar{\psi}_+(\ell^{(3)}; \mathbf{v}_F^{(3)}) t^a \psi_+(\ell^{(1)}; \mathbf{v}_F^{(1)}) \right] \left[\bar{\Psi}_+(\mathbf{k}^{(4)}) t^a \Psi_+(\mathbf{k}^{(2)}) \right]. \quad (391)$$

Note again that the recoil effect is negligible in the heavy-quark limit, or, in other words, the spatial translational invariance is broken by the localized impurity. Accordingly, the above interaction term does not have a delta function for the spatial momentum conservation. Plugging the scaling dimensions of the fields and of the momenta discussed above, we find that the light-heavy four-Fermi operator is marginal.

From the above simple analysis, one expect that the four-Fermi interaction acquires logarithmic quantum corrections from the next-to-leading order scattering diagrams shown in Fig. 34. However, we will see in Sec. 7.3 that, without noncommutative matrices on the interaction vertices, the logarithmic corrections from the two diagrams exactly cancel each other. Therefore, in the Kondo systems, a non-Abelian property of the interaction is essential to make the logarithmic contributions physical. In the QCD Kondo effect, the color matrices naturally play a role so that such a complete cancellation does not occur.⁷⁶

Let us discuss the magnetically induced QCD Kondo effect that is caused by the scatterings between the LLL fermions and heavy quark. In the heavy-quark limit $m_{\text{H}}^2 \gg eB$, effects of the magnetic field on the heavy quark, such as the Lorentz force, are suppressed, so that we do not consider those effects directly acting on the heavy quark. Then, the role of the magnetic field is to confine the light quarks in the LLL, and the four-Fermi operator is given by

$$S_{\text{LLL}}^{\text{int}} = \int dt \int \frac{dp_z^{(1)}}{2\pi} \frac{dp_z^{(3)}}{2\pi} \int \frac{d^3 \mathbf{k}^{(2)}}{(2\pi)^3} \frac{d^3 \mathbf{k}^{(4)}}{(2\pi)^3} G \left[\psi_{\text{LLL}}^{\dagger}(p_z^{(3)}) t^a \psi_{\text{LLL}}(p_z^{(1)}) \right] \left[\Psi_+^{\dagger}(\mathbf{k}^{(4)}) t^a \Psi_+(\mathbf{k}^{(2)}) \right]. \quad (392)$$

We find that the four-Fermi operator (392) in the magnetic field has a scaling dimension s^0 , and thus is marginal as in the Kondo effect in the dense system discussed above. Also, the non-Abelian properties of QCD are again essential for the incomplete cancellation of logarithmic effects, leading to the magnetically induced Kondo effect [336]. In Sec. 7.3, we will explicitly see how the logarithm survives with non-Abelian interactions.

7.2 Magnetic catalysis of the chiral symmetry breaking

The very early studies of the chiral symmetry breaking/restoration in external electric and magnetic fields were carried out based on the effective models of QCD in Refs. [371–373], Refs. [374, 375], and

⁷⁶The original Kondo effect would be the first observation of asymptotic freedom with a non-Abelian interaction. However, the mechanism of the Kondo effect by the effective dimensional reduction should be distinguished from that of the asymptotic freedom in the (3+1) dimensional QCD. The latter is induced by nonlinear gluon dynamics arising as a consequence of the non-Abelian gauge symmetry, which manifests itself in the negative contribution to the (leading-order) beta function [268, 269].

Ref. [376].⁷⁷ The authors of these papers observed tendencies toward chiral symmetry restoration in electric fields and toward stronger dynamical breaking in magnetic fields, compared to the case without the external fields. The basic and intuitive interpretations were based on the facts that the electric fields act to separate the quark and antiquark both in the coordinate and momentum spaces and that the magnetic fields stabilize their spin-singlet configuration. This picture is in contrast to the effects of the external fields on the Cooper pairs in a superconductor, because the Cooper pairs are composed of like-sign charges. Also, the authors of Ref. [376] discussed a possibility that the spatial localization due to the formation of the cyclotron orbits may enhance the $q\bar{q}$ pairing in a strong magnetic field.

It was Gusynin, Miransky, and Shovkovy who clearly pointed out a deep analogy between the low-energy dynamics near the Fermi surface and in the strong magnetic fields (see Ref. [324] for a concise discussion). They initiated the paradigm of the dimensional reduction in the strong magnetic fields first in the (2+1)-dimensional systems [399, 400] and soon later in the (3+1)-dimensional systems [106, 324, 326] (see also brief summary in the proceedings [401]). The concept of the dynamical symmetry breaking due to the dimensional reduction, *the magnetic catalysis*, was established by focusing on the Nambu–Jona-Lasinio (NJL) model and QED at weak coupling. Namely, the dynamical chiral symmetry breaking was shown to occur no matter how small the coupling strengths are, without the help of any inherent nonperturbative interaction in the model/theory.⁷⁸ In the previous subsection, we have already seen that the four-Fermi operator for the LLL fermions is marginal only for the dimensional reason irrespective of the coupling constants in the underlying theories.

The mechanism of the magnetic catalysis was confirmed by various methods. Presumably, the most established method is solving the gap equations derived from the Schwinger-Dyson (SD) equation with appropriate approximations or from the stationary condition of the effective potential. Those studies are summarized already in comprehensive review articles in Refs. [101, 228, 402] (see also Sec. 6.2). The spontaneous chiral symmetry breaking is also characterized by a nontrivial solution of the Bethe-Salpeter equation for the Nambu-Goldstone (NG) mode [106, 326], in which the constituent mass is identified with the dynamical mass gap induced by the magnetic catalysis. It was also discussed that existence of the NG modes indicates avoidance of the Coleman-Mermin-Wagner theorem that states the absence of spontaneous breaking of continuous symmetries in the spacetime dimensions equal to or lower than (1+1) dimensions. The point is that, while the charged fermion in the LLL is confined in (1 + 1) dimensions, the neutral composite particles, say π^0 , do not form the Landau levels and are not subject to the dimensional reduction.⁷⁹ Their fluctuations are, therefore, not large enough to prevent the system from rolling into the broken phase.

In the following, we shed light on the method of renormalization group (RG) [325, 395, 396, 403, 404]. In line with the scaling argument given in the previous subsection, we explicitly obtain the size of the dynamical mass gap which agrees with the result from the aforementioned methods. We first focus on the (3+1)-dimensional systems with the NJL model and weak-coupling theories, or more specifically QED. The magnetic catalysis in a planar system shares the same idea of the dimensional reduction, but has different features due to the dimensional reasons. The interested reader is referred to review articles [101, 402]. Then, we proceed to the magnetic catalysis in QCD in Sec. 7.4 with detailed summary of stimulating results from recent lattice QCD simulations.

⁷⁷Large portions of these studies by the first two groups were aimed at the investigation of the chiral symmetry breaking/restoration in chromo-electromagnetic fields, as a mimic of color flux tubes, rather than in ordinary electromagnetic fields. A recent lattice QCD simulation supports the partial restoration of the chiral symmetry in the color flux tube spanned between a quark and an antiquark [398].

⁷⁸Without a magnetic field, the dynamical symmetry breaking in the NJL model only occurs for a large enough coupling strength beyond the critical value (see below).

⁷⁹Charged pions are no longer NG modes in a magnetic field due to the explicit breaking of the isospin symmetry. Note also that a strong enough magnetic field can resolve the inner structure of the composite particles. One needs to investigate the dispersion relation of a neutral pion on the basis of the fundamental degrees of freedom in QCD in such a strong field (see Sec. 7.4).

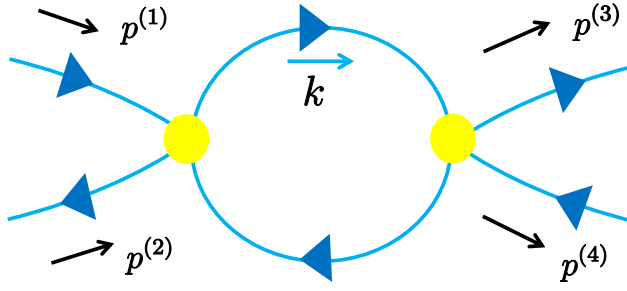


Figure 35: Scattering diagram for the chiral condensate.

7.2.1 Renormalization-group analysis

We derive the RG equation for the effective four-Fermi interaction. More specifically, we shall compute the scattering amplitudes $\mathcal{M}(\Lambda)$ at a given energy scale Λ for the fermion and antifermion pair that forms the chiral condensate. Since the four-Fermi operator in the LLL has a marginal scaling dimension, we anticipate that the effective coupling constant acquires a logarithmic quantum correction which drives the system toward a strong-coupling regime. When the energy scale is reduced from Λ to $\Lambda - \delta\Lambda$, the energy-scale dependence of $\mathcal{M}(\Lambda)$ is captured by the integration of the loop momentum over this infinitesimal energy band. Since the LLL excitation has the linear dispersion relation, the integral can be schematically written as

$$\delta\mathcal{M}(\Lambda) = \# \int_{\Lambda-\delta\Lambda}^{\Lambda} \frac{dk_z}{2\pi} \frac{1}{k_z}. \quad (393)$$

The logarithmic IR correction will be then absorbed by the renormalization of the effective coupling constant, and we are naturally led to the RG equation. By solving the RG equation with a given initial condition, we will find a Landau pole emerging at a certain IR scale. The size of the dynamically generated mass gap should be associated with this dynamical IR scale.

The relevant scattering channels for the formation of the chiral condensate are those between the fermion-antifermion pairs in the opposite chiralities, so that the two relevant spinor structures are given by $[\bar{u}_{R/L}(p_{\parallel}^{(3)})\gamma_{\parallel\mu}u_{R/L}(p_{\parallel}^{(1)})][v_{L/R}(p_{\parallel}^{(4)})\gamma_{\parallel}^{\mu}\bar{v}_{L/R}(p_{\parallel}^{(2)})]$ with the spinors of the fermion u and the antifermion v in the LLL. The chirality is denoted as R/L. The scattering amplitudes are the same for the both channels, so that we suppress these trivial spinor structures below for notational simplicity.

First, we take the NJL model as one of the simplest examples. The coupling constant G_{NJL} does not have any energy-scale dependence in the classical Lagrangian. Then, the leading-order scattering amplitude is just given by the four-Fermi coupling constant as

$$\mathcal{M}_0 = G_{\text{NJL}}. \quad (394)$$

Next, by using the propagator in the LLL (137), the one-loop amplitude shown in Figs. 35 is written down as

$$i\mathcal{M}_1 = G_{\text{NJL}}^2 \rho_B \int \frac{d^2k_{\parallel}}{(2\pi)^2} \left[\bar{u}(p_{\parallel}^{(3)})\gamma_{\parallel}^{\mu}S_{\parallel}(k_{\parallel})\gamma_{\parallel}^{\nu}u(p_{\parallel}^{(1)}) \right] \left[v(p_{\parallel}^{(4)})\gamma_{\parallel\mu}S_{\parallel}(k_{\parallel} - P_{\parallel})\gamma_{\parallel\nu}\bar{v}(p_{\parallel}^{(2)}) \right], \quad (395)$$

where $P_{\parallel} = p_{\parallel}^{(1)} + p_{\parallel}^{(2)}$ is the total momentum of the pair and the longitudinal part of the propagator is given by $S_{\parallel}(k_{\parallel}) = ik_{\parallel}/(k_{\parallel}^2 + i\epsilon)\mathcal{P}_+$. The Landau degeneracy factor $\rho_B = |eB|/(2\pi)$ is reproduced from the transverse-momentum integral, so that we are left with the two-dimensional loop integral as a natural consequence of the dimensional reduction. After performing the elementary k^0 -integral (see

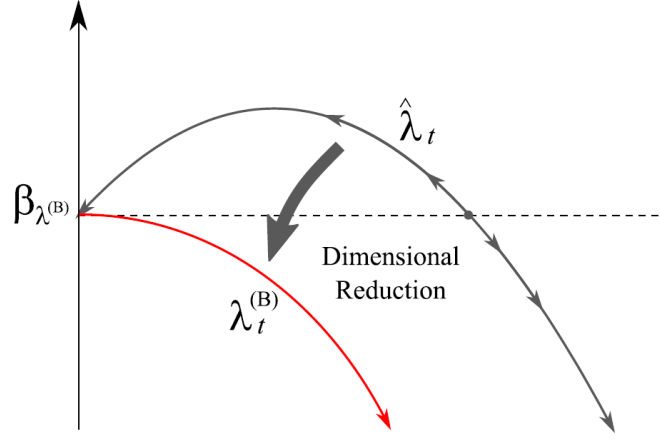


Figure 36: The beta function for the four-Fermi interaction in vacuum (black) and in a strong magnetic field (red) [325] (See also Fig. 2 in Ref. [403]). The horizontal axis shows the coupling constant. When the effective spacetime dimension is reduced to the (1+1) dimensions, the beta function is negative for any value of the coupling constant.

an appendix in Ref. [404]), one finds the origin of the magnetic catalysis:

$$\delta\mathcal{M}_1(\Lambda) = \rho_B G_{\text{NJL}}^2 \int_{\Lambda-\delta\Lambda}^{\Lambda} \frac{dk_z}{2\pi} \frac{1}{|k_z|}. \quad (396)$$

Performing the integral, the logarithmic increment from the one-loop correction is found to be

$$\delta\mathcal{M}_1(\Lambda) = \rho_B \frac{G_{\text{NJL}}^2(\Lambda)}{\pi} \ln \frac{\Lambda}{\Lambda - \delta\Lambda}, \quad (397)$$

where we have introduced the effective coupling $G_{\text{NJL}}(\Lambda)$ at the energy scale Λ .

From the scattering amplitudes in Eqs. (394) and (397), the RG equation is obtained as

$$\Lambda \frac{d}{d\Lambda} [\rho_B G_{\text{NJL}}(\Lambda)] = -\frac{1}{\pi} [\rho_B G_{\text{NJL}}(\Lambda)]^2, \quad (398)$$

where $\rho_B G_{\text{NJL}}(\Lambda)$ is a dimensionless combination. One can immediately read off the beta function from Eq. (398), which is found to be negative. When the interaction is attractive ($G_{\text{NJL}} > 0$), the magnitude of the interaction strength increases in the low-energy domain. Namely, we find that the four-Fermi interaction is a marginally relevant operator. The effect of a magnetic field on the beta function can be clearly summarized in Fig. 36 [325] (cf. also Fig. 2 in Ref. [403]). When $B = 0$, the chiral symmetry breaking occurs only when the initial value of the coupling constant in the RG evolution is larger than the critical value located at the UV fixed point. Namely, the chiral symmetry breaking cannot occur without the help of the strong-coupling nature in the low-energy QCD. While an analogy between QCD and superconductor has provided fruitful insights into high-energy physics in the history [323, 405, 406], the microscopic mechanisms of the symmetry breaking are actually quite different in this regard. The effect of the magnetic field pushes the beta function down to the negative region as we increase the magnetic field, and the beta function finally becomes negative in the entire region. Then, the broken phase is favored irrespective of the initial value of the coupling constant. We have emphasized the dimensional mechanism through the evaluation of the (1+1)-dimensional integral and the scaling argument in the previous subsection; In this regard, the magnetic catalysis of the chiral symmetry breaking provides a closer analogy to superconductivity. We also discussed the dimensional reduction in terms of the effective potential in Sec. 6.2.

It is now easy to solve the RG equation (398). Starting from an initial UV scale Λ_0 , the solution at the energy scale $\Lambda (< \Lambda_0)$ is obtained as

$$G_{\text{NJL}}(\Lambda) = \frac{G_{\text{NJL}}(\Lambda_0)}{1 + \pi^{-1} \rho_B G_{\text{NJL}}(\Lambda_0) \ln(\Lambda/\Lambda_0)}. \quad (399)$$

The effective coupling $G_{\text{NJL}}(\Lambda)$ grows with a decreasing Λ , and diverges at a Landau pole. This implies a breakdown of the perturbative picture and an emergence of nonperturbative dynamics. The presence of the Landau pole gives rise to a dynamical IR scale

$$\Lambda_{\text{IR}} = \Lambda_0 \exp\left(-\frac{\pi}{\rho_B G_{\text{NJL}}(\Lambda_0)}\right). \quad (400)$$

One may take an initial UV scale $\Lambda_0 = \sqrt{eB}$, below which the dynamics is dominated by the LLL fermions. The size of the dynamical mass should be associated with the emergent scale, so that $m_{\text{dyn}} \sim \Lambda_{\text{IR}}$. Therefore, the order of the dynamical mass gap is found to be⁸⁰ [325, 404]

$$m_{\text{dyn}} \sim \sqrt{eB} \exp\left(-\frac{\pi}{\rho_B G_{\text{NJL}}(\sqrt{eB})}\right). \quad (401)$$

This result agrees with that obtained from the solution of the gap equation [324, 325] (see Sec. 6.2). Because of the dimensional reduction, each fermion-antifermion pair in the chiral condensate $\langle \bar{f}f \rangle$ is squeezed within the size of the cyclotron motion $\sim 1/\sqrt{eB}$, and the size of the chiral condensate is given by that of the squeezed condensate multiplied by the Landau degeneracy factor, $\langle \bar{f}f \rangle \sim \Lambda_{\text{IR}} \cdot |eB|/(2\pi)$.

Since we have examined the scaling argument for superconductivity in the previous section, it is instructive to revisit the analogy between superconductivity and the magnetic catalysis. The above mass gap indeed has a quite similar form as that of the energy gap emerging in superconductivity [324]: $\Delta \sim \omega_{\text{D}} \exp(-c'/\rho_{\text{F}} G_{\text{S}})$, where G_{S} and c' are the coupling constant and a numerical constant of order one, respectively. The Debye frequency ω_{D} specifies the band width near the Fermi surface where an attractive phonon interaction is effective, while ρ_{F} is the density of states at the Fermi surface. They are counterparts of the UV scale Λ_0 and the Landau degeneracy factor ρ_B in the magnetic field, respectively. The physics behind this similarity is of course the analogous dimensional reductions occurring in the IR dynamics (cf. Fig. 33).

7.2.2 Magnetic catalysis in weak-coupling gauge theories

In the above, we explicitly identified the origin of the logarithmic quantum correction to the four-Fermi interaction and discussed the similarity to superconductivity. It should be noticed that, in both the magnetic catalysis and superconductivity, the exponent depends on the effective coupling constant multiplied by the density of states (see Eq. (401) and discussions below it). This dependence arises because the coupling constant of the four-Fermi interaction model G_{NJL} has a mass dimension that needs to be compensated by another dimensionful quantity in the exponent. Putting it differently, this exponent is not a universal quantity and depends on details of the interactions. Therefore, the next natural issue is investigating the magnetic catalysis with different types of interactions. Especially, it is interesting to apply the RG analysis to gauge theories where the four-Fermi interaction is generated by gauge-boson exchanges with a dimensionless coupling constant. Below, we examine the magnetic catalysis in the weak-coupling QED which serves as a theoretically well-controlled and nontrivial example of the chiral symmetry breaking in gauge theories.

⁸⁰Hereafter, a quantity eB is understood as a positive value. We omit the symbols of absolute value for notational simplicity.

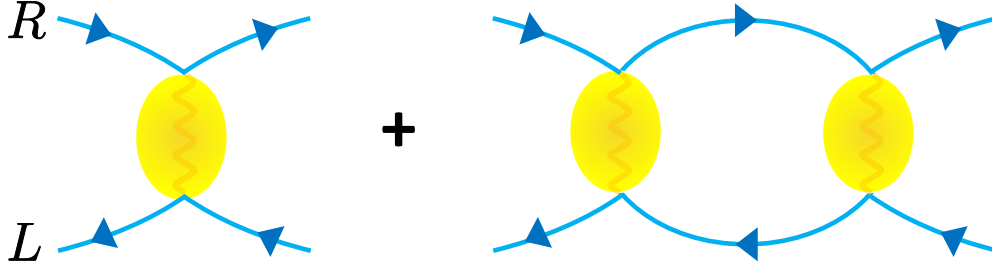


Figure 37: Scattering diagrams contributing to the RG flow in the magnetic catalysis. Yellow blobs denote the effective coupling which are defined by integrating the photon propagator in Eq. (404).

To build a bridge to the scaling argument, we first construct an effective four-Fermi interaction from a photon exchange interaction (cf. Fig. 37). An important point in this treatment is that the effective four-Fermi coupling potentially acquires an energy-scale dependence arising from the photon propagator. This is indeed the case because the photon propagator has an obvious energy-scale dependence in the UV region which behaves as the inverse square momentum. Moreover, this dependence will be modified in the IR region if there is a screening effect. Therefore, the effective coupling could have multiple origins of the energy-scale dependences in addition to the quantum correction stemming from the dimensional reduction, reflecting properties of the interactions in underlying theories. We establish a simple method to include such multiple energy-scale dependences into the RG equations. This enables us to keep track of the modifications and clarify how they are finally reflected in the mass gap [404]. This effective theory should be distinguished from the naïve four-Fermi interactions, like the NJL model discussed above, which do not respect intrinsic energy-scale dependences in underlying theories such as QCD.

We introduce the photon propagator in the strong magnetic field *a la* Gusynin et al. [407, 408]:

$$iD_{\mu\nu}(q) = \frac{g_{\parallel}^{\mu\nu}}{q^2 - m_{\gamma}^2} + \frac{g_{\perp}^{\mu\nu}}{q^2} - \frac{q_{\perp}^{\mu} q_{\perp}^{\nu} + q_{\perp}^{\mu} q_{\parallel}^{\nu} + q_{\parallel}^{\mu} q_{\perp}^{\nu}}{(q^2)^2}. \quad (402)$$

The polarization of the LLL fermion and antifermion pairs induces the static screening mass (see Sec. 5.2.3 and Appendix F)

$$m_{\gamma}^2 = N_f \rho_B \cdot \frac{e^2}{\pi}, \quad (403)$$

where N_f is the number of fermion flavors. This screening mass is a gauge-invariant quantity and is a close analog of the Schwinger mass [197, 198]. Properties of this screening effect have been discussed in the literature [214, 216, 242, 407–409]. The second and third terms are coupled to neither the LLL fermion loop nor the scattering LLL fermions because the LLL fermion current, $j_{\text{LLL}}^{\mu} = \bar{\psi}_{\text{LLL}} \gamma_{\parallel}^{\mu} \psi_{\text{LLL}}$, is longitudinal to the magnetic field. Thus, those terms are irrelevant in the present discussion. Now, we note that the photons live in the ordinary four dimensions while the LLL fermion has the (1+1)-dimensional dispersion relation (381). Therefore, we define the effective coupling constant G by integrating out the transverse momentum in the photon propagator as [61, 336]

$$G(\sqrt{-q_{\parallel}^2}) \equiv (-ie)^2 \int \frac{d^2 \mathbf{q}_{\perp}}{(2\pi)^2} \frac{1}{q^2 - \mathbf{q}_{\perp}^2 - m_{\gamma}^2} e^{-\frac{q_{\perp}^2}{2eB}} e^{-i\frac{P_y q_x}{eB}}. \quad (404)$$

In this way, we obtain an effective (1+1)-dimensional interaction in the form of Eq. (389). The Gaussian factor comes from the transverse part of the fermion wave functions as discussed in Sec. 2.3. This factor

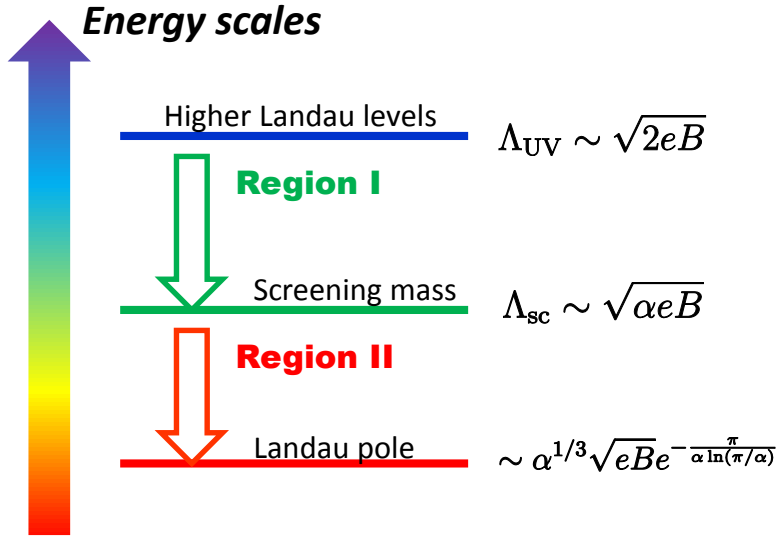


Figure 38: Hierarchy of the energy scales in the RG evolution. The relevant region from the UV cutoff down to the Landau pole is divided into two regions by the scale of the screening mass [404].

cuts off the UV region of the integral. We note that the Schwinger phase is not written explicitly. In general, the Schwinger phases from the vertices remain in Eq. (404) [61]. The resultant Schwinger phase factor $\exp(-iP_y q_x / |eB|)$ with $\mathbf{P} \equiv \mathbf{p}^{(1)} + \mathbf{p}^{(2)}$ can be ignored in the region of our interest with a small q_\perp (see below).

When the energy and momentum scales of the fermions and antifermions are of the order of Λ , the momentum transfer is $-\Lambda^2 \lesssim q_\parallel^2 \lesssim 0$, where we are only interested in the space-like region contributing to the fermion-antifermion scatterings. If the momentum transfer is much larger than the screening mass scale ($\Lambda \gg \Lambda_{\text{sc}} = m_\gamma$), the photon propagator reduces to the free propagator, and the effective coupling constant depends on the energy scale $G(\sqrt{-q_\parallel^2}) \sim G(\Lambda)$. In the opposite limit, if the momentum scale Λ is much smaller than m_γ , the photon exchange can be well approximated by the four-Fermi contact interaction that is independent of the momentum transfer q_\parallel^2 . In this case, the effective theory reduces to the (1+1)-dimensional four-Fermi interaction discussed in the previous section. Therefore, it is important to specify the hierarchy of the scales in the problem. The relevant scales are the initial UV scale Λ_{UV} , the screening mass $\Lambda_{\text{sc}} = m_\gamma$, and a possible emergent IR scale Λ_{IR} from the Landau pole. The initial UV scale Λ_{UV} can be taken at \sqrt{eB} so that the higher Landau levels are decoupled from the LLL dynamics. One can consider three cases:

$$\Lambda_{\text{sc}} \gg \Lambda_{\text{UV}} \gg \Lambda_{\text{IR}}, \quad (405a)$$

$$\Lambda_{\text{UV}} \gg \Lambda_{\text{sc}} \gg \Lambda_{\text{IR}}, \quad (405b)$$

$$\Lambda_{\text{UV}} \gg \Lambda_{\text{IR}} \gg \Lambda_{\text{sc}}. \quad (405c)$$

In the first case, the classical effective coupling is a constant independent of the momentum transfer q_\parallel^2 all the way through the RG evolution from Λ_{UV} to Λ_{IR} . In the second case, the effective coupling has an energy-scale dependence even at the classical level in the regime between Λ_{UV} and Λ_{sc} , while it again reduces to a constant below Λ_{sc} . Figure 38 shows the hierarchy in this case. In the third case, or simply when the screening effect is neglected, the classical effective coupling has an energy-scale dependence arising from the free photon propagator all the way through the RG evolution. We shall examine how those differences in the photon exchanges manifest themselves in the magnitude of the emergent IR scale resulting from the RG evolution driven by the quantum logarithmic corrections.

Contact interaction in “many-flavor QED”

We first consider the case of a strong screening effect (405a). The screening mass scale Λ_{sc} becomes much larger than the initial UV scale at Λ_{UV} if the number of fermion flavors N_f is sufficiently large [410]. This theory is realized when $N_f\alpha \gg 1$ according to Eq. (403) and may be called the “many-flavor QED.” Though this is a sort of hypothetical theories, we can use the many-flavor QED as a control test for our understanding of interaction effects. In this case, explicit integration in Eq. (404) provides

$$G = \rho_B \cdot \frac{e^2}{m_\gamma^2} = \frac{\pi}{N_f}, \quad (406)$$

which is a constant up to possible quantum corrections. The mass gap is simply given by the previous result in Eq. (401) by identifying $\rho_B G_{\text{NJL}} \rightarrow G$. Therefore, we get the mass gap

$$m_{\text{dyn}} \sim \sqrt{eB} e^{-N_f}. \quad (407)$$

This agrees with the result from the SD equation [410].

Unscreened QED as an example of non-contact interactions

We consider the third case (405c). When there is no screening mass ($m_\gamma = 0$), the photon propagator has an obvious energy dependence $\sim q_{\parallel}^{-2}$. Here, we call this model “unscreened QED.” When the energy scale of the fermionic degrees of freedom is reduced from Λ to $\Lambda - \delta\Lambda$, the lower boundary of the photon momentum scale changes from $-\Lambda^2 \lesssim q_{\parallel}^2$ to $-(\Lambda - \delta\Lambda)^2 \lesssim q_{\parallel}^2$. As a consequence, even the tree-level amplitude acquires an increment, which contrasts to the constant (classical) coupling constant discussed in the many-flavor QED and the NJL model in Eq. (394). In Eq. (404), the energy-scale dependence only appears from a small $|\mathbf{q}_{\perp}|$ regime such that $|\mathbf{q}_{\perp}|^2 \lesssim |q_{\parallel}^2| \lesssim \Lambda_{\text{UV}}$, where the Gaussian factor and the Schwinger phase factor reduce to unity and the Λ specifies the lower cut-off of the integral. Thus, the increment is immediately obtained as

$$\delta\mathcal{M}_0(\Lambda) = G(\Lambda - \delta\Lambda) - G(\Lambda) \sim \alpha \int_{(\Lambda - \delta\Lambda)^2}^{\Lambda^2} \frac{d(q_{\perp}^2)}{q_{\perp}^2}. \quad (408)$$

Importantly, this increment gives rise to a logarithm

$$\delta\mathcal{M}_0(\Lambda) = 2\alpha \ln \frac{\Lambda}{\Lambda - \delta\Lambda}, \quad (409)$$

which partly drives the RG flow and will be finally reflected in the mass gap.

This situation is somewhat, though not exactly, similar to that in color superconductivity in dense quark matter. There is only a dynamical screening effect in the color-magnetic interaction in the dense QCD, so that the color-magnetic interaction has a rather long-range nature as compared to the color-electric interaction which is cut off by a static Debye screening effect. In Ref. [393], Son showed that the energy-scale dependence of the color-magnetic interaction plays an important role in obtaining the correct RG equation. Similar to Eq. (409), there is an additional logarithm from the one-gluon exchange diagram that finally modifies the exponent of the emergent IR scale from $\exp(-c_1/g^2)$ to $\exp(-c_2/g)$ with $c_{1,2}$ being numerical constants. This is a significant effect when the QCD coupling constant g is a small number. We should learn a lesson from this result that the color-magnetic interaction, or any kind of energy-scale dependent interactions, cannot be naively approximated by the NJL-type contact interaction.

From the one-loop contribution \mathcal{M}_1 , we again obtain the logarithmic quantum correction. This contribution is the same as that of the NJL model up to possible differences in subleading corrections.

Therefore, combining the logarithms from the tree-level contribution (409) and the quantum correction (397), the RG equation for the unscreened QED is obtained as

$$\Lambda \frac{d}{d\Lambda} G(\Lambda) = -2\alpha - \frac{1}{\pi} G^2(\Lambda). \quad (410)$$

Note that the first term on the right-hand side was absent in Eq. (398) and that a similar inhomogeneous RG equation was obtained in the aforementioned color superconductivity [393, 394]. The solution of the above RG equation is obtained as

$$G(\Lambda) = \sqrt{2\alpha\pi} \tan \left[-\sqrt{\frac{\alpha}{2\pi}} \ln \frac{\Lambda^2}{\Lambda_{\text{UV}}^2} + \arctan \left(\frac{G(\Lambda_{\text{UV}})}{\sqrt{2\pi\alpha}} \right) \right]. \quad (411)$$

Taking the initial scale $\Lambda_{\text{UV}} = \sqrt{eB}$, the initial value of the effective coupling (404) is evaluated as

$$G(\Lambda_{\text{UV}}) \simeq \alpha \int_{\Lambda_{\text{UV}}^2}^{2eB} \frac{d(q_{\perp}^2)}{q_{\perp}^2} = \alpha \ln(2eB/\Lambda_{\text{UV}}^2) \ll 1. \quad (412)$$

Neglecting the higher-order terms in $G(\Lambda_{\text{UV}}) \ll 1$, the above solution of the RG equation reads

$$G(\Lambda) \simeq \sqrt{2\alpha\pi} \tan \left(-\sqrt{\frac{\alpha}{2\pi}} \ln \frac{\Lambda^2}{2eB} \right). \quad (413)$$

As we reduce the energy scale Λ , the solution (413) hits the Landau pole. The emergent IR scale can be determined from the location of the Landau pole

$$-\sqrt{\frac{\alpha}{2\pi}} \ln \frac{\Lambda_{\text{IR}}^2}{2eB} = \frac{\pi}{2}, \quad (414)$$

which immediately yields

$$m_{\text{dyn}} \sim \Lambda_{\text{IR}} \sim \sqrt{2eB} \exp \left(-\frac{\pi}{2} \sqrt{\frac{\pi}{2\alpha}} \right). \quad (415)$$

Notice that the exponent of this mass gap is different from that in the NJL model (401), because of the long-range photon interaction. There is no explicit dependence on the magnetic field in the exponent, so that the dependence of m_{dyn} on the magnetic field is milder than that in the NJL model.

As mentioned earlier, the dynamical mass (415) was also obtained as the constituent mass of the NG mode which emerges when the chiral symmetry is spontaneously broken in a magnetic field [106, 326]. Namely, it was shown that there exists a nontrivial solution of the Bethe-Salpeter equation for the NG boson of which the spectrum is composed of the constituent mass of the same form as in Eq. (415). Consistent results were obtained with the Schwinger-Dyson equation in the rainbow approximation [67, 411] and the RG analysis [404] up to differences in order-one constants. This is not an accidental coincidence. From the diagrammatic point of view, the RG equation corresponds to the resummation of the ladder diagrams with the multiple photon exchanges (cf. Fig. 37). This is nothing but the Bethe-Salpeter equation in the ladder approximation. Also, one can notice a similarity between the rainbow and ladder diagrams since the rainbow approximation of the SD equation only holds the planar diagrams of the fermion self-energy. Cutting the intermediate fermion propagator in the SD equation provides the same ladder diagrams.

Taking the unscreened QED as an example, we have discussed how the energy-scale dependences from the underlying theory, together with the quantum corrections, can be consistently taken into account in the effective theory in terms of the RG evolution.

RG analysis with the static screening effect

Lastly, we consider the second case (405b), where the screening mass sets an intermediate scale $\Lambda_{\text{sc}} \equiv m_\gamma$ in between the UV and IR scales (see Fig. 38). A successful effective theory should correctly take into account the intrinsic energy-scale hierarchy in the underlying theories. This is an important issue which is shared with various systems involving multiple scales. We will find a prescription to reproduce the correct form of the dynamical mass gap in the “screened QED” [404] that has been obtained with other methods [407, 408].

The basic strategy is summarized in Fig. 38, where the RG evolution from the UV to IR scales are divided into two stages by the screening mass scale Λ_{sc} . When the scale of interest Λ is larger than Λ_{sc} , we call it Region I ($\Lambda > \Lambda_{\text{sc}}$), while the deeper IR region is called Region II ($\Lambda < \Lambda_{\text{sc}}$). An important difference in these regions is found in the integral for the effective coupling (404). The screening mass is negligible in Region I, while it is important in Region II as the IR cutoff of the integral. As we have learned with the unscreened QED just above, one should include the energy-scale dependence from the tree-level amplitude in Region I. On the other hand, the effective coupling does not have such an energy-scale dependence in Region II since the integral region is bounded by the constant IR cutoff Λ_{sc} , instead of the floating scale of interest $-q_{\parallel}^2 \sim \Lambda^2$ [see a discussion below Eq. (404)]. As a consequence, the RG evolutions in these regions are governed by different RG equations.

We construct a set of RG equations, one for each region. When solving the RG equations, we switch over from the RG equation for Region I to that for Region II by smoothly connecting the two solutions at the intermediate scale Λ_{sc} . This strategy was proposed in Ref. [336] for the RG analysis of the Kondo effect in a magnetic field (see Sec. 7.3) and then applied to the magnetic catalysis [404]. Performing the integral in Eq. (404), we obtain the effective coupling in each region

$$G(\Lambda) \simeq \begin{cases} \alpha \ln(2eB/\Lambda^2) & \text{Region I} \\ \alpha \ln(2eB/m_\gamma^2) & \text{Region II} \end{cases} . \quad (416)$$

To emphasize the energy-scale dependence, it would be useful to put the results in different forms

$$G(\Lambda - \delta\Lambda) - G(\Lambda) \simeq \begin{cases} 2\alpha \ln\left(\frac{\Lambda}{\Lambda - \delta\Lambda}\right) & \text{Region I} \\ 0 & \text{Region II} \end{cases} . \quad (417)$$

As discussed above, there is the logarithmic dependence in Region I, while no such dependence in Region II. We have already learned all machinery to construct RG equations with the previous models. The RG equation in each region reads

$$\Lambda \frac{d}{d\Lambda} G(\Lambda) = -2\alpha - \frac{1}{\pi} G^2(\Lambda) \quad \text{Region I,} \quad (418a)$$

$$\Lambda \frac{d}{d\Lambda} G(\Lambda) = -\frac{1}{\pi} G^2(\Lambda) \quad \text{Region II.} \quad (418b)$$

Now, we solve the RG equations and connect the two solutions at the intermediate scale Λ_{sc} . From the solution for the RG equation (418a), one finds the running coupling constant at the lower boundary of Region I ($\Lambda = \Lambda_{\text{sc}}$)

$$G(\Lambda_{\text{sc}}) \simeq \alpha \ln \frac{2eB}{m_\gamma^2} + \frac{\alpha^2}{6\pi} \left(\ln \frac{2eB}{m_\gamma^2} \right)^3 , \quad (419)$$

where we performed an expansion with respect to a small quantity $\alpha \ln(2eB/m_\gamma^2) = \alpha \ln(\pi/\alpha) \ll 1$. The leading-order term in α corresponds to the tree-level coupling constant (404), while the subsequent terms explain the growth of the coupling constant driven by the quantum correction in Region I.

When the scale Λ enters Region II, we use the RG equation (418b) with the initial condition at the upper boundary of Region II, i.e., Λ_{sc} , which has been obtained as the result of the RG evolution in

Region I in Eq. (419). Then, we find the solution in Region II

$$G(\Lambda) = \frac{G(\Lambda_{\text{sc}})}{1 + \pi^{-1}G(\Lambda_{\text{sc}})\ln(\Lambda/\Lambda_{\text{sc}})}. \quad (420)$$

Clearly, this solution has a Landau pole and indicates the emergence of the dynamical IR scale at

$$\Lambda_{\text{IR}} = \Lambda_{\text{sc}} e^{-\pi/G(\Lambda_{\text{sc}})}. \quad (421)$$

Therefore, plugging Eq. (419) into $G(\Lambda_{\text{sc}})$, we obtain the magnitude of the dynamical mass gap [404]

$$m_{\text{dyn}} \sim \Lambda_{\text{IR}} \sim m_\gamma \exp \left\{ -\frac{\pi}{\alpha \ln(\pi/\alpha)} + \ln \left(\frac{\pi}{\alpha} \right)^{\frac{1}{6}} \right\} = \sqrt{2eB} \left(\frac{\alpha}{\pi} \right)^{\frac{1}{3}} \exp \left(-\frac{\pi}{\alpha \ln(\pi/\alpha)} \right), \quad (422)$$

where the first and second terms in the exponent correspond to those in Eq. (419), respectively.

Remarkably, the result in Eq. (422) agrees with that from the SD equation [407, 408]. One can identify the origins of the overall factors of \sqrt{eB} , $\alpha^{1/3}$, and the exponent in Eq. (422) in the language of the RG method [404]. Especially, in the passing from Eq. (421) to Eq. (422), the factor of $\alpha^{1/3}$ is obtained as a product of the α dependences from different origins in $\Lambda_{\text{sc}} = m_\gamma$ and $G(\Lambda_{\text{sc}})$. Reproducing the correct fractional power of $\alpha^{1/3}$ serves as a consistency check of the hierarchy scheme implemented above.

Short summary

Here, we summarize the results of the RG analyses on the magnetic catalysis. As suggested by the scaling argument, the logarithmic quantum correction gives rise to the Landau pole in the RG evolution of the effective four-Fermi coupling. The energy-scale dependence of the photon-exchange interaction, which is intrinsic in QED, can be included in the RG analysis with the effective four-Fermi coupling (404) constructed from the photon propagator. Depending on the hierarchy shown in Eq. (405), we constructed the appropriate RG equations and obtained the correct forms of the dynamical mass gap, which are itemized as

- $m_\gamma \gg \Lambda_{\text{UV}}$ (“Many-flavor QED” or equivalent to the NJL model)

$$m_{\text{dyn}} \sim \sqrt{eB} \exp(-N_f) \ll \sqrt{eB} \exp\left(-\frac{1}{\alpha}\right)$$

- $\Lambda_{\text{UV}} \gg m_\gamma \gg \Lambda_{\text{IR}}$ (“Screened QED”)

$$m_{\text{dyn}} \sim \sqrt{2eB} \alpha^{1/3} \exp\left(-\frac{\pi}{\alpha \ln(\pi/\alpha)}\right)$$

- $\Lambda_{\text{IR}} \gg m_\gamma$ or $m_\gamma = 0$ (“Unscreened QED”)

$$m_{\text{dyn}} \sim \sqrt{2eB} \exp\left(-\frac{\pi}{2} \sqrt{\frac{\pi}{2\alpha}}\right)$$

In the many-flavor QED, an inequality $N_f \gg \alpha^{-1}$ as well as $\alpha \ll 1$ need to be satisfied although there is no explicit coupling dependence in the exponent. In case of the second hierarchy ($\Lambda_{\text{UV}} \gg m_\gamma \gg \Lambda_{\text{IR}}$), the photon exchange is screened below the scale m_γ , but is not screened above this scale. We constructed the two separate RG equations for these regions, and connected their solutions at the intermediate scale m_γ . For $\alpha \sim 1/137$, the mass gap is suppressed in the screened QED as compared to that in the unscreened QED as expected. All these results agree with those from other equivalent methods as discussed above.

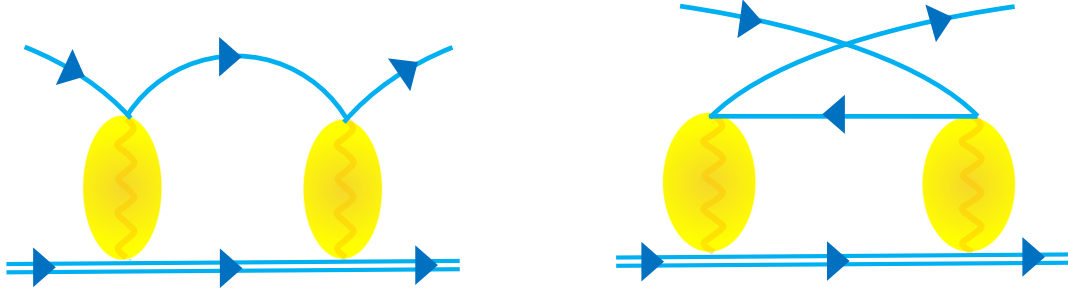


Figure 39: Kondo diagrams. If there were not a non-Abelian interaction, the logarithmic enhancements from those one-loop diagrams completely cancel each other.

7.3 The QCD Kondo effect

In this subsection, we proceed to the “QCD Kondo effect” occurring in dense quark matter and in a strong magnetic field. In condensed matter physics, an anomalous temperature dependence of the electric resistivity, which is now called the Kondo effect, has been experimentally discovered a long time before J. Kondo pointed out the essential mechanism [412]. The existence of a minimum at a certain temperature was a puzzle since the electrical resistivity arising from impurity scatterings had been thought to monotonically decrease with a decreasing temperature and converge to a constant value at zero temperature. Then, J. Kondo showed a logarithmic enhancement of the resistivity arising from the next-to-leading order scattering diagrams. This quantum correction overwhelms classical impurity effects at low temperature, and thus gives rise to a minimum in the temperature dependence of the resistivity. We can anticipate this result from our scaling argument examined in the early this section. The resistivity would increase in the low temperature if there is an emergent strong-coupling regime in the interaction between the conduction electrons and an impurity. We will see how the strong-coupling regime arises on the basis of the RG method which we are already familiar with.

There are three important conditions for the occurrence of the Kondo effect. They are (i) the existence of the Fermi surface, (ii) quantum fluctuations (loop effects), and (iii) a non-Abelian property of the interaction between charge carriers and an impurity. As we have seen in the scaling argument in Sec. 7.1, the interplay between Conditions (i) and (ii) induces logarithmic enhancements of the scattering amplitudes between light and heavy particles, e.g., a conduction electron and an impurity. There are two relevant diagrams in the next-to-leading order as shown in Fig. 39 (see also Fig. 34). The intermediate state in the left diagram is a particle-like state, while that in the right diagram is a hole-like state with an annihilation on the vertex. As we will see explicitly, the logarithms from those diagrams have opposite signs. This is because the boundaries of the loop integrals approach the Fermi surface from above or below depending on whether a diagram is dominated by a particle or hole contribution. Then, one needs to satisfy Condition (iii) so that the logarithms from the two diagrams do not completely cancel each other with noncommutative matrix structures on the vertices. The third condition is satisfied with the (pseudo)spin interaction in condensed matter physics. Once the necessary conditions and their roles are identified, one can look for analogous systems which also satisfy those conditions.

Recently, it is proposed that the Kondo effect occurs in dense quark matter with heavy-quark impurities [377] (see also an earlier work [413] and a short review [414]). The non-Abelian interaction is naturally provided by the color-exchange interaction in QCD, and we do not need a spin interaction as a possible origin of non-Abelian interactions.⁸¹ This is called the QCD Kondo effect. Based on the analogy between the dimensional reductions at high density and in a strong magnetic field, the QCD

⁸¹In fact, the Bohr magneton and thus the spin interaction are suppressed by the heavy-quark mass.

Kondo effect was shown to occur in a strong magnetic field even in the absence of the Fermi surface [336]. It should be noticed that a strong magnetic field spoils the spin flip interaction since the spin direction is frozen in a strong magnetic field due to the Zeeman effect: It may be difficult to expect a spin interaction as an origin of non-Abelian interactions. The “magnetically induced QCD Kondo effect” can still occur as a result of the interplay between the light quarks strongly interacting with a magnetic field and gluons indifferent to a magnetic field.

Below, we discuss an essence of the QCD Kondo effect in dense quark matter, and then proceed to the magnetically induced QCD Kondo effect, focusing on the role of the dimensional reductions.

7.3.1 The QCD Kondo effect in dense quark matter

Here, we briefly review the RG approach to the QCD Kondo effect in dense quark matter. We consider the amplitude of the light-quark excitations near the Fermi surface scattering off a heavy-quark impurity at a certain energy scale Λ . This amplitude defines the effective coupling between the light and heavy quarks. Then, we derive an RG equation that governs the evolution of the effective coupling when we reduce the energy scale Λ . In this analysis, we assume a sufficiently large chemical potential $\mu \gg \Lambda_{\text{QCD}}$, so that a perturbative analysis with respect to a small value of the QCD coupling constant g is justified. We also assume that the heavy-quark mass is much larger than typical scales of the system such as the chemical potential, i.e., $m_{\text{H}} \gg \mu$.

Based on the perturbation theory for the effective interaction at high density (391), we can evaluate the scattering amplitude between a light quark and a heavy-quark impurity. In the high-density QCD, the effective coupling G in Eq. (391) can be obtained from the one-gluon exchange. When a heavy-quark mass is much larger than the other scales in the system, one may organize an expansion with respect to $1/m_{\text{H}}$. In the leading order of the expansion, i.e., in the heavy-quark limit $m_{\text{H}} \rightarrow \infty$, only the temporal component of the gauge field is coupled to the heavy quark. Therefore, the color electric interaction becomes the dominant interaction in this system, and the color magnetic interaction is suppressed by $1/m_{\text{H}}$ at the vertices. Below, we consider the S -wave scattering channel. Then, the S -wave projection of the color-electric interaction gives the effective coupling⁸²

$$\begin{aligned}
G \delta^{ab} &= -(ig)^2 \frac{1}{2} \int_{-1}^1 d \cos \theta D_{00}^{ab}(p^{(1)} - p^{(3)}; \mu) \\
&\simeq \frac{g^2}{4\mu^2} \delta^{ab} \int_{-1}^1 \frac{d \cos \theta}{(1 - \cos \theta) + m_{\text{D}}^2/(2\mu^2)} \\
&\simeq \frac{g^2}{4\mu^2} \ln \left(\frac{4\mu^2}{m_{\text{D}}^2} \right) \delta^{ab}. \tag{423}
\end{aligned}$$

The Debye mass is given as $m_{\text{D}}^2 = \alpha_s \mu^2 / \pi$. We put the initial and final momenta of the light quark on the Fermi surface since the Kondo effect occurs in such a low-energy regime. Then, we have integrated the angle between the Fermi velocities $\mathbf{v}_{\text{F}}^{(1)}$ and $\mathbf{v}_{\text{F}}^{(3)}$. Note that the effective interaction is diagonal in the color space. Using this effective coupling, the tree amplitude is expressed as

$$\mathcal{M}_0^{S\text{-wave}} = G \sum_{r=1}^{N_c^2-1} (t^r)_{ij} (t^r)_{lm}, \tag{424}$$

where we have suppressed the trivial spinor structure and summed over the color matrix t^r .

⁸²We use the hard dense loop (HDL) gluon propagator $D^{\mu\nu}(k) = P_L^{\mu\nu}/(k^2 - \Pi_L) + P_T^{\mu\nu}/(k^2 - \Pi_T)$ where $P_T^{\mu\nu} = \delta^{\mu i} \delta^{\nu j} (\delta^{ij} - k^i k^j / |\mathbf{k}|^2)$ and $P_L^{\mu\nu} = -(g^{\mu\nu} - k^\mu k^\nu / k^2) - P_T^{\mu\nu}$. The longitudinal component of the gluon self-energy provides the screening mass $\Pi_L \rightarrow m_{\text{D}}$ in the static limit. Note also that a similar S -wave projection was performed for the Cooper pairing in Refs. [390, 393, 394].

Next, we consider the one-loop amplitudes. There are two relevant diagrams for the Kondo effect, i.e., the box and crossed diagrams shown in Fig. 39. Based on the effective coupling G and the effective Lagrangians (386) and (390), those amplitudes are written down as (see Ref. [389] for further details)

$$i\mathcal{M}_{1,\text{box}}^{S\text{-wave}} = -(iG)^2 \mathcal{T}^{(a)} \sum_{\mathbf{v}_F} \int \frac{d^4\ell}{(2\pi)^4} \frac{i^2}{(-\ell^0 + i\epsilon)(\ell^0 - \ell_{\parallel} + i\ell^0\epsilon)}, \quad (425a)$$

$$i\mathcal{M}_{1,\text{crossed}}^{S\text{-wave}} = -(iG)^2 \mathcal{T}^{(b)} \sum_{\mathbf{v}_F} \int \frac{d^4\ell}{(2\pi)^4} \frac{i^2}{(+\ell^0 + i\epsilon)(\ell^0 - \ell_{\parallel} + i\ell^0\epsilon)}, \quad (425b)$$

where the infinitesimal imaginary part is assigned so that a positive (negative) value of ℓ^0 corresponds to a particle (hole) excitation near the Fermi surface. Again, we put the initial and final momenta of the light quark on the Fermi surface, i.e., $\ell_i^\mu = \ell_f^\mu = 0$. As required by Condition (iii), there is a difference between the color-matrix structures in the two diagrams, of which the explicit forms are given as

$$\mathcal{T}_{ij;lm}^{(a)} = \sum_{s,r}^{N_c^2-1} \sum_{k,k'}^{N_c} (t^r)_{ik} (t^s)_{kj} (t^r)_{lk'} (t^s)_{k'm}, \quad (426a)$$

$$\mathcal{T}_{ij;lm}^{(b)} = \sum_{s,r}^{N_c^2-1} \sum_{k,k'}^{N_c} (t^r)_{ik} (t^s)_{kj} (t^s)_{lk'} (t^r)_{k'm}. \quad (426b)$$

Performing the integrals in Eq. (425), we have

$$\mathcal{M}_{1,\text{box}}^{S\text{-wave}} = -G^2 \mathcal{T}^{(a)} \rho_F \int \frac{d\ell_{\parallel}}{\ell_{\parallel}} \theta(\ell_{\parallel}), \quad (427a)$$

$$\mathcal{M}_{1,\text{crossed}}^{S\text{-wave}} = -G^2 \mathcal{T}^{(b)} \rho_F \int \frac{d\ell_{\parallel}}{\ell_{\parallel}} \theta(-\ell_{\parallel}), \quad (427b)$$

where the spinor structures are the same as that of the tree amplitude and are suppressed for notational simplicity. The step functions stem from the locations of the poles with the infinitesimal imaginary parts,⁸³ and indicate that the box and crossed diagrams correspond to the particle and hole contributions. The density of states on the Fermi surface ρ_F has been obtained as⁸⁴

$$\rho_F = \sum_{\mathbf{v}_F} \int \frac{d^2\ell_{\perp}}{(2\pi)^3} = \frac{4\pi\mu^2}{(2\pi)^3} = \frac{\mu^2}{2\pi^2}. \quad (428)$$

As in the analysis of the magnetic catalysis, we obtain the one-loop amplitude given by a product of the density of states and the logarithm from the remaining integrals in Eq. (427).

Then, the sum of the two one-loop amplitudes, integrated over a thin momentum shell, is obtained as

$$\begin{aligned} \mathcal{M}_1^{S\text{-wave}} &= \mathcal{M}_{1,\text{box}}^{S\text{-wave}} + \mathcal{M}_{1,\text{crossed}}^{S\text{-wave}} \\ &= -G^2 \rho_F \ln\left(\frac{\Lambda}{\Lambda - \delta\Lambda}\right) (\mathcal{T}^{(a)} - \mathcal{T}^{(b)}). \end{aligned} \quad (429)$$

⁸³One obtains the same result in the both cases where the contour is enclosed in the upper- and lower-half planes.

⁸⁴In the high-density effective theory, the Fermi velocity \mathbf{v}_F is the label of patches on the Fermi surface [388]. Therefore, the combination of the sum over the Fermi velocity and the two-dimensional integral on a patch cover the whole Fermi sphere.

The relative minus sign in the curly brackets originates from the step functions in Eq. (427), and would lead to a cancellation between the logarithms if the interaction were an Abelian type. In case of a non-Abelian interaction, one may use the following decomposition

$$\mathcal{T}_{ij;lm}^{(a)} = \frac{N_c^2 - 1}{4N_c^2} \delta_{ij} \delta_{lm} - \frac{1}{N_c} \sum_r^{N_c^2 - 1} (t^r)_{ij} (t^r)_{lm}, \quad (430a)$$

$$\mathcal{T}_{ij;lm}^{(b)} = \frac{N_c^2 - 1}{4N_c^2} \delta_{ij} \delta_{lm} + \left(\frac{N_c}{2} - \frac{1}{N_c} \right) \sum_r^{N_c^2 - 1} (t^r)_{ij} (t^r)_{lm}. \quad (430b)$$

To get the above expressions, one can apply an identity in Eq. (A.38) of Ref. [66] to Eq. (426). In this case, the cancellation is not complete, and we find a term surviving in the sum

$$\mathcal{M}_1^{S\text{-wave}} = G^2 \frac{N_c}{2} \rho_F \ln \left(\frac{\Lambda}{\Lambda - \delta\Lambda} \right) \sum_r^{N_c^2 - 1} (t^r)_{ij} (t^r)_{lm}. \quad (431)$$

There remains a logarithmic quantum correction that modifies the effective coupling G .

Now, combining the results in Eqs. (424) and (431), we obtain the RG equation

$$\Lambda \frac{dG}{d\Lambda} = -\frac{N_c}{2} \rho_F G^2. \quad (432)$$

The solution of this RG equation is found to be

$$G(\Lambda) = \frac{G(\Lambda_0)}{1 + 2^{-1} N_c \rho_F G(\Lambda_0) \ln(\Lambda/\Lambda_0)}. \quad (433)$$

Here, Λ_0 is the initial energy scale, and the initial condition of G is given by the tree-level result in Eq. (423) as $G(\Lambda_0) = (g^2/4\mu^2) \ln(4\mu^2/m_D^2)$. When the interaction is attractive [$G(\Lambda_0) > 0$], the effective coupling (433) is enhanced according to a negative beta function as the energy scale Λ is reduced. This behavior is characteristic in the Kondo effect as pointed out first by J. Kondo [412]. We know analogous patterns in the occurrence of the Landau poles for superconductivity and the asymptotic freedom in QCD, though the asymptotic freedom in QCD is induced by nonlinear gluon interactions instead of the dimensional reduction as mentioned in Sec. 7.1. We read off the location of the Landau pole that is called the Kondo scale:

$$\Lambda_K = \Lambda_0 \exp \left(-\frac{2}{N_c \rho_F G(\Lambda_0)} \right) = \mu \exp \left(-\frac{4\pi}{N_c \alpha_s \ln(4\pi/\alpha_s)} \right), \quad (434)$$

where we took the initial energy scale as $\Lambda_0 = \mu$. As we approach the Kondo scale, the system becomes non-perturbative no matter how small the initial coupling $G(\Lambda_0)$ and α_s are. Intuitively, the carriers are more strongly trapped around an impurity due to this strong-coupling nature. Therefore, the resistance is enhanced below the Kondo temperature $T_K \sim \Lambda_K$, and there emerges a local minimum at T_K in the temperature dependence of the resistance. The reader is referred to Ref. [415] for estimates of the transport coefficients.

The Kondo effect contains rich nonperturbative physics. One of important observations among those is that the sign of the two-loop beta function depends on the number of scattering channels. In case of the QCD Kondo effect, the number of channels k corresponds to that of the flavor degrees of freedom, while the non-Abelian group corresponds to the color symmetry group $SU(N_c)$. This is called the multi-channel Kondo effect in which the sign of the beta function could be changed for a sufficiently large number of the flavor channels as compared to N_c . This perturbative observation already suggests that

it is not straightforward to settle the fate of the Kondo effect below the Kondo scale, and one needs to ultimately invoke on nonperturbative methods. There are seminal works in condensed matter physics which developed powerful nonperturbative methods such as the Wilson’s numerical renormalization group [43] and applications of the Bethe ansatz [416, 417] and of the (1+1)-dimensional conformal field theory (CFT) [418, 419]. For the quark matter, the multi-channel Kondo effect was first investigated in Ref. [420], and the CFT approach was applied in Ref. [421, 422] (see also Ref. [423]). In the latter, the CFT analysis was generalized to the k -channel $SU(N)$ Kondo effect with general integers k and N . Besides, there are a number of developments in the QCD Kondo effect including the mean-field analyses [389, 415, 424–436].

7.3.2 The magnetically induced QCD Kondo effect

Next, we discuss the magnetically induced QCD Kondo effect [336]. We will derive the RG equation for the amplitude of the light quark, which carries the electric charge q_f , scattering off the heavy-quark impurity in the strong magnetic field. Here, we take $q_f B \gg T^2$ so that the dynamics of light quarks is dominated by the LLL. Under this assumption, the gluon screening is also dominantly provided by the quark loop in the LLL. Effects of the magnetic field directly exerting on the heavy quark are suppressed by an inverse factor of the heavy quark mass m_H , so that those effects are assumed to be small, $q_f B/m_H^2 \ll 1$.

The computation below goes in parallel to that for the QCD Kondo effect with a similar kinematics in the heavy-light quark scattering and is also partly similar to that for the magnetic catalysis in the LLL (cf. Sec. 7.2.1). Also, we take the same strategy as in the RG analysis of the magnetic catalysis in the “screened QED.” Namely, the RG evolution starts from the initial scale $\Lambda_0 \sim \sqrt{q_f B}$,⁸⁵ and is divided into the two stages above and below the scale of the gluon screening mass (cf. Fig. 38). Similar to Eq. (404), we introduce an effective coupling for the heavy-light system

$$G = (ig)^2 \int \frac{d^2 \mathbf{q}_\perp}{(2\pi)^2} \frac{g_{00}}{q_\parallel^2 - \mathbf{q}_\perp^2 - m_g^2} e^{-\frac{q_\perp^2}{4q_f B}}. \quad (435)$$

The temporal component of the metric g^{00} reflects the fact that only the electric gluon is relevant in the leading order of the heavy-quark expansion. The temporal component of the gluon propagator has a static screening mass $m_g^2 = (\alpha_s/\pi)q_f B$ in the strong magnetic field which is a half of the photon mass (403) due to the color trace (up to the replacement of α_s by α and $q_f B$ by eB for $N_f = 1$). While the numerical factor in the Gaussian was one half in Eq. (404), it is now one fourth since only the light quarks are subject to the Landau-level discretization. For the same reason, the Schwinger phase has a slightly different form which is however negligible in the current computation [336].

We shall perform the integral in Eq. (435) with respect to the transverse momentum \mathbf{q}_\perp . Remember that we performed a similar integral to get the results in Eq. (416). As discussed there, the lower boundary of the integral is given by Λ in Region I ($\Lambda > m_g$), while it should be replaced by m_g in Region II ($\Lambda < m_g$). In both regions, the upper boundary of the integral is given by $4q_f B$ due to the Gaussian factor. With these integral regions, we find that

$$G \simeq \begin{cases} \alpha_s \ln \left(\frac{4q_f B}{\Lambda^2} \right) & \text{Region I} \\ \alpha_s \ln \left(\frac{4q_f B}{m_g^2} \right) & \text{Region II} \end{cases}. \quad (436)$$

Based on the effective interaction term in Eq. (392), we evaluate the scattering amplitude at the energy

⁸⁵As in Sec. 7.2.1, we omit the symbols of absolute value for $|q_f B|$.

scale Λ . In terms of the effective coupling G , the tree-level amplitude can be expressed as

$$\mathcal{M}_0^{\text{LLL}} = G \sum_r^{N_c^2-1} (t^r)_{ij} (t^r)_{lm}. \quad (437)$$

The trivial spinor structures are again suppressed for notational simplicity. The logarithmic dependence of the effective coupling on Λ contributes to the RG evolution in Region I.

Next, we consider the one-loop scattering amplitudes. The two relevant one-loop diagrams in the Kondo system (cf. Fig. 39) can be written down as

$$\mathcal{M}_{1,\text{box}}^{\text{LLL}} = G^2 \mathcal{T}^{(a)} \int_{\Lambda-\delta\Lambda}^{\Lambda} \frac{dk_z}{2\pi} \frac{1}{-k_z}, \quad (438a)$$

$$\mathcal{M}_{1,\text{crossed}}^{\text{LLL}} = G^2 \mathcal{T}^{(b)} \int_{\Lambda-\delta\Lambda}^{\Lambda} \frac{dk_z}{2\pi} \frac{1}{k_z}, \quad (438b)$$

where the spinor part is the same as that of the tree-level amplitude and the color factors are already given in Eq. (426). The total one-loop amplitude at the energy scale $\Lambda - \delta\Lambda$ is thus found to be

$$\begin{aligned} \mathcal{M}_1^{\text{LLL}} &= \mathcal{M}_{1,\text{box}}^{\text{LLL}} + \mathcal{M}_{1,\text{crossed}}^{\text{LLL}} \\ &= G^2 \frac{N_c}{2} \ln \left(\frac{\Lambda}{\Lambda - \delta\Lambda} \right) \sum_r^{N_c^2-1} (t^r)_{ij} (t^r)_{lm}. \end{aligned} \quad (439)$$

The logarithmic contributions from the box and crossed diagrams do not cancel each other thanks to the non-Abelian property of QCD. The strong magnetic field does not spoil the non-Abelian property, and the QCD Kondo effect is compatible with the dimensional reduction induced by the Landau quantization; The non-Abelian property would be lost in a strong magnetic field if it needed a spin interaction.

Combining the scattering amplitudes at the tree and one-loop levels, we find the RG equations for the effective coupling G :

$$\Lambda \frac{d}{d\Lambda} G(\Lambda) = -2\alpha_s - \frac{N_c}{4\pi} G^2(\Lambda) \quad \text{Region I}, \quad (440a)$$

$$\Lambda \frac{d}{d\Lambda} G(\Lambda) = -\frac{N_c}{4\pi} G^2(\Lambda) \quad \text{Region II}. \quad (440b)$$

The first term in the RG equation (440a) originates from the logarithmic dependence of the tree-level amplitude. These RG equations are quite similar to those for the magnetic catalysis in Eq. (418). As in the previous analysis, we successively solve the RG equations in Region I and II, and connect the solutions at the screening mass [336] (see Sec. 7.2.1). Explicitly, the solution at $\Lambda = m_g$ is obtained from Eq. (440a) as

$$G(m_g) = \alpha_s \ln \frac{4q_f B}{m_g^2} \left\{ 1 + \frac{1}{3} \left(\sqrt{\frac{N_c \alpha_s}{8\pi}} \ln \frac{4q_f B}{m_g^2} \right)^2 + \dots \right\}. \quad (441)$$

Then, the final solution for $\Lambda < m_g$ is obtained from Eq. (440b) as

$$G(\Lambda) = \frac{G(m_g)}{1 + \frac{1}{4\pi} N_c G(m_g) \ln(\Lambda/m_g)}. \quad (442)$$

The solution (442) has a Landau pole, of which the location gives rise to the Kondo scale

$$\Lambda_K \simeq \sqrt{q_f B} \alpha_s^{1/3} \exp \left\{ -\frac{4\pi}{N_c \alpha_s \ln(4\pi/\alpha_s)} \right\}. \quad (443)$$

The expression of the Kondo scale resembles that of the dynamical mass induced by the magnetic catalysis (422) as a result of the screening effects included by the same hierarchy scheme.

If the Kondo scale (443) only depends on the magnetic field through the prefactor, it rapidly increases with an increasing B . However, the QCD coupling may be evaluated at $\sqrt{q_f B}$ consistently to the fact that the effective coupling in the Kondo scale must be evaluated at the initial scale $\Lambda \sim \sqrt{q_f B}$. In that case, the dependence of the running QCD coupling constant α_s on the magnetic field strength induces a nontrivial B -dependence of the Kondo scale. Inserting the running QCD coupling $\alpha_s(q_f B)^{-1} \simeq b_0 \ln(q_f B/\Lambda_{\text{QCD}}^2)$ with $b_0 = (11N_c - 2N_f)/12\pi$ into Eq. (443), we find the following B -dependence:

$$\frac{\Lambda_K^2}{\Lambda_{\text{QCD}}^2} \simeq \left[b_0 \ln \left(\frac{q_f B}{\Lambda_{\text{QCD}}^2} \right) \right]^{-2/3} \left(\frac{q_f B}{\Lambda_{\text{QCD}}^2} \right)^{1-2\gamma}, \quad (444)$$

where $\gamma = (4\pi b_0/N_c)/\ln\{4\pi b_0 \ln(q_f B/\Lambda_{\text{QCD}}^2)\}$ corresponds to the anomalous dimension for $\Lambda_K(B)$. The Kondo scale (444) increases slowly, but monotonically, as we increase the magnetic field. A similar behavior was discussed for the dynamical quark mass generated by the magnetic catalysis in the weak-coupling regime of QCD [437].

We have seen strong statements in the presence of a strong magnetic field: No matter how small the coupling strength is, an interaction between light fermions and antifermions induces the spontaneous chiral symmetry breaking [106, 324, 326] and an interaction between light and heavy fermions induces the Kondo effect [336]. Then, what if there are both light-light and light-heavy interactions? Which of the magnetic catalysis and the Kondo effect is stronger? This is like *the shield and spear paradox* in ancient China. The competition gives rise to a quantum phase transition [438].

7.4 Magnetic catalysis in QCD

In Sec. 7.2, we discussed the magnetic catalysis occurring in a weak-coupling theory, i.e., QED, as a consequence of the dimensional reduction. One might wonder what happens in QCD as a natural extension, where the chiral symmetry breaking plays a crucial role in the formation of the hadron spectrum. Indeed, the chiral symmetry in magnetic fields was first investigated with the effective models of QCD in the early works [371–376]. It then attracted even more attention after the clear recognition of the dimensional reduction mechanism [106, 324, 326]. An incomplete list of numerous studies on the QCD extensions includes those by the chiral perturbation theory [439–448], various types of chiral models [449–478], and holographic models [479–481].

The most interesting part of studying the magnetic catalysis in QCD is the interplay between the intrinsic strong-coupling nature in the asymptotic-free gauge theory and that induced by the quantum many-body effect via the dimensional reduction irrespective of the coupling strength in underlying microscopic theories. Such interplay has been investigated with the first-principle lattice QCD simulations over the last decade. The Monte-Carlo simulation is feasible since external magnetic fields do not cause the notorious sign problem (as long as the action is free of the sign problem in the absence of the magnetic field). This is opposed to the cases of electric fields. A lot of studies after around 2010 is driven by outcome of the lattice QCD simulations which we summarize below in detail. The reader is also referred to Ref. [482] for a review on the lattice formulation, Refs. [402, 483–485] for complementary review articles written in the early stages just after the lattice QCD results came out, and Refs. [228, 486] for a large volume of references and summary of technical details that may be missed in the discussions below.

7.4.1 Results from lattice QCD simulations

Here, we summarize the major results from the lattice QCD simulations at zero baryon density. In most cases, we do not mention details of each simulation set-up, for which the reader is referred to original papers in the reference list.

Summary of summary

First, let us summarize what we summarize. The main body of the summary will be somewhat long as we cite as many simulation results as possible in a chronicle way to clarify the issues resolved and not yet resolved as of the end of 2022. We also would like to give some comments and interpretations. Before doing so, we summarize minimum materials.

- Chiral condensate at zero temperature: The lattice QCD simulations have shown the enhancement of the chiral condensate at zero temperature as expected from the magnetic catalysis. However, there appeared a deviation between the results from the lattice QCD simulation and the chiral perturbation theory in the regime of strong magnetic fields.
- Chiral symmetry restoration at finite temperature: The simulation results at finite temperature were thought to be puzzling. The magnitude of the chiral condensate decreases as we increase the magnetic-field strength in spite of the increase at zero temperature. This phenomenon was named the *inverse magnetic catalysis*. It also appeared that the pseudo-critical temperature for the crossover chiral phase transition *decreases* as we increase the magnetic-field strength in contrast to the increase in QED and the NJL model (cf. Sec. 6.2.2).
- Deconfinement phase transition: The deconfinement phase transition temperatures read off from the Polyakov loop and the strange-quark susceptibility decrease as we increase the magnetic-field strength in a similar manner as the chiral phase transition temperature. Also, the heavy-quark potential has been measured. The string tension along the magnetic-field direction decreases as we increase the magnetic-field strength.
- Diagnosis of the inverse magnetic catalysis I - III: A magnetic field couples to quarks in the QCD action and observable operators. To identify the mechanism leading to the inverse magnetic catalysis, simulations were performed by turning off either of these couplings. It appeared that the chiral condensate is suppressed by the coupling to the QCD action near the transition temperature, while the coupling to the QCD action at low temperature as well as the coupling to the observable operators at any temperature act to enhance the chiral condensate.

One can also tune the quark mass as a part of simulation set-up and confirm that the inverse magnetic catalysis only occurs with a nearly physical-point quark mass where the dynamical quarks are well excited. Nevertheless, even with a large quark mass, the chiral phase transition temperature was found to decrease irrespective of the presence/absence of the inverse magnetic catalysis. In this respect, it is more useful to regard the inverse magnetic catalysis and the decrease of the chiral phase transition temperature as separate phenomena, and rather discuss the decreasing behaviors of all the aforementioned pseudocritical temperatures in parallel as a consequence of the magnetic enhancement of the dynamical-quark effects, that is, an enhancement of the screening effect.

- Exploring the further strong-field regime: When we increase the magnetic-field strength, the simulation results exhibit a systematic tendency for an enhancement of the strength of the chiral phase transition. Very recent simulation results suggested that the chiral phase transition is still a crossover transition at $eB = 4 \text{ GeV}^2$ but turns into a first-order transition at $eB = 9 \text{ GeV}^2$.

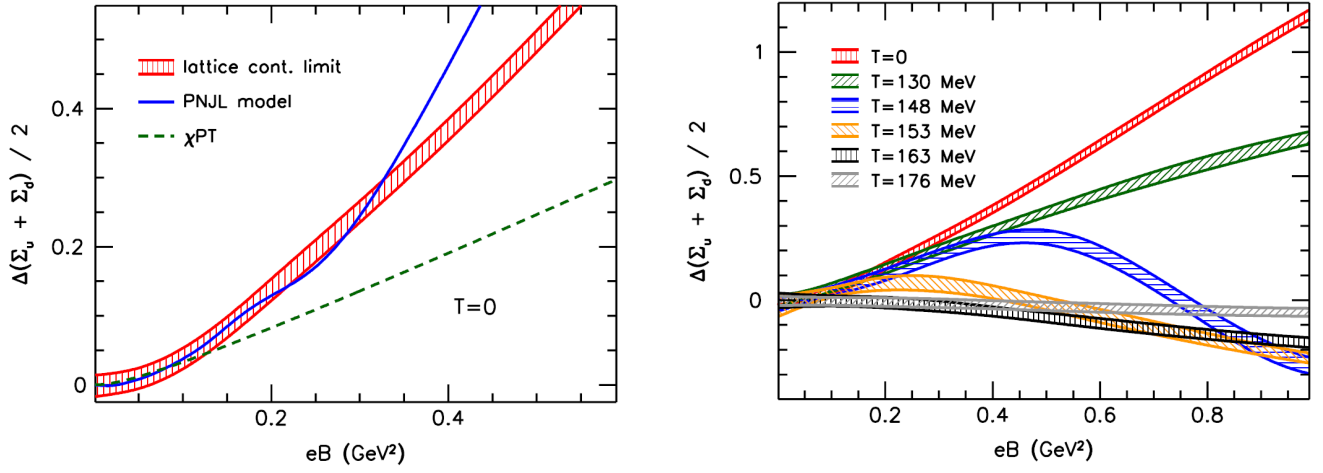


Figure 40: Lattice QCD simulation of the chiral condensate at $T = 0$ (left) and $T \neq 0$ (right) with the physical quark mass [487]. The chiral condensate at nonzero eB is shown as the difference, $\Delta\Sigma = \Sigma(eB) - \Sigma(0)$, and is averaged over the contributions of u and d quarks. The lattice simulation result is compared with the results from the NJL model [460] and the two-loop chiral perturbation theory [447, 448].

This can be the first indication of a first-order phase transition emerging directly from the QCD action once it is confirmed. There are also discussions about the existence of a first-order phase transition and an associated critical point in the deconfinement phase transition.

- Hadron spectrum: Simulation results for neutral and charged π , ρ , K , K^* are available so far at zero temperature. Very recent results from dynamical simulations suggest drastic modifications of the results from the quenched simulations. The Gell-Mann–Oaks–Renner relation in magnetic fields was confirmed by the lattice QCD simulation for the first time. The measurement of the heavy-quark potential was extended to the ever strongest magnetic field $eB = 9 \text{ GeV}^2$. At finite temperature, the meson correlation length, or the screening mass, was measured very recently.
- Magnetization: The magnetic susceptibility of the QCD matter was measured in the temperature range $100 \lesssim T \lesssim 300 \text{ MeV}$, indicating diamagnetism at $T \lesssim 150 \text{ MeV}$ and paramagnetism in the higher temperature region. The quark spin contribution was measured separately by an independent method. The quark spin contribution is found to be diamagnetic within the available data set up to $T \lesssim 200 \text{ MeV}$. However, the quark spin and orbital contributions should converge to the Pauli paramagnetism and the Landau diamagnetism, respectively, at asymptotically high temperature where quarks and gluons are expected to behave as free particles. The convergence could be slow with the logarithmic running of the QCD coupling constant.

Chiral condensate at zero temperature

As expected from the magnetic catalysis, the lattice QCD simulations, performed at zero temperature, have shown an enhancement of the chiral condensate with an increasing magnetic-field strength. A numerical simulation in a background magnetic field was first performed for the two-color and quenched QCD [488]⁸⁶ and then the three-color and quenched QCD [491]. The simulation was refined with the inclusion of the dynamical quarks [492, 493].

⁸⁶We add that the earliest numerical simulations were performed in an abelianized chromo-magnetic field [489, 490].

A lot of numerical improvements, such as simulations with the physical quark mass, larger system volumes, and finer lattice spacings, were achieved in Ref. [487]. In the left panel of Fig. 40, the lattice QCD simulation result is compared with the two-loop chiral perturbation theory [447, 448] and Polyakov-loop extended NJL model [460]. The chiral condensate exhibits a quadratic increase in the small eB region. This is a natural behavior since the chiral condensate is a charge-conjugation even quantity. The chiral perturbation theory indeed reproduces the quadratic increase $\sim \mathcal{O}(eB^2/(f_\pi^2 m_\pi^2))$ with f_π and m_π being the pion decay constant and pion mass, respectively [444, 493].⁸⁷ However, it should be noticed that the simulation result turns into a linear increase in the large eB region.⁸⁸ In this region, the chiral perturbation theory deviates from the simulation result. A very recent work suggests that this linear increase continues to the ever largest magnetic-field strength at $eB = 9 \text{ GeV}^2$ [494].

The chiral perturbation theory is a low-energy effective theory of QCD with the low-lying degrees of freedom, pions as the most important contribution [439–448]. Thus, its results should agree with the first-principle calculations for QCD in relatively weak magnetic fields $eB/\Lambda_{\text{QCD}}^2 \ll 1$. The computation at small values of m_π^2 , $eB \ll \Lambda_{\text{QCD}}^2$, but for an arbitrary ratio m_π^2/eB , was performed in Ref. [444, 445] as an extension of the computation at the chiral limit ($m_\pi^2/eB = 0$) [439]. The chiral perturbation theory, however, would not work as we increase the magnetic field strength, which appears as the deviation observed in the left panel of Fig. 40. This is because the low-lying degrees of freedom can be strongly modified by strong magnetic fields. For example, due to the explicit isospin-symmetry breaking in magnetic fields, charged pions are no longer the Nambu-Goldstone (NG) bosons; This is consistent with the observation that the ground-state energy levels of spinless charged particles are gapped out by the Landau quantization $m_{\pi^\pm}^2(B) = m_{\pi^\pm}^2(B=0) + |eB|$. Also, even neutral pions could be modified when internal motion of quarks and antiquarks are strongly constrained by strong magnetic fields. Eventually, naive hadronic effective theories break down when a large number of magnetic lines penetrates through the composite particles with the flux density larger than the QCD scale $eB \sim \Lambda_{\text{QCD}}^2 \sim 0.04 \text{ GeV}^2$. One needs to reconstruct hadrons with quarks and gluons in strong magnetic fields.

Chiral symmetry restoration at finite temperature

The next question would be how the chiral symmetry restoration occurs at finite temperature. One may think that the transition temperature T_c increases as we increase the magnetic field. We have indeed found that $T_c \sim \sqrt{|eB|} \sim m_{\text{dyn}}$ in Sec. 6.2 for the NJL model [325] and for QED [329, 330]. One can expect such results in these theory and model since the long-range correlation can be screened by the thermal excitations only when the excitations are activated over the mass gap of the order of $m_{\text{dyn}} \sim \sqrt{|eB|}$. In other words, the emergent scale is only one available scale that characterizes both m_{dyn} and T_c associated with the magnetic catalysis. In QCD, we, however, have an intrinsic scale, i.e., the QCD scale Λ_{QCD} , which could change the story.

Temperature dependence of the chiral condensate and associated chiral susceptibility has been studied with the lattice QCD simulations. The simulation result at the physical point, i.e., at the physical value of the current quark mass, has shown that the transition temperature *decreases* with an increasing magnetic field [495]. We summarize this surprising outcome and follow-up results in the followings.

In the right panel of Fig. 40, one finds that, while the chiral condensate is an increasing function of eB at zero and low temperatures, it turns into a decreasing function at higher temperatures. This turnover is more clearly seen in the left panel in Fig. 41; While the magnitudes of the chiral condensate is in an ascending order in the low temperature region, it becomes a descending order in the high temperature

⁸⁷The symmetry argument for the quadratic dependence assumes an analytic dependence of the chiral condensate on $|eB|$ at $eB = 0$; Otherwise, the leading correction could be $|eB|^\nu$ with $0 < \nu < 2$. If there is any non-analytic dependence, it should be studied with a finite pion mass so that one has a dimensionless expansion parameter eB/m_π^2 [444, 493].

⁸⁸The earlier result with a heavier quark mass had shown a quadratic increase [493] (see below for comments on the quark mass dependence.)

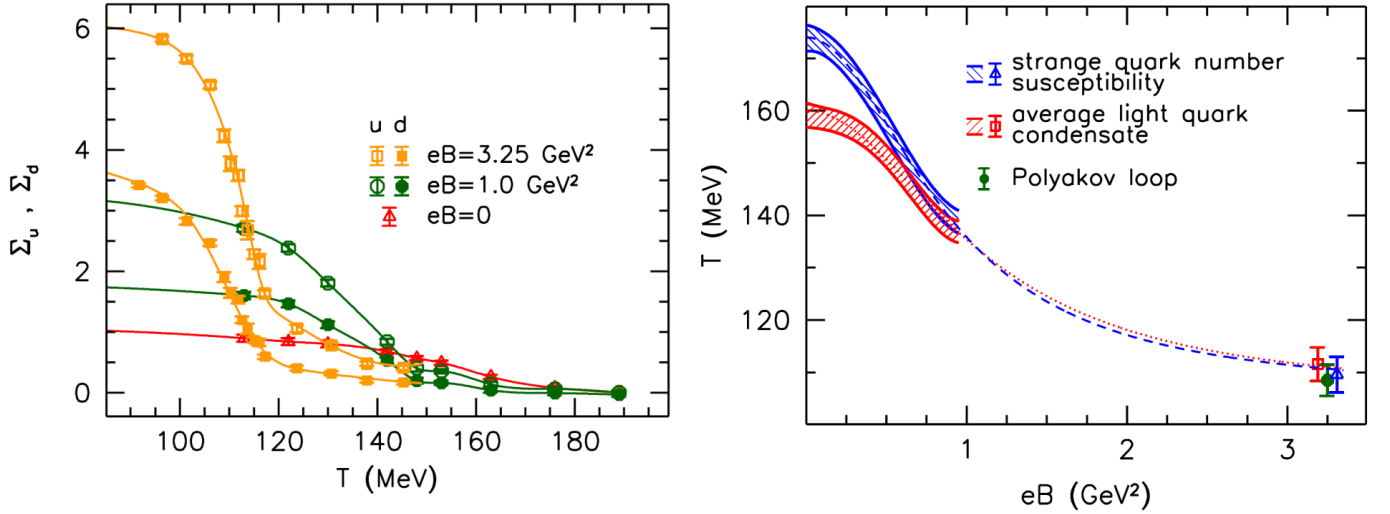


Figure 41: The temperature dependence of the u (d)-quark condensate Σ_u (Σ_d) (left) and the decreasing behavior of the transition temperatures T_c read off from the strange-quark susceptibility, the light-quark condensate, and the Polyakov loop (right), both taken from [368].

region. Furthermore, the transition temperature, read off from the chiral condensate, decreases with an increasing eB . The suppression of the chiral condensate observed near the transition temperature is dubbed the “inverse magnetic catalysis.” To be specific, we shall call the suppression of the chiral condensate the inverse magnetic catalysis rather than the decrease of the transition temperature. It appeared that those two phenomena are not necessarily equivalent with each other as observed in more recent simulation results (see Diagnosis II below).

In the right panel of Fig. 41, the decreasing behavior of the transition temperature is shown by a red band with error estimates [368]. Interpolation to a newer data point at $eB = 3.25 \text{ GeV}^2$, which appeared after the original work [495], suggests a monotonic decrease up to $eB = 3.25 \text{ GeV}^2$. The other data for the transition temperatures, read off from different observables, are discussed just below. Summary of the early numerical studies is available in Ref. [496] (see also Refs. [348, 349] for the two-color QCD).

Deconfinement phase transition

Phases of QCD in high and low temperature regions are distinguished by the color confinement property, as well as by the magnitude of the chiral condensate discussed above. The Polyakov loop serves as an order parameter for the deconfinement phase transition in a pure gluon theory. The strange-quark susceptibility is also studied as an alternative indicator for the deconfinement phase transition with quarks (see, e.g., Refs. [497–500]) since the Polyakov loop is not a strict order parameter when the center symmetry is explicitly broken by inclusion of quarks (cf. Sec. 6.6 and references therein).⁸⁹ For the sake of reference, we note that the transition temperatures at a vanishing magnetic field, which are read off from the Polyakov loop and the strange-quark susceptibility, are 170 MeV and 169 MeV up to error estimates, respectively [498]; The difference between those transition temperatures are much smaller than the magnetic-field effects shown in the right panel of Fig. 41.

⁸⁹While sensitivity of the Polyakov loop to the deconfinement phase transition should increase as the quark mass is increased to approach infinity, the sensitivity is yet questionable with light quarks near the physical point. The strange-quark susceptibility is not a strict order parameter either, but is expected to capture a difference between the confinement and deconfinement phases. That is, the strange-quark density fluctuation is enhanced in the deconfinement phase where the expected temperature scale $\gtrsim 150 \text{ MeV}$ is larger than the current strange-quark mass. In the confinement phase, the fluctuation is suppressed since strangeness is confined in hadrons heavier than the temperature scale. Accordingly, the strange-quark susceptibility can work better as an indicator of the confinement property than light-quark observables.

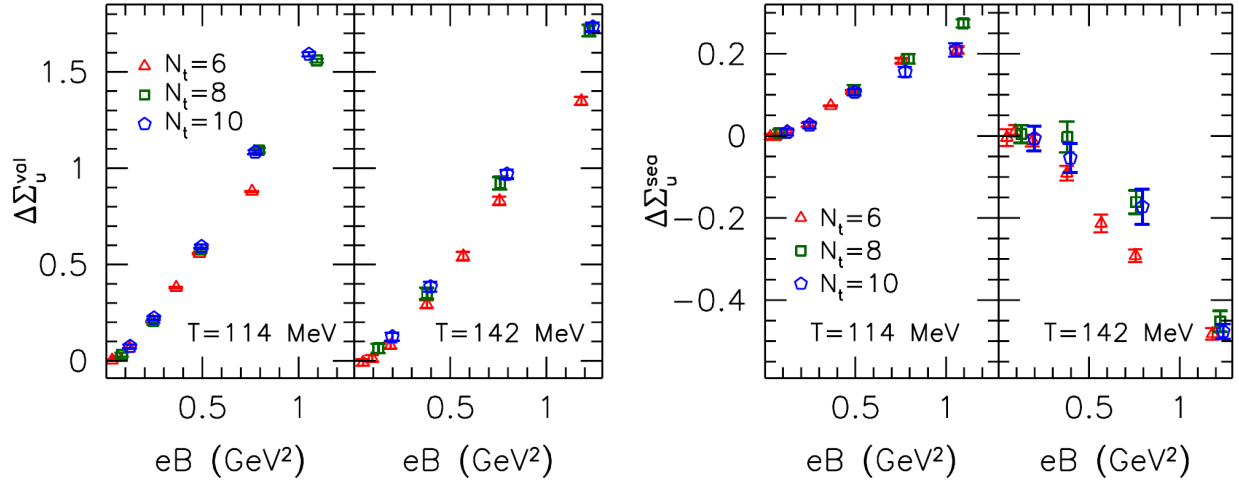


Figure 42: Magnitudes of the chiral condensate with the valence-quark effect (left) and with the sea-quark effect (right), taken from Ref. [367]. The chiral condensate at a vanishing magnetic field is subtracted to isolate the magnetic-field effects.

In the right panel of Fig. 41, the phase transition temperature read off from the strange-quark susceptibility is shown by the blue line [496] with a new data point at $eB = 3.25 \text{ GeV}^2$ [368]. This transition temperature decreases as we increase the magnetic-field strength.

The Polyakov loop was also measured in Refs. [367, 368, 492, 501–504]. In the right panel of Fig. 41, the transition temperature read off from the Polyakov loop is shown by a marker at $eB = 3.25 \text{ GeV}^2$ [368]. The transition temperature at a vanishing magnetic field is about 170 MeV as mentioned above [498]. Interpolation between those two points suggests a decrease of the transition temperature read off from the Polyakov loop as well (see also Ref. [502] for the decreasing behavior observed at a larger pion mass $m_\pi = 440 \text{ MeV}$).

Those observations suggest that the deconfinement phase transition occurs significantly at lower temperatures in strong magnetic fields than at a vanishing magnetic field *albeit* in a crossover manner. Those two transition temperatures as well as that from the chiral condensate exhibit the similar decreasing behaviors. Also, the three data points at $eB = 3.25 \text{ GeV}^2$ indicates degeneracy among the three transition temperatures, while, at a vanishing magnetic field, there is splitting between the transition temperatures from the chiral condensate and strange-quark susceptibility by about 10 – 15 MeV.

Measurement of the heavy-quark potential provides complementary information of the confinement properties and a more direct access to modification of the confinement potential profile such as the spatial anisotropy induced by magnetic fields [351, 494, 505–507] (see the summary of hadron spectrum given below for more discussions). It is worth adding that a heavy-quark potential in a strong *electric* field was also investigated with lattice simulation *albeit* for a sign-problem free theory that contains two fermions having the same magnitudes and opposite signs of electric charges [508]. A strong electric field gives rise to a tendency towards deconfinement because the linear confinement potential is diminished by a voltage that is also a linear function of the distance. The critical electric field, which cancels the confinement potential, is given by the string tension.

Diagnosis of the inverse magnetic catalysis I: Sea-quark effect

The inverse magnetic catalysis, which refers to the suppression of the chiral condensate, and the decrease of the chiral transition temperature shed light on distinctive properties of QCD not seen in QED and the chiral models. It should be a consequence of nonperturbative aspects of QCD probed by strong magnetic fields. The deconfinement transition temperatures, read off from the Polyakov loop and the

strange-quark susceptibility, also show the decreasing behaviors similar to that of the chiral transition temperature.

To identify the mechanism leading to the inverse magnetic catalysis, it is useful to investigate the breakdown of the magnetic-field effects as originally proposed in Ref. [493]. In the lattice QCD simulations, magnetic fields couple to the quark fields in the observable operator $\bar{\psi}\psi$ and the QCD action; We shall call them the “valence-quark effect” and “sea-quark effect,” respectively, according to Ref. [367] where improved numerical simulations were reported. The simulation results have shown that the “valence-quark effect” from the former coupling enhances the chiral condensate at any temperatures as expected from the magnetic catalysis [367]. Along with the Banks-Casher relation (in the massless limit), this effect may be rephrased as an enhancement of quark zero modes by the Landau degeneracy. Similar interpretation holds with the low-energy spectral density in massive cases. On top of this picture for non-interacting quarks, QCD interaction effects can change the dependence on the magnetic-field strength through modification of the spectral density at the quantitative level (see Ref. [509] for a distribution of the Dirac eigenvalues for interacting quarks on the lattice).

In contrast to the valence-quark effect, the sea-quark effect exhibits a turnover from an enhancement of the chiral condensate in low temperature to a suppression near the transition temperature [367]. The breakdown is shown in Fig. 42.⁹⁰ The plot origin is located with subtraction of the chiral condensate at a vanishing magnetic field. The left panel shows the valence-quark effect on the magnitude of the chiral condensate, where the magnetic field in the fermion determinant, resulting from the fermionic Gaussian path integral of the QCD action, is switched off by hand. Plots at two different temperatures exhibit similar increasing behaviors. The right panel shows the sea-quark effect, where the magnetic field acting on the observable operator is switched off by hand. The sea-quark effect acts to enhance the chiral condensate at the lower temperature (see also Ref. [493] for a consistent result with a larger quark mass). However, the sea-quark effect turns to suppressing the chiral condensate near the transition temperature. The inverse magnetic catalysis occurs when this turnover occurs in the sea-quark effect and the suppression due to the sea-quark effect is strong enough to overwhelm the enhancement due to the valence-quark effect. Therefore, the sea quarks, which are also often called the dynamical quarks, are identified as the main player in the inverse magnetic catalysis. More recent simulations have shown the valence- and sea-quark effects on the light-quark condensate at various temperatures [510], which confirms the results in Fig. 42.

The sea-quark effect is also identified by measuring the gluon condensate. There is no counterpart of the valence-quark effect in the gluon condensate simply because magnetic fields do not directly couple to gluons. The simulation results have shown that the gluon condensate gives rise to a turnover similar to that of the sea-quark effect on the chiral condensate. That is, the gluon condensate is enhanced in low temperature but is suppressed near the transition temperature [350], which may be interpreted as a consequence of the sea-quark effect on the gluon condensate. Notice also that the Polyakov loop discussed above is another purely gluonic observable, and thus the decreasing transition temperature read off from the Polyakov loop should originate from the sea-quark effect.

Also, one should note that the sea-quark effect is blind to the charges of observable operators by definition, while the valence-quark effect can depend on electric charges of quark fields if the quark flavor sum is not taken in an observable operator. Note also that the flavor sum in the QCD action is always taken for the sea-quark effect. Numerical simulation results have shown that there is no significant difference between the transition temperatures read off from the u -quark condensate and the d -quark condensate [368]; Both of the transition temperatures exhibit almost the same decrease in spite of the charge difference. Such a charge-blind effect should originate from the sea-quark effect. On the other hand, a charge-dependent effect is found in the absolute magnitudes of the u -quark condensate and the

⁹⁰Note that the full result for the chiral condensate is not simply reconstructed as a sum of the valence-quark and sea-quark contributions beyond the linear order in the magnetic-field strength.

d -quark condensate shown in the left panel of Fig. 41; The magnitude for d quark is almost a half of that for u quark (see also Ref. [493] for an earlier simulation result). This difference may imply the existence of an overall degeneracy factor $\sim |q_f B|/(2\pi)$ with a quark electric charge q_f stemming from the valence-quark spectrum distribution as mentioned above as well. See below for a dependence on the valence-quark mass.

Diagnosis of the inverse magnetic catalysis II: Quark mass dependences

While the sea-quark effect was identified as the driving force for the inverse magnetic catalysis, the magnitude of the sea-quark effect depends on a value of the current quark mass in the numerical simulation set-up. The sea-quark effect is absent in the infinitely heavy quark limit, i.e., the quenched simulations, and becomes larger as the quark mass is reduced to the physical point. Thus, the quark mass can be an important control parameter among other simulation parameters [487, 493]. Besides, there could be a dependence on the valence-quark mass as well because the effective coupling strengths between quark fields in observable operators and gauge fields is suppressed by a quark mass. This dependence can be studied by comparing the light-quark condensate and the strange-quark condensate (with the same sea-quark mass) [510].

In the early studies, neither the suppression of the chiral condensate nor the decrease of the transition temperature was observed in quenched simulations [488, 491] and simulations with a large current quark mass [492, 493] where the sea-quark effect is suppressed. Comparing the simulation set-ups, a large current quark mass and/or the unimproved staggered fermion used in the early works [492, 493] were thought to be possible reasons why those phenomena were not observed [502].

The quark-mass dependence was elaborated in recent works with improved staggered fermions [502, 503] and with the unimproved staggered fermion [511]. With improved staggered fermions, the simulation results exhibit the inverse magnetic catalysis near the transition temperature when the quark mass is small, but the magnetic catalysis at any temperature when the quark mass is large [502, 503]. Namely, it was found that, as the current quark mass is increased at a fixed temperature, a turnover from the inverse magnetic catalysis to the magnetic catalysis occurs somewhere between the corresponding pion masses $m_\pi = 343$ MeV and $m_\pi = 664$ MeV when $eB = 0.425, 0.85$ GeV² [502]. An updated work provided a consistent estimate of the turnover point to be $m_\pi \sim 500$ MeV when $eB = 0.6$ GeV² (see Ref. [503] for the exact value, the issue of scale setting, and the simulation setup).

However, from the above simulations with the *improved* staggered fermions, it appeared that the transition temperature still *decreases* even when the inverse magnetic catalysis, the suppression of the chiral condensate, does not occur with a large quark mass [502, 503]. To disentangle possible lattice artifacts due to the discretization methods, numerical simulations were performed with the *unimproved* staggered fermion in Refs. [511, 512] as a mimic of the early works [492, 493]. In this set-up, the transition temperature *increases* with an increasing magnetic-field strength and the inverse magnetic catalysis does not occur at any temperature. Therefore, it was concluded that the increasing transition temperature observed in the early works [492, 493] is not ascribed to a large quark mass but to the use of unimproved staggered fermion [504].

One can also study a dependence on the valence-quark mass. This serves as not only a control test but also a physical set-up that provides us with an insight into possible differences between the light-quark and strange-quark condensates. The strange-quark condensate as well as the light-quark and light-strange mixed condensates were computed very recently with dynamical simulations [510]. The results for the strange-quark condensate suggests that the valence-quark effect is stronger than the sea-quark effect at any temperatures and the inverse magnetic catalysis does not occur when the valence-quark mass is as large as the physical strange-quark mass. Nevertheless, the transition temperature, read off from the strange-quark condensate, decreases with an increasing magnetic-field strength. Namely, the balance between the valence-quark and sea-quark effects is affected by the valence-quark mass. In

this simulation, the strange-quark and light-quark masses are fixed at the physical value and one tenth of the strange-quark mass, respectively, which corresponds to kaon mass ~ 507 MeV and pion mass ~ 220 MeV.

It appeared in the last decade that the decreases of the transition temperatures are commonly seen in various observables of QCD thermodynamics, i.e., the u -quark condensate, the d -quark condensate, the s -quark condensate, the gluon condensate, the Polyakov loop, and the strange-quark susceptibility, in spite of the distinctive properties of the observable operators. The common main player is the sea-quark effect, of which the temperature dependence was found to be particularly important. In contrast, we have seen just above that whether or not the inverse magnetic catalysis occurs depends on the observable operators, i.e., the valence-quark mass, due to the competition with the valence-quark and sea-quark effects. Therefore, one can get a better insight if we regard the inverse magnetic catalysis of the chiral condensate as a separate issue from the common decreases of the transition temperatures.

It is worth adding that, to investigate connections between the chiral restoration and meson properties at finite temperature, a Ward-Takahashi identity was derived for the chiral transformation in Ref. [513] (see also Ref. [359]) and was confirmed with the aforementioned dynamical simulations at finite temperature [510]. The Ward-Takahashi identity relates the chiral condensate to the spacetime integral of the meson-meson correlator in the pseudoscalar channel. The same authors investigated possible correlations between the chiral condensate and the meson screening mass that is read off from the exponential decay of the meson-meson correlator at the long *spatial* distance limit as originally computed in Ref. [514, 515] (see the section of “hadron spectrum” below for a difference between the screening mass and the pole mass). The dynamical simulation results have shown that the valence-quark and sea-quark effects act on the screening mass with opposite tendencies. That is, the screening masses in the pseudoscalar channels are enhanced by the sea-quark effect as we increase the magnetic-field strength, while they are suppressed by the valence-quark effect [510]. Here, the valence-quark effect refers to a direct coupling of a magnetic field to the meson operator in the correlator.

Also, comparison between the light-quark and strange-quark channels suggested a correlation that the sea-quark effect overwhelms the valence-quark effect both on the meson screening mass and the chiral condensate when the inverse magnetic catalysis occurs [510]. However, a direct connection between the screening mass and the chiral restoration are yet elusive. This may be partly due to lack of clear understanding of what the temperature dependence of the screening mass tells us in the confinement phase and near the transition temperature even in the absence of magnetic fields; Note that this screening mass is not of gluons or the confinement force. It may be interesting, for instance, to check degeneracy between the scalar and pseudoscalar channels as well as between the vector and axial ones as a signal of chiral symmetry restoration rather than temperature dependences in single channels; There are such studies in the absence of magnetic fields (see Refs. [516, 517] and references therein).

Diagnosis of the inverse magnetic catalysis III: Interpreting the sea-quark effect

We have seen that the temperature dependence of the sea-quark effect is particularly important as observed in Fig. 42 (see also Ref. [510]). Now, we shall speculate how the sea-quark effect can enhance the chiral condensate in low temperature and suppress it near the transition temperature. In Sec. 7.2, we have identified two-fold effects of magnetic fields on the formation of the chiral condensate *albeit* with perturbative calculations. The modification of the screening effect, through the fermion loops inserted in the gauge-boson propagators, corresponds to the sea-quark effect, while the dimensional reduction on the scattering fermions, leading to the magnetic catalysis, corresponds to the valence-quark effect. In general, screening effects diminish the magnitude of particle pairing or condensation.

According to the above correspondence, the overall tendency in the temperature dependence can be understood as follows. The sea-quark effect leads to the *enhancement* of the chiral condensate in low temperature because of a *suppression* of the screening effect by a dynamical quark mass in strong

magnetic fields that is larger than that at a vanishing magnetic field. The dynamical quarks can be, nevertheless, excited by thermal energy at finite temperature. Once the minimum energy cost, the dynamical quark mass, is overcome by thermal energy, the screening effect is *enhanced* by abundant low-energy excitations in the Landau degeneracy as opposed to the low temperature case. Then, the sea-quark effect leads to the *suppression* of the chiral condensate because of the *enhancement* of the screening effect.

An implicit condition assumed above is that the quarks in strong magnetic fields have a small mass enough to develop the screening effect near the transition temperature. Once the mass threshold is well overcome by thermal energy, the screening effect is enhanced as mentioned just above. However, the quark mass could grow as we increase the magnetic-field strength. In such a case, the suppression of the screening effect, and associated enhancement of the chiral condensate by the sea-quark effect, would continue all the way from zero to transition temperatures; We would not see the inverse magnetic catalysis. This is the case of QED and the NJL model mentioned earlier due to the monotonic growth of the dynamical quark mass and may also be what is going on in the lattice QCD simulations with a large current quark mass [502, 503] (where generation of a large dynamical mass is also expected due to a suppression of the screening effect by the large current mass).

One should investigate whether the total quark mass from the current and dynamical contributions remains small enough in strong magnetic fields. This question was posed and investigated in Refs. [73, 518]. As discussed in Sec. 7.2, the magnitude of the dynamical mass is sensitive to interaction details. We will discuss this point later in this section with a QCD-motivated interaction. This is an interesting and basic issue for understanding QCD in strong magnetic fields.

Exploring the further strong-field regime

We have seen that the transition temperatures decrease up to $eB = 3.25\text{GeV}^2$. Here, we pay attention to the order of phase transition as well. In the left panel of Fig. 41, the chiral phase transition remains a crossover transition without a singularity or discontinuity in the curves. Nevertheless, we notice that the slope in the transition region becomes steeper as we increase the magnetic-field strength, which has been pointed out in the very early studies [492, 495]. One might expect that the phase transition could turn into a singular one as we further increase the magnetic-field strength.

More careful numerical analyses by the finite-size scaling method yet confirm the crossover transition up to $eB = 3.25\text{ GeV}^2$ and, at the same time, the tendency toward the singular phase transition [368]. Those results motivate us to explore the phase structures in further strong magnetic fields. A first-order phase transition was indeed observed with the unimproved staggered fermion [504],⁹¹ while determining the critical temperature and magnetic field was left to improved simulations. Very recent improved simulation results suggested that the chiral phase transition remains a crossover transition at $eB = 4\text{ GeV}^2$ but is a first-order transition at $eB = 9\text{ GeV}^2$ [507]. The first-order phase transition temperature was estimated to be around 63 MeV, while the pseudo-critical temperature at $eB = 4\text{ GeV}^2$ is around 98 MeV. The transition temperature still keeps decreasing from 113 MeV at $eB = 3.25\text{ GeV}^2$ shown in Fig. 41, though one needs to be careful about comparison among the data obtained with different simulation set-ups. Those are the very first reports of the indication for a first-order phase transition in QCD, including the case in the absence of magnetic fields, and certainly deserves further confirmation and extensions, which requires improvements in simulation set-ups (see discussions in Ref. [507]). Scanning the phase structures at various magnetic-field strengths is a necessary extension to draw the first-order transition line and locate an associated critical point. In this perspective, it is interesting to investigate the critical phenomena near the possible critical point.

⁹¹Without improved staggered fermion, the transition temperature increases with an increasing magnetic field as mentioned in the above diagnosis. The first-order phase transition is observed in the measurement of the Polyakov loop as well [504].

In Ref. [507], the same authors also investigated the quark-antiquark potential obtained from the Wilson loop at the above magnetic-field strengths $eB = 4, 9 \text{ GeV}^2$. Temperature is fixed at a single point $T \sim 86 \text{ MeV}$ that is in between the transition temperatures at $eB = 4 \text{ GeV}^2$ and $eB = 9 \text{ GeV}^2$ mentioned above. It was shown that the linear confinement potential disappears at $eB = 9 \text{ GeV}^2$, while there remains a linear potential at $eB = 4 \text{ GeV}^2$ though the potential becomes anisotropic. Provided that those results suggest the deconfinement transition, the system is in a confinement and chirally broken phase at $eB = 4 \text{ GeV}^2$ and $T \sim 86 \text{ MeV}$ and in a deconfinement and chirally symmetric phase at $eB = 9 \text{ GeV}^2$ and $T \sim 86 \text{ MeV}$. Those data are still consistent with the degeneracy between the chiral and deconfinement phase transition temperatures, which is explicitly observed in case of $eB = 3.25 \text{ GeV}^2$ (see Fig. 41).

It is interesting to further investigate the confinement properties in strong magnetic fields. It was suggested that a critical point exists in the *deconfinement phase transition* in strong magnetic fields [519]. This argument is based on an assumption that the dynamical quark mass keeps increasing by the magnetic catalysis in the asymptotic magnetic-field strength. In such a case, all the “heavy” quarks are decoupled from the low-energy dynamics, which leaves a pure gluonic system realized in the low-energy regime. The order of a deconfinement phase transition in a pure gluonic system may be first order [520]. On the other hand, the deconfinement phase transition is known to be crossover at a vanishing magnetic field due to the existence of quarks. Therefore, one can expect the existence of a critical point somewhere in between the vanishing and asymptotic magnetic-field strengths.

There are two issues to be clarified. Assuming the “infinitely heavy” quarks means that the chiral symmetry is broken at the deconfinement phase transition temperature in the effective pure gluonic system. On the other hand, we have seen the degeneracy of the transition temperatures read off from the chiral condensate, the strange-quark susceptibility, and the Polyakov loop up to the magnetic-field strength mentioned above. Especially, the deconfinement phase transition for the pure gluonic system should be well captured by the Polyakov loop. Thus, it should be clarified whether or not there is room for splitting between the transition temperatures from the chiral condensate and the Polyakov loop in further strong magnetic fields. The other issue is related to an anisotropic nature of the possible pure gluonic system with respect to the direction of the strong magnetic field. While magnetic fields do not directly couple to gluons, the pure gluonic action may contain an anisotropic dielectric constant due to an anisotropic screening effect stemming from the quark loops in magnetic fields [437] (see also Sec. 5 for a QED analog). The issue is whether the deconfinement phase transition is first order in such an anisotropic pure gluonic system [519]. The lattice simulation has been performed for the anisotropic gluonic system by treating the anisotropic dielectric constant as a free parameter [368]. A first-order deconfinement phase transition in the anisotropic pure gluonic system was concluded with the finite-size scaling method. Determining the phase transition temperature in physical units is left as an open question.

Hadron spectrum

As mentioned earlier, strong magnetic fields can modify internal structures of composite particles and resulting spectra when dense magnetic lines penetrate through the bodies. Besides an interest in the composite structures on its own, studying QCD thermodynamics requires information of how pions and other low-lying hadron spectra get modified in strong magnetic fields since hadrons, rather than quark quasiparticles, serve as elementary excitations in the confinement phase. Lattice simulations have been providing light-meson spectrum [356–359, 495, 513, 521] as well as baryon spectrum [522] (see also Ref. [523] for the two-color QCD). All of those measurements were performed with the quenched simulations except for a charged pion in Ref. [495], a neutral pion in Ref. [359],⁹² and the recent paper

⁹²A neutral pion mass was measured by the use of the gauge configuration generated in Ref. [495] for the sake of comparison to the quenched and Wilson-fermion result in Ref. [359].

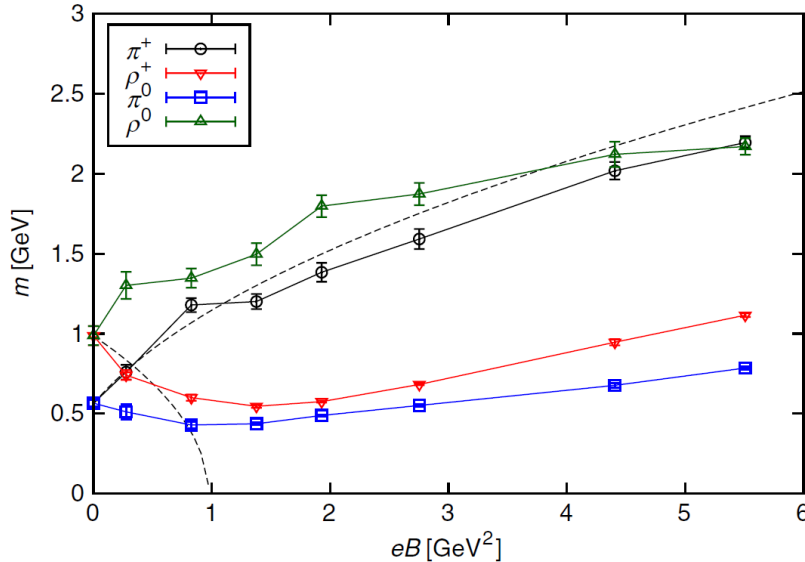


Figure 43: Light-meson spectra in magnetic fields [356]. The dashed lines show the Landau quantization of a point-like charged pion and rho-meson in a naive hadronic picture.

[513]. The dynamical simulation in the last paper was extended to measurements of neutral pseudoscalar mesons at finite temperature for the study of QCD thermodynamics [510]. One can also measure other properties such as the decay constants⁹³ [513, 525] and the anisotropic wave functions of light mesons [526].

Figure 43 shows the simulation results on the light-meson spectra [356]. The dashed lines show the Landau quantization of a point-like charged pion and rho-meson with the lowest Zeeman energy. In the charged-pion spectrum, one finds that the simulation result increases in a similar way to the dashed line. Other simulation results also showed increasing behaviors [357, 359, 495]. However, a recent dynamical simulation suggested a turnover to a decreasing behavior with a peak near $eB \sim 0.6$ GeV² [513]. No such peak structure has been observed with the quenched simulations in Fig. 43 and Refs. [357, 359] or the dynamical simulation up to $eB \sim 0.4$ GeV² [495]. A charged kaon from the dynamical simulation also exhibits a similar peak structure at almost the same position (see Fig. 9 in Ref. [513]). Notice also that, even though no such drastic behavior is seen in the quenched simulations, there is still a systematic tendency for a deviation from the point-like spectrum in the strong-field regime in Fig. 43 and Refs. [357, 359, 495], where the point-like spectrum for a charged pion overshoots the quenched simulation results. Those findings may suggest modification of composite structures and deserve further study in the strong-field regime.

As for the charged rho-meson states,⁹⁴ while the dashed line for the lowest Zeeman energy follows the simulation result up to an intermediate magnetic-field strength, there is a significant deviation in the strong-field regime $eB \gtrsim 0.5$ GeV². This is not very surprising since the magnetic-field strength is already much larger than Λ_{QCD}^2 and becomes comparable to the decreasing rho-meson mass. Whereas a vanishing rho-meson mass was thought to be an indication for a rho-meson condensation in strong magnetic field [353, 354],⁹⁵ the simulation result exhibits a slow down of the decreasing behavior (red

⁹³Due to a preferred spatial orientation provided by a magnetic field, there appear two decay constants that parametrize the hadronic matrix element of the weak current which has one Lorentz index [524].

⁹⁴Note that, in quenched simulations, rho mesons are stable against the dominant decay channel to two pions unlike in reality.

⁹⁵A negative Zeeman energy dominates over the zero-point energy in the Landau quantization when charged particles have spin larger one, leading to a vanishing mass at a certain critical magnetic field. This applies to charged rho-mesons

curve), and a discussion with the QCD inequality does not support this scenario either [356]. No indication for a rho-meson condensate, at least that conjectured with the point-like picture, is observed in later simulations [357–359]. There is a discrepancy among those simulation results in the asymptotic behavior: The later results exhibit a saturating behavior rather than the increasing behavior seen in the strong-field regime of Fig. 43. This discrepancy needs to be resolved in the future studies. Increasing behaviors in the other two spin states (not discussed in Fig. 43) were observed in Ref. [359]. One of those spin states needs investigation for the mixing with a charged pion,⁹⁶ which was, however, concluded to be small [359].

In Fig. 43, the neutral pion and rho-meson spectra also vary as we increase the magnetic-field strength, though they are just constants in a naive hadronic picture. While one finds a non-monotonic behavior in the neutral pion in Fig. 43 [356], a monotonic decreasing behavior was observed in a later simulation [521]. The origin of the discrepancy was pointed out in Ref. [359] as a lattice artifact inherent in the Wilson fermions used in Ref. [356]. The Wilson term, added to the Dirac operator to kill the doublers, generates an artificial magnetic-field dependence of the Dirac eigenvalue at finite lattice spacing, which acts to increase the quark mass as we increase the magnetic-field strength.⁹⁷ Renormalizing the quark mass to subtract the magnetic-field dependence, it was shown that the neutral pion spectrum monotonically decreases and then almost saturates with an increasing magnetic field, which resolves the discrepancy mentioned above [359]. A recent dynamical simulation confirmed the monotonic decrease and also suggested that the effect of dynamical quarks on a neutral pion is negligible at *zero temperature* (see below for a finite temperature case) [513]. Note that they are “connected pions” where a quark-antiquark pair annihilation is not taken into account. The mass of neutral kaon was also measured in Ref. [513], exhibiting a similar, but weaker, decreasing behavior due to a physical strange-quark mass heavier than those of up and down quarks.

As for neutral rho mesons, one finds an increasing behavior in Fig. 43 for the nonzero spin states that do not suffer from the mixing with a neutral pion. Such an increasing behavior was observed in later simulations as well [359, 521]. Neglecting the mixing effect, the spin-zero state was measured in Ref. [521], exhibiting a decreasing behavior. The effects of the mixing and the disconnected diagrams for neutral pion and rho-meson yet await final conclusions (see discussions in Ref. [513]). Once the mass splitting between the spin-zero and -nonzero states is confirmed, this tendency may be understood from spin configurations favored in magnetic fields. Spin configurations inside neutral mesons, where a valence quark and antiquark pair has the opposite electric charges, favor the spin-zero states (including neutral pions) and disfavor the nonzero spin states due to the Zeeman energy cost.⁹⁸

Fitting the measured mass shifts by a polynomial of the magnetic-field strength, one can quantify the effect of composite structures by the polynomial coefficients. The g -factor, which appears as the linear-order coefficient, was read off for rho mesons [357–359] as well as vector kaons K^* [358]. The dipole magnetic polarizability, which appears as the quadratic-order coefficient, was read off for vector mesons [357, 521] and pseudoscalar mesons [359, 504, 521].

It was shown for the first time by lattice QCD simulation that the Gell-Mann–Oaks–Renner (GOR) relation holds in magnetic fields by separately computing the chiral condensate, neutral meson mass, and decay constant at zero temperature [513] (see also Ref. [442] for chiral perturbation theory). The

granted that they are point-like particles.

⁹⁶Due to the breaking of a spatial rotational symmetry in magnetic fields, only the spin component along a magnetic field remains a good quantum number. Therefore, a spinless particle and the spin-zero state of spin-1 particle can have the same quantum numbers and can be mixed with each other.

⁹⁷The Wilson term is proportional to the Klein-Gordon operator. Recall that the lowest eigenvalue of the (non-interacting) Klein-Gordon operator increases linearly with an increasing magnetic field due to the Landau quantization (see Appendix A in Ref. [359]).

⁹⁸In the Landau quantization picture, this means that the spin-zero states can be configured with a quark and antiquark both in the LLL, while the spin-nonzero states have to include at least a hLL which costs energy (see, e.g., an appendix in Ref. [61]).

corrections to the GOR relation was found to be small for light quarks and mild for strange quark that actually become smaller than the corrections at a vanishing magnetic field. Recall that neutral meson mass decreases with an increasing magnetic field though the chiral condensate increases at zero temperature. Those behaviors are compatible with one another in the GOR relation with the aid of an increasing decay constant. The decreasing neutral meson masses may imply a decreasing chiral transition temperature as thermal fluctuations of the (NG) bosons drive chiral restoration.

At finite temperature, the meson correlation length was measured in Ref. [510] as we mentioned earlier in the discussions about the sea-quark effect on the chiral condensate. The correlation length is defined by the long-distance behavior of the meson-meson correlator [514, 515], where the correlator is expected to decay exponentially, characterized by the correlation length on the shoulder. The spatial direction is taken along a magnetic field. The dynamical simulations were performed in the pseudoscalar channels not only for light quarks but also strange quarks. As an overall tendency, the correlation lengths take almost constant values below 100 MeV and rapidly decrease as we further increase temperature across the transition temperature. Understanding those results is left as an open question. It will be important to first understand the high-temperature behavior with the dimensionally reduced effective theory as discussed in the absence of a magnetic field [527–533].⁹⁹ The inverse of the correlation length is called the static screening mass that is different from the pole mass, i.e., an energy gap in a dispersion relation (cf. Appendix F.4.2 for the difference between these two masses seen in a perturbative analog).¹⁰⁰ The dispersion relations of the NG bosons may be, nevertheless, determined by a combination of the screening mass, decay constant, and axial isospin susceptibility that are all *static* quantities as pointed out in Refs [534, 535]; The axial isospin susceptibility could be measured in the future studies. It is interesting to explicitly see correlations between QCD thermodynamics and the NG-boson spectrum at finite temperature.

Besides the light-quark observables above, the heavy-quark potential was also measured at zero and finite temperatures and fitted by the Cornell potential [351, 494, 505, 507]. The left panel in Fig. 44 shows the latest results in Ref. [494] for the heavy-quark potential $V(r)$ in the ever strongest magnetic fields as a function of the distance r between a quark and antiquark pair. The subscripts “L” and “T” denote the cases where the pair is located along the longitudinal and transverse directions to the magnetic field, respectively. One can clearly see an anisotropy in the heavy-quark potential especially in a long-distance part beyond $r = 0.4$ fm. This anisotropy is captured as the magnetic-field dependence of the string tension $\sigma(B)$ in the Cornell potential. The right panel of Fig. 44 shows the string tension normalized by that at a vanishing magnetic field. In the longitudinal case, the string tension is suppressed and almost vanishes at the strongest magnetic field, though it still has a finite value. In the transverse case, the string tension is enhanced to seemingly saturate in strong magnetic fields. By plugging the measured heavy-quark potential into the Schrödinger equation, one can study quarkonium spectra as done with the earlier data [57] (see also Refs. [12, 56, 58–60, 536–539] for related works). Medium effect at finite temperature generally suppresses the string tension [505]. It

⁹⁹One can construct an effective theory at high-temperature by utilizing a property in the imaginary-time formalism that the compact temporal coordinate shrinks in the high-temperature limit. Regarding the remaining spatial three dimensions as an analytic continuation from a fictitious (2+1) dimensional Minkowski spacetime, the screening mass can be formulated as a “quarkonium spectrum” in this effective theory with a large fermion mass given by the lowest Matsubara frequency [527–533] (see Ref. [517] for recent simulation in the (very) high-temperature region).

¹⁰⁰The energy gap of the lowest-lying state is measured with the exponential decay in the long (Euclidean) time correlation, while the screening mass is measured with the long spatial correlation. By construction of the imaginary-time formalism, the length of temporal coordinate is fixed by an inverse temperature, and energy gaps cannot be directly measured in this static formulation. There is not an energy selection in the measurement of the screening mass that should, therefore, include a contribution of the whole spectral function up to the temperature scale. The screening mass approaches the energy gap at zero temperature as anticipated from the Lorentz symmetry and confirmed by the recent simulation [516] and approaches twice the lowest quark Matsubara frequency in the high-temperature limit where quarks are free of the confinement.

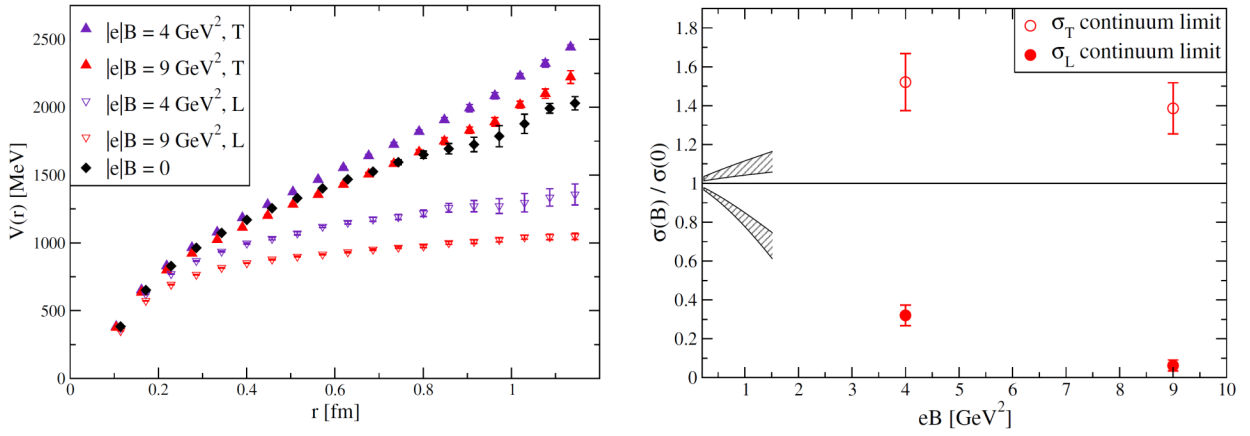


Figure 44: The heavy-quark potential in strong magnetic fields (left) and the ratio of the string tension σ in a magnetic field to that at a vanishing magnetic field (right). Both are taken from Ref. [494]. The subscripts “L” and “T” denote the cases where the quark and antiquark pair is located along the longitudinal and transverse directions to the magnetic field, respectively. The dashed gray regions show the continuum extrapolations of the earlier results in Ref. [505].

is interesting to pursue a signal of the deconfinement transition at finite temperature in line with the aforementioned work [507].

As a complementary measurement, one can measure a strength of the chromo-electric field along the color flux tube spanned between a heavy-quark pair, which is the dominant source of the confinement force (especially in the heavy-quark limit) [494, 540]. This quantity can be defined in a gauge-invariant way. The simulation results confirm that the chromo-electric field and the string tension exhibit the same tendency in the spatial anisotropy. The screening mass in the deconfinement phase was also measured for both the electric and magnetic components [506].

The above tendency in the confinement force can be understood from the screening effect on the chromo-electric field by quark excitations in the LLL that can only excite along magnetic fields in the strong-field limit. In the longitudinal case, the LLL quarks can couple to the chromo-electric field extending along the magnetic field. The screening effect is enhanced by the Landau degeneracy, which *suppresses* the string tension as compared to the case at a vanishing magnetic field (see the right panel of Fig. 44). In the transverse case, the LLL quarks do not couple to the chromo-electric field extending in perpendicular to the magnetic field, and the chromo-electric field is less screened. Therefore, as we increase the magnetic field, the transverse string tension is *enhanced* since quarks fall into the LLL from the hLL. Eventually, the transverse string tension *saturates* after quarks are completely decoupled. The saturation value is determined by the residual screening effect by gluon excitations, which explains the saturation of the transverse string tension in the right panel of Fig. 44.

Magnetization

Response of vacuum and/or medium to an external magnetic field induces magnetization. In Sec. 6.5.3, we have discussed the vacuum responses that lead to renormalization of divergent bare quantities. Here, we summarize finite temperature results from lattice QCD simulations. Magnetization manifests itself in an energy shift in thermodynamic systems, and can be defined as a derivative of the partition function by a magnetic-field strength. However, one cannot simply compute this derivative on periodic lattices, or a compact surface in general, due to the quantization of a magnetic field required by uniqueness

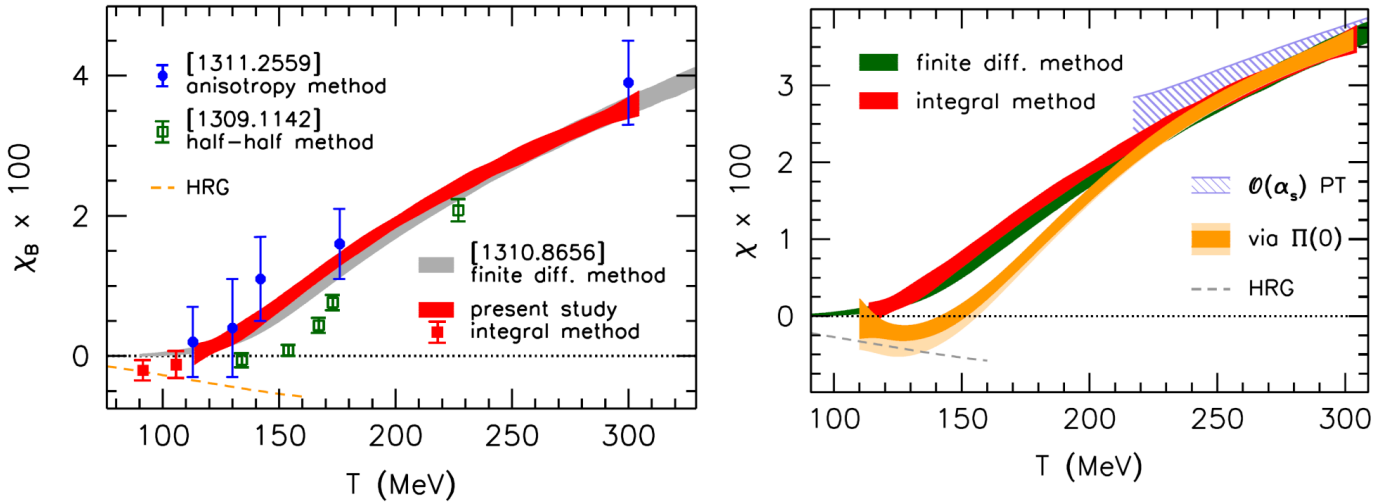


Figure 45: Magnetic susceptibility χ_B (left), taken from Ref. [544]. Shown data are from Refs. [543–546]. The latest update is shown with the orange band (right) [547] together with the results from hadron resonance gas (HRG) model and perturbation theory (PT).

of the phase.¹⁰¹ Magnetization has been nevertheless investigated with lattice QCD simulations by bypassing this issue. We also note that the magnetization studied with lattice QCD simulation so far is in the linear response regime with respect to a magnetic field. Namely, the magnetization is regarded as a linear function of a magnetic field and the magnetic susceptibility corresponds to the linear slope parameter independent of a magnetic field. Investigating the nonlinear effects, which become important in strong magnetic fields, are left as open issues (cf. Sec. 5.2 for nonlinear magnetic permeability).

Various approaches to the issue of the magnetic-field quantization have been proposed as indicated in the left panel of Fig.45. The first result was obtained with a physics-motivated approach denoted as the “anisotropy method” where the magnetization is read off from the pressure anisotropy between the parallel and perpendicular components with respect to the magnetic-field direction [350, 545] (see a review paper [312] for magnetization captured by the energy-momentum tensor). Subsequent results were obtained with the “finite difference method” where an interval between the quantized magnetic fields is interpolated by artificial systems with the Dirac strings [542, 543], the “half-and-half” method where each half of the system volume is exposed to magnetic fields in the opposite directions so that the total magnetic flux is maintained vanishing [546], and the “integral method” where a simple mathematical trick relates the pressure anisotropy at the physical point to that at the infinite quark mass that can be analyzed by a large-mass expansion [544]. Overall, those approaches provided consistent results for the magnetic susceptibility χ as shown in the left panel of Fig.45. Some of those results are compared with the latest result in the right panel [547] where the magnetic susceptibility was tied to the current-current correlator Π of the Kubo formula type with a suitably chosen perturbation. As long as one focuses on the linear response regime, numerical simulations at a vanishing magnetic field should suffice as in this method, reducing numerical costs. See also a recent work [548] for magnetization at finite density within the two-color QCD.

Now, we discuss the results in Fig. 45 at finite temperature. Those results are renormalized in such a way that the susceptibility vanishes at zero temperature with subtraction of the (divergent) vacuum contribution. In the high-temperature limit, the simulation results approach the free-quark contribution denoted as the perturbation theory (PT) and exhibit paramagnetism $\chi > 0$. Remember that, according to the discussions in Sec. 6.5.3, free fermions with spin-1/2 give rise to paramagnetism as a difference

¹⁰¹An arbitrary closed path on a compact surface is a common perimeter of an area S and of the rest of the surface, which requires uniqueness of the phase, i.e., $\exp(iq_f \oint A_\mu dx^\mu) = \exp(iq_f SB) = \exp(-iq_f(S_0 - S)B)$ with the total area S_0 , and thus the quantization $q_f B = 2\pi n/S_0$ (see, e.g., Refs. [50, 541–543] for more details).

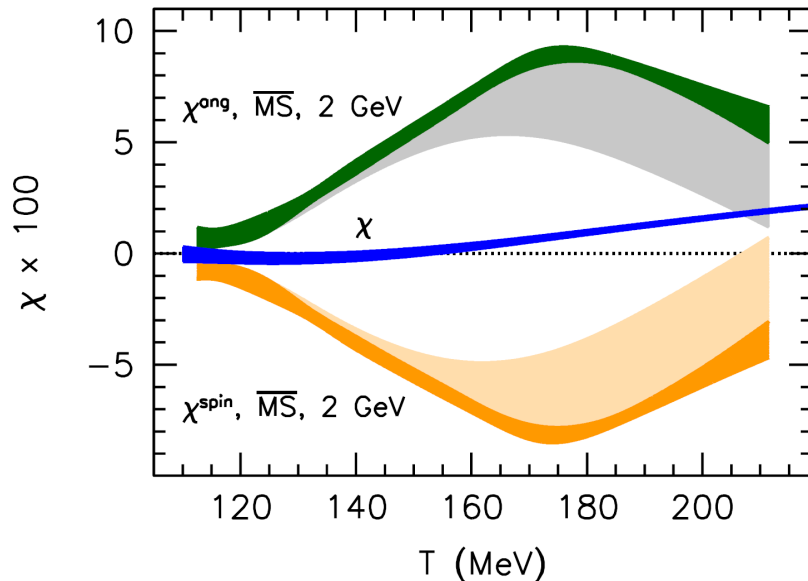


Figure 46: The total and quark-spin magnetic susceptibility shown by the blue and orange bands, respectively [552]. Each of them are renormalized to vanish at zero temperature. The green line shows the difference between the total amount and quark-spin contribution.

between the Pauli paramagnetism from a spin polarization and the Landau diamagnetism from eddy currents; The absolute magnitude of the former is three times larger than that of the latter. This ratio holds at finite temperature as well since the magnetic-field dependence in the effective action (329) is factorized as an overall factor in front of the sum of the vacuum and finite-temperature contributions when an electric field is absent in the medium rest frame (see Refs. [544, 547] for details in finite temperature calculations).

A significant update was made by carefully taking a continuum limit as shown by the orange band [547]. One finds a diamagnetic region below the chiral phase transition temperature ~ 155 MeV where the magnetic susceptibility takes negative values.¹⁰² The diamagnetic region was observed in the preceding result in lower temperature $\lesssim 100$ MeV [544] (see the left panel in Fig. 45), but appeared to extend to a higher temperature as shown in the right panel. The existence of the diamagnetic region may be attributed to the contribution of abundant charged pions in the confinement phase that only provide diamagnetic contributions without spin (cf. Sec. 6.5.3). The simulation result indicates a rough agreement with that from the hadron resonance gas (HRG) model shown by the dashed line that includes contributions of other hadrons as well as pions up to around 1 GeV masses (see Ref. [549] for a list of included hadrons). Also, the reader is referred to results from functional renormalization group [550] and chiral perturbation theory [551].

Spin and orbital contributions to magnetic susceptibility

The simulation results in Fig. 45 suggest that, as we decrease temperature starting from the asymptotically high temperature, the paramagnetic region is smoothly connected to the diamagnetic region in the chirally broken phase. Since the asymptotically high temperature region is governed by free particles, this transition should stem from the QCD interaction effects. To investigate interaction effects, it is useful to separate spin and orbital contributions. The simulation results showed that the quark-spin contribution is diamagnetic below $T \lesssim 200$ MeV which is still far from the Pauli paramagnetism due

¹⁰²A nice global parameterization over the whole temperature region is available in Ref. [547], covering both the paramagnetic and diamagnetic regions.

to the free quarks at the asymptotically high temperature.

To investigate the breakdown, one should decompose the fermion determinant in the partition function (cf. Eq. (180) for the version without gluon fields). Similar to the decomposition in Eq. (75), one can decompose the product of the Dirac operators as $\not{D}\not{D} = D_\mu D^\mu + \frac{g}{2} G^{\mu\nu} \sigma_{\mu\nu} + \frac{q_f}{2} F^{\mu\nu} \sigma_{\mu\nu}$ with $\sigma^{\mu\nu} = i/2[\gamma^\mu, \gamma^\nu]$, where $F^{\mu\nu}$ is for a constant magnetic field and $G^{\mu\nu} = G^{a\mu\nu} t^a$ is the gluon field strength tensor. The covariant derivative contains the gluon field as well as the constant magnetic field. The last term gives rise to the Zeeman effect in the fermion dispersion relation (see Sec. 2.3.1). Therefore, it is reasonable to define a quark-spin contribution to magnetization by the contribution from the Zeeman term.¹⁰³ Accordingly, an orbital contribution is defined as the contribution from the rest of the above decomposition. Note that the orbital contribution defined here contains not only quark contributions but also gluon contributions.

A nonzero gluon contribution to magnetization was indeed observed by measuring the anisotropic pressure, that is more specifically, the gluon field strength tensor squared and traced over the color index [350, 352]. The chromo-magnetic field has a larger magnitude along the magnetic field than in the perpendicular direction, while the chromo-electric field has a smaller magnitude along the magnetic field. This tendency is also seen in a perturbative expansion of the Heisenberg-Euler effective action to the second orders in the gluon fields and the magnetic field, i.e., the quantum correction from the box diagrams [350]. A full-order analysis both in the magnetic field and chromo-magnetic field, but without a chromo-electric field, is performed in Ref. [305]; See Sec. 6.5.4 and the discussions about Fig. 30 there. The magnitude of anisotropy in the gluon contribution is found to be smaller than that from the quark contribution, and was neglected in the ‘‘anisotropy method’’ [350, 553]. However, the gluon contributions are included in the other methods in Fig. 45 where any decomposition is not performed.

Since the quark-spin contribution is defined by the Zeeman term proportional to $\sigma^{\mu\nu}$, one can make a connection to measurement of the tensor condensate $\langle \bar{\psi} \sigma^{\mu\nu} \psi \rangle$ [547, 552]. The tensor condensate can be nonzero because of a preferred orientation provided by the magnetic field, and thus is proportional to the magnetic-field strength in the linear response regime.¹⁰⁴ The magnetic susceptibility is accordingly read off from the linear slope parameter of the tensor condensate or is tied to a correlator at a vanishing magnetic field similarly to the aforementioned method for the total susceptibility [547]; It was concluded that the former method with the simulation at nonzero magnetic fields works better with a smaller statistical error for the measurement of the tensor condensate. We add that the tensor condensate can be probed in terms of the operator product expansion as well [554–558]; Some of those results were compared with the simulation results [547, 552].

The earlier simulation results suggested a diamagnetic quark-spin contribution up to $T \lesssim 170$ MeV [552]. This result was confirmed in Ref. [547] where precision of the renormalization procedure was improved and temperature dependence was explicitly studied as shown in Fig. 46. The blue and orange bands show the total magnetic susceptibility from the correlator method (cf. Fig. 45) and the quark-spin contribution from the tensor condensate, respectively.¹⁰⁵ They are the results of two independent measurements and are both renormalized to vanish at zero temperature. The green band shows the contribution other than the quark-spin contribution, i.e., the difference between the total and the quark-spin contribution (and is not from an independent measurement). The lighter orange band shows systematic uncertainties originating from an approximation (see Ref. [547] for details). One finds that the *diamagnetic quark-spin* contribution, which corresponds to negative values, extends from a low

¹⁰³More precisely speaking, this is a polarization of magnetic moment instead of spin itself and thus has additive contributions from antiquarks and quark flavors, while the spin angular momentum is subject to cancellation among particles with opposite electric charges when the magnetic moment is polarized in a magnetic field.

¹⁰⁴Also, note that, since $\sigma^{\mu\nu}$ and γ^5 commute with each other, the tensor condensate is nonzero only when there is chirality mixing on the quark propagator induced by a nonzero current quark mass and/or the chiral symmetry breaking.

¹⁰⁵For clarity, one should note that the orange band in Fig. 46 is for the quark-spin contribution. The total magnetic susceptibility shown by the orange band in Fig. 45 is shown by the blue band in Fig. 46.

temperature to above the chiral and deconfinement phase transition temperatures. Accordingly, the rest part, shown by the green band, appeared to be positive, indicating a paramagnetic contribution. As compared to the Pauli paramagnetism for free fermions, the QCD interaction effects even induce a sign change in the spin magnetic susceptibility, exhibiting a significant impact on magnetism.

The quark-spin contribution should eventually approaches the Pauli paramagnetism in higher temperature in consistent with the asymptotic freedom. Approaching the free-quark limit appears to require a sign change in the quark-spin contribution at a certain temperature $T \gtrsim 200$ MeV. This behavior has not been directly confirmed by simulations; Though, it may be natural to expect that the orange band in Fig. 46 keeps increasing above the phase transition temperatures to eventually reach the free-quark limit. Recall also that the total susceptibility is confirmed to approach the free-quark limit above $T \gtrsim 250$ MeV in Fig. 45. In the lower temperature, the QCD interaction effects should be responsible for the deviation between the simulation result and the free-quark limit. One such effect is the color confinement where quark spin is forced to configure hadron spin. Inside charged pions, not both of the spin magnetic moments can be aligned in parallel to an external magnetic field, which diminishes the paramagnetic response of quark spin. One can see within the rather large uncertainties that the spin magnetic susceptibility takes a minimum value near the phase transition temperatures.

The rest part, shown by the green band, is interpreted as a sum of the quark and gluon orbital contributions since gluon spin does not directly respond to a magnetic field. A nonzero gluon orbital contribution has been observed in the form of an anisotropic gluon pressure as mentioned above, but should become negligible in the high-temperature limit where free gluons do not respond to a magnetic field. Therefore, the green band is expected to approach the orbital contribution from free quarks that is the Landau diamagnetism with a negative susceptibility. This behavior has not been directly confirmed by simulations either; Within the plot range, the green band yet exhibits a positive sign and is required to change its sign above $T \gtrsim 200$ MeV to approach the free-quark limit.

Phases of magnetism

More studies are demanded to understand the QCD interaction effects on magnetization near the phase transition region. It is useful to explicitly confirm whether and how the spin and orbital contributions approach their high-temperature limits. Approach to the free-quark limit could be slow since the run of the QCD coupling constant is logarithmic in nature; Lattice QCD simulations have shown a slow approach of the energy density and pressure of the quark-gluon plasma to the Stefan-Boltzmann limit (see, e.g., Refs. [559, 560]). Also, it is useful to pin down the temperature at which the spin magnetic susceptibility takes its minimum value. This temperature can be correlated with the chiral/deconfinement phase transition temperature. Along this line, it is interesting to pursue the correlation between magnetism and the chiral/deconfinement phase transition in stronger magnetic fields. The simulation results in Fig. 45 shows a crossover transition in consistent with the chiral and deconfinement crossover transitions at a vanishing magnetic field. However, the strengths of the chiral phase transition is enhanced with an increasing magnetic-field strength as we discussed above. This tendency may manifest itself in the magnetic susceptibility in the form of a sharper transition than the smooth behaviors seen in Figs. 45 and 46. Magnetism in strong magnetic fields is left as an open question.

7.4.2 Quark excitations in strong magnetic fields

We saw three main challenges regarding the chiral symmetry breaking and restoration in QCD. (i) The magnitude of the chiral condensate at zero temperature is not fully understood at the quantitative level; Effective models of QCD and the chiral perturbation theory do not explain the linear dependence on the magnetic-field strength observed by the lattice simulations in the strong magnetic fields, though the increasing behavior is in a qualitative agreement with the picture of the magnetic catalysis. (ii)

In spite of the increase of the chiral condensate in low temperature, the chiral condensate decreases as we increase the magnetic-field strength in higher temperature, which is known as the inverse magnetic catalysis. (iii) The transition temperature decreases as we increase the magnetic-field strength. Those issues can be related to one another since the transition temperature should be basically correlated with the dynamical quark mass as mentioned earlier.

What would be a possible mechanism that suppresses the magnetic catalysis of the chiral symmetry breaking? As mentioned in the beginning of Sec. 7.2, one crucial point in the realization of the magnetic catalysis was that the NG bosons remain (3+1) dimensional excitations, avoiding the Coleman-Mermin-Wigner theorem that inhibits the spontaneous symmetry breaking in (1+1) dimensions [324, 399, 400]. This is simply because neutral mesons do not feel the Lorentz force and, on the other hand, charged mesons are no longer the NG bosons in magnetic fields. Neutral pion fluctuations are parametrically smaller than the quark fluctuations that are enhanced by the logarithmic factor and the Landau degeneracy.

However, the composite structures of mesons need more investigation when the magnetic-field strength becomes larger than their typical scales $\sim \Lambda_{\text{QCD}}$. Such strong magnetic fields can cause strong modifications of their inner structures because the quarks and antiquarks are subject to the dimensional reduction inside mesons. Then, the NG bosons could be also subject to the dimensional reduction and acquire the Landau degeneracy. If the dimensional reduction occurs at the level of neutral mesons as well, the magnitude of the chiral symmetry breaking should be diminished by the mesonic fluctuations as stated by the Coleman-Mermin-Wigner theorem [561]. In the language of the effective potential (see Sec. 6.2), the dimensionally reduced mesonic fluctuations provide the logarithmic singularity multiplied by the Landau degeneracy factor. In that case, the magnitude of the mesonic fluctuations is comparable in magnitude to the logarithmic singularity from the quark fluctuations that is the origin of the magnetic catalysis. Those two logarithmic fluctuations compete with each other due to opposite overall signs originating from the statistics.

The above argument suggests importance of investigating the meson spectra in strong magnetic fields. It was shown within the resummation of ring diagrams that the dispersion relation of the neutral pion indeed exhibits the dimensional reduction in the strong magnetic field, and the resulting logarithmic singularity diminishes the magnitude of the chiral symmetry breaking [561]. This mechanism was named the *magnetic inhibition*. The enhancement of the mesonic fluctuations is in favor of the milder slope of the chiral condensate at zero temperature and the inverse magnetic catalysis at finite temperature.

Yet, there are more to be clarified at the fundamental level. The transverse size of the mesonic fluctuations should depend on the interaction range between the quark and antiquark pair. One may thus wonder what aspects of the QCD interaction could give rise to the dimensionally reduced mesonic fluctuations as compared to QED and typical effective models. The mesonic excitations were more systematically studied by explicit construction of the Bethe-Salpeter equations not only for the NG bosons but also light charged mesons [61, 73]. Below, we discuss roles of QCD-motivated interactions in the spectra of mesonic fluctuations. However, even before constructing mesons, one needs to determine the constituent quark mass in strong magnetic fields because the low-lying meson spectrum is predominantly determined by the constituent quark mass. One should discuss roles of QCD-motivated interactions on the determination of the constituent quark mass.

Saturation of the dynamical quark mass

Remember that we obtained the phase transition temperature for the NJL model in Eq. (299) that is proportional to the dynamical mass at zero temperature [328]

$$T_c \sim m_{\text{dyn}}(T = 0). \quad (445)$$

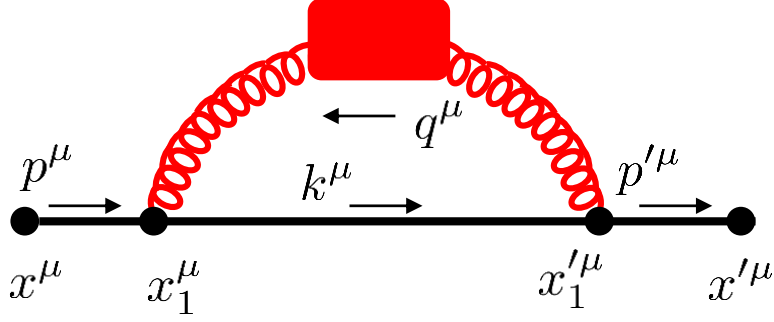


Figure 47: Quark self-energy in the coordinate space. The quark lines, denoted by the black lines, are dressed by a magnetic field.

A similar relation is established in QED [67, 329, 330] (see also, e.g., Ref. [331] for an analogous relation in the BCS theory). Therefore, the critical temperature of the chiral symmetry restoration is naturally interpreted as the point at which the thermal energy becomes large enough to overcome the mass gap and to fill the fermion states with thermal excitations. This just means that the chiral symmetry would not be restored without a significant amount of thermal excitations. This simple observation is expected to hold on general grounds. Thus, the magnitude of the dynamical mass, rather than of the chiral condensate, may provide a direct clue to understand the results from the lattice QCD simulations.

The mass gap, the excitation energy of quasiparticle and antiparticles, can be determined by the Schwinger-Dyson (SD) equation in magnetic fields. The SD equation has been used for QED and the NJL model at zero temperature [411, 439] and finite temperature [67, 329, 330]. It may be worth mentioning that the temperature dependence of the superconducting gap, the counterpart of the dynamical mass, has been also often discussed on the basis of the BCS theory in the weak-coupling limit (see, e.g., Ref. [331]). However, in the nonperturbative QCD, the excitation energy could be quite different from that in weak-coupling theories.

We shall try to grab a key aspect of the nonperturbative gluon interactions. Such effects on the SD equation were first discussed by Kojo and Su [73, 518] and further in Refs. [61, 74, 75, 562]. Below, we discuss the SD equation in the rainbow approximation. All the fermions on the external and internal lines are assumed to stay in the LLLs since the inter-Landau-level transition is suppressed by a large Landau spacing in the strong-field limit.

As discussed in Sec. 3, the quark propagator is factorized into the Schwinger phase and the translation-invariant part as $S(x^\mu, x'^\mu) = e^{i\Phi_A(x^\mu, x'^\mu)} \bar{S}(x^\mu - x'^\mu)$. The Schwinger phase is given as $\Phi(x^\mu, x'^\mu) = \frac{q_f B}{2}(x + x')(y - y')$ in the Landau gauge specified in Eq. (53).¹⁰⁶ Plugging those ingredients, the coordinate representation of the tree-level quark propagator can be arranged as

$$\begin{aligned}
S_{\text{LLL}}^{(0)}(x, x') &:= e^{i\Phi_A(x, x')} \int \frac{d^4 p}{(2\pi)^4} e^{-ip \cdot (x' - x)} S_{\text{LLL}}(p) \\
&= \mathcal{P}_+ \int \frac{d^2 p_{\parallel}}{(2\pi)^2} \int \frac{dp_y}{2\pi} \frac{i}{\not{p}_{\parallel} - m} \\
&\quad \times e^{-ip_{\parallel} \cdot (x'_{\parallel} - x_{\parallel})} e^{ip_y (y' - y)} \phi_{\text{LLL}}\left(\frac{x - s_f \ell_f^2 p_y}{\ell_f}\right) \phi_{\text{LLL}}\left(\frac{x' - s_f \ell_f^2 p_y}{\ell_f}\right), \quad (446)
\end{aligned}$$

where $S_{\text{LLL}}(k)$ is the translation-invariant part of the fermion propagator (137) in the momentum space. We explicitly extracted the wave function in the Landau gauge (57) which is here denoted as

¹⁰⁶Note that x and y (x' and y') are the first and second spatial components of x^μ (x'^μ).

$\phi_{\text{LLL}}(\xi) = e^{-\xi^2/2}/\sqrt{\pi^{1/2}\ell_f}$ without the plane-wave factor for the y direction. The above arrangement is essentially a basis change from the Fourier basis to the Ritus basis (see Appendix B.3). Then, the one-loop quark propagator with the gluon dress can be written as (cf. Fig. 47)

$$\begin{aligned}
S_{\text{LLL}}^{(1)}(x, x') &:= \int d^4x_1 \int d^4x'_1 S(x^\mu, x_1^\mu) \gamma^{\mu_1} S(x_1^\mu, x'^\mu) D_{\mu_1\nu_1}(x_1^\mu, x'^\mu) \gamma^{\nu_1} S(x'^\mu, x'^\mu) \\
&= \mathcal{P}_+ \int \frac{d^2p_\parallel}{(2\pi)^2} \int \frac{dp_y}{2\pi} e^{ip_\parallel \cdot x_\parallel - ip_y y} \phi_{\text{LLL}}\left(\frac{x - s_f \ell_f^2 p_y}{\ell_f}\right) \\
&\quad \times \int \frac{d^2p'_\parallel}{(2\pi)^2} \int \frac{dp'_y}{2\pi} e^{-ip_\parallel \cdot x'_\parallel + ip'_y y'} \phi_{\text{LLL}}\left(\frac{x' - s_f \ell_f^2 p'_y}{\ell_f}\right) \\
&\quad \times \frac{i}{\not{p}_\parallel - m} \left[-i \Sigma_{\text{LLL}}^{(1)}(p_\parallel^\mu, p_y) (2\pi)^4 \delta^{(2)}(p_\parallel^\mu - p'_\parallel^\mu) \delta(p_y - p'_y) \rho_B \right] \frac{i}{\not{p}'_\parallel - m}. \quad (447)
\end{aligned}$$

The external quark lines are factorized as the three-dimensional integral measures and the quark wave functions, and we are left with the amputated quark self-energy $\Sigma_{\text{LLL}}^{(1)}(p_\parallel^\mu, p_y)$. The three-dimensional delta functions and the Landau degeneracy factor are also factorized as we know that the integrals of the wave functions should provide them. The explicit form of the amputated quark self-energy reads

$$\begin{aligned}
&-i \Sigma_{\text{LLL}}^{(1)}(p_\parallel^\mu, p_y) (2\pi)^4 \delta^{(2)}(p_\parallel^\mu - p'_\parallel^\mu) \delta(p_y - p'_y) \rho_B \\
&= (ig)^2 C_2 \mathcal{P}_+ \int d^4x \int d^4x' e^{-i(p_\parallel^\mu x_\mu - ip_y y) + i(p'_\parallel^\mu x'_\mu - ip'_y y')} \phi_{\text{LLL}}\left(\frac{x - s_f \ell_f^2 p_y}{\ell_f}\right) \phi_{\text{LLL}}^*\left(\frac{x' - s_f \ell_f^2 p'_y}{\ell_f}\right) \\
&\quad \times e^{i\Phi_A(x^\mu, x'^\mu)} \int \frac{d^4k}{(2\pi)^4} e^{-ik \cdot (x' - x)} \int \frac{d^4q}{(2\pi)^4} e^{-iq \cdot (x - x')} \gamma_\parallel^\mu S_{\text{LLL}}(k) \gamma_\parallel^\nu D_{\mu\nu}(q),
\end{aligned}$$

where $D_{\mu\nu}(q)$ is the gluon propagator in the momentum space. Note that the gluon propagator is not necessarily a free propagator but is a resummed one that includes nonperturbative effects. We assumed that the gluon propagator is diagonal in the color space, so that the self-energy is also diagonal in the color space with the factor of $C_2 = (N_c^2 - 1)/(2N_c)$. All the fermion lines in the LLLs come with the spin projection operators \mathcal{P}_+ , and the gamma matrices sandwiched in between them can take only the parallel components, i.e., $\mathcal{P}_+ \gamma^\mu \mathcal{P}_+ = \mathcal{P}_+ \gamma_\parallel^\mu$. We suppress the spinor and diagonal color indices of the self-energy.

One can extract the three-dimensional momentum conservation by changing the integral variables to $X^\mu = (x^\mu + x'^\mu)/2$ and $\tilde{x}^\mu = x^\mu - x'^\mu$. After this arrangement, we find that

$$\begin{aligned}
\Sigma_{\text{LLL}}^{(1)}(p_\parallel^\mu, p_y) &= i(ig)^2 C_2 \mathcal{P}_+ \rho_B^{-1} \int dX \int d\tilde{x} \phi_{\text{LLL}}\left(\frac{X + \frac{\tilde{x}}{2} - s_f \ell_f^2 p_y}{\ell_f}\right) \phi_{\text{LLL}}^*\left(\frac{X - \frac{\tilde{x}}{2} - s_f \ell_f^2 p_y}{\ell_f}\right) \\
&\quad \times \int \frac{d^4k}{(2\pi)^4} \int \frac{d^4q}{(2\pi)^4} e^{-i(k_x - q_x) \tilde{x}} (2\pi)^3 \delta^{(2)}(p_\parallel - k_\parallel + q_\parallel) \delta(p_y - k_y + q_y - q_f B X) \\
&\quad \times \gamma_\parallel^\mu S_{\text{LLL}}(k) \gamma_\parallel^\nu D_{\mu\nu}(q), \quad (448)
\end{aligned}$$

where the remaining integral variables X and \tilde{x} are the first spatial components of X^μ and \tilde{x}^μ . Inserting the explicit forms of the LLL wave function and the LLL propagator, we arrive at

$$\Sigma_{\text{LLL}}^{(1)}(p_\parallel^\mu, p_y) = \mathcal{P}_+ \int \frac{d^2k_\parallel}{(2\pi)^2} \gamma_\parallel^\mu \frac{\tilde{D}_{\mu\nu}(k_\parallel - p_\parallel)}{\not{k}_\parallel} \gamma_\parallel^\nu, \quad (449)$$

where we defined

$$\tilde{D}_{\mu\nu}(k_\parallel) = g^2 C_2 \int \frac{d^2q_\perp}{(2\pi)^2} e^{-\frac{|\mathbf{q}_\perp|^2}{2|q_f B|}} D_{\mu\nu}(k_\parallel; \mathbf{q}_\perp). \quad (450)$$

The three components of the external momentum, p_{\parallel}^{μ} and p_y , are conserved in the Landau gauge. p_y labels the degenerate fermion states in homogeneous magnetic fields. The self-energy does not depend on p_y (except for the delta function), meaning that all the degenerate states acquire the same self-energy correction as expected. The rotational symmetry with respect to the magnetic-field direction has been restored despite of the use of the Landau gauge. This implies that the self-energy does not depend on the gauge choice for the external magnetic field.

Now, we proceed to the SD equation in the rainbow approximation, following familiar procedures in the absence of a magnetic field. We resum the quark self-energy linked by the tree-level quark propagators $S_{\text{LLL}}^{(0)}(x, x')$ in the form of the geometrical series. Further, nesting the fermion self-energy, we obtain the SD equation in the rainbow approximation

$$\Sigma_{\text{LLL}}(p_{\parallel}^{\mu}) = \mathcal{P}_+ \int \frac{d^2 k_{\parallel}}{(2\pi)^2} \gamma_{\parallel}^{\mu} \frac{\tilde{D}_{\mu\nu}(k_{\parallel} - p_{\parallel})}{\not{k}_{\parallel} - \Sigma_{\text{LLL}}(k_{\parallel})} \gamma_{\parallel}^{\nu}. \quad (451)$$

We denote the solution for the SD equation as Σ_{LLL} that contains higher loop effects within the rainbow approximation. Notice that this equation has a (1+1)-dimensional form after the transverse gluon momentum is integrated out in the reduced propagator (450). The magnetic-field dependence is not explicit in this (1+1)-dimensional form, and is solely encoded in the Gaussian factor in the reduced gluon propagator (450). Below, we discuss how the reduced gluon propagator controls the density of intermediate virtual states that contribute to the self-energy correction. This is a crucial point since the magnitude of the self-energy correction depends on how much of the degenerate LLLs, spread over the transverse plane, participates in the intermediate state.

The semi-classical picture helps us with understanding the basic physics involved in the SD equation (451). Initially, a quark on the external line is confined in a cyclotron orbit and can propagate only in the longitudinal direction. By emitting a gluon in the intermediate virtual state, the quark can hop from the initial orbit to any one of the degenerate orbits aligned in the transverse plane. Then, it comes back to the original position by absorbing the gluon back. Here, we understand that all the degenerate LLL states contribute to the self-energy if this transverse hopping distance can be infinite, while a limited number of the degenerate states contributes if the hopping distance is finite.

More specifically, in the Landau gauge (53), one of the canonical transverse momentum $x_c = p_y/(q_f B)$ specifies the location of the cyclotron orbit. A quark at x_c hops to another position $x_c' = k_y/(q_f B)$ in the intermediate virtual state. According to the canonical-momentum conservation, the hopping distance is specified by the gluon momentum q_y as $\Delta x := x_c' - x_c = q_y/(q_f B)$. It should be emphasized that the *soft* gluon momentum corresponds to a *short* distance in the transverse plane instead of a long distance in usual Fourier analyses. This difference stems from the specific property, i.e., $x_c = p_y/(q_f B)$, of the basis in the presence of magnetic fields. At the quantum level, the hopping rate should be captured by the overlap among the two quark wave functions and the plane-wave basis for the gluon. This convolution results in the Gaussian factor in the reduced gluon propagator (450) where the integrand depends on the ratio of the hopping distance to the magnetic length $\Delta x^2/\ell_f^2$ as expected from the above observation.

Now, we focus on the gluon spectrum since it controls the transverse size of the virtual fluctuations. Namely, a typical hopping distance is determined by the momentum dependence of the gluon propagator. One can examine two extreme cases.

- *Momentum-independent interactions.*— If the gluon propagator is constant or extremely flat in the transverse-momentum dependence, the hopping can occur at any spatial scale. This means that all the degenerate states participate in the fluctuations, enhancing the quark self-energy by the Landau degeneracy factor. Indeed, the Gaussian integral in Eq. (450) results in the Landau degeneracy factor when the gluon propagator does not depend on the transverse momentum.

- *IR-dominant interactions.*— In the opposite extreme case where the gluon propagator has a dominant support in the soft momentum region $\Delta x^2/\ell_f^2 = |\mathbf{q}_\perp|^2/|q_f B| \ll 1$, the Gaussian factor is approximately a constant in the integral. What is remarkable is that the integral no longer depends on the magnetic-field strength, and neither does the quark self-energy [73]. The dimensionful factor may be provided by a typical momentum scale characterizing the gluon propagator instead of the Landau degeneracy factor. This scale works as an effective cutoff of the hopping distance.

What should we expect to happen in the low-energy QCD? One should expect that the momentum dependence of the gluon propagator has a larger weight in the IR regime $|\mathbf{q}_\perp|^2 \ll \Lambda_{\text{QCD}}^2$ than the UV regime, where Λ_{QCD} is the QCD scale. The existence of this emergent IR scale is a definite property of QCD that divides the perturbative and nonperturbative regimes and distinguishes QCD from QED. This situation is close to the latter of the above two extreme cases. Therefore, the dynamical quark mass approaches a value $\sim \Lambda_{\text{QCD}}$ as we increase the magnetic-field strength to the regime $\Delta x^2/\ell_f^2 = \Lambda_{\text{QCD}}^2/|q_f B| \ll 1$. This offers a saturation mechanism of the dynamical quark mass when we increase the magnetic-field strength beyond Λ_{QCD}^2 . The saturation of the dynamical quark mass was first illustrated with a confinement-potential model [73] and is supported by other approaches [61, 74, 75, 518, 562].

One can interpret the reduced gluon propagator (450) as a quasi-(1+1)-dimensional interaction realized by the cooperative effects of the IR-dominant gluon propagator and the Landau quantization in the quark and antiquark eigenstates. Accordingly, both quarks and gluon interactions are subject to effective dimensional reductions even though magnetic fields do not directly couple to gluons. Then, one can expect that bound states or particle pairing, such as the chiral condensate and mesons, also reduce to (1+1) dimensional forms as speculated earlier.

It would be also interesting to investigate the saturation mechanism of the dynamical quark mass with the RG method (see Refs. [325, 404, 462, 475, 478, 562–564] for RG analyses). In Sec. 7.2.2, we discussed the equivalence between the analyses by the RG method and the Schwinger-Dyson equation and stressed the importance of the scale hierarchy in the RG evolution (cf. Fig. 38). The IR-dominant gluon interactions may modify the RG evolution of the four-Fermi operator below the QCD scale from that in QED.

Parametric estimate of the chiral condensate

One can construct a relation between the dynamical quark mass and the chiral condensate in the spirit of the constituent quark model. With insertion of the self-energy Σ_{LLL} into the quark propagator (137), the chiral condensate is given by a loop of the resummed quark propagator as [73, 439]¹⁰⁷

$$\langle \bar{\psi}\psi \rangle = 2i \int \frac{d^4 p}{(2\pi)^4} e^{-\frac{|\mathbf{p}_\perp|^2}{|q_f B|}} \text{Tr} \left[\frac{1}{\not{p}_\parallel - \Sigma_{\text{LLL}}} \right] \sim \frac{|q_f B|}{2\pi} m_{\text{dyn}}. \quad (452)$$

The transverse momentum integral results in the Landau degeneracy factor. The remaining integral is dominated by the infrared contribution, and is proportional to $m_{\text{dyn}} = \Sigma_{\text{LLL}}(0)$ for the dimensional reason in a qualitative estimate. The dynamical quark mass quantifies the magnitude of the (1+1) dimensional pairing between a quark and an antiquark, while the Landau degeneracy factor counts the density of the (1+1) dimensional pairing aligned in the transverse plane.

The above factorization is a universal consequence of the dimensional reduction, so that the microscopic details of the low-energy QCD is solely captured by the magnitude of m_{dyn} . When the saturation mechanism works for the constituent quark mass $m_{\text{dyn}} \sim \Lambda_{\text{QCD}}$ in the strong magnetic fields, the

¹⁰⁷The Schwinger phase cancels for the one-point function, indicating that the chiral condensate is independent of the gauge choice for the external magnetic fields.

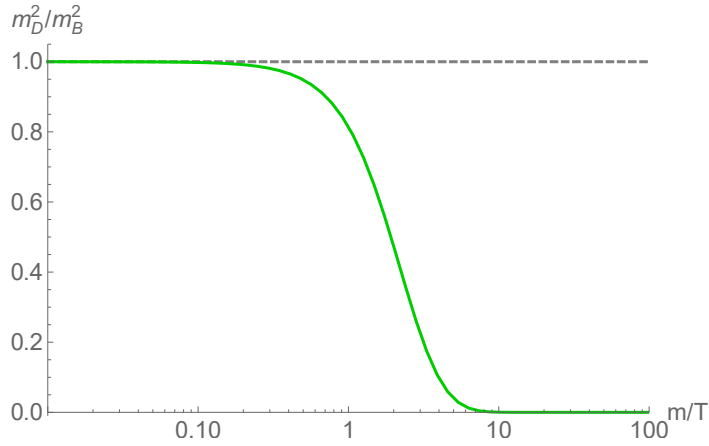


Figure 48: Debye screening mass from the massive quark loop in the LLL (454).

magnitude of the chiral condensate is estimated to be [73, 518]

$$\langle \bar{\psi}\psi \rangle \sim \frac{|q_f B|}{2\pi} \Lambda_{\text{QCD}}. \quad (453)$$

This estimate is in favor of the linear dependence of the chiral condensate on the magnetic-field strength that has been observed in the lattice QCD simulations at zero and low temperature (cf. Fig. 40).

Putting it in the other way around, the linear increase of the chiral condensate does not necessarily imply an increase of the dynamical quark mass. As long as the dynamical quark mass remains as small as the QCD scale Λ_{QCD} , the chiral restoration temperature can also remain as small as the QCD scale or should even decrease because the Landau degeneracy factor enhances the thermal fluctuations [73]. Therefore, the above scenario can offer a consistent explanation of the magnetic-field dependence of the magnetic catalysis in the low-temperature region and the decrease of the transition temperature; Those two issues are intimately related to one another via the quark excitation spectrum of the strongly coupled QCD in the strong magnetic fields.

In the above estimate, one can see that the estimate of the chiral condensate (453) overshoots the lattice QCD result if the dynamical quark mass grows with the magnetic field strength $m_{\text{dyn}} \sim q_f B$ as seen in Fig. 40. Such a problem occurs when the whole degenerate states contribute to the quark self-energy with short-range interactions as discussed below Eq. (451).

7.4.3 Debye screening effect and the deconfinement phase transition

Based on the estimate of the dynamical quark mass, one can also discuss the deconfinement phase transition in QCD. Once the thermal excitations are activated, the quark-antiquark pair excitations develop the Debye screening effect on long-range gluon interactions, weakening the confinement force. We have discussed the interpretation for the suppression of the longitudinal string tension observed in the lattice QCD simulations (See Fig. 44).

The effective potential for the Polyakov loop, the approximate order parameter of the deconfinement phase transition, explicitly indicates that the deconfined phase is favored when the Debye screening effect becomes larger (see Sec. 6.6). As we have discussed around Eq. (380), the Debye screening mass is enhanced by the Landau degeneracy factor in the strong magnetic field, giving rise to the tendency of lowering phase transition temperature. This computation was done with massless quarks. Here, we revisit the Debye screening effect with a finite quark mass that is identified with the dynamical quark mass discussed above.

The screening effect is captured by the gluon self-energy $\Pi_{\parallel}^{\text{med}}(q)$ with q^μ being the gluon momentum. In QCD, there are both quark- and gluon-loop contributions. We focus on the quark-loop contribution

since it is enhanced by the Landau degeneracy factor and dominates over the gluon-loop contribution in the strong magnetic fields. Computational details of the gluon self-energy at finite temperature are summarized in Appendix F (see also Ref. [565]). Using the one-loop gluon self-energy with an arbitrary fermion mass on the loop, the Debye screening mass m_D is defined as¹⁰⁸ [see Eq. (664)]:

$$m_D^2 = -m_B^2 \lim_{q_z \rightarrow 0} \frac{m^2}{q_z} \mathcal{P} \int_{-\infty}^{\infty} \frac{dp_z}{\epsilon_p} \frac{n(\epsilon_p)}{p_z - q_z}. \quad (454)$$

The integral is defined with the Cauchy principal value denoted by \mathcal{P} . The LLL dispersion relation and the thermal distribution function are given as $\epsilon_p = \sqrt{p_z^2 + m^2}$ and $n(\epsilon) = 1/(e^{\epsilon_p/T} + 1)$, respectively. In the massless limit ($m = 0$), the Debye screening effect is given by the Schwinger mass $m_B^2 = g^2 |q_f B| / (2\pi)^2$ multiplied by the Landau degeneracy factor and a color group factor 1/2. While the integral in Eq. (454) looks vanishing when $m/T \rightarrow 0$, the singularity at the origin ($p_z = 0$) reproduces the nonzero value in the massless limit $m_D = m_B$ [see Eq. (665)]. After the factorization of the Landau degeneracy factor, the result of integration can only be a function of the dimensionless combination m/T . It is clear that the result of integration is sizable only when the Fermi distribution function has a support in the low-energy region $p_z \sim q_z \sim 0$; The Debye screening mass can be developed only when the quark mass is small enough to have thermal excitations, i.e., $m/T \lesssim 1$. In Fig. 48, one can confirm those behaviors from the numerical integration of Eq. (454).

For a qualitative discussion, we identify the fermion mass m with the dynamical quark mass m_{dyn} . This provides a good approximation when the quark self-energy is inserted in the quark propagator and the loop integral is dominated by the infrared contribution (and this should be the case in the dimensionally reduced system). When the saturation mechanism of the dynamical quark mass gives $m \sim \Lambda_{\text{QCD}}$, the Debye screening mass is developed when $T \sim \Lambda_{\text{QCD}}$ or even lower with the help of the Landau degeneracy factor. This observation suggests a decrease of the deconfinement phase transition temperature in favor of the observation by the lattice QCD simulation [367, 368]. The decrease of the phase transition temperatures in the deconfinement transition, as well as the chiral restoration discussed above, may not be explained if the dynamical quark mass increases with an increasing magnetic-field strength.

To quantify the above discussions, we discuss the Polyakov loop with a finite quark mass [305, 566]. We parametrize the nonperturbative gluonic potential from the quenched lattice QCD results as [567]

$$\mathcal{U}[C] = -\frac{1}{2}a(T)\Phi^2 + b(T) \ln [1 - 6\Phi^2 + 8\Phi^3 - 3\Phi^4], \quad (455)$$

with

$$a(T) = a_0 + a_1(T_0/T) + a_2(T_0/T)^2, \quad b(T) = b_3(T_0/T)^3. \quad (456)$$

The C variable is related to the Polyakov loop Φ via Eq. (370). Here, the parameters are given as $a_0 = 3.51$, $a_1 = -2.47$, $a_2 = 15.2$, $b_3 = -1.75$, and $T_0 = 270$ MeV for $N_c = 3$. This fitting result replaces the perturbative one $V_{\text{YM}}[C]$ in Eq. (376). On top of this, we include the quark contribution to examine the tendency of the magnetic-field effects. The quark contribution is included at the one-loop level as in Sec. 6.6.2, so that the strong-coupling effects in QCD are approximately included through the magnitude of the dynamical quark mass. For simplicity, we take the color eigenvalues $w_i = \pm 1/2, 0$. Then, the quark part $V_{\text{quark}}[C, B]$ in Eq. (377) takes the same form for $N_c = 2$ and 3 because the quark with the eigenvalue $w_3 = 0$ does not contribute to the potential. Therefore, we obtain the quark contribution to the effective potential by performing the numerical integration (378) as previously.

¹⁰⁸We first take the static limit $q^0 \rightarrow 0$ and then the long wavelength limit $q_z \rightarrow 0$. We also take the homogeneous limit $|q_{\perp}| \rightarrow 0$ in the transverse plane.

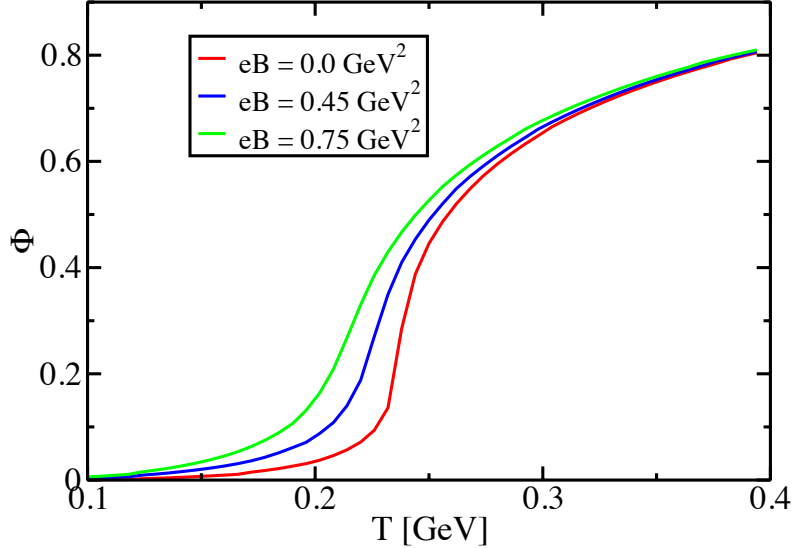


Figure 49: Temperature dependence of the Polyakov loop Φ determined from the effective potential at different values of the magnetic-field strength [305].

In Fig. 49, we show the temperature dependence of the Polyakov loop Φ determined from the stationary point of the effective potential [305]. In this analysis, we fix the dynamical quark mass at 350 MeV that is independent of the magnetic field and is of the order of Λ_{QCD} . The quark contribution is enhanced as we increase the magnetic-field strength, leading to an enhancement of explicit breaking of the center symmetry. In turn, this gives rise to a tendency of decreasing transition temperature $T_c(B) < T_c(B = 0)$ in the strong magnetic field $|eB| > \Lambda_{\text{QCD}}^2$.

7.4.4 Mesonic excitations toward the phase transitions

In the low-energy QCD, hadronic states should serve as a good basis rather than quarks and gluons because of the color confinement. Therefore, it is important to identify the hadron spectra in strong magnetic fields. Knowing the hadron spectra enables us to compute the pressure function (or the partition function) in the so-called hadron resonance gas model. It is a tradition to discuss the deconfinement phase transition with the hadron resonance gas model. Also, the chiral condensate can be in principle computed by taking a derivative of the pressure function (or the partition function) with respect to the current quark mass.

Magnetic-field effects have been included into the hadron resonance gas model as the Landau quantization and the Zeeman effect on point-like charged hadrons [549]. Such point-like picture works in the weak magnetic field regime, but may break down in the strong magnetic field regime. Indeed, when the Zeeman energy becomes larger than a hadron mass at the zero magnetic field, the squared energy falls into a negative value. However, we have seen in the above that lattice QCD simulations do not support such collapsing behaviors (see Fig. 43). The internal structures need to be reconstructed when dense magnetic lines penetrate through hadrons, which can cure problems in the naive treatment. It is particularly important to investigate neutral pions that remain the NG boson and govern the thermodynamics. Those issues are also related to one of the original issues posed in the beginning of this subsection; The conventional chiral perturbation theory does not work in the strong magnetic field regime $q_f B \gtrsim \Lambda_{\text{QCD}}^2$.

Magnetic-field effects on meson properties were studied with various frameworks [61, 73, 106, 326,

353, 354, 356, 371, 372, 447, 448, 524, 561, 568–583] (see also Refs. [522, 584, 585] for baryons). Among others, meson states can be constructed from the Bethe-Salpeter equation in a traditional way. The quark propagator should be dressed by the self-energy that gives the dynamical quark mass. Another ingredient is the gluon-exchange interactions between a quark and an antiquark. One can start with the simplest set-up, for example, in the LLL approximation and the ladder approximation [61]. Similar to the case of the SD equation discussed above, one will find a convolution among the quark and antiquark wave functions and the gluon propagator on the ladder. As a result, one finds a reduced gluon propagator analogous to that in Eq. (450), though they are not exactly the same due to different kinematics (see Ref. [61] for an explicit form). The effective interaction range in the transverse plane is again determined by the ratio of the cyclotron radius to $1/\Lambda_{\text{QCD}}$ when the gluon interaction is dominated by the infrared region below Λ_{QCD} .

When there is an IR dominance in the gluon propagator, soft gluons only mediate the interactions among nearby quark and antiquark states in the transverse plane. Therefore, the meson wave functions are squeezed in (1+1)-dimensional forms. Indeed, prolate shapes of mesonic wave functions have been observed with lattice QCD simulations [526]. The formation of such squeezed mesons saves the energy cost due to the string extension in the transverse direction. The meson spectrum is dominantly determined by the internal eigenmodes along the magnetic field, and the spectrum of “light” mesons will not strongly depend on the magnetic-field strength once we are in the strong-field regime [61].¹⁰⁹ Therefore, a typical light meson mass should remain of the order of the saturation value of the dynamical quark mass $\sim \Lambda_{\text{QCD}}$. Moreover, the meson spectrum should succeed the Landau degeneracy of its constituent quark and antiquark unless the gluon interaction breaks the translation invariance in the transverse plane.

When the low-energy dynamics is governed by such light and degenerate meson excitations, the system is more easily boiled up at finite temperature with the aid of the large degeneracy, as compared to the case without magnetic fields when the same amounts of energy are injected to the systems. Namely, near the phase transition region $T \sim \Lambda_{\text{QCD}}$ and in the strong-field regime $eB \gtrsim \Lambda_{\text{QCD}}^2$, the thermodynamic pressure grows as $eB \times T^2$ with an increasing magnetic field, and is enhanced as compared to the Stefan-Boltzmann law $T^4 \sim \Lambda_{\text{QCD}}^4$ in the (3+1) dimensions. The magnetically enhanced pressure will lead to a decrease of the phase transition temperatures [61, 73]. Numerical analyses are yet left as an open problem (see Ref. [586] for recent demonstration within a nonrelativistic model). Further studies are desired in cooperation with the progress in lattice QCD simulations on the hadron spectrum. It is also very interesting to discuss the magnetization and the possible critical point suggested by the lattice QCD simulations. Those simulation results are summarized earlier in this section.

8 Quantum anomaly in transport phenomena

In the last section, we discuss the transport phenomena in magnetic fields. Computing the vector and axial-vector currents, we find the *chiral magnetic effect* and *chiral separation effect* that belong to a family of the anomaly-induced transport phenomena or, in short, *anomalous transport phenomena* named after their relations to quantum anomaly. We then discuss the dynamics of helicities driven by the chiral magnetic effect.

8.1 Chiral magnetic/separation effect

We focus on the currents transported by massless fermion carriers. Mass effects are discussed in the subsequent section and Appendix G. Since the chirality is a good quantum number for massless fermions,

¹⁰⁹Good quantum numbers for meson states are different from those in the absence of magnetic fields (see an appendix in Ref. [61]). Light mesons here mean the low lying modes in the strong magnetic field.

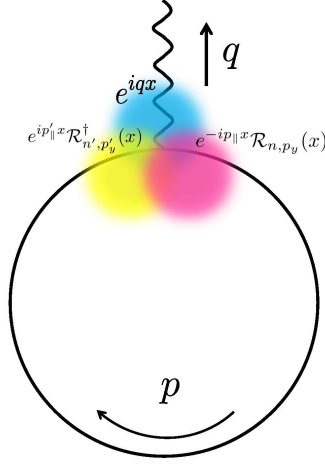


Figure 50: Current in an external magnetic field with the Ritus basis.

we compute the current in the chirality basis

$$j_{R/L}^\mu(x) = \langle \bar{\psi}(x) \gamma^\mu \mathcal{P}_{R/L} \psi(x) \rangle, \quad (457)$$

where the chirality projection operator is defined by $\mathcal{P}_{R/L} = (1 \pm \gamma^5)/2$ with γ^5 given below Eq. (6). In this subsection, the upper and lower signs are understood as those for the right- and left-handed chirality, respectively. The brackets denote the thermal average at finite temperature and density with a finite chemical potential $\mu_{R/L}$ in the chirality basis.

Recall that we examined the Landau levels of the relativistic fermions in Sec. 2.3.1. The Ritus basis (84) provides the eigenspinor in a magnetic field, so that the spatially homogeneous currents may be decomposed into contributions from the Landau levels according to the Ritus-basis mode expansion (93) in the Landau gauge. Assuming that the magnetic field is applied in the third direction without loss of generality, the currents along the magnetic field are given as

$$\begin{aligned} j_{R/L}^3(q=0) &= \frac{1}{L_x L_y} \int d^3x e^{-i0 \cdot x} j_{R/L}^3(x) \\ &= \frac{1}{L_x L_y} \int d^3x \sum_{\kappa=\pm} \sum_{\kappa'=\pm} \sum_{n=0}^{\infty} \sum_{n'=0}^{\infty} \int \frac{dp_z}{2\pi} \int \frac{dp_y dp'_y}{(2\pi)^2} \frac{1}{\sqrt{4\epsilon_n \epsilon_{n'}}} \\ &\quad \times \left[\langle a_{p_{n'}, p'_y}^{\kappa'\dagger} a_{p_n, p_y}^\kappa \rangle \bar{u}^{\kappa'}(p_{n'}) \mathcal{R}_{n', p'_y}^\dagger(x_\perp) \gamma^3 \mathcal{P}_{R/L} \mathcal{R}_{n, p_y}(x_\perp) u^\kappa(p_n) e^{i(\epsilon_{n'} - \epsilon_n)t} \right. \\ &\quad \left. + \langle b_{\bar{p}_{n'}, p'_y}^{\kappa'} b_{\bar{p}_n, p_y}^{\kappa\dagger} \rangle \bar{v}^{\kappa'}(\bar{p}_{n'}) \mathcal{R}_{n', p'_y}^\dagger(x_\perp) \gamma^3 \mathcal{P}_{R/L} \mathcal{R}_{n, p_y}(x_\perp) v^\kappa(\bar{p}_n) e^{-i(\epsilon_{n'} - \epsilon_n)t} \right], \end{aligned} \quad (458)$$

with $L_{x,y}$ being the system lengths in the transverse directions. The Landau levels are given as $\epsilon_n = \sqrt{p_z^2 + 2n|q_f B|}$ and $\epsilon_0 = |p_z|$ is understood.¹¹⁰ We use the fact that \mathcal{P}_\pm commutes with γ^3 and $\mathcal{P}_{R/L}$ and then the orthogonal relation (94b) to find that

$$\begin{aligned} j_{R/L}^3(q=0) &= \frac{|q_f B|}{2\pi} \sum_{\kappa=\pm} \sum_{\kappa'=\pm} \sum_{n=0}^{\infty} \int \frac{dp_z}{2\pi} \frac{1}{2\epsilon_n} \\ &\quad \times \left[\langle a_{p_n, p_y}^{\kappa'\dagger} a_{p_n, p_y}^\kappa \rangle \bar{u}^{\kappa'}(p_n) \gamma^3 I_n \mathcal{P}_{R/L} u^\kappa(p_n) + \langle b_{\bar{p}_n, p_y}^{\kappa'} b_{\bar{p}_n, p_y}^{\kappa\dagger} \rangle \bar{v}^{\kappa'}(\bar{p}_n) \gamma^3 I_n \mathcal{P}_{R/L} v^\kappa(\bar{p}_n) \right]. \end{aligned} \quad (459)$$

The Landau degeneracy factor is reproduced from the y integral in the Landau gauge (see the last part of Sec. 2.2.1). The thermal expectation value is assumed to be diagonal in the spin basis, i.e.,

¹¹⁰ ϵ_0 is the positive-energy part of the massless dispersion relation (97). Here, the positive- and negative-energy solutions are already separated explicitly in Eq. (458).

$\langle a_{p_n, p_y}^{\kappa' \dagger} a_{p_n, p_y}^{\kappa} \rangle = \delta_{\kappa \kappa'} f(\epsilon_n - \mu_{R/L})$, where $f(\epsilon) = 1/[\exp(\epsilon/T) + 1]$ is the Fermi-Dirac distribution function. Likewise, we have $\langle b_{\bar{p}_n, p_y}^{\kappa'} b_{\bar{p}_n, p_y}^{\kappa \dagger} \rangle = -\delta_{\kappa \kappa'} f(\epsilon_n + \mu_{R/L})$, where the contribution from the Dirac sea is dropped.

Taking the summation with Eq. (92), we have

$$j_{R/L}^3(q=0) = \frac{|q_f B|}{2\pi} \sum_{n=0}^{\infty} \int \frac{dp_z}{2\pi} \frac{1}{2\epsilon_n} \{f(\epsilon_n - \mu_{R/L}) - f(\epsilon_n + \mu_{R/L})\} \text{Tr}[\not{p}_n \gamma^3 I_n \mathcal{P}_{R/L}]. \quad (460)$$

Because of the ‘‘unit matrix I_n ’’ defined in Eq. (95), the result of trace depends on the Landau levels. In case of the hLLs ($n \geq 1$), one finds that the chirality projection operator does not play any role:

$$\text{Tr}[\not{p}_n \gamma^3 I_n \mathcal{P}_{R/L}] = \frac{1}{2} \text{Tr}[\not{p}_n \gamma^3] = 2p_z. \quad (461)$$

Remarkably, the p_z integral in Eq. (459) exactly vanishes for all the hLLs due to the linear dependence of the trace on p_z , and there is no contribution to the current. This is because there are an equal number of the carriers moving in parallel and antiparallel to the magnetic field due to the spin degeneracy, which leads to the vanishing net currents.¹¹¹

In the LLL, because of the spin projection operator from I_0 , the chirality projection operator plays a crucial role. The trace result depends on the chirality as

$$\text{Tr}[\not{p}_0 \gamma^3 I_0 \mathcal{P}_{R/L}] = \frac{1}{4} \left(\text{Tr}[\not{p}_n \gamma^3] + \text{Tr}[\not{p}_0 \gamma^3 (i s_f \gamma^1 \gamma^2)(\pm \gamma^5)] \right) = p_z \pm s_f \epsilon_0. \quad (462)$$

After cancellation of all the hLLs, the LLL contribution is left as

$$j_{R/L}^3(q=0) = \pm s_f \frac{|q_f B|}{2\pi} \int_0^{\infty} \frac{dp_z}{2\pi} \{f(\epsilon_0 - \mu_{R/L}) - f(\epsilon_0 + \mu_{R/L})\}. \quad (463)$$

The overall sign depends on the chirality since the chirality and the momentum flow are locked with each other in the LLL (cf. Figs. 7 and 8). Notice that the currents are odd functions of $\mu_{R/L}$ as also expected from the charge-conjugation properties. The linear term should not depend on temperature for the mass dimensions to work on the both sides. In Eq. (463), the Landau degeneracy factor provides mass-dimension two instead. The integrals can be exactly performed as

$$\int_0^{\infty} \frac{dp_z}{2\pi} \{f(\epsilon_0 - \mu_{R/L}) - f(\epsilon_0 + \mu_{R/L})\} = \frac{\mu_{R/L}}{2\pi}. \quad (464)$$

We have found that the currents do not explicitly depend on temperature. Although each integral in Eq. (464) yields temperature-dependent terms, they are canceled out when we take the difference between the two integrals.

Wrapping up the above computation, we have found that the hLL contributions exactly vanish and that the LLL contributions do not depend on temperature in the massless limit. Since the LLL fermions can only move along the magnetic field, the current in the LLL only has the longitudinal component as easily proven with the identity $\mathcal{P}_{\pm} \gamma \mathcal{P}_{\pm} = \gamma_{\parallel} \mathcal{P}_{\pm}$. Therefore, one can restore the vector forms of the currents

$$\mathbf{j}_V = \mathbf{j}_R + \mathbf{j}_L = q_f \frac{\mu_A}{2\pi^2} \mathbf{B}, \quad (465a)$$

¹¹¹This contrasts to the case of the Ohmic current induced by an electric field, which has a finite net current. The difference can be understood with the parity property: An electric field is a parity-odd quantity, while a magnetic field is a parity-even quantity. Accordingly, acceleration by the electric field induces an asymmetric momentum distribution of carriers with respect to the sign flip $p_z \rightarrow -p_z$, resulting in a nonzero Ohmic current [76, 77, 587, 588].

$$\mathbf{j}_A = \mathbf{j}_R - \mathbf{j}_L = q_f \frac{\mu_V}{2\pi^2} \mathbf{B}, \quad (465b)$$

where the chemical potentials in the V/A basis are related to those in the R/L basis as $\mu_{V/A} = (\mu_R \pm \mu_L)/2$ [589, 590]. The vector and axial-vector currents induced by the magnetic field are now called the chiral magnetic effect (CME) and chiral separation effect (CSE), respectively [79, 303, 589–594]. It is instructive to compare the CME with the familiar Ohmic current $q_f \mathbf{j}_V = \sigma_{\text{Ohm}} \mathbf{E}$. Since the electric and magnetic fields have opposite parity, so do the CME and Ohmic conductivities. This means that the CME only occurs in a parity-odd environment that is characterized by the axial chemical potential μ_A as clear from the asymmetric dependence on the R and L chiralities in the definition of μ_A . The vector chemical potential in the CSE is also necessary for satisfying the charge-conjugation and parity properties. Notice that the CME/CSE will induce a vector/axial charge separation, which acts as a source of the subsequent CSE/CME. This mutual induction gives rise to a longitudinal wave propagating along the magnetic field, which is called the *chiral magnetic wave* [594–597].

8.2 Manifestation of the chiral anomaly

The above results on the currents (465) have been confirmed with various methodologies in terms of quantum field theory [72, 589–591, 594, 598–602], hydrodynamics [311, 603–609], the AdS/CFT correspondence [594, 610–614], quantum kinetic theories [615–626], and lattice gauge theories [523, 627–631].¹¹² The central issue addressed in these studies was the relation of the CME/CSE currents to the chiral anomaly. It has been established by those studies that the factors of $1/(2\pi^2)$ in Eq. (465) stem from the “anomaly coefficient C_A ” involved in the anomalous axial Ward identity [82, 83]

$$\partial_\mu j_A^\mu = q_f^2 C_A \mathbf{E} \cdot \mathbf{B}, \quad (466)$$

where we have $C_A = 1/(2\pi^2)$ for a single-flavor (colorless) Dirac fermion coupled to the electromagnetic field.

Figure 51 shows a quick view of the intimate relation of the chiral magnetic effect to the chiral anomaly. The left panel shows the “spectral flow” across the level-crossing point at the origin when an electric field is applied in parallel to the magnetic field. We discussed the spectral flow in Sec. 2.3.3. After the spectral flow occurred, one finds currents due to acceleration of (negative-energy) particles by an electric field¹¹³ as well as a nonzero chirality imbalance ($\mu_R = -\mu_L$) from the bottomless Dirac. Since the currents and the chirality imbalance are created by the same mechanism, their coefficients should be related to one another.

In the right panel of Fig. 51, we more explicitly identify the relation of the currents to the chiral anomaly in a diagrammatic language. This two-point correlator composed of the LLL loop is nothing but the chiral anomaly diagram in the (1+1) dimensions (see Appendix F.2.2). On the other hand, this diagram identifies the nonzero contribution among the tadpole diagrams in Fig. 50 which we used to compute the currents. We have found that the currents only have the contributions from the LLL and are linear in the chemical potential, whereas the tadpole diagrams originally include contributions from all the Landau levels and all orders in the chemical potential. Therefore, what we computed previously was nothing but the chiral anomaly diagram.

¹¹²These studies have also shown an analogy/difference between the effects of a magnetic field and a vorticity in a chiral fluid (see also other early studies in Refs. [632–635]). Induction of the currents by a vorticity is called the chiral vortical effect. More recent studies include analyses of the interplay between a magnetic field and a vorticity/rotation [636–643] (see Ref. [644] for a review).

¹¹³The acceleration of negative-energy particles, as an analog of valence electrons, would not induce currents if the dispersion relation were not directly connected to the positive-energy states or the conduction band. The linear dispersion relation is a special property of the massless LLL where the particle and antiparticle states, as an analog of the conduction and valence bands, are directly connected with each other. See Appendix G for a massive case.

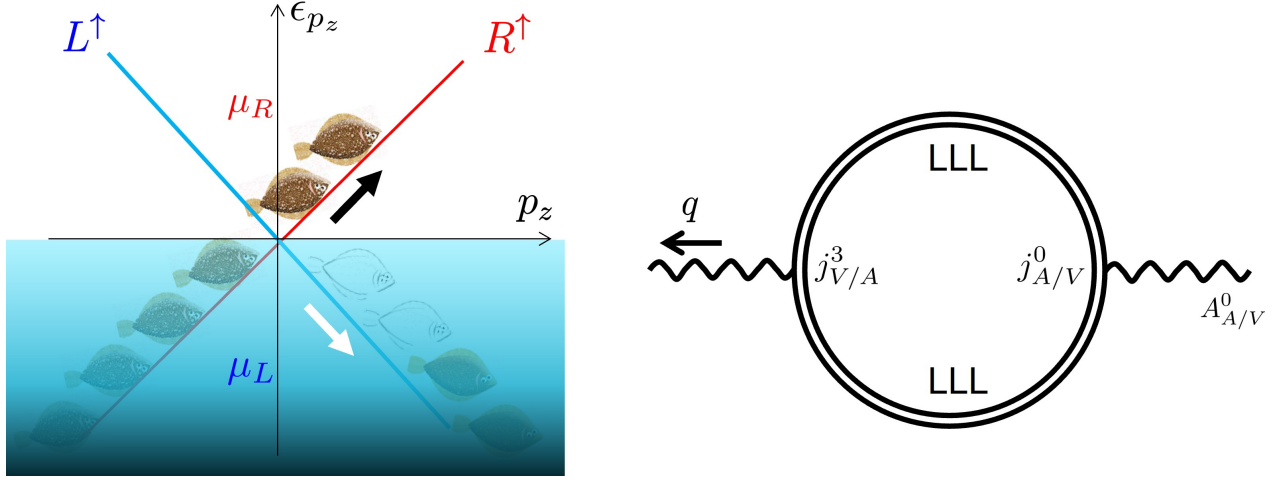


Figure 51: Quick views of the chiral anomaly. Perturbed by an electric field ($q_f E > 0$), right-handed (left-handed) flounders appear (disappear) across the surface of the bottomless Dirac sea (left panel, see also Fig. 7). Fishermen can only catch the right-handed ones. Reinterpretation of the tadpole diagram in Fig. 50 by getting rid of all vanishing pieces (right panel). Internal double lines show the LLL fermion propagators coupled to the vector/axial chemical potential $A_{V/A}^0$.

In order to explicitly see the currents reproduced from the anomaly diagram in Fig. 51, one can construct the Kubo formulas, that is, relations between the currents and the thermal correlators:

$$j_V^3 = \lim_{\omega, \mathbf{q} \rightarrow 0} \Pi_{(VA)}^{30}(\omega, \mathbf{q}) A_A^0, \quad (467a)$$

$$j_A^3 = \lim_{\omega, \mathbf{q} \rightarrow 0} \Pi_{(AV)}^{30}(\omega, \mathbf{q}) A_V^0. \quad (467b)$$

The axial/vector chemical potential is introduced as a temporal component of a constant axial/vector gauge field $A_{A/V}^0 = \mu_{A/V}$, which are coupled to the axial/vector current as $(j_{A/V})_\mu A_{A/V}^\mu$. Thus, the retarded correlator is given by $\Pi_{(VA)/(AV)}^{\mu\nu}(x) = \langle [j_{V/A}^\mu, j_{A/V}^\nu] \theta(x^0) \rangle$ where $j_{V/A}^\mu$ is the current in the LLL. Similar to the purely (1+1) dimensional system, the vector and axial-vector currents are related to each other via a simple identity $\gamma_{\parallel}^\mu \gamma^5 \mathcal{P}_\pm = \mp s_f \epsilon_{\parallel}^{\mu\nu} \gamma_\nu \mathcal{P}_\pm$ with the antisymmetric tensor $\epsilon_{\parallel}^{03} = -\epsilon_{\parallel}^{30} = 1$, i.e., $j_A^\mu = \mp s_f \epsilon_{\parallel}^{\mu\nu} j_{V\nu}$. Therefore, all we need to do is calculating the vector-vector correlator in the LLL which is an analog of that in the Schwinger model [197, 198]. This is a simple exercise given in Appendix F.2.1, and the result is shown in Eq. (605) for the massless case.¹¹⁴ Plugging the correlator into Eq. (467), we have

$$\begin{aligned} j_{V/A}^3 &= -\frac{q_f B}{2\pi} \cdot \frac{\mu_{A/V}}{\pi} \lim_{\omega, \mathbf{q} \rightarrow 0} e^{-\frac{|\mathbf{q}_\perp|^2}{2|q_f B|}} \frac{1}{q_{\parallel}^2} \epsilon_{\parallel}^3 (q_{\parallel}^2 g_{\parallel}^{\rho 0} - q_{\parallel}^\rho q_{\parallel}^0) \\ &= \frac{q_f B}{2\pi} \cdot \frac{\mu_{A/V}}{\pi} \left[\lim_{\omega, q_z \rightarrow 0} \frac{-q_z^2}{\omega^2 - q_z^2} \right]. \end{aligned} \quad (468)$$

The two limits do not commute with each other (see discussions below). Taking the zero-frequency limit first, one can reproduce the CME/CSE currents (465).

According to the above Kubo-formula results, one can interpret those currents as the anomalous currents in the (1+1) dimensions multiplied by the Landau degeneracy factor. As shown in Appendix F.4, there is no temperature correction to the anomalous two-point correlator in the massless case. This is consistent with the previous observation in Eq. (464). The anomalous currents succeed the salient feature of the chiral anomaly, that is, nonrenormalizability in the hydrodynamic limit ($\omega, \mathbf{q} \rightarrow 0$), meaning

¹¹⁴One should just remove the trace of color matrices and set $g = 1$ to match the result in Eq. (605) to the present case.

that the functional forms of the currents do not depend on interactions and energy scales. Indeed, all the theories mentioned in the beginning, from ultraviolet to infrared (effective) theories, confirmed the same form of the anomalous current (465). In Appendix F.3, we also discuss a relation of the chiral anomaly from the LLL two-point correlator in the effective (1+1) dimensions to the chiral anomaly from the familiar triangle diagrams in (3+1) dimensions. They agree with one another in the homogeneous limit such that $|\mathbf{q}_\perp|/|q_f B| \rightarrow 0$. This implies that, in the hydrodynamic limit ($\omega, \mathbf{q} \rightarrow 0$), a perturbative computation linear in the magnetic field as well as the chemical potential provides the same currents as the above LLL result because one can construct an anomalous triangle diagram with a perturbative magnetic field, axial current (vector current), and vector chemical potential (axial chemical potential).

We now briefly return to the issue of the noncommutative limits in Eq. (468). In general, the vanishing frequency and momentum limits of a function may not agree with each other without the Lorentz symmetry which can be broken by, e.g., the presence of a medium. Nevertheless, it was pointed out in Ref. [645] that the hydrodynamic limit for the anomalous currents can be taken irrespective of the ordering of the two limits after appropriate resummation of interaction effects. This could be one of special, and thus specific, properties of the anomalous currents, but can be understood in the following intuitive way. Notice that the hydrodynamic limit is a long spacetime limit, while the one-loop calculation corresponds to a non-interacting limit. To achieve the hydrodynamic limit, one needs to resum interaction effects even when the coupling constant is small since the mean-free time and path are finite and are smaller than the hydrodynamic spacetime scale, which is taken to be infinite. Interestingly, the authors also showed that the interaction effects cancel out in the final expression of the CME current if one takes the hydrodynamic limit. This result supports the nonrenormalizability of the CME current in the hydrodynamic limit. Similar issues of noncommutative limits had been known in the one-loop diagram calculation of the currents in a weak magnetic field [598, 601].

Finally, we add that the effect of the color confinement, i.e., nonzero contributions of hadronic operators to the CME current, was shown on the basis of the Wess-Zumino-Witten action [646], while a vanishing contribution was found in an earlier work [647]. The discrepancy originates from the difference between the Wess-Zumino-Witten actions employed there (see Ref. [646] for discussions about the discrepancy and evaluation of the hadronic operators).

Experimental realization of the chiral magnetic effect

The CME discussed in relativistic heavy-ion collisions [303, 590] have triggered diverse research activities in many other systems including astrophysics, cosmology, and condensed matter physics (see Refs. [11–16, 101, 648, 649] for reviews), *albeit* there had been various proposals equivalent to the CME in the chronicle [see the references above Eq. (466)].

Among the recent progress, we first briefly mention a remarkable experiment in condensed matter physics. In early times, the anomalous current, which is now called the CME, was proposed in a lattice system [79]. However, experimental measurement was achieved only recently thanks to development of the Dirac/Weyl semimetals [650, 651]. In such materials, the axial charge is dynamically created with a parallel electric and magnetic field, so that one will get a chiral imbalance $\mu_A \propto EB$. This imbalance induces the CME contribution to the longitudinal current $j_\parallel = (\sigma_{\text{Ohm}} + cB^2)E$ together with the Ohmic current. A constant c depends on competition between the anomaly effect and relaxation effects due to chirality-flipping processes which may depend on details of materials. The CME gives rise to a suppression of the resistance as we increase the applied magnetic-field strength. This quadratic suppression signals the occurrence of the CME in the Weyl/Dirac semimetals and is referred to as the (anomalous) negative magnetoresistance [652–656]. In experiments, one can study the dependence of the current on the relative angle between the electric and magnetic fields. The negative magnetoresistance has been observed only when an electric and magnetic field are applied nearly in parallel to each other (see Fig. 52) [657–660], where the chiral anomaly plays a dominant role. The reader is referred to

Refs. [661–664] for recent reviews and lists of other experimental papers.

In case of relativistic heavy-ion collisions, one cannot directly measure the current induced in the quark-gluon plasma (QGP) and has less control of electromagnetic-field configurations. Nevertheless, the former issue could be solved by measuring the two-particle angle correlations that have different tendencies for the like-sign and unlike-sign pairs when a charge separation in QGP is induced by the CME current (see Refs. [12, 14–16, 648, 665] for reviews).

In early measurements, nonzero signals were observed by the STAR collaboration at Relativistic Heavy Ion Collider (RHIC)[666–668] and the ALICE collaboration at the Large Hadron Collider (LHC) [669] at the top collision energies. The collision energy dependence was studied in the Beam Energy Scan program I by the STAR collaboration where the signal decreases as the collision energy is decreased [670]. However, the CMS collaboration at the LHC pointed out that the same magnitudes of signals are observed in high-multiplicity proton-nucleus collisions as well as nucleus-nucleus collisions [671, 672]. This implies contamination of the signal due to non-CME effects stemming from the momentum correlations driven by collective motion and/or resonance decay since the CME signal is not expected to be seen in proton-nucleus collisions where the induced magnetic fields have less spatial homogeneity. The STAR collaboration confirmed the presence of such background effects with proton-nucleus and deuteron-nucleus collisions at RHIC [673]. Since then, there have been lots of efforts to disentangle the CME signals from the background effects by those collaborations as well as the ALICE collaboration [674–678] (see also Ref. [679] for an experimental review).

The magnetic-field effects could be disentangled from the background effects if one can compare different collision events with appropriately chosen nuclides. The comparison between the proton-nucleus and nucleus-nucleus collisions posed an important challenge, but one has to deal with the backgrounds and the magnetic fields both in different magnitudes. We need to change either of the magnitudes while keeping the other magnitude intact. A way to achieve distinct magnitudes of the flow backgrounds, without changing the magnitude of the magnetic field, is proposed with the use of deformed uranium nuclei [680]. The tip-tip and body-body collisions generate different magnitudes of the collective flows with similar magnitudes of the magnetic fields. On the other hand, distinct magnitudes of the magnetic fields can be achieved by the “isobar collisions” [680, 681]. Isobars have different atomic numbers but have the same mass numbers, so that one can create different magnitudes of magnetic fields without changing the QCD background effects that are blind to electrical charges carried by protons. Results of the isobar data analysis had been awaited for a few years and were released after careful blind analyses in Ref. [682]. However, the results did not satisfy the predefined criteria for the CME signature and rather exhibited different magnitudes of the background effects for different isobars. Seemingly, the background effects are blind to electric charges but have relevant sensitivities to the shapes and nuclear structures of isobars. One can find a nice summary of the experimental progress in the proceedings [683]. Those effects are still under investigation as of the end of 2022.

8.3 Axial-charge dynamics: Helicity conversion and the chiral plasma instability

The CME conductivity is invariant under the time-reversal transformation since both the vector current and the magnetic field are odd under this transformation, implying the non-dissipative nature of the CME current [606]. However, this is true only if the axial charge was a conserved quantity. One should note that the axial charge is only a conserved quantity in the classical and massless-fermion theory. Namely, the chiral symmetry is explicitly broken by the chiral anomaly at the quantum level and/or by a finite fermion mass. In such situations, the axial chemical potential, which works as the source of the CME, is no longer a static or conserved quantity protected by a symmetry. The chirality imbalance dissipates in real-time dynamics. Therefore, the dynamics of the axial charge can break the time-reversal symmetry, and a consistent description of the coupled dynamics of the axial charge and

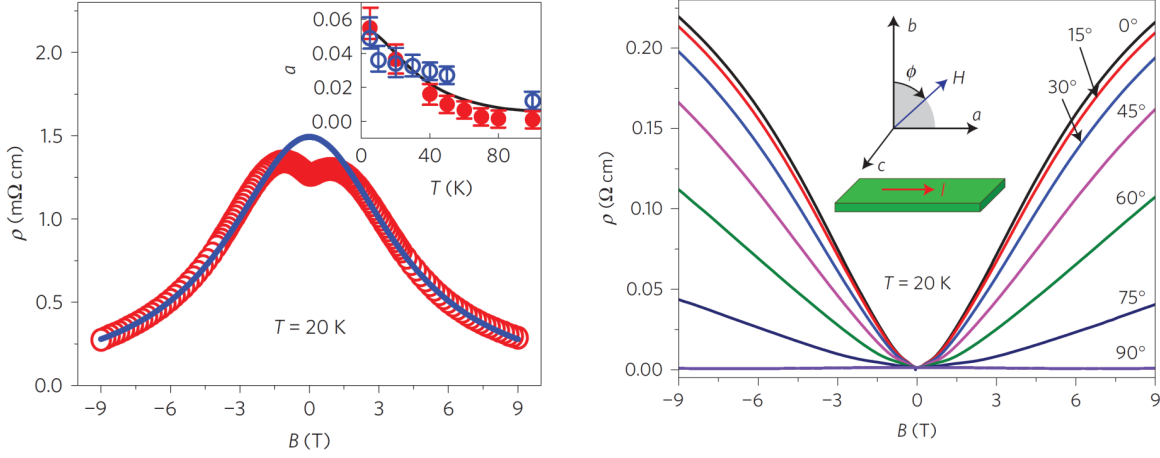


Figure 52: “Negative magnetoresistance” measured with the Weyl semimetal [658]. The resistance ρ decreases with an increasing magnetic field strength (left), which is observed only when the electric and magnetic fields are applied nearly in parallel ($\phi = 90^\circ$ in the right panel). Note that the scales of the vertical axes in the left and right figures are different by three orders.

the CME is important for the long-time off-equilibrium evolution. Prohibition of the *equilibrium* CME current in an external magnetic field has been shown with the generalized Bloch theorem [684] (see also Refs. [649, 685–687]). In contrast, the vector charge is a conserved quantity protected by the $U(1)_V$ symmetry, and the associated vector chemical potential is a well-defined equilibrium quantity. This means that one can investigate mass corrections to the CSE in a thermal equilibrium state specified by a vector chemical potential [593, 688, 689] (see Appendix. G).

The triangle anomaly diagrams give rise to the nonzero divergence of the axial-vector current (466) in the massless case. Computing the triangle diagrams but with massive fermion loops, one finds that the triangle diagrams split into two terms and result in two terms in the divergence of axial-vector current as [82, 83]

$$\partial_\mu j_A^\mu = q_f^2 C_A \mathbf{E} \cdot \mathbf{B} + 2im_f \langle \bar{\psi} \gamma^5 \psi \rangle. \quad (469)$$

In Appendix F.3, we reproduce this computation and provide an explicit form of $\langle \bar{\psi} \gamma^5 \psi \rangle$ in Eq. (631). The first term on the right-hand side is the same as that in the massless case (466). In spite of the mass dependences of the fermion propagators, the mass dependences in this term go away in the end of the day. Mass dependences of the triangle diagrams yield the other term in the form of the pseudoscalar condensate $\langle \bar{\psi} \gamma^5 \psi \rangle$ at the leading nonvanishing order in insertion of external fields. More generally, the pseudoscalar condensate $\langle \bar{\psi} \gamma^5 \psi \rangle$ may have higher-order corrections as well as medium corrections [84]. The presence of this term is suggested by the massive Dirac equation as well. The massive triangle diagrams, i.e., the sum of two terms on the right-hand side as a whole, are suppressed as the fermion mass becomes large and eventually vanish in the infinite-mass limit as shown in Eq. (632). The absence of the axial-charge generation is also understood from the pattern of spectral flow on the parabolic dispersion curves for massive fermions [80] (see also Ref. [85]).

Integrating the anomaly equation (469) for a massive fermion, we find that

$$\frac{d}{dt} [Q_A + q_f^2 \frac{C_A}{2} Q_M] = \Gamma_m, \quad (470)$$

where the fermion chirality, the magnetic helicity, and the chirality mixing rate are, respectively, given by

$$Q_A = \int d^3 \mathbf{x} j_A^0, \quad (471a)$$

$$Q_M = \int d^3\mathbf{x} \mathbf{A} \cdot \mathbf{B}, \quad (471b)$$

$$\Gamma_m = 2im_f \int d^3\mathbf{x} \langle \bar{\psi} \gamma^5 \psi \rangle. \quad (471c)$$

The magnetic helicity Q_M , which originates from the Chern-Simons current, is a gauge-invariant quantity if the surface term vanishes. In the massless case ($\Gamma_m = 0$), we may define the conserved total helicity

$$Q_{\text{tot}} = Q_A + q_f^2 \frac{C_A}{2} Q_M \quad (472)$$

such that $dQ_{\text{tot}}/dt = 0$. However, the two helicities are not conserved separately. Namely, the chiral-anomaly effect allows for the mutual conversion between the fermionic chirality and magnetic helicity when the electromagnetic field is dynamical. As we will see shortly, the CME current actually serves as a physical mechanism for this mutual conversion. On the other hand, the mass effect explicitly breaks the conservation law due to the chirality mixing as shown in Eq. (470). If one invokes on QCD effects, the QCD sphaleron transition is another mechanism of the helicity change [690–692], though its transition rate is suppressed in the weak-coupling regime.

We shall examine the dynamics of helicities with simple equations. The time evolution of the electromagnetic field is governed by the Maxwell equation

$$\nabla \times \mathbf{B} - \frac{\partial \mathbf{E}}{\partial t} = \mathbf{j} = \sigma_{\text{CME}}(t) \mathbf{B} + \sigma_{\text{Ohm}} \mathbf{E}. \quad (473)$$

For simplicity, we assume that the Ohmic conductivity σ_{Ohm} is a constant quantity and that the CME current is given by $\mathbf{j}_{\text{CME}}(t, \mathbf{x}) = \sigma_{\text{CME}}(t) \mathbf{B}(t, \mathbf{x})$ with $\sigma_{\text{CME}}(t) = q_f^2 C_A \mu_A(t)$. Remember that the relation of the CME conductivity σ_{CME} to C_A and μ_A is only proven in the hydrodynamic limit in the presence of a constant axial chemical potential, and the CME conductivity at a finite frequency can be subject to interaction effects [693, 694] (see also Ref. [598]). We here intend to exemplify the dynamics of the axial charge in the slow-variation limit.

An important observation is that Eq. (473) can be regarded as an eigenvalue equation for the magnetic field, i.e., $\nabla \times \mathbf{B} = \sigma_{\text{CME}}(t) \mathbf{B}$, when the electric field is absent. Such eigenvectors are given by the circular-polarization vectors in case of the plane-wave solutions such as $(1, \pm i, 0)e^{ik_z z}$ and by the Chandrasekhar-Kendall (CK) states $\mathbf{W}_{\ell, m}^{\pm}(\mathbf{x}, k)$ as the most general solution [695]. The CK states have desired good properties

$$\nabla \times \mathbf{W}_{\ell, m}^{\pm}(\mathbf{x}, k) = \pm k \mathbf{W}_{\ell, m}^{\pm}(\mathbf{x}, k), \quad (474a)$$

$$\int d^3\mathbf{x} \mathbf{W}_{\ell, m}^a(\mathbf{x}, k) \cdot \mathbf{W}_{\ell', m'}^b(\mathbf{x}, k') = \delta_{ab} \frac{\pi}{k^2} \delta(k - k') \delta_{\ell, \ell'} \delta_{mm'}, \quad (474b)$$

where k is the modulus of the momentum vector and ℓ, m are angular-momentum indices.¹¹⁵ The first equation implies the transversality, $\nabla \cdot \mathbf{W}_{\ell, m}^{\pm}(\mathbf{x}, k) = 0$. By using the CK state, we can decompose the

¹¹⁵The CK states, or the Beltrami fields, are defined as (see Refs. [696–698] and references therein for more details)

$$\mathbf{W}_{\ell m}^{\pm}(\mathbf{x}, k) = \mathbf{T}_{\ell, m}^{\pm}(\mathbf{x}, k) \mp \mathbf{P}_{\ell, m}^{\pm}(\mathbf{x}, k) \quad (475)$$

where

$$\mathbf{T}_{\ell, m}^{\pm}(\mathbf{x}, k) = -\frac{i}{\sqrt{\ell(\ell+1)}} j_{\ell}(kr) (\mathbf{x} \times \nabla) Y_{\ell}^m(\theta, \phi), \quad \mathbf{P}_{\ell, m}^{\pm}(\mathbf{x}, k) = \frac{i}{k} \nabla \times \mathbf{T}_{\ell, m}^{\pm}(\mathbf{x}, k),$$

with the spherical Bessel function $j_{\ell}(kr)$ and the spherical harmonic function $Y_{\ell}^m(\theta, \phi) = e^{im\phi} P_{\ell}^m(\cos \theta)$.

gauge potential \mathbf{A} , magnetic field \mathbf{B} , and electric field \mathbf{E} as

$$\mathbf{A}(t, \mathbf{x}) = \sum_{\ell, m} \int_0^\infty \frac{dk}{\pi} k [\mathcal{A}_{\ell, m}^+(t, k) \mathbf{W}_{\ell, m}^+(\mathbf{x}, k) + \mathcal{A}_{\ell, m}^-(t, k) \mathbf{W}_{\ell, m}^-(\mathbf{x}, k)], \quad (476a)$$

$$\mathbf{B}(t, \mathbf{x}) = \sum_{\ell, m} \int_0^\infty \frac{dk}{\pi} k^2 [\mathcal{A}_{\ell, m}^+(t, k) \mathbf{W}_{\ell, m}^+(\mathbf{x}, k) - \mathcal{A}_{\ell, m}^-(t, k) \mathbf{W}_{\ell, m}^-(\mathbf{x}, k)], \quad (476b)$$

$$\mathbf{E}(t, \mathbf{x}) = -\sum_{\ell, m} \int_0^\infty \frac{dk}{\pi} k [\dot{\mathcal{A}}_{\ell, m}^+(t, k) \mathbf{W}_{\ell, m}^+(\mathbf{x}, k) + \dot{\mathcal{A}}_{\ell, m}^-(t, k) \mathbf{W}_{\ell, m}^-(\mathbf{x}, k)], \quad (476c)$$

where $\mathcal{A}_{\ell, m}^\pm$ is the power spectrum of each helicity mode. Accordingly, the magnetic helicity and the magnetic and electric energies are decomposed as

$$Q_M(t) = \sum_{\ell, m} \int_0^\infty \frac{dk}{\pi} k [(\mathcal{A}_{\ell, m}^+(t, k))^2 - (\mathcal{A}_{\ell, m}^-(t, k))^2], \quad (477a)$$

$$\mathcal{E}_M(t) = \frac{1}{2} \int d^3 \mathbf{x} |\mathbf{B}(t, \mathbf{x})|^2 = \frac{1}{2} \sum_{\ell, m} \int_0^\infty \frac{dk}{\pi} k^2 [(\mathcal{A}_{\ell, m}^+(t, k))^2 + (\mathcal{A}_{\ell, m}^-(t, k))^2], \quad (477b)$$

$$\mathcal{E}_E(t) = \frac{1}{2} \int d^3 \mathbf{x} |\mathbf{E}(t, \mathbf{x})|^2 = \frac{1}{2} \sum_{\ell, m} \int_0^\infty \frac{dk}{\pi} [(\dot{\mathcal{A}}_{\ell, m}^+(t, k))^2 + (\dot{\mathcal{A}}_{\ell, m}^-(t, k))^2]. \quad (477c)$$

Applying the CK decomposition (476) to the Maxwell-Chern-Simons equation (473), we obtain the equation of motion for the helicity components of the gauge field

$$\ddot{\mathcal{A}}_{\ell, m}^\pm(t, k) = -\{k^2 \mp k \sigma_{\text{CME}}(t)\} \mathcal{A}_{\ell, m}^\pm(t, k) - \sigma_{\text{Ohm}} \dot{\mathcal{A}}_{\ell, m}^\pm(t, k). \quad (478)$$

Note that the k modes are still coupled through $\sigma_{\text{CME}}(t)$ that depends on the k spectrum. Without the CME term, the first term on the right-hand side serves as a “restoring force” that induces an oscillation mode near the center position at $\mathcal{A}_{\ell, m}^\pm(t, k) = 0$. However, the CME term pushes the motion away from the origin if the sign of the coefficient, $k^2 \mp k \sigma_{\text{CME}}(t)$, is flipped. Then, the magnetic spectrum $\mathcal{A}_{\ell, m}^\pm(t, k)$ could grow as long as the constrains from the total energy and helicity conservations are satisfied. The Ohmic current works as a “friction” that provides a damping effect.

One can visualize the above observations by constructing an effective potential. Without the dissipative effects ($\sigma_{\text{Ohm}} = 0$ and $m_f = 0$), we find an integral of motion [$d\mathcal{E}_{\ell, m}^\pm(k)/dt = 0$]:

$$\mathcal{E}_{\ell, m}^\pm(k) = \frac{1}{2} (\dot{\mathcal{A}}_{\ell, m}^\pm(t, k))^2 + V_k^\pm[\mathcal{A}_{\ell, m}^\pm(t, k)], \quad (479)$$

where the effective potential is given by

$$V_k^\pm[\mathcal{A}_{\ell, m}^\pm(t, k)] = \frac{1}{2} k^2 (\mathcal{A}_{\ell, m}^\pm(t, k))^2 \mp \frac{1}{2} k \int_0^t dt' \sigma_{\text{CME}}(t') \frac{d}{dt'} (\mathcal{A}_{\ell, m}^\pm(t', k))^2. \quad (480)$$

We dropped the constant of integration which does not play a role in the following. The total energy is found to be

$$\mathcal{E}_{\text{tot}} = \sum_{\ell, m} \sum_{h=\pm} \int \frac{dk}{\pi} \mathcal{E}_{\ell, m}^h(k) = \mathcal{E}_E(t) + \mathcal{E}_M(t) + \int_0^t dt' \int d^3 \mathbf{x} \mathbf{j}_{\text{CME}}(t', \mathbf{x}) \cdot \mathbf{E}(t', \mathbf{x}). \quad (481)$$

As mentioned above, this total energy is a conserved quantity in the absence of the dissipative effects ($\sigma_{\text{Ohm}} = 0$ and $m_f = 0$). The third term shows an energy conservation between the fermionic and

electromagnetic sectors due to the CME current. Here, we only consider a dynamical electric field without an external one.

We are now interested in how the magnetic spectrum evolves, starting with a vanishing initial spectrum $\mathcal{A}_{\ell,m}^{\pm}(0, k) = 0$ and magnetic helicity $Q_M(0) = 0$, but with a finite CME current $\sigma_{\text{CME}}(0) \neq 0$. To examine the stability of the effective potential within the present initial conditions, we shall focus on the quadratic terms near the origin ($\mathcal{A}_{\ell,m}^{\pm}(t, k) = 0$). Then, we can replace $\sigma_{\text{CME}}(t)$ by an initial value $\sigma_{\text{CME}}(0)$. Performing the integral, we get [699]

$$V_k[\mathcal{A}_{\ell,m}^{\pm}(t, k)] \sim \frac{1}{2}\{(k \mp k_*)^2 - k_*^2\}(\mathcal{A}_{\ell,m}^{\pm}(t, k))^2 + \mathcal{O}((\mathcal{A}_{\ell,m}^{\pm}(t, k))^4), \quad (482)$$

where $k_* \equiv \sigma_{\text{CME}}(0)/2 = q_f^2 C_A \mu_A(0)/2$. Either of the helicity modes have a semipositive-definite coefficient in front of the quadratic term, depending on the sign of $\mu_A(0)$. This means a stability at the origin in that helicity mode. On the other hand, the coefficient in the other mode takes a negative value when $0 \leq k \leq |k_*|$, indicating an upward convexity near the origin (cf. Fig. 53 for each ℓ, m, k). Therefore, in this momentum regime, the latter helicity mode is selectively excited in response to an infinitesimal perturbation. As a consequence, a helical magnetic field is generated by the CME current. The presence of such an instability was recognized in early works [700, 701] and was investigated as a possible mechanism for generation of the primordial magnetic field in the inflation era [701] and the electroweak phase transition [702–705]¹¹⁶ or, in the opposite way, for the baryogenesis from the magnetic helicity [709–711]. Now, it is often referred to as the chiral plasma instability (CPI) [712]. As shown in Fig. 53, the CPI can be understood as a cycle of positive feedbacks as follows [713]. First, when there is an initial μ_A and a seed magnetic field B_z , they induce the CME current J_z and subsequently a magnetic field B_θ according to the Ampère’s law. Then, the CME current J_θ induced by B_θ provides a *positive* feedback to the seed magnetic field B_z .

More recently, the instability has been reinvestigated in cosmology [714–723], neutron-star/supernova physics [699, 712, 724–729], and relativistic heavy-ion collisions [696, 697, 730–732]. The presence of the instability was also shown with the chiral magnetohydrodynamics [311] (see also Ref. [312] and references therein for a review and detailed discussions about the recent reformulation of magnetohydrodynamics).

What would be the fate of the instability leading to the helical magnetic field generation? The effective potential $V_k[\mathcal{A}_{\ell,m}^{\pm}(t, k)]$ at a large $\mathcal{A}_{\ell,m}^{\pm}(t, k)$ should be bounded so that the total energy of the system is conserved. The presence of such a quartic term was explicitly constructed for a non-interacting Fermi gas [699]. Then, the unstable mode will oscillate in the vicinity of the local minimum at a non-vanishing helical spectrum. It depends on the energy constraint how large the helical spectrum is at the position of the local minimum. On top of this, if one maintains the Ohmic current in Eq. (478), the oscillatory mode will be damped out due to the energy dissipation and the system will fall in the local minimum. Since the total helicity Q_{tot} is conserved, the gain in the magnetic helicity Q_M needs to be supplied from the fermion chirality Q_A . Therefore, the CME, and thus the instability, will be diminished as Q_A is consumed.

What about effects of the mode coupling through the conservation of the total energy and helicity? In Eq. (477), we notice that a unit magnetic helicity stores an energy k . Therefore, a larger spatial structure is energetically favored for the magnetic field to carry a nonzero magnetic helicity. Under the constraint of the total-helicity conservation, this implies a tendency that short-scale structures of the magnetic-field lines are transformed to large-scale structures. This phenomenon was pointed out as the *inverse energy cascade* of the magnetic helicity in the dynamo theory with the magnetohydrodynamic turbulence (without the CME current) [733–735] and has been applied as the mechanism for extending

¹¹⁶A similar idea with the chiral vortical effect was considered in Ref. [706]. Note also that, when the Lagrangian has an axion term or a topological term $\mathcal{L}_a \propto \theta F^{\mu\nu} \tilde{F}_{\mu\nu}$, we get a current $j^\mu \propto (\partial_\nu \theta) \tilde{F}^{\mu\nu}$. This current can be identified with the CME current with $\mu_A \propto \partial_t \theta$ in Eq. (473). Therefore, the axion electrodynamics [707] contains the same type of instability as implied in Ref. [708].

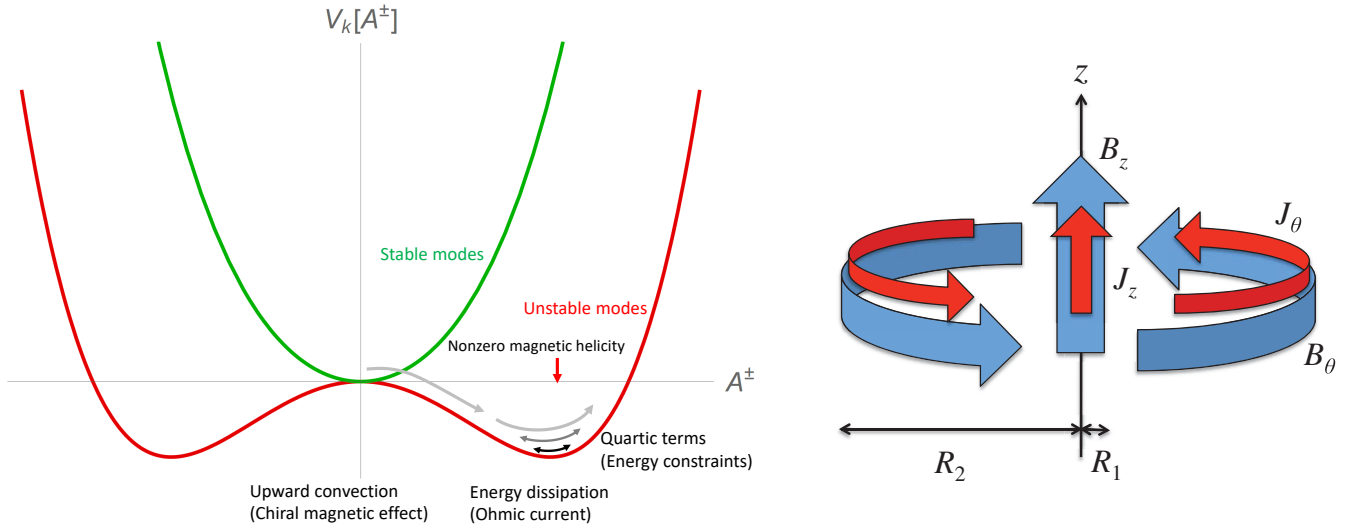


Figure 53: An effective potential for the magnetic spectrum with an unstable convexity at the origin (left). A schematic picture of the positive feedback leading to the chiral plasma instability (right) [713].

the correlation length of the primordial magnetic field in the universe [703, 736–739] (see Refs. [27, 28] for reviews). We point out that the CME term has the same form as the “ α -effect” in the dynamo theory, where the pseudo-scalar coefficient is provided by the fluid kinetic helicity associated with the rotational motion instead of the fermion chirality (see, e.g., textbooks [740, 741]). Subsequently, the inverse energy cascade with the chiral anomaly was intensively investigated [696, 697, 714–717, 719, 727, 732, 742, 743] and the effects of an inhomogeneous $\mu_A(t, \mathbf{x})$ were also examined [744, 745]. Numerical simulation of the chiral MHD evolution in supernovae was performed in Ref. [729].

However, the total helicity also dissipates due to the chirality mixing by the mass term in Eq. (470). In the presence of the explicit chiral symmetry breaking, the chirality is not a conserved quantity and should vanish once a system reaches an equilibrium state: The CME current vanishes in the equilibrium state. A question is if the unstable mode grows fast enough in a transient state before the chirality imbalance is damped out. An answer depends on details of individual systems. The helicity-flipping effects had been mostly neglected in the aforementioned works for the high-temperature epoch in cosmology, but are investigated in Ref. [714] for the electroweak theory and more recently in Refs. [716, 746, 747] in detail. In case of neutron-star/supernovae physics, there is an estimate suggesting that the Rutherford scatterings of electrons off ambient protons have a significant impact on the dissipation of the electron helicity [699, 726]. Also, an estimate of the maximal field strength from the total energy conservation was performed in Ref. [727]. Currently, it is still a challenging issue to create magnetic fields over the cosmological/astrophysical spatial scales in the universe and in the neutron stars/magnetars on the basis of the CPI.

There have been also a number of studies on the axial-charge dynamics in the context of the quark-gluon plasma. The helicity-flip rate by the gluon Compton scattering was estimated in Ref. [732]. Such a perturbative process gives a much longer relaxation time than the lifetime of the quark-gluon plasma. However, it has been known that the relativistic heavy-ion collisions create a “strongly-coupled” quark-gluon plasma, which may demand further estimates beyond the perturbation theory as well. More recently, the kinetic theories for massive fermions are being developed to describe the coupled off-equilibrium dynamics among the vector and axial charges [748–753], which may be called the “axial kinetic theory” (see Ref. [754] for a review). Compared to the “chiral kinetic theory” for massless fermions [615–626], the axial kinetic theory contains a larger number of dynamical degrees of freedom since fermion spin is no longer aligned to the momentum in the massive theories. A smooth connection

between the massive and massless theories are shown in Ref. [750] (see also Ref. [752]). It is the next indispensable step toward description of the relaxation dynamics to implement the collisional effects in the quantum kinetic equations [755, 756]. Also, there has been progress in the real-time numerical simulation for the axial-charge generation, the CME, and the CPI [757–762].

In the context of QCD thermodynamics, the theta angle in the presence of a magnetic field and an Euclidean electric field was measured by the Monte Carlo lattice QCD simulation [541]. Another simulation for the topological susceptibility in a magnetic field (without an electric field) showed that the magnitude of the spatial correction of the topological charge fluctuation is enhanced, but an anisotropy with respect to the parallel and perpendicular directions to the magnetic field is small at $eB = 1.1$ GeV [350].

9 Summary

In this review article, we presented fundamentals and applications of the quantum dynamics under strong fields. In the first half, we summarized the fundamental points in a pedagogical way so that the reader can get the techniques required in the strong-field physics. We discussed the Landau quantization by a gauge-invariant formulation, the Ritus basis, and the proper-time method. In the proper-time resummation, the external fields are extended to non-Abelian fields within the covariantly constant fields.

All of these concepts and techniques were then applied to computation of physical quantities in the second half. We discussed the nonlinear QED effects such as the Schwinger mechanism and the vacuum birefringence. The interplay between QED and QCD was discussed on the bases of the Heisenberg-Euler effective action in the coexistent QED and QCD background fields, including the discussion about the Polyakov loop in strong magnetic fields at finite temperature. Then, starting with the basic concept of the dimensional reduction in strong magnetic fields, we discussed the magnetic catalysis of the chiral condensate and the magnetically induced Kondo effect. These nonperturbative phenomena are induced by quantum many-body effects irrespective of the strength of the coupling constant in the underlying theories. We emphasized this point based on the analogy between the systems in the strong magnetic fields and in the dense matter. What is even more interesting is the interplay between such nonperturbative many-body effects and the intrinsic nonperturbative interaction in the low-energy QCD. We provided detailed summary of the novel results from the lattice QCD simulations in the last decade and interpretations putting an emphasis on the importance of the infrared-dominant interaction in QCD. Finally, we discussed the anomaly-induced transport phenomena, called the chiral magnetic effect. As we discussed on the basis of the effective potential, the vector current in the chiral magnetic effect induces the chiral plasma instability and the associated conversion of the fermion helicity to the magnetic helicity as a consequence of chiral anomaly; This instability is expected to be a potential mechanism of amplifying coherent magnetic fields over the astronomical scales.

The strong-field physics is still a growing research field with the advent of experiments using high-intensity laser field, condensed matter materials, and heavy-ion collisions as well as astrophysical observations. The interested reader is referred to the references and the topical review papers cited in the previous sections. We hope that this review article provides useful introduction for many readers who would like to understand the basic aspects of the strong-field physics.

Acknowledgement

The authors thank Gergely Endrődi, Kenji Fukushima, Yoshimasa Hidaka, Masaru Hongo, Xu-Guang Huang, Toru Kojo, Gergely Markó, Daisuke Satow, Igor Shovkovy, Hidetoshi Taya, Naoki Yamamoto, and Di-Lun Yang for useful discussions and comments. KH thanks Norihiro Hizawa, Hiroki Ohata,

and Kotaro Uzawa, brilliant students in Kyoto University, for carefully reading the manuscript and providing useful feedbacks. K.H. and S.O. thank KEK for hospitalities and financial supports where a part of this work was achieved. This work is partially supported by JSPS KAKENHI under grant Nos. 20K03948 and 22H02316. The research of S.O. is supported by MEXT-Supported Program for the Strategic Foundation at Private Universities, “Topological Science” under Grant No. S1511006.

A Wave functions in magnetic fields

A.1 Landau gauge

The wave function of the ground state can be obtained by solving an equation

$$\langle x|\hat{a}|0, x_c\rangle = 0. \quad (483)$$

Now, in the Landau gauge, the coordinate representation of the annihilation operator is given by

$$\hat{a} = -i\frac{\ell_f}{\sqrt{2}}\left\{\frac{\partial}{\partial x} + \ell_f^{-2}(\hat{x} - x_c)\right\} = -i\frac{1}{\sqrt{2}}e^{-\frac{\xi^2}{2}}\frac{\partial}{\partial \xi}e^{\frac{\xi^2}{2}}, \quad (484)$$

where $\xi = (x - x_c)/\ell_f$. The derivative is assumed to act on what follows on the right as well as on the Gaussian. The explicit form of the above condition reads

$$\frac{\partial}{\partial \xi}\left(e^{\frac{\xi^2}{2}}\tilde{\phi}_0\right) = 0, \quad (485)$$

where the wave function at $n = 0$ is denoted as $\tilde{\phi}_0 = \langle x|0, x_c\rangle$. Therefore, we find

$$\tilde{\phi}_0(\xi) = C_L e^{-\frac{\xi^2}{2}}, \quad (486)$$

with a factor of $C_L = (\ell_f\pi^{\frac{1}{2}})^{-1/2}$ that comes from the normalization

$$\int dx|\tilde{\phi}(x)|^2 = 1. \quad (487)$$

The wave function of the higher Landau levels can be obtained by multiplying the creation operators as

$$\tilde{\phi}_n(\xi) = \langle x|\frac{(a^\dagger)^n}{\sqrt{n!}}|0, x_c\rangle. \quad (488)$$

The coordinate representation of the creation operator is

$$\hat{a}^\dagger = -i\frac{\ell_f}{\sqrt{2}}\left\{\frac{\partial}{\partial x} - \ell_f^{-2}(\hat{x} - x_c)\right\} = -i\frac{1}{\sqrt{2}}e^{\frac{\xi^2}{2}}\frac{\partial}{\partial \xi}e^{-\frac{\xi^2}{2}}. \quad (489)$$

Therefore, the wave function in the general Landau level is obtained as¹¹⁷

$$\tilde{\phi}_n(\xi) = \frac{1}{\sqrt{n!}}\left(-\frac{i}{\sqrt{2}}\right)^n e^{\frac{\xi^2}{2}}\frac{\partial^n}{\partial \xi^n}\left(e^{-\frac{\xi^2}{2}}\tilde{\phi}_0(\xi)\right) = C_L\frac{i^n}{\sqrt{2^n n!}}e^{-\frac{\xi^2}{2}}H_n(\xi), \quad (490)$$

where the Hermite polynomial is defined in Eq. (59). Including the plane-wave part, we get the wave function shown in Eq. (57).

¹¹⁷Since the overall phase $i^n = \exp(in\pi/2)$ depends on the Landau level n , it is important to maintain it when considering the overlap between the wave functions of different Landau levels. Here are two of examples: Only when we maintain this factor, the fermion propagator from the Ritus method agrees with that from the proper-time method [cf. Eq. (526)] and the Ward identity is satisfied (see an appendix in Ref. [65]). This phase does not appear if one takes an alternative choice of the Landau gauge, $A_x = -By$ or interchange π_x and π_y in the definition of the canonical pair in Eq. (15).

A.2 Symmetric gauge

As in the case of the Landau gauge, one can get the explicit form of the wave function by using the coordinate representation of the creation and annihilation operators. In the symmetric gauge, we, however, have the two sets of the operators, of which the coordinate representation are given by

$$\hat{a}, \hat{a}^\dagger = -i \frac{\ell_f}{\sqrt{2}} \left[\left(\frac{\partial}{\partial x} \pm is_f \frac{\partial}{\partial y} \right) \pm \frac{1}{2\ell_f^2} (x \pm is_f y) \right], \quad (491)$$

$$\hat{b}, \hat{b}^\dagger = \pm \frac{\ell_f}{\sqrt{2}} \left[\left(\frac{\partial}{\partial x} \mp is_f \frac{\partial}{\partial y} \right) \pm \frac{1}{2\ell_f^2} (x \mp is_f y) \right], \quad (492)$$

where the upper (lower) signs on the right-hand side are for \hat{a} and \hat{b} (\hat{a}^\dagger and \hat{b}^\dagger).¹¹⁸ Introducing a complex coordinate

$$\zeta = \frac{1}{\ell_f} (x + is_f y), \quad \bar{\zeta} = \frac{1}{\ell_f} (x - is_f y), \quad (493)$$

the coordinate representation of the annihilation operators are given by

$$\hat{a} = -i\sqrt{2}e^{-\frac{|\zeta|^2}{4}} \frac{\partial}{\partial \bar{\zeta}} e^{\frac{|\zeta|^2}{4}}, \quad \hat{b} = \sqrt{2}e^{-\frac{|\zeta|^2}{4}} \frac{\partial}{\partial \zeta} e^{\frac{|\zeta|^2}{4}}. \quad (494)$$

Then, Eq. (62) can be written as

$$\frac{\partial}{\partial \bar{\zeta}} \left(e^{\frac{|\zeta|^2}{4}} \phi_{00}(\zeta, \bar{\zeta}) \right) = \frac{\partial}{\partial \zeta} \left(e^{\frac{|\zeta|^2}{4}} \phi_{00}(\zeta, \bar{\zeta}) \right) = 0. \quad (495)$$

Therefore, we obtain the LLL wave function as

$$\phi_{00}(\zeta, \bar{\zeta}) = C_S e^{-\frac{|\zeta|^2}{4}}, \quad (496)$$

where the normalization constant $C_S = (2\pi\ell_f^2)^{-\frac{1}{2}}$ is determined from an integral

$$\int dx \int dy |\phi_{00}|^2 = 1. \quad (497)$$

The wave functions of the other states $\phi_{nm} = \langle \mathbf{x} | n, m \rangle$ can be obtained by operating the creation operators

$$\hat{a}^\dagger = -i\sqrt{2}e^{\frac{|\zeta|^2}{4}} \frac{\partial}{\partial \bar{\zeta}} e^{-\frac{|\zeta|^2}{4}}, \quad \hat{b}^\dagger = -\sqrt{2}e^{\frac{|\zeta|^2}{4}} \frac{\partial}{\partial \zeta} e^{-\frac{|\zeta|^2}{4}}. \quad (498)$$

Noting that $\hat{a}^\dagger + i\hat{b} = i\bar{\zeta}/\sqrt{2}$, we find

$$\phi_{nm}(\zeta, \bar{\zeta}) = \frac{1}{\sqrt{n!m!}} \langle \mathbf{x} | (\hat{b}^\dagger)^m (-i\hat{b} + i\frac{\bar{\zeta}}{\sqrt{2}})^n | 0, 0 \rangle = \frac{i^n}{\sqrt{2^n n! m!}} \langle \mathbf{x} | (\hat{b}^\dagger)^m \bar{\zeta}^n | 0, 0 \rangle. \quad (499)$$

To make a connection to a special function, we further arrange the derivative operators as

$$\phi_{nm}(\zeta, \bar{\zeta}) = \frac{i^n (-1)^m 2^{\frac{\ell}{2}}}{\sqrt{n!m!}} e^{\frac{|\zeta|^2}{4}} \frac{\partial^m}{\partial \bar{\zeta}^m} \left(\bar{\zeta}^n e^{-\frac{|\zeta|^2}{4}} \phi_{00}(\zeta, \bar{\zeta}) \right)$$

¹¹⁸While the above explicit forms are specific to the symmetric gauge, the algebra of \hat{b}, \hat{b}^\dagger , as well as \hat{a}, \hat{a}^\dagger , holds independently of the gauge choice since \hat{b}, \hat{b}^\dagger are originally defined with the center coordinates in Eq. (26)

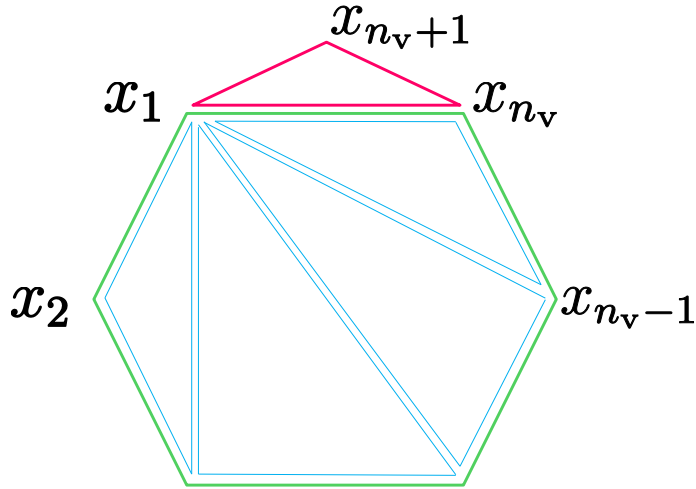


Figure 54: Schwinger phases on the $(n_v + 1)$ -gon, which can be obtained as the sum of those on the n_v -gon (green) and the triangle (magenta).

$$= C_S \frac{i^n (-1)^m}{2^{\frac{\ell}{2}} \sqrt{n!m!}} e^{\frac{\ell}{2} \zeta^\ell} \frac{\partial^m}{\partial \rho^m} (\rho^n e^{-\rho}), \quad (500)$$

where we have put $\ell = m - n$ and $\rho = |\zeta|^2/2$. Then, one can immediately apply the definition of the associated Laguerre polynomial (69). When the angular momentum ℓ is a negative integer, the upper index of the Laguerre polynomial is positive ($\alpha = -\ell$). To maintain the upper index positive for a positive ℓ as well, one may use a formula

$$L_m^{-\ell}(\rho) = \frac{(m - \ell)!}{m!} (-\rho)^\ell L_{m-\ell}^\ell(\rho). \quad (501)$$

The final result is shown in Eq. (68) with $r = \ell_f \sqrt{|\zeta|^2}$.

B Solutions for the resummed propagators

B.1 Schwinger phases on polygons

In Fig. 10, we show closed loops with different numbers of vertices, $n_v = 1, 2$, and 3. When $n_v = 1$ which includes the case of the Heisenberg-Euler effective action discussed in Sec. 4, one finds a vanishing phase as in Eq. (115). However, when $n_v \geq 2$, the integrand differs on each segment by the initial coordinate y in the argument of the propagator (113). in the gauge choice (109). Therefore, one finds in general that

$$\Phi_A^{(n_v)} := \Phi_A(x_2, x_1) + \Phi_A(x_3, x_2) \cdots + \Phi_A(x_1, x_{n_v}) \neq \Phi_A(x_1, x_1). \quad (502)$$

This statement can be checked by choosing a particular path in Eq. (114), that is, a straight path parametrized as $\xi^\mu(w) = y^\mu + (x^\mu - y^\mu)w$, $w \in [0, 1]$. This straight line is shown by blue lines in Fig. 10. In this case, the translation-breaking term in Eq. (114) vanishes, and we find that

$$\Phi_A(x, y) = -q_f \int_0^1 A_\mu(\xi(w)) \frac{d\xi^\mu}{dw} dw. \quad (503)$$

The integrand explicitly depends on the line element $\xi(w)$ on which one performs the integral. For $n_v = 3$, we immediately notice the fact that the phase $\Phi_A(z, x)$ on the segment from x to z is different from the sum of phases $\Phi_A(y, x) + \Phi_A(z, y)$ when one takes a detour via the vertex y . Therefore, the Schwinger phase is nonvanishing for $n_v \geq 3$. We have an exceptional case, that is, $n_v = 2$, which includes the vacuum polarization diagrams. In this case, the Jacobians on the two lines only differ by an overall sign, so that the Schwinger phase identically vanishes thanks to the cancellation. An explicit form of this integral is computed with the Landau gauge in Eq. (524).

While the Schwinger phase is not a gauge- or translation-invariant quantity on each segment, one can show that the sum of the Schwinger phases associated with a closed fermion loop is a gauge-invariant quantity and can be cast into a translation-invariant form. To see this, notice first that the sum of the first two terms in Eq. (114) is by itself a curl-free quantity and does not depend on a specific coordinate y^ν . Therefore, they do not contribute to an integral along a closed path. This readily means invariance of closed fermion loops with respect to the gauge of external fields. The only one nonzero contribution comes from the third term that depends on y^ν . Assembling this contribution from all the segments, one finds the total Schwinger phase on a closed path with n_v vertices:¹¹⁹

$$\Phi_A^{(n_v)} = \frac{q_f}{2} F_{\mu\nu} \sum_{m=1}^{n_v} x_{m+1}^\mu x_m^\nu, \quad (504)$$

where $x_{n_v+1}^\mu \equiv x_1^\mu$ is understood for the closed path. One can arrange this total phase in a manifestly translation-invariant form as follows. Explicitly, the first few cases read

$$\Phi_A^{(2)} = \frac{q_f}{2} F_{\mu\nu} (x_2^\mu x_1^\nu + x_1^\mu x_2^\nu) = 0, \quad (505a)$$

$$\Phi_A^{(3)} = \frac{q_f}{2} F_{\mu\nu} (x_3^\mu - x_2^\mu)(x_2^\nu - x_1^\nu), \quad (505b)$$

$$\Phi_A^{(4)} = \frac{q_f}{2} F_{\mu\nu} \{ (x_4^\mu - x_3^\mu)(x_3^\nu - x_1^\nu) + (x_3^\mu - x_2^\mu)(x_2^\nu - x_1^\nu) \}. \quad (505c)$$

As shown just below, the Schwinger phase on an n_v -gon can be arranged as

$$\Phi_A^{(n_v)} = \frac{q_f}{2} \sum_{m=1}^{n_v-1} F_{\mu\nu} (x_{m+2}^\mu - x_{m+1}^\mu)(x_{m+1}^\nu - x_1^\nu), \quad (506)$$

where again $x_{n_v+1}^\mu \equiv x_1^\mu$. This expression only depends on positions in the form of differences. Therefore, one can conclude that the total Schwinger phase on a closed fermion loop is a gauge- and translation-invariant quantity.

One can prove the general relation (506) by the use of mathematical induction. Assuming that this statement is true for the Schwinger phase $\Phi_A^{(n_v)}$ for a n_v -gon, we construct a $(n_v + 1)$ -gon by inserting a vertex between x_1 and x_{n_v} (see Fig. 54). This suggests to consider a quantity

$$\phi \equiv \Phi_A^{(n_v)} + \frac{q_f}{2} F_{\mu\nu} (x_{n_v+1}^\mu - x_{n_v}^\mu)(x_{n_v}^\nu - x_1^\nu), \quad (507)$$

¹¹⁹One can confirm the total Schwinger phase (504) starting from the integral along the straight path (503). The Schwinger phase on a segment can be arranged as

$$\begin{aligned} \Phi_A(x, y) &= q_f \int_0^1 [\partial_{\xi^\nu} A_\mu(\xi)] \frac{d\xi^\nu}{dw} \xi^\mu dw \\ &= \frac{q_f}{2} F_{\mu\nu} x^\mu y^\nu + \frac{q_f}{2} \int_y^x [\partial_{\xi^\mu} A_\nu(\xi) + \partial_{\xi^\nu} A_\mu(\xi)] \xi^\mu d\xi^\nu. \end{aligned}$$

One can show that the integrand in the second term is a curl-free quantity. Therefore, the contribution of this term vanishes when integrated along a closed path, and the sum of the first term results in Eq. (504).

where the second term is the Schwinger phase for a triangle attached on the n_ν -gon. Since the second term has a manifest translational invariance, the ϕ also has the translational invariance according to the assumption for $\Phi_A^{(n_\nu)}$. Expanding the ϕ , we find a cancellation of the Schwinger phases associated with the diagonal line between the vertices x_1 and x_{n_ν} as

$$\phi = \frac{q_f}{2} F_{\mu\nu} \left[\left(\sum_{m=1}^{n_\nu-1} x_{m+1}^\mu x_m^\nu + x_1^\mu x_{n_\nu}^\nu \right) + \left(x_{n+1}^\mu x_{n_\nu}^\nu + x_1^\mu x_{n_\nu+1}^\nu - x_1^\mu x_{n_\nu}^\nu \right) \right] = \frac{q_f}{2} F_{\mu\nu} \sum_{m=1}^{n_\nu+1} x_{m+1}^\mu x_m^\nu, \quad (508)$$

where $x_{n_\nu+2}^\mu \equiv x_1^\mu$. The rightmost side is nothing but $\Phi_A^{(n_\nu+1)}$, indicating that $\Phi_A^{(n_\nu+1)}$ has a translational invariance when $\Phi_A^{(n_\nu)}$ does. In Eqs. (505b) and (505c), we have already explicitly seen that the first two nonzero cases $\Phi_A^{(3)}$ and $\Phi_A^{(4)}$ have translational invariances. Therefore, we conclude that the Schwinger phase $\Phi_A^{(n_\nu)}$ for an arbitrary n_ν (≥ 3) has a translational invariance. In other words, an explicit expression for $n_\nu \geq 3$ is simply obtained by summing the translation-invariant Schwinger phases on the triangle sub-diagrams [cf. Fig. 54 and Eq. (506)]. Since the phases on the diagonal lines cancel each other in the sum, we get the sum of the phases on the sides as demanded.

One can take a derivative of the Schwinger phase by using the fact that the integral is path-independent once the initial and terminal points are fixed, i.e., $\left[\int_y^x + \int_x^{x+\delta x} + \int_{x+\delta x}^y \right] d\xi^\alpha f_\alpha(\xi; y) = 0$, where we put the integrand of the Schwinger phase (114) as $f_\mu(\xi; y) = A_\mu(\xi) + \frac{1}{2} F_{\mu\nu}(\xi^\nu - y^\nu)$. Following the definition of partial derivative, one finds that

$$\begin{aligned} \frac{\partial}{\partial x^\mu} \Phi_A(x, y) &= -q_f \lim_{\Delta \rightarrow 0} \frac{1}{\Delta} \left[\int_y^{x+\delta x} - \int_y^x \right] d\xi^\alpha f_\alpha(\xi; y) \\ &= -q_f \lim_{\Delta \rightarrow 0} \frac{1}{\Delta} \int_x^{x+\delta x} d\xi^\alpha f_\alpha(\xi; y) \\ &= -q_f f_\mu(x; y), \end{aligned} \quad (509)$$

where only the μ -th component is displaced as $\delta x^\alpha = \Delta \delta^{\mu\alpha}$ by definition. The above result readily means that

$$D_x^\mu e^{i\Phi_A(x, y)} = e^{i\Phi_A(x, y)} \left\{ \partial_x^\mu - \frac{i}{2} q_f F^{\mu\nu} (x_\nu - y_\nu) \right\},$$

which is shown in Eq. (116) in the main text. After the derivative went through the Schwinger phase, the terms between the braces are given in a manifestly gauge- and translation-invariant form and are actually the covariant derivative expressed in the Fock-Schwinger gauge (108) with $x_0^\mu = y^\mu$ as expected from the covariance of the covariant derivative.

B.2 Fermion propagator

We solve Eq. (122) by using an ansatz [99]. Since the operator in Eq. (122) contains the squared momentum p^2 and the second derivative $\partial_p \partial_p$, we assume an ansatz given by

$$\Delta(p|A) = \frac{1}{i} \int_0^\infty ds e^{-i\kappa^2 s + M(s)}, \quad (510)$$

with a momentum bilinear

$$M(s) = ip^\alpha X_{\alpha\beta}(s) p^\beta + Y(s), \quad (511)$$

where $X^{\alpha\beta}(s) = X^{\beta\alpha}(s)$ is a symmetric tensor. Substituting the ansatz for Eq. (122), we find that the equation has a structure

$$1 = \frac{1}{i} \int_0^\infty ds g(s) e^{-f(s)} , \quad (512)$$

in terms of

$$f(s) = -ip^\alpha X_{\alpha\beta}(s) p^\beta - Y(s) + i\kappa^2 s , \quad (513a)$$

$$g(s) = p^\alpha \left(\mathbb{1}_\alpha^\beta - q_f^2 X_{\alpha\rho}(s) F^{\rho\sigma} F_{\sigma\lambda} X^{\lambda\beta}(s) \right) p_\beta + \frac{iq_f^2}{2} F_{\alpha\beta} X^{\beta\gamma}(s) F_\gamma^\alpha - \kappa^2 . \quad (513b)$$

Therefore, if these functions satisfy the following three conditions

$$\frac{d}{ds} f(s) = \frac{1}{i} g(s) , \quad (514a)$$

$$\lim_{s \rightarrow \infty} \text{Re} f(s) \rightarrow \infty , \quad (514b)$$

$$f(0) = 0 , \quad (514c)$$

our ansatz (510) works well. That is, the integral with respect to the proper-time variable s would be simply carried out as

$$\frac{1}{i} \int_0^\infty ds g(s) e^{-f(s)} = - [e^{-f(s)}]_0^\infty = 1 , \quad (515)$$

indicating that Eq. (512) is satisfied.

We shall look for the explicit expressions of $X(s)$ and $Y(s)$ that satisfy the first condition (514a). Then, we check if they meet the second and third conditions. and a finite value $e^{-f(0)} = 1$ at the lower boundary. Inserting Eqs. (513a) and (513b) into Eq. (514a), one finds that $X_\alpha^\beta(s)$ and $Y(s)$ should satisfy a set of equations

$$\frac{d}{ds} X_\alpha^\beta(s) = \mathbb{1}_\alpha^\beta - q_f^2 X_{\alpha\rho}(s) F^{\rho\sigma} F_{\sigma\lambda} X^{\lambda\beta}(s) , \quad (516a)$$

$$\frac{d}{ds} Y(s) = -\frac{q_f^2}{2} F_{\alpha\beta} X^{\beta\gamma}(s) F_\gamma^\alpha . \quad (516b)$$

Owing to elementary relations among the hyperbolic functions, the solution of the first equation (516a) is found to be

$$X_{\alpha\beta}(s) = [(q_f F)^{-1} \tanh(q_f F s)]_{\alpha\beta} , \quad (517)$$

where $(F^{-1})^{\alpha\beta}$ is the inverse matrix of the field strength tensor. Inserting this solution into the second equation (516b), we have

$$\frac{d}{ds} Y(s) = -\frac{q_f}{2} [\tanh(q_f F s)]_{\mu\nu} F^{\nu\mu} . \quad (518)$$

Then, the solution is found to be

$$Y(s) = -\frac{1}{2} \text{Tr} [\ln \{ \cosh(q_f F s) \}] . \quad (519)$$

Now, we check if the conditions in Eqs. (514b) and (514c) are satisfied. To see this, one should note the following two points. First, $X^{\alpha\beta}(s)$ is a real-valued matrix, so that we have $\text{Re} f(s) = -Y(s)$.

Second, the logarithm in $Y(s)$ diverges in the limit, $s \rightarrow \infty$. The second point is valid regardless of the sign of any element in $F_{\mu\nu}$ since the hyperbolic cosine is an even function. We confirm that the second condition (514b) is satisfied as

$$\lim_{s \rightarrow \infty} \text{Re } f(s) = \lim_{s \rightarrow \infty} \frac{1}{2} \text{Tr} [\ln \{ \cosh(q_f F s) \}] + \epsilon s = \infty . \quad (520)$$

On the other hand, in the limit of vanishing s , we have an expansion

$$\lim_{s \rightarrow 0} f(s) = \lim_{s \rightarrow 0} \left[-ip^2 s + \frac{1}{2} \text{Tr} [\ln (\mathbb{1} + O(s^2))] + i\kappa^2 s \right] = 0 , \quad (521)$$

which indicates that the third condition (514c) is successfully satisfied.

This completes solving Eq. (122). The results of this appendix is summarized in Eqs. (123a)–(123c).

B.3 Equivalence with the Ritus basis method

Here, we show an equivalence of the proper-time method discussed in Sec. 3.2.2 with the Ritus-basis method discussed in Sec. 2.3. They should be equivalent with one another since the difference between those methods merely consists in the choice of basis used to define fermion excitations. We have seen in Sec. 2.3 that the Ritus-basis is the eigenfunction of the Dirac operator, while the plane-wave basis used in the proper-time method, as in the familiar perturbation theory without external fields, is no longer an eigenfunction of the Dirac operator in external fields. In short, we examine the change of basis below.

According to the operation of the Dirac operator on the Ritus basis (87), one can find the propagator

$$S(x, x'|A_L) = \sum_{n=0}^{\infty} \int \frac{d^2 p_{\parallel}}{(2\pi)^2} \int \frac{dp_y}{2\pi} e^{-ip_{\parallel}(x-x')} \mathcal{R}_{n,p_y}(x_{\perp}) \left[\frac{i}{\not{p}_n - m} \right] \mathcal{R}_{n,p_y}^{\dagger}(x'_{\perp}), \quad (522)$$

where A_L refers to the external field in the Landau gauge that we used to implement the explicit form of the Ritus basis in Sec. 2.3. Here, the transformation kernel is given by the Ritus basis instead of the familiar Fourier basis. By using the orthogonal relation (94a), one can immediately confirm that $S(x, x'|A_L)$ is the Green's function of the Dirac operator, i.e., $(i\not{D}_x - m)S(x, x'|A_L) = i\delta^{(4)}(x - x')$. In the Ritus-basis space, the propagator has a simple form $i/(\not{p}_n - m)$ in contrast to the resummed propagator (136) in the proper-time method. This is simply because the propagator (522) is an inverse Dirac operator evaluated with its eigenfunction. A drawback in the Ritus-basis method is appearance of complex interaction vertices. In case of the QED interaction, the vertex functions are given by convolutions of the two Ritus basis for fermions and the Fourier basis for a photon, and are no longer the delta functions for the four-dimensional momentum conservation (see, e.g., Ref. [65]).

Below, we show that the propagator (522) agrees with that in the proper-time method (136) up to the Schwinger phase for the Landau gauge. The wave function in the Landau gauge (57) depends on the coordinate and momentum in a particular combination, i.e., $x - s_f \ell_f^2 p_y$. Therefore, by shifting the integral variable $p_y \rightarrow p'_y = p_y - s_f(x + x')/(2\ell_f^2)$ in Eq. (522), one finds that

$$S(x, x'|A_L) = e^{i\frac{q_f B}{2}(x+x')(y-y')} \bar{S}(x - x'), \quad (523)$$

$$\bar{S}(x - x') \equiv \sum_{n=0}^{\infty} \int \frac{d^2 p_{\parallel}}{(2\pi)^2} \int \frac{dp'_y}{2\pi} e^{-ip_{\parallel}(x_{\parallel}-x'_{\parallel})} \mathcal{R}_{n,p'_y} \left(\frac{1}{2}(x - x') \right) S(p_n) \mathcal{R}_{n,p'_y}^{\dagger} \left(-\frac{1}{2}(x - x') \right) .$$

Notice that the phase factor, arising from the shift of the plane-wave part, is factorized from the residual part $\bar{S}(x - x')$ that has a manifest translational invariance. This phase is nothing but the Schwinger

phase introduced in Sec. 3.2.1. This can be confirmed as follows by taking the Landau gauge (53) in Eq. (503):

$$\Phi_A = -q_f \int_0^1 A_2 \frac{d\xi^2}{dw} dw = q_f B \int_0^1 \{x' + (x - x')w\}(y - y') dw = q_f B \frac{x + x'}{2}(y - y'), \quad (524)$$

where the straight path starts from x'^μ toward x^μ , and is parametrized as $\xi^\mu(w) = x'^\mu + (x^\mu - x'^\mu)w$, $w \in [0, 1]$. The rightmost side agrees with the Schwinger phase in Eq. (523) that has an explicit dependence on the gauge field and breaks the translational invariance in the transverse plane. In case of the Landau gauge, this factor also explicitly breaks the rotational invariance around the magnetic field.

Below, we focus on the Fourier transformation of the translation-invariant part:

$$\bar{S}(p) = \int d^4x e^{ip \cdot x} \bar{S}(x). \quad (525)$$

Inserting the explicit form of the Ritus basis (84) in the Landau gauge (57), we find that

$$\bar{S}(p) = \sum_{n=0}^{\infty} \frac{i}{p_n^2 - m^2} \left[(\not{p}_\parallel + m) (\bar{\mathcal{H}}_{n,n} \mathcal{P}_+ + \bar{\mathcal{H}}_{n-1,n-1} \mathcal{P}_-) + i \sqrt{2n|q_f B|} \gamma^1 (\bar{\mathcal{H}}_{n-1,n} \mathcal{P}_+ - \bar{\mathcal{H}}_{n,n-1} \mathcal{P}_-) \right]. \quad (526)$$

The imaginary unit in front of γ^1 is a remnant of a factor of i^n in the wave function (57). We have split \not{p}_n in Eq. (523) into the longitudinal part \not{p}_\parallel and the transverse part $\gamma^1 p_n^\perp$, motivated by the properties of the spin projection operators: $\mathcal{P}_\pm \gamma_\parallel^\mu \mathcal{P}_\pm = \mathcal{P}_\pm \gamma_\parallel^\mu$, $\mathcal{P}_\pm \gamma_\parallel^\mu \mathcal{P}_\mp = 0$, $\mathcal{P}_\pm \gamma_\perp^\mu \mathcal{P}_\pm = 0$, and $\mathcal{P}_\pm \gamma_\perp^\mu \mathcal{P}_\mp = \mathcal{P}_\pm \gamma_\perp^\mu$. Remember that each Landau level has the two-fold spin degeneracy. In Eq. (526), the first and second terms correspond to the spin-up and -down states (depending on s_f), while the remaining two terms the mixing between the degenerate spin states. The overlap between two wave functions is encoded in the coefficient function

$$\bar{\mathcal{H}}_{n,n'}(p_x, p_y) \equiv \int dx e^{ip_x x} \mathcal{H}_n \left(\frac{x/2 - s_f \ell_f^2 p_y}{\ell_f} \right) \mathcal{H}_{n'} \left(\frac{-x/2 - s_f \ell_f^2 p_y}{\ell_f} \right). \quad (527)$$

By using an identity $\mathcal{H}_n(-x) = (-1)^n \mathcal{H}_n(x)$ and inserting Eq. (58) into the above, one can further arrange it as

$$\bar{\mathcal{H}}_{n,n'}(p_x, p_y) = (-1)^{n'} c_n c_{n'} e^{-\ell_f^2 |\mathbf{p}_\perp|^2} \times 2\ell_f \int dx e^{-\frac{1}{4\ell_f^2} x^2} H_n(x + i\ell_f p_\perp) H_{n'}(x + i\ell_f p_\perp^*), \quad (528)$$

where $c_n = 1/(2^n n! \pi^{\frac{1}{2}} \ell_f)^{1/2}$. We also defined a complex variable $p_\perp := p_x + i s_f p_y$ with its complex conjugate p_\perp^* and norm $|p_\perp|^2 = p_x^2 + p_y^2 = |\mathbf{p}_\perp|^2$. By the use of the formula

$$\int dx e^{-x^2} H_m(x+y) H_n(x+z) = 2^n \sqrt{\pi} m! z^{n-m} L_m^{n-m}(-2yz), \quad (529)$$

for $n - m \geq 0$,¹²⁰ we find that

$$\bar{\mathcal{H}}_{n,n}(|\mathbf{p}_\perp|) = 2(-1)^n e^{-\ell_f^2 |\mathbf{p}_\perp|^2} L_n(2\ell_f^2 |\mathbf{p}_\perp|^2), \quad (530a)$$

$$\bar{\mathcal{H}}_{n-1,n}(|\mathbf{p}_\perp|) = \bar{\mathcal{H}}_{n,n-1}^*(|\mathbf{p}_\perp|) = 2i(-1)^n e^{-\ell_f^2 |\mathbf{p}_\perp|^2} \sqrt{\frac{2}{n}} \ell_f p_\perp L_{n-1}^1(2\ell_f^2 |\mathbf{p}_\perp|^2). \quad (530b)$$

¹²⁰When $m - n > 0$, one can simply interchange roles of the two Hermite polynomials to have a positive index on the Laguerre polynomial: $\int dx e^{-x^2} H_m(x+y) H_n(x+z) = 2^m \sqrt{\pi} n! y^{m-n} L_n^{m-n}(-2yz)$. This agrees with an expression obtained by applying the formula (501) to Eq. (529) for $m - n > 0$.

It turns out that those coefficients depend on p_\perp^μ only in the form of the norm $|\mathbf{p}_\perp|$. This indicates restoration of the rotational invariance in the transverse plane, though it is not quite obvious before combining the two wave functions in the Landau gauge.

Inserting those expressions back to Eq. (526), we obtain the fermion propagator in the Fourier basis:

$$\bar{S}(p) = 2ie^{-\ell_f^2 |\mathbf{p}_\perp|^2} \sum_{n=0}^{\infty} (-1)^n \frac{(\not{p}_\parallel + m)(L_n \mathcal{P}_+ - L_{n-1} \mathcal{P}_-) - 2\not{p}_\perp L_{n-1}^1}{p_n^2 - m^2}, \quad (531)$$

where we omitted the arguments of the Laguerre polynomials, $2\ell_f^2 |\mathbf{p}_\perp|^2 = 2|\mathbf{p}_\perp|^2 / |q_f B|$. This expression agrees with the propagator (136) obtained in the proper-time method. $\bar{S}(p)$ has a manifest rotational invariance around the direction of the magnetic field in spite of the use of the Landau gauge that breaks the rotational invariance. This implies that the gauge dependence has been completely factorized in the Schwinger phase Φ_A , and that the other part in Eq. (523) is a gauge-invariant quantity. The spin-mixing terms mentioned below Eq. (526) are nonzero only when the transverse momentum p_\perp^μ is finite. Recall that p_\perp^μ is introduced as the Fourier mode in Eq. (525) and is different from the components in p_n^μ defined below Eq. (88). The square of the latter momentum is given as $p_n^2 = (p^0)^2 - p_z^2 - 2n|q_f B|$ and reproduces the pole positions at the Landau levels.

B.4 Gluon propagator

We solve Eq. (170) for the resummed gluon propagator in parallel to the procedure performed in Appendix B.2 for fermions. In this subsection, we drop the color indices for notational simplicity. Similar to Eq. (510), we assume an ansatz

$$\Delta_{\mu\nu}^{(a)}(p|\mathcal{A}_{\text{FS}}) = \frac{1}{i} \int_0^\infty ds e^{\bar{M}(s)} [e^{-isv^a(\mathcal{F}_{\alpha\beta}\mathcal{J}^{\alpha\beta})}]_{\mu\nu}, \quad (532)$$

with a momentum bilinear

$$\bar{M}(s) = -ip^\alpha X_{\alpha\beta}(s)p^\beta + Y(s), \quad (533)$$

where $X^{\alpha\beta}(s) = X^{\beta\alpha}(s)$ is again a symmetric tensor.¹²¹ Inserting the ansatz (532) into Eq. (170), one finds an equation of the form

$$\delta_\mu^\sigma = \frac{1}{i} \int_0^\infty ds \hat{\mathbf{g}}_{\mu\nu}(s) e^{-\hat{v}^\nu(s)}, \quad (534)$$

and the problem reduces to solving the following equations for $X^{\alpha\beta}(s)$ and $Y(s)$:

$$\hat{\mathbf{f}}_{\mu\nu}(s) = (ip^\alpha X_{\alpha\beta}(s)p^\beta - Y(s))g_{\mu\nu} + isv^a(\mathcal{F}_{\alpha\beta}\mathcal{J}^{\alpha\beta})_{\mu\nu}, \quad (535a)$$

$$\begin{aligned} \hat{\mathbf{g}}_{\mu\nu}(s) = & -p^\alpha \{ \delta_\alpha^\beta - (v^a)^2 X_{\alpha\rho}(s) \mathcal{F}^{\rho\sigma} \mathcal{F}_{\sigma\lambda} X^{\lambda\beta}(s) \} p_\beta g_{\mu\nu} \\ & + i \frac{(v^a)^2}{2} (\mathcal{F}_{\alpha\beta} X^{\beta\gamma}(s) \mathcal{F}_\gamma^\alpha) g_{\mu\nu} - v^a (\mathcal{F}_{\alpha\beta} \mathcal{J}^{\alpha\beta})_{\mu\nu}. \end{aligned} \quad (535b)$$

These equations are very similar to (512)–(513b). The major difference is just the additional Lorentz structures. As in Sec. B.2, we notice that our ansatz in terms of $X^{\alpha\beta}(s)$ and $Y(s)$ works if the above functions $\hat{\mathbf{f}}_{\mu\nu}(s)$ and $\hat{\mathbf{g}}_{\mu\nu}(s)$ satisfy a relation

$$\frac{d}{ds} \hat{\mathbf{f}}_{\mu\nu}(s) = \frac{1}{i} \hat{\mathbf{g}}_{\mu\nu}(s). \quad (536)$$

¹²¹It is convenient to put a minus sign in front of the momentum bilinear for gluons, while it was a positive sign in Eq. (510) for the fermions. In the vanishing field limit, this relative sign correctly reproduces the overall sign of the free propagator.

This leads to the same differential equations as those in Eqs. (516a) and (516b) up to the replacement of the coupling constant $q_f \rightarrow -v^a$. We already have the solutions in Eqs. (517) and (519). Therefore, by using the same $X^{\alpha\beta}(s)$ and $Y(s)$ as those for the fermion propagator, the resummed gluon propagator is obtained as shown in Eq. (171).

C Perturbative propagators in weak external fields

Here, we examine a perturbative interaction between a charged particle and an external field and obtain propagators for a charged scalar particle and a fermion with perturbative insertion of external fields. We also confirm that those propagators agree with those obtained from a perturbative expansion of the resummed propagator shown in Sec. 3.

C.1 Scalar QED

The scalar QED Lagrangian (138) is expanded as

$$\mathcal{L} = \phi^* (-\partial^2 - iq_f \partial^\mu A_\mu + 2iq_f A^\mu \partial_\mu + q_f^2 A^2 - m^2) \phi, \quad (537)$$

where the covariant derivative D^μ is defined in Eq. (73). As in the resummed propagator, we use the Fock-Schwinger gauge (108). Then, we have $\partial_\mu A_{\text{FS}}^\mu = 0$ and $A_{\text{FS}}^\nu \partial_\nu = \frac{1}{4} F^{\mu\nu} (x_\mu \partial_\nu - x_\nu \partial_\mu)$. The last factor in this expression is a generator of the Lorentz group. Since $\phi(x)$ is a scalar field, a Lorentz transform $F^{\mu\nu} \Lambda_{\mu\nu} \phi(x)$ by an ‘‘angle’’ $F^{\mu\nu}$ vanishes. Therefore, the three-point vertex $\phi^* A^\mu \partial_\mu \phi$ does not play any role in the Fock-Schwinger gauge. Removing those vanishing terms, we have

$$\mathcal{L} = \phi^* (-\partial^2 + q_f^2 A_{\text{FS}}^2 - m^2) \phi. \quad (538)$$

Now, an exact propagator is formally written as

$$\begin{aligned} G(p) &= \frac{i}{p^2 - m^2 + q_f^2 A_{\text{FS}}^2} \\ &= G_0(p) \sum_{n=0}^{\infty} [iq_f^2 A_{\text{FS}}^2 G_0(p)]^n, \end{aligned} \quad (539)$$

where the free propagator is given by $G_0(p) = i/(p^2 - m^2)$. We have defined the translation-invariant part by $G_n(p_1, p_2) = (2\pi)^4 \delta(p_1 - p_2) G_n(p_1)$. This expansion provides explicit expressions of perturbative propagators on an order-by-order basis which we denote as $G(p) = \sum_{n=0}^{\infty} G_n(p)$. This series contains the free propagator $G_0(p)$ as the first term. Note that the Schwinger phase, which breaks the translation symmetry, is not shown explicitly in the above exact propagator.

We shall see the perturbative propagator at $n = 1$ which comes with the squared gauge field. Following the above expansion, we find that¹²²

$$\begin{aligned} G_1(p_1, p_2) &= \int dx \int dy \int dz e^{ip_1 x - ip_2 y} G_0(x - z) [iq_f^2 A_{\text{FS}}^2(z)] G_0(z - y) \\ &= (2\pi)^4 \delta(p_1 - p_2) \times (-i) \frac{q_f^2}{2^2} F^{\mu\alpha} F^\nu{}_\alpha G_0(p_1) \frac{\partial^2 G_0(p_1)}{\partial p_1^\mu \partial p_1^\nu}. \end{aligned} \quad (540)$$

¹²²The absence of the three-point vertex can be explicitly seen as follows. Inserting an external field between two free propagators, we have $A_{\text{FS}}^\mu \partial_\mu G_0(z - y) \propto F^{\mu\nu} \int d^4 k e^{-i(z-y)k} \frac{\partial}{\partial k^\mu} [k_\nu G_0(k)]$. However, the derivative of the free propagator is symmetric in the Lorentz indices, and vanishes when contracted with the field strength tensor. This is true in all orders.

It is important to take the origin of the Fock-Schwinger gauge field as $x_0^\mu = y^\mu$. Otherwise, one would get an additional term given by a derivative of delta function. This choice is similar to the one we made in Sec. 3.2, and, thus, the Schwinger phase has the same form as shown in Sec. 3.2.1. The appearance of the delta function in Eq. (540) indicates that the other part has a manifest translational invariance as expected. Inserting the second derivative of the free propagator, we obtain the leading correction to the propagator

$$G_1(p) = \frac{2iq_f^2}{(p^2 - m^2)^3} F_{\mu\alpha} F_\nu^\alpha \left(\frac{p^\mu p^\nu}{p^2 - m^2} - \frac{1}{4} g^{\mu\nu} \right). \quad (541)$$

The same result is obtained from an expansion of the resummed propagator (143) with respect to $q_f F^{\mu\nu}$. In the leading order of the external field strength, we have

$$X^{\mu\nu}(s) \sim s - \frac{q_f^2}{3} F^{\mu\alpha} F_\alpha^\nu s^3, \quad (542a)$$

$$Y(s) \sim -\frac{q_f^2}{4} F_\mu^\alpha F_\alpha^\mu s^2, \quad (542b)$$

Plugging these approximations into the resummed propagator (143), the proper-time integral is performed as

$$\begin{aligned} G(p|A_{\text{FS}}) &\sim \int_0^\infty ds e^{is(p^2 - m^2 + i\epsilon)} \left[1 + q_f^2 \left(\frac{is^3}{3} p_\mu F^{\mu\alpha} F_\alpha^\nu p_\nu + \frac{s^2}{4} F^{\mu\nu} F_{\mu\nu} \right) \right] \\ &= G_0(p) + G_1(p). \end{aligned} \quad (543)$$

The leading term is the free propagator. The next term agrees with $G_1(p)$ in Eq. (541). In this way, the higher-order propagators can be obtained straightforwardly with a systematic expansion of the resummed propagator.

For example, when parallel electric and magnetic fields are applied, one can use Eq. (5a) to simplify the above propagator. Especially, when one of the field, e.g., an electric field, is absent ($E = 0$), we have a simple form

$$G_1(p) = -\frac{i(q_f B)^2}{(p^2 - m^2)^4} [(p_\parallel^2 - p_\perp^2) - m^2]. \quad (544)$$

C.2 Spinor QED

The perturbative fermion propagators are obtained in the same manner as the boson propagators discussed just above. We show the first two terms in the perturbative expansion. The leading correction term is obtained by inserting one external field between free fermion propagators as

$$\begin{aligned} S_1(p_1, p_2) &= (-iq_f) \int dx \int dy e^{ip_1 x - ip_2 y} S_0(x - z) \mathcal{A}_{\text{FS}}(z) S_0(z - y) \\ &= (2\pi)^4 \delta^4(p_2 - p_1) \left(-\frac{1}{4} q_f F^{\mu\nu} \right) \left(\frac{\partial}{\partial p_2^\mu} - \frac{\partial}{\partial p_1^\mu} \right) S_0(p_1) \gamma_\nu S_0(p_2), \end{aligned} \quad (545)$$

where the free propagator is given by $S_0(p) = i/(\not{p} + m)$. Carrying out the derivatives acting on the free propagator, we find that

$$S_1(p) = \frac{i}{4} q_f F_{\mu\nu} \frac{(\not{p} + m) \sigma^{\mu\nu} + \sigma^{\mu\nu} (\not{p} + m)}{(p^2 - m^2)^2}. \quad (546)$$

Similarly, the second-order term is obtained as

$$S_2(p) = -\frac{i}{4}q_f^2 F_{\alpha\beta} F_{\mu\nu} \frac{(\not{p} + m)(f^{\alpha\beta\mu\nu} + f^{\alpha\mu\beta\nu} + f^{\alpha\mu\nu\beta})(\not{p} + m)}{(p^2 - m^2)^5}, \quad (547)$$

where $f^{\alpha\beta\mu\nu} = \gamma^\alpha(\not{p} + m)\gamma^\beta(\not{p} + m)\gamma^\mu(\not{p} + m)\gamma^\nu$. As shown in the previous subsection for the boson propagator, these propagators can be obtained from an expansion of the resummed propagator (124) with respect to $q_f B$. It is worth mentioning that these propagators were used to compute the Wilson coefficients for the gluon operators in the operator product expansion [103, 104, 763] and in magnetic fields [536, 537, 558, 764]. In Sec. F.5, we will use those perturbative propagators to compute the photon/gluon self-energy in a weak magnetic field.

D QCD Lagrangian in external chromo-electromagnetic fields

D.1 Decomposition into external and fluctuation fields

We summarize the QCD Lagrangian in an external chromo-electromagnetic field. According to Eq. (147), the field strength tensor $\mathcal{F}^{a\mu\nu}$ is also decomposed into two parts, that is, the external and fluctuation fields. After a simple arrangement, the field strength tensor is decomposed as

$$\mathcal{F}_{\mu\nu}^a \rightarrow \mathcal{F}_{\mu\nu}^a + D_\mu^{ac} a_\nu^c - D_\nu^{ac} a_\mu^c + g a_\mu^b a_\nu^c f^{abc}, \quad (548)$$

where the field strength tensor on the right-hand side is for the external field $\mathcal{F}_{\mu\nu}^a t^a = \frac{i}{g}[D_\mu, D_\nu]$ which follows from the covariant derivative defined in Eq. (149). Then, the Yang-Mills Lagrangian is expanded into a kinetic term, three- and four-point vertices of the fluctuation field as

$$-\frac{1}{4}\mathcal{F}^{a\mu\nu}\mathcal{F}_{\mu\nu}^a \rightarrow \mathcal{L}_{\text{gluon}}^{\text{kin}} + \mathcal{L}_{\text{gluon}}^{(3)} + \mathcal{L}_{\text{gluon}}^{(4)}, \quad (549)$$

where

$$\mathcal{L}_{\text{gluon}}^{\text{kin}} = -\frac{1}{4}\{(D_\mu^{ac} a_\nu^c - D_\nu^{ac} a_\mu^c)^2 + 2g\mathcal{F}^{a\mu\nu} a_\mu^b a_\nu^c f^{abc}\}, \quad (550)$$

$$\mathcal{L}_{\text{gluon}}^{(3)} = -g(D_\mu^{ad} a_\nu^d) a^{b\mu} a^{c\nu} f^{abc}, \quad (551)$$

$$\mathcal{L}_{\text{gluon}}^{(4)} = -\frac{g^2}{4}(a_\mu^b a_\nu^c f^{abc})(a^{d\mu} a^{e\nu} f^{ade}). \quad (552)$$

The three-point vertex $\mathcal{L}_{\text{gluon}}^{(3)}$ contains the external field in the covariant derivative. Diagrammatically, this coupling is understood by replacing one of the legs in the four-point gluon vertex by the external field.

We shall fix the gauge of the fluctuation field $a^{a\mu}$. For a given external field, the gauge transformation of $a^{a\mu}$ by an angle α^a reads

$$a_\mu^a \rightarrow a_\mu^a + \frac{1}{g}D_\mu \alpha^a + f^{abc} a_\mu^b \alpha^c. \quad (553)$$

Compared with the usual gauge transformation, the derivative in the second term has been replaced by the covariant derivative with the external field. Therefore, the derivative in the gauge-fixing term in terms of the Faddeev-Popov trick is also replaced by the covariant derivative as

$$\mathcal{L}_{\text{gauge}} = -\frac{1}{2\xi_g}(D^{ab\mu} a_\mu^b)^2. \quad (554)$$

Integrating the kinetic term by parts, the gauge-fixed kinetic term is obtained as

$$\mathcal{L}_{\text{gluon}}^{\text{kin}} + \mathcal{L}_{\text{gauge}} = -\frac{1}{2}a_\mu^a \left\{ -(D^2)^{ac} g^{\mu\nu} + \left(1 - \frac{1}{\xi_g}\right) (D^\mu D^\nu)^{ac} - 2g\mathcal{F}^{b\mu\nu} f^{abc} \right\} a_\nu^c. \quad (555)$$

Also, associated with the above gauge-fixing procedure, there arises the ghost term

$$\mathcal{L}_{\text{ghost}} = -\bar{c}^a (D^2)^{ac} c^c - g\bar{c}^a (D_\mu^{ab} a^{d\mu} f^{bdc}) c^c, \quad (556)$$

which also contains the external field in the form of the covariant derivative.

Including all the terms for quarks, gluons, and ghosts, the Lagrangian \mathcal{L} in the external field is wrapped up as

$$\mathcal{L} = \mathcal{L}_{\text{quark}} + \mathcal{L}_{\text{gluon}} + \mathcal{L}_{\text{ghost}}, \quad (557)$$

where

$$\mathcal{L}_{\text{quark}} = \bar{\psi} (i\not{D} - m)\psi - ig\bar{\psi}\not{a}^a(t^a)\psi, \quad (558a)$$

$$\mathcal{L}_{\text{gluon}} = (\mathcal{L}_{\text{gluon}}^{\text{kin}} + \mathcal{L}_{\text{gauge}}) + \mathcal{L}_{\text{gluon}}^{(3)} + \mathcal{L}_{\text{gluon}}^{(4)}, \quad (558b)$$

$$\mathcal{L}_{\text{ghost}} = -\bar{c}^a (D^2)^{ac} c^c - g\bar{c}^a (D_\mu^{ab} a^{d\mu} f^{bdc}) c^c. \quad (558c)$$

The first term in each line provides the kinetic term, of which the inverse is the resummed propagator shown in Sec. 3.4. The other terms provide the perturbative vertices that connect those resummed propagators, assembled as

$$\mathcal{L}_{\text{int}} = -ig\bar{\psi}\not{a}^a(t^a)\psi + \mathcal{L}_{\text{gluon}}^{(3)} + \mathcal{L}_{\text{gluon}}^{(4)} - g\bar{c}^a (D_\mu^{ab} a^{d\mu} f^{bdc}) c^c. \quad (559)$$

D.2 Covariantly constant external fields

As shown in Eq. (154) for the covariantly constant field, the field strength tensor is decomposed into the color direction and the strength. Therefore, the covariant derivative is also decomposed as

$$D^\mu = \partial^\mu - ig(n^a t^a) \mathcal{A}_{\text{ext}}^\mu, \quad (560)$$

where the Abelian-like field $\mathcal{A}_{\text{ext}}^\mu$ does not have the color index. The color matrix $\mathcal{T} \equiv n^a t^a$ in Eq. (560) can be diagonalized because the $N^2 - 1$ generators of $SU(N)$ are Hermitian matrices. Below, we explicitly find the diagonal forms in the fundamental and adjoint representations.

D.2.1 Fundamental representation

We notice that the diagonalized matrix should have $N - 1$ independent components, because the generators are traceless. Since the rank of $SU(N)$, namely the dimension of the Cartan subgroup, is $N - 1$, we can decompose the matrix \mathcal{T}_f by using the simultaneously diagonalized $SU(N)$ generators, where the subscript denotes the matrix \mathcal{T} in the fundamental representation.

We shall discuss the case of $SU(3)$. In order to represent the diagonalized \mathcal{T}_f , we can use the two diagonal matrices out of the eight Gell-Mann matrices. They are $t^3 = \text{diag}(1/2, -1/2, 0)$ and $t^8 = \text{diag}(1/(2\sqrt{3}), 1/(2\sqrt{3}), -1/\sqrt{3})$. Thus, the diagonalized form will be

$$U\mathcal{T}_f U^\dagger = \alpha_1 t^3 + \alpha_2 t^8, \quad (561)$$

where U is the unitary matrix that diagonalizes \mathcal{T}_f . To get convenient forms of the coefficients α_1 and α_2 , we square and cube the both sides of Eq. (561) and then carry out the trace of those quantities. Then, the left-hand side results in (one half of) the following quantities

$$C_1 = n^a n^a = 1, \quad (562a)$$

$$C_2 = d^{abc}n^a n^b n^c, \quad (562b)$$

where the first and second lines are for the square and cube, respectively. We used the normalization $n^a n^a = 1$ and a completely symmetric constant $d^{abc} \equiv \text{Tr}[\{t^a, t^b\}t^c]$. The coefficients C_1 and C_2 are the Casimir invariants in $SU(3)$. Comparing the above expressions with the square and cube of the right-hand side, we obtain two relations

$$C_1 = \alpha_1^2 + \alpha_2^2, \quad (563a)$$

$$C_2 = \frac{1}{2\sqrt{3}}(3\alpha_1^2\alpha_2 - \alpha_2^3). \quad (563b)$$

The first relation suggests to parametrize the coefficients as $\alpha_1 = \sqrt{C_1} \cos \theta$ and $\alpha_2 = \sqrt{C_1} \sin \theta$, respectively. Thus, the angle θ is specified by the gauge invariant quantities $C_1 = 1$ and C_2 as

$$\sin 3\theta = 2\sqrt{3}C_2. \quad (564)$$

The three diagonal elements, $U\mathcal{T}_f U^\dagger = \text{diag}(\lambda^1, \lambda^2, \lambda^3)$, are then specified as

$$\lambda^k = \frac{1}{\sqrt{3}} \sin\left(\frac{2}{3}k\pi - \theta\right), \quad (k = 1, 2, 3). \quad (565)$$

The diagram in Fig. 55 shows the magnitude of λ^k specified by the angle θ in the color space. Multiplying the QCD coupling constant g , we have Eq. (156). Following the properties of the generators, one gets useful identities:

$$\sum_{k=1}^{N_c} \lambda^k = \sum_{a=1}^{N_c^2-1} \text{Tr}[t^a]n^a = 0, \quad (566a)$$

$$\sum_{k=1}^{N_c} (\lambda^k)^2 = \sum_{a=1}^{N_c^2-1} \sum_{b=1}^{N_c^2-1} \text{Tr}[t^a t^b]n^a n^b = \frac{1}{2}. \quad (566b)$$

D.2.2 Adjoint representation

Similar to the case of the fundamental representation, one can diagonalize the Hermitian matrix $\mathcal{T}_{\text{ad}}^{ac} = if^{abc}n^b$ in the adjoint representation as well. In the case of $SU(3)$, the number of independent degrees of freedom is again two. This can be explicitly seen as follows.

We first count the number of independent eigenvalues. Since the eigenvalue λ of the Hermitian matrix is real, the complex conjugate of the eigenvalue equation reads $\mathcal{T}_{\text{ad}}^{*ac}u^{*c} = \lambda u^{*a}$ with u^a being the eigenvector corresponding to λ . The completely antisymmetric property of the structure constant, together with the Hermitian property of the generator, indicates that all components of f^{abc} are real, and thus $\mathcal{T}_{\text{ad}}^{*ac} = -\mathcal{T}_{\text{ad}}^{ac}$. This fact leads to $\mathcal{T}_{\text{ad}}^{ac}u^{*c} = -\lambda u^{*a}$, meaning that the eigenvalue λ appears with a partner which has the opposite sign. The associated eigenvector is given by the complex conjugate u^{*a} . Also, we find that n^c is a trivial eigenvector of $\mathcal{T}_{\text{ad}}^{ac}$ giving a zero eigenvalue. Therefore, apart from the pair of zero eigenvalues, the number of the independent eigenvalues in $SU(3)$ is equal to $(8-2)/2 - 1 = 2$, where the minus one stems from a constraint $\mathcal{T}_{\text{ad}}^{ac}\mathcal{T}_{\text{ad}}^{ca} = N\delta^{ac}n^a n^c = N$ for the adjoint representation of the $SU(N)$ group.

Based on this observation, the diagonalized form can be decomposed by two independent diagonal matrices as

$$U\mathcal{T}_{\text{ad}}U^\dagger = \beta_1 T^3 + \beta_2 T^8, \quad (567)$$

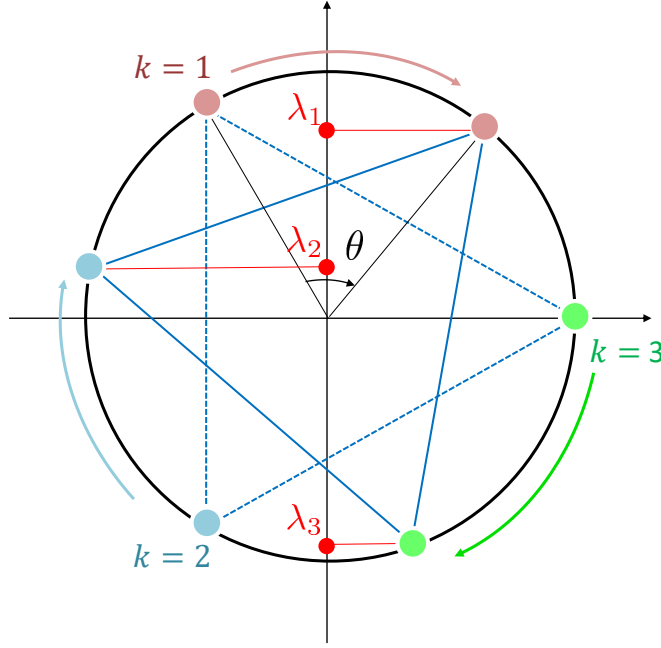


Figure 55: Diagrammatic representation of the eigenvalues λ^k that determine the effective color charges in the covariantly constant field. Note a difference from the definition of θ in Ref. [114].

where we may choose $T^3 = \text{diag}(t^3, 0, -t^3, 0)$ and $T^8 = \text{diag}(t^8, 0, -t^8, 0)$ by using the diagonal Gell-Mann matrices and two vanishing components. Then, computing the square of Eq. (567), we have

$$NC_1 = \beta_1^2 + \beta_2^2, \quad (568)$$

where $C_1 = n^a n^a$ is normalized to be one. As in the fundamental representation, this relation suggests to put $\beta_1 = \sqrt{NC_1} \cos \theta_{\text{ad}}$ and $\beta_2 = \sqrt{NC_1} \sin \theta_{\text{ad}}$. Thus far, it is similar to what we have done for the fundamental representation. However, we find that the symmetric tensor d^{abc} identically vanishes in the adjoint representation, so that it does not make any sense to compute the cube. We, therefore, compute the sixth power of Eq. (567) to find

$$\theta_{\text{ad}} = \frac{1}{6} \cos^{-1} \left(10 - \frac{144C'_2}{C_1^3} \right), \quad (569)$$

where

$$C'_2 = \text{Tr}[(t_{\text{ad}}^a t_{\text{ad}}^b t_{\text{ad}}^c n^a n^b n^c)^2]. \quad (570)$$

These equations establish the connection between the angle θ_{ad} in the adjoint representation and the gauge invariant quantities C_1 and C'_2 . We are now able to specify the eight diagonal elements, $\hat{\mathcal{T}}_{\text{ad}} = \text{diag}(\lambda_{\text{ad}}^1, \lambda_{\text{ad}}^2, \lambda_{\text{ad}}^3, 0, -\lambda_{\text{ad}}^1, -\lambda_{\text{ad}}^2, -\lambda_{\text{ad}}^3, 0)$, in a gauge-invariant way by using the angle θ_{ad} as

$$\lambda_{\text{ad}}^a = \frac{\sqrt{NC_1}}{2\sqrt{3}} \sin \left(\frac{2}{3} a\pi - \theta_{\text{ad}} \right), \quad (a = 1, 2, 3). \quad (571)$$

Multiplying the QCD coupling constant g , we have Eq. (157). The counterparts of identities (566a) and (566b) are obtained as

$$\sum_{a=1}^{N_c^2-1} \lambda_{\text{ad}}^a = \sum_{a=1}^{N_c^2-1} \text{Tr}[t_{\text{ad}}^a] n^a = 0, \quad (572a)$$

$$\sum_{a=1}^{N_c^2-1} (\lambda_{\text{ad}}^a)^2 = \sum_{a=1}^{N_c^2-1} \sum_{b=1}^{N_c^2-1} \text{Tr}[t_{\text{ad}}^a t_{\text{ad}}^b] n^a n^b = N_c. \quad (572b)$$

E QCD effective action in a chromo-magnetic field

We provide supplementary computational notes on the QCD effective action in a chromo- and Abelian magnetic field discussed in Sec. 6.5.

E.1 Vacuum energy in the Landau levels

Here, we find an alternative form of the Landau-level representation (325). Performing the transverse-momentum integral in Eq. (322), there remain the longitudinal-momentum and proper-time integrals in the form

$$\mathcal{L}_{\text{YM}}^{(1)} = -i \frac{|v^a \mathcal{B}|}{2\pi} \sum_{n=0}^{\infty} \frac{1}{2} (2 - \delta_{n0} - \delta_{n1}) \int \frac{d^2 p_{\parallel}}{(2\pi)^2} \int_0^{\infty} \frac{ds}{s} e^{-is\{p_{\parallel}^2 - i\epsilon - (2n-1)|v^a \mathcal{B}|\}}. \quad (573)$$

The energy and proper-time integrals can be also performed as

$$\begin{aligned} & \lim_{\delta \rightarrow 0} \mu^{2\delta} \int \frac{d^2 p_{\parallel}}{(2\pi)^2} \int_0^{\infty} \frac{ds}{s^{1-\delta}} e^{-i\{p_{\parallel}^2 - (2n-1)|v^a \mathcal{B}| - i\epsilon\}s} \\ &= \frac{(-i)^{\frac{1}{2}}}{2\sqrt{\pi}} \lim_{\delta \rightarrow 0} \mu^{2\delta} \int \frac{dp_z}{2\pi} \int_0^{\infty} \frac{ds}{s^{\frac{3}{2}-\delta}} e^{i\{p_z^2 + (2n-1)|v^a \mathcal{B}| + i\epsilon\}s} \\ &= \frac{(-i)^{\frac{1}{2}}}{2\sqrt{\pi}} \lim_{\delta \rightarrow 0} \mu^{2\delta} \int \frac{dp_z}{2\pi} \Gamma(\delta - \frac{1}{2}) [-i(p_z^2 + (2n-1)|v^a \mathcal{B}| + i\epsilon)]^{\frac{1}{2}-\delta} \\ &= i \int \frac{dp_z}{2\pi} \sqrt{p_z^2 + (2n-1)|v^a \mathcal{B}| + i\epsilon}, \end{aligned} \quad (574)$$

where we regularized the UV divergences with a displacement δ and $\Gamma(z) = \int_0^{\infty} ds s^{z-1} e^{-s}$. Plugging this result back into Eq. (573), we obtain the expression in Eq. (347) that is given by the integration of the energy levels, i.e., the vacuum energy in the form of the Landau levels [62].

We shall focus on the region where $p_z^2 + (2n-1)|v^a \mathcal{B}| < 0$. This only occurs in the IR regime where $n = 0$ and $p_- < p_z < p_+$ with $p_{\pm} = \pm \sqrt{|v^a \mathcal{B}|}$. Then, we can rotate the contour to the lower half plane to get

$$\begin{aligned} \int \frac{d^2 p_{\parallel}}{(2\pi)^2} \int_0^{\infty} \frac{ds}{s} e^{-i(p_{\parallel}^2 + |v^a \mathcal{B}| - i\epsilon)s} &= \frac{(-i)^{\frac{1}{2}}}{2\sqrt{\pi}} \int_{p_-}^{p_+} \frac{dp_z}{2\pi} (-i)^{-\frac{1}{2}} \int_0^{\infty} \frac{ds}{s^{\frac{3}{2}}} e^{-|p_z^2 - |v^a \mathcal{B}||s} \\ &= - \int_{p_-}^{p_+} \frac{dp_z}{2\pi} \sqrt{|v^a \mathcal{B}| - p_z^2}. \end{aligned} \quad (575)$$

The contribution from this IR regime gives rise to an imaginary part of the Yang-Mills effective Lagrangian

$$i\Im m[\mathcal{L}_{\text{YM}}^{(1)}] = i \frac{|v^a \mathcal{B}|}{2\pi} \frac{1}{2} \int_{p_-}^{p_+} \frac{dp_z}{2\pi} \sqrt{|v^a \mathcal{B}| - p_z^2} = i \frac{|v^a \mathcal{B}|}{2\pi} \cdot \frac{1}{8} |v^a \mathcal{B}|. \quad (576)$$

A consistent result is also shown in Eq. (348).

E.2 Yang-Mills part

We first identify the origins of the overall factors in the regularized integral (349). To understand each factor in the regularized integral (349), one needs to track it back to the Gaussian integral in Eq. (314b). In the d_{\parallel} dimensions, the Gaussian integral is defined and performed as

$$4 \int \frac{d^2 p_{\perp} d^{d_{\parallel}} p_{\parallel}}{(2\pi)^{2+d_{\parallel}}} \exp \left[-i \frac{p_{\perp}^2}{|v^a \mathcal{B}|} \tan(|v^a \mathcal{B}|s) - ip_{\parallel}^2 s \right] = \frac{4}{(2\pi)^{2+d_{\parallel}}} \cdot \frac{|v^a \mathcal{B}| \pi}{i \tan(|v^a \mathcal{B}|)} \cdot i \left(\frac{\pi}{is} \right)^{d_{\parallel}/2}$$

$$= \left[-\frac{i}{4\pi^2} \frac{|v^a \mathcal{B}|}{\tan(|v^a \mathcal{B}|s)} \cdot \frac{1}{s} \right] \left(\frac{-i}{4\pi s} \right)^{-\delta}, \quad (577)$$

where $\delta := (2 - d_{\parallel})/2$. The overall factor of $\mu^{2\delta}$ is inserted to compensate the mass dimension as before (cf. Sec. 5.2.2). The last factor on the right-hand side $[-i/(4\pi s)]^{-\delta}$ is taken over to the regularized integral $I_{\text{YM}}^{(1)}$. The first factor $|v^a \mathcal{B}|^{-\delta}$ in Eq. (349) appears from the rescaling of the integral variable $s \rightarrow s' = |v^a \mathcal{B}|s$.

The integrals in Eqs. (351a) and (351b) for the Nielsen-Olesen (NO) and residual modes are performed separately. The proper-time integral for the NO mode (351a) is rotated to the upper-half plane, i.e., $\int_0^\infty ds f(s) = i \int_0^\infty ds f(+is)$, since the integral diverges in the lower-half plane. Then, the integral for the NO mode is straightforwardly performed along the positive imaginary axis as

$$\begin{aligned} I_{\text{NO}}^{(1)} &= \left(\frac{4\pi i \mu^2}{|v^a \mathcal{B}|} \right)^\delta \frac{i^2}{i^{2-\delta}} \int_0^\infty \frac{ds}{s^{2-\delta}} e^{-s} \\ &= \left(\frac{4\pi \mu^2}{|v^a \mathcal{B}|} \right)^\delta i^{2\delta} \Gamma(-1 + \delta) \\ &= -\kappa \left(\frac{\mu^2}{2|v^a \mathcal{B}|} \right) - \ln 2 - 1 - i\pi + \mathcal{O}(\delta^1), \end{aligned} \quad (578)$$

where we used an identity $a^\delta = e^{\delta \ln a}$. This result has an imaginary part as foreseen in Eq. (348). We defined a UV-divergent quantity $\kappa(x) := [1/\delta - \gamma_E + \ln(4\pi)] + \ln x$ as in Eq. (353) with the Euler-Mascheroni constant γ_E .

On the other hand, the integral for the residual part $I_{\text{res}}^{(1)}$ can be computed as usual by rotating the integral contour to the lower-half plane:

$$I_{\text{res}}^{(1)} = \left(\frac{4\pi i \mu^2}{|v^a \mathcal{B}|} \right)^\delta \frac{1}{(-i)^{2-\delta}} \int_0^\infty \frac{ds}{s^{2-\delta}} \left[\frac{\cosh(2s)}{\sinh s} - e^{+s} \right]. \quad (579)$$

Notice that the overall imaginary units cancel out in this expression in contrast to the case in the NO mode (578) that gives rise to the imaginary part in the final result (352). The regularized integral (579) can be expressed with the Hurwitz zeta function introduced in Sec. 5.2.2 via another formula.¹²³ Applying the formula (580) to the proper-time integral (579), we get

$$I_{\text{res}}^{(1)} = - \left(\frac{4\pi \mu^2}{|v^a \mathcal{B}|} \right)^\delta \times \Gamma(-1 + \delta) [2(1 - 2^{1-\delta})\zeta_R(-1 + \delta) - 1]$$

¹²³Starting from the integral representation of the Hurwitz zeta function (258), one can easily show a relation

$$\zeta(w; \frac{x+3}{2}) = -\zeta(w; \frac{x+1}{2}) + \frac{2^w}{\Gamma(w)} \left[-\int_0^\infty \frac{ds}{s^{1-w}} e^{-xs} e^s + \int_0^\infty \frac{ds}{s^{1-w}} e^{-xs} \frac{\cosh(2s)}{\sinh s} \right],$$

which, when $x = 0$ for massless gluons, reduces to

$$\int_0^\infty \frac{ds}{s^{1-w}} \left[\frac{\cosh(2s)}{\sinh s} - e^s \right] = \Gamma(w) [2(1 - 2^{-w})\zeta_R(w) - 1]. \quad (580)$$

In the above, we used relations to the Riemann zeta function $\zeta_R(w)$, i.e., $\zeta(w, 1/2) = (2^w - 1)\zeta_R(w)$ and $\zeta(w, 3/2) = \zeta_R(w, 1/2) - 2^w$ (cf. Ref. [229]). An expansion of the Riemann zeta function reads

$$\zeta_R(-1 + \delta) = -\frac{1}{12} + \left(\frac{1}{12} - \ln G \right) \delta + \mathcal{O}(\delta^2),$$

with G being the Glaisher constant $G = 1.2824 \dots$ [327].

$$= -\frac{5}{6}\kappa\left(\frac{\mu^2}{2|v^a\mathcal{B}|}\right) - 1 + 2\ln G + \frac{11}{6}\ln 2 + \mathcal{O}(\delta^1), \quad (581)$$

where $\kappa(x)$ is defined above. Combining the contributions of the NO and residual modes, we obtain the complex-valued result in Eq. (352).

E.3 Quark part

As in the Yang-Mills part, we first identify the origins of the overall factors in the regularized integral (354). One should maintain an overall factor of $(-1)^\delta$ which comes from the determinant $\det(-1)$ associated with the arrangement below Eq. (180). Explicitly, one should note that $\det[(-1)(\mathbb{D}\mathbb{D} + m^2)]^{\frac{1}{2}} = (-1)^\delta \det[\mathbb{D}\mathbb{D} + m^2]^{\frac{1}{2}}$ in Eq. (311a). Also, similar to Eq. (577), the Gaussian integral for fermions (187) yields

$$4 \int \frac{d^2 p_\perp d^d p_\parallel}{(2\pi)^{2+d}} \exp\left(i \frac{p_\perp^2}{\mathbf{b}_{i,f}} \tan(\mathbf{b}_{i,f}s) + ip_\parallel^2 s\right) = \left[-\frac{i}{4\pi^2} \frac{\mathbf{b}_{i,f}}{\tan(\mathbf{b}_{i,f}s)} \cdot \frac{1}{s} \right] \left(\frac{i}{4\pi s} \right)^{-\delta}, \quad (582)$$

where the sign of the imaginary unit is, however, opposite to that in Eq. (577). Combining those factors, we arrive at the regularized integral (354).

Remember that we have performed the proper-time integral for the fermionic effective action in Sec. 5.2.2, albeit it was for electrons in an Abelian magnetic field. In the same manner, one can rotate the integral contour to the lower-half plane and use the formula (259). Then, the regularized integral (354) reads

$$\begin{aligned} I_{\text{quark}}^{(1)} &\equiv \frac{(4\pi i \mu^2)^\delta}{\mathbf{b}_{i,f}} \int_0^\infty \frac{ds}{s^{2-\delta}} e^{-i(m^2 - i\epsilon)s} \cot(\mathbf{b}_{i,f}s) \\ &= -\left(\frac{4\pi\mu^2}{\mathbf{b}_{i,f}}\right)^\delta \int_0^\infty \frac{ds}{s^{2-\delta}} e^{-2\bar{\mathbf{b}}_{i,f}^{-1}s} \coth s \\ &= -\left(\frac{4\pi\mu^2}{\mathbf{b}_{i,f}}\right)^\delta \Gamma(-1 + \delta) \left[2^{2-\delta} \zeta(-1 + \delta, \bar{\mathbf{b}}_{i,f}^{-1}) - (2\bar{\mathbf{b}}_{i,f}^{-1})^{1-\delta} \right], \end{aligned} \quad (583)$$

where $\bar{\mathbf{b}}_{i,f} = 2\mathbf{b}_{i,f}/m_f^2$. The imaginary units are canceled out in the second line after the rotation of the integral contour, leaving a real-valued integral. The divergent pieces can be isolated in the expansion with respect to δ :

$$I_{\text{quark}}^{(1)} = -\left(\frac{1}{3} + 2\bar{\mathbf{b}}_{i,f}^{-2}\right) \left\{ \kappa\left(\frac{\mu^2}{m_f^2}\right) + 1 \right\} + 4\zeta(-1, \bar{\mathbf{b}}_{i,f}^{-1}) \ln \bar{\mathbf{b}}_{i,f}^{-1} + 4\zeta'(-1, \bar{\mathbf{b}}_{i,f}^{-1}), \quad (584)$$

where $\zeta'(z, a) \equiv \partial\zeta(z, a)/\partial z$ and $\zeta(-1, a) = -(2a^2 - 2a + 1/3)/4$ as mentioned below Eq. (260). We arrive at the result in Eq. (355) with $\kappa(x)$ defined below Eq. (578) in the previous subsection for the YM part.

E.4 Scalar QED

The Gaussian integral for scalar QED is the same as that for the quark part (582). Therefore, the regularized integral is given as

$$\mathcal{L}_{\text{scalar}}^{(1)} = -\frac{1}{16\pi^2} I_{\text{scalar}}^{(1)},$$

$$I_{\text{scalar}}^{(1)} \equiv \frac{(4\pi i\mu^2)^\delta}{q_f B} \int_0^\infty \frac{ds}{s^{2-\delta}} e^{-i(m^2-i\epsilon)s} \frac{1}{\sin(q_f B s)}, \quad (585)$$

The above integral can be identified with an integral formula that can be derived from the integral representation of the Hurwitz zeta function (258):

$$\zeta(w; \frac{x+1}{2}) = \frac{2^{w-1}}{\Gamma(w)} \int_0^\infty \frac{ds}{s^{1-w}} e^{-xs} \frac{1}{\sinh s}. \quad (586)$$

Applying this formula, we have

$$\begin{aligned} I_{\text{scalar}}^{(1)} &= - \left(\frac{4\pi\mu^2}{q_f B} \right)^\delta \int_0^\infty \frac{ds}{s^{2-\delta}} e^{-\frac{m^2}{q_f B} s} \frac{1}{\sinh s} \\ &= - \left(\frac{4\pi\mu^2}{q_f B} \right)^\delta \Gamma(-1+\delta) 2^{2-\delta} \zeta(-1+\delta, \frac{m^2}{2q_f B} + \frac{1}{2}) \\ &= 4\zeta(-1, \frac{m^2}{2q_f B} + \frac{1}{2}) \left[\kappa\left(\frac{\mu^2}{q_f B}\right) + 1 - \ln 2 \right] + 4\zeta'(-1, \frac{m^2}{2q_f B} + \frac{1}{2}), \end{aligned} \quad (587)$$

where $\zeta(-1, \frac{\zeta+1}{2}) = (1 - 3\zeta^2)/24$. Therefore, the one-loop correction in scalar QED also contains a logarithmic divergence with a quadratic dependence on B . The numerical coefficient in front of κ is found to be $-1/(16\pi^2) \times (4/24) = -1/(2 \cdot 8\pi^2)(1/6)$, which results in the beta function (363). Note that a factor of $1/2$ is canceled in the renormalization-group equation since the logarithmic dependence on the renormalization scale has a quadratic form in the above expressions.

F Gluon/photon self-energy in magnetic fields

Photons/gluons are not directly coupled to an external $U_{\text{em}}(1)$ field since they do not carry electric charges. Nevertheless, their self-energies are affected by the external fields through fermion loops. Such effects give rise to various consequences. For example, photons propagating in the external fields exhibit the vacuum birefringence (see Sec. 5). Also, we will see below that they acquire a gauge-invariant mass in a strong magnetic field due to the effective dimensional reduction to the (1+1) dimensions as an analog of the Schwinger mass [197, 198] that is also related to chiral anomaly. Besides, it is widely known that the medium-induced self-energies are important to obtain the collective excitations and the screening effects (see, e.g., Refs. [307, 765] and references therein in the absence of external fields). The screening effect is a necessary ingredient when computing transport coefficients and production rate of the electromagnetic probes. In the last part of this appendix, we discuss how the external magnetic fields give rise to novel properties of the photons/gluons via interplay with the medium effects. Below, we first summarize various properties of the gluon/photon propagator in the presence of both the external field and the medium. While we focus on the perturbative computations, it is worth mentioning that the screening effect has been also investigated by the lattice QCD simulations as a nonperturbative method [351, 505, 506].

F.1 General form of gluon/photon propagator

We shall consider the tensor structure of the photon/gluon propagator that can be constrained by the structure of the photon/gluon self-energy. In Eq. (239), we found the tensor structures that satisfy the Ward identity in QED. There are two new tensor structures in addition to the one in the ordinary vacuum because the external field breaks a part of the spatial rotational symmetries. The gluon/photon propagator with the resummation of the self-energies was discussed in Ref. [214] at zero temperature

and density. There is an additional tensor structure when there is both constant electric and magnetic fields (see, e.g., Ref. [102]).

More recently, this result was generalized to the gluon/photon propagator in the presence of both a magnetic field and medium [216]. In such a case, one needs to take into account splitting of the longitudinal and transverse modes with respect to the gluon/photon momentum because the Lorentz symmetry is broken in the medium. Correspondingly, the transverse projection tensor, $g^{\mu\nu} - q^\mu q^\nu / q^2$, for the Lorentz-symmetric system is split into two structures. Then, the tensor structure of the self-energy can be written as

$$\Pi_R^{\mu\nu}(q) = \sum_{i=T,L,\parallel,\perp} \Pi_i(q) P_i^{\mu\nu}(q), \quad (588)$$

where the projection operators are defined by

$$P_T^{\mu\nu}(q) = g^{\mu i} g^{\nu j} \left(\delta_{ij} - \frac{q_i q_j}{q^2} \right), \quad P_L^{\mu\nu}(q) = \left(g^{\mu\nu} - \frac{q^\mu q^\nu}{q^2} \right) - P_T^{\mu\nu}(q), \quad (589)$$

for the splitting of the longitudinal and transverse components in the medium rest frame, and

$$P_{\parallel}^{\mu\nu}(q) = g_{\parallel}^{\mu\nu} - \frac{q_{\parallel}^{\mu} q_{\parallel}^{\nu}}{q_{\parallel}^2}, \quad P_{\perp}^{\mu\nu}(q) = g_{\perp}^{\mu\nu} - \frac{q_{\perp}^{\mu} q_{\perp}^{\nu}}{q_{\perp}^2}, \quad (590)$$

for the splitting of the parallel and perpendicular components with respect to the external magnetic field (applied in the z direction). These four transverse structures have been known to appear in the perturbative computation of the self-energies in the magnetic field and in the medium with the hard thermal loop approximation. Whereas they exhaust the transverse tensor structures in QED, there could appear non-transverse structures from general consideration in QCD where the color current is not necessarily conserved within the fermion sector due to color charges carried by gluons. Below, we, however, do not take into account those potential structures since nonzero components have not been found thus far in perturbative computation in magnetic fields. It is still an open problem to investigate those potential components. The reader is referred to Ref. [216] for more discussions, where useful properties of the projection tensors are also summarized.

Including the self-energy (588), the retarded gluon/photon propagator $D_R^{\mu\nu}(q)$ is given by

$$iD_{\mu\nu}^R(q) = [(iD_0(q))^{-1} + \Pi^R(q)]_{\mu\nu}^{-1}, \quad (591)$$

where we suppressed the color indices for the notational simplicity and the inverse matrix in the Minkowski space is defined as $D^{\mu\nu} D_{\nu\alpha}^{-1} = \delta_{\alpha}^{\mu}$. A relatively simple form of the resummed propagator is obtained in the covariant gauge, so that we use a bare propagator

$$iD_0^{\mu\nu}(q) = \frac{1}{q^2} \left(g^{\mu\nu} - \frac{q^\mu q^\nu}{q^2} \right) + \xi_g \frac{q^\mu q^\nu}{(q^2)^2}, \quad (592)$$

where ξ_g is the gauge-fixing parameter. The photon/gluon energy q^0 contains an infinitesimal imaginary part ($q^0 + i\epsilon$) for the retarded function. Plugging these ingredients, we find the resummed propagator

$$iD_R^{\mu\nu}(q) = \frac{1}{\Delta} \left[(q^2 - \Pi_{\parallel} - \Pi_L) P_T^{\mu\nu}(q) + (q^2 - \Pi_{\parallel} - \Pi_T) P_L^{\mu\nu}(q) + \Pi_{\parallel} P_{\parallel}^{\mu\nu}(q) + D_{\perp}(q) P_{\perp}^{\mu\nu}(q) \right] + \xi_g \frac{q^\mu q^\nu}{(q^2)^2}, \quad (593)$$

where two functions are defined by

$$\Delta \equiv (q^2 - \Pi_T)(q^2 - \Pi_L) - \Pi_{\parallel} \left[q^2 - \Pi_T a \frac{q^2}{q_{\parallel}^2} - \Pi_L (1 - a) \frac{(q^0)^2}{q_{\parallel}^2} \right], \quad (594)$$

$$D_{\perp}(q) \equiv \frac{1}{q^2 - \Pi_T - \Pi_{\perp}} \left[\Pi_{\parallel}(\Pi_L - \Pi_T)(1 - a) \frac{(q^0)^2}{q_{\parallel}^2} + \Pi_{\perp}(q^2 - \Pi_L - \Pi_{\parallel}) \right], \quad (595)$$

with $a \equiv (q_z)^2/|\mathbf{q}|^2$. We assumed that the self-energy corrections (588) are diagonal in the color space. Once the above propagator is obtained, one can, for example, extract dispersion relations of the gluons/photons from pole positions and also use it as a building block in diagram computations. More information including the Coulomb-gauge propagator, physical meaning of each mode, collective excitations, and screening effects are available in Ref. [84, 216, 565].

F.2 Anomalous dynamics in the lowest Landau level

One can estimate the order of each self-energy component associated with a magnetic field and a medium as $\Pi_{\parallel} \sim \alpha_s eB$ and $\Pi_{L,T} \sim \alpha_s T^2$, respectively.¹²⁴ The physical scales of the system are the magnetic field strength eB , temperature T , and/or chemical potential μ . The former dependence originates from the Landau degeneracy factor. When a magnetic field is so strong that $eB \gg T^2$, the magnetized fermion-loop contribution $\Pi_{\parallel} \sim \alpha_s eB$ is much larger than the thermal-loop contributions $\Pi_{L,T} \sim \alpha_s T^2$. Also, we have a vanishing component $\Pi_{\perp} = 0$ in the strong-field limit as discussed in Sec. 5 because the LLL fermions do not have fluctuations perpendicular to the magnetic field. Therefore, considering the momentum regime $p^2 \sim \Pi_{\parallel} \sim eB$ where the thermal contribution is negligible (see Ref. [216] for discussions in other regimes), we have a simple expression of the photon/gluon propagator

$$iD_R^{\mu\nu}(q) = \frac{1}{q^2} \left[P_0^{\mu\nu} + \frac{\Pi_{\parallel}}{q^2 - \Pi_{\parallel}} P_{\parallel}^{\mu\nu} + \xi_g \frac{q^{\mu} q^{\nu}}{q^2} \right]. \quad (596)$$

Especially, when the on-shell LLL current j_{LLL}^{μ} is coupled to the photon/gluon propagator, we have

$$j_{\text{LLL}\mu} iD_R^{\mu\nu}(q) = \frac{j_{\text{LLL}}^{\nu}}{q^2 - \Pi_{\parallel}}, \quad (597)$$

where we used the Ward identity $q_{\mu} j_{\text{LLL}}^{\mu} = 0$ and the fact that the LLL current j_{LLL}^{μ} is only nonvanishing in the 0, 3 components. Those expressions motivate us to elaborate the computation of the self-energy, focusing on the relevant component in the strong magnetic field

$$\Pi_R^{\mu\nu} = \Pi_{\parallel} P_{\parallel}^{\mu\nu}. \quad (598)$$

The screening effect arising from this component has been discussed in various contexts [12, 76, 77, 216, 242, 336, 404, 407–409, 766, 767]. Note that only one of the photon/gluon modes is screened; This mode has the electric field oscillating along the strong magnetic field [214, 404]. The other modes are neither screened nor play any role in the dynamics of the LLL fermions, simply because those modes are not coupled to the LLL fermions confined in the (1+1) dimensions, like electrons confined in polarizers. We first summarize rather technical aspects in computation of the one-loop self-energy in the strong magnetic field and then discuss physical consequences of the self-energy correction.

F.2.1 Vacuum contribution: Massless and massive cases

We first briefly summarize computation of the vacuum contribution. By using the LLL propagator (137), the self-energy in the strong magnetic field is written as

$$i\Pi_R^{\mu\nu}(q) = -(ig)^2 \int \frac{d^4 p}{(2\pi)^4} \text{Tr}[\gamma^{\mu} S_{\text{LLL}}(p) \gamma^{\nu} S_{\text{LLL}}(p+q)]. \quad (599)$$

¹²⁴Here, we have α_s for the coupling between a dynamical gluon and the one-loop polarization, which should be replaced by α_{em} for a photon. Note also that we do not consider an external chromo fields discussed in Sections 3.4 and 6 which would induce an additional contribution of a gluon loop to Π_{\parallel} .

The color factor $\text{Tr}[t^a t^b] = 1/2\delta^{ab}$ should be attached for gluons, which we suppress for the notational simplicity. For notational simplicity, we do not explicitly write the flavor sum or the color sum. The latter simply yields an overall factor of N_c in the quark-loop contributions to the photon self-energy (with the replacement of the coupling constant, $g \rightarrow q_f$) and is absent for a lepton loop. Also, one should take care of the difference in the electric charges q_f as well as the mass when carrying out the flavor sum. Remember that the gauge-dependent Schwinger phase goes away in this self-energy diagram [see discussions below Eq. (503)].

Inserting the explicit form of the LLL propagator (137) which is factorized into the parallel and perpendicular parts, we find that the one-loop self-energy (599) is also factorized as

$$i\Pi_R^{\mu\nu}(q) = I_{\perp}(q_{\perp}^2) i\Pi_{1+1}^{\mu\nu}(q_{\parallel}), \quad (600)$$

where

$$I_{\perp}(q_{\perp}^2) = 2^2 \int \frac{d^2 p_{\perp}}{(2\pi)^2} e^{-\frac{1}{|q_f B|}(|\mathbf{p}_{\perp}|^2 + |\mathbf{p}_{\perp} + \mathbf{q}_{\perp}|^2)}, \quad (601a)$$

$$i\Pi_{1+1}^{\mu\nu}(q_{\parallel}) = -(ig)^2 \int \frac{d^2 p_{\parallel}}{(2\pi)^2} \frac{\text{Tr}[\gamma_{\parallel}^{\mu} i(\not{p}_{\parallel} + m) \mathcal{P}_+ \gamma_{\parallel}^{\nu} i(\not{p}_{\parallel} + \not{q}_{\parallel} + m) \mathcal{P}_+]}{(p_{\parallel}^2 - m^2)((p_{\parallel} + q_{\parallel})^2 - m^2)}. \quad (601b)$$

Here, the spinor trace is taken at the four dimensions. Performing the elementary integral for the transverse momentum, we find that

$$I_{\perp}(q_{\perp}^2) = \rho_B e^{-\frac{|q_{\perp}|^2}{2|q_f B|}}. \quad (602)$$

The transverse integral results in the Landau degeneracy factor $\rho_B = |q_f B|/(2\pi)$.

On the other hand, the longitudinal part is the polarization tensor in the (1+1)-dimensional QED, i.e., the Schwinger model [198]. After the standard treatment with the help of the Feynman parameter, the longitudinal integral is cast into the form

$$i\Pi_{1+1}^{\mu\nu}(q_{\parallel}) = -g^2 \frac{4}{2} \int_0^1 dx \left[\int \frac{d^2 \ell_{\parallel}}{(2\pi)^2} \frac{2\ell_{\parallel}^{\mu} \ell_{\parallel}^{\nu} - \ell_{\parallel}^2 g_{\parallel}^{\mu\nu}}{(\ell_{\parallel}^2 - \Delta_{\parallel})^2} + \alpha^{\mu\nu} \int \frac{d^2 \ell_{\parallel}}{(2\pi)^2} \frac{1}{(\ell_{\parallel}^2 - \Delta_{\parallel})^2} \right], \quad (603)$$

where $\ell_{\parallel}^{\mu} = p_{\parallel}^{\mu} + x(1-x)q_{\parallel}^{\mu}$, $\Delta_{\parallel} = m^2 - x(1-x)q_{\parallel}^2$, and $\alpha^{\mu\nu} = m^2 g_{\parallel}^{\mu\nu} + x(1-x)(q_{\parallel}^2 g_{\parallel}^{\mu\nu} - 2q_{\parallel}^{\mu} q_{\parallel}^{\nu})$. The factor of 4 from the four-dimensional trace is multiplied by the factor of 1/2 from the spin projection operator, resulting in the factor of 2 just like the two-dimensional trace. Also, one needs to be careful about the gauge-invariant regularization. We use the dimensional regularization, and the numerator of the first integral is proportional to $\epsilon_2 g_{\parallel}^{\mu\nu}$ with $\epsilon_2 \equiv (2-d)$, which appears to vanish in the two dimensions. However, a factor of $1/\epsilon_2$ arises from the integral that provides a finite contribution and is necessary for the gauge-invariant result:

$$\Pi_{1+1}^{\mu\nu}(q_{\parallel}) = -\frac{g^2}{\pi} (q_{\parallel}^2 g_{\parallel}^{\mu\nu} - q_{\parallel}^{\mu} q_{\parallel}^{\nu}) \int_0^1 dx x(1-x) \Delta_{\parallel}^{-1}. \quad (604)$$

The x integral can only be a function of q_{\parallel}^2/m^2 (up to an overall factor of $1/q_{\parallel}^2$) as a consequence of the Landau degeneracy and the gauge-invariance. Especially, without the mass scale ($m=0$), the integral can only be a pure number. Below, we consider the massless and massive cases in order.

The integral (604) is quite simple in the massless case, i.e., $\int_0^1 dx x(1-x) \Delta_{\parallel}^{-1} = -1/q_{\parallel}^2$. Plugging the expressions in Eqs. (602) and (604), we have

$$\Pi_R^{\mu\nu}(q) = m_B^2 e^{-\frac{|q_{\perp}|^2}{2|q_f B|}} \frac{q_{\parallel}^2 g_{\parallel}^{\mu\nu} - q_{\parallel}^{\mu} q_{\parallel}^{\nu}}{q_{\parallel}^2 + i\omega\epsilon}, \quad (605)$$

where $\omega \equiv q^0$ and we put $\omega \rightarrow \omega + i\epsilon$ for the retarded correlator. We defined

$$m_B^2 := \rho_B \cdot \frac{g^2}{\pi}, \quad (606)$$

where a factor of 1/2 from the color factor should be attached for gluons. Then, the self-energy correction to the propagator (596) is found to be

$$\Pi_{\parallel} = m_B^2 e^{-\frac{|\mathbf{q}_{\perp}|^2}{2|q_f B|}}. \quad (607)$$

This function is independent of ω and q_z . Therefore, the photon propagator (596) acquires a pole mass in a gauge-invariant manner as a consequence of the $1/q_{\parallel}^2$ pole in Eq. (605) that is required on the dimensional ground. This mechanism is an analog with that in the Schwinger model [197, 198]. In the vanishing momentum limit ($|\mathbf{q}_{\perp}| \rightarrow 0$), the gauge-invariant mass is given by m_B in Eq. (606) that is the Schwinger mass g^2/π multiplied by the Landau degeneracy factor ρ_B .

The imaginary part in Eq. (605) is proportional to $(q_{\parallel}^2 g_{\parallel}^{\mu\nu} - q_{\parallel}^{\mu} q_{\parallel}^{\nu})\delta(q_{\parallel}^2)$, that vanishes when contracted with the photon/gluon polarization vectors and summed over the polarization modes. This implies that the pair production in the LLL is strictly prohibited in the massless limit since the imaginary part provides the squared tree amplitude of the pair production from a single photon/gluon. The physical reason behind this prohibition is the absence of chirality mixing. Namely, fermions and antifermions, which would satisfy the momentum conservation, belong to different chirality eigenstates (see Sec. 2.3.3), and are not directly coupled with each other. A similar prohibition mechanism is known as the ‘‘helicity suppression’’ in the leptonic decay of charged pions, where the muon channel dominates over the electron channel due to a mass suppression factor in the decay rate [768, 769].

In terms of kinematics, it is rather natural that a vanishing energy-momentum transfer ($q_{\parallel}^2 = 0$) does not create a pair. A vanishing energy-momentum transfer implies an adiabatic process, and may not create a particle and an antiparticle that usually belong to different energy bands even in the massless limit. There is, however, an exception in the (1+1) dimensions, where the particle and antiparticle branches are directly connected with each other. This is the spectral flow discussed in Sec. 2.3.3, where particles and antiparticles can be created in adiabatic shifts along single energy bands. Nevertheless, the net charge creation vanishes as seen above. Instead, the adiabatic shift creates a nonzero axial charge and breaks the chiral symmetry as we further discuss below.

In the massive case, we need to perform the remaining integral in Eq. (604). This can be done analytically as¹²⁵

$$\Pi_{\parallel} = m_B^2 e^{-\frac{|\mathbf{q}_{\perp}|^2}{2|q_f B|}} \left[1 - I\left(\frac{q_{\parallel}^2}{4m^2}\right) \right]. \quad (608)$$

Because of the mass scale, the expressions between the square brackets can be a function of a dimensionless combination $q_{\parallel}^2/(4m^2)$. The explicit form of the integral is obtained as

$$I(x + i\omega\epsilon) = \begin{cases} \frac{1}{2} \frac{1}{\sqrt{x(x-1)}} \ln \frac{\sqrt{x(x-1)}-x}{\sqrt{x(x-1)}+x} & x < 0 \\ \frac{1}{\sqrt{x(1-x)}} \arctan \frac{x}{\sqrt{x(1-x)}} & 0 \leq x < 1 \\ \frac{1}{2} \frac{1}{\sqrt{x(x-1)}} \left[\ln \frac{x-\sqrt{x(x-1)}}{x+\sqrt{x(x-1)}} + i \operatorname{sgn}(\omega)\pi \right] & 1 \leq x \end{cases}. \quad (609)$$

¹²⁵The correspondence between the notations in this appendix and in Sec. 5.2.3 is summarized as $P_{\parallel}^{\mu\nu} \leftrightarrow P_2^{\mu\nu}/q_{\parallel}^2$, $\Pi_{\parallel} \leftrightarrow -q_{\parallel}^2 \chi_1^{\text{LLL}}$, and $I(q_{\parallel}^2) \leftrightarrow I_{0\Delta}^0(q_{\parallel}^2)/2$ [cf. Eqs. (239) and (588)].

This function is plotted in Fig. 23. We took the retarded prescription $\omega \rightarrow \omega + i\epsilon$ that yields an infinitesimal displacement $q_{\parallel}^2 \rightarrow q_{\parallel}^2 + i\omega\epsilon$.¹²⁶ The advanced and causal correlators can be computed in the same manner. As discussed in Sec. 5, the polarization tensor acquires an imaginary part in the regime $q_{\parallel}^2 \geq 4m^2$, indicating decay of photon/gluon into a fermion and antifermion pair. One can consider the light- and heavy-fermion limits relative to the photon energy, i.e., $m^2 \ll |q_{\parallel}^2|$ and $m^2 \gg |q_{\parallel}^2|$, respectively. In those limits, one finds that

$$\lim_{x \rightarrow \infty} I(x) = 0, \quad \lim_{x \rightarrow 0} I(x) = 1 \quad (610)$$

In the light-fermion limit, one finds the finite photon mass $\sim m_B$ that is induced by the polarization of the nearly massless fermions. In contrast, in the heavy-fermion limit, one finds that $\Pi_{\parallel} \rightarrow 0$, meaning that the polarization effects are suppressed. This is simply because the fermions have too large a mass gap to be excited by a soft photon momentum.¹²⁷

The massless limit of the imaginary part is more subtle. Let us carefully examine how the massless limit (605) is reproduced. Notice that the integral (609) vanishes everywhere in the massless limit except the pair production threshold at $q_{\parallel}^2 = 4m^2$, where the imaginary part diverges as q_{\parallel}^2 approaches $4m^2$ from above. Thus, the functional form of the imaginary part approaches a delta function in the massless limit:

$$\begin{aligned} \lim_{m \rightarrow 0} \frac{1}{q_{\parallel}^2} \Im m \Pi_{\parallel}(q_{\parallel}^2 + i\omega\epsilon) &= - \lim_{m \rightarrow 0} \frac{1}{q_{\parallel}^2} \Im m I\left(\frac{q_{\parallel}^2}{4m^2} + i\omega\epsilon\right) m_B^2 e^{-\frac{|q_{\perp}|^2}{2|q_f B|}} \\ &\rightarrow -C_0 \delta(q_{\parallel}^2) \{\theta(\omega) - \theta(-\omega)\} m_B^2 e^{-\frac{|q_{\perp}|^2}{2|q_f B|}}. \end{aligned} \quad (611)$$

The coefficient C_0 can be fixed by the fact that the imaginary part satisfies a sum rule

$$\begin{aligned} \int_{-\infty}^{\infty} dq_{\parallel}^2 \frac{1}{q_{\parallel}^2} \Im m I\left(\frac{q_{\parallel}^2}{4m^2} + i\omega\epsilon\right) &= \pi \{\theta(\omega) - \theta(-\omega)\} \int_1^{\infty} dx \frac{1}{2x\sqrt{x(x-1)}} \\ &= \pi \{\theta(\omega) - \theta(-\omega)\}. \end{aligned} \quad (612)$$

Remarkably, the result of the integral is independent of the mass parameter [770–772], so that this sum rule should hold in the massless limit. Such a sum rule was shown in the four dimensions even earlier [773, 774]. Therefore, we get $C_0 = \pi$, and can reproduce the correct massless limit for the imaginary part that agrees with Eq. (605). The integral in Eq. (612) is dominated by the contribution of an integrable singularity at the threshold $q_{\parallel}^2 = 4m^2$ (cf. Fig. 23). The threshold behavior depends on the number of phase-space dimensions in a factor of $(q^2 - E_{\text{th}}^2)^{(d-2)/2}$ with d and E_{th} being the number of dimensions and the threshold energy. Here, we have $d = 1$ because of the effective dimensional reduction.

F.2.2 Chiral anomaly: Massless and massive cases

Now, consider the currents carried by the LLL fermions

$$j_V^{\mu} = q_f \bar{\psi}_{\text{LLL}} \gamma^{\mu} \psi_{\text{LLL}}, \quad (613a)$$

¹²⁶We used a relation $\arctan \frac{x}{\sqrt{x(1-x)}} = \frac{i}{2} \ln \frac{\sqrt{x(x-1)}-x}{\sqrt{x(x-1)+x}}$ when $x < 0$ or $1 \geq x$. When $x \geq 1$, the argument of the logarithm takes a negative value, so that the logarithm becomes a complex-valued function, $\arctan \frac{x}{\sqrt{x(1-x)}} = \frac{i}{2} [\ln \frac{|\sqrt{x(x-1)}-x|}{\sqrt{x(x-1)+x}} + i \text{sgn}(\omega)\pi]$. The sign of the imaginary part depends on that of the infinitesimal displacement. When $x < 0$, the argument of the logarithm is semi-positive definite, i.e., $\frac{\sqrt{x(x-1)}-x}{\sqrt{x(x-1)+x}} = \frac{-x}{(\sqrt{x(x-1)+x})^2} \geq 0$.

¹²⁷The author (K.H.) thanks Toru Kojo for useful discussions about those limiting behaviors and differences/similarities in finite temperature/density.

$$j_A^\mu = \bar{\psi}_{\text{LLL}} \gamma^\mu \gamma^5 \psi_{\text{LLL}}, \quad (613b)$$

where ψ_{LLL} is the fermion spinor in the LLL that is an eigenstate of the spin projection operator \mathcal{P}_+ (cf. Sec. 2.3). Those currents can be induced in response to an external $U(1)$ gauge field A^μ .¹²⁸ By the use of a relation among the gamma matrices $\gamma_\parallel^\mu \gamma^5 \mathcal{P}_\pm = \mp s_f \epsilon_\parallel^{\mu\nu} \gamma_{\parallel\nu} \mathcal{P}_\pm$, we find a relation between the LLL contributions to the vector and axial-vector currents along the magnetic field¹²⁹

$$q_f j_A^\mu = -s_f \epsilon_\parallel^{\mu\nu} j_{V\nu}, \quad (614)$$

where we introduced an antisymmetric tensor $\epsilon_\parallel^{\mu\nu}$ which only has two non-vanishing components, $\epsilon_\parallel^{03} = -\epsilon_\parallel^{30} = 1$. This relation is an analog of the well-known relation in the (1+1) dimensional QED and is understood as a consequence of the effective dimensional reduction and the spin polarization in the LLL. Equation (614) relates the vector–vector correlator $\Pi_R^{\mu\nu}$, which we just computed, to the vector–axial-vector correlator

$$\langle j_A^\mu j_V^\nu \rangle_R = -s_f \epsilon_\parallel^\mu{}_\rho q_f^{-1} \Pi_R^{\rho\nu}. \quad (615)$$

We shall consider a linear response to the gauge field A_μ . According to the transverse form of the polarization tensor (604), the divergences of the currents read [84]

$$\text{F.T. } \partial_\mu j_V^\mu = -i q_\mu \Pi_R^{\mu\nu} A_\nu = 0, \quad (616a)$$

$$\text{F.T. } \partial_\mu j_A^\mu = -i q_\mu \langle j_A^\mu j_V^\nu \rangle_R A_\nu = s_f q_f^{-1} \Pi_\parallel \tilde{E}_\parallel, \quad (616b)$$

where F.T. stands for the Fourier transform and $\tilde{E}_\parallel(q) = -i \epsilon_\parallel^{\mu\nu} q_\mu A_\nu$ is the parallel (or antiparallel) component of an electric field along the magnetic field. Note that $\tilde{E}_\parallel(q)$ is the Fourier spectrum, while B is a constant magnitude. In case of the quark-loop contributions, one should count the number of color degrees of freedom circulating on the loop, that comes from the simple color trace $\text{Tr}[\mathbb{1}_c] = N_c$. The Ward identity (616a) is a consequence of the gauge invariance in QED. However, the axial current may not be conserved in Eq. (616b) in general.

We first consider the massless case. Inserting the polarization tensor (607) into Eq. (616b), one finds the axial Ward identity (AWI)

$$\text{F.T. } \partial_\mu j_A^\mu = s_f \rho_B \frac{q_f}{\pi} \tilde{E}_\parallel e^{-\frac{|\mathbf{q}_\perp|^2}{2|q_f B|}} = \frac{q_f^2}{2\pi^2} \tilde{\mathbf{E}} \cdot \mathbf{B} e^{-\frac{|\mathbf{q}_\perp|^2}{2|q_f B|}}. \quad (617)$$

The expression in the middle of Eq. (617) is given by the Landau degeneracy factor ρ_B multiplied by the chiral anomaly in purely (1+1) dimensions (without any other external line), i.e., $-i q_\mu \langle j_A^\mu j_V^\nu \rangle_{(1+1)} A_\nu = (q_f/\pi) \tilde{E}$ (see, e.g., Ref. [66]). This is a consequence of the dimensional reduction in the strong magnetic field [79]. At the same time, the rightmost side in Eq. (617) exhibits the same form as the chiral anomaly in the (3+1) dimensions from the triangle diagrams. Notice that the correlator $\Pi_R^{\mu\nu}$ indeed contains the triangle diagrams as a part of the resummed series with respect to the external magnetic field. However, due to the Gaussian factor that originates from the transverse wave functions, the contribution of the LLL fermions only saturates the (3+1)-dimensional chiral anomaly relation in the long-wavelength and/or strong-field limits where $|\mathbf{q}_\perp|^2/|q_f B| \rightarrow 0$. In such a limit, the total current

¹²⁸This is an additional external gauge field superimposed on the one inducing the external magnetic field. Note also that the color trace in Eq. (605) should be removed as we consider a coupling to the $U(1)$ gauge field and that the coupling constant should be replaced as $g \rightarrow q_f$. There is no mixing between the photon and gluon (without an external color field).

¹²⁹Here, the axial-vector current (613b) does not carry an electric charge, which is, however, included in the vector current (613a) and the electromagnetic coupling $j_V^\mu A_\mu$ in Eq (616b).

is composed of copies of the (1+1)-dimensional currents with the transverse density ρ_B since the axial current and the electromagnetic fields do not resolve the cyclotron motion of the radius $\sim 1/\sqrt{|q_f B|}$.¹³⁰

In the massive case, Π_{\parallel} in Eq. (608) provides the AWI

$$\text{F.T. } \partial_{\mu} j_A^{\mu} = \frac{q_f^2}{2\pi^2} \tilde{\mathbf{E}} \cdot \mathbf{B} \left[1 - I\left(\frac{q_{\parallel}^2}{4m^2}\right) \right] e^{-\frac{|q_{\perp}|^2}{2|q_f B|}}. \quad (618)$$

We have already seen that Π_{\parallel} approaches the expression in the massless case when $m^2/q_{\parallel}^2 \rightarrow 0$. In the opposite limit, we have $\Pi_{\parallel} \rightarrow 0$ when $m^2/q_{\parallel}^2 \rightarrow \infty$, so that the axial current is effectively conserved, i.e., $\partial_{\mu} j_A^{\mu} = 0$ in such a heavy-mass and/or soft-photon limit. This is a natural result because the weak electric field, perturbatively applied in Eq. (616b), cannot create any massive on-shell fermions over the mass gap. The mass dependence plays a crucial role in determining the magnitude of the divergence of the current.

It should be emphasized that the effective conservation of j_A^{μ} in the above limit does not contradict with the chiral anomaly at all. Actually, the term proportional to the I function in Eq. (608) is nothing but the matrix element of the pseudoscalar condensate $2im\langle\bar{\psi}\gamma^5\psi\rangle$ that arises from the explicit chiral symmetry breaking by a finite fermion mass. Namely, as explicitly shown in Sec. F.3, the anomaly diagrams composed of the massive fermion loops are split into two terms that are the mass-independent anomalous term and mass-dependent matrix element of the pseudoscalar condensate. The anomaly diagram as a whole vanishes when the fermion mass is sent to infinity just because all the internal lines go far off-shell. One could rephrase this vanishing result as an exact cancellation between the anomalous term and the pseudoscalar condensate term [80, 770]. While the above result and discussion hold only for a perturbative electric field, the cancellation was further shown for arbitrary electric-field strength as long as the electromagnetic fields are taken to be constant fields [85].¹³¹ The cancellation may not be always exact when there is an energy-momentum transfer from inhomogeneous electromagnetic fields (or dynamical photons) as discussed in Sec. F.3 (see also Refs. [80, 84]).

F.2.3 Chiral anomaly from dispersion integral

Chiral anomaly is often explained, a little bit technically, as a consequence of the gauge-invariant regularization of the UV divergence. The UV divergence appears in the real part of the polarization tensor. On the other hand, the real part can be tied to the imaginary part via the dispersion integral. One may, therefore, identify the origin of the chiral anomaly with the physical processes captured by the imaginary part [770, 773]. Of course, the imaginary part is free of any UV divergence since it corresponds to the squared amplitude of the tree diagram (at the lowest order in the coupling constant). In short, the chiral anomaly from the (superficially divergent) UV dynamics is connected to the IR dynamics.¹³²

We shall first confirm that the polarization tensor satisfies the dispersion integral that captures the analyticity in the complex plane (see Fig. 56). We begin with a simple identity stemming from a contour

¹³⁰At the mathematical level, it is not obvious how the chiral anomaly in the (3+1) dimensions is reproduced from the LLL contribution. The familiar triangle diagrams are the lowest-order contribution in the series expansion with respect to the coupling constant. On the other hand, the LLL contribution is obtained only after summing the all-order one-loop diagrams with respect to the external-field insertion and then expanding it in another series in terms of the Landau levels: The LLL contribution contains the higher-order diagrams in the coupling constant that give rise to a non-analytic dependence of the Gaussian on the coupling constant. The leading terms in those two expansions could differ from each other in general.

¹³¹It was also shown that a nonzero axial charge is created by the Schwinger mechanism in the real-time formalism.

¹³²It is also worth emphasizing that the anomaly diagram does not yield any UV-divergent term in the end. Remember that, in Eq. (603), we only needed the regularization not to miss the terms of order $(\epsilon_2)^0$, and that there were no divergent poles like $1/\epsilon_2$ after all. This ‘‘marginal’’ degree of the divergence is precisely the reason why the anomalous term gets independent of the fermion mass (see Sec. F.3).

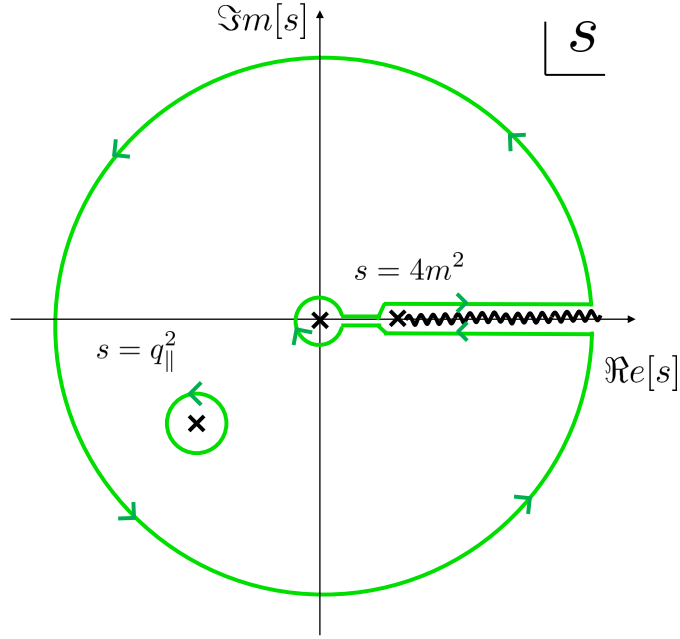


Figure 56: Dispersion relation from analyticity in the complex s plane.

integral that encloses a pole at $s = q_{\parallel}^2$:

$$f(q_{\parallel}^2) = \frac{1}{2\pi i} \oint ds \frac{f(s)}{s - q_{\parallel}^2}, \quad (619)$$

where $f(s)$ is an arbitrary complex function that is analytic inside the closed contour. We apply the above formula to $f(s) = \Pi_{\parallel}(s)/s$. Expanding the integral contour to an infinitely large arc, we find that

$$\frac{1}{q_{\parallel}^2} \Pi_{\parallel}(q_{\parallel}^2) = -\frac{\Pi_{\parallel}(0)}{-q_{\parallel}^2} + \frac{1}{\pi} \int_{4m^2}^{\infty} ds \frac{\Im m \Pi_{\parallel}(s)}{s(s - q_{\parallel}^2)}, \quad (620)$$

which is often called the dispersion integral and is another kind of sum rules [cf. Eq. (612)]. For the moment, we assume a kinematical condition $q_{\parallel}^2 < 4m^2$, which can be relaxed with the help of the analytic continuation afterwards.

In the massive case, the polarization tensor (608) has a branch cut along the real axis $s \geq 4m^2$ that corresponds to the pair creation from a single photon. This continuum contributes to the second term in the dispersion integral (620). On the other hand, we have $\Pi_{\parallel}(0) = 0$ as discussed below Eq. (609), so that the first term vanishes. Inserting the imaginary part in Eq. (609) into the dispersion relation leads to an elementary integral

$$\begin{aligned} \frac{1}{q_{\parallel}^2} \Pi_{\parallel}(q_{\parallel}^2) &= \text{sgn}(\omega) m_B^2 e^{-\frac{|\mathbf{q}_{\perp}|^2}{2|q_f B|}} \frac{1}{2} \int_{4m^2}^{\infty} ds \frac{-4m^2}{s(s - q_{\parallel}^2) \sqrt{s(s - 4m^2)}} \\ &= \text{sgn}(\omega) m_B^2 e^{-\frac{|\mathbf{q}_{\perp}|^2}{2|q_f B|}} \frac{1}{q_{\parallel}^2} \left[1 - I\left(\frac{q_{\parallel}^2}{4m^2}\right) \right]. \end{aligned} \quad (621)$$

This result agrees with the right-hand side of Eq. (608), indicating that the polarization tensor satisfies the dispersion relation. Therefore, we identify the pair creation from a single photon or a finite-frequency electric field as the physical process that induces the non-conservation of the axial current in the massive case. Namely, a fermion and antifermion pair of the same helicity, which belong to different chirality

sectors, is created thanks to the chirality mixing by a finite mass term. This 1-to-2 process is not allowed in the (3+1) dimensions but is allowed in the effective (1+1) dimensions with the Landau levels. The created axial charge contains the contribution of the explicit breaking term $2im\langle\bar{\psi}\gamma^5\psi\rangle$ as discussed below Eq. (618), and thus does not necessarily agree with that in the massless case (617) except for in some limits.

The above 1-to-2 process is different from the physical process encoded in the imaginary part of the triangle diagrams, that is, the Compton scattering [773]. Interestingly, the same non-conservation equations are induced by the different physical processes in the weak and strong magnetic fields, up to the aforementioned difference in the Gaussian factor. In the subsequent appendix, we will discuss an explicit connection between the triangle diagrams and the polarization diagram in the LLL.

The dispersion integral (620) is simpler in the strictly massless case ($m = 0$). In Eq. (605), the polarization tensor does not have a branch cut due to the prohibition of the photon/gluon decay in the absence of chirality mixing as discussed below (606). It is this prohibition that makes the chiral anomaly so simple in the massless theory by excluding the physical processes other than the spectral flow discussed in Sec. 2.3.3. The spectral flow stems from the residue at the origin $\Pi_{\parallel}(0)$. One can immediately find that the dispersion relation (620) is satisfied in the strictly massless case [cf. Eq. (607)]. Clearly, the analytic structures in the complex s plane are different in the strictly massless and massive cases. They are not continuously related.

Summarizing the dispersion analysis, we found that the relevant physical processes are different in the strictly massless and massive cases. In the strictly massless case, the spectral flow gives rise to the chiral anomaly from the adiabatic shifts of the whole occupied states along the dispersion lines from the UV to IR regions (see Sec. 2.3.3). This is the only process that can occur without the chirality mixing, which is the reason for the simplicity in the massless case. In the massive case, the 1-to-2 pair creation gives rises to the axial charge creation. This is a diabatic process dominated by the IR contribution, i.e., the near-threshold divergence. There can be contributions from the higher-order processes. In the massive case, there is no contribution from the adiabatic spectral flow in vacuum [80], while there are finite contributions at finite temperature and/or density [84] (see Sec. F.4.3).

F.3 Fermion-mass dependences of the anomaly diagrams

We here explicitly see that the anomaly diagrams with massive-fermion loops can be split into two terms that are nothing but the anomalous and pseudoscalar-condensate terms. More specifically, this means that the term proportional to I function in Eq. (608) is identified with the matrix element of the pseudoscalar condensate. Also, we show that the familiar triangle diagrams in the four dimensions are split into the two terms in the same manner.

It is often said that the chiral anomaly is independent of the fermion mass since the anomalous term originates from a UV divergence. We further clarify this statement and carefully discuss mass dependences of the anomaly diagrams. The nonzero divergence of the axial-vector current (616b), which we refer to as the axial Ward identity (AWI), certainly has mass dependences as a whole. What one can explicitly show is that the anomalous term is independent of the fermion mass. The reason is rather because the anomaly diagrams are *not* divergent after all, though they are superficially divergent. They are even not logarithmically divergent. This “marginal” degree of divergence gives rise to the mass independence of the anomalous term.

The remaining term is explicitly identified with the matrix element of the pseudoscalar condensate and depends on the fermion mass. This term vanishes in the massless limit, reproducing the chiral anomaly. In contrast, this term exactly offsets the anomalous term in the large-mass limit, leading to effective *conservation* of the axial-vector current. Therefore, the mass dependence plays a crucial to control the behaviors of the total AWI. The above exact cancellation is anticipated because both of the terms originate from the same diagram which is only split into the two terms *a posteriori*. The

cancellation is nothing more than a simple statement that diagrams generically vanish when all internal lines go far off-shell due to an infinitely large mass.

The presence of mass dependences in the AWI may be further anticipated as follows. (1) In general, finite terms in divergent diagrams do have mass dependences; A mass term just does not change the degree of divergence. The anomaly diagrams are even *not* divergent after all, and should have mass dependences as a whole. (2) The imaginary part of the anomaly diagrams correspond to the scattering rates of the on-shell processes. In case of the LLL, it is the pair creation from a single gluon/photon as discussed above [84, 770]. In case of the triangle diagrams, it is an interference between the amplitudes of the Compton scattering and decay of the axial current to a fermion pair [773]. No one would believe that those processes are independent of the fermion mass. The real part, reconstructed from the imaginary part via the dispersion integral, should also have mass dependences as seen above for the LLL. No UV regularization procedure is involved. (3) If there were not any mass dependence in the AWI, heavy fermions, or even undiscovered heavy fermions if any, contribute to the anomalous term with the same magnitudes as the light fermions do, changing the chiral-anomaly coefficients by factors. However, we have not detected such “anomalous” contributions to the chiral anomaly. This may imply that the cancellation with the pseudoscalar-condensate term occurs for heavy fermions when they are too heavy to be excited by the axial-vector current of a given energy scale.

Below, we follow the conventions and strategy given in the standard textbook [66], where the authors explain the chiral anomaly from the familiar triangle diagrams in the massless case with the dimensional regularization. We thus first examine the triangle diagrams with massive fermions so that the reader can directly compare the massive and massless cases. We then examine the anomaly diagram from the LLL massive fermions.

F.3.1 Massive triangle diagrams and the limit of constant magnetic fields

Following the strategy with the dimensional regularization described in Ref. [66], we compute the triangle diagrams with the massive-fermion loops. We essentially compute the matrix element $\mathcal{M}^{\mu\nu\lambda}$ such that

$$\int d^4x e^{-iqx} \langle p, k | \partial_\mu j_A^\mu(x) | 0 \rangle = (2\pi)^4 \delta^{(4)}(p + k - q) i q_\mu \mathcal{M}^{\mu\nu\lambda}(q; p, k) \epsilon_\nu^*(p) \epsilon_\lambda^*(k), \quad (622)$$

where p, k are the photon momenta and ϵ_ν is the photon polarization vector. There are two triangle diagrams with the opposite fermion charge flows:

$$\mathcal{M}_1^{\mu\nu\lambda} = (-1)(-ie)^2 \int \frac{d^4\ell}{(2\pi)^4} \frac{i^3 \text{Tr}[\gamma^\mu \gamma^5 (\ell - \not{k} + m) \gamma^\lambda (\ell + m) \gamma^\nu (\ell + \not{p} + m)]}{\{(\ell - k)^2 - m^2\} \{\ell^2 - m^2\} \{(\ell + p)^2 - m^2\}}, \quad (623a)$$

$$\mathcal{M}_2^{\mu\nu\lambda} = (-1)(-ie)^2 \int \frac{d^4\ell}{(2\pi)^4} \frac{i^3 \text{Tr}[\gamma^\mu \gamma^5 (\ell - \not{p} + m) \gamma^\nu (\ell + m) \gamma^\lambda (\ell + \not{k} + m)]}{\{(\ell - p)^2 - m^2\} \{\ell^2 - m^2\} \{(\ell + k)^2 - m^2\}}, \quad (623b)$$

where $\mathcal{M}^{\mu\nu\lambda} = \mathcal{M}_1^{\mu\nu\lambda} + \mathcal{M}_2^{\mu\nu\lambda}$. Each integral is linearly divergent, and one needs to regularize it in a gauge-invariant manner. To apply the dimensional regularization, it is important to make sure the properties of the γ^5 . The γ^5 is extended in such a way that $\{\gamma^5, \gamma^\mu\} = 0$ for $\mu = 0, 1, 2, 3$ and $[\gamma^5, \gamma^\mu] = 0$ for the other components. The extra components in the momentum is denoted with tilde like $\tilde{\ell}^\mu$.¹³³ The external momenta q^μ, p^μ, k^μ have vanishing components in the extra dimensions, $\tilde{q}^\mu = \tilde{p}^\mu = \tilde{k}^\mu = 0$. The extra components of γ^μ commute with γ^5 , i.e., $[\tilde{\ell}, \gamma^5] = 0$.

Then, by the use of an identity

$$q_\mu \gamma^\mu \gamma^5 = (\ell + \not{p} - m) \gamma^5 + \gamma^5 (\ell - \not{k} - m) - 2\gamma^5 (\tilde{\ell} - m), \quad (624)$$

¹³³This corresponds to ℓ_1^μ in the notations of Ref. [66]. We do not use their notations with \parallel, \perp to avoid possible confusions with the parallel and perpendicular components with respect to the magnetic field in this paper.

we find the regularized matrix element

$$iq_\mu \mathcal{M}_1^{\mu\nu\lambda} = iq_\mu \Delta \mathcal{M}_{1(a)}^{\mu\nu\lambda} + iq_\mu \Delta \mathcal{M}_{1(m)}^{\mu\nu\lambda}, \quad (625)$$

where

$$iq_\mu \Delta \mathcal{M}_{1(a)}^{\mu\nu\lambda} = -2(-1)(-ie)^2 \int \frac{d^d \ell}{(2\pi)^d} \frac{\text{Tr}[\gamma^5 \tilde{\ell}(\ell - \not{k} + m)\gamma^\lambda(\ell + m)\gamma^\nu(\ell + \not{p} + m)]}{\{(\ell - k)^2 - m^2\}\{\ell^2 - m^2\}\{(\ell + p)^2 - m^2\}}, \quad (626a)$$

$$iq_\mu \Delta \mathcal{M}_{1(m)}^{\mu\nu\lambda} = 2m(-1)(-ie)^2 \int \frac{d^d \ell}{(2\pi)^d} \frac{\text{Tr}[\gamma^5(\ell - \not{k} + m)\gamma^\lambda(\ell + m)\gamma^\nu(\ell + \not{p} + m)]}{\{(\ell - k)^2 - m^2\}\{\ell^2 - m^2\}\{(\ell + p)^2 - m^2\}}. \quad (626b)$$

We denote the corresponding terms from the other triangle diagram as $\Delta \mathcal{M}_{2(a)}^{\mu\nu\lambda}$ and $\Delta \mathcal{M}_{2(m)}^{\mu\nu\lambda}$, respectively, and have dropped the terms that cancel each other between $\mathcal{M}_1^{\mu\nu\lambda}$ and $\mathcal{M}_2^{\mu\nu\lambda}$. Moreover, we will not need to compute those two triangle diagrams separately since they provide the same contributions. The point is that there appears $q_\mu \Delta \mathcal{M}_{1(a)}^{\mu\nu\lambda}$ proportional to $\tilde{\ell}$ after the regularization. Below, we demonstrate how $q_\mu \Delta \mathcal{M}_{1(a)}^{\mu\nu\lambda}$ results in the *mass-independent* anomalous term, though the above expression yet contains mass terms. Also, the second term $q_\mu \Delta \mathcal{M}_{1(m)}^{\mu\nu\lambda}$ is identified with the leading nonvanishing matrix element of the pseudoscalar condensate in the coupling-constant expansion.

We first compute the anomalous term $q_\mu \mathcal{M}_{1(a)}^{\mu\nu\lambda}$. Introducing the Feynman parameter integral and then performing the momentum shift $\ell'^\mu = \ell^\mu - xk^\mu + yp^\mu = \ell^\mu + P^\mu$, the integral is arranged as

$$iq_\mu \Delta \mathcal{M}_{1(a)}^{\mu\nu\lambda} = (-2)2!e^2 \int_0^1 dx \int_0^{1-x} dy \times \int \frac{d^d \ell}{(2\pi)^d} \frac{\text{Tr}[\gamma^5 \tilde{\ell}(\ell - \not{k} - \not{P} + m)\gamma^\lambda(\ell - \not{P} + m)\gamma^\nu(\ell + \not{p} - \not{P} + m)]}{(\ell^2 - \Delta)^3}, \quad (627)$$

where $\Delta = m^2 - \{x(1-x)k^2 + y(1-y)p^2 + 2xyp \cdot k\}$. Note that the external momenta p^μ, k^μ do not have nonzero components in the extra dimensions, so that $\tilde{\ell}^\mu$ is not shifted by P^μ . Performing the spinor trace, one arrives at only one integral

$$\int \frac{d^d \ell}{(2\pi)^d} \frac{\tilde{\ell}^\mu \tilde{\ell}^\nu}{(\ell^2 + \Delta)^3} = \frac{d-4}{d} g^{\mu\nu} \times \frac{i(-1)^2}{(4\pi)^{d/2}} \frac{d}{2} \frac{\Gamma(-\frac{d-4}{2})}{\Gamma(3)} \Delta^{\frac{d-4}{2}}. \quad (628)$$

Notice that this integral is *not* divergent because of the overall dimensional factor that suppresses the divergent pole as $(d-4)\Gamma(-\frac{d-4}{2}) = -2 + \mathcal{O}(d-4)$. This means that one can take the limit $d \rightarrow 4$ in all the places, indicating that the mass-dependent factor goes away, $\Delta^{\frac{d-4}{2}} \rightarrow 1$. If there remained a divergence, the mass-dependent factor Δ , as well as a divergent pole, would remain in the result of the integral. We have found the mass-independent anomaly coefficient

$$iq_\mu [\Delta \mathcal{M}_{1(a)}^{\mu\nu\lambda} + \Delta \mathcal{M}_{2(a)}^{\mu\nu\lambda}] \epsilon_\nu^*(p) \epsilon_\lambda^*(k) = -\frac{e^2}{16\pi^2} \epsilon^{\alpha\nu\beta\lambda} \langle p, k | F_{\alpha\nu} F_{\beta\lambda} | 0 \rangle, \quad (629)$$

where the two terms on the left-hand side provide the same contributions. The antisymmetric tensor comes from the spinor trace with γ^5 . This is only a part of the triangle diagrams (622).

Now, we consider the other term $\mathcal{M}_{1(m)}^{\mu\nu\lambda}$ proportional to the fermion mass in Eq. (626b). Only one difference of $\mathcal{M}_{1(m)}^{\mu\nu\lambda}$ from the original triangle (623a) is the replacement of the axial vector vertex $\not{q}\gamma^5$ by the pseudoscalar vertex γ^5 via the identity (624). Thus, $\mathcal{M}_{1(m)}^{\mu\nu\lambda}$ is the matrix element of the pseudoscalar operator $\bar{\psi}\gamma^5\psi$ instead of the axial-vector operator $\bar{\psi}\gamma^\mu\gamma^5\psi$. Explicitly, it is identified with the matrix element of the pseudoscalar condensate as

$$iq_\mu [\mathcal{M}_{1(m)}^{\mu\nu\lambda} + \mathcal{M}_{2(m)}^{\mu\nu\lambda}] \epsilon_\nu^*(p) \epsilon_\lambda^*(k) = 2im \int d^4 x e^{-iqx} \langle p, k | \bar{\psi}\gamma^5\psi | 0 \rangle, \quad (630)$$

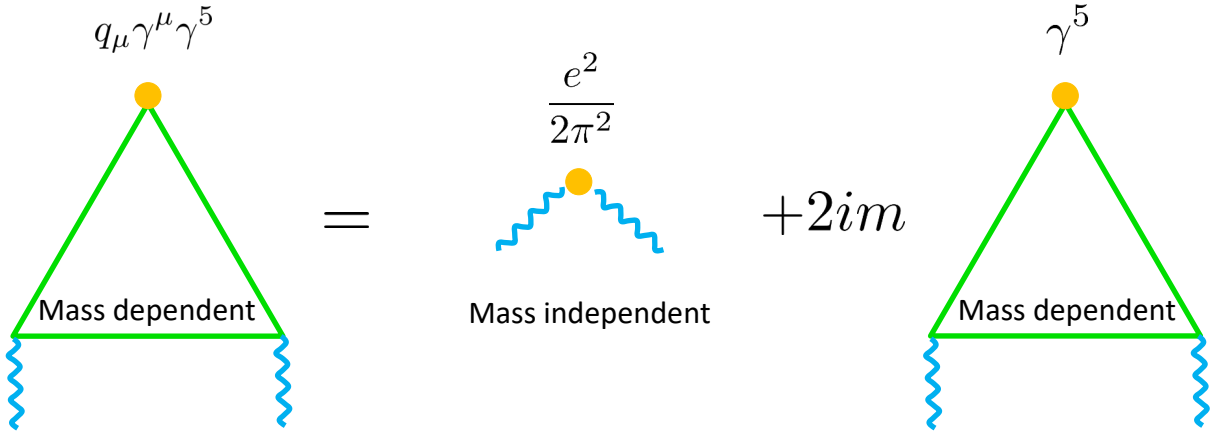


Figure 57: Splitting the massive triangle diagram into the anomalous and pseudoscalar-condensate terms.

where the sum of the two triangle diagrams provides a factor of 2. The presence of this term is consistent with the explicit symmetric breaking, $\partial_\mu j_A^\mu = 2im\bar{\psi}\gamma^5\psi$, from the Dirac equation. Notice that the matrix element of the pseudoscalar condensate $\langle\bar{\psi}\gamma^5\psi\rangle$ cannot be finite without insertions of the external photon legs. For example, the simplest one-loop integral without any insertion reads $\langle\bar{\psi}\gamma^5\psi\rangle \propto \text{Tr}[\gamma^5(\not{p}+m)] = m\text{Tr}[\gamma^5] = 0$; One has to take the mass term to mix the right and left chirality as they are mixed in the bilinear spinor $\bar{\psi}\gamma^5\psi$. It turns out that the lowest nonzero contribution needs two external photon legs. That is, the matrix element (630) is the leading nonvanishing contribution and its diagrammatic representation still has the triangle form (cf. Fig. 57). This pseudoscalar triangle diagram (626b) does not have a divergence and can be computed quite straightforwardly.

Summarizing the above, we obtain the AWI as the sum of the anomalous term (629) and the pseudoscalar triangles (630) as [82, 83]

$$\begin{aligned} \langle p, k | \partial_\mu j_A^\mu | 0 \rangle &= \langle p, k | -\frac{e^2}{8\pi^2} F^{\mu\nu} \tilde{F}_{\mu\nu} + 2im\bar{\psi}\gamma^5\psi | 0 \rangle \\ &= -\frac{e^2}{8\pi^2} \langle p, k | F^{\mu\nu} \tilde{F}_{\mu\nu} | 0 \rangle \left[1 + \int_0^1 dx \int_0^{1-x} dy \frac{2m^2}{x(1-x)k^2 + y(1-y)p^2 + 2xy p \cdot k - m^2} \right]. \end{aligned} \quad (631)$$

We emphasize that both the mass-independent anomalous term and the mass-dependent pseudoscalar condensate stem from the same triangle diagrams with the massive fermion loops (cf. Fig. 57). The remaining integral is only a function of normalized photon momenta $\bar{p}^\mu = p^\mu/m$ and $\bar{k}^\mu = k^\mu/m$, so that the magnitude of the mass correction depends on the relative magnitudes between the photon momenta and the fermion mass.

We shall examine the remaining integral. In the massless limit, the second term simply vanishes, reproducing the triangle anomaly in the strictly massless theory. On the other hand, in the large-mass limit such that $\bar{p}^\mu, \bar{k}^\mu \ll 1$, we have

$$\langle p, k | \partial_\mu j_A^\mu | 0 \rangle \rightarrow -\frac{e^2}{8\pi^2} \langle p, k | F^{\mu\nu} \tilde{F}_{\mu\nu} | 0 \rangle \left[1 + \int_0^1 dx \int_0^{1-x} dy \frac{2m^2}{-m^2} \right] = 0. \quad (632)$$

The axial-vector current is *conserved* in this limit. As shown just below, a vanishing momentum limit $\bar{p}^\mu, \bar{k}^\mu \rightarrow 0$ corresponds to the constant electromagnetic fields. Therefore, one finds that the axial-vector current carried by massive fermions is conserved in the constant and perturbatively weak electromagnetic fields.¹³⁴

¹³⁴In the above, we only discussed the perturbatively weak electromagnetic fields with the triangle diagrams. We could have a contribution of the Schwinger pair production when there is a strong electric field even if it is a constant field.

When the two photons are on-shell ($p^2 = k^2 = 0$), we have $2p \cdot k = q^2$ according to the momentum conservation. Therefore, the integral is only a function of the normalized momentum q^2/m^2 . Considering the neutral-pion decay $\pi^0 \rightarrow 2\gamma$, which is one of the representative consequences of the chiral anomaly, we put $q^2 = m_\pi^2$ to find a ratio to the current quark mass $m^2/q^2 \sim (5/140)^2 \sim 0.001$. Therefore, the quark-mass correction to the decay rate is expected to be quite small. The integral can be written with the polylogarithmic functions in this limit if necessary.

Limit of a constant magnetic field

Finally, we examine one more limit in Eq. (631) where one of the photon momentum is zero while the other is finite. We take $p^\mu \rightarrow 0$, and then $q^\mu = k^\mu$ led by the momentum conservation. One can show that the vanishing momentum limit corresponds to a constant electromagnetic field as follows. For simplicity, we may consider a parallel electromagnetic field in the z direction. Other configurations can be generated by the Lorentz transformation. Such a parallel field can be described by a linear gauge configuration

$$A^\mu = (-c_0 z E_0(\mathbf{x}_\perp), -d_1 y B_0(t, z), d_2 x B_0(t, z), -c_3 t E_0(\mathbf{x}_\perp)), \quad (633)$$

with constants such that $c_0 + c_3 = 1$ and $d_1 + d_2 = 1$. The gauge transformation does not change the following observations since we consider the strengths of the electric and magnetic fields

$$\tilde{E}_z(q^\mu) = \tilde{E}_0(\mathbf{q}_\perp) [c_3 \omega \delta'(\omega) \delta(q_z) + c_0 q_z \delta'(q_z) \delta(\omega)] = (2\pi)^2 \delta(\omega) \delta(q_z) \tilde{E}_0(\mathbf{q}_\perp), \quad (634a)$$

$$\tilde{B}_z(q^\mu) = \tilde{B}_0(\omega, p_z) [d_2 q_x \delta'(q_x) \delta(q_y) + d_1 q_y \delta(q_x) \delta'(q_y)] = (2\pi)^2 \delta(q_x) \delta(q_y) \tilde{B}_0(\omega, q_z). \quad (634b)$$

where the tildes on the fields stand for the Fourier spectrum. When the electric field is independent of t and z , its Fourier spectrum corresponds to vanishing ω and q_z in spite of the facts that q^μ is the momentum of the gauge field and that the gauge field itself depends on t and z . In a similar manner, when the magnetic field is independent of x and y , its Fourier spectrum corresponds to vanishing q_x and q_y . When the electromagnetic field is independent of all the spacetime coordinate, one gets the four-dimensional delta functions

$$\tilde{E}_z(q) = (2\pi)^4 \delta^{(4)}(q) E, \quad (635a)$$

$$\tilde{B}_z(q) = (2\pi)^4 \delta^{(4)}(q) B, \quad (635b)$$

where E and B are constant strengths.

When $p^\mu \rightarrow 0$, the AWI (631) reads

$$\text{F.T. } \langle p, k | \partial_\mu j_A^\mu | 0 \rangle_{p^\mu \rightarrow 0} = \frac{q_f^2}{2\pi^2} \frac{1}{2} [\tilde{\mathbf{E}}(q) \cdot \mathbf{B} + \tilde{\mathbf{B}}(q) \cdot \mathbf{E}] \left[1 - I\left(\frac{q^2}{4m^2}\right) \right] V_4, \quad (636)$$

with the constant field strengths \mathbf{E} and \mathbf{B} and the system volume $V_4 = (2\pi)^4 \delta^{(4)}(0)$. Remarkably, the integral agrees with the I function (609).¹³⁵ Adding the two cases where either p^μ or k^μ is sent to zero,

¹³⁵To see the agreement, first notice that

$$\int_0^1 dx \int_0^{1-x} dy \frac{2m^2}{x(1-x)q^2 - m^2} = \int_0^1 dx \frac{2m^2(1-x)}{x(1-x)q^2 - m^2} = \int_0^1 dx \frac{2m^2 x}{(1-x)xq^2 - m^2}, \quad (637)$$

where the last expression is obtained via a change of the integral variable. Then, summing the latter two expressions, we get

$$\int_0^1 dx \frac{2m^2(1-x)}{x(1-x)q^2 - m^2} = \frac{1}{2} \int_0^1 dx \frac{2m^2}{x(1-x)q^2 - m^2} = -I(q^2/4m^2). \quad (638)$$

When one sends the other momentum k^μ to zero the integral reduces to the I function in the same manner.

one finds that the AWI in a constant and perturbatively weak magnetic field reads

$$\text{F.T. } \langle p, k | \partial_\mu j_A^\mu | 0 \rangle = \frac{q_f^2}{2\pi^2} \tilde{\mathbf{E}}(q) \cdot \mathbf{B} \left[1 - I\left(\frac{q^2}{4m^2}\right) \right] V_4, \quad (639)$$

where we assumed that there is not a constant electric field, i.e., $\mathbf{E} = 0$. This expression agrees with Eq. (618) in the constant and strong magnetic field when the electric field is homogeneous in the transverse plane, i.e., $|\mathbf{q}_\perp| \rightarrow 0$.

F.3.2 The lowest Landau level in effective (1+1) dimensions

We next examine the AWI in the effective (1+1) dimensions realized in the LLL. One can find more computational details in the appendix of Ref. [84]. The anomaly diagram here is the two-point function composed of the LLL fermion loop:

$$\int d^4x e^{-iqx} \langle k | \partial_\mu j_A^\mu(x) | 0 \rangle = \rho_B e^{-\frac{|\mathbf{q}_\perp|^2}{2|q_f B|}} (2\pi)^2 \delta^{(2)}(k_\parallel - q_\parallel) i q_\mu \Pi_{1+1(A)}^{\mu\nu}(q_\parallel) \epsilon_\nu^*(q). \quad (640)$$

The Landau degeneracy factor and the Gaussian come from the transverse-momentum integral as in the computation of the vector-current correlator (600). The residual (1+1)-dimensional longitudinal part is given as

$$i q_\mu \Pi_{1+1(A)}^{\mu\nu}(q_\parallel) = (-1)(-i q_f) \int \frac{d^2 p_\parallel}{(2\pi)^2} \frac{\text{Tr}[\not{q}_\parallel \gamma^5 i(\not{p}_\parallel + m) \mathcal{P}_+ \gamma_\parallel^\nu i((\not{p}_\parallel + \not{q}_\parallel) + m) \mathcal{P}_+]}{(p_\parallel^2 - m^2)((p_\parallel + q_\parallel)^2 - m^2)}. \quad (641)$$

The two-dimensional integral is (superficially) logarithmically divergent, and we use the dimensional regularization with a displacement from two dimensions, i.e., $2 \rightarrow d$. Similar to the identity (624), we here use another identity

$$\not{q}_\parallel \gamma^5 = \gamma^5(\not{p}_\parallel - m) + (\not{q}_\parallel + \not{p}_\parallel - m) \gamma^5 + 2(m - \tilde{p}_\parallel) \gamma^5. \quad (642)$$

Plugging the above identity to the (1+1)-dimensional part, we have

$$\begin{aligned} i q_\mu \Pi_{1+1(A)}^{\mu\nu}(q_\parallel) \epsilon_\nu^*(q) &= -2q_f \epsilon_\nu^*(q) \int \frac{d^d p_\parallel}{(2\pi)^d} \frac{\text{Tr}[\tilde{\not{p}}_\parallel \gamma^5 (\not{p}_\parallel + m) \mathcal{P}_+ \gamma_\parallel^\nu i((\not{p}_\parallel + \not{q}_\parallel) + m) \mathcal{P}_+]}{(p_\parallel^2 - m^2)((p_\parallel + q_\parallel)^2 - m^2)} \\ &\quad + 2im \langle \bar{\psi} \gamma^5 \psi \rangle, \end{aligned} \quad (643)$$

where we have

$$\langle \bar{\psi} \gamma^5 \psi \rangle = (-1)[-i q_f \epsilon_\nu^*(q)] \int \frac{d^2 p_\parallel}{(2\pi)^2} \frac{\text{Tr}[\gamma^5 i(\not{p}_\parallel + m) \mathcal{P}_+ \gamma_\parallel^\nu i((\not{p}_\parallel + \not{q}_\parallel) + m) \mathcal{P}_+]}{(p_\parallel^2 - m^2)((p_\parallel + q_\parallel)^2 - m^2)}. \quad (644)$$

This is the leading nonvanishing matrix element of the pseudoscalar condensate, which is represented by the diagram with one-insertion of the external photon leg. The first term in Eq. (643) will result in the anomalous term.

We shall first examine the anomalous term. Introducing the Feynman parameter and performing the spinor trace to the first term in Eq. (643), one arrives at a momentum integral

$$\int \frac{d^d p_\parallel}{(2\pi)^d} \frac{\tilde{p}_\parallel^2}{(p_\parallel^2 - \Delta_\parallel)^2} = \frac{d-2}{d} \times \frac{(-1)i}{(4\pi)^{d/2}} \frac{d \Gamma(-\frac{d-2}{2})}{2 \Gamma(2)} \Delta_\parallel^{\frac{d-2}{2}} = \frac{i}{4\pi}, \quad (645)$$

where we used $(d-2)\Gamma(-\frac{d-2}{2}) = -2 + \mathcal{O}(d-2)$. As in the integral (628) for the triangle diagrams, the above integral is finite because of the overall dimensional factor and all the mass dependence goes away on the rightmost side after the limit $(d \rightarrow 2)$ is taken. the correlator (643) results in

$$iq_\mu \Pi_{1+1(A)}^{\mu\nu}(q_\parallel) \epsilon_\nu^*(k) = -\frac{q_f}{\pi} \langle k | \tilde{E}_\parallel | 0 \rangle + 2im \langle \bar{\psi} \gamma^5 \psi \rangle, \quad (646)$$

where the momentum conservation in Eq. (640) is understood (with the delta function suppressed). The electric field is defined as $\tilde{E}_\parallel = -i\epsilon_{\parallel}^{\mu\nu} q_\mu A_\nu$ with $\epsilon_{\parallel}^{\mu\nu} = \epsilon^{\mu\nu 12}$ as below Eq. (616).

One can straightforwardly compute the matrix element of the pseudoscalar condensate (644) to find that

$$2im \langle \bar{\psi} \gamma^5 \psi \rangle = \frac{s_f q_f}{\pi} \tilde{E}_\parallel I\left(\frac{q_\parallel^2}{4m^2}\right). \quad (647)$$

Notice that we have the I function defined in Eq. (609). As discussed below Eq. (630) for the triangle diagrams, one needs insertion of external photon legs to have a nonvanishing matrix element of $\langle \bar{\psi} \gamma^5 \psi \rangle$. In the present case, one needs to include one external photon leg that results in \tilde{E}_\parallel in addition to the resummed magnetic-field legs.

Combining the anomalous term and pseudoscalar condensate in the above, we obtain

$$\text{F.T. } \partial_\mu j_A^\mu = \frac{q_f^2}{2\pi^2} \tilde{\mathbf{E}}(q) \cdot \mathbf{B} \left[1 - I\left(\frac{q_\parallel^2}{4m^2}\right) \right] e^{-\frac{|\mathbf{q}_\perp|^2}{2|q_f B|}}. \quad (648)$$

This result reproduces the AWI (618) obtained from Π_\parallel in Eq. (608). As in the discussions about the triangle diagrams, we emphasize that both the mass-independent anomalous term and the mass-dependent pseudoscalar condensate stem from a single diagram with the massive fermion loop. The massive fermion loop vanishes as a whole in the large-mass limit, $\lim_{x \rightarrow 0} I(x) = 1$. This clearly explains the conservation of the axial current observed below Eq. (618). Notice again that this expression (648) agrees with the AWI (639) from the triangle diagrams in a weak and constant magnetic field when the electric field is homogeneous in the transverse plane ($|\mathbf{q}_\perp| = 0$).

F.4 Thermal contributions at finite temperature and density

When there are thermally populated particles and antiparticles, their polarization can contribute to the polarization tensor $\Pi^{\mu\nu}$. Below, we discuss such a medium contribution to Π_\parallel in Eq. (598) within the LLL in strong magnetic fields. We write it as $\Pi_\parallel = \Pi_\parallel^{\text{vac}} + \Pi_\parallel^{\text{med}}$ where the vacuum contribution discussed in Appendix F.2.1 and the medium contribution discussed below are denoted as $\Pi_\parallel^{\text{vac}}$ and $\Pi_\parallel^{\text{med}}$, respectively. To compute the medium contribution, one can use either the real-time formalism [409, 565, 770, 771, 775] or the imaginary-time formalism [776]). The equivalence between those results is commented below. Since all the computational details are summarized in the appendix of Ref. [565]. We here only quote the essential results.

In the strictly massless case, one can show that the medium correction to the polarization tensor exactly vanishes, i.e., $\Pi_\parallel^{\text{med}} = 0$. This result can be also confirmed by the use of the bosonization technique (see, e.g., Refs. [409, 777]). This result implies the absence of medium corrections to the AWI (617) in the massless case.

Even in the massive case, one finds a partial cancellation. As anticipated from the complete cancellation in the massless case, the residual terms are all proportional to the fermion mass squared m^2 . After some computational efforts (see Ref. [565]), the medium contribution is obtained as [409]

$$\Pi_\parallel^{\text{med}}(\omega, q_z) = \pi m_B^2 e^{-\frac{|\mathbf{q}_\perp|^2}{2|q_f B|}} m^2 \int_{-\infty}^{\infty} \frac{dp_z}{2\pi \epsilon_p} \frac{(q_\parallel^2 + 2q_z p_z) [n_+(\epsilon_p) + n_-(\epsilon_p)]}{q_\parallel^2 (p_z - \frac{1}{2}q_z)^2 - \frac{\omega^2}{4} (q_\parallel^2 - 4m^2)}, \quad (649)$$

where $\epsilon_p = \sqrt{p_z^2 + m^2}$ and $n_{\pm}(p^0) = [e^{(p^0 \mp \mu)/T} + 1]^{-1}$ with temperature T and chemical potential μ . The LLL contribution does not yield tensor structures other than $P_{\parallel}^{\mu\nu}$. In fact, there is no other transverse tensor structure that can be constructed in the (1+1) dimensions, whereas the projection operator is usually split into two components in a medium due to the absence of the Lorentz symmetry. Instead, the absence of the Lorentz symmetry manifests itself in the remaining p_z integral that separately depends on the external gluon/photon energy ω and momentum q_z in separate forms in addition to the boost-invariant form $q_{\parallel}^2 = \omega^2 - q_z^2$. After some algebra, the above expression reduces to the one shown in Eq. (7) of Ref. [776].¹³⁶

Noticing that the integrand in Eq. (649) has poles, one can rearrange it in a more transparent form

$$\Pi_{\parallel}^{\text{med}}(\omega, q_z) = \frac{2\pi m^2 m_B^2}{q_{\parallel}^2 \sqrt{1 - 4m^2/q_{\parallel}^2}} e^{-\frac{|q^2|}{2|q_f B|}} \int_{-\infty}^{\infty} \frac{dp_z}{2\pi \epsilon_p} [n_+(\epsilon_p) + n_-(\epsilon_p)] \left(\frac{\epsilon_p^+ s_+}{p_z - p_z^+} - \frac{\epsilon_p^- s_-}{p_z - p_z^-} \right). \quad (650)$$

With the infinitesimal imaginary part $\omega \rightarrow \omega + i\epsilon$ for the retarded correlator, the pole positions are found to be

$$p_z^{\pm} = \frac{1}{2} \left(q_z \pm \omega \sqrt{1 - 4m^2/q_{\parallel}^2} \right) \pm i\epsilon. \quad (651)$$

Accordingly, we define corresponding energies

$$\epsilon_p^{\pm} \equiv \sqrt{(p_z^{\pm})^2 + m^2} = \frac{1}{2} \left| \omega \pm q_z \sqrt{1 - 4m^2/q_{\parallel}^2} \right|. \quad (652)$$

Note that those are complex-valued quantities when $1 - 4m^2/q_{\parallel}^2 < 0$, meaning that there is no pole contribution to the integral in this kinematical region. We also introduced sign functions

$$s_{\pm} := \text{sgn} \left(\omega \pm q_z \sqrt{1 - 4m^2/q_{\parallel}^2} \right), \quad (653)$$

for $1 - 4m^2/q_{\parallel}^2 > 0$. When $1 - 4m^2/q_{\parallel}^2 \leq 0$ and thus ϵ_p^{\pm} is complex-valued, we define that $s_{\pm} = 1$ just to maintain the original form $\epsilon_p^{\pm} s_{\pm} = \frac{1}{2} \left(\omega \pm q_z \sqrt{1 - 4m^2/q_{\parallel}^2} \right)$.

F.4.1 Thermally induced imaginary parts

We closely look into the medium effects contained in the imaginary part of the integral expression (650). Since the imaginary part is related to the squared amplitude of on-shell processes, it helps us to intuitively understand how the interplay between the effects of the strong magnetic field and medium work in the relevant processes.

The denominator of the integrand in Eq (650) has a definite sign as long as $1 - 4m^2/q_{\parallel}^2 < 0$, that is, $0 < q_{\parallel}^2 < 4m^2$. In this kinematics, the regular p_z -integral does not generate any imaginary part. However, when $q_{\parallel}^2 \leq 0$ or $q_{\parallel}^2 \geq 4m^2$, the integral picks up the pole contributions (651), implying existence of an imaginary part in these regimes. By the use of the formula $1/(x \pm i\epsilon) = P(1/x) \mp i\pi\delta(x)$, one can extract the imaginary part of the polarization tensor: We obtain the total imaginary part

$$\Im m \Pi_{\parallel} = \Im m \Pi_{\parallel}^{\text{vac}} + \Im m \Pi_{\parallel}^{\text{med}} \quad (654)$$

¹³⁶In Ref. [776], the imaginary-time formalism was applied to the computation of the polarization tensor in the massive Schwinger model. To confirm the agreement, notice that the numerator in the integrand can be rewritten as $\{(\epsilon_{\mp} - \omega)^2 - \epsilon_{\pm}^2\} + \{(\epsilon_{\mp} + \omega)^2 - \epsilon_{\pm}^2\} = 2(\omega^2 \mp 2p'_z q_z) = 2(q_{\parallel}^2 \mp 2p_z q_z)$ where $\epsilon_{\pm} = \sqrt{(p'_z \pm q_z/2)^2 + m^2}$ is defined in Ref. [776]. We utilized shifts of the integral variable $p'_z = \mp p_z \pm \frac{1}{2} q_z$. The denominator can be arranged in the same way.

$$= -\pi m_B^2 e^{-\frac{|q_\perp|^2}{2|q_f^B|}} \frac{2m^2}{q_\parallel^2 \sqrt{1 - 4m^2/q_\parallel^2}} \left[(1 - N_+) \theta(q_\parallel^2 - 4m^2) \text{sgn}(\omega) - N_- \theta(-q_\parallel^2) \right],$$

where we defined $s_\pm = \theta(q_\parallel^2 - 4m^2) \text{sgn}(\omega) \pm \theta(-q_\parallel^2)$ and $N_\pm = \frac{1}{2} \{n_+(\epsilon_p^+) + n_-(\epsilon_p^+)\} \pm \frac{1}{2} \{n_+(\epsilon_p^-) + n_-(\epsilon_p^-)\}$. The above result is symmetric under the sign flip of the chemical potential $\mu \rightarrow -\mu$ as expected. One can combine the two kinematical regions $q_\parallel^2 < 0$ and $q_\parallel^2 - 4m^2 > 0$ to get another expression by hyperbolic functions:

$$\Im m \Pi_\parallel = -\pi m_B^2 e^{-\frac{|q_\perp|^2}{2|q_f^B|}} \frac{2m^2}{q_\parallel^2 \sqrt{1 - 4m^2/q_\parallel^2}} \cdot \frac{1}{2} \sum_{c=\pm} \frac{\sinh(\frac{\omega}{2T}) \theta(1 - 4m^2/q_\parallel^2)}{\cosh(\frac{\omega}{2T}) + \cosh(\frac{q_z}{2T} \sqrt{1 - 4m^2/q_\parallel^2} + c \frac{\mu}{T})}. \quad (655)$$

At a vanishing chemical potential $\mu \rightarrow 0$, this expression essentially agrees with those in Ref. [776] (up to a typo there) and in Ref. [771] where the authors compute the Feynman causal correlator instead of the retarded correlator. One can immediately find that the above result (654), and thus (655) as well, is an odd function of ω , which originates from a general property of the spectral density (see, e.g., Ref. [306]).

Now, we shall examine the physical processes that give rise to the imaginary part in the regions $q_\parallel^2 > 4m^2$ and $q_\parallel^2 < 0$ separately. Below, we refer those regions “time-like” and “space-like” as in the (1+1)-dimensional case. Notice that the “time-like” condition $q_\parallel^2 > 4m^2$ can be compatible with the light-like on-shell condition $q^2 = q_\parallel^2 + q_\perp^2 = 0$ in the four dimensions.

Finite temperature

Here, we consider the zero-density case $\mu = 0$, and both the fermion and antifermion distribution functions reduce to the same form $n_\pm(p^0) \rightarrow n(p^0) = [e^{p^0/T} + 1]^{-1}$. We first focus on the high-temperature limit where $T \gg \omega, q_z$. Observe that the leading term in the high-temperature expansion of N_+ exactly cancels the vacuum contribution in Eq. (654), i.e.,

$$1 - N_+ \sim \frac{1}{4T} (\epsilon_p^+ + \epsilon_p^-) = \frac{|\omega|}{4T}. \quad (656)$$

Consequently, the total imaginary part is highly suppressed in the time-like region by a factor of $|\omega|/(4T) \ll 1$. One can interpret this result in the following way. In vacuum, the imaginary part indicates a pair creation from an incident photon/gluon. However, in the presence of a heat bath, its inverse process is also activated because thermal fermions and antifermions can annihilate into a photon/gluon.¹³⁷ Due to the detail balance between these processes, the net imaginary part in the time-like regime is suppressed at high temperature. One can confirm this observation with a simple identity

$$1 - N_+ = [1 - n(\epsilon_p^+)] [1 - n(\epsilon_p^-)] - n(\epsilon_p^+) n(\epsilon_p^-). \quad (657)$$

The first term corresponds to the pair-creation channel $\gamma \rightarrow f\bar{f}$ that is subject to the Pauli-blocking effect in the final state, while the second term corresponds to the pair-annihilation channel $f\bar{f} \rightarrow \gamma$. Here, we also confirm the energy conservation $|\omega| = \epsilon_p^+ + \epsilon_p^-$ according to Eq. (652). The net pair creation occurs with a significant rate only in a sufficiently high energy regime $\omega, q_z \gg T$, where the thermal contribution is exponentially suppressed. In such cases, the vacuum contribution stands as the dominant contribution to the imaginary part.

¹³⁷Note that kinematics of the 1-to-2 and 2-to-1 processes is allowed in a magnetic field even for an on-shell photon, though it is forbidden in the four dimensions without a magnetic field.

On the other hand, one finds a new medium-induced channel in the space-like regime, that is, a contribution from the Landau damping proportional to N_- . The Landau damping is purely a medium effect where a medium fermion (antifermion) is scattering off a space-like photon. In case of vacuum, the imaginary parts in the space-like regime cancel out in the final expression of the polarization tensor in all order of the Landau levels [214]. One finds an identity

$$-N_- = n(\epsilon_p^-)[1 - n(\epsilon_p^+)] - n(\epsilon_p^+)[1 - n(\epsilon_p^-)], \quad (658)$$

where the first (second) term corresponds to the gain (loss) term for the phase-space volume at $p^0 = \epsilon_p^+$. Namely, this identity shows the detail balance between the scatterings $f + \gamma^* \rightarrow f$ and $f \rightarrow f + \gamma^*$. The Pauli blocking effect appears in the final states on the right-hand side of the above identity. We confirm the energy conservation $\omega + \epsilon_p^- = \epsilon_p^+$ according to Eq. (652).

Finite density

At nonzero density ($\mu \neq 0$), the fermion and antifermion distribution functions should be distinguished. Nevertheless, we can interpret the pair creation/annihilation and the Landau damping in a similar way to the zero-density case discussed above.

Similar to the zero-density case (657), one finds an identity

$$1 - N_+ = \sum_{\alpha=\pm} \frac{1}{2} \left[\{1 - n_+(\epsilon_p^\alpha)\} \{1 - n_-(\epsilon_p^{-\alpha})\} - n_+(\epsilon_p^\alpha) n_-(\epsilon_p^{-\alpha}) \right]. \quad (659)$$

This expression has the same form as in Eq. (657) up to the difference between the fermion and antifermion distribution functions. In the pair creation/annihilation channel, the fermion and antifermion can have different energies ϵ_p^+ and ϵ_p^- when the photon momentum is nonzero, i.e., $q_z \neq 0$. Thus, there are two kinematical windows depending on either a fermion or antifermion takes ϵ_p^+ . Clearly, interchanging ϵ_p^+ and ϵ_p^- brings one kinematics to the other. A finite chemical potential distinguishes those two cases, whereas they are degenerate at zero density (657).

In the space-like region, the Landau damping of the fermions and antifermions occurs with different magnitudes. Separating the fermion and antifermion distribution functions, we find an identity

$$-N_- = \sum_{c=\pm} \frac{1}{2} \left[n_c(\epsilon_p^-) \{1 - n_c(\epsilon_p^+)\} - n_c(\epsilon_p^+) \{1 - n_c(\epsilon_p^-)\} \right]. \quad (660)$$

The sum over $c = + (-)$ is for the Landau damping of fermions (antifermions), assuming that $\mu > 0$ without lose of generality.

Notice that, at zero temperature, the fermion distribution functions reduce to step functions, and the Pauli blocking factors vanish, i.e., $1 - n_\pm \rightarrow 0$ below the Fermi surface. That is, the Pauli blocking at zero temperature requires photons/gluons to be energetic enough for the above on-shell processes to occur, leading to threshold shifts. This can be also confirmed on the basis of the analytic result of the integral (650) that can be performed exactly at zero temperature [565].

F.4.2 Photon masses from the polarization effects

We discuss physical applications of the in-medium polarization tensor given in Eq. (650). The first application is the in-medium gluon/photon masses [565] and another is the AWI at finite temperature and/or density [84] in the next subsection. According to the resummed propagator (596), the pole position of the parallel mode is given as

$$q^2 - \Pi_{\parallel}(q_{\parallel}; q_{\perp}) = 0. \quad (661)$$

The other mode is not modified by the polarization of the LLL fermions as already discussed there. In the massless limit, there is no medium modification on the polarization tensor (607), so that the gluon/photon dispersion relation is immediately obtained as

$$\omega^2 = |\mathbf{q}|^2 + m_B^2 e^{-\frac{|\mathbf{q}_\perp|^2}{2|q_f B|}}. \quad (662)$$

Computing the gluon/photon dispersion relation with massive fermions is more involved due to the momentum dependence of the polarization tensor; one needs to solve Eq. (661) with respect to the frequency. In general, the polarization tensor exhibits different limiting behaviors in the vanishing frequency and momentum limits; those limits do not commute with each other. Thus, there are two different gluon/photon masses (see, e.g., Ref. [307]). They are called the Debye screening mass and the plasma frequency, which we discuss below in order.

It should be emphasized that the medium contribution (649) gives rise to finite gluon/photon masses even in the massive case, in contrast to the absence of a static mass in the vacuum contribution [see discussions below Eq. (609)]. This is simply because the thermal fermions populated above the mass gap respond to the gluon/photon fields. From this observation, the masses may be sizeable when m/T , $m/\mu \lesssim 1$, and approach m_B in the high-temperature or -density limit, $m/T \rightarrow 0$ or $m/\mu \rightarrow 0$.

The Debye screening mass is the inverse of the screening length of a static (heavy) charge embedded in medium. In the static limit, the pole position is given as $|\mathbf{q}|^2 + \Pi_\parallel(\omega = 0) = 0$, and the polarization tensor cuts off the long-range propagation of spatial gluons/photons. The Debye screening mass is defined as

$$m_D^2 = \lim_{q_z/m \rightarrow 0} \Pi_\parallel^{\text{med}}(\omega = 0, q_z; q_\perp = 0) \quad (663)$$

We have first taken the vanishing frequency limit and the vanishing transverse-momentum limit ($q_\perp = 0$). The ordering of the limits does not matter for q_\perp in the present case. There is no vacuum contribution to m_D^2 as long as the fermion mass m is finite according to the property of the I function in Eq. (610); Massive fermions are not excited by photons with an infinitesimal energy. Inserting the medium contribution (650), we have

$$m_D^2 = -m_B^2 \lim_{\bar{q}_z \rightarrow 0} \frac{1}{2\bar{q}_z} \mathcal{P} \int_{-\infty}^{\infty} \frac{d\bar{p}_z}{\bar{\epsilon}_p} \frac{n_+(m\bar{\epsilon}_p) + n_-(m\bar{\epsilon}_p)}{\bar{p}_z - \bar{q}_z}. \quad (664)$$

We introduced a dimensionless variable $\bar{q}_z = q_z/(2m)$, and scaled the integral variable as $p_z \rightarrow p'_z = p_z/m$ accordingly. Other variables are also normalized as $\bar{\epsilon}_p = \epsilon_p/m$, $\bar{T} = T/m$, and $\bar{\mu} = \mu/m$. The integral should be understood as the Cauchy principal value denoted with \mathcal{P} . The Debye mass is determined by the first derivative of the integral value with respect to \bar{q}_z . The integral value is dominated by the infrared contribution such that $\bar{p}_z \sim \bar{q}_z \rightarrow 0$ due to the effective dimensional reduction of the integral measure.

We first examine the high-temperature or -density limit. The fermion distribution functions provide a cutoff scale at temperature T or chemical potential μ as

$$m_D^2 = -m_B^2 \lim_{\Lambda/m \rightarrow \infty} \lim_{\bar{q}_z \rightarrow 0} \frac{1}{2\bar{q}_z} \mathcal{P} \int_{-\Lambda/m}^{\Lambda/m} \frac{d\bar{p}_z}{\bar{\epsilon}_p} \frac{1}{\bar{p}_z - \bar{q}_z} = m_B^2, \quad (665)$$

where the cut-off Λ is given by a large value of either T or μ . In this limit, the Debye mass agrees with the Schwinger mass. Note that the hierarchy $T/\mu \gg 1$ ($T/\mu \ll 1$) needs to be satisfied for the above replacement in addition to the high-temperature limit $\bar{T} \rightarrow \infty$ (high-density limit $\bar{\mu} \rightarrow \infty$).

In Fig. 58, we show numerical results for the temperature dependence of the Debye screening mass at several values of density. We take $\bar{\mu} = \{0, 0.8, 1, 1.2, 2\}$ for the lines shown in {green, brown, gray,

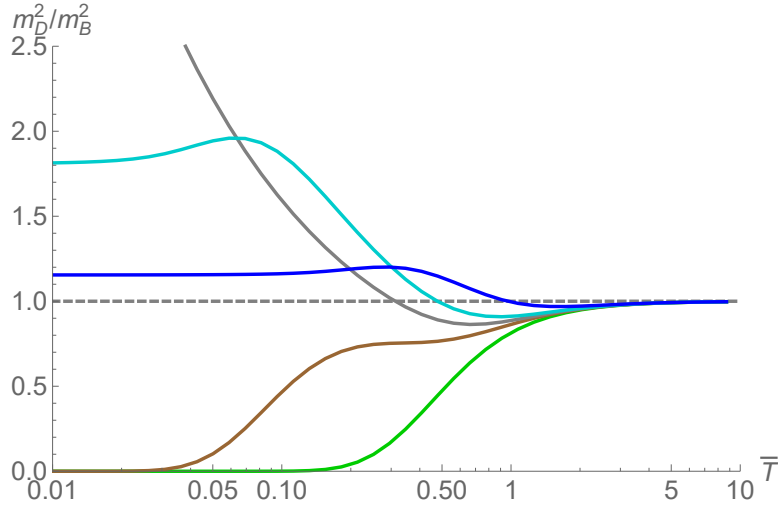


Figure 58: Temperature dependence of the Debye screening mass at $\bar{\mu} = \{0, 0.8, 1, 1.2, 2\}$ shown in {green, brown, gray, blue, cyan}.

blue, cyan}. One can confirm that the Debye mass approaches the Schwinger mass when $\bar{T} \gg 1$ for all the shown values of $\bar{\mu}$. As we decrease temperature, the lines splits near $\bar{T} = 1$ depending on the value of $\bar{\mu}$. The Debye mass approaches zero when $\bar{\mu} < 1$ due to the absence of thermal excitations, while it increases when $\bar{\mu} \geq 1$. This contrast behavior stems from a simple fact that the density of occupied low-energy states increases near the Fermi surface as we decrease temperature in the latter case. The reader is referred to Ref. [565] for more results and discussions.

In short, the Debye screening mass is dominantly induced by the fermions in the low-energy regime, and is enhanced when those states are occupied. Notice also that the Debye mass is scaled by the Schwinger mass m_B^2 . The Debye screening mass only depends on the magnetic-field strength through the Landau degeneracy factor in m_B^2 . The density of degenerate states increases as we increase the magnetic-field strength, and thus naturally enhances the Debye screening mass.

Next, we discuss the plasma frequency that appears in the dispersion relation of an on-shell gluon/photon in medium, which can be regarded as a collective excitation composed of a gluon/photon and oscillating plasma. The dispersion relations may be no longer gapless in the absence of the Lorentz symmetry. To find the magnitude of the energy gap at $|\mathbf{q}| = 0$, one should take the vanishing momentum limit first. Therefore, the plasma frequency ω_p is determined by the following equation

$$\omega_p^2 = \Pi_{\parallel}(\omega_p, 0) = m_B^2 \left[1 - I\left(\frac{\omega_p^2}{4m^2}\right) + 2m^2 \mathcal{P} \int_{-\infty}^{\infty} \frac{dp_z}{\epsilon_p} \frac{n_+(\epsilon_p) + n_-(\epsilon_p)}{(2\epsilon_p)^2 - \omega_p^2} \right]. \quad (666)$$

The right-hand side is still a function of the frequency ω_p , so that one needs to solve the above equation explicitly. Note that the first two terms in the brackets come from the vacuum contribution. One needs to maintain those terms in addition to the medium contribution because the medium contributions does not necessarily dominate over the vacuum contribution due to the effective dimensional reduction. This contrasts to the four dimensional case where the medium contribution, which is proportional to $(q_f T)^2$ or $(q_f \mu)^2$, governs the polarization effects at the high temperature/density regime.

One can show that Eq. (666) always has a solution as follows [565]. When $\omega_p \rightarrow 0$, the vacuum contribution exactly vanishes and the integral for the medium contribution gives Π_{\parallel} a positive value. On the other hand, the behavior of the right-hand side is dominated by the I function that gives Π_{\parallel} a divergence to negative infinity as $\omega_p^2 \rightarrow 4m^2$. This divergence is associated with the pair creation threshold as we discussed repeatedly. Therefore, one can find a solution in the range $0 < \omega_p^2 < 4m^2$

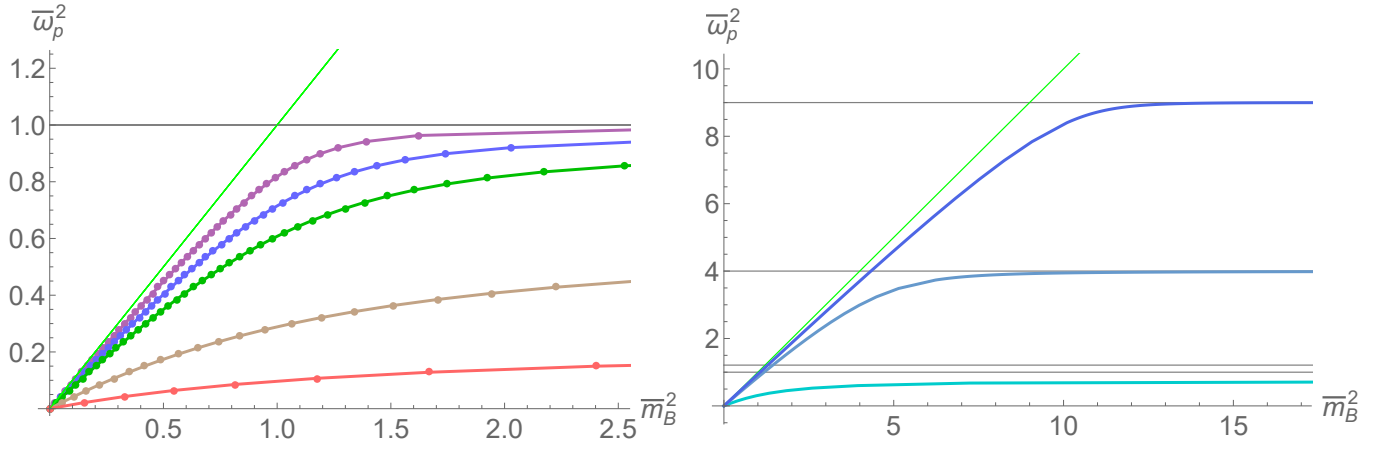


Figure 59: The plasma frequency as a function of the normalized magnetic-field strength \bar{m}_B^2 (left). We take $\bar{\mu} = 0$ and $\bar{T} = \{0.5, 1, 3, 5, 10\}$ from bottom to top. The plasma frequency as a function of the normalized magnetic-field strength \bar{m}_B^2 (right). We take $\bar{\mu} = \{1.1, 2, 3\}$ from bottom to top.

as long as temperature is finite. At zero temperature case, the upper bound is shifted with a chemical potential since the Pauli-blocking effect induces the threshold shift as we discussed below Eq. (660).

In the left panel of Fig. 59, we show the normalized plasma frequency $\bar{\omega}_p^2 = \omega_p^2/(4m^2)$ as a function of the normalized magnetic-field strength \bar{m}_B^2 . We take a set of temperature $\bar{T} = \{0.5, 1, 3, 5, 10\}$ at vanishing chemical potential $\bar{\mu} = 0$. All the curves increase as we increase the magnetic-field strength \bar{m}_B^2 . The plasma frequency approaches the Schwinger mass, shown with the light green line, and saturates at $\bar{\omega}_p^2 = 1$ as we increase temperature. The former behavior is naturally expected from that in the massless limit $\bar{T} \rightarrow \infty$. The latter behavior may be more subtle, implying that an infinitesimal mass makes the curve approach $\bar{\omega}_p^2 = 1$ rather than the Schwinger mass. The deviation from the Schwinger mass gets larger as we increase \bar{m}_B^2 , and the plasma frequency is strongly suppressed in such a strong-field limit, meaning that the fermion-mass effect becomes sizable in the photon dispersion relation.

In the right panel of Fig. 59, we show the plasma frequency as a function of \bar{m}_B^2 at $\bar{\mu} = \{1.1, 2, 3\}$. The plasma frequency approaches the Schwinger mass as we increase $\bar{\mu}$. As we increase \bar{m}_B^2 , the plasma frequency saturates at $\bar{\omega}_p^2 = \bar{\mu}^2$ [$\omega_p^2 = (2\mu)^2$] at zero temperature, whereas we have seen that the saturation value is always given by $\bar{\omega}_p^2 = 1$ [$\omega_p^2 = (2m)^2$] at finite temperature. This difference originates from the shift of the pair-creation threshold induced by the Pauli blocking effect.

Here is one caveat; For the LLL approximation to work, all the physical scales should be smaller than the magnetic-field strength, i.e., $m^2, \omega_p^2, T^2, \mu^2, \ll q_f B$. Otherwise, the higher Landau levels come into play a role. Noticing that $\bar{m}_B^2 = \alpha_{\text{em}} \rho_B / m^2 \sim |q_f B| / m^2 \times 10^{-3}$, the LLL approximation should work for the lines shown in Fig. 59, except for the regime where \bar{m}_B^2 is too small.

F.4.3 Axial Ward identity at finite temperature and density

We now come back to the AWI (616b). In case of zero temperature, the axial current is conserved in the massive case $m^2 \gg q_{\parallel}^2$ where $\Pi_{\parallel} \rightarrow 0$. This is because there are no fermions that respond to the soft photon. In contrast, even a soft photon can perturb the system when there are thermal fermions at finite temperature as already discussed below Eq. (649). In this case, the spectral flow of thermal fermions, which is induced by a constant electric field, can create the axial charge due to the helicity flip during the acceleration [84]. Also, a gauge field A^μ at finite frequency can induce helicity flop of massive fermions by scattering and can decay into a pair of fermion and antifermion with the same helicity, both of which contribute to creation of the axial charge.

Including both the vacuum contribution (608) and the thermal contribution (650), we obtain the

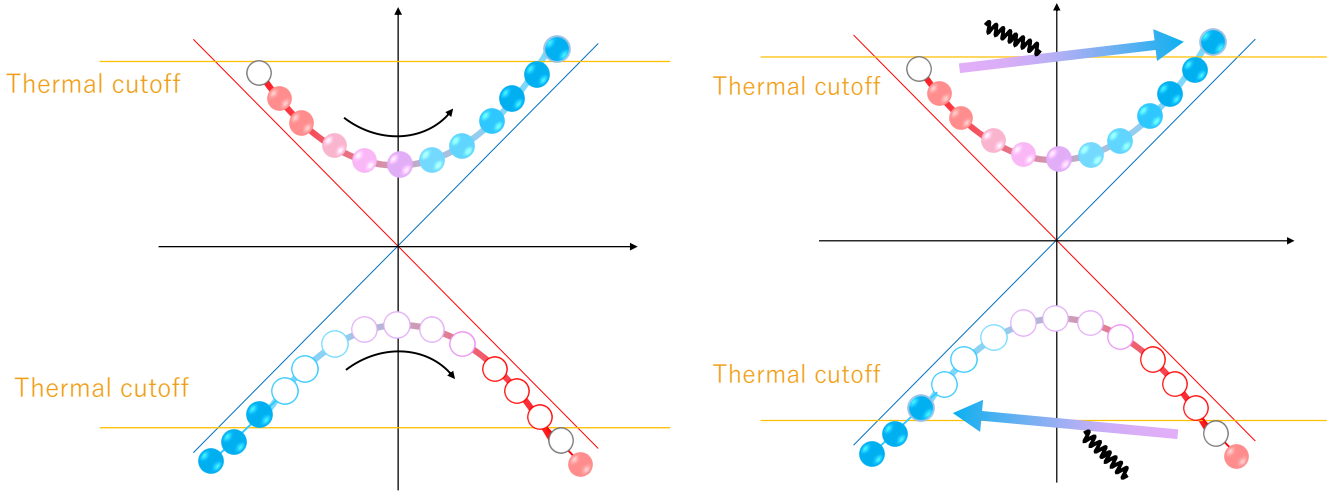


Figure 60: Axial-charge creation by the thermal spectral flow (left) and by the Landau damping (right) in the plane of fermion dispersion relation. Those processes are regarded as transitions from the left to right half planes (and in the inverse direction) that are accompanied by helicity flip.

in-medium AWI

$$\text{F.T. } \partial_\mu j_A^\mu = \frac{q_f^2}{2\pi^2} \tilde{\mathbf{E}}(q) \cdot \mathbf{B} e^{-\frac{|\mathbf{q}_\perp|^2}{2|q_f B|}} + 2im \langle \bar{\psi} \gamma^5 \psi \rangle, \quad (667a)$$

where

$$2im \langle \bar{\psi} \gamma^5 \psi \rangle = \frac{q_f^2}{2\pi^2} \tilde{\mathbf{E}}(q) \cdot \mathbf{B} e^{-\frac{|\mathbf{q}_\perp|^2}{2|q_f B|}} \times \left[-I\left(\frac{q_\parallel^2}{4m^2}\right) + m^2 \int_{-\infty}^{\infty} \frac{dp_z}{\epsilon_p} \frac{n_+(\epsilon_p) + n_-(\epsilon_p)}{q_\parallel^2 \sqrt{1 - 4m^2/q_\parallel^2}} \left(\frac{\epsilon_p^+ s_+}{p_z - p_z^+} - \frac{\epsilon_p^- s_-}{p_z - p_z^-} \right) \right]. \quad (668)$$

This is an extension of the vacuum expression (648). The first term in Eq. (667) is the anomalous term as in the vacuum massless case (617). The remaining terms are proportional to the fermion mass and are identified with matrix elements of the pseudoscalar condensate (668) as confirmed with explicit computation of the anomaly diagrams in Eq. (647). The first and second terms in Eq. (668) are the vacuum and thermal contributions, respectively. Note that the expression between the square brackets is dimensionless and should be a function of dimensionless combinations of the parameters.

In the “massless” limit $q_\parallel^2/m^2 \rightarrow \infty$, there is no thermal correction, and the AWI takes the same form as in vacuum with massless fermions (648). While we here does not discuss radiative corrections, the absence of temperature correction to the anomalous term was shown to all orders in the coupling constant in the strictly massless case [778]. Note that the above limit, $q_\parallel^2/m^2 \rightarrow \infty$, needs to be defined with a nonzero energy ω and/or momentum q_z of the electric field \tilde{E}_\parallel along the magnetic-field direction. If q_\parallel^2 goes to zero faster than m^2 , it is rather the adiabatic limit discussed below. This is the case where the electric field is homogeneous over the Compton length $1/m$ and includes the case of a constant electric field (see Sec. F.3.1).

One can recognize a qualitative difference between the vacuum and in-medium cases in the adiabatic limit $q_\parallel^2/m^2 \rightarrow 0$. As explicitly shown around Eq. (633), this limit corresponds to constant electric fields. The axial current is conserved in vacuum since a massive fermion and antifermion pair cannot be created in an adiabatic process. The spectral flow of the negative-energy states is always there, but does not give rise to axial-charge creation in the infrared regime because the spectral flow along the parabolic

dispersion curve turns back to the bottom of the Dirac sea [80] (see the left panel in Fig. 60). In contrast, the spectral flow can occur to the thermal particles in medium and give rise to a nonzero divergence of the axial current. This is because acceleration of thermal (on-shell) particles by electric fields induces a momentum flip and thus a helicity flip when the spectral flow goes through the bottom of the parabolic dispersion curve for the positive-energy states. What remains in the adiabatic limit is only the thermal contribution to the pseudoscalar condensate, which, therefore, is responsible for the thermal spectral flow. Interestingly, the AWI nevertheless takes the same form as the anomalous term in the high-temperature or density limit (m/T , $m/\mu \rightarrow 0$). Namely, one finds that

$$\lim_{\omega/m \rightarrow 0} \lim_{q_z/m \rightarrow 0} \text{F.T. } \partial_\mu j_A^\mu = \lim_{q_z/m \rightarrow 0} \lim_{\omega/m \rightarrow 0} \text{F.T. } \partial_\mu j_A^\mu = \frac{q_f^2}{2\pi^2} \tilde{\mathbf{E}}(q_\perp) \cdot \mathbf{B} e^{-\frac{|q_\perp|^2}{2|q_f B|}}, \quad (669)$$

where the integrals can be performed as in the previous subsection for the photon masses. One gets the same results irrespective of the order of limits. In the thermal spectral flow, the axial-charge imbalance appears near the thermal cutoff of the order of temperature or density instead of the infrared regime. Therefore, effects of the finite curvature along the dispersion curve is negligible in the high temperature or density limit defined as m/T , $m/\mu \rightarrow 0$.

Diabatic processes can also give rise to a nonzero divergence of the axial-vector current. In the present case, those processes have been identified with the pair creation and the Landau damping. We already discussed the contribution from the pair creation in vacuum. A net chirality carried by a pair of massive fermion and antifermion belonging to different chirality sectors. The pair creation rate is captured by the imaginary part of the polarization tensor inspected in the preceding subsection. The Landau damping can also contribute because a fermion or antifermion can be back-scattered during this process, implying occurrence of the helicity flip. Those contributions were numerically studied in Ref. [84].

Overall, one can only get simple results in the adiabatic limit that can be understood with the spectral-flow picture. However, the flow pattern crucially depends on the fermion mass, temperature, and density. Once diabatic processes are activated, fermions do not follow such a collective flow. Then, one needs to investigate the frequency and wavelength dependences of the AWI with the explicit form of the response function, which do not exhibit universal behaviors. The AWI takes the simple universal form in the massless case only because those diabatic processes are kinematically prohibited. In a sense, this situation is similar to that in quantum Hall systems and topological insulators where clean edge currents can be measured thanks to the absence of non-universal metallic currents in the bulk; Noises are muted by inherent mechanisms. The massless nature strongly restricts possible processes to those that occur in the right- and left-handed sectors independently.

F.5 Gluon/photon self-energy in a weak magnetic field

In this subsection, we discuss the vacuum polarization, or the photon/gluon self-energy, in the weak field limit that can be addressed with perturbative insertion of the external-field lines to the self-energy diagram. Such computation was well-investigated in a somewhat different context in the computation of the Wilson coefficients for the operator product expansion (see Ref. [104] for a review). There is an established algorithm useful for analytic computation of the self-energy diagrams [763]. We will summarize the flow chart of the computation and the result of the leading-order correction below.

The zeroth-order diagram is a familiar vacuum polarization tensor without any insertion of the external field. The computation and properties of this diagram is given in standard textbooks, e.g., in Ref. [66], so that we do not discuss this diagram. The diagrams with one insertion of the external-field line vanish according to the Furry's theorem. Therefore, the perturbative corrections by the external field start at the second-order diagrams shown in Fig. 61. Corresponding to those diagrams, one may

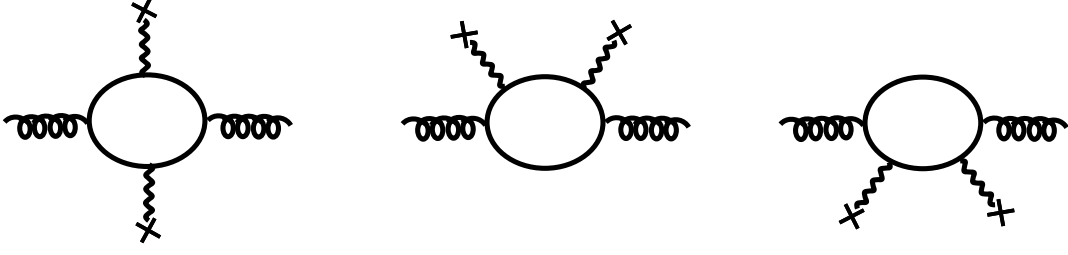


Figure 61: Leading-order perturbative corrections to the gluon/photon self-energy with two insertions of an external field (wavy lines with crosses).

write the leading-order correction as

$$\Pi^{\mu\nu}(q) = \Pi_{(1)}^{\mu\nu}(q) + 2\Pi_{(2)}^{\mu\nu}(q). \quad (670)$$

The latter two diagrams provide the same contributions when the quark pair carry an identical mass and charge, resulting in a factor of two. These terms can be written down by the use of the fermion propagators (546)-(547) with the insertions of one and two external fields [104, 763] as

$$i\Pi_{(1)}^{\mu\nu}(q) = g^2 \text{Tr}[t^a t^b] \int \frac{d^4 p}{(2\pi)^4} \text{Tr}[\gamma^\mu S_1(p) \gamma^\nu S_1(p-q)], \quad (671a)$$

$$i\Pi_{(2)}^{\mu\nu}(q) = g^2 \text{Tr}[t^a t^b] \int \frac{d^4 p}{(2\pi)^4} \text{Tr}[\gamma^\mu S_2(p) \gamma^\nu S_0(p-q)]. \quad (671b)$$

Note that the product of the coupling constant and the color trace, $g^2 \text{Tr}[t^a t^b]$, for the gluon self-energy should be replaced by $q_f^2 \text{Tr}[\mathbb{1}]_{\text{color}}$ for the photon self-energy with a quark loop. Inclusion of leptons needs a modification of the electric charge and removal of the color matrix as obvious.

At the second order, one can decompose the field strength tensor as

$$q_f^2 F_{\mu\nu} F_{\alpha\beta} = \frac{1}{12} (g_{\mu\alpha} g_{\nu\beta} - g_{\mu\beta} g_{\nu\alpha}) H + \frac{1}{2} (g_{\mu\alpha} H_{\nu\beta} - g_{\mu\beta} H_{\nu\alpha} + g_{\nu\beta} H_{\mu\alpha} - g_{\nu\alpha} H_{\mu\beta}) - \frac{2}{4!} \epsilon_{\mu\nu\alpha\beta} \tilde{H}, \quad (672)$$

where the scalar, the symmetric and traceless, and the antisymmetric parts are, respectively, given by

$$H = q_f^2 F_{\mu\nu} F^{\mu\nu}, \quad (673a)$$

$$H_{\mu\nu} = q_f^2 \left(F_{\mu\sigma} F_{\nu}{}^\sigma - \frac{1}{4} g_{\mu\nu} F_{\lambda\sigma} F^{\lambda\sigma} \right), \quad (673b)$$

$$\tilde{H} = q_f^2 F_{\mu\nu} \tilde{F}^{\mu\nu}. \quad (673c)$$

Accordingly, the self-energy can be also decomposed into the scalar and symmetric-tensor parts as

$$\Pi^{\mu\nu} = \frac{g^2}{\pi^2} \text{Tr}[t^a t^b] (\Pi_s^{\mu\nu} + \Pi_t^{\mu\nu}), \quad (674)$$

with

$$\Pi_s^{\mu\nu} = H \left[-\frac{1}{12} \phi^{(1)\mu\nu} - m^2 \phi^{(2)\mu\nu} \right], \quad (675a)$$

$$\Pi_t^{\mu\nu} = H^{\alpha\beta} \left[\frac{1}{2} \psi_{\alpha\beta}^{(1)\mu\nu} + 4 \left(\psi_{\alpha\beta}^{(21)\mu\nu} - \psi_{\alpha\beta}^{(22)\mu\nu} \right) \right]. \quad (675b)$$

The antisymmetric part does not contribute in usual environments where the correlator is symmetric in the Lorentz indices. More specifically, one needs an odd number of γ^5 so that the spinor trace yields an antisymmetric tensor.¹³⁸ The coefficients in Eqs. (675a) and (675b) are obtained by performing the loop integrals:

$$\phi^{(1)\mu\nu} = -i\frac{(4\pi)^2}{32} \int \frac{d^4p}{(2\pi)^4} \frac{1}{A^2 B^2} \text{Tr}[\gamma^\mu \{\sigma^{\delta\gamma}, \not{p}\} \gamma^\nu \{\sigma_{\delta\gamma}, (\not{p} - \not{q})\} + (2m)^2 \gamma^\mu \sigma^{\delta\gamma} \gamma^\nu \sigma_{\delta\gamma}], \quad (676a)$$

$$\phi^{(2)\mu\nu} = -i\frac{(4\pi)^2}{4} \int \frac{d^4p}{(2\pi)^4} \frac{1}{A^4 B^1} \text{Tr}[\gamma^\mu \gamma^\nu p^2 + \gamma^\mu \not{p} \gamma^\nu (\not{p} - \not{q})], \quad (676b)$$

and

$$\psi_{\alpha\beta}^{(1)\mu\nu} = i\frac{(4\pi)^2}{16} \int \frac{d^4p}{(2\pi)^4} \frac{1}{A^2 B^2} \text{Tr}[\gamma^\mu \{\sigma_{\alpha\lambda}, \not{p}\} \gamma^\nu \{\sigma_\beta{}^\lambda, (\not{p} - \not{q})\} + (2m)^2 \gamma^\mu \sigma_{\alpha\lambda} \gamma^\nu \sigma_\beta{}^\lambda], \quad (677a)$$

$$\psi_{\alpha\beta}^{(21)\mu\nu} = -i\frac{(4\pi)^2}{8} \int \frac{d^4p}{(2\pi)^4} \frac{1}{A^3 B^1} \text{Tr}[\gamma^\mu (p_\alpha \gamma_\beta + p_\beta \gamma_\alpha) \gamma^\nu (\not{p} - \not{q})], \quad (677b)$$

$$\psi_{\alpha\beta}^{(22)\mu\nu} = -i\frac{(4\pi)^2}{4} \int \frac{d^4p}{(2\pi)^4} \frac{p_\alpha p_\beta}{A^4 B^1} \text{Tr}[m^2 \gamma^\mu \gamma^\nu + \gamma^\mu p \gamma^\nu (\not{p} - \not{q})], \quad (677c)$$

where $A = p^2 - m^2$ and $B = (p - q)^2 - m^2$. One can arrange the above expressions into compact ones by the use of a nice algorithm [763]. We briefly summarize the procedure in the following.

As in the standard procedure [66], the propagators are combined with the help of the Feynman parameter:

$$\frac{1}{A^m B^n} = \frac{\Gamma(n+m)}{\Gamma(m)\Gamma(n)} \int \frac{x^{m-1}(1-x)^{n-1} dx}{[x(p^2 - m^2) + (1-x)\{(p-q)^2 - m^2\}]^{m+n}}. \quad (678)$$

Then, replacing an integral variable as $\ell = p - (1-x)q$, the loop integral can be performed as

$$\int \frac{d^4\ell}{(2\pi)^4} \frac{(\ell^2)^r}{(\ell^2 - \Delta)^s} = i \frac{(-1)^{r-s} \Gamma(r+2)\Gamma(s-r-2)}{(4\pi)^2 \Gamma(s)} \Delta^{r-s+2}, \quad (679)$$

where we introduced $\Delta = m^2 - x(1-x)q^2$. After the integration, one will obtain an expression with single integrals with respect to the Feynman parameter, of which the general form is given by

$$I_n^m(N) = \int_0^1 \frac{x^m(1-x)^n}{[m^2 + x(1-x)Q^2]^N} dx, \quad (680)$$

with integers m, n, N . By using recursive relations¹³⁹

$$I_{n-1}^n(N) = \frac{1}{2} I_{n-1}^n(N), \quad (681a)$$

$$I_{n-2}^n(N) = -I_{n-1}^n(N) + \frac{1}{2} I_{n-2}^n(N), \quad (681b)$$

$$I_{n-3}^n(N) = -\frac{3}{2} I_{n-2}^n(N) + \frac{1}{2} I_{n-3}^n(N), \quad (681c)$$

¹³⁸Possible examples are the presence of an axial chemical potential, or a mixing between the currents which have different parities.

¹³⁹From a simple identity $x^n(1-x)^{n-1} = x^{n-1}(1-x)^{n-1} - x^{n-1}(1-x)^n$, we have $I_{n-1}^n(N) = I_{n-1}^n(N) - I_n^{n-1}(N)$. Thus, noting that $I_m^n(N) = I_n^m(N)$, the first recursive equation is readily obtained. The other relations are also obtained in a similar way.

one can reduce the difference between the upper and lower indices, and arrive at the expression given by $I_n(N) \equiv I_n^n(N)$, that is,

$$I_n(N) = \int_0^1 \frac{x^n(1-x)^n}{[m^2 - x(1-x)q^2]^N} dx =: \frac{1}{(m^2)^N} J_N^n, \quad (682)$$

where we introduced a dimensionless integral J_N^n . Furthermore, one can immediately get another recursive relation

$$J_N^n = y^{-1} (J_{N-1}^{n-1} - J_N^{n-1}). \quad (683)$$

By the use of this relation, one can reduce the order n in the numerator, and finally reach the integrals that do not have the Feynman parameters in the numerators, i.e.,

$$J_N := J_N^0 = \int_0^1 [1 + x(1-x)y]^{-N} dx, \quad (684)$$

with $y = -q^2/m^2$. Then, the integral with an arbitrary index N can be obtained recursively as

$$J_N = \frac{(2N-3)!!}{(N-1)!} \left(\frac{a-1}{2a} \right)^{N-1} \left[J_1 + \sum_{k=0}^{N-2} \frac{k!}{(2k+1)!!} \left(\frac{a-1}{2a} \right)^{-k} \right], \quad (685)$$

where $a = 1 + 4/y$, and

$$J_1 = \left(\frac{a-1}{2a} \right) \sqrt{a} \ln \frac{\sqrt{a}+1}{\sqrt{a}-1}. \quad (686)$$

Now, performing a lengthy but straightforward calculation outlined above, we obtain the leading-order correction (674) to the vacuum polarization as

$$\Pi_s^{\mu\nu} = \frac{1}{2} H w P_0^{\mu\nu}, \quad (687a)$$

$$\Pi_t^{\mu\nu} = \frac{1}{2} H_{\alpha\beta} [v P_0^{\mu\nu} q^\alpha q^\beta + u \{ -g^{\mu\nu} q^\alpha q^\beta + g^{\mu\alpha} q^\nu q^\beta + g^{\nu\alpha} q^\mu q^\beta - g^{\mu\alpha} g^{\nu\beta} q^2 \}], \quad (687b)$$

where $P_0^{\mu\nu} = (g^{\mu\nu} - q^\mu q^\nu / q^2)$ and

$$w = \frac{1}{12q^2} (1 - 3J_2 + 2J_3), \quad (688a)$$

$$v = \frac{1}{q^4} \left[-\frac{2}{3} + 2J_1 - 2J_2 + \frac{2}{3} J_3 \right], \quad (688b)$$

$$u = \frac{1}{q^4} \left[\frac{1}{2} + \left(1 - \frac{1}{3} y \right) J_1 - \frac{3}{2} J_2 \right]. \quad (688c)$$

The tensor part $\Pi_t^{\mu\nu}$ has been obtained as the Wilson coefficient for the twist-two gluon condensate in medium [779] (up to the differences in color factors). Choosing the Lorentz frame where the electric and magnetic fields are parallel/antiparallel to each other, we find the leading correction to the gluon/photon self-energy (674) as

$$\Pi_s^{\mu\nu} = q_f^2 (B^2 - E^2) w P_0^{\mu\nu}, \quad (689a)$$

$$\Pi_t^{\mu\nu} = -\frac{1}{4} q_f^2 (B^2 + E^2) [v (q_{\parallel}^2 - q_{\perp}^2) P_0^{\mu\nu} - 2u (q_{\parallel}^2 P_{\parallel}^{\mu\nu} - q_{\perp}^2 P_{\perp}^{\mu\nu})]. \quad (689b)$$

Here, without the medium effect, the self-energy contains the transversal tensor structures discussed around Eq. (588) in the beginning of this section. The results at $B \neq 0$, $E = 0$ were used to investigate charmonium spectroscopy in an external magnetic field by means of the QCD sum rule [536, 537].

G Chiral magnetic/separation effect with massive fermions

We discuss mass effects on the anomalous transport phenomena in a magnetic field. Here, we focus on a straightforward extension of the computation in Sec. 8.1 by the use of the mode expansion of fermion fields in the Ritus basis. This extension assumes existence of constant axial and vector chemical potentials in the thermal equilibrium. Then, we will reach a somewhat misleading conclusion that there is no mass effect on the CME. Does this really mean that the same amount of the CME current is transported no matter how heavy the fermion is? In reality, this should not be taken literary since the axial charge density is not a conserved quantity due to the explicit chiral symmetry breaking by a fermion mass and the CME current is implicitly, but possibly significantly, dependent on a fermion mass. The axial charge will be damped out in an equilibrium due to the helicity flipping processes (unless there is an external pumping effect, which may realize a steady state). One should keep these caveats in mind when computing the CME current with an axial chemical potential μ_A as a static parameter. On the other hand, the vector charge and associated vector chemical potential μ_V are well-defined equilibrium quantity protected by a $U(1)_V$ symmetry, so that we will find a simpler and more robust conclusion on the mass correction to the CSE.

Computation of the currents goes almost in parallel to that in the massless case performed in Sec. 8.1. Here, we should use the V/A basis to compute the currents since the chirality is no longer a good quantum number of massive fermions. We focus on the spatial component along the magnetic field

$$j_{V/A}^\mu(x) = \langle \bar{\psi}(x) \gamma_{V/A}^\mu \psi(x) \rangle, \quad (690)$$

where $\gamma_V^3 = \gamma^3$ and $\gamma_A^3 = \gamma^3 \gamma^5$. The convention of γ^5 is given below Eq. (6).

To organize the mode expansion similar to Eq. (93), we first find solutions for the Dirac equation with the chemical potentials. In addition to the vector chemical potential, we introduce an axial chemical potential as a temporal component of the axial gauge field that is coupled to the right- and left-handed helicity modes with opposite signs (Note that this procedure itself does not justify the existence of the static axial chemical potential). The Dirac operator with nonzero vector and axial chemical potentials read [cf. Eq. (86)]

$$(i\mathcal{D} + \mu_V \gamma^0 + \mu_A \gamma^0 \gamma^5 - m) = (i\mathcal{D}_\parallel + \mu_V \gamma^0 + \mu_A \gamma^0 \gamma^5 - m) - \sqrt{2n|q_f B|} \gamma^1 (\hat{a} \mathcal{P}_+ + \hat{a}^\dagger \mathcal{P}_-). \quad (691)$$

As usual, the origin of energy is shifted by the vector chemical potential μ_V . On the other hand, the longitudinal momentum is shifted by the axial chemical potential μ_A with spin-dependent signs as implied by an identity $\gamma^0 \gamma^5 \mathcal{P}_\pm = \pm s_f \gamma^3 \mathcal{P}_\pm$. Since the LLL has the unique spin state, we simply have a shift of the momentum when the Dirac operator acts on the Ritus basis in the LLL:

$$(i\mathcal{D} + \mu_V \gamma^0 + \mu_A \gamma^0 \gamma^5 - m) \psi_{\text{LLL}}(x) = e^{-ip_\parallel x} \mathcal{R}_{n=0, \chi} \{ (p^0 + \mu_V) \gamma^0 - (p^3 - s_f \mu_A) \gamma^3 - m \} u, \quad (692)$$

where we assumed the ansatz (85) for positive-energy solutions. On the other hand, the spin degeneracy in the hLLs is resolved by the inclusion of μ_A as

$$\begin{aligned} (i\mathcal{D} + \mu_V \gamma^0 + \mu_A \gamma^0 \gamma^5 - m) \psi_{\text{hLL}}(x) &= e^{-ip_\parallel x} \mathcal{R}_{n, \chi} (\not{p}_n - m) u + (\mu_V \gamma^0 + \mu_A \gamma^0 \gamma^5) \psi_{\text{hLL}}(x) \\ &= e^{-ip_\parallel x} \mathcal{R}_{n, \chi} \left[\mathcal{P}_+ (\not{p}_n^+ - m) + \mathcal{P}_- (\not{p}_n^- - m) \right] u, \end{aligned} \quad (693)$$

where we used $\mathcal{P}_\pm \mathcal{P}_\mp = 0$ and defined the shifted momenta $p_n^\pm = (p^0 + \mu_V, \sqrt{2n|q_f B|}, 0, p^3 \mp s_f \mu_A)$. Correspondingly, one can decompose the spinor basis as $u = u^+ \mathcal{P}_+ + u^- \mathcal{P}_-$ where the spinors u^\pm satisfy distinct ‘‘free’’ Dirac equations $(\not{p}_n^\pm - m) u^\pm = 0$. Similarly, the negative-energy solutions satisfy the

above equations with the sign of momentum flipped; The spin basis v^\pm is provided by the solutions for $(\not{p}_n^\pm + m)v^\pm = 0$ with $\bar{p}_n^\pm = (p^0 - \mu_V, -\sqrt{2n|q_f B|}, 0, p^3 \pm s_f \mu_A)$. One can then perform the mode expansion in the same manner as in Eq. (93) but with the distinct dispersion relations for the two spin states.

Now, we are ready to compute the current. Inserting the mode expansion as in Eq. (458), we get the currents expressed by the Ritus basis. This amounts to replacement of the gamma matrices and the dispersion relations as

$$\begin{aligned}
j_{V/A}^3(q=0) &= \frac{1}{L_x L_y} \int d^3x e^{-i0 \cdot x} j_{V/A}^3(x) \\
&= \frac{1}{L_x L_y} \int d^3x \sum_{\kappa=\pm} \sum_{\kappa'=\pm} \sum_{n=0}^{\infty} \sum_{n'=0}^{\infty} \int \frac{dp_z}{2\pi} \int \frac{dp_y dp_y'}{(2\pi)^2} \\
&\quad \times \left[\frac{1}{\sqrt{4\epsilon_n^\kappa \epsilon_{n'}^\kappa}} \langle a_{p_{n'}, p_y'}^{\kappa'\dagger} a_{p_n, p_y}^\kappa \rangle \bar{u}^{\kappa'}(p_{n'}^{\kappa'}) \mathcal{R}_{n', p_y'}^\dagger(x_\perp) \gamma_{V/A}^3 \mathcal{R}_{n, p_y}(x_\perp) u^\kappa(p_n^\kappa) e^{i(\epsilon_{n'}^\kappa - \epsilon_n^\kappa)t} \right. \\
&\quad \left. + \frac{1}{\sqrt{4\bar{\epsilon}_n^\kappa \bar{\epsilon}_{n'}^\kappa}} \langle b_{\bar{p}_{n'}, p_y'}^{\kappa'\dagger} b_{\bar{p}_n, p_y}^{\kappa\ddagger} \rangle \bar{v}^{\kappa'}(\bar{p}_{n'}^{\kappa'}) \mathcal{R}_{n', p_y'}^\dagger(x_\perp) \gamma_{V/A}^3 \mathcal{R}_{n, p_y}(x_\perp) v^\kappa(\bar{p}_n^\kappa) e^{-i(\bar{\epsilon}_{n'}^\kappa - \bar{\epsilon}_n^\kappa)t} \right],
\end{aligned} \tag{694}$$

with $L_{x,y}$ being the system lengths in the transverse directions. The temporal component of the momentum is given by the shifted Landau levels as $(p_n^\kappa)^0 = \sqrt{(p_z \mp s_f \mu_A)^2 + m^2 + 2n|q_f B|} =: \epsilon_n^\kappa$ and $(\bar{p}_n^\kappa)^0 = \sqrt{(p_z \pm s_f \mu_A)^2 + m^2 + 2n|q_f B|} =: \bar{\epsilon}_n^\kappa$. We use the fact that \mathcal{P}_\pm commutes with γ^3 and γ^5 and then the orthogonal relation (94b) to find that

$$\begin{aligned}
j_{V/A}^3(q=0) &= \frac{|q_f B|}{2\pi} \sum_{\kappa=\pm} \sum_{\kappa'=\pm} \sum_{n=0}^{\infty} \int \frac{dp_z}{2\pi} \\
&\quad \times \left[\frac{1}{2\epsilon_n} \langle a_{p_n, p_y}^{\kappa'\dagger} a_{p_n, p_y}^\kappa \rangle \bar{u}^{\kappa'}(p_n^{\kappa'}) \gamma_{V/A}^3 I_n u^\kappa(p_n^\kappa) + \frac{1}{2\bar{\epsilon}_n} \langle b_{\bar{p}_n, p_y}^{\kappa'\dagger} b_{\bar{p}_n, p_y}^{\kappa\ddagger} \rangle \bar{v}^{\kappa'}(\bar{p}_n^{\kappa'}) \gamma_{V/A}^3 I_n v^\kappa(\bar{p}_n^\kappa) \right].
\end{aligned} \tag{695}$$

The Landau degeneracy factor is reproduced from the y integral in the Landau gauge (see the last part of Sec. 2.2.1). The thermal expectation value is assumed to be diagonal in the spin basis, i.e., $\langle a_{p_n, p_y}^{\kappa'\dagger} a_{p_n, p_y}^\kappa \rangle = \delta_{\kappa\kappa'} f(\epsilon_n^\kappa - \mu_V)$, where $f(\epsilon) = 1/[\exp(\epsilon/T) + 1]$ is the Fermi-Dirac distribution function. Likewise, we have $\langle b_{\bar{p}_n, p_y}^{\kappa'\dagger} b_{\bar{p}_n, p_y}^{\kappa\ddagger} \rangle = \delta_{\kappa\kappa'} \{1 - f(\bar{\epsilon}_n^\kappa + \mu_V)\}$. Then, we arrive at

$$\begin{aligned}
j_{V/A}^3(q=0) &= \frac{|q_f B|}{2\pi} \sum_{\kappa=\pm} \sum_{n=0}^{\infty} \int \frac{dp_z}{2\pi} \left[\frac{\text{Tr}[\gamma_{V/A}^3 I_n (\not{p}_n^\kappa + m) \mathcal{P}_\kappa]}{2\epsilon_n^\kappa} f(\epsilon_n^\kappa - \mu_V) \right. \\
&\quad \left. + \frac{\text{Tr}[\gamma_{V/A}^3 I_n (\not{\bar{p}}_n^\kappa - m) \mathcal{P}_\kappa]}{2\bar{\epsilon}_n^\kappa} \{1 - f(\bar{\epsilon}_n^\kappa + \mu_V)\} \right].
\end{aligned} \tag{696}$$

The mass term in the numerator vanishes due to the spinor trace, meaning that the chirality cannot be flipped by the mass term in those tadpole diagrams. Therefore, mass dependences could appear only through the energy levels $\epsilon^\pm, \bar{\epsilon}^\pm$ if any. Below, we examine the vector and axial-vector currents separately.

Carrying out the spinor trace, we find the vector current

$$\begin{aligned}
j_V^3(q=0) &= \frac{|q_f B|}{2\pi} \sum_{\kappa=\pm} \sum_{n=0}^{\infty} \int \frac{dp_z}{2\pi} \left[\frac{p_z - \kappa s_f \mu_A}{\epsilon_n^\kappa} f(\epsilon_n^\kappa - \mu_V) + \frac{p_z + \kappa s_f \mu_A}{\bar{\epsilon}_n^\kappa} \{1 - f(\bar{\epsilon}_n^\kappa + \mu_V)\} \right] \\
&= \frac{|q_f B|}{2\pi} \sum_{\kappa=\pm} \sum_{n=0}^{\infty} \int_{-\Lambda}^{\Lambda} \frac{dp_z}{2\pi} \frac{p_z + \kappa s_f \mu_A}{\bar{\epsilon}_n^\kappa}.
\end{aligned} \tag{697}$$

After shifting the integral variable in the terms proportional to the distribution functions, one finds that those contributions vanish in contrast to the massless case (464). The vacuum contribution has a subtle structure since the integrand approaches a constant in the UV region. Introducing the cut-off Λ , we find that

$$\begin{aligned} j_V^3(q=0) &= \frac{|q_f B|}{2\pi} \sum_{\kappa=\pm} \sum_{n=0}^{\infty} \frac{1}{2\pi} \lim_{\Lambda \rightarrow \infty} \left[\sqrt{(\Lambda + \kappa s_f \mu_A)^2 + m^2} - \sqrt{(\Lambda - \kappa s_f \mu_A)^2 + m^2} \right] \\ &= \frac{q_f B}{2\pi^2} \mu_A. \end{aligned} \quad (698)$$

The final result stems from the LLL contribution: There is no net contribution from the hLL due to cancellation between the spin states $\kappa = \pm$. This result is independent of the fermion mass and have the same form as in the massless case (464) [653, 780, 781]. However, let us reiterate that this conclusion is obtained under a strong assumption for the existence of a *constant* axial chemical potential, which is not always a good approximation in real systems. Also, the origins of the same results are different as mentioned above. The terms proportional to the distribution functions do not provide any contribution to the current in the massive case. In contrast, the current in the massless case are transported by thermally populated fermions as seen in Sec. 8.1, while the explicit temperature dependence finally goes away because of the cancellation between the particle and antiparticle contributions in the integral (464).

Next, we examine the axial-vector current. Carrying out the spinor trace in Eq. (696), we find that

$$\begin{aligned} j_A^3(q=0) &= s_f \frac{|q_f B|}{2\pi} \sum_{\kappa=\pm} \sum_{n=0}^{\infty} \int \frac{dp_z}{2\pi} \kappa \left[f(\epsilon_n^\kappa - \mu_V) + \{1 - f(\bar{\epsilon}_n^\kappa + \mu_V)\} \right] \\ &= \frac{q_f B}{2\pi} \int \frac{dp_z}{2\pi} [f(\epsilon_0 - \mu_V) - f(\epsilon_0 + \mu_V)], \end{aligned} \quad (699)$$

where $\epsilon_0 = \sqrt{p_z^2 + m^2}$. We dropped the divergent vacuum term which depends on neither T , μ_V , nor μ_A and shifted the integral variable p_z to absorb the dependence on μ_A , which is allowed in the convergent integrals. The particle and antiparticle contributions have opposite signs because their spins are aligned in the opposite directions in the LLL. The hLL contributions are canceled out between the two spin states in each hLL.

Wrapping up the computation in the massive case, the net vector and axial-vector currents are transported by fermions in the LLL; there are no contributions from the hLLs to either vector or axial-vector current due to the cancellations. This fact is common to the massless case. We have obtained

$$\mathbf{j}_V = q_f \frac{\mu_A}{2\pi^2} \mathbf{B}, \quad (700a)$$

$$\mathbf{j}_A = q_f \frac{\lambda}{2\pi^2} \mathbf{B}. \quad (700b)$$

While the vector current has the same form as in the massless case (465), the axial current is subject to the mass correction encoded in an integral

$$\lambda = \frac{1}{2} \int_{-\infty}^{\infty} dp_z [f(\epsilon_0 - \mu_V) - f(\epsilon_0 + \mu_V)], \quad (701)$$

which agrees with the results from the Kubo formula calculation without the explicit Landau quantization [689]. Note again that the origins of the vector current are different in the massless and massive cases [780, 781]. The vector current in the massive case originates from the vacuum contribution in

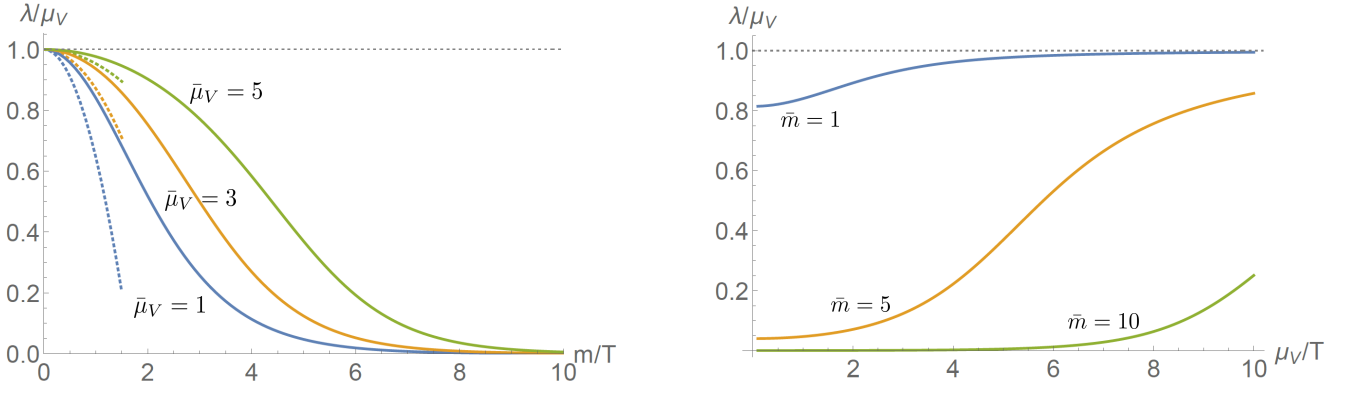


Figure 62: Mass corrections to the integral λ for the axial current with $\bar{\mu}_V = \mu_V/T$ and $\bar{m} = m/T$. Solid lines show the results of numerical integration, while the dotted lines show those of the small-mass expansion in $\mathcal{O}(\bar{m}^2)$.

Eq. (698) with vanishing finite-temperature contributions, while the finite-temperature contributions in the massless case result in the temperature-independent result (464).

In the rest of this appendix, we more closely look into the mass corrections to the axial-vector current (700b). In the massless limit, one can get an analytic result of the integral

$$\lambda = \mu_V, \quad (702)$$

which reproduces the previous result in the massless case (465). One should expect sizeable mass effects when the mass is larger than both temperature and chemical potential. Otherwise, the mass scale may be negligible as compared to either of them. Numerical results on mass corrections to the integral λ are shown in Fig. 62, where we introduce normalized variables, $\bar{\mu}_V = \mu_V/T$ and $\bar{m} = m/T$. In the left figure, we confirm that the curves start at $\lambda = \mu_V$ where $\bar{m} = 0$ and approach zero as we increase \bar{m} , indicating a suppression of the axial current by mass effects (at a given temperature and chemical potential). Dotted curves show a small-mass expansion (704) shown just below. In the right figure, when the normalized mass is small $\bar{m} \lesssim 1$, the integral λ exhibits an almost linear dependence on $\bar{\mu}_V$ like the massless case. As we increase the mass, the integral λ is significantly suppressed when the chemical potential is smaller than the mass $\bar{\mu}_V \lesssim \bar{m}$. However, the integral λ again approaches a linear dependence on $\bar{\mu}_V$ as the chemical potential exceeds the mass scale, $\bar{m} \ll \bar{\mu}_V$.

One can find some analytic forms of the integral λ . At zero temperature, one can easily perform the integral. There is no contribution from antiparticles (particles) when $\mu_V > 0$ ($\mu_V < 0$), so that the direction of the current depends on the sign of μ_V . The result is immediately obtained as [593, 688, 689]

$$\mathbf{j}_A = q_f \frac{\sqrt{\mu_V^2 - m^2}}{2\pi^2} \mathbf{B} \theta(\mu_V^2 - m^2) \text{sgn}(\mu_V), \quad (703)$$

where $\theta(x)$ is the step function. At finite temperature, a small-mass expansion was shown in Ref. [689], which is reproduced as

$$\begin{aligned} \mathbf{j}_A &= q_f \frac{\mu_V}{2\pi^2} \mathbf{B} \left[1 - \frac{\bar{m}^2}{2\bar{\mu}_V} \int_0^\infty \frac{d\bar{p}_z}{\bar{p}_z} \frac{\partial}{\partial \bar{\mu}_V} \left(\frac{1}{e^{\bar{p}_z - \bar{\mu}_V} + 1} + \frac{1}{e^{\bar{p}_z + \bar{\mu}_V} + 1} \right) + \mathcal{O}(\bar{m}^4) \right] \\ &= q_f \frac{\mu_V}{2\pi^2} \mathbf{B} \left[1 + \frac{\bar{m}^2}{2\bar{\mu}_V} \lim_{s \rightarrow 0} \frac{\partial}{\partial \bar{\mu}_V} \Gamma(s) \{ \text{Li}_s(-e^{-\bar{\mu}_V}) + \text{Li}_s(-e^{\bar{\mu}_V}) \} + \mathcal{O}(\bar{m}^4) \right] \\ &= q_f \frac{\mu_V}{2\pi^2} \mathbf{B} \left[1 - \frac{\bar{m}^2}{2\bar{\mu}_V} \frac{\partial}{\partial s} \{ \text{Li}_s(-e^{-\bar{\mu}_V}) - \text{Li}_s(-e^{\bar{\mu}_V}) \} \Big|_{s=-1} + \mathcal{O}(\bar{m}^4) \right], \end{aligned} \quad (704)$$

where $\Gamma(x)$ and $\text{Li}_s(x)$ are gamma and polylogarithmic functions, respectively.¹⁴⁰ Note that each integral in the leading mass correction has a singularity at $p_z = 0$ which manifests itself as a divergence of the gamma function in the intermediate line. Nevertheless, the expansion coefficient in the last line is finite thanks to a cancellation of the divergences originating from the particle and antiparticle contributions. The leading mass correction (704) is shown by the dotted curves in Fig. 62.

References

- [1] W. Heisenberg and H. Euler, “Consequences of Dirac’s theory of positrons,” *Z. Phys.* **98**, 714 (1936), [arXiv:physics/0605038 \[physics\]](#) .
- [2] E. Fermi, “Über die theorie des stosses zwischen atomen und elektrisch geladenen teilchen,” *Z. Phys.* **29**, 315-327 (1924).
- [3] C. von Weizsacker, “Ausstrahlung beim stossen sehr schneller elektronen,” *Z. Phys.* **88**, 612-625 (1934).
- [4] E. Williams, “Correlation of certain collision problems with radiation theory,” *Kgl. Danske Videnskab. Selskab Mat.-fys. Medd.* **13**, No. 4 (1935).
- [5] G. Breit and J. A. Wheeler, “Collision of two light quanta,” *Phys. Rev.* **46**, 1087 (1934).
- [6] V. Skokov, A. Yu. Illarionov, and V. Toneev, “Estimate of the magnetic field strength in heavy-ion collisions,” *Int. J. Mod. Phys. A* **24**, 5925 (2009), [arXiv:0907.1396 \[nucl-th\]](#) .
- [7] V. Voronyuk, V. D. Toneev, W. Cassing, E. L. Bratkovskaya, V. P. Konchakovski, and S. A. Voloshin, “(Electro-)Magnetic field evolution in relativistic heavy-ion collisions,” *Phys. Rev.* **C83**, 054911 (2011), [arXiv:1103.4239 \[nucl-th\]](#) .
- [8] A. Bzdak and V. Skokov, “Event-by-event fluctuations of magnetic and electric fields in heavy ion collisions,” *Phys. Lett.* **B710**, 171 (2012), [arXiv:1111.1949 \[hep-ph\]](#) .
- [9] W.-T. Deng and X.-G. Huang, “Event-by-event generation of electromagnetic fields in heavy-ion collisions,” *Phys. Rev.* **C85**, 044907 (2012), [arXiv:1201.5108 \[nucl-th\]](#) .
- [10] W.-T. Deng and X.-G. Huang, “Electric fields and chiral magnetic effect in Cu+Au collisions,” *Phys. Lett.* **B742**, 296 (2015), [arXiv:1411.2733 \[nucl-th\]](#) .
- [11] X.-G. Huang, “Electromagnetic fields and anomalous transports in heavy-ion collisions — A pedagogical review,” *Rept. Prog. Phys.* **79**, 076302 (2016), [arXiv:1509.04073 \[nucl-th\]](#) .
- [12] K. Hattori and X.-G. Huang, “Novel quantum phenomena induced by strong magnetic fields in heavy-ion collisions,” *Nucl. Sci. Tech.* **28**, 26 (2017), [arXiv:1609.00747 \[nucl-th\]](#) .
- [13] D. Kharzeev, K. Landsteiner, A. Schmitt, and H.-U. Yee, “Strongly Interacting Matter in Magnetic Fields,” *Lect. Notes Phys.* **871**, pp.1 (2013).
- [14] D. E. Kharzeev, “The Chiral Magnetic Effect and Anomaly-Induced Transport,” *Prog. Part. Nucl. Phys.* **75**, 133 (2014), [arXiv:1312.3348 \[hep-ph\]](#) .

¹⁴⁰To get the above result, use the following formulas [334]: $\int_0^\infty dp p^s / (e^{p-\mu} + 1) = -\Gamma(s+1)\text{Li}_{s+1}(-e^\mu)$, $\frac{\partial}{\partial x}\text{Li}_s(x) = x^{-1}\text{Li}_{s-1}(x)$, and $\text{Li}_m(x) + (-1)^m\text{Li}_m(1/x) = 0$ for a negative integer m .

- [15] J. Liao, “Anomalous transport effects and possible environmental symmetry ‘violation’ in heavy-ion collisions,” *Pramana* **84**, 901 (2015), [arXiv:1401.2500 \[hep-ph\]](#) .
- [16] D. E. Kharzeev, J. Liao, S. A. Voloshin, and G. Wang, “Chiral magnetic and vortical effects in high-energy nuclear collisions—status report,” *Prog. Part. Nucl. Phys.* **88**, 1 (2016), [arXiv:1511.04050 \[hep-ph\]](#) .
- [17] M. Aaboud *et al.* (ATLAS), “Evidence for light-by-light scattering in heavy-ion collisions with the ATLAS detector at the LHC,” *Nature Phys.* **13**, 852 (2017), [arXiv:1702.01625 \[hep-ex\]](#) .
- [18] A. M. Sirunyan *et al.* (CMS), “Evidence for light-by-light scattering and searches for axion-like particles in ultraperipheral PbPb collisions at $\sqrt{s_{\text{NN}}} = 5.02$ TeV,” *Phys. Lett. B* **797**, 134826 (2019), [arXiv:1810.04602 \[hep-ex\]](#) .
- [19] G. Aad *et al.* (ATLAS), “Observation of light-by-light scattering in ultraperipheral Pb+Pb collisions with the ATLAS detector,” *Phys. Rev. Lett.* **123**, 052001 (2019), [arXiv:1904.03536 \[hep-ex\]](#) .
- [20] G. Aad *et al.* (ATLAS), “Measurement of light-by-light scattering and search for axion-like particles with 2.2 nb^{-1} of Pb+Pb data with the ATLAS detector,” *JHEP* **03**, 243 (2021), [Erratum: *JHEP* 11, 050 (2021)], [arXiv:2008.05355 \[hep-ex\]](#) .
- [21] J. Adam *et al.* (STAR), “Measurement of e^+e^- Momentum and Angular Distributions from Linearly Polarized Photon Collisions,” *Phys. Rev. Lett.* **127**, 052302 (2021), [arXiv:1910.12400 \[nucl-ex\]](#) .
- [22] A. K. Harding and D. Lai, “Physics of Strongly Magnetized Neutron Stars,” *Rept. Prog. Phys.* **69**, 2631 (2006), [arXiv:astro-ph/0606674 \[astro-ph\]](#) .
- [23] T. Enoto, S. Kisaka, and S. Shibata, “Observational diversity of magnetized neutron stars,” *Rept. Prog. Phys.* **82**, 106901 (2019).
- [24] D. Grasso and H. R. Rubinstein, “Magnetic fields in the early universe,” *Phys. Rept.* **348**, 163 (2001), [arXiv:astro-ph/0009061 \[astro-ph\]](#) .
- [25] M. Giovannini, “The Magnetized universe,” *Int. J. Mod. Phys. D* **13**, 391 (2004), [arXiv:astro-ph/0312614 \[astro-ph\]](#) .
- [26] A. Kandus, K. E. Kunze, and C. G. Tsagas, “Primordial magnetogenesis,” *Phys. Rept.* **505**, 1 (2011), [arXiv:1007.3891 \[astro-ph.CO\]](#) .
- [27] R. Durrer and A. Neronov, “Cosmological Magnetic Fields: Their Generation, Evolution and Observation,” *Astron. Astrophys. Rev.* **21**, 62 (2013), [arXiv:1303.7121 \[astro-ph.CO\]](#) .
- [28] K. Subramanian, “The origin, evolution and signatures of primordial magnetic fields,” *Rept. Prog. Phys.* **79**, 076901 (2016), [arXiv:1504.02311 \[astro-ph.CO\]](#) .
- [29] K. Kamada, N. Yamamoto, and D.-L. Yang, “Chiral effects in astrophysics and cosmology,” *Prog. Part. Nucl. Phys.* **129**, 104016 (2023), [arXiv:2207.09184 \[astro-ph.CO\]](#) .
- [30] G. A. Mourou, T. Tajima, and S. V. Bulanov, “Optics in the relativistic regime,” *Rev. Mod. Phys.* **78**, 309 (2006).

- [31] A. Di Piazza, C. Muller, K. Z. Hatsagortsyan, and C. H. Keitel, “Extremely high-intensity laser interactions with fundamental quantum systems,” *Rev. Mod. Phys.* **84**, 1177 (2012), [arXiv:1111.3886 \[hep-ph\]](#) .
- [32] A. Ejlli, F. Della Valle, U. Gastaldi, G. Messineo, R. Pengo, G. Ruoso, and G. Zavattini, “The PVLAS experiment: A 25 year effort to measure vacuum magnetic birefringence,” *Phys. Rept.* **871**, 1 (2020), [arXiv:2005.12913 \[physics.optics\]](#) .
- [33] P. Zhang, S. S. Bulanov, D. Seipt, A. V. Arefiev, and A. G. R. Thomas, “Relativistic Plasma Physics in Supercritical Field,” (2020), [arXiv:2001.00957 \[physics.plasm-ph\]](#) .
- [34] A. Fedotov, A. Ilderton, F. Karbstein, B. King, D. Seipt, H. Taya, and G. Torgrimsson, “Advances in QED with intense background fields,” *Phys. Rept.* **1010**, 1 (2023), [arXiv:2203.00019 \[hep-ph\]](#) .
- [35] A. A. Sokolov and I. M. Ternov, *Radiation from relativistic electrons* (AIP, 1986).
- [36] V. Canuto and J. Ventura, “Quantizing Magnetic Fields in Astrophysics,” *Fund. Cosmic Phys.* **2**, 203 (1977).
- [37] P. Mészáros, *High-energy radiation from magnetized neutron stars* (University of Chicago press, 1992).
- [38] D. Yoshioka, *The quantum Hall effect*, Vol. 133 (Springer Science & Business Media, 2013).
- [39] D. Tong, “Lectures on the Quantum Hall Effect,” (2016), [arXiv:1606.06687 \[hep-th\]](#) .
- [40] Y. Nambu, “The use of the Proper Time in Quantum Electrodynamics,” *Prog. Theor. Phys.* **5**, 82 (1950).
- [41] R. P. Feynman, “Mathematical formulation of the quantum theory of electromagnetic interaction,” *Phys. Rev.* **80**, 440 (1950).
- [42] J. S. Schwinger, “On gauge invariance and vacuum polarization,” *Phys. Rev.* **82**, 664 (1951).
- [43] K. G. Wilson, “The Renormalization Group: Critical Phenomena and the Kondo Problem,” *Rev. Mod. Phys.* **47**, 773 (1975).
- [44] L. Landau, “Diamagnetismus der metalle,” *Z. Phys.* **64**, 629 (1930), english translation available in “Collected papers of L.D. Landau,” edited by D. ter Haar, Pergamon, (1965).
- [45] L. D. Landau and E. M. Lifshits, *Quantum Mechanics*, Course of Theoretical Physics, Vol. v.3 (Butterworth-Heinemann, Oxford, 1991).
- [46] L. Hoddeson, E. Braun, J. Teichmann, and S. Weart, *Out of the crystal maze: chapters from the history of solid state physics* (Oxford University Press, 1992).
- [47] S. M. Girvin, in *Aspects topologiques de la physique en basse dimension. Topological aspects of low dimensional systems: Session LXIX. 7–31 July 1998* (Springer, 2002) pp. 53–175.
- [48] J. J. Sakurai and J. Napolitano, *Modern Quantum Mechanics*, 2nd ed. (Cambridge University Press, 2017).
- [49] M. H. Johnson and B. A. Lippmann, “Motion in a constant magnetic field,” *Phys. Rev.* **76**, 828 (1949).

- [50] M. H. Al-Hashimi and U. J. Wiese, “Discrete Accidental Symmetry for a Particle in a Constant Magnetic Field on a Torus,” *Annals Phys.* **324**, 343 (2009), [arXiv:0807.0630 \[quant-ph\]](#) .
- [51] J. Zak, “Magnetic Translation Group,” *Phys. Rev.* **134**, A1602 (1964).
- [52] E. Brown, “Bloch electrons in a uniform magnetic field,” *Physical Review* **133**, A1038 (1964).
- [53] M. Kohmoto, “Topological invariant and the quantization of the hall conductance,” *Annals of Physics* **160**, 343 (1985).
- [54] J. Avron, I. Herbst, and B. Simon, “Separation of center of mass in homogeneous magnetic fields,” *Annals of Physics* **114**, 431 (1978).
- [55] H. Herold, H. Ruder, and G. Wunner, “The two-body problem in the presence of a homogeneous magnetic field,” *Journal of Physics B: Atomic and Molecular Physics* **14**, 751 (1981).
- [56] J. Alford and M. Strickland, “Charmonia and Bottomonia in a Magnetic Field,” *Phys. Rev.* **D88**, 105017 (2013), [arXiv:1309.3003 \[hep-ph\]](#) .
- [57] C. Bonati, M. D’Elia, and A. Rucci, “Heavy quarkonia in strong magnetic fields,” *Phys. Rev.* **D92**, 054014 (2015), [arXiv:1506.07890 \[hep-ph\]](#) .
- [58] K. Suzuki and T. Yoshida, “Cigar-shaped quarkonia under strong magnetic field,” *Phys. Rev.* **D93**, 051502 (2016), [arXiv:1601.02178 \[hep-ph\]](#) .
- [59] T. Yoshida and K. Suzuki, “Heavy meson spectroscopy under strong magnetic field,” (2016), [arXiv:1607.04935 \[hep-ph\]](#) .
- [60] S. Iwasaki, M. Oka, and K. Suzuki, “A review of quarkonia under strong magnetic fields,” *Eur. Phys. J. A* **57**, 222 (2021), [arXiv:2104.13990 \[hep-ph\]](#) .
- [61] K. Hattori, T. Kojo, and N. Su, “Mesons in strong magnetic fields: (I) General analyses,” *Nucl. Phys.* **A951**, 1 (2016), [arXiv:1512.07361 \[hep-ph\]](#) .
- [62] N. K. Nielsen and P. Olesen, “An Unstable Yang-Mills Field Mode,” *Nucl. Phys.* **B144**, 376 (1978).
- [63] V. I. Ritus, “Radiative corrections in quantum electrodynamics with intense field and their analytical properties,” *Annals Phys.* **69**, 555 (1972).
- [64] V. I. Ritus, “Method of eigenfunctions and mass operator in quantum electrodynamics of a constant field,” *Sov. Phys. JETP* **48**, 788 (1978), [*Zh. Eksp. Teor. Fiz.*75,1560(1978)].
- [65] K. Hattori, H. Taya, and S. Yoshida, “Di-lepton production from a single photon in strong magnetic fields: vacuum dichroism,” *JHEP* **01**, 093 (2021), [arXiv:2010.13492 \[hep-ph\]](#) .
- [66] M. E. Peskin and D. V. Schroeder, *An Introduction to quantum field theory* (1995).
- [67] D. S. Lee, C. N. Leung, and Y. J. Ng, “Chiral symmetry breaking in a uniform external magnetic field,” *Phys. Rev.* **D55**, 6504 (1997), [arXiv:hep-th/9701172 \[hep-th\]](#) .
- [68] E. Elizalde, E. J. Ferrer, and V. de la Incera, “Neutrino selfenergy and index of refraction in strong magnetic field: A New approach,” *Annals Phys.* **295**, 33 (2002), [arXiv:hep-ph/0007033 \[hep-ph\]](#) .

- [69] A. Ayala, A. Bashir, A. Raya, and E. Rojas, “Dynamical mass generation in strongly coupled quantum electrodynamics with weak magnetic fields,” *Phys. Rev.* **D73**, 105009 (2006), [arXiv:hep-ph/0602209 \[hep-ph\]](#) .
- [70] E. J. Ferrer, V. de la Incera, and C. Manuel, “Color-superconducting gap in the presence of a magnetic field,” *Nucl. Phys.* **B747**, 88 (2006), [arXiv:hep-ph/0603233 \[hep-ph\]](#) .
- [71] J. L. Noronha and I. A. Shovkovy, “Color-flavor locked superconductor in a magnetic field,” *Phys. Rev.* **D76**, 105030 (2007), [Erratum: *Phys. Rev.*D86,049901(2012)], [arXiv:0708.0307 \[hep-ph\]](#) .
- [72] H. J. Warringa, “Dynamics of the Chiral Magnetic Effect in a weak magnetic field,” *Phys. Rev.* **D86**, 085029 (2012), [arXiv:1205.5679 \[hep-th\]](#) .
- [73] T. Kojo and N. Su, “The quark mass gap in a magnetic field,” *Phys. Lett.* **B720**, 192 (2013), [arXiv:1211.7318 \[hep-ph\]](#) .
- [74] P. Watson and H. Reinhardt, “Quark gap equation in an external magnetic field,” *Phys. Rev.* **D89**, 045008 (2014), [arXiv:1310.6050 \[hep-ph\]](#) .
- [75] N. Mueller, J. A. Bonnet, and C. S. Fischer, “Dynamical quark mass generation in a strong external magnetic field,” *Phys. Rev.* **D89**, 094023 (2014), [arXiv:1401.1647 \[hep-ph\]](#) .
- [76] K. Hattori, S. Li, D. Satow, and H.-U. Yee, “Longitudinal Conductivity in Strong Magnetic Field in Perturbative QCD: Complete Leading Order,” *Phys. Rev.* **D95**, 076008 (2017), [arXiv:1610.06839 \[hep-ph\]](#) .
- [77] K. Hattori and D. Satow, “Electrical Conductivity of Quark-Gluon Plasma in Strong Magnetic Fields,” *Phys. Rev.* **D94**, 114032 (2016), [arXiv:1610.06818 \[hep-ph\]](#) .
- [78] K. Hattori, X.-G. Huang, D. H. Rischke, and D. Satow, “Bulk Viscosity of Quark-Gluon Plasma in Strong Magnetic Fields,” *Phys. Rev.* **D96**, 094009 (2017), [arXiv:1708.00515 \[hep-ph\]](#) .
- [79] H. B. Nielsen and M. Ninomiya, “The Adler-Bell-Jackiw anomaly and Weyl fermions in a crystal,” *Phys. Lett.* **130B**, 389 (1983).
- [80] J. Ambjorn, J. Greensite, and C. Peterson, “The Axial Anomaly and the Lattice Dirac Sea,” *Nucl. Phys.* **B221**, 381 (1983).
- [81] M. Creutz, “Aspects of Chiral Symmetry and the Lattice,” *Rev. Mod. Phys.* **73**, 119 (2001), [arXiv:hep-lat/0007032 \[hep-lat\]](#) .
- [82] S. L. Adler, “Axial vector vertex in spinor electrodynamics,” *Phys. Rev.* **177**, 2426 (1969).
- [83] J. S. Bell and R. Jackiw, “A PCAC puzzle: $\pi^0 \rightarrow \gamma\gamma$ in the sigma model,” *Nuovo Cim.* **A60**, 47 (1969).
- [84] K. Hattori and K. Itakura, “In-medium polarization tensor in strong magnetic fields (II): Axial Ward identity at finite temperature and density,” *Annals Phys.* **446**, 169115 (2022), [arXiv:2205.06411 \[hep-ph\]](#) .
- [85] P. Copinger, K. Fukushima, and S. Pu, “Axial Ward identity and the Schwinger mechanism – Applications to the real-time chiral magnetic effect and condensates,” *Phys. Rev. Lett.* **121**, 261602 (2018), [arXiv:1807.04416 \[hep-th\]](#) .
- [86] V. Fock, “Proper time in classical and quantum mechanics,” *Phys. Z. Sowjetunion* **12**, 404 (1937).

- [87] M. D. Schwartz, *Quantum Field Theory and the Standard Model* (Cambridge University Press, 2013).
- [88] C. Schubert, “Perturbative quantum field theory in the string inspired formalism,” *Phys. Rept.* **355**, 73 (2001), [arXiv:hep-th/0101036 \[hep-th\]](#) .
- [89] K. Hattori, K. Itakura, and S. Ozaki, “Note on all-order Landau-level structures of the Heisenberg-Euler effective actions for QED and QCD,” (2020), [arXiv:2001.06131 \[hep-ph\]](#) .
- [90] I. K. Affleck, O. Alvarez, and N. S. Manton, “Pair Production at Strong Coupling in Weak External Fields,” *Nucl. Phys.* **B197**, 509 (1982).
- [91] Z. Bern and D. A. Kosower, “Efficient calculation of one loop QCD amplitudes,” *Phys. Rev. Lett.* **66**, 1669 (1991).
- [92] E. S. Fradkin and D. M. Gitman, “Path integral representation for the relativistic particle propagators and BFV quantization,” *Phys. Rev. D* **44**, 3230 (1991).
- [93] M. J. Strassler, “Field theory without Feynman diagrams: One loop effective actions,” *Nucl. Phys. B* **385**, 145 (1992), [arXiv:hep-ph/9205205](#) .
- [94] M. G. Schmidt and C. Schubert, “On the calculation of effective actions by string methods,” *Phys. Lett. B* **318**, 438 (1993), [arXiv:hep-th/9309055](#) .
- [95] M. Reuter, M. G. Schmidt, and C. Schubert, “Constant external fields in gauge theory and the spin 0, 1/2, 1 path integrals,” *Annals Phys.* **259**, 313 (1997), [arXiv:hep-th/9610191](#) .
- [96] C. Schubert, “QED in the worldline representation,” *AIP Conf. Proc.* **917**, 178 (2007), [arXiv:hep-th/0703186](#) .
- [97] M. R. Brown and M. J. Duff, “Exact Results for Effective Lagrangians,” *Phys. Rev.* **D11**, 2124 (1975).
- [98] W. Dittrich, “One Loop Effective Potentials in QED,” *J. Phys. A* **9**, 1171 (1976).
- [99] W. Dittrich and M. Reuter, “Effective lagrangians in quantum electrodynamics,” *Lect. Notes Phys.* **220**, 1 (1985).
- [100] T. Hayata, Y. Hidaka, and A. Yamamoto, “Temporal chiral spiral in QCD in the presence of strong magnetic fields,” *Phys. Rev.* **D89**, 085011 (2014), [arXiv:1309.0012 \[hep-ph\]](#) .
- [101] V. A. Miransky and I. A. Shovkovy, “Quantum field theory in a magnetic field: From quantum chromodynamics to graphene and Dirac semimetals,” *Phys. Rept.* **576**, 1 (2015), [arXiv:1503.00732 \[hep-ph\]](#) .
- [102] W. Dittrich and H. Gies, “Probing the quantum vacuum. Perturbative effective action approach in quantum electrodynamics and its application,” *Springer Tracts Mod. Phys.* **166**, 1 (2000).
- [103] V. A. Novikov, M. A. Shifman, A. I. Vainshtein, and V. I. Zakharov, “Calculations in External Fields in Quantum Chromodynamics. Technical Review,” *Fortsch. Phys.* **32**, 585 (1984).
- [104] L. J. Reinders, H. Rubinstein, and S. Yazaki, “Hadron Properties from QCD Sum Rules,” *Phys. Rept.* **127**, 1 (1985).

- [105] A. Chodos, K. Everding, and D. A. Owen, “QED With a Chemical Potential: 1. The Case of a Constant Magnetic Field,” *Phys. Rev.* **D42**, 2881 (1990).
- [106] V. P. Gusynin, V. A. Miransky, and I. A. Shovkovy, “Dimensional reduction and catalysis of dynamical symmetry breaking by a magnetic field,” *Nucl. Phys.* **B462**, 249 (1996), [arXiv:hep-ph/9509320 \[hep-ph\]](#) .
- [107] I. A. Batalin, S. G. Matinyan, and G. K. Savvidy, “Vacuum Polarization by a Source-Free Gauge Field,” *Sov. J. Nucl. Phys.* **26**, 214 (1977), [*Yad. Fiz.*26,407(1977)].
- [108] A. Yildiz and P. H. Cox, “Vacuum Behavior in Quantum Chromodynamics,” *Phys. Rev.* **D21**, 1095 (1980).
- [109] J. Ambjorn and R. J. Hughes, “Canonical Quantization in Nonabelian Background Fields. 1.” *Annals Phys.* **145**, 340 (1983).
- [110] M. Gyulassy and A. Iwazaki, “Quark and gluon pair production in $su(n)$ covariant constant fields,” *Phys. Lett.* **B165**, 157 (1985).
- [111] H. Suganuma and T. Tatsumi, “Chiral symmetry and quark - anti-quark pair creation in a strong color electromagnetic field,” *Prog. Theor. Phys.* **90**, 379 (1993).
- [112] G. C. Nayak and P. van Nieuwenhuizen, “Soft-gluon production due to a gluon loop in a constant chromo-electric background field,” *Phys. Rev.* **D71**, 125001 (2005), [arXiv:hep-ph/0504070 \[hep-ph\]](#) .
- [113] G. C. Nayak, “Non-perturbative quark-antiquark production from a constant chromo-electric field via the Schwinger mechanism,” *Phys. Rev.* **D72**, 125010 (2005), [arXiv:hep-ph/0510052 \[hep-ph\]](#) .
- [114] N. Tanji, “Quark pair creation in color electric fields and effects of magnetic fields,” *Annals Phys.* **325**, 2018 (2010), [arXiv:1002.3143 \[hep-ph\]](#) .
- [115] S. Ozaki, “QCD effective potential with strong $U(1)_{em}$ magnetic fields,” *Phys. Rev.* **D89**, 054022 (2014), [arXiv:1311.3137 \[hep-ph\]](#) .
- [116] N. K. Nielsen and P. Olesen, “Electric Vortex Lines From the Yang-Mills Theory,” *Phys. Lett.* **B79**, 304 (1978).
- [117] J. Ambjorn and P. Olesen, “A Color Magnetic Vortex Condensate in QCD,” *Nucl. Phys.* **B170**, 265 (1980).
- [118] F. Cooper and E. Mottola, “Quantum Back Reaction in Scalar QED as an Initial Value Problem,” *Phys. Rev.* **D40**, 456 (1989).
- [119] Y. Kluger, J. M. Eisenberg, B. Svetitsky, F. Cooper, and E. Mottola, “Pair production in a strong electric field,” *Phys. Rev. Lett.* **67**, 2427 (1991).
- [120] I. Bialynicki-Birula, P. Gornicki, and J. Rafelski, “Phase space structure of the Dirac vacuum,” *Phys. Rev.* **D44**, 1825 (1991).
- [121] Y. Kluger, J. M. Eisenberg, B. Svetitsky, F. Cooper, and E. Mottola, “Fermion pair production in a strong electric field,” *Phys. Rev.* **D45**, 4659 (1992).
- [122] N. Tanji, “Dynamical view of pair creation in uniform electric and magnetic fields,” *Annals Phys.* **324**, 1691 (2009), [arXiv:0810.4429 \[hep-ph\]](#) .

- [123] F. Gelis and N. Tanji, “Formulation of the Schwinger mechanism in classical statistical field theory,” *Phys. Rev.* **D87**, 125035 (2013), [arXiv:1303.4633 \[hep-ph\]](#) .
- [124] H. Taya, “Quark and gluon production from a boost-invariantly expanding color electric field,” *Phys. Rev.* **D96**, 014033 (2017), [arXiv:1609.06189 \[nucl-th\]](#) .
- [125] G. V. Dunne, in *From fields to strings: Circumnavigating theoretical physics. Ian Kogan memorial collection (3 volume set)*, edited by M. Shifman, A. Vainshtein, and J. Wheeler (2004) pp. 445–522, [arXiv:hep-th/0406216 \[hep-th\]](#) .
- [126] G. V. Dunne, “The Heisenberg-Euler Effective Action: 75 years on,” *Proceedings, 10th Conference on Quantum field theory under the influence of external conditions (QFEXT 11): Benasque, Spain, September 18-24, 2011*, *Int. J. Mod. Phys.* **A27**, 1260004 (2012), [*Int. J. Mod. Phys. Conf. Ser.*14,42(2012)], [arXiv:1202.1557 \[hep-th\]](#) .
- [127] F. Gelis and N. Tanji, “Schwinger mechanism revisited,” *Prog. Part. Nucl. Phys.* **87**, 1 (2016), [arXiv:1510.05451 \[hep-ph\]](#) .
- [128] A. Casher, H. Neuberger, and S. Nussinov, “Chromoelectric Flux Tube Model of Particle Production,” *Phys. Rev.* **D20**, 179 (1979).
- [129] A. Casher, H. Neuberger, and S. Nussinov, “Multiparticle production by bubbling flux tubes,” *Phys. Rev.* **D21**, 1966 (1980).
- [130] T. S. Biro, H. B. Nielsen, and J. Knoll, “Color Rope Model for Extreme Relativistic Heavy Ion Collisions,” *Nucl. Phys.* **B245**, 449 (1984).
- [131] K. Kajantie and T. Matsui, “Decay of strong color electric field and thermalization in ultrarelativistic nucleus-nucleus collisions,” *Phys. Lett.* **164B**, 373 (1985).
- [132] W. H. Furry, “A Symmetry Theorem in the Positron Theory,” *Phys. Rev.* **51**, 125 (1937).
- [133] H. W. Lee, P. Y. Pac, and H. K. Shin, “Derivative expansions in quantum electrodynamics,” *Phys. Rev.* **D40**, 4202 (1989).
- [134] V. P. Gusynin and I. A. Shovkovy, “Derivative expansion for the one loop effective Lagrangian in QED,” *Can. J. Phys.* **74**, 282 (1996), [arXiv:hep-ph/9509383 \[hep-ph\]](#) .
- [135] V. P. Gusynin and I. A. Shovkovy, “Derivative expansion of the effective action for QED in (2+1)-dimensions and (3+1)-dimensions,” *J. Math. Phys.* **40**, 5406 (1999), [arXiv:hep-th/9804143 \[hep-th\]](#) .
- [136] G. V. Dunne and T. Hall, “On the QED effective action in time dependent electric backgrounds,” *Phys. Rev. D* **58**, 105022 (1998), [arXiv:hep-th/9807031](#) .
- [137] I. Huet, M. Rausch de Traubenberg, and C. Schubert, “Asymptotic behavior of the QED perturbation series,” *5th Winter Workshop on Non-Perturbative Quantum Field Theory (WWNPQFT) Sophia-Antipolis, France, March 22-24, 2017*, *Adv. High Energy Phys.* **2017**, 6214341 (2017), [arXiv:1707.07655 \[hep-th\]](#) .
- [138] H. Gies and F. Karbstein, “An Addendum to the Heisenberg-Euler effective action beyond one loop,” *JHEP* **03**, 108 (2017), [arXiv:1612.07251 \[hep-th\]](#) .
- [139] F. Karbstein, “All-Loop Result for the Strong Magnetic Field Limit of the Heisenberg-Euler Effective Lagrangian,” *Phys. Rev. Lett.* **122**, 211602 (2019), [arXiv:1903.06998 \[hep-th\]](#) .

- [140] F. Sauter, “Über das Verhalten eines Elektrons im homogenen elektrischen Feld nach der relativistischen Theorie Diracs,” *Z. Phys.* **69**, 742 (1931).
- [141] A. I. Nikishov, “Pair production by a constant external field,” *Zh. Eksp. Teor. Fiz.* **57**, 1210 (1969).
- [142] A. I. Nikishov, “Barrier scattering in field theory removal of klein paradox,” *Nucl. Phys.* **B21**, 346 (1970).
- [143] J. Ambjorn and R. J. Hughes, “Particle Creation in Color Electric Fields,” *Phys. Lett.* **113B**, 305 (1982).
- [144] B. R. Holstein, “Strong field pair production,” *Am. J. Phys.* **67**, 499 (1999).
- [145] J. Haro, “Schwinger formula revisited,” *International Journal of Theoretical Physics* **42**, 2839 (2003).
- [146] T. D. Cohen and D. A. McGady, “The Schwinger mechanism revisited,” *Phys. Rev.* **D78**, 036008 (2008), [arXiv:0807.1117 \[hep-ph\]](#) .
- [147] J. Ambjorn, R. J. Hughes, and N. K. Nielsen, “Action Principle of Bogolyubov Coefficients,” *Annals Phys.* **150**, 92 (1983).
- [148] H. Taya, *Schwinger Mechanism in QCD and its Applications to Ultra-relativistic Heavy Ion Collisions*, *Ph.D. thesis*, Tokyo U. (2017).
- [149] N. Glendenning and T. Matsui, “Creation of anti-q q pair in a chromoelectric flux tube,” *Phys. Rev. D* **28**, 2890 (1983).
- [150] S. P. Kim and D. N. Page, “Schwinger pair production via instantons in a strong electric field,” *Phys. Rev.* **D65**, 105002 (2002), [arXiv:hep-th/0005078 \[hep-th\]](#) .
- [151] S. P. Kim and D. N. Page, “Schwinger pair production in electric and magnetic fields,” *Phys. Rev.* **D73**, 065020 (2006), [arXiv:hep-th/0301132 \[hep-th\]](#) .
- [152] Y. Hidaka, T. Iritani, and H. Suganuma, in *International Conference on Physics in Intense Fields (PIF 2010) KEK, Tsukuba, Japan, November 24-26, 2010* (2011) [arXiv:1102.0050 \[hep-ph\]](#) .
- [153] Y. Hidaka, T. Iritani, and H. Suganuma, “Fast Vacuum Decay into Quark Pairs in Strong Color Electric and Magnetic Fields,” *Proceedings, 12th International Conference : The structure of baryons (Baryons 10): Osaka, Japan, December 7-11, 2010*, *AIP Conf. Proc.* **1388**, 516 (2011), [arXiv:1103.3097 \[hep-ph\]](#) .
- [154] E. Brezin and C. Itzykson, “Pair production in vacuum by an alternating field,” *Phys. Rev.* **D2**, 1191 (1970).
- [155] G. V. Dunne and C. Schubert, “Worldline instantons and pair production in inhomogeneous fields,” *Phys. Rev.* **D72**, 105004 (2005), [arXiv:hep-th/0507174 \[hep-th\]](#) .
- [156] G. V. Dunne, Q.-h. Wang, H. Gies, and C. Schubert, “Worldline instantons. II. The Fluctuation prefactor,” *Phys. Rev. D* **73**, 065028 (2006), [arXiv:hep-th/0602176](#) .
- [157] J. R. Oppenheimer, “Three Notes on the Quantum Theory of Aperiodic Effects,” *Phys. Rev.* **31**, 66 (1928).

- [158] L. V. Keldysh, “Ionization in the Field of a Strong Electromagnetic Wave,” *J. Exp. Theor. Phys.* **20**, 1307 (1965).
- [159] V. S. Popov, “Tunnel and multiphoton ionization of atoms and ions in a strong laser field (Keldysh theory),” *Physics-Uspekhi* **47**, 855 (2004).
- [160] L. Keldysh, “Dynamic tunneling,” *Herald of the Russian Academy of Sciences* **86**, 413 (2016).
- [161] C. Zener, “Nonadiabatic crossing of energy levels,” *Proc. Roy. Soc. Lond.* **A137**, 696 (1932).
- [162] C. Zener, “A theory of the electrical breakdown of solid dielectrics,” *Proceedings of the Royal Society A* **145**, 523 (1934).
- [163] T. Oka (2011) [arXiv:1102.2482 \[cond-mat.stat-mech\]](https://arxiv.org/abs/1102.2482) .
- [164] E. W. Weisstein, “Associated Laguerre polynomial,” *From MathWorld—A Wolfram Web Resource.* <http://mathworld.wolfram.com/AssociatedLaguerrePolynomial.html> ().
- [165] X.-L. Sheng, R.-H. Fang, Q. Wang, and D. H. Rischke, “Wigner function and pair production in parallel electric and magnetic fields,” *Phys. Rev.* **D99**, 056004 (2019), [arXiv:1812.01146 \[hep-ph\]](https://arxiv.org/abs/1812.01146) .
- [166] L. Keldysh *et al.*, “Ionization in the field of a strong electromagnetic wave,” *Sov. Phys. JETP* **20**, 1307 (1965).
- [167] H. Taya, H. Fujii, and K. Itakura, “Finite pulse effects on e^+e^- pair creation from strong electric fields,” *Phys. Rev.* **D90**, 014039 (2014), [arXiv:1405.6182 \[hep-ph\]](https://arxiv.org/abs/1405.6182) .
- [168] R. Schutzhold, H. Gies, and G. Dunne, “Dynamically assisted Schwinger mechanism,” *Phys. Rev. Lett.* **101**, 130404 (2008), [arXiv:0807.0754 \[hep-th\]](https://arxiv.org/abs/0807.0754) .
- [169] A. Di Piazza, E. Lotstedt, A. I. Milstein, and C. H. Keitel, “Barrier control in tunneling $e^+ - e^-$ photoproduction,” *Phys. Rev. Lett.* **103**, 170403 (2009), [arXiv:0906.0726 \[hep-ph\]](https://arxiv.org/abs/0906.0726) .
- [170] G. Torgrimsson, C. Schneider, J. Oertel, and R. Schutzhold, “Dynamically assisted Sauter-Schwinger effect — non-perturbative versus perturbative aspects,” *JHEP* **06**, 043 (2017), [arXiv:1703.09203 \[hep-th\]](https://arxiv.org/abs/1703.09203) .
- [171] M. F. Linder, C. Schneider, J. Sicking, N. Szpak, and R. Schutzhold, “Pulse shape dependence in the dynamically assisted Sauter-Schwinger effect,” *Phys. Rev.* **D92**, 085009 (2015), [arXiv:1505.05685 \[hep-th\]](https://arxiv.org/abs/1505.05685) .
- [172] I. A. Aleksandrov, G. Plunien, and V. M. Shabaev, “Pulse shape effects on the electron-positron pair production in strong laser fields,” *Phys. Rev.* **D95**, 056013 (2017), [arXiv:1701.01058 \[hep-ph\]](https://arxiv.org/abs/1701.01058) .
- [173] F. Fillion-Gourdeau, F. Hebenstreit, D. Gagnon, and S. MacLean, “Pulse shape optimization for electron-positron production in rotating fields,” *Phys. Rev.* **D96**, 016012 (2017), [arXiv:1704.08919 \[hep-ph\]](https://arxiv.org/abs/1704.08919) .
- [174] W. Franz, “Einfluß eines elektrischen felde auf eine optische absorptionskante,” *Zeitschrift für Naturforschung A* **13**, 484 (1958).
- [175] L. Keldysh, “The effect of a strong electric field on the optical properties of insulating crystals,” *Sov. Phys. JETP* **7**, 788 (1958).

- [176] S. Y. Kruchinin, F. Krausz, and V. S. Yakovlev, “Colloquium: Strong-field phenomena in periodic systems,” *Rev. Mod. Phys.* **90**, 021002 (2018).
- [177] H. Taya, “Franz-Keldysh effect in strong-field QED,” *Phys. Rev.* **D99**, 056006 (2019), [arXiv:1812.03630 \[hep-ph\]](#) .
- [178] R.-C. Wang and C. Y. Wong, “Finite Size Effect in the Schwinger Particle Production Mechanism,” *Phys. Rev.* **D38**, 348 (1988).
- [179] C. Martin and D. Vautherin, “Finite Size and Dynamical Effects in Pair Production by an External Field,” *Phys. Rev.* **D40**, 1667 (1989).
- [180] S. P. Gavrilov and D. M. Gitman, “Scattering and pair creation by a constant electric field between two capacitor plates,” *Phys. Rev.* **D93**, 045033 (2016), [arXiv:1511.02915 \[hep-th\]](#) .
- [181] K. Tuchin, “Electromagnetic fields in high energy heavy-ion collisions,” *Int. J. Mod. Phys.* **E23**, 1430001 (2014).
- [182] S. P. Kim and D. N. Page, “Improved Approximations for Fermion Pair Production in Inhomogeneous Electric Fields,” *Phys. Rev.* **D75**, 045013 (2007), [arXiv:hep-th/0701047 \[hep-th\]](#) .
- [183] H. Gies and G. Torgrimsson, “Critical Schwinger pair production,” *Phys. Rev. Lett.* **116**, 090406 (2016), [arXiv:1507.07802 \[hep-ph\]](#) .
- [184] H. Gies and G. Torgrimsson, “Critical Schwinger pair production II - universality in the deeply critical regime,” *Phys. Rev.* **D95**, 016001 (2017), [arXiv:1612.00635 \[hep-th\]](#) .
- [185] B. Damski, “The Simplest quantum model for the Kibble-Zurek mechanism of topological defect production: Landau-Zener transitions from a new perspective,” *Phys. Rev. Lett.* **95**, 035701 (2005), [arXiv:cond-mat/0411004](#) .
- [186] B. Damski and W. H. Zurek, “Adiabatic-impulse approximation for avoided level crossings: From phase transition dynamics to Landau-Zener evolutions and back again,” *Phys. Rev. A* **73**, 063405 (2006), [arXiv:cond-mat/0511709](#) .
- [187] T. W. B. Kibble, “Topology of Cosmic Domains and Strings,” *J. Phys. A* **9**, 1387 (1976).
- [188] T. W. B. Kibble, “Some Implications of a Cosmological Phase Transition,” *Phys. Rept.* **67**, 183 (1980).
- [189] W. H. Zurek, “Cosmological Experiments in Superfluid Helium?” *Nature* **317**, 505 (1985).
- [190] A. del Campo and W. H. Zurek, “Universality of phase transition dynamics: Topological Defects from Symmetry Breaking,” *Int. J. Mod. Phys. A* **29**, 1430018 (2014), [arXiv:1310.1600 \[cond-mat.stat-mech\]](#) .
- [191] Y. R. Shen, *The principles of nonlinear optics* (Oxford University Press, 2007).
- [192] L. D. Landau, E. M. Lifshits, and L. Pitaevskii, *Electrodynamics of continuous media*, Vol. 8 (Pergamon press Oxford, 1984).
- [193] V. Weisskopf, “The electrodynamics of the vacuum based on the quantum theory of the electron,” *Kong. Dan. Vid. Sel. Mat. Fys. Med.* **14N6**, 1 (1936).

- [194] A. I. Miller, *The electrodynamics of the vacuum based on the quantum theory of the electron* (English translation in “Early Quantum. Electrodynamics: A Source Book”, A. I. Miller. (Cambridge University Press, 1994).).
- [195] R. Battesti and C. Rizzo, “Magnetic and electric properties of quantum vacuum,” *Rept. Prog. Phys.* **76**, 016401 (2013), [arXiv:1211.1933 \[physics.optics\]](#) .
- [196] V. B. Berestetskii, E. M. Lifshitz, and L. P. Pitaevskii, *QUANTUM ELECTRODYNAMICS*, Course of Theoretical Physics, Vol. 4 (Pergamon Press, Oxford, 1982).
- [197] J. S. Schwinger, “Gauge Invariance and Mass,” *Phys. Rev.* **125**, 397 (1962).
- [198] J. S. Schwinger, “Gauge Invariance and Mass. 2.” *Phys. Rev.* **128**, 2425 (1962).
- [199] J. S. Toll, *The Dispersion relation for light and its application to problems involving electron pairs*, Ph.D. thesis, Princeton U. (1952).
- [200] J. J. Klein and B. P. Nigam, “Dichroism of the Vacuum,” *Phys. Rev.* **136**, B1540 (1964).
- [201] R. Baier and P. Breitenlohner, “Photon Propagation in External Fields,” *Acta Phys. Austriaca* **25**, 212 (1967).
- [202] R. Baier and P. Breitenlohner, “The Vacuum refraction Index in the presence of External Fields,” *Nuovo Cim.* **B47**, 117 (1967).
- [203] Z. Bialynicka-Birula and I. Bialynicki-Birula, “Nonlinear effects in Quantum Electrodynamics. Photon propagation and photon splitting in an external field,” *Phys. Rev.* **D2**, 2341 (1970).
- [204] E. Brezin and C. Itzykson, “Polarization phenomena in vacuum nonlinear electrodynamics,” *Phys. Rev.* **D3**, 618 (1971).
- [205] S. L. Adler, “Photon splitting and photon dispersion in a strong magnetic field,” *Annals Phys.* **67**, 599 (1971).
- [206] I. Batalin and A. Shabad, “Green’s function of a photon in a constant homogeneous electromagnetic field of general form,” *Zh. Eksp. Teor. Fiz* **60**, 894 (1971).
- [207] W.-y. Tsai and T. Erber, “Photon Pair Creation in Intense Magnetic Fields,” *Phys. Rev.* **D10**, 492 (1974).
- [208] W.-y. Tsai and T. Erber, “The Propagation of Photons in Homogeneous Magnetic Fields: Index of Refraction,” *Phys. Rev.* **D12**, 1132 (1975).
- [209] W.-y. Tsai, “Vacuum Polarization in Homogeneous Magnetic Fields,” *Phys. Rev.* **D10**, 2699 (1974).
- [210] D. B. Melrose and R. J. Stoneham, “The polarization tensor for a magnetized vacuum,” *J. Phys.* **A10**, 1211 (1977).
- [211] L. F. Urrutia, “Vacuum Polarization in Parallel Homogeneous Electric and Magnetic Fields,” *Phys. Rev.* **D17**, 1977 (1978).
- [212] J. S. Heyl and L. Hernquist, “An Analytic form for the effective Lagrangian of QED and its application to pair production and photon splitting,” *Phys. Rev.* **D55**, 2449 (1997), [arXiv:hep-th/9607124 \[hep-th\]](#) .

- [213] J. S. Heyl and L. Hernquist, “Birefringence and dichroism of the QED vacuum,” *J. Phys.* **A30**, 6485 (1997), [arXiv:hep-ph/9705367 \[hep-ph\]](#) .
- [214] K. Hattori and K. Itakura, “Vacuum birefringence in strong magnetic fields: (I) Photon polarization tensor with all the Landau levels,” *Annals Phys.* **330**, 23 (2013), [arXiv:1209.2663 \[hep-ph\]](#) .
- [215] K. Hattori and K. Itakura, “Vacuum birefringence in strong magnetic fields: (II) Complex refractive index from the lowest Landau level,” *Annals Phys.* **334**, 58 (2013), [arXiv:1212.1897 \[hep-ph\]](#) .
- [216] K. Hattori and D. Satow, “Gluon Spectrum in Quark-Gluon Plasma under Strong Magnetic Fields,” *Phys. Rev.* **D97**, 014023 (2018), [arXiv:1704.03191 \[hep-ph\]](#) .
- [217] E. Hecht, *Optics* (Pearson education, 2002).
- [218] H. Euler and B. Kockel, “Ueber die Streuung von Licht an Licht nach der Diracschen Theorie,” *Naturwiss.* **23**, 246 (1935).
- [219] S. L. Adler, J. N. Bahcall, C. G. Callan, and M. N. Rosenbluth, “Photon splitting in a strong magnetic field,” *Phys. Rev. Lett.* **25**, 1061 (1970).
- [220] E. Zavattini *et al.* (PVLAS), “Experimental observation of optical rotation generated in vacuum by a magnetic field,” *Phys. Rev. Lett.* **96**, 110406 (2006), [Erratum: *Phys. Rev. Lett.* 99,129901(2007)], [arXiv:hep-ex/0507107 \[hep-ex\]](#) .
- [221] E. Zavattini *et al.* (PVLAS), “New PVLAS results and limits on magnetically induced optical rotation and ellipticity in vacuum,” *Phys. Rev.* **D77**, 032006 (2008), [arXiv:0706.3419 \[hep-ex\]](#) .
- [222] F. Della Valle, A. Ejlli, U. Gastaldi, G. Messineo, E. Milotti, R. Pengo, G. Ruoso, and G. Zavattini, “The PVLAS experiment: measuring vacuum magnetic birefringence and dichroism with a birefringent Fabry-Perot cavity,” *Eur. Phys. J.* **C76**, 24 (2016), [arXiv:1510.08052 \[physics.optics\]](#) .
- [223] E. L. I. (ELI), <http://www.eli-beams.eu/science/exotic-physics-and-theory/> .
- [224] “Topical issue on Fundamental physics and ultra-high laser fields,” *Euro. Phys. J. D* **55** (2009).
- [225] T. Heinzl, B. Liesfeld, K.-U. Amthor, H. Schworer, R. Sauerbrey, and A. Wipf, “On the observation of vacuum birefringence,” *Opt. Commun.* **267**, 318 (2006), [arXiv:hep-ph/0601076 \[hep-ph\]](#) .
- [226] A. Salam and J. A. Strathdee, “Transition Electromagnetic Fields in Particle Physics,” *Nucl. Phys.* **B90**, 203 (1975).
- [227] W. Dittrich, W.-y. Tsai, and K.-H. Zimmermann, “On the Evaluation of the Effective Potential in Quantum Electrodynamics,” *Phys. Rev.* **D19**, 2929 (1979).
- [228] J. O. Andersen, W. R. Naylor, and A. Tranberg, “Phase diagram of QCD in a magnetic field: A review,” *Rev. Mod. Phys.* **88**, 025001 (2016), [arXiv:1411.7176 \[hep-ph\]](#) .
- [229] E. W. Weisstein, “Hurwitz zeta function,” [From MathWorld—A Wolfram Web Resource. https://mathworld.wolfram.com/HurwitzZetaFunction.html](https://mathworld.wolfram.com/HurwitzZetaFunction.html) ().

- [230] J. S. Heyl and N. J. Shaviv, “Polarization evolution in strong magnetic fields,” *Mon. Not. Roy. Astron. Soc.* **311**, 555 (2000), [arXiv:astro-ph/9909339 \[astro-ph\]](#) .
- [231] J. S. Heyl, N. J. Shaviv, and D. Lloyd, “The high-energy polarization-limiting radius of neutron star magnetospheres. 1. Slowly rotating neutron stars,” *Mon. Not. Roy. Astron. Soc.* **342**, 134 (2003), [arXiv:astro-ph/0302118 \[astro-ph\]](#) .
- [232] M. van Adelsberg and D. Lai, “Atmosphere Models of Magnetized Neutron Stars: QED Effects, Radiation Spectra, and Polarization Signals,” *Mon. Not. Roy. Astron. Soc.* **373**, 1495 (2006), [arXiv:astro-ph/0607168 \[astro-ph\]](#) .
- [233] R. P. Mignani, V. Testa, D. G. Caniulef, R. Taverna, R. Turolla, S. Zane, and K. Wu, “Evidence for vacuum birefringence from the first optical polarimetry measurement of the isolated neutron star RX J1856.5–3754,” *Mon. Not. Roy. Astron. Soc.* **465**, 492 (2017), [arXiv:1610.08323 \[astro-ph.HE\]](#) .
- [234] PRAXyS, <https://asd.gsfc.nasa.gov/praxys/> .
- [235] J. D. Brandenburg, J. Seger, Z. Xu, and W. Zha, “Report on Progress in Physics: Observation of the Breit-Wheeler Process and Vacuum Birefringence in Heavy-Ion Collisions,” (2022), [arXiv:2208.14943 \[hep-ph\]](#) .
- [236] V. N. Baier and V. M. Katkov, “Pair creation by a photon in a strong magnetic field,” *Phys. Rev.* **D75**, 073009 (2007), [arXiv:hep-ph/0701119 \[hep-ph\]](#) .
- [237] F. Karbstein, L. Roessler, B. Dobrich, and H. Gies, “Optical Probes of the Quantum Vacuum: The Photon Polarization Tensor in External Fields,” *Int. J. Mod. Phys. Conf. Ser.* **14**, 403 (2012), [arXiv:1111.5984 \[hep-ph\]](#) .
- [238] C. Schubert, “Vacuum polarization tensors in constant electromagnetic fields. Part 1.” *Nucl. Phys.* **B585**, 407 (2000), [arXiv:hep-ph/0001288 \[hep-ph\]](#) .
- [239] W. Dittrich and R. Shaisultanov, “Vacuum polarization in QED with worldline methods,” *Phys. Rev.* **D62**, 045024 (2000), [arXiv:hep-th/0001171 \[hep-th\]](#) .
- [240] K. Kohri and S. Yamada, “Polarization tensors in a strong magnetic field,” *Phys. Rev.* **D65**, 043006 (2002), [arXiv:astro-ph/0102225 \[astro-ph\]](#) .
- [241] K.-I. Ishikawa, D. Kimura, K. Shigaki, and A. Tsuji, “A numerical evaluation of vacuum polarization tensor in constant external magnetic fields,” *Int. J. Mod. Phys.* **A28**, 1350100 (2013), [arXiv:1304.3655 \[hep-ph\]](#) .
- [242] K. Fukushima, “Magnetic-field Induced Screening Effect and Collective Excitations,” *Phys. Rev.* **D83**, 111501 (2011), [arXiv:1103.4430 \[hep-ph\]](#) .
- [243] K. Tuchin, “Photon decay in strong magnetic field in heavy-ion collisions,” *Phys. Rev.* **C83**, 017901 (2011), [arXiv:1008.1604 \[nucl-th\]](#) .
- [244] K. Tuchin, “Particle production in strong electromagnetic fields in relativistic heavy-ion collisions,” *Adv. High Energy Phys.* **2013**, 490495 (2013), [arXiv:1301.0099 \[hep-ph\]](#) .
- [245] A. Yatabe and S. Yamada, “Vacuum Polarization and Photon Propagation in an Electromagnetic Plane Wave,” *PTEP* **2018**, 033B04 (2018), [arXiv:1801.05430 \[hep-ph\]](#) .

- [246] W. Greiner and J. Reinhardt, *Quantum electrodynamics* (Springer Science & Business Media, 2008).
- [247] D. d’Enterria and G. G. da Silveira, “Observing light-by-light scattering at the Large Hadron Collider,” *Phys. Rev. Lett.* **111**, 080405 (2013), [Erratum: Phys.Rev.Lett. 116, 129901 (2016)], [arXiv:1305.7142 \[hep-ph\]](#) .
- [248] A. I. Milstein and M. Schumacher, “Present status of Delbruck scattering,” *Phys. Rept.* **243**, 183 (1994).
- [249] G. Jarlskog, L. Joensson, S. Pruenster, H. D. Schulz, H. J. Willutzki, and G. G. Winter, “Measurement of delbrueck scattering and observation of photon splitting at high energies,” *Phys. Rev. D*, **8**, 3813 (1973).
- [250] S. Z. Akhmadaliev *et al.*, “Experimental investigation of high-energy photon splitting in atomic fields,” *Phys. Rev. Lett.* **89**, 061802 (2002), [arXiv:hep-ex/0111084 \[hep-ex\]](#) .
- [251] M. G. Baring, “Photon Splitting and Pair Conversion in Strong Magnetic Fields,” *AIP Conf. Proc.* **1051**, 53 (2008), [arXiv:0804.0832 \[astro-ph\]](#) .
- [252] M. G. Baring and A. K. Harding, “Magnetic photon splitting: Computations of proper time rates and spectra,” *Astrophys. J.* **482**, 372 (1997), [arXiv:astro-ph/9704210 \[astro-ph\]](#) .
- [253] M. V. Chistyakov, A. V. Kuznetsov, and N. V. Mikheev, “Photon splitting above the pair creation threshold in a strong magnetic field,” *Phys. Lett. B***434**, 67 (1998), [arXiv:hep-ph/9804444 \[hep-ph\]](#) .
- [254] M. G. Baring and A. K. Harding, “Radio-quiet pulsars with ultrastrong magnetic fields,” *The Astrophysical Journal Letters* **507**, L55 (1998).
- [255] J. I. Weise, M. G. Baring, and D. B. Melrose, “Photon splitting in strong magnetic fields: S matrix calculations,” *Phys. Rev. D***57**, 5526 (1998), [Erratum: Phys. Rev.D60,099901(1999)].
- [256] V. N. Baier, A. I. Milshstein, and R. Z. Shaisultanov, “Photon Splitting in a Strong Electromagnetic Field,” *Sov. Phys. JETP* **63**, 665 (1986), [*Zh. Eksp. Teor. Fiz.*90,1141(1986)].
- [257] V. N. Baier, A. I. Milshstein, and R. Z. Shaisultanov, “Photon splitting in a very strong magnetic field,” *Phys. Rev. Lett.* **77**, 1691 (1996), [arXiv:hep-th/9604028 \[hep-th\]](#) .
- [258] S. L. Adler and C. Schubert, “Photon splitting in a strong magnetic field: Recalculation and comparison with previous calculations,” *Phys. Rev. Lett.* **77**, 1695 (1996), [arXiv:hep-th/9605035 \[hep-th\]](#) .
- [259] M. G. Baring and A. K. Harding, “Photon splitting and pair creation in highly magnetized pulsars,” *Astrophys. J.* **547**, 929 (2001), [arXiv:astro-ph/0010400 \[astro-ph\]](#) .
- [260] M. G. Baring, “Magnetic photon splitting: The S matrix formulation in the Landau representation,” *Phys. Rev. D***62**, 016003 (2000), [arXiv:hep-th/0003186 \[hep-th\]](#) .
- [261] M. V. Chistyakov, D. A. Rumyantsev, and N. S. Stus’, “Photon splitting and Compton scattering in strongly magnetized hot plasma,” *Phys. Rev. D***86**, 043007 (2012), [arXiv:1207.6273 \[hep-ph\]](#) .
- [262] K. Hattori and K. Itakura, in *Proceedings, 7th International Conference on Hard and Electromagnetic Probes of High-Energy Nuclear Collisions (Hard Probes 2015): Montréal, Québec, Canada, June 29-July 3, 2015* (2016) [arXiv:1509.03217 \[hep-ph\]](#) .

- [263] M. J. Duff and M. Ramon-Medrano, “On the effective lagrangian for the yang-mills field,” *Phys. Rev.* **D12**, 3357 (1975).
- [264] G. K. Savvidy, “Infrared Instability of the Vacuum State of Gauge Theories and Asymptotic Freedom,” *Phys. Lett.* **B71**, 133 (1977).
- [265] S. G. Matinyan and G. K. Savvidy, “Vacuum Polarization Induced by the Intense Gauge Field,” *Nucl. Phys.* **B134**, 539 (1978).
- [266] G. Savvidy, “From Heisenberg-Euler Lagrangian to the discovery of chromomagnetic gluon condensation,” (2019), [arXiv:1910.00654 \[hep-th\]](https://arxiv.org/abs/1910.00654) .
- [267] V. S. Vanyashin and M. V. Terentev, “The Vacuum Polarization of a Charged Vector Field,” *Zh. Eksp. Teor. Fiz.* **48**, 565 (1965), [*Sov. Phys. JETP*21,no.2,375(1965)].
- [268] D. J. Gross and F. Wilczek, “Ultraviolet Behavior of Nonabelian Gauge Theories,” *Phys. Rev. Lett.* **30**, 1343 (1973), [,271(1973)].
- [269] H. D. Politzer, “Reliable Perturbative Results for Strong Interactions?” *Phys. Rev. Lett.* **30**, 1346 (1973), [,274(1973)].
- [270] R. J. Hughes, “Some comments on asymptotic freedom,” *Phys. Lett.* **97B**, 246 (1980).
- [271] N. K. Nielsen, “Asymptotic freedom as a spin effect,” *Am. J. Phys.* **49**, 1171 (1981).
- [272] R. J. Hughes, “More comments on asymptotic freedom,” *Nucl. Phys.* **B186**, 376 (1981).
- [273] D. J. Gross, “Nobel lecture: The discovery of asymptotic freedom and the emergence of qcd,” *Rev. Mod. Phys.* **77**, 837 (2005).
- [274] A. Grozin (2008) [arXiv:0803.2589 \[physics.hist-ph\]](https://arxiv.org/abs/0803.2589) .
- [275] W. Dittrich and M. Reuter, “Effective QCD Lagrangian With Zeta Function Regularization,” *Phys. Lett.* **128B**, 321 (1983).
- [276] E. Elizalde and J. Soto, “Zeta Regularized Lagrangians for Massive Quarks in Constant Background Mean Fields,” *Annals Phys.* **162**, 192 (1985).
- [277] W.-Y. Tsai and A. Yildiz, “Motion of charged particles in a homogeneous magnetic field,” *Phys. Rev. D* **4**, 3643 (1971).
- [278] J. Ambjorn and P. Olesen, “On the Formation of a Random Color Magnetic Quantum Liquid in QCD,” *Nucl. Phys.* **B170**, 60 (1980).
- [279] M. Claudson, A. Yildiz, and P. H. Cox, “Vacuum behavior in quantum chromodynamics. ii,” *Phys. Rev.* **D22**, 2022 (1980).
- [280] W. Dittrich and V. Schanbacher, “Effective qcd lagrangian at finite temperature,” *Phys. Lett.* **B100**, 415 (1981).
- [281] B. Muller and J. Rafelski, “Temperature Dependence of the Bag Constant and the Effective Lagrangian for Gauge Fields at Finite Temperatures,” *Phys. Lett.* **101B**, 111 (1981).
- [282] J. I. Kapusta, “Thermodynamics of Chromomagnetism,” *Nucl. Phys.* **B190**, 425 (1981).

- [283] H. Gies, “Effective action for the order parameter of the deconfinement transition of Yang-Mills theories,” *Phys. Rev.* **D63**, 025013 (2001), [arXiv:hep-th/0005252 \[hep-th\]](#) .
- [284] W. Dittrich, “Effective Lagrangian at Finite Temperature,” *Phys. Rev.* **D19**, 2385 (1979).
- [285] M. Loewe and J. C. Rojas, “Thermal effects and the effective action of quantum electrodynamics,” *Phys. Rev.* **D46**, 2689 (1992).
- [286] P. Elmfors, D. Persson, and B.-S. Skagerstam, “QED effective action at finite temperature and density,” *Phys. Rev. Lett.* **71**, 480 (1993), [arXiv:hep-th/9305004 \[hep-th\]](#) .
- [287] P. Elmfors, D. Persson, and B.-S. Skagerstam, “Real time thermal propagators and the QED effective action for an external magnetic field,” *Astropart. Phys.* **2**, 299 (1994), [arXiv:hep-ph/9312226 \[hep-ph\]](#) .
- [288] P. Elmfors and B.-S. Skagerstam, “Electromagnetic fields in a thermal background,” *Phys. Lett.* **B348**, 141 (1995), [Erratum: *Phys. Lett.*B376,330(1996)], [arXiv:hep-th/9404106 \[hep-th\]](#) .
- [289] H. Gies, “QED effective action at finite temperature,” *Phys. Rev.* **D60**, 105002 (1999), [arXiv:hep-ph/9812436 \[hep-ph\]](#) .
- [290] P. Cea, “SU(2) Gauge Theory in a Constant Chromomagnetic Background Field,” *Phys. Rev.* **D37**, 1637 (1988).
- [291] H. Pagels and E. Tomboulis, “Vacuum of the Quantum Yang-Mills Theory and Magnetostatics,” *Nucl. Phys.* **B143**, 485 (1978).
- [292] S. L. Adler, “Effective Action Approach to Mean Field Nonabelian Statics, and a Model for Bag Formation,” *Phys. Rev.* **D23**, 2905 (1981).
- [293] S. L. Adler and T. Piran, “Flux Confinement in the Leading Logarithm Model,” *Phys. Lett.* **B113**, 405 (1982), [Erratum: *Phys. Lett.*B121,455(1983)].
- [294] Y. M. Cho and D. G. Pak, “Monopole condensation in SU(2) QCD,” *Phys. Rev.* **D65**, 074027 (2002), [arXiv:hep-th/0201179 \[hep-th\]](#) .
- [295] K.-I. Kondo, “Magnetic condensation, Abelian dominance, and instability of Savvidy vacuum,” *Phys. Lett.* **B600**, 287 (2004), [arXiv:hep-th/0404252 \[hep-th\]](#) .
- [296] K.-I. Kondo, “Gauge-invariant gluon mass, infrared Abelian dominance and stability of magnetic vacuum,” *Phys. Rev.* **D74**, 125003 (2006), [arXiv:hep-th/0609166 \[hep-th\]](#) .
- [297] K.-I. Kondo, “Stability of chromomagnetic condensation and mass generation for confinement in SU(2) Yang-Mills theory,” *Phys. Rev.* **D89**, 105013 (2014), [arXiv:1309.2337 \[hep-th\]](#) .
- [298] E. Iancu and R. Venugopalan, in *In *Hwa, R.C. (ed.) et al.: Quark gluon plasma* 249-3363* (2003) [arXiv:hep-ph/0303204 \[hep-ph\]](#) .
- [299] F. Gelis, E. Iancu, J. Jalilian-Marian, and R. Venugopalan, “The Color Glass Condensate,” *Ann. Rev. Nucl. Part. Sci.* **60**, 463 (2010), [arXiv:1002.0333 \[hep-ph\]](#) .
- [300] A. Kovner, L. D. McLerran, and H. Weigert, “Gluon production from nonAbelian Weizsacker-Williams fields in nucleus-nucleus collisions,” *Phys. Rev.* **D52**, 6231 (1995), [arXiv:hep-ph/9502289 \[hep-ph\]](#) .

- [301] A. Kovner, L. D. McLerran, and H. Weigert, “Gluon production at high transverse momentum in the McLerran-Venugopalan model of nuclear structure functions,” *Phys. Rev.* **D52**, 3809 (1995), [arXiv:hep-ph/9505320 \[hep-ph\]](#) .
- [302] T. Lappi and L. McLerran, “Some features of the glasma,” *Nucl. Phys.* **A772**, 200 (2006), [arXiv:hep-ph/0602189 \[hep-ph\]](#) .
- [303] D. E. Kharzeev, L. D. McLerran, and H. J. Warringa, “The Effects of topological charge change in heavy ion collisions: ‘Event by event P and CP violation’,” *Nucl.Phys.* **A803**, 227 (2008), [arXiv:0711.0950 \[hep-ph\]](#) .
- [304] B. V. Galilo and S. N. Nedelko, “Impact of the strong electromagnetic field on the QCD effective potential for homogeneous Abelian gluon field configurations,” *Phys. Rev.* **D84**, 094017 (2011), [arXiv:1107.4737 \[hep-ph\]](#) .
- [305] S. Ozaki, T. Arai, K. Hattori, and K. Itakura, “Euler-Heisenberg-Weiss action for QCD+QED,” *Phys. Rev.* **D92**, 016002 (2015), [arXiv:1504.07532 \[hep-ph\]](#) .
- [306] J. I. Kapusta and C. Gale, *Finite-temperature field theory: Principles and applications*, Cambridge Monographs on Mathematical Physics (Cambridge University Press, 2011).
- [307] M. L. Bellac, *Thermal Field Theory* (Cambridge University Press, 2000).
- [308] R. B. Griffiths, *Consistent quantum theory* (Cambridge University Press, 2003).
- [309] D. Cangemi and G. V. Dunne, “Temperature expansions for magnetic systems,” *Annals Phys.* **249**, 582 (1996), [arXiv:hep-th/9601048 \[hep-th\]](#) .
- [310] S. Grozdanov, D. M. Hofman, and N. Iqbal, “Generalized global symmetries and dissipative magnetohydrodynamics,” *Phys. Rev.* **D95**, 096003 (2017), [arXiv:1610.07392 \[hep-th\]](#) .
- [311] K. Hattori, Y. Hirono, H.-U. Yee, and Y. Yin, “MagnetoHydrodynamics with chiral anomaly: phases of collective excitations and instabilities,” *Phys. Rev.* **D100**, 065023 (2019), [arXiv:1711.08450 \[hep-th\]](#) .
- [312] K. Hattori, M. Hongo, and X.-G. Huang, “New Developments in Relativistic Magnetohydrodynamics,” *Symmetry* **14**, 1851 (2022), [arXiv:2207.12794 \[hep-th\]](#) .
- [313] P. H. Cox, W. S. Hellman, and A. Yildiz, “Finite Temperature Corrections to Field Theory: Electron Mass and Magnetic Moment, and Vacuum Energy,” *Annals Phys.* **154**, 211 (1984).
- [314] H. Gies, “QED effective action at finite temperature: Two loop dominance,” *Phys. Rev.* **D61**, 085021 (2000), [arXiv:hep-ph/9909500 \[hep-ph\]](#) .
- [315] S. P. Gavrilov and D. M. Gitman, “One-loop energy-momentum tensor in QED with electric-like background,” *Phys. Rev.* **D78**, 045017 (2008), [arXiv:0709.1828 \[hep-th\]](#) .
- [316] S. P. Kim and H. K. Lee, “Schwinger pair production at finite temperature in scalar QED,” *Phys. Rev.* **D76**, 125002 (2007), [arXiv:0706.2216 \[hep-th\]](#) .
- [317] S. P. Kim, H. K. Lee, and Y. Yoon, “Schwinger Pair Production at Finite Temperature in QED,” *Phys. Rev.* **D79**, 045024 (2009), [arXiv:0811.0349 \[hep-th\]](#) .
- [318] L. Medina and M. C. Ogilvie, “Schwinger Pair Production at Finite Temperature,” *Phys. Rev.* **D95**, 056006 (2017), [arXiv:1511.09459 \[hep-th\]](#) .

- [319] O. Gould and A. Rajantie, “Thermal Schwinger pair production at arbitrary coupling,” *Phys. Rev.* **D96**, 076002 (2017), [arXiv:1704.04801 \[hep-th\]](#) .
- [320] G. Endrődi and G. Markó, “On electric fields in hot QCD: perturbation theory,” *JHEP* **12**, 015 (2022), [arXiv:2208.14306 \[hep-ph\]](#) .
- [321] G. B. Arfken, H. J. Weber, and F. E. Harris, *Mathematical Methods for Physicists (Seventh Edition)*, seventh edition ed. (Academic Press, Boston, 2013).
- [322] E. W. Weisstein, “Modified Bessel function of the second kind,” *From MathWorld—A Wolfram Web Resource*. <http://mathworld.wolfram.com/ModifiedBesselFunctionoftheSecondKind.html> ().
- [323] T. Hatsuda and T. Kunihiro, “QCD phenomenology based on a chiral effective Lagrangian,” *Phys. Rept.* **247**, 221 (1994), [arXiv:hep-ph/9401310 \[hep-ph\]](#) .
- [324] V. P. Gusynin, V. A. Miransky, and I. A. Shovkovy, “Dimensional reduction and dynamical chiral symmetry breaking by a magnetic field in (3+1)-dimensions,” *Phys. Lett.* **B349**, 477 (1995), [arXiv:hep-ph/9412257 \[hep-ph\]](#) .
- [325] K. Fukushima and J. M. Pawłowski, “Magnetic catalysis in hot and dense quark matter and quantum fluctuations,” *Phys. Rev.* **D86**, 076013 (2012), [arXiv:1203.4330 \[hep-ph\]](#) .
- [326] V. P. Gusynin, V. A. Miransky, and I. A. Shovkovy, “Dynamical chiral symmetry breaking by a magnetic field in QED,” *Phys. Rev.* **D52**, 4747 (1995), [arXiv:hep-ph/9501304 \[hep-ph\]](#) .
- [327] E. W. Weisstein, “Riemann zeta function,” *From MathWorld—A Wolfram Web Resource*. <http://mathworld.wolfram.com/RiemannZetaFunction.html> ().
- [328] D. Ebert and V. C. Zhukovsky, “Chiral phase transitions in strong chromomagnetic fields at finite temperature and dimensional reduction,” *Mod. Phys. Lett.* **A12**, 2567 (1997), [arXiv:hep-ph/9701323 \[hep-ph\]](#) .
- [329] V. P. Gusynin and I. A. Shovkovy, “Chiral symmetry breaking in QED in a magnetic field at finite temperature,” *Phys. Rev.* **D56**, 5251 (1997), [arXiv:hep-ph/9704394 \[hep-ph\]](#) .
- [330] D. S. Lee, C. N. Leung, and Y. J. Ng, “Chiral symmetry breaking in a uniform external magnetic field. 2. Symmetry restoration at high temperatures and chemical potentials,” *Phys. Rev.* **D57**, 5224 (1998), [arXiv:hep-th/9711126 \[hep-th\]](#) .
- [331] M. Tinkham, *Introduction to superconductivity* (Courier Corporation, 2004).
- [332] U. Kraemmer and A. Rebhan, “Advances in perturbative thermal field theory,” *Rept. Prog. Phys.* **67**, 351 (2004), [arXiv:hep-ph/0310337 \[hep-ph\]](#) .
- [333] K. Fukushima and V. Skokov, “Polyakov loop modeling for hot QCD,” *Prog. Part. Nucl. Phys.* **96**, 154 (2017), [arXiv:1705.00718 \[hep-ph\]](#) .
- [334] E. W. Weisstein, “Polylogarithm,” *From MathWorld—A Wolfram Web Resource*. <http://mathworld.wolfram.com/Polylogarithm.html> ().
- [335] N. Tanji and K. Itakura, “Schwinger mechanism enhanced by the nielsen-olesen instability,” *Phys. Lett.* **B713**, 117 (2012), [arXiv:1111.6772 \[hep-ph\]](#) .
- [336] S. Ozaki, K. Itakura, and Y. Kuramoto, “Magnetically induced QCD Kondo effect,” *Phys. Rev.* **D94**, 074013 (2016), [arXiv:1509.06966 \[hep-ph\]](#) .

- [337] F. Cooper and G. C. Nayak, “Non-perturbative gluon pair production from a constant chromo-electric field via the Schwinger mechanism in arbitrary gauge,” *Phys. Rev.* **D73**, 065005 (2006), [arXiv:hep-ph/0511053 \[hep-ph\]](#) .
- [338] G. Gatoff, A. K. Kerman, and T. Matsui, “The flux tube model for ultrarelativistic heavy ion collisions: Electrohydrodynamics of a quark gluon plasma,” *Phys. Rev.* **D36**, 114 (1987).
- [339] H. Fujii and K. Itakura, “Expanding color flux tubes and instabilities,” *Nucl. Phys.* **A809**, 88 (2008), [arXiv:0803.0410 \[hep-ph\]](#) .
- [340] H. Fujii, K. Itakura, and A. Iwazaki, “Instabilities in non-expanding glasma,” *Nucl. Phys.* **A828**, 178 (2009), [arXiv:0903.2930 \[hep-ph\]](#) .
- [341] C. Cardona and T. Vachaspati, “Instability of a uniform electric field in pure non-Abelian Yang-Mills theory,” *Phys. Rev. D* **104**, 045009 (2021), [arXiv:2105.08782 \[hep-th\]](#) .
- [342] J. Pereira and T. Vachaspati, “Stability analysis of non-Abelian electric fields,” *Phys. Rev. D* **106**, 096019 (2022), [arXiv:2207.05102 \[hep-th\]](#) .
- [343] T. Vachaspati, “Electric strings in non-Abelian theories,” *Phys. Rev. D* **107**, L031903 (2023), [arXiv:2212.00808 \[hep-th\]](#) .
- [344] T. Vachaspati, “Construction of non-Abelian electric strings,” *Phys. Rev. D* **107**, 096015 (2023), [arXiv:2303.03459 \[hep-th\]](#) .
- [345] M. S. Marinov and V. S. Popov, “Pair production in electromagnetic field (case of arbitrary spin),” *Yad. Fiz.* **15**, 1271 (1972).
- [346] D. Karabali, S. Kurkcuoglu, and V. P. Nair, “Magnetic Field and Curvature Effects on Pair Production II: Vectors and Implications for Chromodynamics,” *Phys. Rev. D* **100**, 065006 (2019), [arXiv:1905.12391 \[hep-th\]](#) .
- [347] V. Schanbacher, “Gluon Propagator and Effective Lagrangian in QCD,” *Phys. Rev.* **D26**, 489 (1982).
- [348] E. M. Ilgenfritz, M. Kalinowski, M. Muller-Preussker, B. Petersson, and A. Schreiber, “Two-color QCD with staggered fermions at finite temperature under the influence of a magnetic field,” *Phys. Rev.* **D85**, 114504 (2012), [arXiv:1203.3360 \[hep-lat\]](#) .
- [349] E. M. Ilgenfritz, M. Muller-Preussker, B. Petersson, and A. Schreiber, “Magnetic catalysis (and inverse catalysis) at finite temperature in two-color lattice QCD,” *Phys. Rev.* **D89**, 054512 (2014), [arXiv:1310.7876 \[hep-lat\]](#) .
- [350] G. S. Bali, F. Bruckmann, G. Endrodi, F. Gruber, and A. Schaefer, “Magnetic field-induced gluonic (inverse) catalysis and pressure (an)isotropy in QCD,” *JHEP* **04**, 130 (2013), [arXiv:1303.1328 \[hep-lat\]](#) .
- [351] C. Bonati, M. D’Elia, M. Mariti, M. Mesiti, F. Negro, and F. Sanfilippo, “Anisotropy of the quark-antiquark potential in a magnetic field,” *Phys. Rev.* **D89**, 114502 (2014), [arXiv:1403.6094 \[hep-lat\]](#) .
- [352] M. D’Elia, E. Meggiolaro, M. Mesiti, and F. Negro, “Gauge-invariant field-strength correlators for QCD in a magnetic background,” *Phys. Rev.* **D93**, 054017 (2016), [arXiv:1510.07012 \[hep-lat\]](#) .

- [353] M. Chernodub, “Superconductivity of QCD vacuum in strong magnetic field,” *Phys. Rev. D* **82**, 085011 (2010), [arXiv:1008.1055 \[hep-ph\]](#) .
- [354] M. Chernodub, “Spontaneous electromagnetic superconductivity of vacuum in strong magnetic field: evidence from the Nambu–Jona-Lasinio model,” *Phys. Rev. Lett.* **106**, 142003 (2011), [arXiv:1101.0117 \[hep-ph\]](#) .
- [355] V. Braguta, P. Buividovich, M. Chernodub, A. Kotov, and M. Polikarpov, “Electromagnetic superconductivity of vacuum induced by strong magnetic field: numerical evidence in lattice gauge theory,” *Phys. Lett. B* **718**, 667 (2012), [arXiv:1104.3767 \[hep-lat\]](#) .
- [356] Y. Hidaka and A. Yamamoto, “Charged vector mesons in a strong magnetic field,” *Phys. Rev. D* **87**, 094502 (2013), [arXiv:1209.0007 \[hep-ph\]](#) .
- [357] E. V. Luschevskaya, O. A. Kochetkov, O. V. Teryaev, and O. E. Solovjeva, “ π^\pm and $\rho^{0,\pm}$ mesons in a strong magnetic field on the lattice,” *JETP Lett.* **101**, 674 (2015).
- [358] E. V. Luschevskaya, O. E. Solovjeva, and O. V. Teryaev, “Determination of the properties of vector mesons in external magnetic field by Quenched $SU(3)$ Lattice QCD,” *JHEP* **09**, 142 (2017), [JHEP09,142(2017)], [arXiv:1608.03472 \[hep-lat\]](#) .
- [359] G. S. Bali, B. B. Brandt, G. Endrodi, and B. Glaesle, “Meson masses in electromagnetic fields with Wilson fermions,” *Phys. Rev. D* **97**, 034505 (2018), [arXiv:1707.05600 \[hep-lat\]](#) .
- [360] H. Leutwyler, “Constant Gauge Fields and their Quantum Fluctuations,” *Nucl. Phys.* **B179**, 129 (1981).
- [361] V. Weisskopf, “On the Self-Energy and the Electromagnetic Field of the Electron,” *Phys. Rev.* **56**, 72 (1939).
- [362] S. R. Coleman and D. J. Gross, “Price of asymptotic freedom,” *Phys. Rev. Lett.* **31**, 851 (1973).
- [363] D. J. Gross, R. D. Pisarski, and L. G. Yaffe, “QCD and Instantons at Finite Temperature,” *Rev. Mod. Phys.* **53**, 43 (1981).
- [364] N. Weiss, “The Effective Potential for the Order Parameter of Gauge Theories at Finite Temperature,” *Phys. Rev.* **D24**, 475 (1981).
- [365] N. Weiss, “The Wilson Line in Finite Temperature Gauge Theories,” *Phys. Rev.* **D25**, 2667 (1982).
- [366] E. W. Weisstein, “Bernoulli polynomial,” [From MathWorld—A Wolfram Web Resource. http://mathworld.wolfram.com/BernoulliPolynomial.html](http://mathworld.wolfram.com/BernoulliPolynomial.html) ().
- [367] F. Bruckmann, G. Endrodi, and T. G. Kovacs, “Inverse magnetic catalysis and the Polyakov loop,” *JHEP* **04**, 112 (2013), [arXiv:1303.3972 \[hep-lat\]](#) .
- [368] G. Endrodi, “Critical point in the QCD phase diagram for extremely strong background magnetic fields,” *JHEP* **07**, 173 (2015), [arXiv:1504.08280 \[hep-lat\]](#) .
- [369] J. Bardeen, L. N. Cooper, and J. R. Schrieffer, “Theory of superconductivity,” *Phys. Rev.* **108**, 1175 (1957).
- [370] J. Kondo, “Resistance minimum in dilute magnetic alloys,” *Progress of theoretical physics* **32**, 37 (1964).

- [371] S. P. Klevansky and R. H. Lemmer, “Chiral symmetry restoration in the Nambu-Jona-Lasinio model with a constant electromagnetic field,” *Phys. Rev.* **D39**, 3478 (1989).
- [372] S. P. Klevansky, J. Janicke, and R. H. Lemmer, “Collective modes of the Nambu-Jona-Lasinio model with an external U(1) gauge field,” *Phys. Rev.* **D43**, 3040 (1991).
- [373] S. P. Klevansky, “The Nambu-Jona-Lasinio model of quantum chromodynamics,” *Rev. Mod. Phys.* **64**, 649 (1992).
- [374] H. Suganuma and T. Tatsumi, “Manifestation of chiral symmetry and the effective potential in a strong color electromagnetic field,” *Phys. Lett.* **B269**, 371 (1991).
- [375] H. Suganuma and T. Tatsumi, “On the Behavior of Symmetry and Phase Transitions in a Strong Electromagnetic Field,” *Annals Phys.* **208**, 470 (1991).
- [376] S. Schramm, B. Muller, and A. J. Schramm, “Quark - anti-quark condensates in strong magnetic fields,” *Mod. Phys. Lett.* **A7**, 973 (1992).
- [377] K. Hattori, K. Itakura, S. Ozaki, and S. Yasui, “QCD Kondo effect: quark matter with heavy-flavor impurities,” *Phys. Rev.* **D92**, 065003 (2015), [arXiv:1504.07619 \[hep-ph\]](#) .
- [378] J. Polchinski, in *Theoretical Advanced Study Institute (TASI 92): From Black Holes and Strings to Particles Boulder, Colorado, June 3-28, 1992* (1992) pp. 0235–276, [arXiv:hep-th/9210046 \[hep-th\]](#) .
- [379] M. Stone, *The Physics of Quantum Fields* (Springer).
- [380] A. C. Hewson, *The Kondo problem to heavy fermions* (Cambridge university press, 1997).
- [381] P. Anderson, “A poor man’s derivation of scaling laws for the kondo problem,” *Journal of Physics C: Solid State Physics* **3**, 2436 (1970).
- [382] D. K. Hong, “An Effective field theory of QCD at high density,” *Phys. Lett.* **B473**, 118 (2000), [arXiv:hep-ph/9812510 \[hep-ph\]](#) .
- [383] D. K. Hong, “Aspects of high density effective theory in QCD,” *Nucl. Phys.* **B582**, 451 (2000), [arXiv:hep-ph/9905523 \[hep-ph\]](#) .
- [384] D. K. Hong, “High density effective theory of QCD,” *Superdense QCD matter and compact stars. Proceedings, NATO Advanced Research Workshop, Erevan, Armenia, September 27-October 4, 2003*, *Prog. Theor. Phys. Suppl.* **153**, 241 (2004), [165(2004)], [arXiv:hep-ph/0401057 \[hep-ph\]](#) .
- [385] R. Casalbuoni, R. Gatto, and G. Nardulli, “Dispersion laws for in-medium fermions and gluons in the CFL phase of QCD,” *Phys. Lett.* **B498**, 179 (2001), [Erratum: *Phys. Lett.*B517,483(2001)], [arXiv:hep-ph/0010321 \[hep-ph\]](#) .
- [386] S. R. Beane, P. F. Bedaque, and M. J. Savage, “Meson masses in high density QCD,” *Phys. Lett.* **B483**, 131 (2000), [arXiv:hep-ph/0002209 \[hep-ph\]](#) .
- [387] G. Nardulli, “Effective description of QCD at very high densities,” *Riv. Nuovo Cim.* **25N3**, 1 (2002), [Riv. Nuovo Cim.25,031(2002)], [arXiv:hep-ph/0202037 \[hep-ph\]](#) .
- [388] T. Schafer, “Hard loops, soft loops, and high density effective field theory,” *Nucl. Phys.* **A728**, 251 (2003), [arXiv:hep-ph/0307074 \[hep-ph\]](#) .

- [389] K. Hattori, X.-G. Huang, and R. D. Pisarski, “Emergent QCD Kondo effect in two-flavor color superconducting phase,” *Phys. Rev.* **D99**, 094044 (2019), [arXiv:1903.10953 \[hep-ph\]](#) .
- [390] N. J. Evans, S. D. H. Hsu, and M. Schwetz, “An Effective field theory approach to color superconductivity at high quark density,” *Nucl. Phys.* **B551**, 275 (1999), [arXiv:hep-ph/9808444 \[hep-ph\]](#) .
- [391] N. J. Evans, S. D. H. Hsu, and M. Schwetz, “Nonperturbative couplings and color superconductivity,” *Phys. Lett.* **B449**, 281 (1999), [arXiv:hep-ph/9810514 \[hep-ph\]](#) .
- [392] T. Schafer and F. Wilczek, “High density quark matter and the renormalization group in QCD with two and three flavors,” *Phys. Lett.* **B450**, 325 (1999), [arXiv:hep-ph/9810509 \[hep-ph\]](#) .
- [393] D. T. Son, “Superconductivity by long range color magnetic interaction in high density quark matter,” *Phys. Rev.* **D59**, 094019 (1999), [arXiv:hep-ph/9812287 \[hep-ph\]](#) .
- [394] S. D. H. Hsu and M. Schwetz, “Magnetic interactions, the renormalization group and color superconductivity in high density QCD,” *Nucl. Phys.* **B572**, 211 (2000), [arXiv:hep-ph/9908310 \[hep-ph\]](#) .
- [395] D. K. Hong, Y. Kim, and S.-J. Sin, “RG analysis of magnetic catalysis in dynamical symmetry breaking,” *Phys. Rev.* **D54**, 7879 (1996), [arXiv:hep-th/9603157 \[hep-th\]](#) .
- [396] D. K. Hong, “Magnetic catalysis in quantum electrodynamics,” *Phys. Rev.* **D57**, 3759 (1998), [arXiv:hep-ph/9707432 \[hep-ph\]](#) .
- [397] A. V. Manohar and M. B. Wise, “Heavy quark physics,” *Camb. Monogr. Part. Phys. Nucl. Phys. Cosmol.* **10**, 1 (2000).
- [398] T. Iritani, G. Cossu, and S. Hashimoto, “Partial restoration of chiral symmetry in the color flux tube,” *Phys. Rev.* **D91**, 094501 (2015), [arXiv:1502.04845 \[hep-lat\]](#) .
- [399] V. P. Gusynin, V. A. Miransky, and I. A. Shovkovy, “Catalysis of dynamical flavor symmetry breaking by a magnetic field in (2+1)-dimensions,” *Phys. Rev. Lett.* **73**, 3499 (1994), [Erratum: *Phys. Rev. Lett.* 76,1005(1996)], [arXiv:hep-ph/9405262 \[hep-ph\]](#) .
- [400] V. P. Gusynin, V. A. Miransky, and I. A. Shovkovy, “Dynamical flavor symmetry breaking by a magnetic field in (2+1)-dimensions,” *Phys. Rev.* **D52**, 4718 (1995), [arXiv:hep-th/9407168 \[hep-th\]](#) .
- [401] V. A. Miransky, “Catalysis of dynamical symmetry breaking by a magnetic field,” *From the standard model to grand unified theories. Proceedings, 6th Yukawa International Seminar, YKIS’95, Kyoto, Japan, August 21-25, 1995*, *Prog. Theor. Phys. Suppl.* **123**, 49 (1996), [arXiv:hep-th/9511224 \[hep-th\]](#) .
- [402] I. A. Shovkovy, “Magnetic Catalysis: A Review,” *Lect. Notes Phys.* **871**, 13 (2013), [arXiv:1207.5081 \[hep-ph\]](#) .
- [403] D. D. Scherer and H. Gies, “Renormalization Group Study of Magnetic Catalysis in the 3d Gross-Neveu Model,” *Phys. Rev.* **B85**, 195417 (2012), [arXiv:1201.3746 \[cond-mat.str-el\]](#) .
- [404] K. Hattori, K. Itakura, and S. Ozaki, “Anatomy of the magnetic catalysis by renormalization-group method,” *Phys. Lett.* **B775**, 283 (2017), [arXiv:1706.04913 \[hep-ph\]](#) .

- [405] Y. Nambu and G. Jona-Lasinio, “Dynamical Model of Elementary Particles Based on an Analogy with Superconductivity. 1.” *Phys. Rev.* **122**, 345 (1961), [,127(1961)].
- [406] Y. Nambu and G. Jona-Lasinio, “Dynamical model of elementary particles based on an analogy with superconductivity. ii,” *Phys. Rev.* **124**, 246 (1961), [,141(1961)].
- [407] V. P. Gusynin, V. A. Miransky, and I. A. Shovkovy, “Dynamical chiral symmetry breaking in QED in a magnetic field: Toward exact results,” *Phys. Rev. Lett.* **83**, 1291 (1999), [arXiv:hep-th/9811079 \[hep-th\]](#) .
- [408] V. P. Gusynin, V. A. Miransky, and I. A. Shovkovy, “Theory of the magnetic catalysis of chiral symmetry breaking in QED,” *Nucl. Phys.* **B563**, 361 (1999), [arXiv:hep-ph/9908320 \[hep-ph\]](#) .
- [409] K. Fukushima, K. Hattori, H.-U. Yee, and Y. Yin, “Heavy Quark Diffusion in Strong Magnetic Fields at Weak Coupling and Implications for Elliptic Flow,” *Phys. Rev.* **D93**, 074028 (2016), [arXiv:1512.03689 \[hep-ph\]](#) .
- [410] V. P. Gusynin, V. A. Miransky, and I. A. Shovkovy, “Large N dynamics in QED in a magnetic field,” *Phys. Rev.* **D67**, 107703 (2003), [arXiv:hep-ph/0304059 \[hep-ph\]](#) .
- [411] C. N. Leung, Y. J. Ng, and A. W. Ackley, “Schwinger-Dyson equation approach to chiral symmetry breaking in an external magnetic field,” *Phys. Rev.* **D54**, 4181 (1996), [arXiv:hep-th/9512114 \[hep-th\]](#) .
- [412] J. Kondo, “Resistance Minimum in Dilute Magnetic Alloys,” *Prog. Theor. Phys.* **32**, 37 (1964).
- [413] S. Yasui and K. Sudoh, “Heavy-quark dynamics for charm and bottom flavor on the Fermi surface at zero temperature,” *Phys. Rev.* **C88**, 015201 (2013), [arXiv:1301.6830 \[hep-ph\]](#) .
- [414] S. Yasui, “Kondo Effect in Dense Matter,” *Proceedings, Workshop on Quarks and Compact Stars (QCS2017): Kyoto, Japan, February 19-22, 2017*, *JPS Conf. Proc.* **20**, 011011 (2018).
- [415] S. Yasui and S. Ozaki, “Transport coefficients from the QCD Kondo effect,” *Phys. Rev.* **D96**, 114027 (2017), [arXiv:1710.03434 \[hep-ph\]](#) .
- [416] N. Andrei, “Diagonalization of the Kondo Hamiltonian,” *Phys. Rev. Lett.* **45**, 379 (1980).
- [417] P. Wiegmann, “Diagonalization of the Kondo Hamiltonian,” *ETP. Lett.* **31**, 364 (1980).
- [418] I. Affleck and A. W. W. Ludwig, “Critical theory of overscreened Kondo fixed points,” *Nucl. Phys.* **B360**, 641 (1991).
- [419] I. Affleck, “Conformal field theory approach to the Kondo effect,” *Bosonization and conformal field theories in high-energy and condensed matter physics. Proceedings, 35th Cracow School of Theoretical Physics, Zakopane, Poland, June 4-14, 1995*, *Acta Phys. Polon.* **B26**, 1869 (1995), [arXiv:cond-mat/9512099 \[cond-mat\]](#) .
- [420] T. Kanazawa and S. Uchino, “Overscreened Kondo effect, (color) superconductivity and Shiba states in Dirac metals and quark matter,” *Phys. Rev.* **D94**, 114005 (2016), [arXiv:1609.00033 \[cond-mat.str-el\]](#) .
- [421] T. Kimura and S. Ozaki, “Fermi/non-Fermi mixing in $SU(N)$ Kondo effect,” *J. Phys. Soc. Jap.* **86**, 084703 (2017), [arXiv:1611.07284 \[cond-mat.str-el\]](#) .

- [422] T. Kimura and S. Ozaki, “Conformal field theory analysis of the QCD Kondo effect,” *Phys. Rev. D* **99**, 014040 (2019), [arXiv:1806.06486 \[hep-ph\]](#) .
- [423] T. Kimura, “ABCD of Kondo effect,” *J. Phys. Soc. Jpn.* **90**, 024708 (2021), [arXiv:2011.08301 \[cond-mat.str-el\]](#) .
- [424] S. Yasui, K. Suzuki, and K. Itakura, “Kondo phase diagram of quark matter,” *Nucl. Phys. A* **983**, 90 (2019), [arXiv:1604.07208 \[hep-ph\]](#) .
- [425] S. Yasui, “Kondo cloud of single heavy quark in cold and dense matter,” *Phys. Lett. B* **773**, 428 (2017), [arXiv:1608.06450 \[hep-ph\]](#) .
- [426] S. Yasui, K. Suzuki, and K. Itakura, “Topology and stability of the Kondo phase in quark matter,” *Phys. Rev. D* **96**, 014016 (2017), [arXiv:1703.04124 \[hep-ph\]](#) .
- [427] K. Suzuki, S. Yasui, and K. Itakura, “Interplay between chiral symmetry breaking and the QCD Kondo effect,” *Phys. Rev. D* **96**, 114007 (2017), [arXiv:1708.06930 \[hep-ph\]](#) .
- [428] R. Fariello, J. C. Macías, and F. S. Navarra, “The QCD Kondo phase in quark stars,” (2019), [arXiv:1901.01623 \[nucl-th\]](#) .
- [429] D. Suenaga, K. Suzuki, and S. Yasui, “QCD Kondo excitons,” *Phys. Rev. Research* **2**, 023066 (2020), [arXiv:1909.07573 \[nucl-th\]](#) .
- [430] D. Suenaga, K. Suzuki, Y. Araki, and S. Yasui, “Kondo effect driven by chirality imbalance,” *Phys. Rev. Research* **2**, 023312 (2020), [arXiv:1912.12669 \[hep-ph\]](#) .
- [431] T. Kanazawa, “Random matrix model for the QCD Kondo effect,” (2020), [arXiv:2006.00200 \[hep-th\]](#) .
- [432] Y. Araki, D. Suenaga, K. Suzuki, and S. Yasui, “Two relativistic Kondo effects: Classification with particle and antiparticle impurities,” *Phys. Rev. Research* **3**, 013233 (2021), [arXiv:2008.08434 \[hep-ph\]](#) .
- [433] Y. Araki, D. Suenaga, K. Suzuki, and S. Yasui, “Spin-orbital magnetic response of relativistic fermions with band hybridization,” *Phys. Rev. Research* **3**, 023098 (2021), [arXiv:2011.00882 \[cond-mat.mes-hall\]](#) .
- [434] D. Suenaga, Y. Araki, K. Suzuki, and S. Yasui, “Chiral separation effect catalyzed by heavy impurities,” *Phys. Rev. D* **103**, 054041 (2021), [arXiv:2012.15173 \[hep-ph\]](#) .
- [435] T. Ishikawa, K. Nakayama, and K. Suzuki, “Kondo effect with Wilson fermions,” *Phys. Rev. D* **104**, 094515 (2021), [arXiv:2107.07270 \[hep-lat\]](#) .
- [436] D. Suenaga, Y. Araki, K. Suzuki, and S. Yasui, “Heavy-quark spin polarization induced by the Kondo effect in a magnetic field,” *Phys. Rev. D* **105**, 074028 (2022), [arXiv:2109.14799 \[hep-ph\]](#) .
- [437] V. A. Miransky and I. A. Shovkovy, “Magnetic catalysis and anisotropic confinement in QCD,” *Phys. Rev. D* **66**, 045006 (2002), [arXiv:hep-ph/0205348 \[hep-ph\]](#) .
- [438] K. Hattori, D. Suenaga, K. Suzuki, and S. Yasui, “Dirac Kondo effect under magnetic catalysis,” (2022), [arXiv:2211.16150 \[hep-ph\]](#) .
- [439] I. A. Shushpanov and A. V. Smilga, “Quark condensate in a magnetic field,” *Phys. Lett.* **B402**, 351 (1997), [arXiv:hep-ph/9703201 \[hep-ph\]](#) .

- [440] N. O. Agasian and I. A. Shushpanov, “The Quark and gluon condensates and low-energy QCD theorems in a magnetic field,” *Phys. Lett.* **B472**, 143 (2000), [arXiv:hep-ph/9911254 \[hep-ph\]](#) .
- [441] N. O. Agasian, “Phase structure of the QCD vacuum in a magnetic field at low temperature,” *Phys. Lett.* **B488**, 39 (2000), [arXiv:hep-ph/0005300 \[hep-ph\]](#) .
- [442] N. O. Agasian and I. A. Shushpanov, “Gell-Mann-Oakes-Renner relation in a magnetic field at finite temperature,” *JHEP* **10**, 006 (2001), [arXiv:hep-ph/0107128 \[hep-ph\]](#) .
- [443] N. O. Agasian, “Chiral thermodynamics in a magnetic field,” *Phys. Atom. Nucl.* **64**, 554 (2001), [*Yad. Fiz.*64,608(2001)], [arXiv:hep-ph/0112341 \[hep-ph\]](#) .
- [444] T. D. Cohen, D. A. McGady, and E. S. Werbos, “The Chiral condensate in a constant electromagnetic field,” *Phys. Rev.* **C76**, 055201 (2007), [arXiv:0706.3208 \[hep-ph\]](#) .
- [445] E. S. Werbos, “The Chiral condensate in a constant electromagnetic field at $O(p^{**6})$,” *Phys. Rev.* **C 77**, 065202 (2008), [arXiv:0711.2635 \[hep-ph\]](#) .
- [446] N. O. Agasian and S. M. Fedorov, “Quark-hadron phase transition in a magnetic field,” *Phys. Lett.* **B663**, 445 (2008), [arXiv:0803.3156 \[hep-ph\]](#) .
- [447] J. O. Andersen, “Thermal pions in a magnetic background,” *Phys. Rev.* **D86**, 025020 (2012), [arXiv:1202.2051 \[hep-ph\]](#) .
- [448] J. O. Andersen, “Chiral perturbation theory in a magnetic background - finite-temperature effects,” *JHEP* **10**, 005 (2012), [arXiv:1205.6978 \[hep-ph\]](#) .
- [449] A. Yu. Babansky, E. V. Gorbar, and G. V. Shchepanyuk, “Chiral symmetry breaking in the Nambu-Jona-Lasinio model in external constant electromagnetic field,” *Phys. Lett.* **B419**, 272 (1998), [arXiv:hep-th/9705218 \[hep-th\]](#) .
- [450] D. Ebert, K. G. Klimenko, M. A. Vdovichenko, and A. S. Vshivtsev, “Magnetic oscillations in dense cold quark matter with four fermion interactions,” *Phys. Rev.* **D61**, 025005 (2000), [arXiv:hep-ph/9905253 \[hep-ph\]](#) .
- [451] T. Inagaki, D. Kimura, and T. Murata, “Four fermion interaction model in a constant magnetic field at finite temperature and chemical potential,” *Prog. Theor. Phys.* **111**, 371 (2004), [arXiv:hep-ph/0312005 \[hep-ph\]](#) .
- [452] E. S. Fraga and A. J. Mizher, “Chiral transition in a strong magnetic background,” *Phys. Rev.* **D78**, 025016 (2008), [arXiv:0804.1452 \[hep-ph\]](#) .
- [453] K. G. Klimenko and V. C. Zhukovsky, “Does there arise a significant enhancement of the dynamical quark mass in a strong magnetic field?” *Phys. Lett.* **B665**, 352 (2008), [arXiv:0803.2191 \[hep-ph\]](#) .
- [454] D. P. Menezes, M. Benghi Pinto, S. S. Avancini, and C. Providencia, “Quark matter under strong magnetic fields in the SU(3) Nambu-Jona-Lasinio Model,” *Phys. Rev.* **C80**, 065805 (2009), [arXiv:0907.2607 \[nucl-th\]](#) .
- [455] J. K. Boomsma and D. Boer, “The Influence of strong magnetic fields and instantons on the phase structure of the two-flavor NJL model,” *Phys. Rev.* **D81**, 074005 (2010), [arXiv:0911.2164 \[hep-ph\]](#) .

- [456] S. Fayazbakhsh and N. Sadooghi, “Phase diagram of hot magnetized two-flavor color superconducting quark matter,” *Phys. Rev.* **D83**, 025026 (2011), [arXiv:1009.6125 \[hep-ph\]](#) .
- [457] K. Fukushima, M. Ruggieri, and R. Gatto, “Chiral magnetic effect in the PNJL model,” *Phys. Rev.* **D81**, 114031 (2010), [arXiv:1003.0047 \[hep-ph\]](#) .
- [458] R. Gatto and M. Ruggieri, “Dressed Polyakov loop and phase diagram of hot quark matter under magnetic field,” *Phys. Rev.* **D82**, 054027 (2010), [arXiv:1007.0790 \[hep-ph\]](#) .
- [459] A. J. Mizher, M. N. Chernodub, and E. S. Fraga, “Phase diagram of hot QCD in an external magnetic field: possible splitting of deconfinement and chiral transitions,” *Phys. Rev.* **D82**, 105016 (2010), [arXiv:1004.2712 \[hep-ph\]](#) .
- [460] R. Gatto and M. Ruggieri, “Deconfinement and Chiral Symmetry Restoration in a Strong Magnetic Background,” *Phys. Rev.* **D83**, 034016 (2011), [arXiv:1012.1291 \[hep-ph\]](#) .
- [461] S.-i. Nam and C.-W. Kao, “Chiral restoration at finite T under the magnetic field with the meson-loop corrections,” *Phys. Rev.* **D83**, 096009 (2011), [arXiv:1103.6057 \[hep-ph\]](#) .
- [462] V. Skokov, “Phase diagram in an external magnetic field beyond a mean-field approximation,” *Phys. Rev.* **D85**, 034026 (2012), [arXiv:1112.5137 \[hep-ph\]](#) .
- [463] K. Kashiwa, “Entanglement between chiral and deconfinement transitions under strong uniform magnetic background field,” *Phys. Rev.* **D83**, 117901 (2011), [arXiv:1104.5167 \[hep-ph\]](#) .
- [464] B. Chatterjee, H. Mishra, and A. Mishra, “Vacuum structure and chiral symmetry breaking in strong magnetic fields for hot and dense quark matter,” *Phys. Rev.* **D84**, 014016 (2011), [arXiv:1101.0498 \[hep-ph\]](#) .
- [465] S. S. Avancini, D. P. Menezes, M. B. Pinto, and C. Providencia, “The QCD Critical End Point Under Strong Magnetic Fields,” *Phys. Rev.* **D85**, 091901 (2012), [arXiv:1202.5641 \[hep-ph\]](#) .
- [466] J. O. Andersen and A. A. Cruz, “Two-color QCD in a strong magnetic field: The role of the Polyakov loop,” *Phys. Rev.* **D88**, 025016 (2013), [arXiv:1211.7293 \[hep-ph\]](#) .
- [467] G. N. Ferrari, A. F. Garcia, and M. B. Pinto, “Chiral Transition Within Effective Quark Models Under Magnetic Fields,” *Phys. Rev.* **D86**, 096005 (2012), [arXiv:1207.3714 \[hep-ph\]](#) .
- [468] E. S. Fraga, J. Noronha, and L. F. Palhares, “Large N_c Deconfinement Transition in the Presence of a Magnetic Field,” *Phys. Rev.* **D87**, 114014 (2013), [arXiv:1207.7094 \[hep-ph\]](#) .
- [469] E. S. Fraga and L. F. Palhares, “Deconfinement in the presence of a strong magnetic background: an exercise within the MIT bag model,” *Phys. Rev.* **D86**, 016008 (2012), [arXiv:1201.5881 \[hep-ph\]](#) .
- [470] M. Ruggieri, M. Tachibana, and V. Greco, “Renormalized vs Nonrenormalized Chiral Transition in a Magnetic Background,” *JHEP* **07**, 165 (2013), [arXiv:1305.0137 \[hep-ph\]](#) .
- [471] E. S. Fraga, B. W. Mintz, and J. Schaffner-Bielich, “A search for inverse magnetic catalysis in thermal quark-meson models,” *Phys. Lett.* **B731**, 154 (2014), [arXiv:1311.3964 \[hep-ph\]](#) .
- [472] J. O. Andersen, W. R. Naylor, and A. Tranberg, “Chiral and deconfinement transitions in a magnetic background using the functional renormalization group with the Polyakov loop,” *JHEP* **04**, 187 (2014), [arXiv:1311.2093 \[hep-ph\]](#) .

- [473] P. G. Allen and N. N. Scoccola, “Quark matter under strong magnetic fields in SU(2) NJL-type models: parameter dependence of the cold dense matter phase diagram,” *Phys. Rev.* **D88**, 094005 (2013), [arXiv:1309.2258 \[hep-ph\]](#) .
- [474] M. Ferreira, P. Costa, and C. Providencia, “Deconfinement, chiral symmetry restoration and thermodynamics of (2+1)-flavor hot QCD matter in an external magnetic field,” *Phys. Rev.* **D89**, 036006 (2014), [arXiv:1312.6733 \[hep-ph\]](#) .
- [475] K. Kamikado and T. Kanazawa, “Chiral dynamics in a magnetic field from the functional renormalization group,” *JHEP* **03**, 009 (2014), [arXiv:1312.3124 \[hep-ph\]](#) .
- [476] M. Ferreira, P. Costa, O. Lourenco, T. Frederico, and C. Providencia, “Inverse magnetic catalysis in the (2+1)-flavor Nambu-Jona-Lasinio and Polyakov-Nambu-Jona-Lasinio models,” *Phys. Rev.* **D89**, 116011 (2014), [arXiv:1404.5577 \[hep-ph\]](#) .
- [477] S. Fayazbakhsh and N. Sadooghi, “Anomalous magnetic moment of hot quarks, inverse magnetic catalysis, and reentrance of the chiral symmetry broken phase,” *Phys. Rev.* **D90**, 105030 (2014), [arXiv:1408.5457 \[hep-ph\]](#) .
- [478] J. O. Andersen, W. R. Naylor, and A. Tranberg, “Inverse magnetic catalysis and regularization in the quark-meson model,” *JHEP* **02**, 042 (2015), [arXiv:1410.5247 \[hep-ph\]](#) .
- [479] F. Preis, A. Rebhan, and A. Schmitt, “Inverse magnetic catalysis in dense holographic matter,” *JHEP* **03**, 033 (2011), [arXiv:1012.4785 \[hep-th\]](#) .
- [480] J. Erdmenger, V. G. Filev, and D. Zoakos, “Magnetic Catalysis with Massive Dynamical Flavours,” *JHEP* **08**, 004 (2012), [arXiv:1112.4807 \[hep-th\]](#) .
- [481] K. A. Mamo, “Inverse magnetic catalysis in holographic models of QCD,” *JHEP* **05**, 121 (2015), [arXiv:1501.03262 \[hep-th\]](#) .
- [482] M. D’Elia, “Lattice QCD Simulations in External Background Fields,” *Lect. Notes Phys.* **871**, 181 (2013), [arXiv:1209.0374 \[hep-lat\]](#) .
- [483] F. Preis, A. Rebhan, and A. Schmitt, “Inverse magnetic catalysis in field theory and gauge-gravity duality,” *Lect. Notes Phys.* **871**, 51 (2013), [arXiv:1208.0536 \[hep-ph\]](#) .
- [484] E. S. Fraga, “Thermal chiral and deconfining transitions in the presence of a magnetic background,” *Lect. Notes Phys.* **871**, 121 (2013), [arXiv:1208.0917 \[hep-ph\]](#) .
- [485] R. Gatto and M. Ruggieri, “Quark Matter in a Strong Magnetic Background,” *Lect. Notes Phys.* **871**, 87 (2013), [arXiv:1207.3190 \[hep-ph\]](#) .
- [486] J. O. Andersen, “QCD phase diagram in a constant magnetic background: Inverse magnetic catalysis: where models meet the lattice,” *Eur. Phys. J. A* **57**, 189 (2021), [arXiv:2102.13165 \[hep-ph\]](#) .
- [487] G. S. Bali, F. Bruckmann, G. Endrodi, Z. Fodor, S. D. Katz, and A. Schafer, “QCD quark condensate in external magnetic fields,” *Phys. Rev.* **D86**, 071502 (2012), [arXiv:1206.4205 \[hep-lat\]](#) .
- [488] P. V. Buividovich, M. N. Chernodub, E. V. Luschevskaya, and M. I. Polikarpov, “Numerical study of chiral symmetry breaking in non-Abelian gauge theory with background magnetic field,” *Phys. Lett.* **B682**, 484 (2010), [arXiv:0812.1740 \[hep-lat\]](#) .

- [489] P. Cea and L. Cosmai, “Color dynamics in external fields,” *JHEP* **08**, 079 (2005), [arXiv:hep-lat/0505007](#) .
- [490] P. Cea, L. Cosmai, and M. D’Elia, “QCD dynamics in a constant chromomagnetic field,” *JHEP* **12**, 097 (2007), [arXiv:0707.1149 \[hep-lat\]](#) .
- [491] V. V. Braguta, P. V. Buividovich, T. Kalaydzhyan, S. V. Kuznetsov, and M. I. Polikarpov, “The Chiral Magnetic Effect and chiral symmetry breaking in SU(3) quenched lattice gauge theory,” *Phys. Atom. Nucl.* **75**, 488 (2012), [arXiv:1011.3795 \[hep-lat\]](#) .
- [492] M. D’Elia, S. Mukherjee, and F. Sanfilippo, “QCD Phase Transition in a Strong Magnetic Background,” *Phys. Rev.* **D82**, 051501 (2010), [arXiv:1005.5365 \[hep-lat\]](#) .
- [493] M. D’Elia and F. Negro, “Chiral Properties of Strong Interactions in a Magnetic Background,” *Phys. Rev.* **D83**, 114028 (2011), [arXiv:1103.2080 \[hep-lat\]](#) .
- [494] M. D’Elia, L. Maio, F. Sanfilippo, and A. Stanzione, “Confining and chiral properties of QCD in extremely strong magnetic fields,” *Phys. Rev. D* **104**, 114512 (2021), [arXiv:2109.07456 \[hep-lat\]](#) .
- [495] G. S. Bali, F. Bruckmann, G. Endrodi, Z. Fodor, S. D. Katz, S. Krieg, A. Schafer, and K. K. Szabo, “The QCD phase diagram for external magnetic fields,” *JHEP* **02**, 044 (2012), [arXiv:1111.4956 \[hep-lat\]](#) .
- [496] G. S. Bali *et al.*, “Thermodynamic properties of QCD in external magnetic fields,” *Proceedings, 10th Conference on Quark Confinement and the Hadron Spectrum (Confinement X): Munich, Germany, October 8-12, 2012*, PoS **ConfinementX**, 197 (2012), [arXiv:1301.5826 \[hep-lat\]](#) .
- [497] Y. Aoki, Z. Fodor, S. D. Katz, and K. K. Szabo, “The QCD transition temperature: Results with physical masses in the continuum limit,” *Phys. Lett. B* **643**, 46 (2006), [arXiv:hep-lat/0609068](#) .
- [498] Y. Aoki, S. Borsanyi, S. Durr, Z. Fodor, S. D. Katz, S. Krieg, and K. K. Szabo, “The QCD transition temperature: results with physical masses in the continuum limit II.” *JHEP* **06**, 088 (2009), [arXiv:0903.4155 \[hep-lat\]](#) .
- [499] S. Borsanyi, Z. Fodor, C. Hoelbling, S. D. Katz, S. Krieg, C. Ratti, and K. K. Szabo (Wuppertal-Budapest), “Is there still any T_c mystery in lattice QCD? Results with physical masses in the continuum limit III,” *JHEP* **09**, 073 (2010), [arXiv:1005.3508 \[hep-lat\]](#) .
- [500] A. Bazavov *et al.*, “The chiral and deconfinement aspects of the QCD transition,” *Phys. Rev. D* **85**, 054503 (2012), [arXiv:1111.1710 \[hep-lat\]](#) .
- [501] V. G. Bornyakov, P. V. Buividovich, N. Cundy, O. A. Kochetkov, and A. Schefer, “Deconfinement transition in two-flavor lattice QCD with dynamical overlap fermions in an external magnetic field,” *Phys. Rev.* **D90**, 034501 (2014), [arXiv:1312.5628 \[hep-lat\]](#) .
- [502] M. D’Elia, F. Manigrasso, F. Negro, and F. Sanfilippo, “QCD phase diagram in a magnetic background for different values of the pion mass,” *Phys. Rev.* **D98**, 054509 (2018), [arXiv:1808.07008 \[hep-lat\]](#) .
- [503] G. Endrodi, M. Giordano, S. D. Katz, T. G. Kovacs, and F. Pittler, “Magnetic catalysis and inverse catalysis for heavy pions,” *JHEP* **07**, 007 (2019), [arXiv:1904.10296 \[hep-lat\]](#) .
- [504] H.-T. Ding, C. Schmidt, A. Tomiya, and X.-D. Wang, “Chiral phase structure of three flavor QCD in a background magnetic field,” *Phys. Rev. D* **102**, 054505 (2020), [arXiv:2006.13422 \[hep-lat\]](#) .

- [505] C. Bonati, M. D’Elia, M. Mariti, M. Mesiti, F. Negro, A. Rucci, and F. Sanfilippo, “Magnetic field effects on the static quark potential at zero and finite temperature,” *Phys. Rev.* **D94**, 094007 (2016), [arXiv:1607.08160 \[hep-lat\]](#) .
- [506] C. Bonati, M. D’Elia, M. Mariti, M. Mesiti, F. Negro, A. Rucci, and F. Sanfilippo, “Screening masses in strong external magnetic fields,” *Phys. Rev.* **D95**, 074515 (2017), [arXiv:1703.00842 \[hep-lat\]](#) .
- [507] M. D’Elia, L. Maio, F. Sanfilippo, and A. Stanzione, “Phase diagram of QCD in a magnetic background,” *Phys. Rev. D* **105**, 034511 (2022), [arXiv:2111.11237 \[hep-lat\]](#) .
- [508] A. Yamamoto, “Lattice QCD with strong external electric fields,” *Phys. Rev. Lett.* **110**, 112001 (2013), [arXiv:1210.8250 \[hep-lat\]](#) .
- [509] F. Bruckmann, G. Endrodi, M. Giordano, S. D. Katz, T. G. Kovacs, F. Pittler, and J. Wellenhofer, “Landau levels in QCD,” *Phys. Rev.* **D96**, 074506 (2017), [arXiv:1705.10210 \[hep-lat\]](#) .
- [510] H. T. Ding, S. T. Li, J. H. Liu, and X. D. Wang, “Chiral condensates and screening masses of neutral pseudoscalar mesons in thermomagnetic QCD medium,” *Phys. Rev. D* **105**, 034514 (2022), [arXiv:2201.02349 \[hep-lat\]](#) .
- [511] H.-T. Ding, S.-T. Li, S. Mukherjee, A. Tomiya, and X.-D. Wang, in *37th International Symposium on Lattice Field Theory (Lattice 2019) Wuhan, Hubei, China, June 16-22, 2019* (2020) [arXiv:2001.05322 \[hep-lat\]](#) .
- [512] A. Tomiya, H.-T. Ding, S. Mukherjee, C. Schmidt, and X.-D. Wang, “Chiral phase transition of three flavor QCD with nonzero magnetic field using standard staggered fermions,” *EPJ Web Conf.* **175**, 07041 (2018), [arXiv:1711.02884 \[hep-lat\]](#) .
- [513] H. T. Ding, S. T. Li, A. Tomiya, X. D. Wang, and Y. Zhang, “Chiral properties of (2+1)-flavor QCD in strong magnetic fields at zero temperature,” *Phys. Rev. D* **104**, 014505 (2021), [arXiv:2008.00493 \[hep-lat\]](#) .
- [514] C. E. Detar and J. B. Kogut, “The Hadronic Spectrum of the Quark Plasma,” *Phys. Rev. Lett.* **59**, 399 (1987).
- [515] C. E. Detar and J. B. Kogut, “Measuring the Hadronic Spectrum of the Quark Plasma,” *Phys. Rev. D* **36**, 2828 (1987).
- [516] A. Bazavov *et al.*, “Meson screening masses in (2+1)-flavor QCD,” *Phys. Rev. D* **100**, 094510 (2019), [arXiv:1908.09552 \[hep-lat\]](#) .
- [517] M. Dalla Brida, L. Giusti, T. Harris, D. Laudicina, and M. Pepe, “Non-perturbative thermal QCD at all temperatures: the case of mesonic screening masses,” *JHEP* **04**, 034 (2022), [arXiv:2112.05427 \[hep-lat\]](#) .
- [518] T. Kojo and N. Su, “A renormalization group approach for QCD in a strong magnetic field,” *Phys. Lett.* **B726**, 839 (2013), [arXiv:1305.4510 \[hep-ph\]](#) .
- [519] T. D. Cohen and N. Yamamoto, “New critical point for QCD in a magnetic field,” *Phys. Rev.* **D89**, 054029 (2014), [arXiv:1310.2234 \[hep-ph\]](#) .
- [520] L. G. Yaffe and B. Svetitsky, “First Order Phase Transition in the SU(3) Gauge Theory at Finite Temperature,” *Phys. Rev. D* **26**, 963 (1982).

- [521] E. V. Luschevskaya, O. E. Solovjeva, O. A. Kochetkov, and O. V. Teryaev, “Magnetic polarizabilities of light mesons in $SU(3)$ lattice gauge theory,” *Nucl. Phys. B* **898**, 627 (2015), [arXiv:1411.4284 \[hep-lat\]](#) .
- [522] G. Endrodi and G. Markó, “Magnetized baryons and the QCD phase diagram: NJL model meets the lattice,” *JHEP* **08**, 036 (2019), [arXiv:1905.02103 \[hep-lat\]](#) .
- [523] P. V. Buividovich, M. N. Chernodub, D. E. Kharzeev, T. Kalaydzhyan, E. V. Luschevskaya, and M. I. Polikarpov, “Magnetic-Field-Induced insulator-conductor transition in $SU(2)$ quenched lattice gauge theory,” *Phys. Rev. Lett.* **105**, 132001 (2010), [arXiv:1003.2180 \[hep-lat\]](#) .
- [524] S. Fayazbakhsh and N. Sadooghi, “Weak decay constant of neutral pions in a hot and magnetized quark matter,” *Phys. Rev. D* **88**, 065030 (2013), [arXiv:1306.2098 \[hep-ph\]](#) .
- [525] G. S. Bali, B. B. Brandt, G. Endródi, and B. Gläfle, “Weak decay of magnetized pions,” *Phys. Rev. Lett.* **121**, 072001 (2018), [arXiv:1805.10971 \[hep-lat\]](#) .
- [526] K. Hattori and A. Yamamoto, “Meson deformation by magnetic fields in lattice QCD,” *PTEP* **2019**, 043B04 (2019), [arXiv:1901.10182 \[hep-lat\]](#) .
- [527] T. H. Hansson and I. Zahed, “Hadronic correlators in hot QCD,” *Nucl. Phys. B* **374**, 277 (1992).
- [528] V. Koch, E. V. Shuryak, G. E. Brown, and A. D. Jackson, “The Propagation of quarks in the spatial direction in hot QCD,” *Phys. Rev. D* **46**, 3169 (1992), [Erratum: *Phys.Rev.D* 47, 2157 (1993)], [arXiv:hep-ph/9204236](#) .
- [529] M. Ishii and T. Hatsuda, “Hadronic screening masses and the magnetic gluon condensate at high temperature,” *Phys. Lett. B* **338**, 319 (1994), [arXiv:hep-ph/9408209](#) .
- [530] T. H. Hansson, M. Sporre, and I. Zahed, “Baryonic and gluonic correlators in hot QCD,” *Nucl. Phys. B* **427**, 545 (1994), [arXiv:hep-ph/9401281](#) .
- [531] M. Laine and M. Vepsalainen, “Mesonic correlation lengths in high temperature QCD,” *JHEP* **02**, 004 (2004), [arXiv:hep-ph/0311268](#) .
- [532] B. B. Brandt, A. Francis, M. Laine, and H. B. Meyer, “A relation between screening masses and real-time rates,” *JHEP* **05**, 117 (2014), [arXiv:1404.2404 \[hep-ph\]](#) .
- [533] E. Shuryak, “Mesonic ”screening masses” in high temperature QCD,” (2022), [arXiv:2212.11825 \[hep-ph\]](#) .
- [534] D. T. Son and M. A. Stephanov, “Pion propagation near the QCD chiral phase transition,” *Phys. Rev. Lett.* **88**, 202302 (2002), [arXiv:hep-ph/0111100](#) .
- [535] D. T. Son and M. A. Stephanov, “Real time pion propagation in finite temperature QCD,” *Phys. Rev. D* **66**, 076011 (2002), [arXiv:hep-ph/0204226](#) .
- [536] S. Cho, K. Hattori, S. H. Lee, K. Morita, and S. Ozaki, “QCD sum rules for magnetically induced mixing between η_c and J/ψ ,” *Phys. Rev. Lett.* **113**, 172301 (2014), [arXiv:1406.4586 \[hep-ph\]](#) .
- [537] S. Cho, K. Hattori, S. H. Lee, K. Morita, and S. Ozaki, “Charmonium Spectroscopy in Strong Magnetic Fields by QCD Sum Rules: S-Wave Ground States,” *Phys. Rev.* **D91**, 045025 (2015), [arXiv:1411.7675 \[hep-ph\]](#) .

- [538] S. Iwasaki, M. Oka, K. Suzuki, and T. Yoshida, “Hadronic Paschen–Back effect,” *Phys. Lett. B* **790**, 71 (2019), [arXiv:1802.04971 \[hep-ph\]](#) .
- [539] S. Iwasaki and K. Suzuki, “Quarkonium radiative decays from the Hadronic Paschen-Back effect,” *Phys. Rev. D* **98**, 054017 (2018), [arXiv:1805.09787 \[hep-ph\]](#) .
- [540] C. Bonati, S. Cali, M. D’Elia, M. Mesiti, F. Negro, A. Rucci, and F. Sanfilippo, “Effects of a strong magnetic field on the QCD flux tube,” *Phys. Rev. D* **98**, 054501 (2018), [arXiv:1807.01673 \[hep-lat\]](#) .
- [541] M. D’Elia, M. Mariti, and F. Negro, “Susceptibility of the QCD vacuum to CP-odd electromagnetic background fields,” *Phys. Rev. Lett.* **110**, 082002 (2013), [arXiv:1209.0722 \[hep-lat\]](#) .
- [542] C. Bonati, M. D’Elia, M. Mariti, F. Negro, and F. Sanfilippo, “Magnetic Susceptibility of Strongly Interacting Matter across the Deconfinement Transition,” *Phys. Rev. Lett.* **111**, 182001 (2013), [arXiv:1307.8063 \[hep-lat\]](#) .
- [543] C. Bonati, M. D’Elia, M. Mariti, F. Negro, and F. Sanfilippo, “Magnetic susceptibility and equation of state of $N_f = 2 + 1$ QCD with physical quark masses,” *Phys. Rev.* **D89**, 054506 (2014), [arXiv:1310.8656 \[hep-lat\]](#) .
- [544] G. S. Bali, F. Bruckmann, G. Endrodi, S. D. Katz, and A. Schafer, “The QCD equation of state in background magnetic fields,” *JHEP* **08**, 177 (2014), [arXiv:1406.0269 \[hep-lat\]](#) .
- [545] G. S. Bali, F. Bruckmann, G. Endrodi, and A. Schafer, “Paramagnetic squeezing of QCD matter,” *Phys. Rev. Lett.* **112**, 042301 (2014), [arXiv:1311.2559 \[hep-lat\]](#) .
- [546] L. Levkova and C. DeTar, “Quark-gluon plasma in an external magnetic field,” *Phys. Rev. Lett.* **112**, 012002 (2014), [arXiv:1309.1142 \[hep-lat\]](#) .
- [547] G. S. Bali, G. Endrődi, and S. Piemonte, “Magnetic susceptibility of QCD matter and its decomposition from the lattice,” *JHEP* **07**, 183 (2020), [arXiv:2004.08778 \[hep-lat\]](#) .
- [548] P. V. Buividovich, D. Smith, and L. von Smekal, “Static magnetic susceptibility in finite-density $SU(2)$ lattice gauge theory,” *Eur. Phys. J. A* **57**, 293 (2021), [arXiv:2104.10012 \[hep-lat\]](#) .
- [549] G. Endrodi, “QCD equation of state at nonzero magnetic fields in the Hadron Resonance Gas model,” *JHEP* **04**, 023 (2013), [arXiv:1301.1307 \[hep-ph\]](#) .
- [550] K. Kamikado and T. Kanazawa, “Magnetic susceptibility of a strongly interacting thermal medium with 2+1 quark flavors,” *JHEP* **01**, 129 (2015), [arXiv:1410.6253 \[hep-ph\]](#) .
- [551] C. P. Hofmann, “Diamagnetic and paramagnetic phases in low-energy quantum chromodynamics,” *Phys. Lett. B* **818**, 136384 (2021), [arXiv:2103.04937 \[hep-ph\]](#) .
- [552] G. S. Bali, F. Bruckmann, M. Constantinou, M. Costa, G. Endrodi, S. D. Katz, H. Panagopoulos, and A. Schafer, “Magnetic susceptibility of QCD at zero and at finite temperature from the lattice,” *Phys. Rev.* **D86**, 094512 (2012), [arXiv:1209.6015 \[hep-lat\]](#) .
- [553] G. S. Bali, F. Bruckmann, G. Endrődi, and A. Schäfer, “Magnetization and pressures at nonzero magnetic fields in QCD,” *PoS LATTICE2013*, 182 (2014), [arXiv:1310.8145 \[hep-lat\]](#) .
- [554] B. L. Ioffe and A. V. Smilga, “Nucleon Magnetic Moments and Magnetic Properties of Vacuum in QCD,” *Nucl. Phys.* **B232**, 109 (1984).

- [555] I. I. Balitsky and A. V. Yung, “Proton and Neutron Magnetic Moments from QCD Sum Rules,” *Phys. Lett. B* **129**, 328 (1983).
- [556] P. Ball, V. M. Braun, and N. Kivel, “Photon distribution amplitudes in QCD,” *Nucl. Phys. B* **649**, 263 (2003), [arXiv:hep-ph/0207307](#) .
- [557] A. Vainshtein, “Perturbative and nonperturbative renormalization of anomalous quark triangles,” *Phys. Lett. B* **569**, 187 (2003), [arXiv:hep-ph/0212231](#) .
- [558] P. Gubler, K. Hattori, S. H. Lee, M. Oka, S. Ozaki, and K. Suzuki, “D mesons in a magnetic field,” *Phys. Rev.* **D93**, 054026 (2016), [arXiv:1512.08864 \[hep-ph\]](#) .
- [559] S. Borsanyi, Z. Fodor, C. Hoelbling, S. D. Katz, S. Krieg, and K. K. Szabo, “Full result for the QCD equation of state with 2+1 flavors,” *Phys. Lett. B* **730**, 99 (2014), [arXiv:1309.5258 \[hep-lat\]](#) .
- [560] A. Bazavov *et al.* (HotQCD), “Equation of state in (2+1)-flavor QCD,” *Phys. Rev. D* **90**, 094503 (2014), [arXiv:1407.6387 \[hep-lat\]](#) .
- [561] K. Fukushima and Y. Hidaka, “Magnetic Catalysis Versus Magnetic Inhibition,” *Phys. Rev. Lett.* **110**, 031601 (2013), [arXiv:1209.1319 \[hep-ph\]](#) .
- [562] N. Mueller and J. M. Pawłowski, “Magnetic catalysis and inverse magnetic catalysis in QCD,” *Phys. Rev.* **D91**, 116010 (2015), [arXiv:1502.08011 \[hep-ph\]](#) .
- [563] J. Braun, W. A. Mian, and S. Rechenberger, “Delayed Magnetic Catalysis,” *Phys. Lett.* **B755**, 265 (2016), [arXiv:1412.6025 \[hep-ph\]](#) .
- [564] K.-I. Aoki, H. Uoi, and M. Yamada, “Functional renormalization group study of the Nambu-Jona-Lasinio model at finite temperature and density in an external magnetic field,” *Phys. Lett.* **B753**, 580 (2016), [arXiv:1507.02527 \[hep-ph\]](#) .
- [565] K. Hattori and K. Itakura, “In-medium polarization tensor in strong magnetic fields (I): Magneto-birefringence at finite temperature and density,” *Annals Phys.* **446**, 169114 (2022), [arXiv:2205.04312 \[hep-ph\]](#) .
- [566] P. M. Lo, M. Szymański, C. Sasaki, and K. Redlich, “Deconfinement in the presence of a strong magnetic field,” *Phys. Rev. D* **102**, 034024 (2020), [arXiv:2004.04138 \[hep-ph\]](#) .
- [567] S. Roessner, C. Ratti, and W. Weise, “Polyakov loop, diquarks and the two-flavour phase diagram,” *Phys. Rev.* **D75**, 034007 (2007), [arXiv:hep-ph/0609281 \[hep-ph\]](#) .
- [568] N. Callebaut, D. Dudal, and H. Verschelde, “Holographic rho mesons in an external magnetic field,” *JHEP* **03**, 033 (2013), [arXiv:1105.2217 \[hep-th\]](#) .
- [569] N. Callebaut and D. Dudal, “A magnetic instability of the non-Abelian Sakai-Sugimoto model,” *JHEP* **01**, 055 (2014), [arXiv:1309.5042 \[hep-th\]](#) .
- [570] R.-G. Cai, S. He, L. Li, and L.-F. Li, “A Holographic Study on Vector Condensate Induced by a Magnetic Field,” *JHEP* **12**, 036 (2013), [arXiv:1309.2098 \[hep-th\]](#) .
- [571] Y.-Y. Bu, J. Erdmenger, J. P. Shock, and M. Strydom, “Magnetic field induced lattice ground states from holography,” *JHEP* **03**, 165 (2013), [arXiv:1210.6669 \[hep-th\]](#) .

- [572] R.-G. Cai, L. Li, L.-F. Li, and Y. Wu, “Vector Condensate and AdS Soliton Instability Induced by a Magnetic Field,” *JHEP* **01**, 045 (2014), [arXiv:1311.7578 \[hep-th\]](#) .
- [573] M. A. Andreichikov, B. O. Kerbikov, V. D. Orlovsky, and Yu. A. Simonov, “Meson Spectrum in Strong Magnetic Fields,” *Phys. Rev.* **D87**, 094029 (2013), [arXiv:1304.2533 \[hep-ph\]](#) .
- [574] G. Colucci, E. S. Fraga, and A. Sedrakian, “Chiral pions in a magnetic background,” *Phys. Lett.* **B728**, 19 (2014), [arXiv:1310.3742 \[nucl-th\]](#) .
- [575] H. Taya, “Hadron Masses in Strong Magnetic Fields,” *Phys. Rev.* **D92**, 014038 (2015), [arXiv:1412.6877 \[hep-ph\]](#) .
- [576] H. Liu, L. Yu, and M. Huang, “Charged and neutral vector ρ mesons in a magnetic field,” *Phys. Rev.* **D91**, 014017 (2015), [arXiv:1408.1318 \[hep-ph\]](#) .
- [577] M. Kawaguchi and S. Matsuzaki, “Vector meson masses from a hidden local symmetry in a constant magnetic field,” *Phys. Rev.* **D93**, 125027 (2016), [arXiv:1511.06990 \[hep-ph\]](#) .
- [578] M. A. Andreichikov, B. O. Kerbikov, E. V. Lushevskaya, Yu. A. Simonov, and O. E. Solovjeva, “The Evolution of Meson Masses in a Strong Magnetic Field,” *JHEP* **05**, 007 (2017), [arXiv:1610.06887 \[hep-ph\]](#) .
- [579] S. Ghosh, A. Mukherjee, M. Mandal, S. Sarkar, and P. Roy, “Spectral properties of ρ meson in a magnetic field,” *Phys. Rev.* **D94**, 094043 (2016), [arXiv:1612.02966 \[nucl-th\]](#) .
- [580] Z. Wang and P. Zhuang, “Meson properties in magnetized quark matter,” *Phys. Rev.* **D97**, 034026 (2018), [arXiv:1712.00554 \[hep-ph\]](#) .
- [581] D. Gómez Dumm, M. F. Izzo Villafañe, and N. N. Scoccola, “Neutral meson properties under an external magnetic field in nonlocal chiral quark models,” *Phys. Rev.* **D97**, 034025 (2018), [arXiv:1710.08950 \[hep-ph\]](#) .
- [582] H. Liu, X. Wang, L. Yu, and M. Huang, “Neutral and charged scalar mesons, pseudoscalar mesons, and diquarks in magnetic fields,” *Phys. Rev.* **D97**, 076008 (2018), [arXiv:1801.02174 \[hep-ph\]](#) .
- [583] S. Mao, “Pions in magnetic field at finite temperature,” *Phys. Rev.* **D99**, 056005 (2019), [arXiv:1808.10242 \[nucl-th\]](#) .
- [584] M. A. Andreichikov, B. O. Kerbikov, V. D. Orlovsky, and Yu. A. Simonov, “Neutron in Strong Magnetic Fields,” *Phys. Rev.* **D89**, 074033 (2014), [arXiv:1312.2212 \[hep-ph\]](#) .
- [585] U. Yakhshiev, H.-C. Kim, and M. Oka, “Nucleon and Δ isobar in a strong magnetic field,” *Phys. Rev.* **D99**, 054027 (2019), [arXiv:1902.00212 \[hep-ph\]](#) .
- [586] T. Kojo, “Neutral and charged mesons in magnetic fields: A resonance gas in a non-relativistic quark model,” *Eur. Phys. J. A* **57**, 317 (2021), [arXiv:2104.00376 \[hep-ph\]](#) .
- [587] K. Fukushima and Y. Hidaka, “Electric conductivity of hot and dense quark matter in a magnetic field with Landau level resummation via kinetic equations,” *Phys. Rev. Lett.* **120**, 162301 (2018), [arXiv:1711.01472 \[hep-ph\]](#) .
- [588] K. Fukushima and Y. Hidaka, “Resummation for the Field-theoretical Derivation of the Negative Magnetoresistance,” *JHEP* **04**, 162 (2020), [arXiv:1906.02683 \[hep-ph\]](#) .

- [589] A. Yu. Alekseev, V. V. Cheianov, and J. Frohlich, “Universality of transport properties in equilibrium, Goldstone theorem and chiral anomaly,” *Phys. Rev. Lett.* **81**, 3503 (1998), [arXiv:cond-mat/9803346 \[cond-mat\]](#) .
- [590] K. Fukushima, D. E. Kharzeev, and H. J. Warringa, “The Chiral Magnetic Effect,” *Phys. Rev.* **D78**, 074033 (2008), [arXiv:0808.3382 \[hep-ph\]](#) .
- [591] A. Vilenkin, “Equilibrium parity violating current in a magnetic field,” *Phys. Rev.* **D22**, 3080 (1980).
- [592] D. T. Son and A. R. Zhitnitsky, “Quantum anomalies in dense matter,” *Phys. Rev.* **D70**, 074018 (2004), [arXiv:hep-ph/0405216 \[hep-ph\]](#) .
- [593] M. A. Metlitski and A. R. Zhitnitsky, “Anomalous axion interactions and topological currents in dense matter,” *Phys. Rev.* **D72**, 045011 (2005), [arXiv:hep-ph/0505072 \[hep-ph\]](#) .
- [594] G. M. Newman and D. T. Son, “Response of strongly-interacting matter to magnetic field: Some exact results,” *Phys. Rev.* **D73**, 045006 (2006), [arXiv:hep-ph/0510049 \[hep-ph\]](#) .
- [595] D. E. Kharzeev and H.-U. Yee, “Chiral Magnetic Wave,” *Phys. Rev.* **D83**, 085007 (2011), [arXiv:1012.6026 \[hep-th\]](#) .
- [596] Y. Burnier, D. E. Kharzeev, J. Liao, and H.-U. Yee, “Chiral magnetic wave at finite baryon density and the electric quadrupole moment of quark-gluon plasma in heavy ion collisions,” *Phys. Rev. Lett.* **107**, 052303 (2011), [arXiv:1103.1307 \[hep-ph\]](#) .
- [597] M. Stephanov, H.-U. Yee, and Y. Yin, “Collective modes of chiral kinetic theory in a magnetic field,” *Phys. Rev.* **D91**, 125014 (2015), [arXiv:1501.00222 \[hep-th\]](#) .
- [598] D. E. Kharzeev and H. J. Warringa, “Chiral Magnetic conductivity,” *Phys. Rev.* **D80**, 034028 (2009), [arXiv:0907.5007 \[hep-ph\]](#) .
- [599] D. K. Hong, “Anomalous currents in dense matter under a magnetic field,” *Phys. Lett.* **B699**, 305 (2011), [arXiv:1010.3923 \[hep-th\]](#) .
- [600] K. Landsteiner, E. Megias, and F. Pena-Benitez, “Gravitational Anomaly and Transport,” *Phys. Rev. Lett.* **107**, 021601 (2011), [arXiv:1103.5006 \[hep-ph\]](#) .
- [601] D. Hou, H. Liu, and H.-c. Ren, “Some Field Theoretic Issues Regarding the Chiral Magnetic Effect,” *JHEP* **05**, 046 (2011), [arXiv:1103.2035 \[hep-ph\]](#) .
- [602] M. Hongo and Y. Hidaka, “Anomaly-induced transport phenomena from the imaginary-time formalism,” *Particles* **2**, 261 (2019), [arXiv:1902.09166 \[hep-th\]](#) .
- [603] D. T. Son and P. Surowka, “Hydrodynamics with triangle anomalies,” *Phys. Rev. Lett.* **103**, 191601 (2009), [arXiv:0906.5044 \[hep-th\]](#) .
- [604] Y. Neiman and Y. Oz, “Relativistic Hydrodynamics with General Anomalous Charges,” *JHEP* **03**, 023 (2011), [arXiv:1011.5107 \[hep-th\]](#) .
- [605] A. V. Sadofyev and M. V. Isachenkov, “The Chiral magnetic effect in hydrodynamical approach,” *Phys. Lett.* **B697**, 404 (2011), [arXiv:1010.1550 \[hep-th\]](#) .

- [606] D. E. Kharzeev and H.-U. Yee, “Anomalies and time reversal invariance in relativistic hydrodynamics: the second order and higher dimensional formulations,” *Phys. Rev.* **D84**, 045025 (2011), [arXiv:1105.6360 \[hep-th\]](#) .
- [607] S. Lin, “An anomalous hydrodynamics for chiral superfluid,” *Phys. Rev.* **D85**, 045015 (2012), [arXiv:1112.3215 \[hep-ph\]](#) .
- [608] K. Jensen, “Triangle Anomalies, Thermodynamics, and Hydrodynamics,” *Phys. Rev.* **D85**, 125017 (2012), [arXiv:1203.3599 \[hep-th\]](#) .
- [609] N. Banerjee, J. Bhattacharya, S. Bhattacharyya, S. Jain, S. Minwalla, and T. Sharma, “Constraints on Fluid Dynamics from Equilibrium Partition Functions,” *JHEP* **09**, 046 (2012), [arXiv:1203.3544 \[hep-th\]](#) .
- [610] G. Lifschytz and M. Lippert, “Anomalous conductivity in holographic QCD,” *Phys. Rev.* **D80**, 066005 (2009), [arXiv:0904.4772 \[hep-th\]](#) .
- [611] H.-U. Yee, “Holographic Chiral Magnetic Conductivity,” *JHEP* **11**, 085 (2009), [arXiv:0908.4189 \[hep-th\]](#) .
- [612] A. Rebhan, A. Schmitt, and S. A. Stricker, “Anomalies and the chiral magnetic effect in the Sakai-Sugimoto model,” *JHEP* **01**, 026 (2010), [arXiv:0909.4782 \[hep-th\]](#) .
- [613] A. Gynther, K. Landsteiner, F. Pena-Benitez, and A. Rebhan, “Holographic Anomalous Conductivities and the Chiral Magnetic Effect,” *JHEP* **02**, 110 (2011), [arXiv:1005.2587 \[hep-th\]](#) .
- [614] T. Kalaydzhyan and I. Kirsch, “Fluid/gravity model for the chiral magnetic effect,” *Phys. Rev. Lett.* **106**, 211601 (2011), [arXiv:1102.4334 \[hep-th\]](#) .
- [615] S. Pu, J.-h. Gao, and Q. Wang, “A consistent description of kinetic equation with triangle anomaly,” *Phys. Rev.* **D83**, 094017 (2011), [arXiv:1008.2418 \[nucl-th\]](#) .
- [616] J.-H. Gao, Z.-T. Liang, S. Pu, Q. Wang, and X.-N. Wang, “Chiral Anomaly and Local Polarization Effect from Quantum Kinetic Approach,” *Phys. Rev. Lett.* **109**, 232301 (2012), [arXiv:1203.0725 \[hep-ph\]](#) .
- [617] D. T. Son and N. Yamamoto, “Berry Curvature, Triangle Anomalies, and the Chiral Magnetic Effect in Fermi Liquids,” *Phys. Rev. Lett.* **109**, 181602 (2012), [arXiv:1203.2697 \[cond-mat.mes-hall\]](#) .
- [618] D. T. Son and N. Yamamoto, “Kinetic theory with Berry curvature from quantum field theories,” *Phys. Rev.* **D87**, 085016 (2013), [arXiv:1210.8158 \[hep-th\]](#) .
- [619] M. A. Stephanov and Y. Yin, “Chiral Kinetic Theory,” *Phys. Rev. Lett.* **109**, 162001 (2012), [arXiv:1207.0747 \[hep-th\]](#) .
- [620] J.-W. Chen, S. Pu, Q. Wang, and X.-N. Wang, “Berry Curvature and Four-Dimensional Monopoles in the Relativistic Chiral Kinetic Equation,” *Phys. Rev. Lett.* **110**, 262301 (2013), [arXiv:1210.8312 \[hep-th\]](#) .
- [621] Y. Hidaka, S. Pu, and D.-L. Yang, “Relativistic Chiral Kinetic Theory from Quantum Field Theories,” *Phys. Rev.* **D95**, 091901 (2017), [arXiv:1612.04630 \[hep-th\]](#) .

- [622] N. Mueller and R. Venugopalan, “The chiral anomaly, Berry’s phase and chiral kinetic theory, from world-lines in quantum field theory,” *Phys. Rev. D* **97**, 051901 (2018), [arXiv:1701.03331 \[hep-ph\]](#) .
- [623] N. Mueller and R. Venugopalan, “Worldline construction of a covariant chiral kinetic theory,” *Phys. Rev. D* **96**, 016023 (2017), [arXiv:1702.01233 \[hep-ph\]](#) .
- [624] S. Carignano, C. Manuel, and J. M. Torres-Rincon, “Consistent Relativistic Chiral Kinetic Theory: a derivation from OSEFT,” (2018), [arXiv:1806.01684 \[hep-ph\]](#) .
- [625] S. Lin and A. Shukla, “Chiral Kinetic Theory from Effective Field Theory Revisited,” (2019), [arXiv:1901.01528 \[hep-ph\]](#) .
- [626] Z. Chen and S. Lin, “Quantum kinetic theory with vector and axial gauge fields,” *Phys. Rev. D* **105**, 014015 (2022), [arXiv:2109.08440 \[hep-ph\]](#) .
- [627] P. V. Buividovich, E. V. Luschevskaya, M. I. Polikarpov, and M. N. Chernodub, “Chiral magnetic effect in SU(2) lattice gluodynamics at zero temperature,” *JETP Lett.* **90**, 412 (2009), [*Pisma Zh. Eksp. Teor. Fiz.*90,456(2009)].
- [628] P. V. Buividovich, M. N. Chernodub, E. V. Luschevskaya, and M. I. Polikarpov, “Numerical evidence of chiral magnetic effect in lattice gauge theory,” *Phys. Rev. D* **80**, 054503 (2009), [arXiv:0907.0494 \[hep-lat\]](#) .
- [629] A. Yamamoto, “Chiral magnetic effect in lattice QCD with a chiral chemical potential,” *Phys. Rev. Lett.* **107**, 031601 (2011), [arXiv:1105.0385 \[hep-lat\]](#) .
- [630] A. Yamamoto, “Lattice study of the chiral magnetic effect in a chirally imbalanced matter,” *Phys. Rev. D* **84**, 114504 (2011), [arXiv:1111.4681 \[hep-lat\]](#) .
- [631] G. S. Bali, F. Bruckmann, G. Endrodi, Z. Fodor, S. D. Katz, and A. Schefer, “Local CP-violation and electric charge separation by magnetic fields from lattice QCD,” *JHEP* **04**, 129 (2014), [arXiv:1401.4141 \[hep-lat\]](#) .
- [632] A. Vilenkin, “Parity Violating Currents in Thermal Radiation,” *Phys. Lett.* **80B**, 150 (1978).
- [633] A. Vilenkin, “Macroscopic parity-violating effects: Neutrino fluxes from rotating black holes and in rotating thermal radiation,” *Phys. Rev. D* **20**, 1807 (1979).
- [634] A. Vilenkin, “Quantum field theory at finite temperature in a rotating system,” *Phys. Rev. D* **21**, 2260 (1980).
- [635] J. Erdmenger, M. Haack, M. Kaminski, and A. Yarom, “Fluid dynamics of R-charged black holes,” *JHEP* **01**, 055 (2009), [arXiv:0809.2488 \[hep-th\]](#) .
- [636] K. Mameda and A. Yamamoto, “Magnetism and rotation in relativistic field theory,” *PTEP* **2016**, 093B05 (2016), [arXiv:1504.05826 \[hep-th\]](#) .
- [637] H.-L. Chen, K. Fukushima, X.-G. Huang, and K. Mameda, “Analogy between rotation and density for Dirac fermions in a magnetic field,” *Phys. Rev. D* **93**, 104052 (2016), [arXiv:1512.08974 \[hep-ph\]](#) .
- [638] K. Hattori and Y. Yin, “Charge redistribution from anomalous magnetovorticity coupling,” *Phys. Rev. Lett.* **117**, 152002 (2016), [arXiv:1607.01513 \[hep-th\]](#) .

- [639] S. Ebihara, K. Fukushima, and K. Mameda, “Boundary effects and gapped dispersion in rotating fermionic matter,” (2016), [arXiv:1608.00336 \[hep-ph\]](#) .
- [640] M. N. Chernodub and S. Gongyo, “Interacting fermions in rotation: chiral symmetry restoration, moment of inertia and thermodynamics,” *JHEP* **01**, 136 (2017), [arXiv:1611.02598 \[hep-th\]](#) .
- [641] M. N. Chernodub and S. Gongyo, “Effects of rotation and boundaries on chiral symmetry breaking of relativistic fermions,” *Phys. Rev.* **D95**, 096006 (2017), [arXiv:1702.08266 \[hep-th\]](#) .
- [642] S. Lin and L. Yang, “Magneto-vortical effect in strong magnetic field,” *JHEP* **06**, 054 (2021), [arXiv:2103.11577 \[nucl-th\]](#) .
- [643] N. Yamamoto and D.-L. Yang, “Helical magnetic effect and the chiral anomaly,” *Phys. Rev. D* **103**, 125003 (2021), [arXiv:2103.13208 \[hep-th\]](#) .
- [644] K. Fukushima, “Extreme matter in electromagnetic fields and rotation,” *Prog. Part. Nucl. Phys.* **107**, 167 (2019), [arXiv:1812.08886 \[hep-ph\]](#) .
- [645] D. Satow and H.-U. Yee, “Chiral Magnetic Effect at Weak Coupling with Relaxation Dynamics,” *Phys. Rev.* **D90**, 014027 (2014), [arXiv:1406.1150 \[hep-ph\]](#) .
- [646] S. Imaki, “Chiral magnetic effect in the hadronic phase,” *Phys. Rev. D* **101**, 074024 (2020), [arXiv:1906.08949 \[hep-ph\]](#) .
- [647] K. Fukushima and K. Mameda, “Wess-Zumino-Witten action and photons from the Chiral Magnetic Effect,” *Phys. Rev.* **D86**, 071501 (2012), [arXiv:1206.3128 \[hep-ph\]](#) .
- [648] D. E. Kharzeev, “Topology, magnetic field, and strongly interacting matter,” *Ann. Rev. Nucl. Part. Sci.* **65**, 193 (2015), [arXiv:1501.01336 \[hep-ph\]](#) .
- [649] K. Landsteiner, “Notes on Anomaly Induced Transport,” *Proceedings, 56th Cracow School of Theoretical Physics : A Panorama of Holography: Zakopane, Poland, May 24-June 1, 2016*, *Acta Phys. Polon.* **B47**, 2617 (2016), [arXiv:1610.04413 \[hep-th\]](#) .
- [650] S. Murakami, “Phase transition between the quantum spin hall and insulator phases in 3d: emergence of a topological gapless phase,” *New Journal of Physics* **9**, 356 (2007).
- [651] X. Wan, A. M. Turner, A. Vishwanath, and S. Y. Savrasov, “Topological semimetal and fermi-arc surface states in the electronic structure of pyrochlore iridates,” *Physical Review B* **83**, 205101 (2011).
- [652] D. T. Son and B. Z. Spivak, “Chiral Anomaly and Classical Negative Magnetoresistance of Weyl Metals,” *Phys. Rev.* **B88**, 104412 (2013), [arXiv:1206.1627 \[cond-mat.mes-hall\]](#) .
- [653] A. A. Zyuzin and A. A. Burkov, “Topological response in Weyl semimetals and the chiral anomaly,” *Phys. Rev. B* **86**, 115133 (2012), [arXiv:1206.1868 \[cond-mat.mes-hall\]](#) .
- [654] A. A. Burkov, “Chiral Anomaly and Diffusive Magnetotransport in Weyl Metals,” *Phys. Rev. Lett.* **113**, 247203 (2014), [arXiv:1409.0013](#) .
- [655] E. V. Gorbar, V. A. Miransky, and I. A. Shovkovy, “Chiral anomaly, dimensional reduction, and magnetoresistivity of Weyl and Dirac semimetals,” *Phys. Rev.* **B89**, 085126 (2014), [arXiv:1312.0027 \[cond-mat.mes-hall\]](#) .

- [656] A. A. Burkov, “Negative longitudinal magnetoresistance in Dirac and Weyl metals,” *Phys. Rev. B* **91**, 245157 (2015).
- [657] H.-J. Kim, K.-S. Kim, J.-F. Wang, M. Sasaki, N. Satoh, A. Ohnishi, M. Kitaura, M. Yang, and L. Li, “Dirac versus Weyl Fermions in Topological Insulators: Adler-Bell-Jackiw Anomaly in Transport Phenomena,” *Phys. Rev. Lett.* **111**, 246603 (2013).
- [658] Q. Li, D. E. Kharzeev, C. Zhang, Y. Huang, I. Pletikosic, A. V. Fedorov, R. D. Zhong, J. A. Schneeloch, G. D. Gu, and T. Valla, “Observation of the chiral magnetic effect in ZrTe₅,” *Nature Phys.* **12**, 550 (2016), [arXiv:1412.6543 \[cond-mat.str-el\]](#) .
- [659] J. Xiong, S. K. Kushwaha, T. Liang, J. W. Krizan, M. Hirschberger, W. Wang, R. J. Cava, and N. P. Ong, “Evidence for the chiral anomaly in the dirac semimetal na₃bi,” *Science* **350**, 413 (2015).
- [660] X. Huang *et al.*, “Observation of the Chiral-Anomaly-Induced Negative Magnetoresistance in 3D Weyl Semimetal TaAs,” *Phys. Rev. X* **5**, 031023 (2015), [arXiv:1503.01304 \[cond-mat.mtrl-sci\]](#) .
- [661] A. A. Burkov, “Chiral anomaly and transport in Weyl metals,” *J. Phys. Condens. Matter* **27**, 113201 (2015), [arXiv:1502.07609 \[cond-mat.mes-hall\]](#) .
- [662] N. P. Armitage, E. J. Mele, and A. Vishwanath, “Weyl and Dirac Semimetals in Three Dimensional Solids,” *Rev. Mod. Phys.* **90**, 015001 (2018), [arXiv:1705.01111 \[cond-mat.str-el\]](#) .
- [663] B. Yan and C. Felser, “Topological materials: Weyl semimetals,” *Annual Review of Condensed Matter Physics* **8**, 337 (2017).
- [664] C. Felser and J. Gooth, “Topology and chirality,” *arXiv preprint arXiv:2205.05809* (2022).
- [665] V. Skokov, P. Sorensen, V. Koch, S. Schlichting, J. Thomas, S. Voloshin, G. Wang, and H.-U. Yee, “Chiral Magnetic Effect Task Force Report,” *Chin. Phys. C* **41**, 072001 (2017), [arXiv:1608.00982 \[nucl-th\]](#) .
- [666] B. I. Abelev *et al.* (STAR), “Azimuthal Charged-Particle Correlations and Possible Local Strong Parity Violation,” *Phys. Rev. Lett.* **103**, 251601 (2009), [arXiv:0909.1739 \[nucl-ex\]](#) .
- [667] B. I. Abelev *et al.* (STAR), “Observation of charge-dependent azimuthal correlations and possible local strong parity violation in heavy ion collisions,” *Phys. Rev. C* **81**, 054908 (2010), [arXiv:0909.1717 \[nucl-ex\]](#) .
- [668] L. Adamczyk *et al.* (STAR), “Fluctuations of charge separation perpendicular to the event plane and local parity violation in $\sqrt{s_{NN}} = 200$ GeV Au+Au collisions at the BNL Relativistic Heavy Ion Collider,” *Phys. Rev. C* **88**, 064911 (2013), [arXiv:1302.3802 \[nucl-ex\]](#) .
- [669] B. Abelev *et al.* (ALICE), “Charge separation relative to the reaction plane in Pb-Pb collisions at $\sqrt{s_{NN}} = 2.76$ TeV,” *Phys. Rev. Lett.* **110**, 012301 (2013), [arXiv:1207.0900 \[nucl-ex\]](#) .
- [670] L. Adamczyk *et al.* (STAR), “Beam-energy dependence of charge separation along the magnetic field in Au+Au collisions at RHIC,” *Phys. Rev. Lett.* **113**, 052302 (2014), [arXiv:1404.1433 \[nucl-ex\]](#) .
- [671] V. Khachatryan *et al.* (CMS), “Observation of charge-dependent azimuthal correlations in *p*-Pb collisions and its implication for the search for the chiral magnetic effect,” *Phys. Rev. Lett.* **118**, 122301 (2017), [arXiv:1610.00263 \[nucl-ex\]](#) .

- [672] A. M. Sirunyan *et al.* (CMS), “Constraints on the chiral magnetic effect using charge-dependent azimuthal correlations in p Pb and PbPb collisions at the CERN Large Hadron Collider,” *Phys. Rev. C* **97**, 044912 (2018), [arXiv:1708.01602 \[nucl-ex\]](#) .
- [673] J. Adam *et al.* (STAR), “Charge-dependent pair correlations relative to a third particle in $p + Au$ and $d + Au$ collisions at RHIC,” *Phys. Lett. B* **798**, 134975 (2019), [arXiv:1906.03373 \[nucl-ex\]](#) .
- [674] S. Acharya *et al.* (ALICE), “Constraining the magnitude of the Chiral Magnetic Effect with Event Shape Engineering in Pb-Pb collisions at $\sqrt{s_{NN}} = 2.76$ TeV,” *Phys. Lett. B* **777**, 151 (2018), [arXiv:1709.04723 \[nucl-ex\]](#) .
- [675] S. Acharya *et al.* (ALICE), “Constraining the Chiral Magnetic Effect with charge-dependent azimuthal correlations in Pb-Pb collisions at $\sqrt{s_{NN}} = 2.76$ and 5.02 TeV,” *JHEP* **09**, 160 (2020), [arXiv:2005.14640 \[nucl-ex\]](#) .
- [676] M. S. Abdallah *et al.* (STAR), “Pair invariant mass to isolate background in the search for the chiral magnetic effect in Au + Au collisions at $s_{NN}=200$ GeV,” *Phys. Rev. C* **106**, 034908 (2022), [arXiv:2006.05035 \[nucl-ex\]](#) .
- [677] M. S. Abdallah *et al.* (STAR), “Search for the Chiral Magnetic Effect via Charge-Dependent Azimuthal Correlations Relative to Spectator and Participant Planes in Au+Au Collisions at $\sqrt{s_{NN}} = 200$ GeV,” *Phys. Rev. Lett.* **128**, 092301 (2022), [arXiv:2106.09243 \[nucl-ex\]](#) .
- [678] “Search for the Chiral Magnetic Effect in Au+Au collisions at $\sqrt{s_{NN}} = 27$ GeV with the STAR forward Event Plane Detectors,” (2022), [arXiv:2209.03467 \[nucl-ex\]](#) .
- [679] J. Zhao and F. Wang, “Experimental searches for the chiral magnetic effect in heavy-ion collisions,” *Prog. Part. Nucl. Phys.* **107**, 200 (2019), [arXiv:1906.11413 \[nucl-ex\]](#) .
- [680] S. A. Voloshin, “Testing the Chiral Magnetic Effect with Central U+U collisions,” *Phys. Rev. Lett.* **105**, 172301 (2010), [arXiv:1006.1020 \[nucl-th\]](#) .
- [681] W.-T. Deng, X.-G. Huang, G.-L. Ma, and G. Wang, “Test the chiral magnetic effect with isobaric collisions,” *Phys. Rev. C* **94**, 041901 (2016), [arXiv:1607.04697 \[nucl-th\]](#) .
- [682] M. Abdallah *et al.* (STAR), “Search for the chiral magnetic effect with isobar collisions at $\sqrt{s_{NN}}=200$ GeV by the STAR Collaboration at the BNL Relativistic Heavy Ion Collider,” *Phys. Rev. C* **105**, 014901 (2022), [arXiv:2109.00131 \[nucl-ex\]](#) .
- [683] F. Wang, in *29th International Conference on Ultra-relativistic Nucleus-Nucleus Collisions* (2022) [arXiv:2207.10044 \[nucl-ex\]](#) .
- [684] N. Yamamoto, “Generalized Bloch theorem and chiral transport phenomena,” *Phys. Rev.* **D92**, 085011 (2015), [arXiv:1502.01547 \[cond-mat.mes-hall\]](#) .
- [685] K. Landsteiner, E. Megias, and F. Pena-Benitez, “Anomalous Transport from Kubo Formulae,” *Lect. Notes Phys.* **871**, 433 (2013), [arXiv:1207.5808 \[hep-th\]](#) .
- [686] M. Vazifeh and M. Franz, “Electromagnetic response of Weyl semimetals,” *Physical review letters* **111**, 027201 (2013).
- [687] M. A. Zubkov, “Absence of equilibrium chiral magnetic effect,” *Phys. Rev.* **D93**, 105036 (2016), [arXiv:1605.08724 \[hep-ph\]](#) .

- [688] E. V. Gorbar, V. A. Miransky, I. A. Shovkovy, and X. Wang, “Radiative corrections to chiral separation effect in QED,” *Phys. Rev.* **D88**, 025025 (2013), [arXiv:1304.4606 \[hep-ph\]](#) .
- [689] S. Lin and L. Yang, “Mass correction to chiral vortical effect and chiral separation effect,” *Phys. Rev. D* **98**, 114022 (2018), [arXiv:1810.02979 \[nucl-th\]](#) .
- [690] L. D. McLerran, E. Mottola, and M. E. Shaposhnikov, “Sphalerons and Axion Dynamics in High Temperature QCD,” *Phys. Rev.* **D43**, 2027 (1991).
- [691] P. B. Arnold, D. T. Son, and L. G. Yaffe, “Effective dynamics of hot, soft nonAbelian gauge fields. Color conductivity and $\log(1/\alpha)$ effects,” *Phys. Rev.* **D59**, 105020 (1999), [arXiv:hep-ph/9810216 \[hep-ph\]](#) .
- [692] G. D. Moore and M. Tassler, “The Sphaleron Rate in SU(N) Gauge Theory,” *JHEP* **02**, 105 (2011), [arXiv:1011.1167 \[hep-ph\]](#) .
- [693] A. Jimenez-Alba and H.-U. Yee, “Second order transport coefficient from the chiral anomaly at weak coupling: Diagrammatic resummation,” *Phys. Rev. D* **92**, 014023 (2015), [arXiv:1504.05866 \[hep-ph\]](#) .
- [694] D. E. Kharzeev, M. A. Stephanov, and H.-U. Yee, “Anatomy of chiral magnetic effect in and out of equilibrium,” *Phys. Rev. D* **95**, 051901 (2017), [arXiv:1612.01674 \[hep-ph\]](#) .
- [695] S. Chandrasekhar and P. C. Kendall, “On force-free magnetic fields.” *Astrophysical Journal* **126**, 457 (1957).
- [696] Y. Hirono, D. Kharzeev, and Y. Yin, “Self-similar inverse cascade of magnetic helicity driven by the chiral anomaly,” *Phys. Rev.* **D92**, 125031 (2015), [arXiv:1509.07790 \[hep-th\]](#) .
- [697] X.-l. Xia, H. Qin, and Q. Wang, “Approach to Chandrasekhar-Kendall-Woltjer State in a Chiral Plasma,” *Phys. Rev.* **D94**, 054042 (2016), [arXiv:1607.01126 \[nucl-th\]](#) .
- [698] Z. Qiu, G. Cao, and X.-G. Huang, “On electrodynamics of chiral matter,” *Phys. Rev.* **D95**, 036002 (2017), [arXiv:1612.06364 \[cond-mat.mes-hall\]](#) .
- [699] D. B. Kaplan, S. Reddy, and S. Sen, “Energy Conservation and the Chiral Magnetic Effect,” *Phys. Rev.* **D96**, 016008 (2017), [arXiv:1612.00032 \[hep-ph\]](#) .
- [700] S. M. Carroll, G. B. Field, and R. Jackiw, “Limits on a Lorentz and Parity Violating Modification of Electrodynamics,” *Phys. Rev.* **D41**, 1231 (1990).
- [701] W. D. Garretson, G. B. Field, and S. M. Carroll, “Primordial magnetic fields from pseudoGoldstone bosons,” *Phys. Rev.* **D46**, 5346 (1992), [arXiv:hep-ph/9209238 \[hep-ph\]](#) .
- [702] M. Joyce and M. E. Shaposhnikov, “Primordial magnetic fields, right-handed electrons, and the Abelian anomaly,” *Phys. Rev. Lett.* **79**, 1193 (1997), [arXiv:astro-ph/9703005 \[astro-ph\]](#) .
- [703] G. B. Field and S. M. Carroll, “Cosmological magnetic fields from primordial helicity,” *Phys. Rev.* **D62**, 103008 (2000), [arXiv:astro-ph/9811206 \[astro-ph\]](#) .
- [704] V. B. Semikoz and D. D. Sokoloff, “Magnetic helicity and cosmological magnetic field,” *Astron. Astrophys.* **433**, L53 (2005), [arXiv:astro-ph/0411496 \[astro-ph\]](#) .
- [705] M. Laine, “Real-time Chern-Simons term for hypermagnetic fields,” *JHEP* **10**, 056 (2005), [arXiv:hep-ph/0508195](#) .

- [706] A. Vilenkin and D. A. Leahy, “PARITY NONCONSERVATION AND THE ORIGIN OF COSMIC MAGNETIC FIELDS,” *Astrophys. J.* **254**, 77 (1982).
- [707] F. Wilczek, “Two Applications of Axion Electrodynamics,” *Phys. Rev. Lett.* **58**, 1799 (1987).
- [708] M. S. Turner and L. M. Widrow, “Inflation Produced, Large Scale Magnetic Fields,” *Phys. Rev.* **D37**, 2743 (1988).
- [709] M. Giovannini and M. E. Shaposhnikov, “Primordial hypermagnetic fields and triangle anomaly,” *Phys. Rev.* **D57**, 2186 (1998), [arXiv:hep-ph/9710234 \[hep-ph\]](#) .
- [710] M. Giovannini, “Primordial hypermagnetic knots,” *Phys. Rev.* **D61**, 063004 (2000), [arXiv:hep-ph/9905358 \[hep-ph\]](#) .
- [711] M. Giovannini, “Hypermagnetic knots, Chern-Simons waves and the baryon asymmetry,” *Phys. Rev.* **D61**, 063502 (2000), [arXiv:hep-ph/9906241 \[hep-ph\]](#) .
- [712] Y. Akamatsu and N. Yamamoto, “Chiral Plasma Instabilities,” *Phys. Rev. Lett.* **111**, 052002 (2013), [arXiv:1302.2125 \[nucl-th\]](#) .
- [713] Y. Akamatsu and N. Yamamoto, “Chiral Langevin theory for non-Abelian plasmas,” *Phys. Rev.* **D90**, 125031 (2014), [arXiv:1402.4174 \[hep-th\]](#) .
- [714] A. Boyarsky, J. Frohlich, and O. Ruchayskiy, “Self-consistent evolution of magnetic fields and chiral asymmetry in the early Universe,” *Phys. Rev. Lett.* **108**, 031301 (2012), [arXiv:1109.3350 \[astro-ph.CO\]](#) .
- [715] H. Tashiro, T. Vachaspati, and A. Vilenkin, “Chiral Effects and Cosmic Magnetic Fields,” *Phys. Rev.* **D86**, 105033 (2012), [arXiv:1206.5549 \[astro-ph.CO\]](#) .
- [716] K. Kamada and A. J. Long, “Evolution of the Baryon Asymmetry through the Electroweak Crossover in the Presence of a Helical Magnetic Field,” *Phys. Rev.* **D94**, 123509 (2016), [arXiv:1610.03074 \[hep-ph\]](#) .
- [717] K. Kamada and A. J. Long, “Baryogenesis from decaying magnetic helicity,” *Phys. Rev.* **D94**, 063501 (2016), [arXiv:1606.08891 \[astro-ph.CO\]](#) .
- [718] T. Fujita and R. Durrer, “Scale-invariant Helical Magnetic Fields from Inflation,” *JCAP* **09**, 008 (2019), [arXiv:1904.11428 \[astro-ph.CO\]](#) .
- [719] V. Domcke, B. von Harling, E. Morgante, and K. Mukaida, “Baryogenesis from axion inflation,” *JCAP* **10**, 032 (2019), [arXiv:1905.13318 \[hep-ph\]](#) .
- [720] J. Schober, T. Fujita, and R. Durrer, “Generation of chiral asymmetry via helical magnetic fields,” *Phys. Rev. D* **101**, 103028 (2020), [arXiv:2002.09501 \[physics.plasm-ph\]](#) .
- [721] K. Mukaida, K. Schmitz, and M. Yamada, “Baryon Asymmetry of the Universe from Lepton Flavor Violation,” *Phys. Rev. Lett.* **129**, 011803 (2022), [arXiv:2111.03082 \[hep-ph\]](#) .
- [722] V. Domcke, K. Kamada, K. Mukaida, K. Schmitz, and M. Yamada, “Wash-in leptogenesis after axion inflation,” *JHEP* **01**, 053 (2023), [arXiv:2210.06412 \[hep-ph\]](#) .
- [723] T. Fujita, J. Kume, K. Mukaida, and Y. Tada, “Effective treatment of U(1) gauge field and charged particles in axion inflation,” *JCAP* **09**, 023 (2022), [arXiv:2204.01180 \[hep-ph\]](#) .

- [724] A. Ohnishi and N. Yamamoto, “Magnetars and the Chiral Plasma Instabilities,” (2014), [arXiv:1402.4760 \[astro-ph.HE\]](#) .
- [725] M. Dvornikov and V. B. Semikoz, “Magnetic field instability in a neutron star driven by the electroweak electron-nucleon interaction versus the chiral magnetic effect,” *Phys. Rev.* **D91**, 061301 (2015), [arXiv:1410.6676 \[astro-ph.HE\]](#) .
- [726] D. Grabowska, D. B. Kaplan, and S. Reddy, “Role of the electron mass in damping chiral plasma instability in Supernovae and neutron stars,” *Phys. Rev.* **D91**, 085035 (2015), [arXiv:1409.3602 \[hep-ph\]](#) .
- [727] G. Sigl and N. Leite, “Chiral Magnetic Effect in Protoneutron Stars and Magnetic Field Spectral Evolution,” *JCAP* **1601**, 025 (2016), [arXiv:1507.04983 \[astro-ph.HE\]](#) .
- [728] N. Yamamoto, “Chiral transport of neutrinos in supernovae: Neutrino-induced fluid helicity and helical plasma instability,” *Phys. Rev. D* **93**, 065017 (2016), [arXiv:1511.00933 \[astro-ph.HE\]](#) .
- [729] Y. Masada, K. Kotake, T. Takiwaki, and N. Yamamoto, “Chiral magnetohydrodynamic turbulence in core-collapse supernovae,” *Phys. Rev. D* **98**, 083018 (2018), [arXiv:1805.10419 \[astro-ph.HE\]](#) .
- [730] M. N. Chernodub, “Free magnetized knots of parity-violating deconfined matter in heavy-ion collisions,” (2010), [arXiv:1002.1473 \[nucl-th\]](#) .
- [731] K. Tuchin, “Electromagnetic field and the chiral magnetic effect in the quark-gluon plasma,” *Phys. Rev.* **C91**, 064902 (2015), [arXiv:1411.1363 \[hep-ph\]](#) .
- [732] C. Manuel and J. M. Torres-Rincon, “Dynamical evolution of the chiral magnetic effect: Applications to the quark-gluon plasma,” *Phys. Rev.* **D92**, 074018 (2015), [arXiv:1501.07608 \[hep-ph\]](#) .
- [733] U. Frisch, A. Pouquet, J. L  Orat, and A. Mazure, “Possibility of an inverse cascade of magnetic helicity in magnetohydrodynamic turbulence,” *Journal of Fluid Mechanics* **68**, 769 (1975).
- [734] A. Pouquet, U. Frisch, and J. L  Orat, “Strong mhd helical turbulence and the nonlinear dynamo effect,” *Journal of Fluid Mechanics* **77**, 321 (1976).
- [735] M. Christensson, M. Hindmarsh, and A. Brandenburg, “Inverse cascade in decaying 3-D magnetohydrodynamic turbulence,” *Phys. Rev. E* **64**, 056405 (2001), [arXiv:astro-ph/0011321](#) .
- [736] G. Baym, D. Bodeker, and L. D. McLerran, “Magnetic fields produced by phase transition bubbles in the electroweak phase transition,” *Phys. Rev.* **D53**, 662 (1996), [arXiv:hep-ph/9507429 \[hep-ph\]](#) .
- [737] J. M. Cornwall, “Speculations on primordial magnetic helicity,” *Phys. Rev.* **D56**, 6146 (1997), [arXiv:hep-th/9704022 \[hep-th\]](#) .
- [738] D. T. Son, “Magnetohydrodynamics of the early universe and the evolution of primordial magnetic fields,” *Phys. Rev.* **D59**, 063008 (1999), [arXiv:hep-ph/9803412 \[hep-ph\]](#) .
- [739] T. Vachaspati, “Estimate of the primordial magnetic field helicity,” *Phys. Rev. Lett.* **87**, 251302 (2001), [arXiv:astro-ph/0101261 \[astro-ph\]](#) .
- [740] D. Biskamp, *Nonlinear magnetohydrodynamics*, Vol. 1 (Cambridge University Press, 1997).

- [741] P. A. Davidson, “An introduction to magnetohydrodynamics,” (2002).
- [742] N. Yamamoto, “Scaling laws in chiral hydrodynamic turbulence,” *Phys. Rev.* **D93**, 125016 (2016), [arXiv:1603.08864 \[hep-th\]](#) .
- [743] A. Brandenburg, J. Schober, I. Rogachevskii, T. Kahniashvili, A. Boyarsky, J. Frohlich, O. Ruchayskiy, and N. Kleeorin, “The turbulent chiral-magnetic cascade in the early universe,” *Astrophys. J. Lett.* **845**, L21 (2017), [arXiv:1707.03385 \[astro-ph.CO\]](#) .
- [744] A. Boyarsky, J. Frohlich, and O. Ruchayskiy, “Magnetohydrodynamics of Chiral Relativistic Fluids,” *Phys. Rev.* **D92**, 043004 (2015), [arXiv:1504.04854 \[hep-ph\]](#) .
- [745] E. V. Gorbar, I. Rudenok, I. A. Shovkovy, and S. Vilchinskii, “Anomaly-driven inverse cascade and inhomogeneities in a magnetized chiral plasma in the early Universe,” *Phys. Rev.* **D94**, 103528 (2016), [arXiv:1610.01214 \[hep-ph\]](#) .
- [746] A. Boyarsky, V. Cheianov, O. Ruchayskiy, and O. Sobol, “Evolution of the Primordial Axial Charge across Cosmic Times,” *Phys. Rev. Lett.* **126**, 021801 (2021), [arXiv:2007.13691 \[hep-ph\]](#) .
- [747] A. Boyarsky, V. Cheianov, O. Ruchayskiy, and O. Sobol, “Equilibration of the chiral asymmetry due to finite electron mass in electron-positron plasma,” *Phys. Rev. D* **103**, 013003 (2021), [arXiv:2008.00360 \[hep-ph\]](#) .
- [748] N. Weickgenannt, X.-L. Sheng, E. Speranza, Q. Wang, and D. H. Rischke, “Kinetic theory for massive spin-1/2 particles from the Wigner-function formalism,” *Phys. Rev. D* **100**, 056018 (2019), [arXiv:1902.06513 \[hep-ph\]](#) .
- [749] J.-H. Gao and Z.-T. Liang, “Relativistic Quantum Kinetic Theory for Massive Fermions and Spin Effects,” *Phys. Rev. D* **100**, 056021 (2019), [arXiv:1902.06510 \[hep-ph\]](#) .
- [750] K. Hattori, Y. Hidaka, and D.-L. Yang, “Axial Kinetic Theory and Spin Transport for Fermions with Arbitrary Mass,” *Phys. Rev. D* **100**, 096011 (2019), [arXiv:1903.01653 \[hep-ph\]](#) .
- [751] Z. Wang, X. Guo, S. Shi, and P. Zhuang, “Mass Correction to Chiral Kinetic Equations,” *Phys. Rev.* **D100**, 014015 (2019), [arXiv:1903.03461 \[hep-ph\]](#) .
- [752] X.-L. Sheng, Q. Wang, and X.-G. Huang, “Kinetic theory with spin: From massive to massless fermions,” *Phys. Rev. D* **102**, 025019 (2020), [arXiv:2005.00204 \[hep-ph\]](#) .
- [753] S. Lin, “Quantum kinetic theory for quantum electrodynamics,” *Phys. Rev. D* **105**, 076017 (2022), [arXiv:2109.00184 \[hep-ph\]](#) .
- [754] Y. Hidaka, S. Pu, Q. Wang, and D.-L. Yang, “Foundations and applications of quantum kinetic theory,” *Prog. Part. Nucl. Phys.* **127**, 103989 (2022), [arXiv:2201.07644 \[hep-ph\]](#) .
- [755] S. Li and H.-U. Yee, “Quantum Kinetic Theory of Spin Polarization of Massive Quarks in Perturbative QCD: Leading Log,” *Phys. Rev. D* **100**, 056022 (2019), [arXiv:1905.10463 \[hep-ph\]](#) .
- [756] D.-L. Yang, K. Hattori, and Y. Hidaka, “Effective quantum kinetic theory for spin transport of fermions with collisional effects,” *JHEP* **07**, 070 (2020), [arXiv:2002.02612 \[hep-ph\]](#) .
- [757] N. Tanji, N. Mueller, and J. Berges, “Transient anomalous charge production in strong-field QCD,” *Phys. Rev.* **D93**, 074507 (2016), [arXiv:1603.03331 \[hep-ph\]](#) .

- [758] N. Mueller, S. Schlichting, and S. Sharma, “Chiral magnetic effect and anomalous transport from real-time lattice simulations,” *Phys. Rev. Lett.* **117**, 142301 (2016), [arXiv:1606.00342 \[hep-ph\]](#) .
- [759] M. Mace, N. Mueller, S. Schlichting, and S. Sharma, “Non-equilibrium study of the Chiral Magnetic Effect from real-time simulations with dynamical fermions,” *Phys. Rev.* **D95**, 036023 (2017), [arXiv:1612.02477 \[hep-lat\]](#) .
- [760] N. Tanji, “Nonequilibrium axial charge production in expanding glasma flux tubes,” *Phys. Rev.* **D98**, 014025 (2018), [arXiv:1805.00775 \[hep-ph\]](#) .
- [761] M. Mace, N. Mueller, S. Schlichting, and S. Sharma, “Chiral instabilities & the onset of chiral turbulence in QED plasmas,” *Phys. Rev. Lett.* **124**, 191604 (2020), [arXiv:1910.01654 \[hep-ph\]](#) .
- [762] S. Schlichting and S. Sharma, “Chiral instabilities & the fate of chirality imbalance in non-Abelian plasmas,” (2022), [arXiv:2211.11365 \[hep-ph\]](#) .
- [763] S. N. Nikolaev and A. V. Radyushkin, “Vacuum Corrections to QCD Charmonium Sum Rules: Basic Formalism and $O(G^3)$ Results,” *Nucl. Phys.* **B213**, 285 (1983).
- [764] C. S. Machado, S. I. Finazzo, R. D. Matheus, and J. Noronha, “Modification of the B Meson Mass in a Magnetic Field from QCD Sum Rules,” *Phys. Rev.* **D89**, 074027 (2014), [arXiv:1307.1797 \[hep-ph\]](#) .
- [765] J.-P. Blaizot and E. Iancu, “The Quark gluon plasma: Collective dynamics and hard thermal loops,” *Phys. Rept.* **359**, 355 (2002), [arXiv:hep-ph/0101103 \[hep-ph\]](#) .
- [766] A. Bandyopadhyay, C. A. Islam, and M. G. Mustafa, “Electromagnetic spectral properties and Debye screening of a strongly magnetized hot medium,” *Phys. Rev.* **D94**, 114034 (2016), [arXiv:1602.06769 \[hep-ph\]](#) .
- [767] S. Li, K. A. Mamo, and H.-U. Yee, “Jet quenching parameter of the quark-gluon plasma in a strong magnetic field: Perturbative QCD and AdS/CFT correspondence,” *Phys. Rev.* **D94**, 085016 (2016), [arXiv:1605.00188 \[hep-ph\]](#) .
- [768] J. F. Donoghue, E. Golowich, and B. R. Holstein, “Dynamics of the standard model,” *Camb. Monogr. Part. Phys. Nucl. Phys. Cosmol.* **2**, 1 (1992), [Camb. Monogr. Part. Phys. Nucl. Phys. Cosmol.35(2014)].
- [769] P. Zyla *et al.* (Particle Data Group), “Review of Particle Physics,” *PTEP* **2020**, 083C01 (2020).
- [770] A. V. Smilga, “Anomaly mechanism at finite temperature,” *Phys. Rev.* **D45**, 1378 (1992).
- [771] R. Baier and E. Pilon, “On the axial anomaly at finite temperature in the Schwinger model,” *Z. Phys.* **C52**, 339 (1991).
- [772] C. Adam, R. A. Bertlmann, and P. Hofer, “Dispersion relation approach to the anomaly in two-dimensions,” *Z. Phys. C* **56**, 123 (1992).
- [773] A. D. Dolgov and V. I. Zakharov, “On Conservation of the axial current in massless electrodynamics,” *Nucl. Phys. B* **27**, 525 (1971).
- [774] J. Horejsi, “Dispersive Derivation of the Triangle Anomaly,” *Phys. Rev. D* **32**, 1029 (1985).
- [775] L. Dolan and R. Jackiw, “Symmetry Behavior at Finite Temperature,” *Phys. Rev.* **D9**, 3320 (1974).

- [776] Y.-C. Kao and Y.-L. Lee, “Screening mass in the massive Schwinger model at infinite temperature,” *Phys. Rev.* **D58**, 067701 (1998).
- [777] K. Fukushima, “QCD matter in extreme environments,” *J. Phys.* **G39**, 013101 (2012), [arXiv:1108.2939 \[hep-ph\]](#) .
- [778] H. Itoyama and A. H. Mueller, “The Axial Anomaly at Finite Temperature,” *Nucl. Phys. B* **218**, 349 (1983).
- [779] F. Klingl, S.-s. Kim, S. H. Lee, P. Morath, and W. Weise, “J / psi and eta(c) in the nuclear medium: QCD sum rule approach,” *Phys. Rev. Lett.* **82**, 3396 (1999), [Erratum: *Phys. Rev. Lett.* 83,4224(1999)], [arXiv:nucl-th/9811070 \[nucl-th\]](#) .
- [780] K. Fukushima, D. E. Kharzeev, and H. J. Warringa, “Electric-current Susceptibility and the Chiral Magnetic Effect,” *Nucl. Phys.* **A836**, 311 (2010), [arXiv:0912.2961 \[hep-ph\]](#) .
- [781] K. Fukushima, “Views of the Chiral Magnetic Effect,” *Lect. Notes Phys.* **871**, 241 (2013), [arXiv:1209.5064 \[hep-ph\]](#) .